Günther Meschke · Rolf Breitenbücher ·
Steffen Freitag · Markus König ·
Markus Thewes *Editors*

Interaction Modeling in Mechanized Tunneling

Springer

Interaction Modeling in Mechanized Tunneling

Günther Meschke · Rolf Breitenbücher · Steffen Freitag · Markus König · Markus Thewes

Editors

Interaction Modeling in Mechanized Tunneling

1st edition 2023

Springer Open

Editors
Günther Meschke
Structural Mechanics
Ruhr-Universität Bochum
Bochum, Germany

Markus König
Computing in Engineering
Ruhr-Universität Bochum
Bochum, Germany

Rolf Breitenbücher
Building Materials
Ruhr-Universität Bochum
Bochum, Germany

Markus Thewes
Tunneling and Construction Management
Ruhr-Universität Bochum
Bochum, Germany

Steffen Freitag
Institute for Structural Analysis
Karlsruhe Institute of Technology
Karlsruhe, Germany

This book is dedicated to memory of the late Tom Schanz, a brilliant researcher, a compassionate PI and Member of the Executive Board of the SFB 837. With his critical mind and creative thinking, he significantly inspired scientific discussions and often provoked out-of-the-box thinking about new research ideas. Although Tom is not with us anymore, we firmly believe he would have enjoyed the successful outcome of the SFB 837 as much as we do now. His legacy lives on in the substantial work he put into the SFB 837, so all members of the SFB 837 therefore gratefully acknowledge the dedication Tom paid to "his" SFB.

Preface

"Modern tunnel construction techniques ... are only tolerant within ranges of variations of the ground. It is therefore apparent that understanding and operating the system become increasingly vital for successful tunnelling."
– Sir Alan Muir Wood, 1921–2009

Ins Bergwerk 'nein, wo die Bergleut sein,
die da graben das Silber und das Gold bei der Nacht
aus Felsgestein
– From the "Steigerlied" (traditional German mining song)

About twelve years ago the Collaborative Research Center (Sonderforschungsbereich) 837 began to pick up its work studying how to understand and improve the process of Machine Tunneling in all its aspects. Although the professors, post-docs, doctorates and students were well-prepared to take on this journey, it is never clear at the outset of a research project–and this was truly a large and involved undertaking–where the research will be headed. So, in the last years many experiments have been executed and monitored, many theories have been set up and validated, many models have been created and verified, many software systems have been programmed and debugged, all without a guarantee that success is around the corner.

Although the word "interaction" is part of the official title of the SFB 837 ("Interaction Modeling in Mechanized Tunneling"), we firmly believe the overall success of the SFB 837 is due to the fact that we took the word "interaction" seriously in our SFB. From the formal meetings of the executive council of the distinguished professors to the informal gatherings of students, post-docs and group leaders in the Academic Lunches, we lived and breathed *interaction* to the point working alone on a sub-project seemed utterly strange . . .

Thus, all the more we are pleased to report to the knowledgeable public that there has been some degree of success in the outcome of the SFB 837 and, in out humble opinion, this level is not of mere nature. To pass the large body of wisdom, insight and expertise gained during the completion of the SFB 837 to the public, we hereby present this work of reference to the engineering community in the hope that it will contribute to

the advancement of underground engineering as was done within the SFB 837, at least to some small, but significant, extent.

We hope the reader will enjoy perusing this literary work with as much pleasure as the co-authors had in preparing the book.

Bochum   Günther Meschke
August 2022

Acknowledgements

Contents

List of Contributors

About the Editors

Günther Meschke Structural Mechanics, Ruhr-Universität Bochum, Bochum, Germany

Rolf Breitenbücher Building Materials, Ruhr-Universität Bochum, Bochum, Germany

Steffen Freitag Institute for Structural Analysis, Karlsruhe Institute of Technology, Karlsruhe, Germany

Markus König Computing in Engineering, Ruhr-Universität Bochum, Bochum, Germany

Markus Thewes Tunneling and Construction Management, Ruhr-Universität Bochum, Bochum, Germany

List of Authors

Michael Alber Applied Geology, Ruhr-Universität Bochum, Bochum, Germany

Abdullah Alsahly Structural Mechanics, Ruhr-Universität Bochum, Bochum, Germany

Wiebke Baille Soil Mechanics, Foundation Engineering and Environmental Geotechnics, Ruhr-Universität Bochum, Bochum, Germany

Matthias Baitsch Bauinformatik und Numerische Verfahren, Bochum University of Applied Sciences, Bochum, Germany

Daniel Balzani Continuum Mechanics, Ruhr-Universität Bochum, Bochum, Germany

Thomas Barciaga Dr. Spang Ingenieurgesellschaft für Bauwesen, Geologie und Umwelttechnik GmbH, Witten, Germany

Lukas Brackmann Materials Technology, Ruhr-Universität Bochum, Bochum, Germany

Hoang-Giang Bui Mechanics of Materials, Ruhr-Universität Bochum, Bochum, Germany

Sahir Butt Structural Mechanics, Ruhr-Universität Bochum, Bochum, Germany

Ba Trung Cao Structural Mechanics, Ruhr-Universität Bochum, Bochum, Germany

Florian Christ Soil Mechanics, Foundation Engineering and Environmental Geotechnics, Ruhr-Universität Bochum, Bochum, Germany

Jan Düllmann Stahl & Stein, Meschede, Meschede, Germany

Sascha Freimann Vössing Ingenieurgesellschaft mbH, Düsseldorf, Germany

Wolfgang Friederich Geophysics, Ruhr-Universität Bochum, Bochum, Germany

Mario Galli Vössing Ingenieurgesellschaft mbH, Düsseldorf, Germany

Klaus Hackl Mechanics of Materials, Ruhr-Universität Bochum, Bochum, Germany

Lukas Heußner Concrete Structures, Ruhr-Universität Bochum, Bochum, Germany

Raoul Hölter Soil Mechanics, Foundation Engineering and Environmental Geotechnics, Ruhr-Universität Bochum, Bochum, Germany

Golnaz Hoormazdi Mechanics of Materials, Ruhr-Universität Bochum, Bochum, Germany

Tagir Iskhakov Structural Mechanics, Ruhr-Universität Bochum, Bochum, Germany

Annika Jodehl Tunneling and Construction Management, Ruhr-Universität Bochum, Bochum, Germany

Christina Krikelis Building Materials, Ruhr-Universität Bochum, Bochum, Germany

Sebastian Kube Tunneling and Construction Management, Ruhr-Universität Bochum, Bochum, Germany

Andre Lamert Geophysics, Ruhr-Universität Bochum, Bochum, Germany

Arash Alimardani Lavasan Soil Mechanics, Foundation Engineering and Environmental Geotechnics, Ruhr-Universität Bochum, Bochum, Germany

Abdiel Ramon Leon Bal Structural Mechanics, Ruhr-Universität Bochum, Bochum, Germany

Elham Mahmoudi Computing in Engineering, Ruhr-Universität Bochum, Bochum, Germany

Peter Mark Concrete Structures, Ruhr-Universität Bochum, Bochum, Germany

Peyman Mianji Soil Mechanics, Foundation Engineering and Environmental Geotechnics, Ruhr-Universität Bochum, Bochum, Germany

Shorash Miro Sicherheitsuntersuchungen, BGE Bundesgesellschaft für Endlagerung mbH, Peine, Germany

Thomas Möller Geophysics, Ruhr-Universität Bochum, Bochum, Germany

Inka Mueller Technical Mechanics, Bochum University of Applied Sciences, Bochum, Germany

Khayal Musayev Mechanics of Materials, Ruhr-Universität Bochum, Bochum, Germany

Tamara Nestorovic Mechanics of Adaptive Systems, Ruhr-Universität Bochum, Bochum, Germany

Gerrit Emanuel Neu Structural Mechanics, Ruhr-Universität Bochum, Bochum, Germany

Markus Obel Mark Ingenieure GmbH, Bochum, Germany

Diego Nicolás Petraroia Concrete Structures, Ruhr-Universität Bochum, Bochum, Germany

Sven Plückelmann Building Materials, Ruhr-Universität Bochum, Bochum, Germany

Sebastian Priebe Structural Mechanics, Ruhr-Universität Bochum, Bochum, Germany

Jörg Renner Experimental Geophysics, Ruhr-Universität Bochum, Bochum, Germany

Christopher Riedel Mechanics of Materials, Ruhr-Universität Bochum, Bochum, Germany

Arne Röttger New Production Technologies and Materials, Bergische Universität Wuppertal, Wuppertal, Germany

Poria Saberi High Performance Computing, Ruhr-Universität Bochum, Bochum, Germany

Yara Salloum Computing in Engineering, Ruhr-Universität Bochum, Bochum, Germany

Steffen Schindler Consult IKS, HOCHTIEF Engineering GmbH, Frankfurt am Main, Germany

Maximilian Schoen Soil Mechanics, Foundation Engineering and Environmental Geotechnics, Ruhr-Universität Bochum, Bochum, Germany

Britta Schößer Tunneling and Construction Management, Ruhr-Universität Bochum, Bochum, Germany

Marius Schröer Tunneling and Construction Management, Ruhr-Universität Bochum, Bochum, Germany

Marcel Stepien Computing in Engineering, Ruhr-Universität Bochum, Bochum, Germany

Jithender J. Timothy Centre for Building Materials, TU Munich, Munich, Germany

Maximilian Trapp Mechanics of Adaptive Systems, Ruhr-Universität Bochum, Bochum, Germany

Andreas Vogel High Performance Computing, Ruhr-Universität Bochum, Bochum, Germany

Andre Vonthron Computing in Engineering, VSK Software GmbH, Bochum, Germany

Rodolfo Javier Williams Moises Structural Mechanics, Ruhr-Universität Bochum, Bochum, Germany

Dennis Wingender Continuum Mechanics, Ruhr-Universität Bochum, Bochum, Germany

Hongwei Yang School of Civil Engineering, Sun Yat-sen University, Guangzhou, China

Yaman Zendaki Structural Mechanics, Ruhr-Universität Bochum, Bochum, Germany

Chenyang Zhao School of Civil Engineering, Sun Yat-sen University, Guangzhou, China

Zdenek Zizka METROPROJEKT PRAHA, Prague, Czech Republic

Introduction

1

Günther Meschke

Abstract

This book summarizes the main results from research performed within the Collaborative Research Center "Interaction Modeling in Mechanized Tunneling" installed at Ruhr University Bochum, Germany. Topics being covered include all relevant aspects of mechanized tunneling ranging from digital design to steering support during tunnel construction. One subject area is concerned with the characterization and modeling of ground conditions, advance exploration methods as well as face support measures. A second subject area covers novel segmental lining designs with enhanced robustness and the interaction between the grout and the surrounding soil. A third subject area is concerned with computational simulation of tunnel advancement, logistics and excavation processes including monitoring strategies and digital models for real-time support of TBM construction. Finally, risk analysis and tunnel information modeling are completing the large range of topics. The individual research topics are each supported by computational models, experimental research and in situ monitoring.

In order to meet the growing demand for an efficient and environmentally friendly transport infrastructure, the use of the subsurface is often without alternative. Major projects, such as the Alpine transversals (e.g. Brenner Base Tunnel), but also the construction or expansion of inner-city underground transport lines to reduce the above ground traffic illustrate the growing importance of tunnel construction, as can be vividly seen in Fig. 1.1.

Mechanized Tunneling has proven itself as an economical and flexible construction method that continues to undergo a dynamic evolution process; shield diameters are con-

G. Meschke (✉)
Structural Mechanics, Ruhr-Universität Bochum, Bochum, Germany
e-mail: guenther.meschke@rub.de

Fig. 1.1 Metro-systems improving the quality of life in urban areas: Example Vienna before [Source: https://de.wikipedia.org/wiki/Kärntner_Strasse] (left) and after (right) completion of the metro system in the city center [Source: https://commons.wikimedia.org/wiki/]

stantly increasing (an example can be seen in Fig. 1.2, right), and the range of scenarios in which tunnel boring machines are deployed is continuously expanding, from clays to granular soils to highly fractured or monolithic rock masses, from partially to fully saturated ground, and from alpine mountain ranges with high overburden pressures to sensitive urban areas with low overburden (Fig. 1.2, left). Today, the application range of tunnel boring machines is being extended to an ever increasing variety of geotechnical conditions.
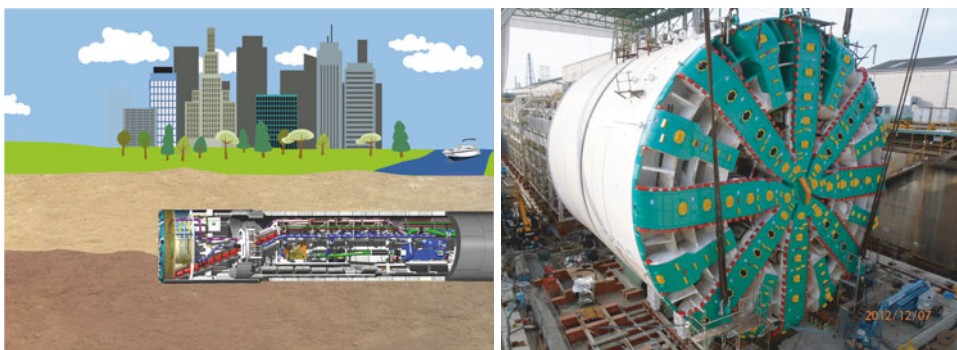
Fig. 1.2 Illustration of mechanized tunneling in urban areas (left), breakthrough of a 17.5 m Tunnel Boring Machine in Seattle [Source: Washington State Department of Transportation (WSDOT) – https://www.flickr.com/photos/wsdot/8260834957/] (right)

Mechanized tunneling is characterized by a number of advantages over competing tunneling methods. As a result of the shield casing, a high level of work safety is guaranteed; due to the prefabrication, a high quality of the segment elements can be ensured and the intended tunnel profile is maintained with great accuracy, without unintended additional excavation. In addition to very high investment costs, these advantages are offset above all by a lack of flexibility with regard to adjustments during tunneling to changing ground conditions, e.g. marl-limestone alternating bedding or difficult geological conditions, such as swelling clay rock.

The reliable, economical and environmentally compatible planning and construction of tunnels on the basis of mechanized driving requires reliable knowledge of the expected effects of tunnel driving on the existing infrastructure and environment, but also of the effects of the geological conditions or existing infrastructure on the tunnel driving process. The generally heterogeneous geological conditions and the often only vaguely detectable ground properties place special demands on prognosis models compared to other engineering tasks. However, such models are indispensable for limiting driving-related risks during the planning and driving stages, especially in the case of difficult geological and tunneling conditions and special boundary conditions, for example, when tunneling underneath existing buildings.

Research goals Heterogeneous geological conditions and often only approximated ground parameters create, in contrast to other engineering projects, special challenges. These circumstances and the constant expansion of the range of deployment of shield-supported tunneling as well as the tendency to always larger shield diameters demand the exploration of new problems that can only be effectively solved through truly interdisciplinary research. Open problems demanding fundamental research arise in almost all aspects of the mechanized tunneling process. Examples are the characterization of the ground properties ahead of the tunnel face, the efficiency of the face support pressure in Earth Pressure Balanced, slurry or variable density machines, the actual mechanism in which the support fluids infiltrate the ground, tool wear, the efficiency of the cutting process in heterogeneous ground conditions or the optimization of design and construction processes based on real-time interactive digital tools. Understanding the relevant aspects and components of the mechanized tunneling process and their interactions is a prerequisite for developing new concepts and improved technological solutions.

Due to the high degree of automation and the interlocking of a large number of sub-processes and components, malfunctions and the failure of individual components often cause delays in the process or even complete shutdowns. On average, tunnel boring machines achieve only 30%–50% of their theoretical performance capacity (Fig. 1.3, left). Deficiencies in design are among the most common causes of failures in underground construction (Fig. 1.3, right).

This and the constant expansion of the range of deployment of shield-supported tunneling to various ground conditions, the tendency to ever larger shield diameters and the strict
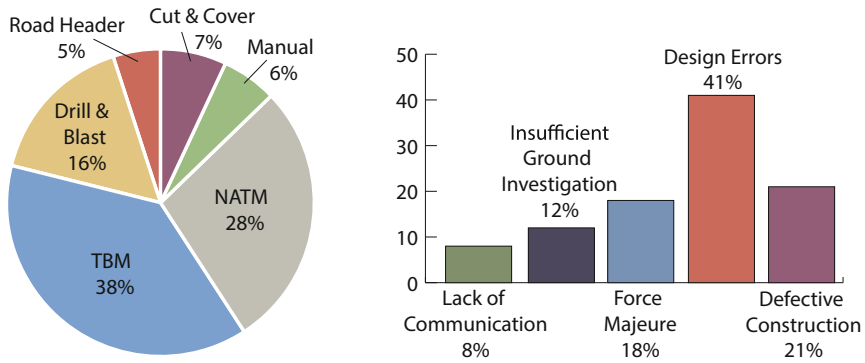
Fig. 1.3 Causes of damage in mechanized tunneling [redrawn according to N. Bilgin, H. Copur & C. Balci. TBM excavation in difficult ground conditions: Case studies from Turkey, Ernst & Sohn, 2016] (left); Frequency of damage events depending on the construction method [redrawn according to T.K. Konstantis. Tunnel projects: Risks exposure, risk management and insurance coverage – A realistic roadmap, Proceedings of the World Tunnel Congress 2017, 2017] (right)

requirements posed by society in regard to safety and impact on the environment during construction, sustainability of the design and durability of the constructed tunnel necessitate new insights into the manifold interactions between individual components, planning phases and partial processes involved in mechanized tunneling. Innovative solutions can only be effectively solved through truly interdisciplinary research.

The transformation to a green economy also induces a strong motivation in the underground construction sector to develop novel designs for segmented tunnel shells with less material consumption and thus a reduced CO_2 footprint of the tunnel linings without sacrificing safety or robustness. In the same spirit, innovation in the design of cutter heads and novel materials for excavation tools both lead to a better wear resistance, and thus to an improved efficiency of the tunnel advancement and less energy consumption. A key ingredient in reducing unexpected standstill in tunnel processes is the knowledge of the ground conditions ahead of the tunnel face, necessitating reliable methods of ground advance exploration.

In order to maintain low settlements, and to ensure an economically feasible as well as environmentally friendly construction process, realistic computational models are indispensable for providing reliable prognoses during the planning and construction stages of a tunnel project. These models become especially critical in difficult geotechnical environments as well as under special boundary conditions, such as driving under existing, possibly fragile constructions. A prerequisite for a reliable numerical prognosis is the assessment of the interactions between the components involved in mechanized tunneling, the surrounding site, the ground, and any pre-existing structures. To render use of complex 3D modeling feasible within a digital workflow requires a smooth integration of all interacting tools.

Digitalization   The use of digital tools places specific demands on the planning processes in tunnel construction, addressing the problems generated by decentralized data management and separate submodels by adequately linking heterogeneous data sources via tunnel information models. Although information model methods were first developed to be applied to improve the organization of above-ground building projects (Building Information Models, BIM), they have been, and currently are, being extended to tunneling projects.

Standardized exchange formats such as the Industry Foundation Classes (IFC) are being developed to ensure a universal data structure, coherent data exchange and interoperability among projects partners. The capability of the Tunnel Information Model (TIM) to connect information databases and graphical representations based on parametric 3D models allows a better visualization, coordination, and management of construction projects and helps to reduce planning errors and project costs. Recent developments in software platforms for tunnel information modeling have enabled a multi-level information representation of the built environment with an adequate Level of Detail (LoD) and collaborative design, and a parameterized analysis of alternative designs (Fig. 1.4).

In the future, tunnel information and simulation models will be used interactively, beyond the visualization of project data, also by real-time analyses of route variants and accompanying risk forecasts, especially in inner-city tunnel construction. This places demands not only on the efficiency of numerical simulation models and a seamless connection to digital tunnel information and logistics models, but also on the real-time capability of complex tunneling and process simulation models.
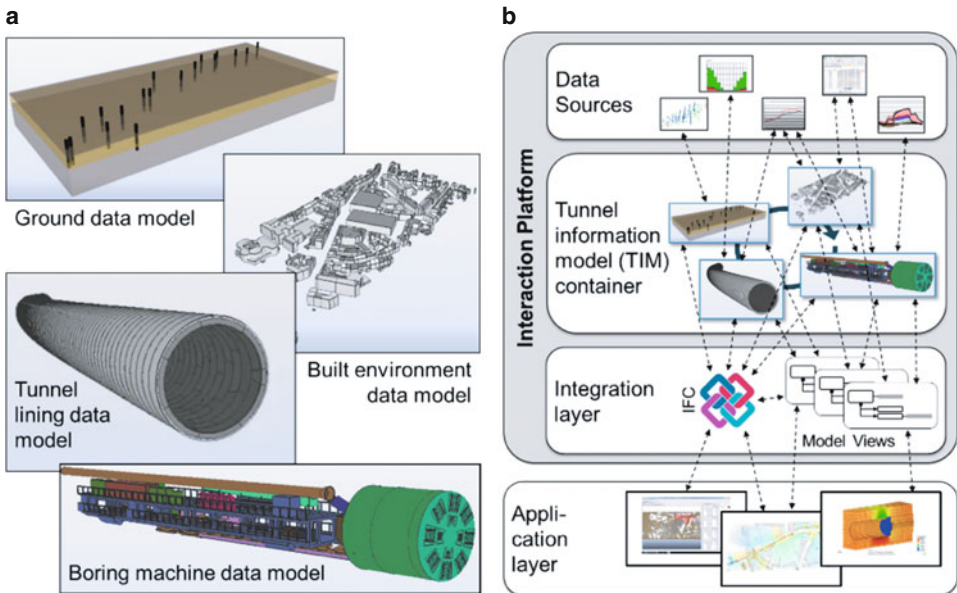
Fig. 1.4   Illustration of the tunnel information modeling framework: Main subdomain data models (**a**), the unified interaction platform and application layer (**b**)

The SFB 837   In this context, the German Research Foundation (Deutsche Forschungs-gemeinschaft, DFG) established the Collaborative Research Center "Interaction Modeling in Mechanized Tunneling" (Sonderforschungsbereich 837, SFB 837) at Ruhr University Bochum since 2010. Collaborative Research Centers are interdisciplinary scientific research groups in which cooperative research is conducted under the umbrella of a central research theme. Within the 20 subprojects of the SFB 837, a range of design concepts, numerical models and new excavation technologies concerning mechanized tunneling have been developed.

While research during the initial project phases focused mainly on tunneling in soft ground, more recent research concentrated additionally on tunneling in difficult geological conditions, which nowadays sets the limits on the application range of mechanized tunneling. Among other topics, research was concerned with the exploration of significant, as yet unexplored factors that control tunneling processes in expansive soils as well as with the design of novel deformation-tolerant tunnel linings to be used in such situations. From interdisciplinary research between material scientists and geophysicists, essential insights have been gained into the wear of excavation tools and the efficiency of excavation in such difficult geological conditions. Simulation and risk models for the excavation, advancement and logistics processes developed in the SFB 837 will enable improved, environmentally-friendly and low-risk planning and construction processes. These models have been extended to enable real-time prognoses and to provide a platform for the interactive digital design of urban tunneling projects. In doing so, the SFB 837 aims to create new perspectives for innovative participative planning instruments in tunneling. Furthermore, by developing continuously updated real-time models, the SFB 837 has taken an important step towards computer-aided steering of the mechanized tunneling process.

The research goals of the SFB 837 are concerned with relevant planning and construction aspects of the many components of the mechanized tunneling process. They are organized into four project areas (Fig. 1.5). Project area A is concerned with the characterization and modeling of the in-situ ground and the disturbed ground conditions in the vicinity of the cutting wheel as well as with advance exploration methods. The topic of research in project area B is the modeling of novel segmental lining designs with enhanced robustness and the interaction between the grout and the surrounding soil. Project area C is concerned with the simulation of the advancement process and real-time prognosis methods to support the TBM steering, as well as with optimal monitoring strategies, the simulation of logistics processes and the modeling of the cutting process and the material transport into the excavation chamber. The last project area D is concerned with research on risk analysis in urban tunneling and model integration. These research themes are each supported by computational models and are all included in an SFB encompassing tunnel information model that was developed in the first period of the SFB.

Furthermore, interaction groups were formed in order to integrate and combine the results of different submodels and analyses. These originated partially through prototypical cause-and-effect relationships, and partially from applications to actual reference tunneling projects.
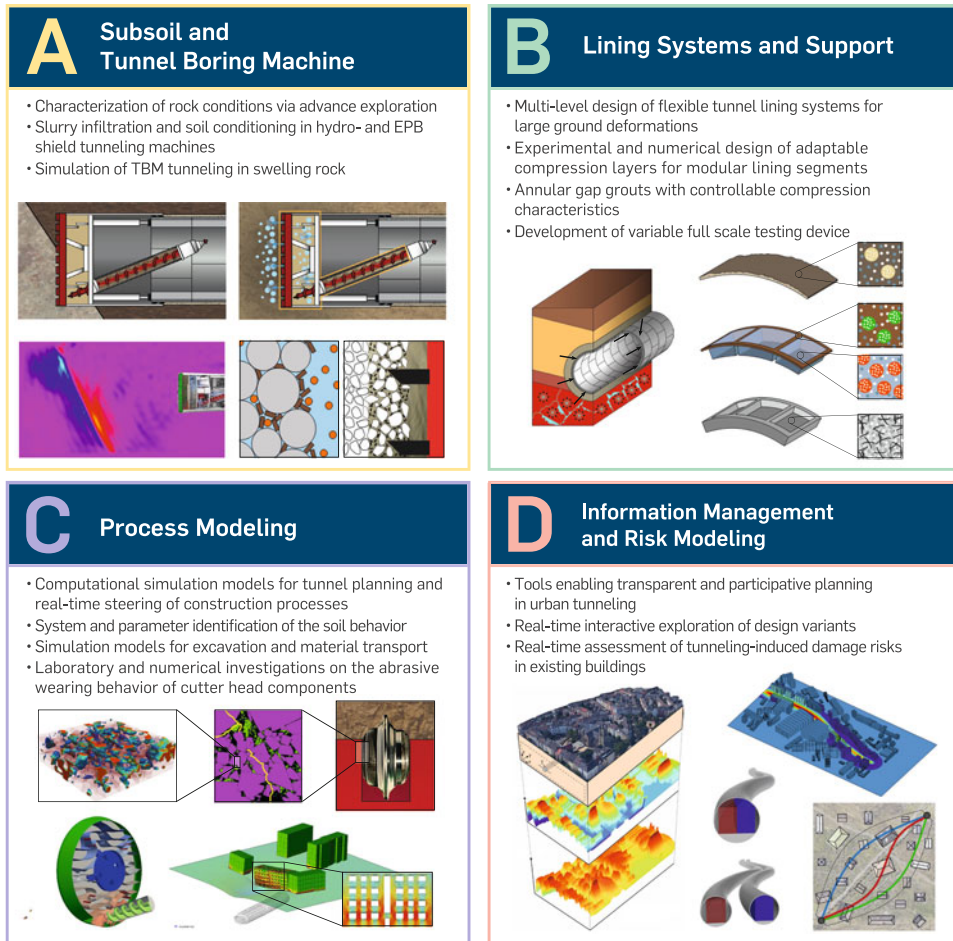
Fig. 1.5 Components and processes involved in mechanized tunneling and their representation within four project areas (A–D) in the SFB 837

Structure of the book This book summarizes the main results from the SFB 837 related to the four project areas included in Fig. 1.5:

A: Characterization of the subsoil and the face support mechanisms;
B: Lining systems and support;
C: Modeling and computational simulation of the tunnel construction processes including the excavation and logistics and
D: Tunnel information modeling and risk assessment in urban tunneling.

Evidently, research within these project areas is highly interlinked. This leads to the structure of this book, which organizes the developed concepts, methods, models for

mechanized tunneling in soft ground and rock conditions as well as the findings from experimental research into 6 chapters.

Chapter 2 is concerned with the characterization of the ground ahead of the tunnel face based on geophysical exploration methods in association with computational methods for the identification of joints and obstacles in the ground.

In Chap. 3, computational models for the analysis of excavation processes at the tunnel face in soft, hard and mixed ground conditions along with the experimental and model-based analysis of wear processes in the cutting tools are presented.

Chapter 4 focuses on the analysis of infiltration processes involved in the support of the tunnel face and the material transport in Earth Pressure Balance and Hydro Shield Machines.

Chapter 5 is concerned with the design of robust- and damage-tolerant segmented linings and the experimental and model-based characterization of the infiltration and the stiffening behavior of various one- and two-component grouting materials.

Methods and models for digital design in mechanized tunneling are described in Chap. 6. Here, the Tunnel Information Model is introduced to facilitate the management of heterogeneous and distributed data and the interoperability of various submodels involved in the design process. Furthermore, computational methods for the modeling of tunnel-ground interaction within a digital workflow, and risk models for existing infrastructure are described. Combining these submodels, a method for the interactive assessment of tunnel alignment variants in urban areas is introduced.

Finally, Chap. 7 presents computational models for the support of the construction process in real-time. This concerns a real-time prediction scheme for the logistics processes and a software for the steering of tunnel boring machines considering different steering targets, such as minimizing the damage risk in existing buildings. Uncertainties, of both epistemic and aleatoric nature arising in mechanized tunneling are considered in the prediction models.

Advance Reconnaissance and Optimal Monitoring

2

Elham Mahmoudi [ID], Jan Düllmann, Lukas Heußner [ID], Raoul Hölter [ID], Andre Lamert, Shorash Miro, Thomas Möller, Khayal Musayev, Christopher Riedel [ID], Steffen Schindler, Maximilian Trapp [ID], Michael Alber, Matthias Baitsch, Wolfgang Friederich, Klaus Hackl [ID], Markus König [ID], Peter Mark [ID], and Tamara Nestorovic [ID]

E. Mahmoudi (✉) · M. König
Computing in Engineering, Ruhr-Universität Bochum, Bochum, Germany
e-mail: elham.mahmoudi@rub.de

M. König
e-mail: koenig@inf.bi.rub.de

J. Düllmann
Stahl & Stein, Meschede, Meschede, Germany
e-mail: stahlundstein@gmx.de

L. Heußner · P. Mark
Concrete Structures, Ruhr-Universität Bochum, Bochum, Germany
e-mail: lukas.heussner@rub.de

P. Mark
e-mail: peter.mark@rub.de

R. Hölter
Soil Mechanics, Foundation Engineering and Environmental Geotechnics, Ruhr-Universität Bochum, Bochum, Germany
e-mail: raoul.hoelter@rub.de

A. Lamert · T. Möller · W. Friederich
Geophysics, Ruhr-Universität Bochum, Bochum, Germany
e-mail: andre.lamert@rub.de

T. Möller
e-mail: thomas.moeller@rub.de

W. Friederich
e-mail: wolfgang.friederich@rub.de

S. Miro
Sicherheitsuntersuchungen, BGE Bundesgesellschaft für Endlagerung mbH, Peine, Germany
e-mail: Shorash.Miro@bge.de

Abstract

Effective exploration techniques during mechanized tunneling are of high importance in order to prevent severe surface settlements as well as a damage of the tunnel boring machine, which in turn would lead to additional costs and a standstill in the construction process. A seismic methodology called full waveform inversion can bring a considerable improvement compared to state-of-the-art seismic methods in terms of precision. Another method of exploration during mechanized tunneling is to continuously monitor subsurface behavior and then use this data to identify disturbances through pattern recognition and machine learning techniques. Various probabilistic methods for conducting system identification and proposing an appropriate monitoring plan are developed in this regard. Furthermore, ground conditions can be determined by studying boring machine data collected during the excavation. The active and passive obtained data during performance of a shield driven machine were used to estimate soil parameters. The monitoring campaign can be extended to include above-ground structural surveillance as well as terrestrial and satellite data to track displacements of existing infrastructure caused by tunneling. The available radar data for the Wehrhahn-line project are displayed and were utilized to precisely monitor the process of anticipated uplift by injections and any subsequent ground building settlements.

K. Musayev · C. Riedel · K. Hackl
Mechanics of Materials, Ruhr-Universität Bochum, Bochum, Germany
e-mail: khmusayev@googlemail.com

C. Riedel
e-mail: christopher.riedel@rub.de

K. Hackl
e-mail: klaus.hackl@rub.de

S. Schindler
Consult IKS, HOCHTIEF Engineering GmbH, Frankfurt am Main, Germany
e-mail: steffen.schindler@hochtief.de

M. Trapp · T. Nestorovic
Mechanics of Adaptive Systems, Ruhr-Universität Bochum, Bochum, Germany
e-mail: maximilian.trapp@rub.de

T. Nestorovic
e-mail: tamara.nestorovic@rub.de

M. Alber
Applied Geology, Ruhr-Universität Bochum, Bochum, Germany
e-mail: michael.alber@rub.de

M. Baitsch
Bauinformatik und Numerische Verfahren, Bochum University of Applied Sciences, Bochum, Germany
e-mail: matthias.baitsch@hs-bochum.de

2.1 Introduction

In mechanized tunneling, which is a highly automated process, a tunnel boring machine (TBM) sequentially excavates the ground and installs the tunnel lining. The high level of automation causes restrictions for a dynamic adaptation of the construction process and makes it vulnerable for unconsidered events. Sudden geological changes may endanger the process of tunnel construction by causing unexpected surface settlements, damage to the TBM or wear of the cutting tools. Since there is only a limited access to the front shield of the TBM during the construction, its maintenance turns out to be cumbersome. Furthermore, damage of the TBM leads to construction delays which may cause accumulation of running costs (e.g. personnel costs). Early identification of geological changes enables the opportunity to initiate countermeasures by, for instance, adapting the excavation velocity, changing the cutting tools or adapting the face pressure. During the planning as well as the construction phase, exploratory drilling is typically performed to characterize properties of the ground. However, such drilling is not sufficient for estimation of the subsoil properties along the whole tunnel track since it is locally limited.

Approaches that are suitable for exploring the space directly in front of the tunnel face are provided by exploration seismics. However, state-of-the-art methods only process the onsets of directly reflected waves and therefore neglect information of later arriving waves. In order to improve today's exploration techniques, the application of a methodology called full waveform inversion (FWI) is proposed. Here, the whole information of the seismic records is taken into account. Different FWI approaches are proposed, investigated and validated with synthetic data and experimental laboratory data in Sect. 2.2.

Another possibility for exploration during mechanized tunneling is to analyze the gathered hydro-mechanical data during the excavation process. Measuring the changes of surface settlement or pore water pressure in various locations around the tunnel line is a common practice, and through analyzing these data the geotechnical pattern of the subsoil can be recognized. Therefore, a pattern recognition approach based on supervised machine learning is proposed and investigated in Sect. 2.3. To evaluate the surrounding geomaterial based on the measurements, one should carefully consider the associated aleatory and epistemic uncertainties in such problems. Uncertainties in geomaterials are mainly due to their geologic origin, which implies their heterogeneity as well as multiphase-nature at different aggregation states. Furthermore, the boundary conditions are frequently complicated as a result of multi-phase interactions in projects such as tunneling, making the conventional approaches of using soil sample and preliminary laboratory studies on limited number of samples to predict soil parameters less trustworthy. The impact of uncertainties on tunneling performance may be precisely assessed utilizing the model adaptation approach, which is primarily concerned with the use of previously acquired datasets in the subsequent prediction and TBM steering process. In this regard, various uncertainty quantification methods like sensitivity analysis, random field and back analysis were employed.

Afterwards, a scenario-based framework pattern recognition is used to explore the geological formation ahead of TBM based on the subsoil response to the excavation process. It takes into account several frequent geometrical variations of geological scenarios in tunnel construction, such as layer change, interlayers, or a large rock boulder. As a result, in the context of pattern identification, machine learning algorithms are used to identify critical changes in geological conditions, such as incoming new soil layers or enormous rock boulders.

Besides obtained data by sensors and gauges in the subsoil, TBMs constantly monitor several variables during excavation. Therefore, one may determine ground conditions by analyzing such machine data. Among all the monitored data, data on the movement of the cutting wheel and the shield in relation to subsoil conditions for a shield driven TBM, in particular, can be considered as formative data. Parameters as thrust force on cutting wheel, torque on cutting wheel and advance speed are referred to as excavation-specific data components, and they may be used as indicators for the Earth's resistance to excavation (ground conditions) and the condition of the cutting wheel (wheel design, tool wear, and clogging), accordingly. The relation between different parameters on various projects and their effectiveness are studied in the Sect. 2.5.

A comprehensive monitoring campaign, which is required to prevent any unexpected or serious damage to above-ground structures, may include the use of available radar data and terrestrial technologies for the above-ground observations in addition to subterranean monitoring. Terrestrial settlement monitoring includes measurements of the interplay of all (settlement) data prior to, during, and after tunnel construction. The data delivered by these technologies may be detailed to the millimeter level for monitoring the settlement or tilting of buildings in the impacted geographical extent of tunnel excavation. Using the radar data, on-site installations, such as those found in buildings, are no longer necessary. The technology captures complicated raw data signals (amplitude and phase information) provided by radar waves (electromagnetic waves) reflect on the upper mantle. These data can be utilized in visualization process besides the actual settlement monitoring. Visualized in space and time, critical conditions such as torsional deformations when underpassing structures in parallel can be recognized easier. Details about the above-ground monitoring methods and data is presented in Sect. 2.6. The following section offers a case study of monitoring displacements of existing infrastructure caused by the excavation of the Wehrhahn railway tunnel in Dusseldorf using a series of 16 TERRASAR-X photos.

2.2   Seismic Reconnaissance

Triggered by man-made explosions or natural earthquakes, energy is induced into the ground and travels through it in the form of seismic body waves. These waves have different propagation modes, e.g. compressional waves that vibrate in propagation direction and shear waves that vibrate perpendicular to the propagation direction. The propagation ve-

locity of the different waves depends on the elastic properties of the ground. These are, in the context of seismological applications, usually described in terms of the compressional wave velocity v_p (or P-wave velocity) and the slower shear wave velocity v_s (or S-wave velocity),

$$v_p = \sqrt{\frac{E(1-\nu)}{\rho(1+\nu)(1-2\nu)}}, \qquad v_s = \sqrt{\frac{E}{2\rho(1+\nu)}}, \qquad (2.1)$$

rather than in terms of Young's modulus E and Poisson's ratio ν. The density of the ground is denoted by ρ. Waves that encounter a stress free surface, e.g. the Earth's surface, are to some part reflected. Another portion of these waves induces surface waves with very high amplitudes that propagate along the surface with a velocity slightly lower than the shear wave velocity. At geological interfaces, reflections, refractions and conversions of the seismic waves occur, whereby the amount of reflected, refracted and converted energy as well as the refraction angle depends on the material contrast.

The physical behavior of the ground can be described by the elastic wave equation

$$\rho(\mathbf{x})\,\ddot{\mathbf{u}}(\mathbf{x},t) - \nabla \cdot (\mathsf{C}(\mathbf{x}) : \nabla\mathbf{u}(\mathbf{x},t)) = \mathbf{f}(\mathbf{x},t), \qquad (2.2)$$

where $\mathsf{C}(\mathbf{x})$ is the fourth-order material stiffness tensor which contains the elastic properties of the ground at the spatial position $\mathbf{x}$. The external force vector at the time t is denoted by $\mathbf{f}(\mathbf{x},t)$ whereas the displacement vector is denoted by $\mathbf{u}(\mathbf{x},t)$ and its second derivative with respect to time by $\ddot{\mathbf{u}}(\mathbf{x},t)$.

For exploration in tunneling, a non-destructive artificial signal is induced into the ground. A wave propagation scenario within a two-dimensional tunnel environment with a disturbance in front of the tunnel is illustrated by Fig. 2.1 for two different points in time.
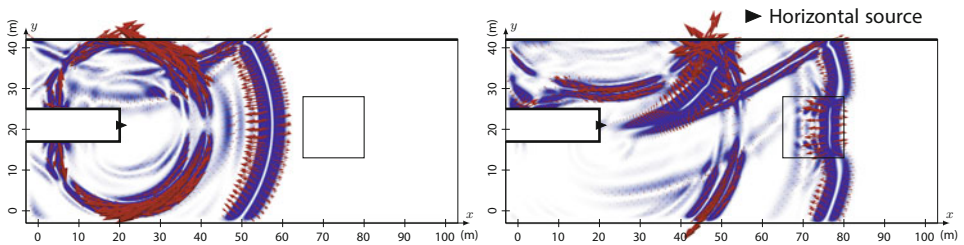
Fig. 2.1 A horizontal single-force source (triangle) at the tunnel face emits a Ricker wavelet with a peak frequency of 500 Hz. The vibration direction and amplitude of the waves are indicated by the red arrows. A rectangular shaped disturbance (indicated by its borders) with lower P- and S-wave velocities is located in front of the tunnel. The reflection of the first P-wave at the Earth's surface can be observed in the left picture. The right picture illustrates the induced surface waves at the Earth's surface as well as the interaction of the waves with the disturbance

The emitted seismic waves interact with anomalies and arrive at the geophones, which record the signal. The gained seismic records contain information about the geological conditions of the ground. Seismic exploration approaches utilize this information for the purpose of inferring the structure of the ground.

2.2.1 State-of-the-art Methods for Seismic Exploration in Mechanized Tunneling

State-of-the-art methods for seismic reconnaissance during mechanized tunneling are based on tomography methods. Certain parts of the seismic waveforms are evaluated, where most commonly reflected P-waves are extracted and processed for the purpose of estimating anomaly locations and properties. Two exemplary systems which are used in practice are Sonic Softground Probing (SSP) [49] and Tunnel Seismic Prediction (TSP) [92]. SSP is used for reconnaissance in soft rock. Sources and receivers are placed at the cutting wheel of the TBM and in the case that reflected waves arrive at the receivers, they are extracted from the waveform and evaluated with migration techniques. The range of SSP is specified to lie at about 40 m [101]. In TSP, sources and receivers are placed in boreholes along the tunnel wall. Also here, reflected waves are analyzed and evaluated using various geotechnical approaches. TSP's range is given with about 150-200 m; however, the error margin increases rapidly with increasing distance to the TBM shield [20]. A methodology which is generally able to provide a detailed image of the subsoil is the concept of full waveform inversion (FWI). The method can be expected to outperform the state-of-the-art systems in terms of ranges, error margins and levels of detail since not only parts of the acquired waveforms are evaluated, but the full measured signal.

2.2.2 Full Waveform Inversion

One of the first FWI approaches is introduced by Tarantola [110, 111] for acoustic as well as elastic media. For FWI, a numerical model is set up which is able to approximate forward wave propagation described by the elastic wave equation (Eq. 2.2). The ground properties (e.g. expressed by the P-wave velocity v_p, the S-wave velocity v_s and the density ρ) are discretized for the numerical application and the corresponding parameters which specify the ground model can be stored in a model **m**.

The goal of FWI is to minimize the difference of the synthetic seismic records and the seismic records from field observations by adapting the ground properties **m** of the numerical model iteratively. The ground model which produces the lowest difference of the seismic data is assumed to be a good representation of the real ground. Since different ground formations are able to produce similar seismic records, FWI has to deal with the ambiguity of the inverse problem. For that purpose, all prior information (e.g. from exploration drilling, other exploration approaches or former construction projects)

can be used to define an initial model which is close to the real subsurface in order to move the inversion to reconstruct a physically meaningful ground model. Or, in different approaches, prior knowledge may be used to implement a parametrization of the ground model directly. Different objective functions can be used to quantify the difference of the seismic records which have, depending on the FWI application, different advantages and disadvantages [13]. The least squares norm is commonly used as misfit function,

$$\chi(\mathbf{m}) = \frac{1}{2} \sum_{s=1}^{N_\mathrm{s}} \sum_{r=1}^{N_\mathrm{r}} \int_T \left(u_r^s(t; \mathbf{m}) - \bar{u}_r^s(t) \right)^2 \mathrm{d}t. \tag{2.3}$$

The considered time interval is denoted by T, the approximated displacements of the current ground model $\mathbf{m}$ by $u_r^s(t; \mathbf{m})$ and the displacements from the field observations by $\bar{u}_r^s(t)$. The squared difference is summed over the number of all receivers N_r and the number of all sequentially used sources N_s.

In the last decades, many different approaches of FWI have been developed, e.g. adjoint time and frequency domain approaches, statistical FWI approaches or machine learning approaches. There exist many different successful applications of FWI, even on the continental scale (e.g. [128]). However, FWI has not been applied yet for reconnaissance in mechanized tunneling projects.

A high number of forward simulations is needed for FWI due to its iterative procedure. Therefore, a real time application with three-dimensional tunnel models is not feasible with nowadays computational resources. Since the efficiency of computational techniques and resources have increased enormously in the last decades, it can be expected that an application of FWI will become practicable in the future. Therefore, an early investigation of the potential of FWI for reconnaissance in mechanized tunneling is necessary. Due to the variety of FWI approaches, an investigation on their characteristics for different ground conditions and scenarios is recommendable.

In Sect. 2.2.3, two Bayesian FWI approaches for application in mechanized tunneling are presented. The application of adjoint inversion approaches is examined for a time domain approach in Sect. 2.2.4 and for a frequency domain approach in Sect. 2.2.6, where synthetic reference data is used for inversion. However, also a validation of the proposed inversion schemes with measured data is crucial. Since seismic measurements during today's tunneling projects are not performed for FWI but for other exploration approaches and since rich field data, suitable for FWI, is difficult to get, a small-scale experiment is constructed in order to acquire seismic data with which some of the proposed inversion approaches are validated (Sect. 2.2.7). The validation with this experimental laboratory is valuable since severe measurement and later modeling errors are included in the inversion. Furthermore, small heterogeneities inside the specimen may be expected to have a large scattering effect on the small-scale, but a vanishing effect in later tunneling scenarios, which makes the inversion even more challenging on the small-scale concerning that point. Therefore, the validation of the methods by the acquired experimental data is evaluated to be reliable.

2.2.3 Bayesian Full Waveform Inversion

Instead of allowing the material properties to vary all over the model domain like in the upcoming adjoint methods, the dimensionality of the inverse problem can be aimed to be reduced. Dimensionality reduction can be achieved by either implementing a generally suitable but simplified parametrization of the subsoil model or even a direct parametrization (e.g. of a boulder or a layer change) which is based on prior knowledge. The search for a set of parameters with a misfit value close to the global minimum can then be performed with Bayesian inference. In this approach, a prior guess with initial uncertainties is specified. Parameter configurations are sampled and the prior guess and uncertainties are multiply updated. The output is a statistical description of the model parameters, revealing the sampled parameter configuration which is most likely representing the true subsurface. Furthermore, uncertainty quantification can be performed in order to find out at which positions anomalies could potentially be missed. If the parametrization can approximately describe the real subsurface, the proposed Bayesian FWI approaches can deliver precise results, which will be shown in the further progress of the chapter.

Two methods are proposed, where both approaches include the unscented Kalman filter (UKF) that is based on Bayesian inference. The first method is called unscented hybrid simulated annealing (UHSA) [80] and the second method is called the UKF-controlled parametric level-set method (UKF-PaLS) [79]. In this section, the working principles of UHSA and UKF-PaLS are briefly explained in words and UKF-PaLS is validated with synthetic data. For a complete description of the two methods, readers are referred to [114].

2.2.3.1 Unscented Hybrid Simulated Annealing (UHSA)

UHSA is a global optimization algorithm which combines the UKF [39] with simulated annealing (SA) [47]. The method is based on implementing prior knowledge in the form of a user-defined parametrization of the disturbance. Commonly, a coarse representation of the subsoil is already available after planning of the tunneling track, e.g. from exploratory drillings, prior seismic surveys, geological maps, or other exploration techniques. Then, for instance, if prior knowledge exists that there is a cuboid boulder somewhere in the model domain, one could define the parametrization with its center location coordinates, three edge lengths and the material properties. With respect to the parametrization, UHSA conducts a global search in order to investigate the whole parameter space. In the course of this, SA acts as the global search algorithm, proposing certain parameter configurations and UKF acts as the local search algorithm, performing a local minimization for some of those parameter configurations, where parameter configurations with comparatively small misfit functionals are more frequently chosen as a starting point for local minimization. Due to the strong dimensionality reduction, results of UHSA can be close to exact if the chosen parametrization of the disturbance is sufficient; even when experimental scenarios are considered [115, 116] or when the parametrization is not fully correct [88]. UHSA results will be demonstrated on experimental examples directly in Sect. 2.2.7.1 and Sect. 2.2.7.2.

2.2.3.2   UKF-Controlled Parametric Level-Set Method (UKF-PaLS)

The previously described method can only be applied if prior knowledge is available, which is different for UKF-PaLS. In this method, the parametric level-set method (PaLS) enables a parametrization of the disturbance domain. Radial basis functions, also called bumps, are used to define the geometry of irregularly shaped objects. Prior to inversion, the centers of the bumps are defined by the user. Placing the bumps, a region of investigation as well as a resolution is defined, where at this stage, also prior knowledge can be included. Each radial basis function is controlled by two parameters, where one parameter basically defines the radial size of the bump, and the other parameter distorts the shapes of the bumps. The UKF seeks to find the optimal configuration of level-set parameters and material properties. In order to facilitate the finding of a parameter configuration corresponding to a misfit functional which is close to the global optimum, a multi-scale approach is implemented (see e.g. [26]). This approach includes a low-pass filter with a stepwise increasing cutoff frequency into the inversion. In early iterations, the simulation and measurement data is filtered with a low cutoff frequency in order to resolve larger structures, while in later iterations, higher cutoff frequencies are used in order to resolve more details.

For UKF-PaLS, a 2D synthetic inversion scenario is presented. For more 2D as well as 3D examples, readers are referred to [114]. The computational model used for generating the synthetic measurements is shown in Fig. 2.2, left. Simulations are conducted with the spectral-element code SPECFEM2D [118]. Two rectangular disturbance domain objects are located close to each other with higher wave velocities than the wave velocities of the background domain, where the material is considered elastic with no attenuation for both sets of material properties. The density is considered constant all over the model domain. The top surface and all tunnel walls obtain free boundary conditions, while the other model boundaries obtain absorbing boundary conditions. The initial UKF model is shown in Fig. 2.2, right. 28 bumps are aligned on a regular grid, so that $2 \times 28 = 56$ level-set parameters and two material properties are to be determined during inversion. The initial level-set parameters are chosen so that small areas of the disturbance material are visible. In order to perform uncertainty quantification, the double standard deviation
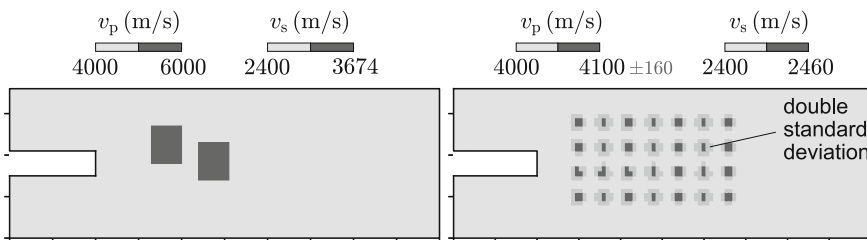
Fig. 2.2 True model (left) and initial UKF-PaLS model (right). Ticks are in distances of 10 m. In the left figure, the double standard deviations of the initial parameters are illustrated by the medium dark gray tone (see marking)
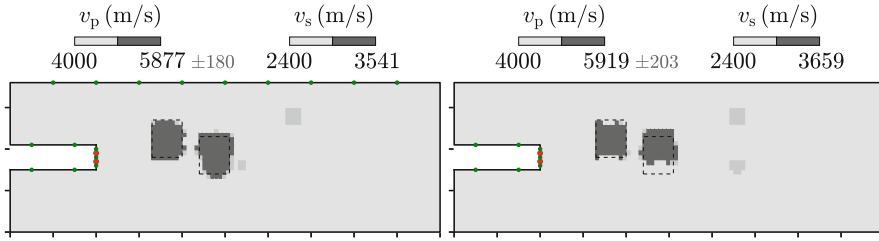
Fig. 2.3 Estimates corresponding to the minimum misfit. The medium dark gray regions illustrate the double standard deviations of the computed covariance matrix of the model parameters. Ticks are in distances of 10 m. Sources illustrated by red dots, receivers illustrated by green dots

of the initial covariance matrix of the model parameters is computed and illustrated by the medium dark gray tone (see marking). Note that for the initial model, this measure does not allow for any physical interpretation.

The inversion method is tested with two different source-receiver configurations, which are visualized together with the inversion results in Fig. 2.3 by the red (sources) and green (receivers) dots. Both configurations include 2 sources placed at the tunnel front and 7 receivers placed inside the tunnel at the front and walls. One configuration additionally includes 9 receivers located at the Earth's surface (compare Fig. 2.3, left). With both source-receiver configurations, a precise estimation of the reference model is achieved, where both objects are clearly resolved without melting together. All front and rear boundaries seen from the tunnel are well reconstructed. Due to the lack of receivers at the Earth's surface, top and bottom borders are slightly less precisely determined for the example shown in Fig. 2.3, right. However, differences remain small. The high precision emphasizes the gain of the dimensionality reduction since especially the resolving of rear boundaries based only on reflected waves is a difficult FWI challenge. The uncertainties which are again visualized by the medium dark gray areas show where objects are most probably missed by the inversion, where the greatest uncertainties lie in the "shadow" of the reconstructed objects.

2.2.4 Adjoint Time Domain Full Waveform Inversion

This section gives an overview of the implementation of the adjoint time domain inversion method into the nodal discontinuous Galerkin solver NEXD [54]. The solution of the forward problem is introduced briefly, the adjoint time domain inversion method is introduced and examples for a successful inversion in 2D and 3D are given.

2.2.4.1 Forward Problem
The solution of the forward problem is an essential part of the inversion process as it has to be performed multiple times during each iteration step. In this approach the discontin-

uous Galerkin (DG) solver NEXD developed by [53] is used to perform these calculations. NEXD is based on a velocity-stress formulation of the wave equation derived by [42] and [43]. The computational model of the target region is divided into triangular or tetrahedral elements and the solution vector containing stress and particle velocity components is expanded into appropriate basis functions defined on the elements. By multiplying with a set of test functions defined on the elements and integrating over each element, the elastic wave equation is replaced by a large coupled system of ordinary differential equations. Interaction and coupling between elements is realized by numerical fluxes. Depending on the choice of basis functions, DG methods are either of modal or nodal type. Modal approaches use sets of orthogonal basis functions whereas nodal ones take multidimensional Lagrange interpolating polynomials anchored to carefully selected nodal points [31]. In the latter case, the expansion coefficients are identical to the values of the velocity-stress vector at the nodal points. As NEXD is based on the nodal version of the DG method, a quick overview of the semi-discrete scheme is given: Let now $l_i(\mathbf{x})$ denote the Lagrange polynomials attached to the nodes $\mathbf{x}_i$ [31]. Moreover, let $\mathbf{q}(\mathbf{x}_j, t)$ denote the solution vector in element k, representing the values of the stress and particle components at node $\mathbf{x}_j$.[1] Then, using the Einstein summation convention, the system of ordinary differential equations for the expansion coefficients can be written as

$$\mathbf{M}_{ij}^k \frac{\partial}{\partial t} \mathbf{q}(\mathbf{x}_j, t) = -\mathbf{A}\mathbf{S}_{ij,x}^k \mathbf{q}(\mathbf{x}_j, t) - \mathbf{B}\mathbf{S}_{ij,y}^k \mathbf{q}(\mathbf{x}_j, t) - \mathbf{C}\mathbf{S}_{ij,z}^k \mathbf{q}(\mathbf{x}_j, t)$$
$$+ \mathbf{M}_{ij}^k \mathbf{s}(\mathbf{x}_j, t) - \int_{\partial D^k} \mathbf{r}_\mathrm{n}(\mathbf{x}, t) \, l_i(\mathbf{x}) \, d\Sigma, \quad 1 \le i, j \le N_\mathrm{p}, \qquad (2.4)$$

where $\mathbf{A}$, $\mathbf{B}$ and $\mathbf{C}$ are matrices containing the material properties of each element, $\mathbf{M}^k$ is the mass matrix, $\mathbf{S}_x^k$, $\mathbf{S}_y^k$ and $\mathbf{S}_z^k$ are the stiffness matrices, $\mathbf{r}_\mathrm{n}(\mathbf{x}, t)$ are normal Riemann fluxes and $\mathbf{s}(\mathbf{x}_j, t)$ is the source term. The number of interpolation points per element is denoted by N_p and ∂D^k denotes a line element of an element edge. Equation 2.4 is a system of coupled ordinary differential equations, as the flux terms depend on the expansion coefficients of adjacent elements. A more comprehensive derivation of Eq. 2.4 is given in [53, 54].

2.2.4.2 Adjoint Inversion
The primary ingredient for the inversion process is the measured data, since this data contains the information on the model that is to be calculated during the inversion process. This data is either generated synthetically using a forward solver, e.g. SPECFEM or NEXD, or data from seismic stations deployed in the field is used. The goal of the inversion process is to recover the model $\bar{\mathbf{m}}$, that best explains the observed data.

---

[1] The solution vector is denoted by the $\mathbf{q}$ in the context of this book to avoid the double definition with displacement. If the interested reader takes a look at the literature detailing the mathematics behind the NDG method the same solution vector will be denoted by $\mathbf{u}$.

The search for the best model $\bar{\mathbf{m}}$ starts with a model $\mathbf{m}_0$ for which synthetic waveforms $\mathbf{u}_r^s(t, \mathbf{m}_0)$ are to be calculated by a forward simulation. These synthetic waveforms are compared to the observed ones, $\bar{\mathbf{u}}$ and the misfit between the observed and measured seismograms is calculated according to Eq. 2.3. The model $\mathbf{m}_0$ is adjusted iteratively into models $\mathbf{m}_j$ with waveforms $\mathbf{u}_r^s(t, \mathbf{m}_j)$ at iteration j where $\mathbf{m}_j$ should approach $\bar{\mathbf{m}}$ with increasing j in the sense of minimizing the misfit between synthetic and observed waveforms as defined by [119].

To minimize the misfit χ an iterative approach is used which exploits information about the misfit gradient [118]. The latter is obtained by taking the Fréchet derivative of Eq. (2.3) with respect to $\mathbf{m}$,

$$\frac{\partial \chi}{\partial \mathbf{m}} = \sum_{s=1}^{N_s} \sum_{r=1}^{N_r} \int_T \left(\mathbf{u}_r^s(t, \mathbf{m}) - \bar{\mathbf{u}}_r^s(t) \right) \cdot \frac{\partial \mathbf{u}_r^s(t, \mathbf{m})}{\partial \mathbf{m}} \, dt \, . \tag{2.5}$$

Calculating the Fréchet derivatives of the wavefield with respect to $\mathbf{m}$, $\partial \mathbf{u}/\partial \mathbf{m}$, for all variations of $\mathbf{m}$ would require large amounts of storage. Instead, [26] shows that the misfit gradient can be more efficiently calculated with the help of an adjoint wave field $\mathbf{u}^\dagger(\mathbf{m}, \mathbf{x}_i, T - t)$, which in turn can be obtained as the time reversed result of a forward simulation with so-called adjoint sources situated at the receiver positions and defined by

$$\mathbf{f}^\dagger(\mathbf{m}, \mathbf{x}_i, t) = \mathbf{u}_r^s(T - t, \mathbf{m}) - \bar{\mathbf{u}}_i^s(T - t) \, . \tag{2.6}$$

Thus, the adjoint sources are the time reversed residuals between observed and predicted waveforms injected at the receiver positions and propagated into the medium.

For a perturbation of density and Lamé parameters in the subsurface, $\Delta m = (\Delta \rho, \Delta \lambda, \Delta \mu)$, the change of misfit is given by

$$\Delta \chi = \int_V \frac{\partial \chi}{\partial \rho} \Delta \rho + \frac{\partial \chi}{\partial \lambda} \Delta \lambda + \frac{\partial \chi}{\partial \mu} \Delta \mu \, dV$$
$$= -\int_V K_\rho \frac{\Delta \rho}{\rho} + K_\lambda \frac{\Delta \lambda}{\lambda} + K_\mu \frac{\Delta \mu}{\mu} \, dV \, , \tag{2.7}$$

where the misfit kernels are introduced according to [56] as

$$K_\rho(\mathbf{x}) := -\rho \frac{\partial \chi}{\partial \rho} = -\int_0^T \rho(\mathbf{x}) \mathbf{u}^\dagger(\mathbf{x}, T - t) \cdot \partial_t^2 \mathbf{u}(\mathbf{x}, t) \, dt,$$

$$K_\lambda(\mathbf{x}) := -\lambda \frac{\partial \chi}{\partial \lambda} = -\int_0^T \lambda(\mathbf{x}) (\mathrm{Tr}(\boldsymbol{\epsilon}^\dagger(\mathbf{x}, T - t)))(\mathrm{Tr}(\boldsymbol{\epsilon}(\mathbf{x}, t))) \, dt, \quad \text{and}$$

$$K_\mu(\mathbf{x}) := -\mu \frac{\partial \chi}{\partial \mu} = -\int_0^T 2\mu(\mathbf{x}) \boldsymbol{\epsilon}^\dagger(\mathbf{x}, T - t) : \boldsymbol{\epsilon}(\mathbf{x}, t) \, dt. \tag{2.8}$$

Here, ϵ denotes the strain tensor and $\text{Tr}(\epsilon)$ its trace. The colon stands for the Frobenius inner product. The kernels are defined with a negative sign, as the misfit is to be minimized and therefore the negative misfit gradient is used. The strain tensor ϵ is calculated from the stress components used as variables in the simulation by inverting the isotropic stress-strain relation.

Corresponding misfit kernels for the density, ρ, P-wave velocity, v_p, and S-wave velocity, v_s are given by

$$
\begin{aligned}
K'_\rho(\mathbf{x}) &= K_\rho(\mathbf{x}) + K_\lambda(\mathbf{x}) + K_\mu(\mathbf{x}), \\
K_{v_\text{p}}(\mathbf{x}) &= 2\rho(\mathbf{x})v_\text{p}(\mathbf{x})K_\lambda(\mathbf{x}), \\
K_{v_\text{s}}(\mathbf{x}) &= 2\rho(\mathbf{x})v_\text{s}(\mathbf{x})(K_\mu(\mathbf{x}) - 2K_\lambda(\mathbf{x})).
\end{aligned} \tag{2.9}
$$

So far, material properties and misfit kernels were defined as continuous functions of position in the subsurface. In order to make the inverse problem finite-dimensional, a discretization of these functions is required. The discretization by elements introduced in context with the forward simulation is used and the model $\mathbf{m}$ is now considered as a vector containing all values of the material properties in the elements. This implies constant values of the material parameters within the elements and it is possible to integrate the kernels over the elements. Hence, pre-integrated element-specific misfit kernels $\bar{K}_\rho^k$ are defined by Lamert [55] (explicitly given here for density)

$$
\bar{K}_\rho^k = -\frac{\rho_k}{V_k} \int_{D^k} \int_0^T \mathbf{u}^\dagger(\mathbf{x}, T - t) \cdot \partial_t^2 \mathbf{u}(\mathbf{x}, t)\, \mathrm{d}t\, \mathrm{d}V, \tag{2.10}
$$

where D_k denotes element k, V_k its volume and ρ_k the value of density within this element.

As mentioned before, in the NDG method field variables at position $\mathbf{x}$ are expanded into Lagrange polynomials anchored at the nodal points. Hence, $\mathbf{u}^\dagger$ and $\mathbf{u}$ are expressed in the form

$$
\mathbf{u}(\mathbf{x}, t) = \sum_{m=1}^{N_\text{p}} \mathbf{u}(\mathbf{x}_m, t)l_m(\mathbf{x}), \ \mathbf{x} \in D^k \tag{2.11}
$$

with the Lagrange polynomials $l_m(\mathbf{x})$ and N_p the number of nodal points. Inserting Eq. 2.11 into Eq. 2.10 and changing the order of volume and time integral results in

$$
\bar{K}_\rho^k = -\frac{\rho_k}{V_k} \int_0^T \sum_{m=1}^{N_\text{p}} \mathbf{u}^\dagger(\mathbf{x}_m, T - t) \sum_{n=1}^{N_\text{p}} \partial_t^2 \mathbf{u}(\mathbf{x}_n, t) \int_{D^k} l_m(\mathbf{x})l_n(\mathbf{x})\, \mathrm{d}V\, \mathrm{d}t. \tag{2.12}
$$

The volume integral on the right hand side is identical to the mass matrix used and computed in the NDG method,

$$M_{mn}^k = \int_{D_k} l_m^k(\mathbf{x}) l_n^k(\mathbf{x}) \, \mathrm{d}V \,. \tag{2.13}$$

Since the elements from the NDG method are used as discretization for the inversion, the mass matrix is already known and the pre-integrated kernels (Eq. 2.12) become

$$\bar{K}_\rho^k = -\frac{\rho_k}{V_k} \int_0^T \sum_{m=1}^{N_\mathrm{p}} \mathbf{u}^\dagger(\mathbf{x}_m, T-t) \sum_{n=1}^{N_\mathrm{p}} \partial_t^2 \mathbf{u}(\mathbf{x}_n, t) M_{mn}^k \, \mathrm{d}t$$

$$= -\frac{\rho_k}{V_k} \int_0^T \mathbf{u}^\dagger(\mathbf{x}_m, T-t) M_{mn}^k \partial_t^2 \mathbf{u}(\mathbf{x}_n, t) \, \mathrm{d}t \,. \tag{2.14}$$

The element kernels $\bar{K}_\lambda$ and $\bar{K}_\mu$ are calculated in a similar way,

$$\bar{K}_\lambda^k = -\frac{\lambda_k}{V_k} \int_0^T (\mathrm{Tr}(\boldsymbol{\epsilon}^\dagger(\mathbf{x}_m, T-t))) M_{mn}^k (\mathrm{Tr}(\boldsymbol{\epsilon}(\mathbf{x}_n, t))) \, \mathrm{d}t,$$

$$\bar{K}_\mu^k = -2\frac{\mu_k}{V_k} \int_0^T \boldsymbol{\epsilon}^\dagger(\mathbf{x}_m, T-t) : (M_{mn}^k \boldsymbol{\epsilon}(\mathbf{x}_n, t)) \, \mathrm{d}t. \tag{2.15}$$

For $\bar{K}_\mu^k$ the sum over n is applied to all components of $\boldsymbol{\epsilon}$ first and the inner product is to be calculated before applying the sum over m.

With this method, it is possible to calculate the misfit gradient without the use of an additional mesh. The values of $\mathbf{u}^\dagger$ and $\mathbf{u}$ at the nodal points $\mathbf{x}$ are directly given by the NDG method. Moreover, since the element size is typically about half a wave length due to computational stability, the resolution potential of FWI is conserved.

2.2.5   Inversion Procedure

Based on the gradients of the misfit function the L-BFGS (Low-memory Broyden-Fletcher-Goldfarb-Shanno) [81] method is applied to find a local minimum. The L-BFGS method uses models and misfit gradients of former inversion steps to approximate the Hessian $\mathbf{H}_j$ of inversion step j, thus boosting the convergence of search for a minimum to superlinear behavior. As proposed by [81] the approximation of the Hessian starts by defining $\mathbf{H}_j^0 = \gamma_j I$ where I is the identity matrix and γ_j is a scalar which can be calculated from the model values and the misfit gradient of the latest inversion step. Afterwards,

gradients and models from L former inversion steps are used to iteratively approximate $\mathbf{H}_j$ based on $\mathbf{H}_j^0$.

The elastic properties of all elements contained in model $\mathbf{m}_j$ are updated in direction of the corrected gradient multiplied by a step length factor α_j,

$$\mathbf{m}_{j+1} = \mathbf{m}_j - \alpha_j \mathbf{H}_j \mathbf{c}_j \,, \tag{2.16}$$

where $\mathbf{c}_j$ is a vector composed of all the element-specific misfit kernels calculated in inversion step j. If $\mathbf{H}_j^0$ is chosen diagonal, $\mathbf{H}_j$ is diagonal as well and no matrix multiplication is needed to calculate $\mathbf{H}_j$. Thus, the multiplication of $\mathbf{H}_j$ and $\mathbf{c}_j$ reduces also to a simple multiplication for each entry of $\mathbf{c}_j$ instead of a matrix-vector multiplication ensuring fast computation of the model correction.

To determine α_j, two trial step length $\alpha_{j,1}$ and $\alpha_{j,2}$ are chosen and a forward simulation is performed for both step length and the resulting waveforms are used to calculated the corresponding misfit. A second order polynomial, $\chi(\alpha_j)$, is fitted to the misfit of the current model and the misfit for the two trial simulations. If existing, the minimum of the polynomial is taken as the optimal step length for the next iteration. In case the optimal step length is beyond the range of the trial step length, the maximum step length, $\alpha_{j,2}$, is doubled. If no minimum is found, the intermediate step length $\alpha_{j,1}$ is halved and the old value of $\alpha_{j,1}$ is used as $\alpha_{j,2}$. In both cases a further forward simulations is needed for the new step length. This procedure is repeated until a minimum $\alpha_{j,0} < \alpha_{\min} \leq \alpha_{j,2}$ is found or until $\alpha_{j,1}$ or $\alpha_{j,2}$ reach a maximum or a minimum value, respectively.

The computational cost of the procedure described above requires one forward simulation for each seismic source to obtain the wave field for the current model, one forward simulation for the adjoint wave field and two forward simulations for the test step lengths. Due to an appropriate choice of γ_j the test step lengths are not changed often. On average, 4-5 forward simulations per inversion step and per source are needed. Additional receivers do not increase the number of forward runs since the adjoint sources at the receiver positions can be fired at the same time. The presented method is most effective for a low number of sources and a high number of receivers within the observed region.

To ensure a stable and smooth convergence towards the minimum of the misfit function, a hierarchical multiscale approach is used. As suggested by several authors [12, 73, 121] the inversion starts with waveforms of low frequency content and higher frequencies are admitted gradually. In this way, large scale structures evolve at the beginning of the inversion which are gradually refined later as higher frequencies are added. Frequency content is controlled by low-pass filtering the observed waveforms and the source time function for the forward simulations in an identical way. This concept avoids the well-known cycle skipping problem where the phase difference between measured data and synthetic waveforms approaches one dominating signal period. Using low frequency content leads to a smoother misfit function making it more likely for the FWI procedure to converge to the global minimum. Adding higher frequencies gradually introduces additional detail in the model and ensures the convergence to at least a local minimum close to the global one.

Without this approach, the inversion tends to converge into a shallow local minimum far away from the global one.

2.2.5.1 FWI in Two Dimensions

A common scenario during tunnel construction is the appearance of fractures in the rock mass in front of the drilling machine. In case of large scale fractures, the location of these fractures is often roughly known from geological surveys. Seismic waves interact with fractures and are partially reflected and partially transmitted at the fracture similar to a material contrast. Nevertheless, the dependency of transmission coefficient, reflection coefficient, and phase shift on the inclination angle differs strongly compared to a material contrast [86]. In this example we first generate synthetic waveforms for a fracture placed ahead of a tunnel interface and investigate the potential of locating the fracture using the inversion process. The synthetic waveforms are calculated using the 2D solver of NEXD. The fracture is not directly modeled but described by an implementation of the Schoenbergs linear slip concept [104] by Möller & Friederich [72]. In this implementation, the response of the fracture is described by a characteristic frequency, ν, that is calculated according to

$$\nu = \frac{Z_1 + Z_2}{\eta Z_1 Z_2}, \tag{2.17}$$

where Z_i are the impedances of the surrounding media and η is the specific compliance, or the inverse of the specific stiffness, of the fracture [72]. According to [86] the reflection coefficient of a fracture is calculated by

$$R_j = \left| \frac{i\omega}{2\frac{\kappa_j}{\rho v_j} - i\omega} \right|, \quad j = \text{p, s} \tag{2.18}$$

where ω is the angular frequency of the incident wave, ρ the density of the surrounding medium, v_j is the P- or S-wave velocity and $\kappa = \frac{1}{\eta}$ is the specific stiffness of the fracture.

In this example, the reflective parameters of the fracture were chosen to emulate a material contrast, were the medium in front of the fracture (closer to the source) has a P-wave velocity of 3000 m/s and an S-wave velocity of 2000 m/s and the medium behind the fracture has a P-Wave velocity of 1600 m/s and an S-wave velocity of 1000 m/s. The density is identical in both media at 2200 kg/m^3. An inversion for this fault structure is discussed in detail by A. Lamert in [55] and [57] and will be referenced here for comparison.

Using the above parameters, reflection coefficients, $R_\text{p} = 0.2$ and $R_\text{s} \approx 0.231$ are obtained for P- and S-waves respectively. Using these reflection coefficients, and a frequency of 500 Hz the specific stiffnesses for P-and S-wave are calculated as: $\kappa_\text{p} \approx 50.79$ GPa/m and $\kappa_\text{s} \approx 23.31$ GPa/m, leading to characteristic frequencies of the fracture

$$\nu_\text{N} = 15.4 \,\text{kHz}, \tag{2.19}$$
$$\nu_\text{T} = 13.2 \,\text{kHz}. \tag{2.20}$$
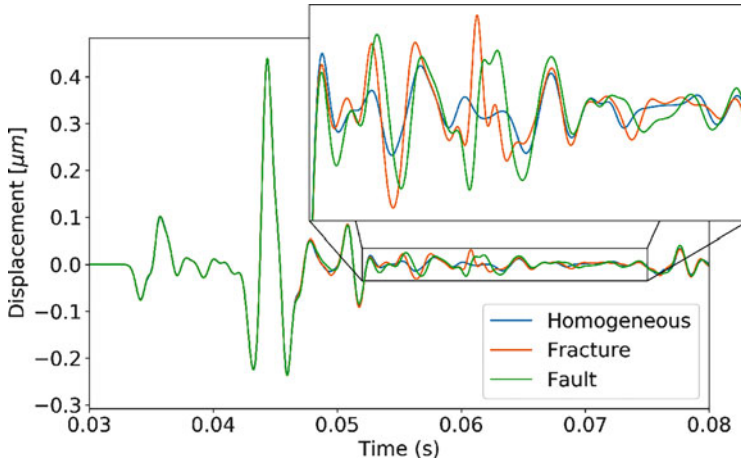
Fig. 2.4 Displacement seismogram of the horizontal component recorded at a surface receiver at the center of the simulation domain for the homogeneous model, the model incorporating a fault, and the model incorporating a fracture. The zoom-in panel highlights waves reflected by the fault or the fracture, respectively. The amount and amplitude of reflected waves is comparable for both cases but the seismograms are not equal due to the different phase shifts introduced by the different reflectors. ([55])

Figure 2.4 shows a comparison of the synthetic seismograms for the homogeneous background model without any reflectors and the seismograms calculated for two cases in which different reflectors were added. The first case shows the seismogram for a forward simulation were a fracture with the above parameters is added to the model (Fracture). The second case is a seismogram recorded at the same station in case of a fault (Fault). The seismograms are not identical due to the inherent difference of the reflectors used in the respective simulations. However, just by analyzing these seismograms, no assumption can be made whether the reflector is a fracture or a fault.

Figure 2.5 shows the model for the generation of the synthetic data and the results of the inversion for the fracture and for the fault. The fracture is best recovered in the P-wave velocity model as a thin low velocity zone almost at the exact position of the fracture in the initial mesh. It should be noted that a homogeneous velocity model with a fracture only defined at the element edges is used to produce the synthetic waveforms but during the inversion it is not possible to invert for the fractures itself. Instead the velocity values of the starting model are changed to represent the data and, thus, will produce an inhomogeneous velocity model without a fracture. The second observation from these results is that even though their parametrization is identical, the results from the inversion differ quite substantially.

From this data alone, no estimation of the true thickness of the fracture can be made, as the resolution of the fractures thickness highly depends on the frequency of the source wavelet. Nevertheless using these results, an operator will be able to determine if the reflector is a fracture or a fault and the location of either.
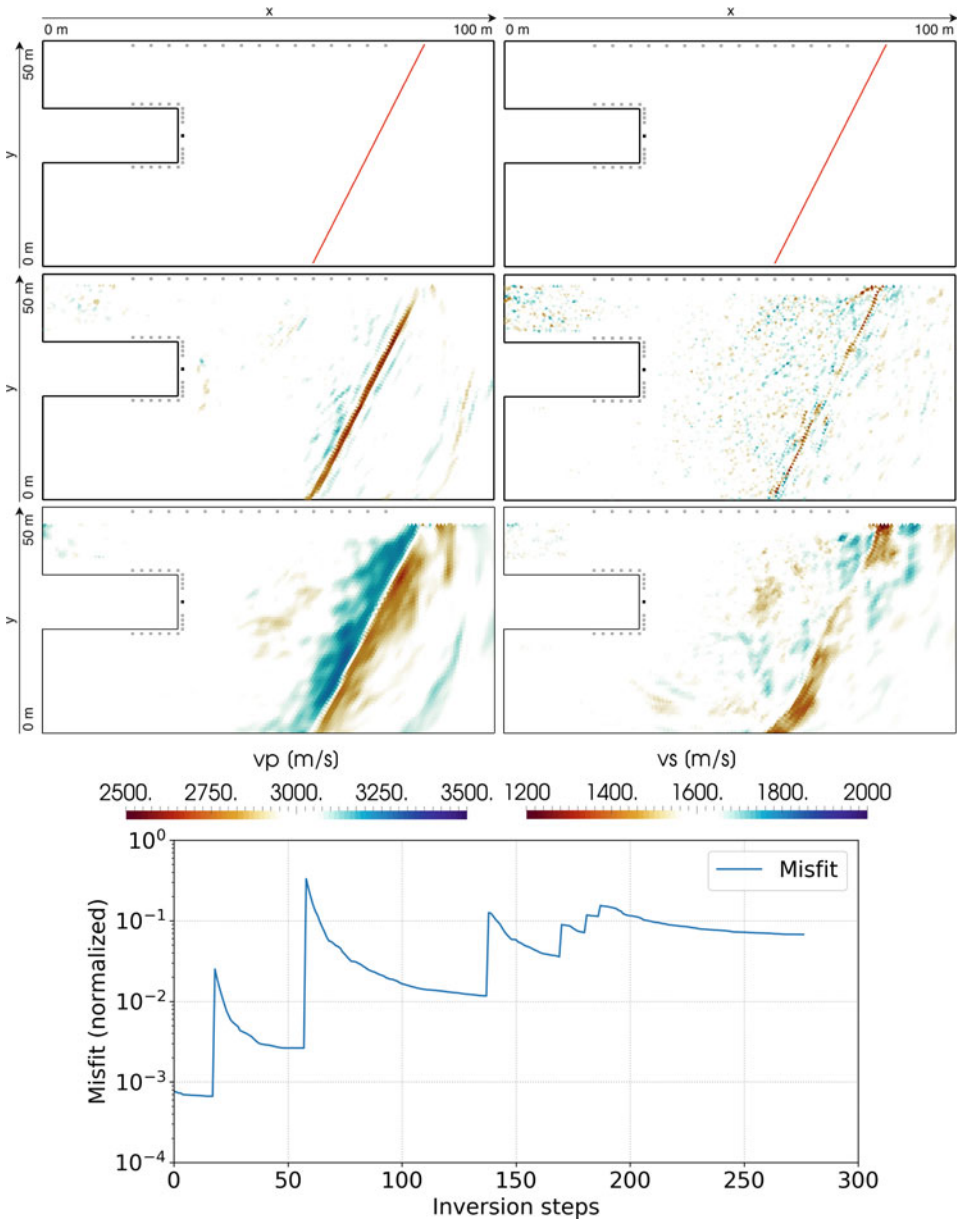
Fig. 2.5 Top: Homogeneous velocity model with fracture characterized by a red line (top row), inversion result after 276 iterations (center row), and inversion result for a fault with comparable reflection behavior like the fracture for comparison (bottom row). Bottom: Evolution of the misfit normalized to the misfit value of the starting model with full frequency content. Jumps correspond to an increase of the frequency content. ([55])

2.2.5.2 FWI in Three Dimensions

This example was originally published as part of the PhD thesis by A. Lamert [55].

To test the capabilities of the inversion procedure on three dimensional data, a synthetic test model is created with 100 m length in x direction and 60 m length in both, y and z direction. A cylindrical tunnel with a diameter of 8 m and 21 m overburden extends 25 m into the medium parallel to the x-axis. The homogeneous background model has elastic properties of $v_p = 3000$ m/s, $v_s = 1700$ m/s, and $\rho = 2000$ kg/m^3 (see top row of Fig. 2.6). A spherical cave with a radius of 1.5 m is located 2 m above the tunnel line and 20 m in front of the tunnel as first inhomogeneity. The cave is modeled as a void with a free surface. A fault is located 46.5 m ahead of the tunnel where the seismic velocities change to $v_p = 2000$ m/s and $v_s = 1100$ m/s. The fault is rotated through 24.8° about the y-axis and afterwards through 20.5° about the z-axis. A seismic source is located centrally at the tunnel face pointing in the direction of $(1, 0, 1)$ to illuminate the ground with both, P- and S-waves. Receivers are placed at the free surface, the tunnel walls and the tunnel face to receive reflected waves as well as possible.

The starting model is a homogeneous model without the cave or the fault but with the tunnel. As elastic parameters, the bed rock properties around the tunnel are used. The mesh of this model consists of 65,747 elements and the simulation needs to be run for 8500 time steps (0.135 s simulation time) ensuring the observation of all reflected waves. With this, the simulation time for a single forward simulation is increased to almost 30 minutes compared to a couple of minutes for the 2D examples. However, the chosen size of the elements only allows to use a Ricker wavelet with a central frequency of 125 Hz leading to a spatial resolution 4 times smaller compared to the 2D examples. Increasing the frequency would lead to excessive computational times since the computational time grows with the fourth power of the frequency.

The inversion starts with a cutoff frequency of 50 Hz increasing step wise to the maximum frequency of the Ricker wavelet during the inversion. Figure 2.6 shows the final inversion result after 200 iterations from different perspectives. The color scale is chosen such that a small band close to velocity values of the homogeneous starting model is completely transparent. From both edges of the transparent velocity band, the transparency decreases to the maximum and minimum values. Thus, clouds of higher and lower wave velocities compared to the bed rock become visible. The true position of the fault and the cave are also depicted in the inversion result by a plane and a sphere, respectively.

Compared to the 2D fault example presented in [55], many more small scale inhomogeneities are created but the fault is still clearly visible. The strongest signal of the fault is created on the left hand side of the tunnel axis for the P-wave velocity model (around the coordinate $(0 \text{ m}, 20 \text{ m}, 0 \text{ m})$) since waves from this area are directly reflected back to the receivers. The strongest signal for the S-wave velocity model appear at the top (around the coordinate $(35 \text{ m}, 0 \text{ m}, 25 \text{ m})$). With the velocity values increasing in front of the fault and decreasing behind it, a change at the fault from higher to lower wave velocities is obvious. However, determining the unknown velocity value behind the fault is only possible
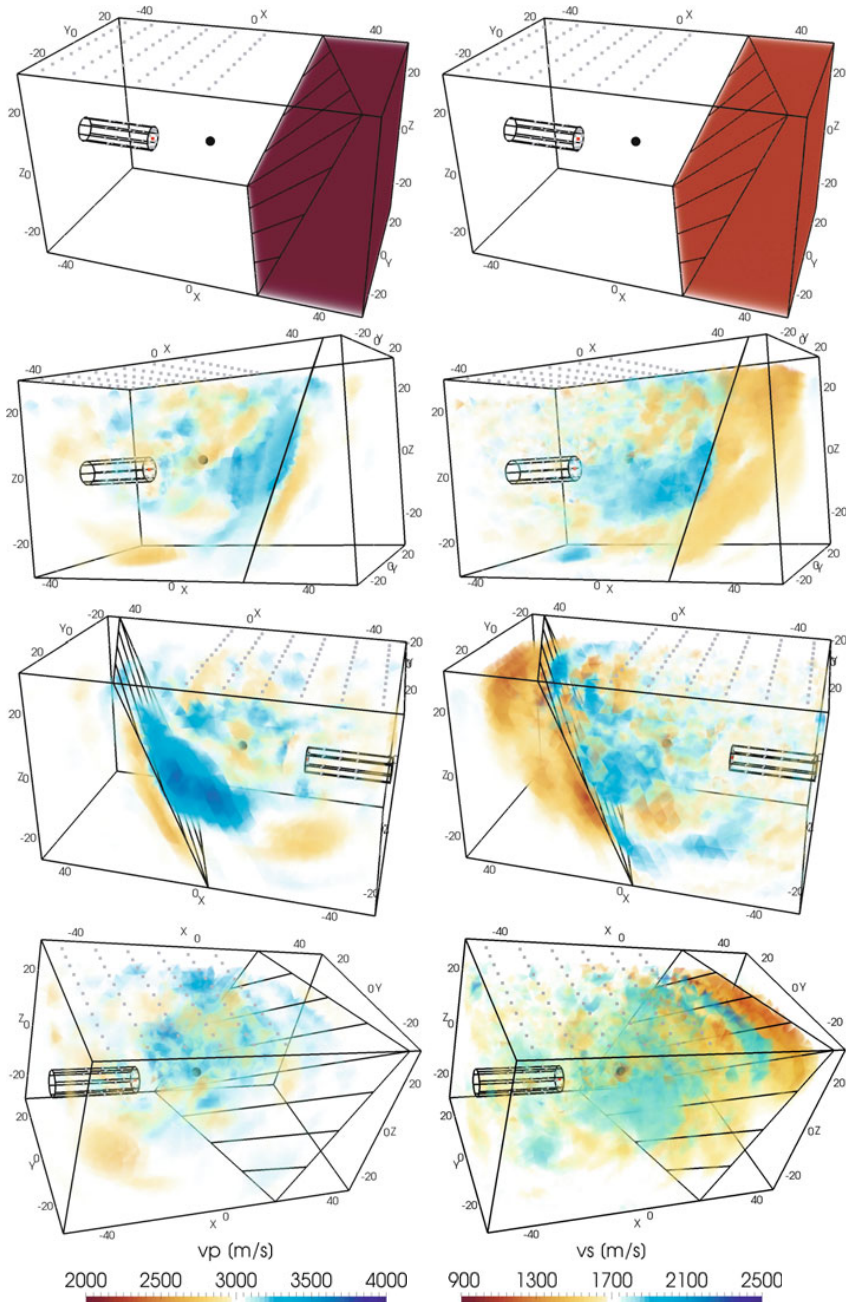
Fig. 2.6 Real model (top) and inversion result after 200 iterations from three different perspectives. All panels show the positions of the two obstacles: a fault illustrated as plane and a cavern illustrated as sphere. Velocity values close to the homogeneous background model are made transparent to show clouds of inhomogeneities. Receivers are represented by grey dots, the source at the tunnel face is shown in red. ([55])

with high uncertainties since the reconstructed values vary strongly in the region where the fault is located. Additionally, the same effect as in the 2D example appears related to the distance between tunnel and fault. Due to the increase of the wave velocity in front of the tunnel, the fault plane is shifted to slightly higher distances from the tunnel. The lower part of the fault appears curved. This is probably caused by the fact that waves from here are mainly reflected to the receivers within the tunnel and only a small portion is recorded by receivers at the surface. Thus, considering only the receivers within the tunnel, a small aperture results. By using higher frequencies within the source signal, it can be expected that most of the small inhomogeneities will disappear and a clear picture of the fault is reconstructed similar to the 2D example. However, the provided computer would need several months for such a calculation.

The size of the cavern is chosen to be slightly higher than the shortest wavelength and is comparable to the size of the mesh elements as necessary for a stable simulation of the highest frequencies. Considering the inversion result for the P-wave velocity, the cavern appears as a small cloud with decreased wave velocity values not significantly smaller compared to the inhomogeneities around it. Within the S-wave velocity model a small cloud with clearly decreased velocity values can be seen with, however, almost the double radius as the real cave. The velocity values do not decrease to very small values and thus do not give a clear indication on the presence of a cavern in that area. Using a source signal containing higher frequencies would be necessary to obtain a clear picture with more reliable velocity values. However, the example clearly shows the potential of the FWI procedure to reconstruct large and small scale objects also in three dimensions. The problems of the computational effort can be expected to get less relevant in the future with increasing computer power.

2.2.6 Adjoint Frequency Domain Full Waveform Inversion

The wave modeling and the application of FWI is more illustrative in the time domain because an accurate selection of the considered period of time and an easy identification of emerging amplitudes in the seismic records is feasible. However, the non-linearity of the inversion is increased by this abundance of information. A separate analysis of single frequency groups by a frequency domain approach allows a mitigation of the non-linearity [1] by an intuitive application of a multi-scale approach where the used frequencies are gradually increased during the inversion scheme.

Frequency domain approaches of FWI have already been studied for other applications like the inversion of seismic records of a cross-hole experiment [85] or the inversion of tomographic seismic data of a physical scale model [84].

The complex-valued frequency domain elastic wave equation

$$-\omega^2 \rho(\mathbf{x})\,\mathbf{u}(\mathbf{x}, \omega) - \nabla \cdot (\mathsf{C}(\mathbf{x}) : \nabla \mathbf{u}(\mathbf{x}, \omega)) = \mathbf{f}(\mathbf{x}, \omega) \tag{2.21}$$

is obtained by a Fourier transformation of the time domain's counterpart in Eq. 2.2. The complex-valued wave field $\mathbf{u}(\mathbf{x}, \omega)$ can be solved for an angular frequency ω and the complex-valued excitation force $\mathbf{f}(\mathbf{x}, \omega)$.

An application of numerical schemes to solve Eq. 2.21 leads to a linear system of equations. Therefore, the initial factorization of the system matrix enables the computation of additional wave fields of the current ground model and the same angular frequency for other source excitations by a comparatively low increase of the computational effort. This makes the frequency domain approach favorable in terms of computational efficiency for applications with a high number of sources.

In time domain modeling, an increase of the discretization level of the ground model for modeling higher frequencies brings a need for a decrease of the time increment to ensure numerical stability. This dilemma is avoided by frequency domain modeling and therefore, the choice of the applied numerical scheme is not limited by this problem. Nevertheless, finite element approaches are favorable because the Neumann boundary condition at the free surfaces, which acts as reflecting surfaces, of the Earth's surface as well as of the tunnel walls are fulfilled implicitly.

A major drawback of the frequency domain modeling is that the artificial borders of the considered computational domain have to be treated very carefully. If no high attenuation effects occur within the subsurface domain, the reflections from the artificial borders contaminate the whole wave field. In time domain modeling only the later points in time are affected by these reflections which can be simply neglected by a reduction of the considered time interval.

An efficient way to suppress these erroneous reflections is an application of small absorbing boundary layers at the artificial borders of the computational domain. The so-called perfectly matched layer method enables a smooth absorption of escaping waves by a coordinate stretching into the imaginary plane [9]. For shallow subsurface models like in the considered tunnel models, an application of convolutional perfectly matched layers is recommended [25].

The frequency domain Green's functions $\mathbf{g}(\mathbf{x}, \omega)$, which are the system response to an impulse excitation, are illustrated in a shallow two-dimensional tunnel environment for excitation by a horizontal single force which is located at the front tunnel face in Fig. 2.7 for a frequency of 500 Hz. An absorption of the elastic waves within the perfectly matched layers (dashed regions) is observed. Even though a homogeneous ground model was used, it is not recognizable by the wave field whether there is a disturbance in front of the tunnel face or not.

Since the wave field is only solved for a limited number of currently investigated frequencies of the ith frequency group the proposed misfit function of Eq. 2.3 is adapted to

$$\chi_i(\mathbf{m}) = \sum_{f=1}^{F_i} \sum_{s=1}^{N_s} \sum_{r=1}^{N_r} \left(u_r^s(\omega_f; \mathbf{m}) - \bar{u}_r^s(\omega_f) \right) \left(u_r^s(\omega_f; \mathbf{m}) - \bar{u}_r^s(\omega_f) \right)^*. \qquad (2.22)$$
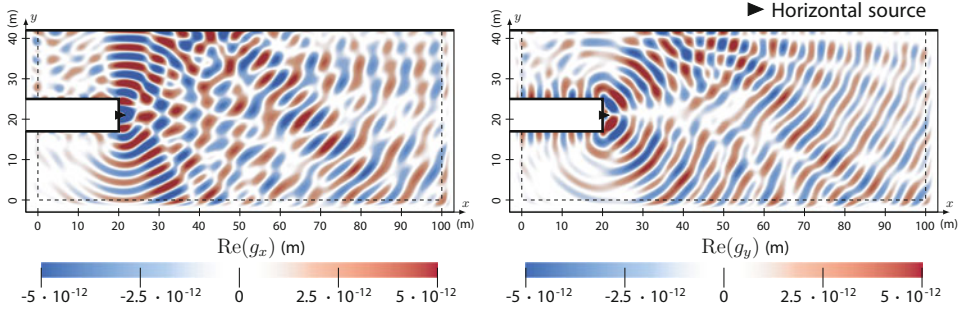
Fig. 2.7 Real part of the Green's functions Re(**g**) in x- (left) and y-direction (right) in a two-dimensional tunnel environment for a frequency of 500 Hz. Free surfaces are located at the Earth's surface and around the tunnel. The origins of the perfectly matched layers are indicated by the dashed lines. The illustrated ground model has a homogeneous P-wave velocity $v_p = 3800$ m/s, S-wave velocity $v_s = 2200$ m/s and density $\rho = 2400$ kg/m^3. The applied source is a horizontal single force

The number of frequencies within the current frequency group is denoted by F_i whereas $(\cdot)^*$ is the complex conjugate. The complex displacements of the reference seismic records $\bar{u}_r^s(\omega_f)$ are calculated by a discrete Fourier transformation. A preservation of low frequency features is guaranteed by combining the increasing frequencies with low frequencies from former iteration steps.

The discrete adjoint gradient of the misfit function is calculated by differentiating the misfit in Eq. 2.22 with respect to the discretized material properties (e.g. discretized within single elements or at every node). For computing the gradient, the product rule has to be applied and the derivative of the displacement with respect to the discretized material properties is evaluated by using the according derivative of numerical representation of Eq. 2.21. The resulting system of equations can be simplified by calculating the adjoint wave field by using the negative derivative of the misfit function with respect to the displacements at the receiver stations as adjoint source [26]. The computation of the adjoint wave field in the frequency domain only needs low additional computational effort since the already factorized system matrix can be reused again.

For minimizing Eq. 2.22 by changing the material properties of the current ground model different techniques as steepest descent method, conjugate gradient method or the L-BFGS method [81] can be applied to find a suitable search direction. The step length can be evaluated by heuristic schemes or by e.g. calculating the minimum of a quadratic approximation of the misfit function with three points [107]. Singularities occur for the wave field at the sources as well as for the adjoint wave field at the receivers. Therefore, the gradient has disproportionately high changes at these positions [83] and makes an exploration of the ground in front of the tunnel more difficult. By a preconditioning of the gradient, e.g. setting the gradient equal to zero around the sources and receivers, the negative impact of this effect on the inversion scheme might be reduced.

A deconvolution of the source function into a spatially dependent impulse part $\delta(\mathbf{x} - \mathbf{s})$, which is equal to zero everywhere except at the considered source position $\mathbf{s}$, and a frequency dependent part $h(\omega)$ is in the frequency domain straightforward,

$$\mathbf{f}(\mathbf{x} - \mathbf{s}, \omega) = h(\omega)\,\delta(\mathbf{x} - \mathbf{s}). \tag{2.23}$$

By neglecting the frequency dependent part $h(\omega)$ for the forward wave modeling, the Green's functions $\mathbf{g}(\mathbf{x}, \omega)$ are calculated. The displacement at the receiver station can be calculated with the Green's functions by a convolution with the frequency dependent source function

$$u_r^s(\omega_f; \mathbf{m}) = h^s(\omega_f)\, g_r^s(\omega_f; \mathbf{m}). \tag{2.24}$$

Under the assumption that the transfer function between the ground and a receiver r is approximately equal for all receivers N_r, a simultaneous approximation of the source signatures during every iteration of the inversion is possible. By setting the derivative of Eq. 2.22 with respect to the source function $h^s(\omega)$ equal to zero to satisfy the necessary condition for a minimum [84], the source function is approximated by

$$h^s(\omega_f) = \frac{\sum_{r=1}^{N_r} \left(g_r^s(\omega_f; \mathbf{m})\right)^* \bar{u}_r^s(\omega_f)}{\sum_{r=1}^{N_r} \left(g_r^s(\omega_f; \mathbf{m})\right)^* g_r^s(\omega_f; \mathbf{m})}. \tag{2.25}$$

The calculated source function depends on the current ground model $\mathbf{m}$. Therefore, the source function is approximated for every iteration of a frequency group. Since the calculation of the displacements is with Eq. 2.24 only a linear operation, the already calculated Green's functions can be reused and no additional forward simulations are performed.

If the assumptions made are valid, the frequency domain approach enables an inversion scheme in which no information of the source signature is needed in advance. This might be a great advantage since a prior estimation of the source function is cumbersome.

In Fig. 2.8, the inversion results for a two-dimensional tunnel environment are illustrated, where different numbers and locations of sources and receivers are used. The resulting P-wave velocity v_p is shown on the left side and the S-wave velocity v_s on the right side. The ambient P-wave velocity is $v_p = 3800$ m/s and the ambient S-wave velocity is $v_s = 2200$ m/s, whereas the density is $\rho = 2400$ kg/m^3 and is assumed to be constant. The reference ground model, which is illustrated on top of Fig. 2.8, contains three disturbances in front of the tunnel track with different shapes and elastic properties. Free surfaces are applied at the Earth's surface and at the tunnel, whereas the absorbing boundary layers are illustrated by the dashed regions.

For the computation of the wave fields, a finite element approach is used, where hierarchical higher-order shape functions [108] are employed for efficiently increasing the accuracy of the numerical scheme for higher frequencies (which lead to shorter wavelengths) by just adding additional shape functions without changing the initial mesh. For
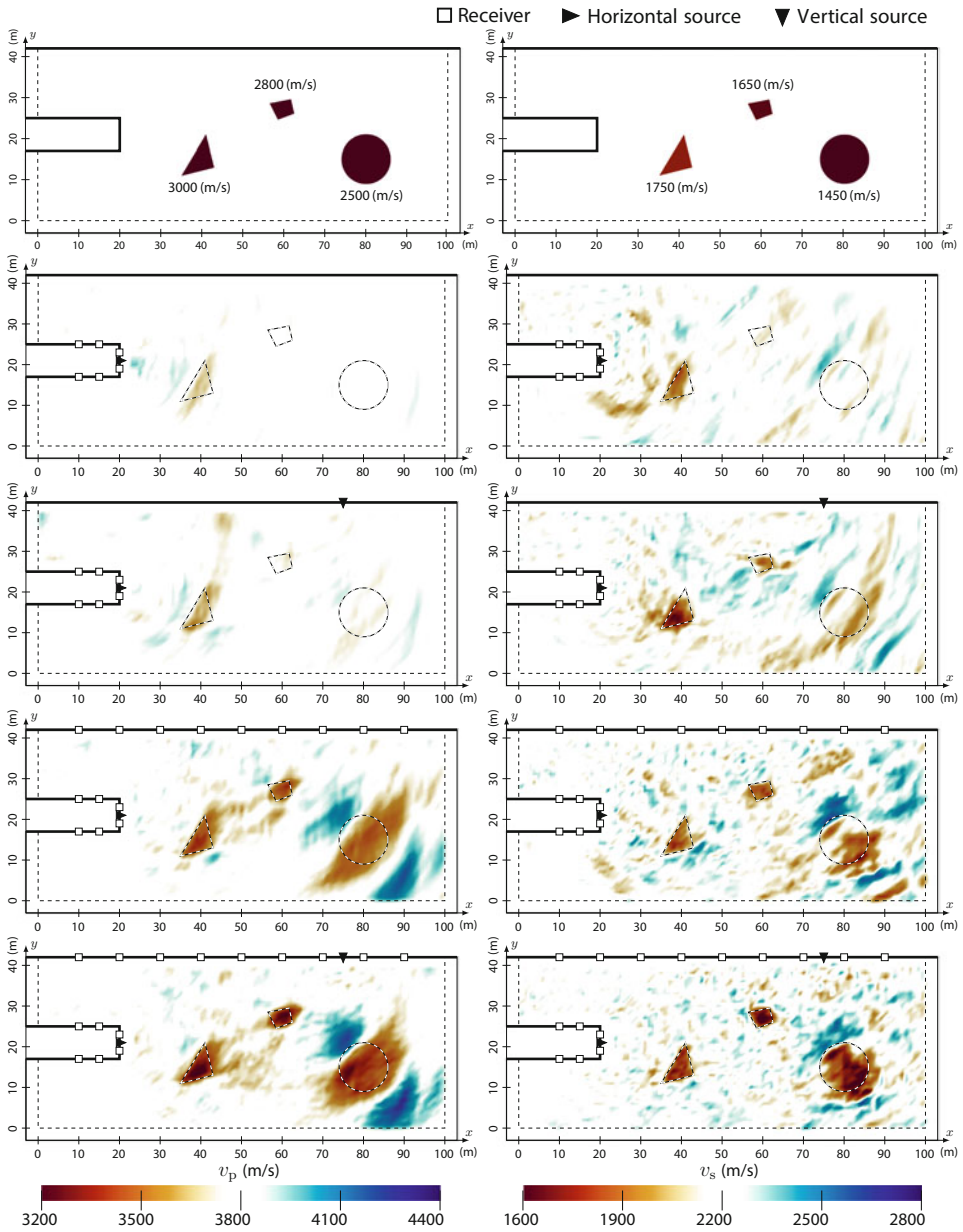
Fig. 2.8 Results of a full waveform inversion with a frequency domain model for a two-dimensional tunnel environment with a different number and position of sources (triangles) and receivers (squares). The P-wave velocity distribution is on the left side and the S-wave velocity distribution is illustrated on the right side. In the first row the wave velocity distribution of the reference model is illustrated. The shapes of the three disturbances are indicated within the inversion results

the illustrated application, the ground properties are discretized in the nodes. The used synthetic reference displacements are calculated with the same approach in advance to the several frequency groups. As reference source functions $\bar{h}^s$ Ricker wavelets with a peak frequency of 500 Hz, without a time delay and a scaling factor of 10^6 are used. A simultaneous approximation of the source function by Eq. 2.25 is applied for all results in Fig. 2.8. For the first eight frequency groups only one frequency is employed. The other thirty frequency groups contain a combination of an increased frequency and a lower frequency. The inversion is performed by using 12 iterations for each frequency group. For all four examples, the displacements in both spatial directions are measured at the indicated receivers.

The used source and receiver configuration of the first example (second row of Fig. 2.8) is likely to be used for today's exploration approaches in mechanized tunneling. Only one source is positioned in the middle of the tunnel face and the receivers are located at the tunnel face as well as at the tunnel walls. The resulting wave velocities allow only a prediction of the position of the first disturbance but neither its shape nor its actual elastic properties are quantifiable accurately. Furthermore, spurious fluctuations of the wave velocities occur which make an unambiguous prediction difficult. For the second example (third row of Fig. 2.8), a source is added at the Earth's surface 55 m in front of the tunnel. Therefore, not only reflected waves are analyzed but also directly refracted waves of the second source are captured. The position of all three disturbances are hinted by the resulting wave velocities, especially by the S-wave velocity. However, only the shapes and properties of the first two disturbances can be predicted by the S-wave velocity. For the third example (fourth row of Fig. 2.8), only nine evenly distributed receivers are added at the Earth's surface in comparison to the first example. The resulting wave velocities enable a good prediction of the position and the properties of all three disturbances whereas only the shape of the first two obstacles are predictable in an accurate way. A rapid increase followed by a sudden decrease of the wave velocities occur at the borders of the third disturbance, which produces a comparable reflection behavior since the gradient of the ground properties is nearly the same as the gradient of the reference ground model. This ambiguity of the seismic records has to be taken into account for evaluating the results of the full waveform inversion. The fourth example (fifth row of Fig. 2.8) combines the additional source of the second example as well as the additional receivers of the third example. An accurate prediction of the position, shape and properties of the disturbances is enabled on the basis of the inversion results.

It is observed that adding sources and receivers at the Earth's surface improves the prediction of geological changes in front of the tunnel face. The application of sources and receivers at the Earth's surface may not be possible in urban areas due to restrictions on the access to the surface. However, as illustrated by the first example, a prediction of the first reflection feature in front of the tunnel is already possible by only using sources and receivers at the tunnel.

As already announced, a simultaneous approximation of the source signature was used. A comparison of the real part of the reference and the approximated source signature of
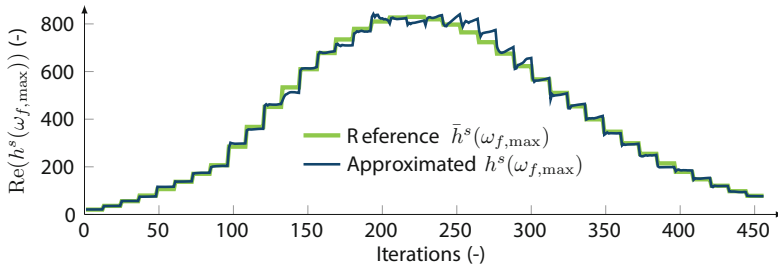
Fig. 2.9 The change of the real part of reference $\bar{h}^s$ and approximated source signature h^s for the highest frequency of a frequency group $\omega_{f,\max}$ of the first full waveform inversion example (second row of Fig. 2.8) during the several iterations is displayed

the first example is illustrated in Fig. 2.9. Only the reference and the approximated value of the highest frequency of the frequency groups is displayed.

A sufficient approximation of the source function is obtained which enables a full waveform inversion scheme without prior knowledge of the source signature.

Since the curvature of the tunnel as well as other effects are not considered by a two-dimensional model, more realistic examples have to be investigated by using three-dimensional tunnel models. Therefore, the proposed inversion scheme is tested on a shallow tunnel domain where the reference ground model includes a spherical disturbance in front of the tunnel track. The ambient wave velocities are $v_p = 4000\,\text{m/s}$ and $v_s = 2400\,\text{m/s}$, whereas the properties of the sphere are $v_{p,\text{sphere}} = 2800\,\text{m/s}$ and $v_{s,\text{sphere}} = 1700\,\text{m/s}$. The density is assumed to be constant with $\rho = 2500\,\text{m/s}$. The tunnel has a diameter of 8 m and its center is located 18 m below the Earth's surface. The sphere has a radius of 8 m and its center is on the level of the tunnel's center with a distance of 25 m to the front tunnel face. The FWI is started again with an homogeneous ground model.

Since the computation demand for the inversion schemes is still very high for three-dimensional problems, only 16 freqeuency groups are used where the first nine groups contain only single frequencies and the other seven groups combine two frequencies within a group. The frequencies are only increased to $f = 381.97\,\text{Hz}$ because the wave field becomes more complex for higher frequencies and therefore a higher discretization would be needed. But for the used disturbance size this frequency range is sufficient.

The full waveform inversion is performed for two different configurations of sources and receivers. The first configuration only employs a source in orthogonal direction at the center of the tunnel face as well as only receivers at the tunnel face and walls. The second configuration uses additional sources and receivers at the Earth's surface. The receivers record the displacements in all three spatial directions. All sources use a Ricker wavelet with a peak frequency of 500 Hz, without a time delay and a scaling factor of 10^6. The resulting wave velocity distributions are illustrated in Fig. 2.10, where the source and receiver positions as well as the position of the disturbance are indicated, too.
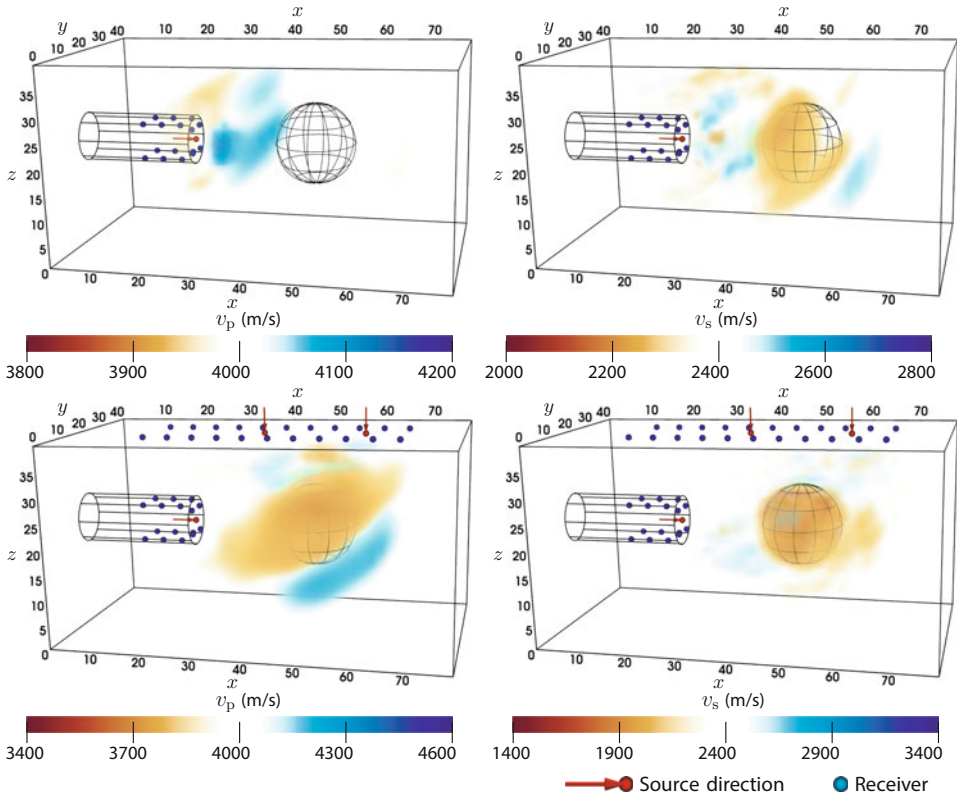
Fig. 2.10 P-wave velocity v_p (left) and S-wave velocity v_s distribution (right) of the full waveform inversion results of a three-dimensional shallow tunnel domain for two different configurations of sources (red spheres) and receivers (blue spheres). The position of the spherical disturbance of the reference model is indicated by grid lines

For the first source-receiver configuration, the S-wave velocity field allows a prediction of the front face of the sphere, whereas the P-wave velocity field only provides spurious fluctuations directly in front of the area where the gradient is preconditioned (around the sources and receivers). Nevertheless, these results allow the guess that a disturbance with decreased wave velocities might be in front of the tunnel. The second source-receiver configuration leads to improved inversion results. The S-wave velocity distribution gives an accurate representation of the the position, shape and S-wave velocity of the sphere. Whereas the P-wave velocity field only gives a blurred image of the sphere but its position and the trend of the P-wave velocity are identifiable. An application of additional frequency groups containing higher frequencies would improve the representation of the sphere by the reconstructed P-wave velocity field. Therefore, these results would allow a more precise prediction of the disturbance.

The three-dimensional results demonstrate that the two-dimensional results give good insights into the influence of the different source-receiver configurations as well as that seismic reconnaissance via full waveform inversion by an adjoint frequency domain approach provides promising results for synthetic seismic records.

2.2.7   Validation with Small-Scale Laser Experiment

In order to validate the FWI methods with real data, a small-scale laser experiment is set up with which ultrasonic measurement can be acquired. The validation with ultrasonic data brings a significant gain compared to the validation with synthetically generated data since noise as well as measurement errors are naturally included. Furthermore, also modeling errors occur when setting up the forward model. All of these error types also occur during field scenarios, but not in synthetic tests, and therefore, the robustness of the FWI methods against these error types can be tested with the laboratory data. Rich field data is difficult to get, while in the small-scale experiment, a broad variety of scenarios can be tested in order to prepare the methods for a later in-situ application. A picture of the experiment with labeled components is provided in Fig. 2.11, while a sketch of the measurement chain of the experiment is illustrated in Fig. 2.12.
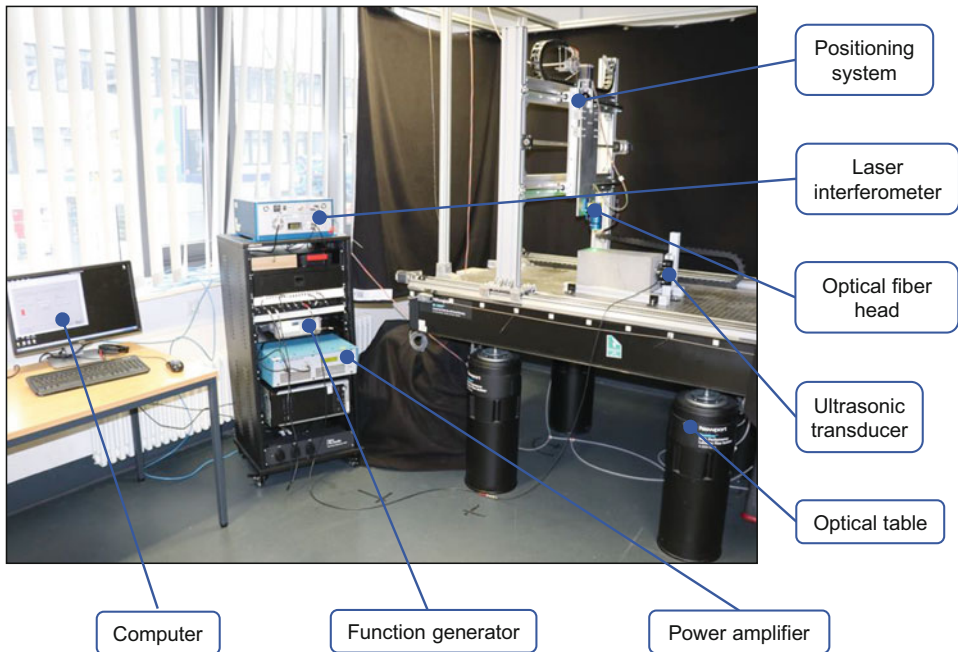
Fig. 2.11 Picture of the experiment with labeled components
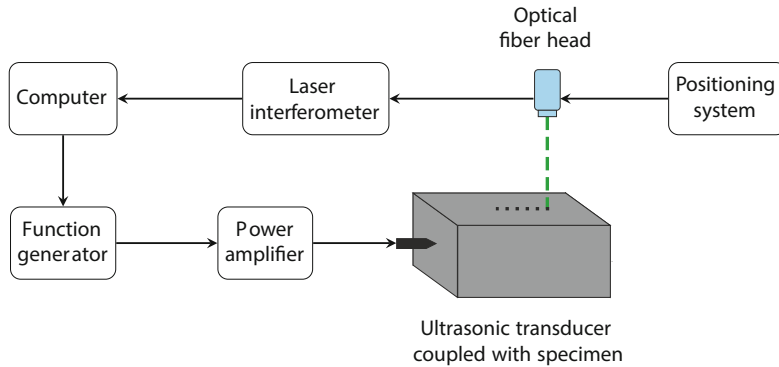
Fig. 2.12 Measurement chain of the experiment

On the computer, the source signal is specified which is forwarded to a function genera-
tor and then to a power amplifier. Arriving at the ultrasonic transducer, the electrical signal
is converted into a mechanical waveform. The transducer applies a force onto the specimen
and thus initiates a seismic wave which propagates through the specimen. A laser inter-
ferometer enables the contactless recording of seismic data, where a positioning system
allows the measurement at various points along predefined lines or areas. The recorded
signal is forwarded to the computer for data acquisition. In order to minimize vibrational
influences from the environment, the setup is placed on an optical table.

Intensive preliminary investigations are conducted with the aim to maximize the re-
peatability of measurements as well as their signal-to-noise ratios [114]. Firstly, it is found
out that a stacking of single measurements is necessary in order to achieve a repeatable
high-quality signal, where a minimum of 100 stacked measurements is recommended.
Secondly, it is shown that the attachment of aluminum tape on the specimen's surface
when measuring on porous material is highly beneficial in order to improve the reflection
of the laser signal. With these methods, a signal-to-noise ratio of 4322 (or 36.4 dB) could
be achieved for 100 stacked measurements acquired on a concrete specimen with alu-
minum tape, where the signal-to-noise ratio of a single measurement without aluminum
tape amounted to 11.3 (or 10.6 dB) only.

2.2.7.1 Hole Imaging in an Aluminum Block

First validation of the methods is performed with ultrasonic data acquired on an aluminum
block which contains a drilling hole. Since a consideration of homogeneity and isotropy
is most widely valid for aluminum, simulation results may be expected to be closer to
the measurement than for rock materials. Therefore, modeling strategies such as the esti-
mation of the material properties and the transducer's source function can be more easily
developed. More information on the experiment, the forward modeling and UHSA may be
found in [114, 117]; more information on the time domain adjoint solution may be found
in [55].
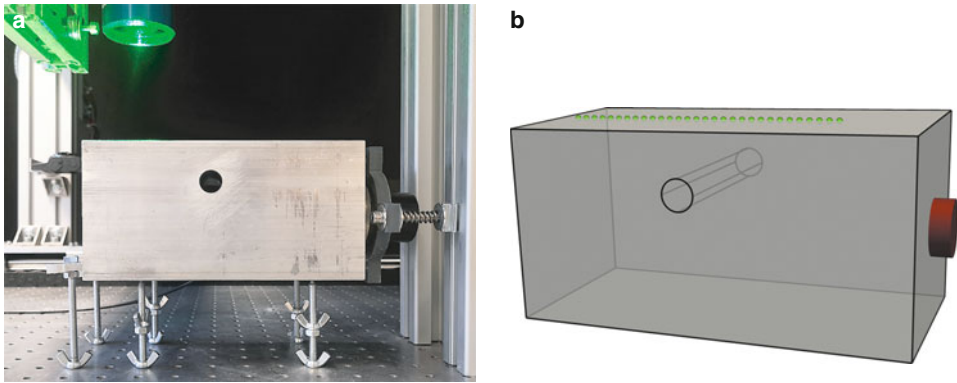
Fig. 2.13 Aluminum block with a drilling hole. **a** Photo of measurement setup, **b** illustration with measurement configuration. The shape of the transducer is illustrated in red. Points of laser measurements are visualized by the green dots

The aluminum block with its drilling hole is shown in Fig. 2.13 with a photo of the measurement setup in Fig. 2.13, left, and an illustration in Fig. 2.13, right. A coordinate system is placed at the center of mass of the ideal block as shown in Fig. 2.13, right. The outer dimension of the aluminum block is $200.4\,\text{mm} \times 103\,\text{mm} \times 100\,\text{mm}$, where a hole of 16 mm diameter is drilled throughout the y-dimension at $(-10, y, 20)$ mm. The green dots illustrate the points of laser measurement, the red cylinder visualizes the shape of the ultrasonic transducer. The source function which is sent to the transducer is a Ricker wavelet with a central frequency of 300 kHz. In order to determine the material properties of the specimen and the transducer's source function, a second undisturbed aluminum block with the same outer dimensions as above is used, which is illustrated in Fig. 2.14 (analogous to the illustration in Fig. 2.13). Here, only a single measurement is acquired on the opposite site of the transducer as illustrated. At all of the above-mentioned points of measurement, 200 single measurements are stacked in order to increase the signal qualities. Offsets of the records are removed by subtraction of average amplitudes before signal arrival. Bandpass filters with cutoff frequencies of 50 and 800 kHz are applied to each trace.

Before an inversion scenario can be set up, a forward model needs to be constructed. In order to estimate the material properties and the transducer's source signature, a model corresponding to the setup shown in Fig. 2.14 is set up. Dimensions are carefully measured and a brick is modeled and meshed, where all surfaces are defined as free boundaries. The material behavior is assumed to be elastic and therefore, material properties reduce to density ρ, compressional wave velocity v_p, and shear wave velocity v_s. Density ρ is determined and implemented into the model. With the spectral-element code SPECFEM3D [50], numerical solutions to various gridded combinations of v_p and v_s are computed, where an ideal Ricker is used as source function. By incorporation of the acquired measurement, the misfit functionals are determined and the wave velocity combination corresponding to the
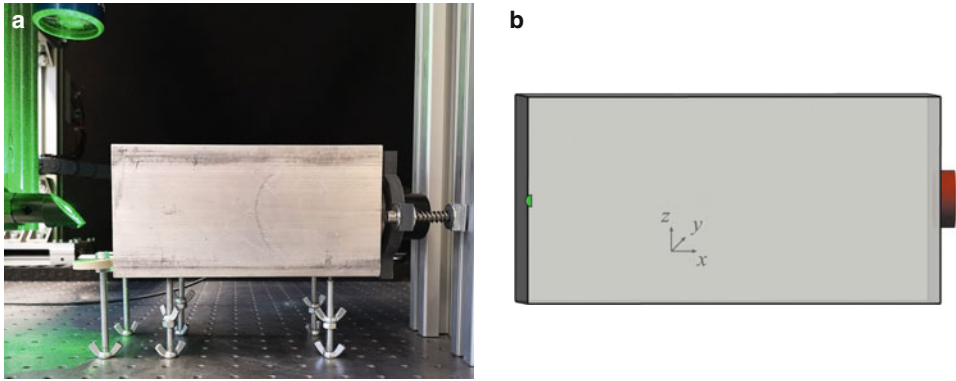
Fig. 2.14 Undisturbed aluminum block. **a** Photo of measurement setup, **b** illustration with measurement configuration. The shape of the transducer is illustrated in red. The single measurement is visualized by the green dot
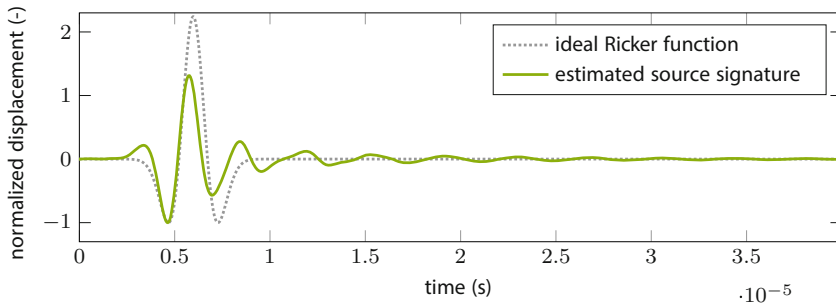
Fig. 2.15 Ideal Ricker source function and estimated source function. The waveforms are normalized with their second local extremum

smallest misfit value is picked, which is $v_p = 6340\,\text{m/s}$ and $v_s = 3110\,\text{m/s}$. In a next step, the transducer's source function is estimated. If it is assumed that the numerical model captures all properties of the experimental model (e.g. in terms of geometry and material properties), the source function in frequency domain $R_{\text{exp}}(\omega)$ can be estimated as [117]

$$R_{\text{exp}}(\omega) = \frac{S_{\text{exp}}(\omega)}{S_{\text{syn}}(\omega)} \cdot R_{\text{syn}}(\omega), \tag{2.26}$$

where $R_{\text{syn}}(\omega)$ is the ideal (Ricker) source function, $S_{\text{exp}}(\omega)$ the acquired waveform, and $S_{\text{syn}}(\omega)$ the simulated waveform in frequency domain for the angular frequency ω.

Figure 2.15 shows the estimated source function after transformation to time domain compared to the ideal Ricker source function. With the estimated waveform as source function, a new simulation is set up, where the outcoming waveform is plotted in Fig. 2.16 (green), together with the measurement (black) and the simulated wavelet generated with
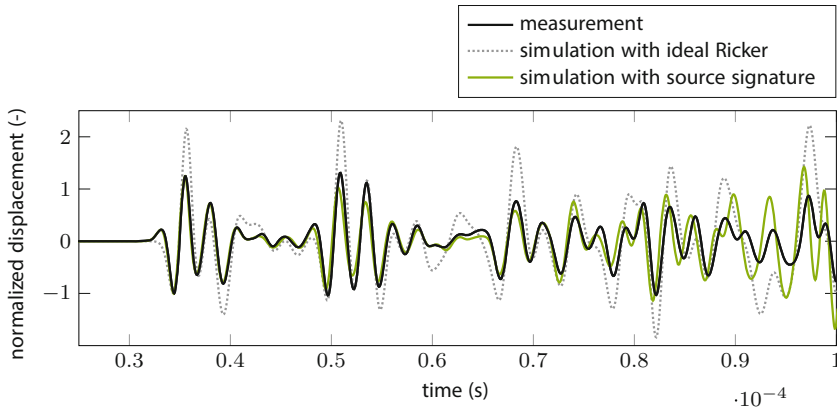
Fig. 2.16 Visualization of the acquired measurement, the synthetic response to an ideal Ricker source function, and the synthetic response to the estimated source signature shown in Fig. 2.15. The waveforms are normalized with their second local extremum

the ideal Ricker (gray dotted). It becomes visible that the waveform agreement to the measurement improves substantially compared to the prior estimation. The high correlation is a sign for well-fitting material properties and a well-estimated source signature, forming the basis for the upcoming inversion scenarios.

UHSA inversion In this section, UHSA is applied to the measurement data (setup shown in Fig. 2.13), where the previously determined material properties and the estimated source signature are used. Since UHSA is based on the implementation of prior knowledge, a parametrization needs to be derived. Here, it is selected to consist of just two center coordinates (x, z) respective to the coordinate system in Fig. 2.13, right, where the corresponding drilling spreads all over the specimen in y-direction. The diameter of the drilling is considered to be known which has the advantage that with this kind of parametrization with only two parameters, a relatively fast computation and a visualization of the misfit functional is possible. The time window of investigation is set to 8.8×10^{-5} s since according to Fig. 2.16, a high agreement of experimental and synthetic waveforms is observed during this time. In a first step, a misfit landscape is computed by linear interpolation of 1024 sampled parameter configurations and visualized in Fig. 2.17.

The abscissa corresponds to the x-axis in Fig. 2.13, while the ordinate corresponds to the z-axis. Several local minima are visible; however, there is a distinct global minimum around the actual center of the boring at $(x, z) = (-10, 20)$ mm. UHSA is set up for 40 cycles, where the course of the algorithm is drawn onto the misfit landscape in Fig. 2.17. It is visible that the SA algorithm rather accepts parameter configurations with smaller misfit functionals as many SA samples lying in the red regions are rejected. If a SA proposal is accepted, the UKF samples different parameter configurations with the aim to move into
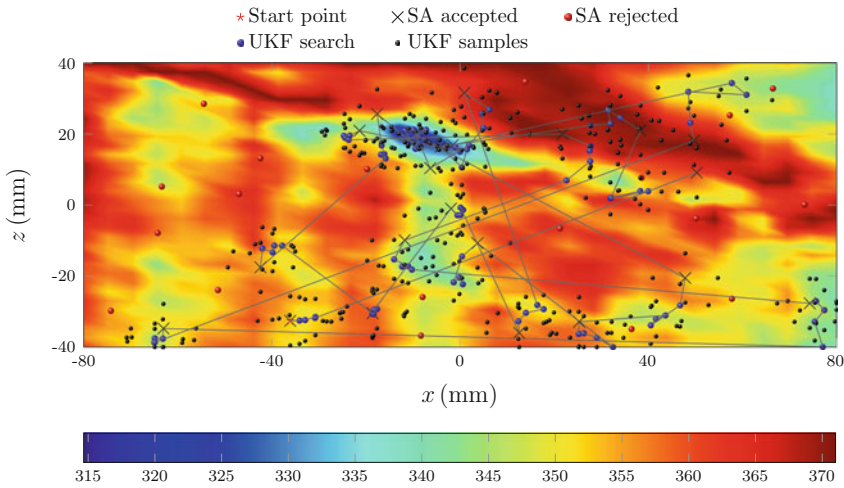
Fig. 2.17 Course of UHSA on the misfit landscape, where a certain location on the map specifies position (x, z) of the hole in the computational model. The color corresponds to the respective misfit functional

the direction of the neighboring local minimum, which succeeds in most cases. The global minimum region is intensively explored and the parameter configuration with the lowest misfit functional is found at $(x, z) = (-8.86, 19.17)$ mm, which is close to the actual expected global minimum. The entire inversion requires 460 forward simulations within 55 hours of computation time on a 26-core computer with 2.4 GHz each and 96 GB RAM.

Time domain adjoint inversion In this section, the results for an inversion scenario using the adjoint time domain FWI on the setup shown in Fig. 2.13 are presented. The initial model is a homogeneous model described by the material parameters determined above. The source time function used here is the green curve shown in Fig. 2.15. The computational mesh consists of 285,588 tetrahedral elements. The computation time for one single simulation on a machine with two Intel Xeon E5-2698 v4 processors with 20 cores each and 256 GB RAM on 40 threads is approximately 1.35 hours.

A comparison of the measured seismograms to synthetic ones showed large discrepancies for the receivers closest to the source. Consequently, only the 20 receivers farthest away from the source were used in the inversion process (see [55]). Figure 2.18 shows the inversion results, where the changes in P- and S-wave velocities are shown in three perspectives. Around the position of the drilling, a decrease of the P-wave velocity is visible. In addition, a number of other regions with altered wave velocities are observed, where possible reasons are described in [55]. For the S-wave model, on the other hand, an increase in velocity at the position of the drilling is observed. In [55], Lamert provides a detailed analysis as to why an increase rather than a decrease is observed in this instance.
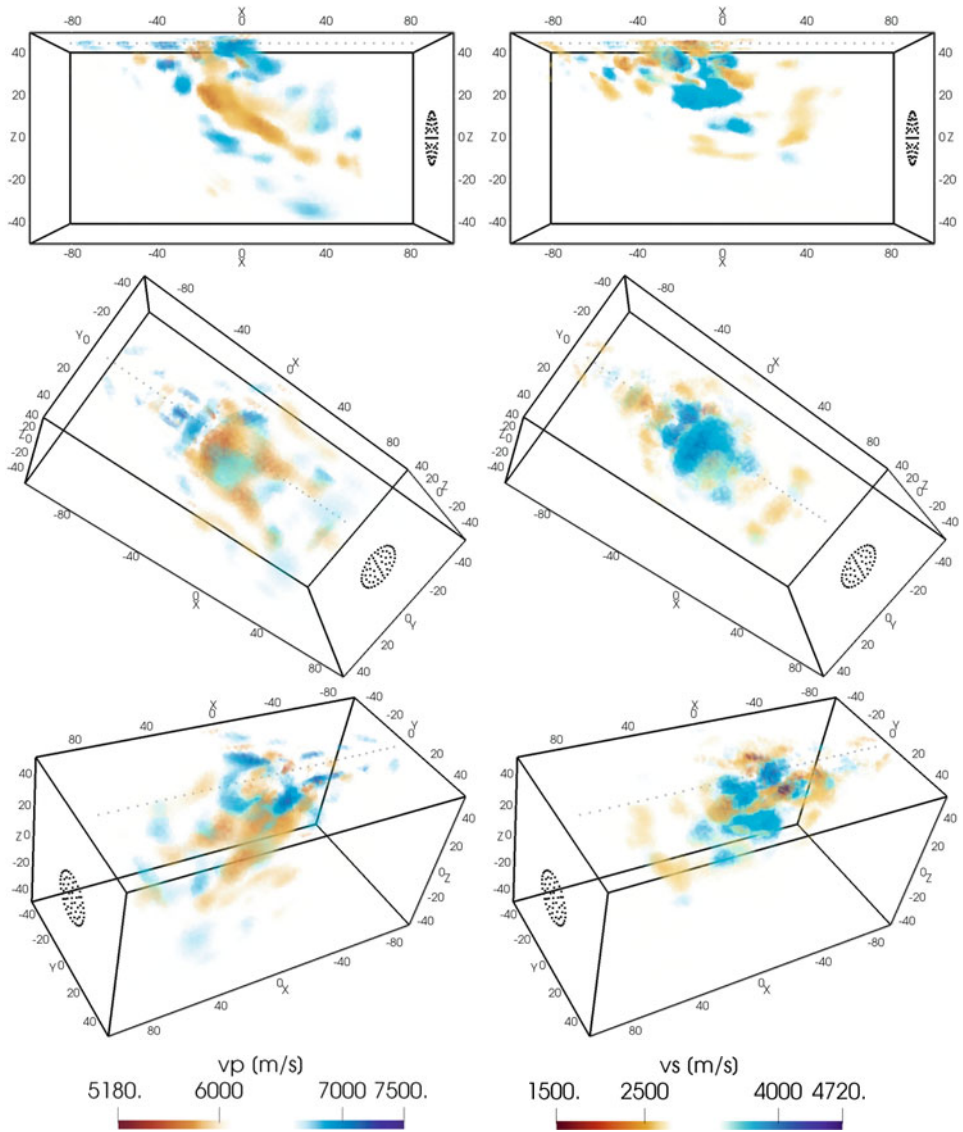
Fig. 2.18 Inversion results of the P-wave velocity model in the left column and the S-wave velocity model in the right column from three different perspectives for the inversion changing both P- and S-wave velocities. Grey dots represent seismic stations and black dots the seismic source. ([55])

Using both velocity models, an inhomogeneity is identified in the vicinity of the true position of the drilling. The center is estimated by [55] at $(x, z) = (-15.5\,\text{mm}, 24.5\,\text{mm})$ with a radius of 6.5 mm, while the true center lies at $(x, z) = (-10.0\,\text{mm}, 20.0\,\text{mm})$ with a radius of 8.0 mm.

2.2.7.2   Layer Change Imaging in a Concrete Block

In this section, an experimental model with certain similarities to field models is used to acquire ultrasonic data with which UHSA and UKF-PaLS are validated. For more information, readers are referred to [114, 115]. The experimental model is shown in Fig. 2.19 with a photo in Fig. 2.19, left, and an illustration of the inner structure in Fig. 2.19, right.

The specimen is a concrete block which has a relatively large dimension in y-direction compared to the other directions, enabling thus to perform the upcoming simulations in 2D instead of in 3D for the gain of a reduced computation time. Into the block, a linear material change is incorporated, where the two materials are composed of different concrete mixtures. In order to illustrate a 2D tunnel geometry in the later simulation model, the block has a material recess at $x = 0$. For the acquisition of the ultrasonic data, two source locations are specified which are illustrated by the red dots. At each source location, two source signals are released in the form of tone burst signals centered at 80 and 100 kHz. For each source signal, data is acquired at 532 receiver points, where the locations of the laser measurements are illustrated by the green lines. In order to improve the laser reflection, aluminum tape is attached along the lines of measurement. At each point of measurement, 100 single measurements are stacked. Bandpass filters with cutoff frequencies of 10 kHz and 150 kHz are applied to each record. A $\sqrt{t}$-filter is applied to the measurement data in order to approximately convert the amplitudes from the 3D spreading to a 2D spreading as for instance performed in [85].

Same as in the previous section, a forward model is to be constructed, where the main tasks are the determination of the background material properties and the estimation of the source signal. For their estimation, only the receivers between $x = 0.1$ m and $x = 0.16$ m are used within a reduced time window in order to minimize the impact resulting from the disturbance. Afterwards, a homogeneous model is set up with the outer dimensions of Fig. 2.19, right. The geometry and the mesh are defined, where again all boundaries obtain free boundary conditions. Simulations are conducted with the spectral-element code SPECFEM2D [118]. The density is determined and implemented into the model. After-
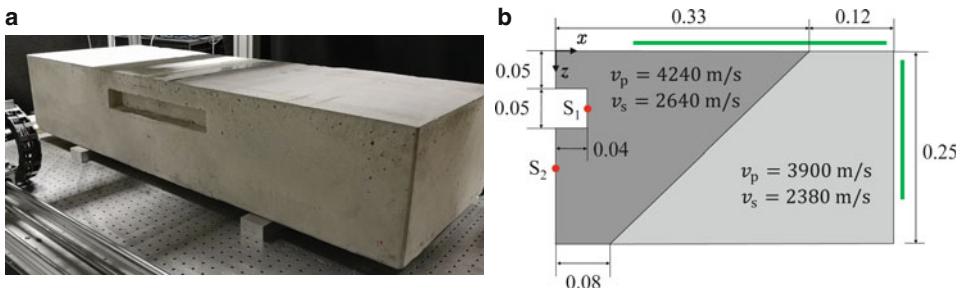
Fig. 2.19 Concrete block with measurement configuration. Dimensions in m. Sources in red, locations of laser measurement in green. Left: Photo of the specimen. Right: Illustration of the ideal inner structure with two materials in different colors

Fig. 2.20 Parametrization and determined geometry for configuration 1 (red) and configuration 2 (blue)
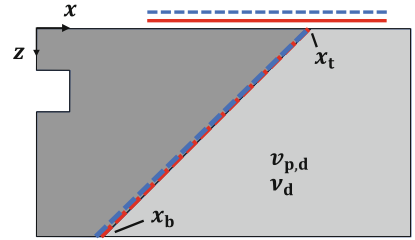
wards, material properties are determined in the same way as explained in Sect. 2.2.7.1, where also attenuation is included. However, the misfit functionals increase for increasing attenuation and thus, elastic material behavior without attenuation is considered for inversion. Disturbance material properties are determined in a similar way like the background material properties, where the material properties for both domains are shown in Fig. 2.19, right. First estimations of the source functions are determined by a direct measurement with a second transducer at the head of the first transducer. Afterwards, the source signal is improved same as in the previous section by applying the relation Eq. 2.26 at a reference receiver. For inversion, the receiver signals are cut in such a way that no reflections arrive from the boundaries of the experimental model Fig. 2.19, left, in positive and negative y-direction. The density is assumed to be constant all over the model domain.

UHSA inversion.   Prior to inversion, a parametrization is set, which is visualized in Fig. 2.20. It is composed of a linear connection of a top border position x_t at $z = 0$ with a bottom border position x_b at $z = 0.25$ m, a disturbance wave velocity $v_{p,d}$ and a Poisson's ratio v_d.

Two source-receiver configurations are tested, where the first configuration includes all receivers along the green lines in Fig. 2.19, right, and where the second configuration includes the receivers only at the top surface $z = 0$. The inversion results are shown in Table 2.1 and a visualization of the determined geometry as well as of the source-receiver configurations is given in Fig. 2.20 for configuration 1 (red) and configuration 2 (blue). It is observed that for both configurations, the determined values are very close to the expected true values. For configuration 2, x_b is determined a little less precise since receivers only occur at the top surface. The inversion scenarios took about 12 hours on a 26-core computer with 2.4 GHz each and 96 GB RAM, where 3762 (configuration 1) or 3933 (configuration 2) forward simulations were required.

Table 2.1 Inversion results of UHSA: expected true value and inversion results

Parameter	Expected true value	UHSA (config 1)	UHSA (config 2)
x_t (m)	0.33	0.3256	0.3297
x_b (m)	0.08	0.0770	0.0622
$v_{p,d}$ (m/s)	3900	3904	3903
v_d (–)	0.2033	0.2088	0.1951

Fig. 2.21 Initial model. The uncertainty measure introduced in Sect. 2.2.3.2 is plotted in medium dark gray

$v_p\,(\mathrm{m/s})$ $v_s\,(\mathrm{m/s})$

$4240_{\pm16}$ 4200 2640 2615

double standard deviation
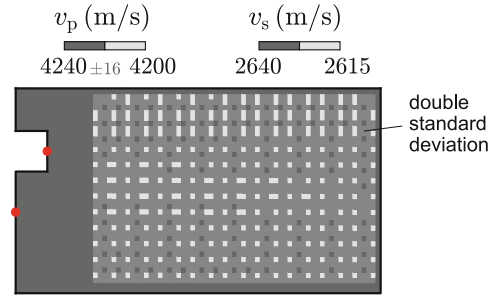
UKF-PaLS inversion   The initial model for UKF-PaLS is set up with 216 bumps and visualized in Fig. 2.21, where analogous to Fig. 2.2, an uncertainty measure is plotted. Same as UHSA, UKF-PaLS is validated with the two source-receiver configurations described in the previous paragraph. Figure 2.22 shows the inversion results for both configurations after 20 iterations compared to the expected true geometry illustrated by black dashed lines. It is observed that for both configurations, most of the bumps outside the region of the actual disturbance domain vanish while parts of the disturbance become visible. The uncertainty measure correctly extends the region of the actual disturbance. However, there a still errors which mainly occur due to measurement errors, noises and modeling errors. At height of the tunnel, the disturbance is determined quite precisely for both configurations, which would be most important for an application during mechanized tunneling. Both computations require about 12 hours on a 26-core computer with 2.4 GHz each and 96 GB RAM, where 17360 forward simulations are consumed.

In summary, both UHSA and UKF-PaLS can determine the inner structure of the concrete block satisfactorily. With the dimensionality reduction applied in UHSA, results are even close to exact. Primarily due to model side reflections which would not occur in a real tunneling model and due to source-receiver configurations, the findings cannot fully be compared with field scenarios. However, the experiment brings similarities enabling a validation with a certain relation to mechanized tunneling.

$v_p\,(\mathrm{m/s})$ $v_s\,(\mathrm{m/s})$ $v_p\,(\mathrm{m/s})$ $v_s\,(\mathrm{m/s})$

$4240_{\pm12}$ 3848 2640 2390 $4240_{\pm13}$ 3921 2640 2325
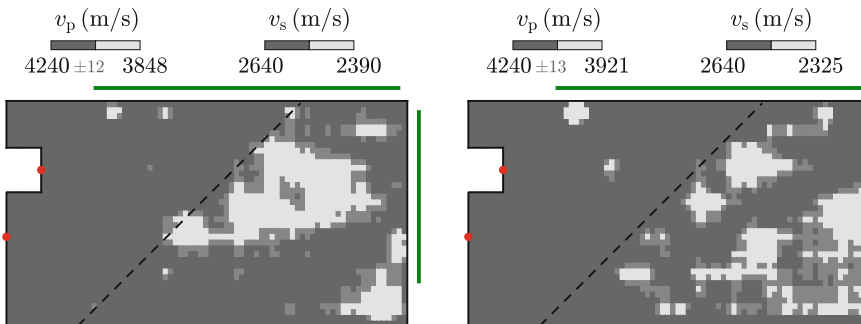
Fig. 2.22 Inversion results after 20 iterations for receiver configuration 1 (left) and receiver configuration 2 (right). The expected true geometry is illustrated by black dashed lines

2.2.8   Summary and Outlook

After the explanation of the principle of seismic reconnaissance in general, state-of-the-art methods for application during mechanized tunneling are shortly presented. Changes for the better are identified, directly leading to the field of full waveform inversion with which a more detailed representation of the subsoil can be achieved. Four different FWI approaches are introduced, that are two Bayesian FWI approaches, one adjoint FWI approach in time domain, and one adjoint FWI approach in frequency domain. Synthetic inversion scenarios are created, where all of the methods are generally able to image the anomalies in a tunnel environment. For the validation of the FWI methods with real data, a small-scale laser experiment is set up with which ultrasonic data is created. Since noise, measurement errors and later modeling errors occur, the grade of validation is evaluated to be high. Two experiments are presented, where the tested inversion methods show a certain robustness against these kinds of errors, being able to reconstruct the anomalies which are incorporated into the specimen. The results give a hint that the methods are generally applicable for exploration during mechanized tunneling. However, it is to mention that the methods are still far from delivering results close to real-time or within a time which would be necessary for an application during mechanized tunneling. Nonetheless, with exponentially growing computational power, full waveform inversion may become applicable in the future.

2.3   System and Parameter Identification Methods for Ground Models in Mechanized Tunneling

Collecting data of excavation-induced changes on surroundings in a linear project like tunneling may enable the engineers to adapt the computational model for subsequent phases through back analysis and reduce uncertainty, subsequently. In this regard, sensitivity analysis methods play a crucial role in selecting the most pertinent input components that must be adjusted using available experimental or field data. The suggested conceptual approach aims to increase the efficiency of measurement-based system identification in mechanized tunneling by using various mathematical approaches such as optimization based back analysis, and optimum experimental design.

2.3.1   Back Analysis

Over the last decade, there has been a growth in the use of numerical models for predicting ground behavior, surface settlements, and the loading and deformation of tunnel linings. The rising power and efficiency of current computer technology, as well as significant advances in computational mechanics, have fueled the development of more complicated numerical models with more characteristics.

In the numerical simulation of mechanized tunneling, more or less severe idealizations are frequently used, such as modeling its stress-strain behavior using a simplified constitutive law or initial boundaries, assuming simplified hydro-mechanical initial boundaries in the subsoil, or a homogenization of soil mass. The epistemic uncertainties that arise as a result of such models may result in either a conservative design or a significant risk of instability. Back analysis techniques are commonly adopted in geotechnical applications to calibrate constitutive parameters for numerical simulation models. For large-scale geotechnical applications where the region of the impacted ground is considerably larger than the tested samples, a calibration technique based on existing measurements is required for an effective evaluation of the soil characteristics.

The observed excavation-induced changes in the measurement logs (ground displacements, stresses, pore water pressures, etc.) will be utilized to update the computational model in this regard through system adaptation. If the observations show that the design values are not being followed, the back analysis may be used to determine realistic soil properties and system performance without the need for additional field surveys. With the significant development of computer technology and advanced algorithms, the concept of back analysis via in-situ measurement can be implemented by an optimization procedure, as illustrated in Fig. 2.23.
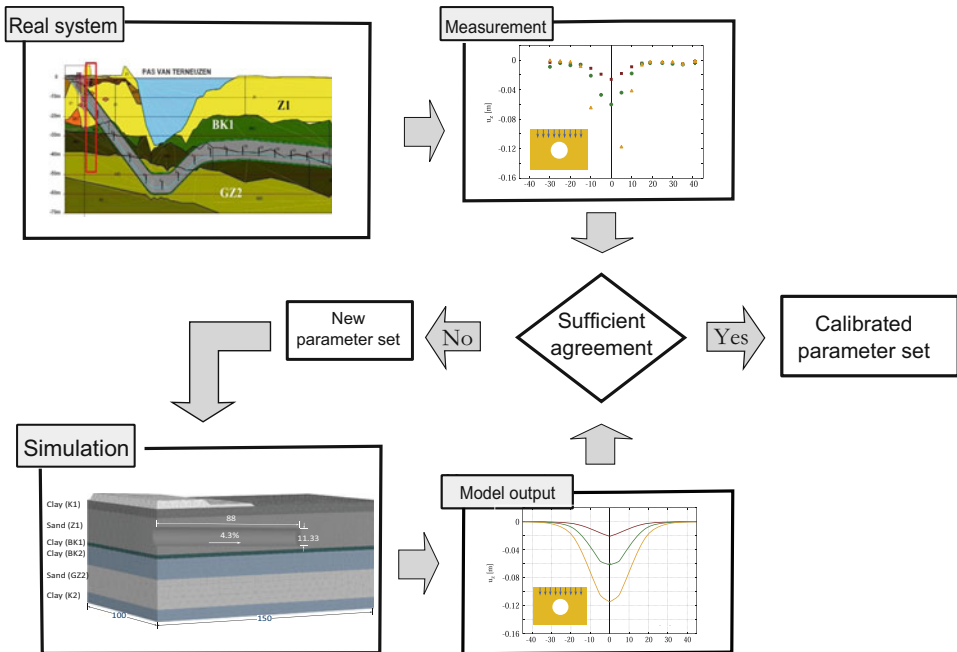
Fig. 2.23 The applied iterative approach via back analysis, from [59]

Observations or measurements $\tilde{\mathbf{y}}$ are compared to model outputs $\mathbf{y}$ obtained from initial assumptions on model parameters $\mathbf{m}$. To reduce the discrepancy between measurement and model response, the model parameters are varied. In the end this corresponds to the formulation of the objective function. The complexity of this problem emerges from the circumstance that there are usually several model parameters that are correlated with each other and that the system behavior is non-linear, explicitly in the considered geotechnical applications. Therefore, finding that optimal parameter combination $\hat{\mathbf{m}}$ that causes the minimum discrepancy between measurement and model response requires so-called optimization algorithms as described in Sect. 2.3.4.

The aforementioned discrepancy between measurements $\tilde{\mathbf{y}}$ and model responses $\mathbf{y}(\mathbf{m})$ is usually described by the objective function J as

$$J_{\min}(\mathbf{m}) = \|\tilde{\mathbf{y}} - \mathbf{y}(\mathbf{m})\|. \tag{2.27}$$

In case some of the measurements are of less relevance for the model or less trustworthy, the objective function can be modified by including a vector of weighting factors $\mathbf{w}$ that reflects the relevance of the individual measurements $\tilde{y}_i$:

$$J_{\min} = \sum_{i=1}^{N} w_i \left| \frac{\tilde{y}_i - y_i(\mathbf{m}).}{\tilde{y}_i} \right| \tag{2.28}$$

It should be highlighted that the back studies must be undertaken immediately after obtaining the recorded measurements in order for the project design and construction procedures to be reviewed and, if necessary, updated without significant delay during the construction/excavation phase [90]. Iterative parameter identification can be automated thanks to the availability of parameter optimization techniques.

A variety of optimization algorithms have been widely utilized to analyse different engineering problems like optimizing geometry, performance optimization, parameter identification, etc. The back analysis techniques are widely used in geotechnical applications primarily for the purpose of calibrating constitutive model parameters for numerical simulation models [48, 65, 70, 93]. Meier et al. [65] provides a detailed review of several optimization algorithms, and their applications in the geotechnical problems.

Despite gradient based methods, evolutionary algorithms are shown to be efficient and reliable in reaching the global optimal solution in a multidimensional space. As a simulation mechanism of Darwinian natural selection, the Genetic Algorithm (GA) starts with a population of solutions and then improves it through repeated applications of selection, crossover, and mutation operators. Khaledi et al. [46] and Müthing et al. [77] used GA to determine the parameters of a time dependent constitutive model.

Particle Swarm Optimization (PSO) is an evolutionary optimization algorithm that was introduced in [44] working with a population (called a swarm) of candidate solutions. This method randomly places a number of "particles" in the search space of a specified function and then evaluates them at each point. Zhao et al. [127] carried out PSO to determine

geotechnical parameters for an actual tunneling project (Western Scheldt tunnel). The optimized parameters successfully captured the tunneling-induced ground motions.

2.3.2 Metamodeling

Depending on the size of the subsurface domain, the excavation length, and the appropriate discretization, 3D finite element simulations of the mechanized tunnel can take anywhere from half an hour to several hours to complete. Therefore, the existence of a tool that allows for the execution of a large number of precise and detailed numerical models is required for the use of most of the non-deterministic approaches. This is due to the fact that uncertainty quantification and reliability analyses need thousands of model runs. As a result, using surrogate modeling approaches to replace the tunnel's original finite element models is essential. Based on a given number of parameter samples conducted in the original finite element (FE) model, several mathematical methodologies have been examined and confirmed. These techniques attempt to determine model input parameters, mainly subsurface mechanical characteristics and boundary conditions, permitting a valid employment of tunneling simulation models.

Surrogate models, also known as metamodels or emulators, are empirically generated models (or mathematical functions) that link the inputs and outputs of a computer model or a complicated system. They originated in the idea of design of experiments (DOE), which employed polynomial functions as a response surface methodology (RSM) [122]. Other metamodels have since been created and used, including kriging [18], artificial neural networks, radial basis functions (RBF) by [51]. RBF later has been extended by [76], and been called extended radial basis functions (ERBF). This method employs more than one basis function for each input which leads to a linear combination of radial- and non-radial basis functions to conduct the approximation. Unlike classic RSM, which simply calculates a least squares distance between data points, these approaches give an interpolation surface that spans all training data points. Furthermore, unlike RSM, which assumes a certain shape for the approximation as polynomials, these approaches often include a series of functions, each associated with individual points in the feature space. [14] presented a surrogate modeling process that combines the proper orthogonal decomposition (POD) method (also known as Karhunen Loe've decomposition [41]) with radial basis functions abbreviated as POD-RBF. This technique showed promising results for approximating finite element simulation responses in [10].

After reviewing the state of the art in metamodeling approaches and comparing their characteristics and considering tunneling simulation as an application [45] presented a hybrid technique that integrated POD and ERBF approaches. Khaledi et al. enhanced the POD-RBF method by replacing the radial basis functions with their extended version [76] and abbreviated it as POD-ERBF. Miro et al. [70] suggested a framework for evaluating and selecting the appropriate surrogate model for the approximation purpose.

Among many researches which used metamodeling techniques to replace complex FE models for system identification purposes as [35, 46], Zhao et al. [126] employed meta-models to develop a hybrid estimation concept. In which a small scale submodel is taken out of a larger complex model and continuous simulations are run in this submodel to reduce computing effort. Metamodels are used in three levels to i) correlate soil parameters and nodal displacements on submodel boundaries, ii) correlate soil parameters and tunneling-induced ground movements according to measurements, and iii) correlate tunneling process parameters and tunneling-induced building settlements.

The purpose of a surrogate model is to approximate the response u of a computational model $f(\mathbf{x}) = u$ with an approximation $\tilde{u}$. As a result, the model output u may be given as

$$u = \tilde{u} + \epsilon, \tag{2.29}$$

where ϵ is the approximation error. The common approach to surrogate modeling is to perform computer runs for n sets of the input parameters $\{\mathbf{x_1}, \mathbf{x_2}, \ldots, \mathbf{x_n}\}$, and then using the generated pair points $(\mathbf{x_i}, u(\mathbf{x_i}))$, as *training data* to construct an approximation to the original model.

Three steps are necessary to do this, namely:

1. Selecting an experimental design to generate training data.
2. Choosing (or developing) a metamodeling approach and fit its features based on the data presented above.
3. Quantifying the approximation utilizing testing data and some error estimates to assess the surrogate model.

Testing data are often created by running the computational model with input parameters different from those used to create the training data. The third step is discussed further below.

2.3.2.1   Accuracy Measures of Surrogate Models

The most significant aspect of a metamodel, as previously stated, is its agreement with the original data, or prediction goodness. One may become aware of the links between model complexity, sample size, and approximation method based on experience obtained from multiple applications of various techniques, but it is difficult to know the metamodel's estimation accuracy in advance. As a result, every metamodel must be evaluated before being used to guarantee that it is trustworthy.

Mahmoudi et al. [71], applied many measures to identify the extent of perfection in a surrogate model, as Root Mean Square Error (RMSE), normalized Root Mean Square Error (NRMSE), Mean Absolute Error (MAE), Mean Bias Error (MBE), Bias Factor, Nash-Sutcliffe Efficiency (NS), Variance Account Factor (VAF), Performance Index (PI), RMSE To Standard Deviation Ratio (RSR), Normalized Mean Bias Factor (NMBE), Mean

Absolute Percentage Error (MAPE), Wilmott's Index (WI), Legate and McCabe's Index (LMI), Expanded Uncertainty ($U_9 5$), t-Statistic, Global Performance Indicator (GPI), and Weighted Mean Absolute Percentage Error (WMAPE).

Additional techniques to investigating the correctness of the metamodel may be found in the literature. The coefficient of prognosis, which is a model-independent statistic to assess model quality, is suggested in [74]. It is used to generate a so-called metamodel of optimum prognosis, which is a rough estimate that excludes irrelevant factors. Atamturktur et al. [4] proposes a coverage metric, in which the coverage of the design space is examined in terms of appropriateness for metamodel development, and where extra samples in the parameter space should be placed to increase the metamodel's accuracy.

2.3.3   Sensitivity Analysis

In the concept of system analysis, the large number of input factors involved in a sophisticated geotechnical computational model is a challenge. The essential elements that control system reaction and must be calibrated using experimental or field data can be identified using sensitivity analysis.

The approaches used in sensitivity analysis are either statistical or deterministic. Two main categories are the so-called local and the global sensitivity analyses (GSA). To address complicated models including non linear phenomena like a 3D numerical simulation of TBM model advancement, GSA methods are recommended [68]. The performance of different global sensitivity analysis techniques was reviewed in [62]. This study examines three distinct global sensitivity analysis approaches, namely Sobol'/Saltelli, Random Balance Design, and Elementary Effect method. A decision graph is presented to aid in the selection of a proper technique, taking into account several model properties such as complexity, processing costs, and the number of input parameters. Based on the model features, the user may use it as a reference to choose the most appropriate and cost-effective strategy. Sophisticated SA approaches such as Sobol'/Saltelli give additional information as detecting non-linearity and interaction effects for a better understanding of the system. Therefore the designer may be ready to spend for their high computational costs in order to get such knowledge.

One major drawback of global sensitivity analysis methodologies is the requirement to construct a relatively large number of input-output data sets. As a result, the need of advanced numerical models, which are computationally expensive, makes such analysis impractical. The metamodeling notion presented in 2.3.2 is used as a solution.

Among the others, the Sobol'/Saltelli technique, has shown to be particularly useful for a variety of geotechnical systems [69, 127] since it prioritizes parameter relevance and highlights any interactions among them. Its main goal is to determine how the variance of input parameters affects the variance of the model output. The total effect sensitivity index $S_{\mathbf{T}_i}$ is a comprehensive index that considers the interaction of variables [91]. In order to employ Sobol'/Saltelli technique, two randomly chosen $K \times 2n$ matrices $\mathbf{C}_1$ and $\mathbf{C}_2$ are

constructed for a generic model with n parameters, where K is the number of samples taken from the model space.

Afterwards, a new matrix $\mathbf{R}_i$ is defined by copying all columns from $\mathbf{C}_2$ except its ith column, which is taken from $\mathbf{C}_1$. Then, model outputs $f(\cdot)$ for $\mathbf{C}_1$ and $\mathbf{C}_2$ are evaluated as

$$\mathbf{y}_{\mathbf{C}_1} = f(\mathbf{C}_1), \quad \mathbf{y}_{\mathbf{C}_2} = f(\mathbf{C}_2) \text{ and } \mathbf{y}_{\mathbf{R}_i} = f(\mathbf{R}_i). \tag{2.30}$$

Finally, the variance-based indices for model inputs are evaluated as

$$S_{\mathbf{T}_i} = 1 - \frac{\mathbf{y}_{\mathbf{C}_2} \cdot \mathbf{y}_{\mathbf{R}_i} - f_0^2}{\mathbf{y}_{\mathbf{C}_1} \cdot \mathbf{y}_{\mathbf{C}_1} - f_0^2}, \tag{2.31}$$

where $\mathbf{y}_{\mathbf{C}_1}$, $\mathbf{y}_{\mathbf{C}_2}$ and $\mathbf{y}_{\mathbf{R}_i}$ are vectors containing model evaluations for matrices $\mathbf{C}_1$, $\mathbf{C}_2$ and $\mathbf{R}_i$, respectively. The mean value f_0 is further defined as

$$f_0 = \left(\frac{1}{K} \sum_{j=1}^{K} \mathbf{y}_{\mathbf{C}_1}^{(j)} \right)^2. \tag{2.32}$$

Variance-based sensitivity method is not merely used to identify the effectiveness of input factors, but also later employed in Sect. 2.3.4 to optimize sensor localisation.

2.3.4 Optimal Experimental Design

The following explanation from [123] can describe the key motivation to pay attention to monitoring design in general: Experiments are expensive and time-consuming to conduct in order to gather a large enough set of experimental data. The goal of optimal experimental design (OED) is to create the necessary dynamic experiments in such a way that the parameters are estimated with the best possible statistical quality from the resulting experimental data, which is usually a measure of the estimated parameters' accuracy. In other words, the goal is to create the best feasible tests based on model candidates in order to make system identification straightforward. Fisher's work [27] is widely regarded as the first methodical and scientific investigation of the subject. Fisher implies that the variance of a distribution obtained as an outcome of an experimental design may be used to explain the discovered information content in order to link data to information. As a result, if some components of the monitoring or experimental design are ignored, the resulting distribution will be different and the information content will be reduced. In this way, the designer may compare which experimental design comes closest to a fully monitored scenario while requiring the least amount of experimental work.

To describe the information content I of the experimental data $\tilde{\mathbf{y}}$ with respect to the parameter m_i, the formulation

$$I = \frac{\partial^2 \tilde{\mathbf{y}}}{\partial^2 m_i}, \; i = 1, \ldots, s \tag{2.33}$$

can be employed, where s is the dimension of the considered parameter space. The matrix that accrues when considering all parameters and their correlations is often called the Fisher-information matrix FIM, whereby several similar formulations exist. In [6], the state of the art up to the 1970s is presented and the concepts of [27] are transferred to more systematic and fundamental approaches. This FIM is still employed in recent publications such as [120] that investigated where to place sensors to survey air pollution. In [52], a more statistical investigation is performed on sensor placements on dams, wherein the mean square error of parameter identification results is employed to define the quality of an experimental design. This approach was further developed by the employment of the bootstrap method in [94], where again repeated parameter identification is performed to obtain a covariance matrix $\mathbf{C_m}$ of all considered parameters $\mathbf{m}$. Another aspect in the framework of OED is that one should differentiate between problems where the parameters of interest need to be back-calculated as it is the case in the present thesis and those where they can directly be measured. An example for the latter case is given in [75] where it is described how to find optimal sensor placements to detect contaminants in a water network. As the water demand in such a network is uncertain, finding these optimal placements is still a complex optimization problem, but it does not require the additional step of parameter identification. With different deterministic and stochastic optimization approaches, including different uncertainty scenarios, the optimal sensor locations are identified exhibiting quite different results and showing the need to consider effects of uncertainty in OED applications. The experimental settings can be modified to make the calibration of an unknown (or uncertain) input component as simple as possible. Furthermore, collecting data from tunnel construction measurements enables for the validation of numerical models and the reduction of parameter uncertainties. The utility $\tilde{U}$ (as inverse equivalent to the cost function) defines how a certain design $\boldsymbol{\delta}$ reduces the uncertainty and is to be maximized. Random output samples y are generated according to the defined initial distribution of the input parameter m and the considered "experimental design," $y = f(m, \boldsymbol{\delta})$.

Hölter et al. [34] used Bootstrap technique to evaluate and compare the specific design scenarios and the aspect of including measurement error in a hydromechanical structure. Among all the various approaches to conduct OED, in this study exclusively employing sensitivity measures for performing OED, and Bayesian updating concept were applied. However, GSA is still performed as first essential step to identify the most relevant model parameters on which the specific OED approach is applied afterwards.

2.3.4.1   Spatial GSA

The benefit of sensitivity analysis in relation to the issue of OED is initially determining which parameters are most relevant. The experimental design should concentrate on these parameters since discovering a parameter that has no impact would be wasteful of the generally limited resources. The conceptual relationship between GSA and OED is that changing the parameters to which the model response is most sensitive results in a wider bandwidth of outcomes. The greater the output variation, the easier it is to identify and

distinguish the effect of particular parameters from uncertainty-related errors. As a result, using a back analysis, as explained before in Sect. 2.3.1 back, it is feasible to determine the most sensitive parameters with the greatest accuracy. First ideas to the concept of sensitivity analysis in a spatially distributed manner for geotechnical purposes can be found in [34]. Modern FE programs enable model answers to be provided for any point of the FE model geometry. A GSA may be done for each of these spots to utilize the position with the highest sensitivity to a given parameter to insert a sensor to identify this specific parameter. However, it should be noted that the sensitivity index S_{T_i} calculated using the variance-based technique yields normalized values in each spot for all the considered parameters. Therefore, they may not be compared in various locations. This issue can be overcome by including the importance of an output via its variance and using the updated sensitivity index $S_{T_i}^*$,

$$S_{T_{i,j,k}}^* = \frac{S_i \; \sigma_{j,k}}{\max_k \sigma_{j,k}}, \tag{2.34}$$

where, $S_{T_{i,j,k}}^*$ denotes the well-known sensitivity index as it was introduced in Sect. 2.3.3 for a certain parameter m_i, but specifically for the jth model response obtained at the kth position. $\sigma_{j,k}$ denotes the standard deviation of the jth model response obtained at the kth position and $\max_k \sigma_{j,k}$ corresponds to the maximum of the standard deviation of the jth model response obtained from all of the considered positions. Contour plots may be constructed via interpolation after getting $S_{T_{i,j,k}}^*$ in each of the grid points, allowing for improved visualization and explanation of the data. In terms of planning an experimental setup, the contour plot areas with the greatest values of $S_{T_{i,j,k}}^*$ are the optimum places to install sensors of the matching response type j. The various values of $S_{T_{i,j,k}}^*$ should be employed as objective function weighting factors w_i in the cost functions defined by Eq. 2.28.

2.3.4.2 Bayesian OED

For several decades, applications of Bayesian updating have been applied in various fields. Miro [68] and Nguyen [78] employed Bayesian interference to update 3D simulation models of tunnel excavations. The uncertainty of the prior estimation of the soil parameters is therein reduced stepwise using measurement data that is obtained after each new excavation step of the tunnel, but each time affected with artificial random noise. As the measurement data used for back calculation is at the same time an extension of the current data knowledge, one might be interested to "update" the previous knowledge. This concept was first formulated in [7] as

$$p(m|y) = \frac{p(y|m) \; p(m)}{p(y)}. \tag{2.35}$$

Herein, $p(y)$ describes the probability distribution function (PDF) of model output that is used to normalise the result. Here, this would typically be noisy measurement data

$\tilde{\mathbf{y}}$ that is somehow distributed around its mean value $\bar{y}$. $p(m)$ accordingly is the PDF of the model parameters. These would usually be soil parameters that are often very uncertain in geotechnical engineering. Within the Bayesian concept, this distribution $p(m)$ is called as "prior knowledge." Accordingly, $p(m|y)$ is called the posterior knowledge as it includes the new information y. The link between prior and posterior distribution is the likelihood $p(y|m)$ that describes how probable the new data y is, given the known probability distribution of m.

2.3.5　Case Study: The Metro Line 5 in Milan

The Metro Line No. 5 in Milan is selected as an exemplary realistic case study to show the use of previously mentioned approaches. This route, which runs from the north to the west of the city, is composed of 2 12.6-kilometer tunnels with a center-to-center distance of 16.7 meters between them. The first tunnel was completed in May 2012, and the second tunnel was completed a month later in June. The outside diameter of the tunnel tubes is $D = 6.7$ m. Tunnel excavation was carried out utilizing EPB machines (tunnel boring machine with earth pressure balance shield). In the segment under consideration, the tunnel axis is 15 meters below ground level. [24] developed an FE investigation to analyse the soil-structure interaction behavior that is induced by the construction of the twin-tunnel. This simulation of three soil layers using the HSsmall model [8], was used in our study as well. The subsoil consists of a 20-meter-deep gravelly sand layer, lies beneath a 5-meter-thick sandy silt soil layer, according to the geotechnical soil research. Finally, a gravelly sand with a thickness of 5 m (i.e. 25–30 m below ground level) was discovered. For the finite element simulation, drained conditions are considered because of the high permeability of the soil (gravelly sand). This model was created with the FE-code Plaxis 3D and is presented in Fig. 2.24 without the soil clusters. Table 2.2 lists the soil parameters derived from the soil study and subsequent laboratory testing, as reported by [23, 24]. The considered twin tunnel is excavated in an urban area and partially underpasses a nine-story building. The building that is specifically considered in this model is selected because an extensive monitoring program has been applied to it. Figure 2.25 depicts the building's location and relationship to the two tunnel tubes. The shallow foundation of the residential structure comprises five strip footings and intermediate concrete slabs. With a height of 0.65 m, the strip footings are placed around 4 m below ground level. Figure 2.25 also shows the monitoring arrangement, comprising 13 sensors placed throughout the building. The sensors capture local vertical displacements. At the same time, the location of the TBM, applied face pressure, and grouting pressure are recorded. This allows the numerical model to be validated, as well as, to some extent, the outcomes of an OED procedure.

　　The ultimate goal of design, monitoring, and back calculation is to prevent compromising the integrity and serviceability of subsurface and above-ground structures. If an appropriate model that can very accurately anticipate building behavior is produced, countermeasures that lead to improved building safety may be more effectively assessed. As
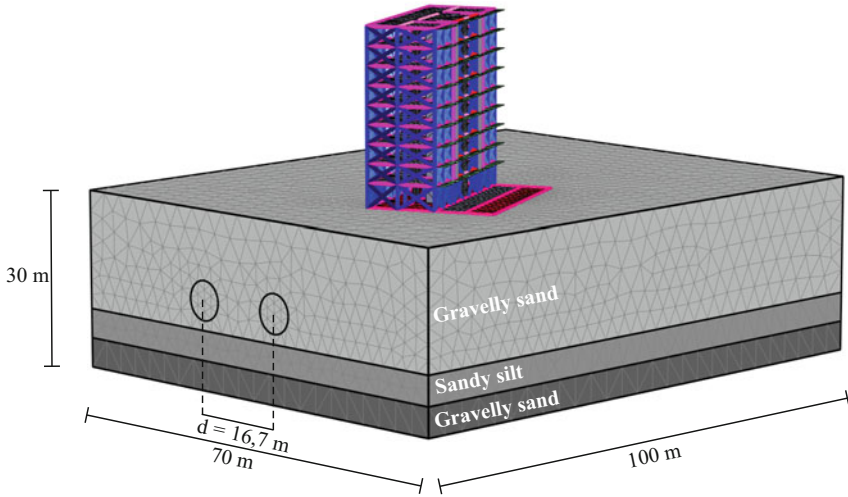
Fig. 2.24 FE model of considered interaction of twin tunnel bypassing the nine-storey building, [103]
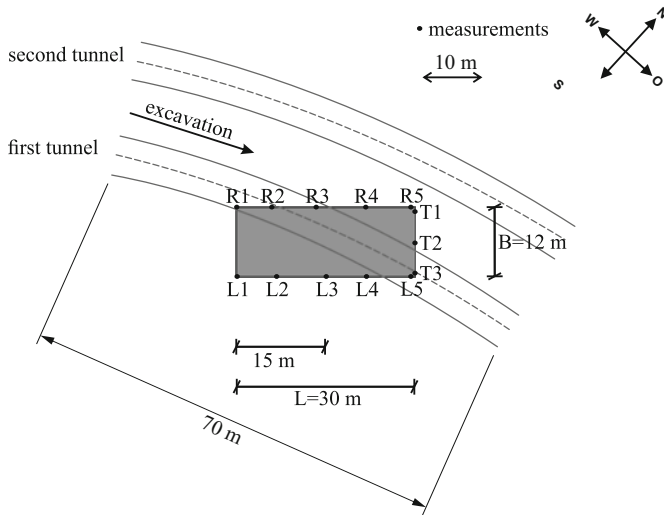
Fig. 2.25 Top view of the considered building and location of applied measurement points [103]

Parameter (description)	Gravelly Sand	Sandy Silt	Unit
γ (Total unit weight)	20	17.5	kN/m^3
Φ (Friction angle)	33	26	°
c (Cohesion)	0	5	kPa

Table 2.2 In-situ soil parameters according to [24]

a result, the goal becomes to produce a trustworthy model by identifying the important soil features using the approach of back analysis outlined in Sect. 2.3.1, which will benefit from incorporating OED principles.

In the previous studies by the authors, e.g., in [103] the in-situ measurement data were employed to back-calculate the constitutive parameters of the surrounding soil. In that study, the grouting pressure p_v and face pressure p_s, the site-related volume loss factor V_L, the friction angle φ_1, the small-strain stiffness $G_{0,1}$, and the secant stiffness $E_{50,1}^{ref}$ of the first and the second soil layer, $E_{50,2}^{ref}$ were evaluated to be the most important parameters. It should be noted that the secant stiffness E_{50}^{ref} is supposed to be associated with the tangent stiffness E_{oed}^{ref} and the unloading-reloading stiffness E_{ur}^{ref}, by a factor of three. When the term "stiffness" is used in the following, it refers to those three factors. Only the measurement data received until the first tunnel tube is completed is used for model validation, so that a forecast for the excavation of the second tunnel tube may be made and compared to the measurement data. As a consequence, the findings shown in Fig. 2.26a, are achieved. The measured settlements obtained after excavation of the first tube in the thirteen measurement points shown in Fig. 2.25 are displayed here, along with the settlements that correspond to the identified parameters using the actual FE-model and the corresponding metamodel. The determined set of parameters is utilized for subsequent experiments and for the prediction of the settlements produced by the excavation of the second tube, as illustrated in Fig. 2.26b. The findings of the FE-model are compared to the data when the second tube is completed. With the exception of R4, T1, T2, and T3 points, there is still a strong agreement. One should keep in mind that, in the considered urban region, there are other buildings just adjacent to the one being studied, that produce pre-stressing of the subsoil and consequently an increase in stiffness, resulting in the lower settlements observed in reality.

Several GSAs are done in [103] to gain a better knowledge of the system behavior, linking the aforementioned soil and system characteristics to average settlements and tilting along different axes of the building. The results of the GSAs performed following excavation of the first and second tunnel tubes are presented in Figs. 2.27 and 2.28, linking the seven examined input parameters to the vertical settlements of each of the thirteen measurement locations. When looking at the shown findings, it is clear that they change with time and space, but that the parameters $E_{50,1}^{ref}$, $G_{0,1}$, and V_L have the most impact on the analyzed outcomes. As a result, all subsequent research, have focused only on these three parameters.

In a further step, a second GSA was run for the previously discovered key parameters to examine the evolution of the sensitivity of the model response in time and space domains with respect to each of the key parameters defined from GSA. The main idea of spatial GSA as a tool for OED concept is introduced in [37]. This GSA is used in the same way as previously to find geometrical sections that are particularly promising for sensor positions, but with the output values of different places in the relevant area. Schoen et al. [102] analysed the spatial and temporal variations in the sensitivity of different parameters in various construction stages, namely during the passage of first tunnel, at the end of

Fig. 2.26 Comparison of measured and **a** back-calculated data of first tunnel excavation and **b** measured and predicted data of second tunnel excavation [33]
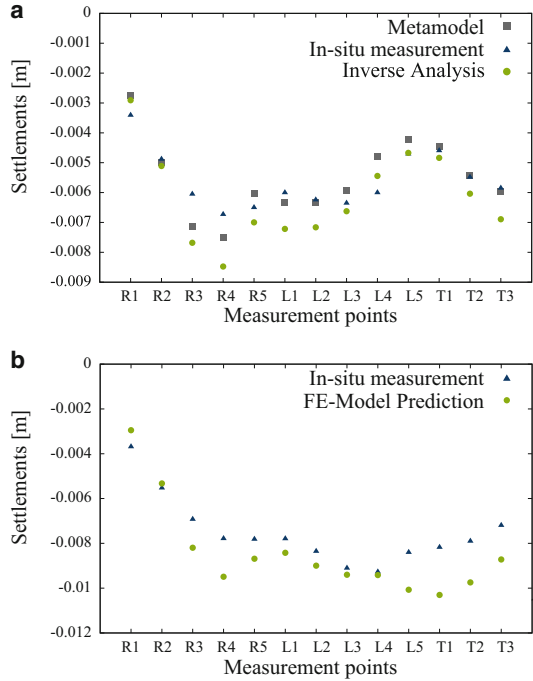
Fig. 2.27 GSA results utilized in thirteen measurement places to examine the influence of the seven factors of interest on settlements after the first tunnel tube was excavated [33]
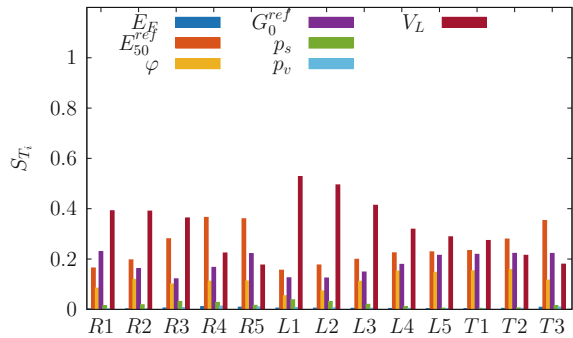
Fig. 2.28 Results of GSA applied in the thirteen measurement points considering the impact of the seven parameters of interest on the settlements after excavation of the second tunnel tube [33]
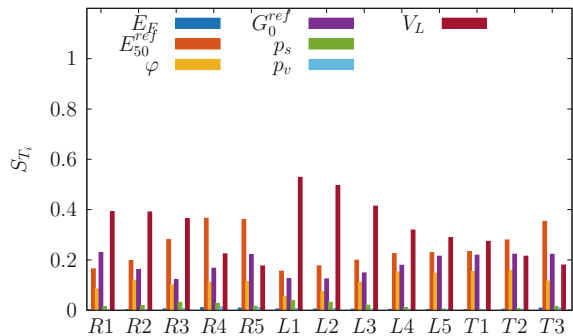
excavation of the first tube, and finally when both tunnels are bored. They concluded that the influence of the secant stiffness E_r^{ref} on the settlements increases with progress of the tunnel excavation. Moreover, V_L has a high influence on the settlements around the TBM as surface settlements are directly related to the volume loss. Zhao et al. [125] also showed that the sensitivity of the volume loss V_L depends on both the location of the TBM, and the magnitude of the surface loads above the tunnel. The spatial GSA findings reveal that the impact of each input parameter changes geographically and temporally depending on the excavation time step and location. As a result, the usefulness of monitored data for parameter identification changes depending on the position of the sensor and the period of monitoring. Therefore, in parameter identification process, it is far more necessary to utilize data from those sensor locations that are particularly impacted by the respective input parameter at the most. Afterwards, the GSA findings are utilized as weighting factors for each monitoring spot and each input parameter in the cost function for back analysis. These weighting variables are chosen based on spatial GSA results to provide more weight to those measuring places where the effect of the corresponding input parameter is considerable, and significant tunneling-induced settlement can be accurately recorded. Therefore, their values vary in different construction phases. Including these weighing factors in the back analysis improves the simulation model's accuracy, bringing it closer to the in-situ records.

Continuation of this research in relation to monitoring optimization, Hölter et al. [36] employed the introduced Bayesian OED using the Approximate Coordinate Exchange (ACE) in Sect. 2.3.4 to use obtained prior knowledge for improving the further searches. After excavating the first tunnel tube, the vertical settlements are acquired at a grid of locations separated by 5 m within the constraints of the employed FE-model. Latin hypercube sampling technique is used to build a sample set of 120 combinations of the three parameters of interest, to generate a metamodel for the FE-model. The metamodel is generated based on quadratic polynomial regression, allowing the settlement result to be received in any of the 259 parameter combinations. To calculate settlement data between these points, the polynomial interpolation approach described in [2] is used.

It is specified that six sensors should be located in this region. Because each sensor location may be swapped in both dimensions of the surface, determining the ideal design $\boldsymbol{\delta}$ becomes a twelve-dimensional optimization issue. To begin, a random 6×2 matrix inside the provided geometric limits should be simply constructed. It should be noted that the initial design $\boldsymbol{\delta}_0$, which determines where the ACE algorithm begins its search, has a significant impact on the method's performance. For example, if certain places of the model's boundaries which are not affected by the building or tunnel excavation at all are chosen, the calculations result in high utilities and the model reaction will always be the same. Accordingly, none of the investigated current designs is accepted as new best design $\boldsymbol{\delta}^{\dagger}$ and the initial design $\boldsymbol{\delta}_0$ is always kept. As a result, it is reasonable to position the starting coordinates of the six sensors anywhere within the tunnel's area of impact, such that the different back analysis runs result in varying responses of the utility function u.

Fig. 2.29 Initial design δ_0 and final design δ^* of the Bayesian OED mapped over displacement field of the ground surface. The position of the building is shown in black [59]
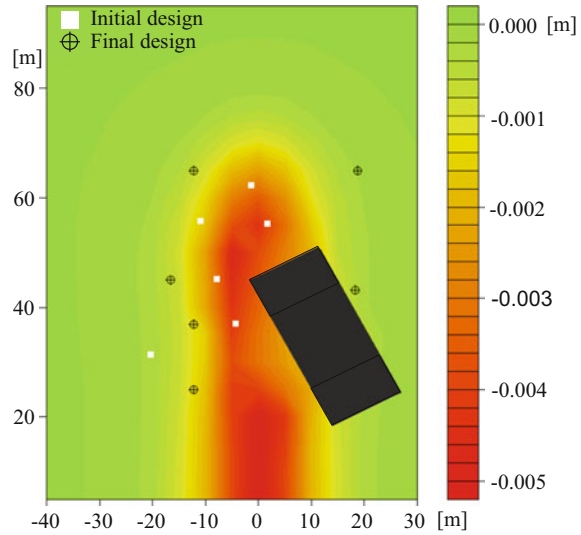
The obtained results are shown in Fig. 2.29. The settlement at the ground surface in the whole model domain is illustrated as a contour plot between red and green for one typical parameter combination, with the position of the building noted as a black block. The locations of the sensors in the first design δ_0 are represented by white squares. They are clearly located in locations where big settlements occur for the reasons stated above. The black crossmarks represent the ultimate design to which the algorithm converges, i.e. the design with the highest utility. The black markings may be seen moving away from the initial design and towards the border of the settlement basin. It should be noted here that the settlement distribution refers to a single arbitrary realization of the input parameters **m**. The settlement distribution may be broader or smaller for various combinations. The resulting sensor configuration does not correlate to a specific set of parameters, but it is expected to be the most reliable throughout the studied range of values.

2.3.5.1 Reliability Measures Updating

As mentioned before, engineers use inverse analysis techniques to increase the dependability of proposed infrastructure projects such as mechanized tunnels by evaluating the uncertainty propagation of soil parameters using recorded data. During different excavation phases, the excavation-induced settlement of the surface structures impacted by tunneling projects is commonly monitored. However, the strength characteristics of geomaterials, on the other hand, shows spatial variability owing to their natural origin. Model adaptation, which is primarily concerned with using previously acquired dataset in further prediction, may be used to precisely analyze the impact of uncertainties on dependability measurements. In this study, a recently developed approach for Bayesian updating of reliability is used while applying random field techniques to account for the geographical

variability of the subsoil. The revised reliability measures may be calculated. They can be used to identify the right steering settings or to select adequate countermeasures in order to minimize long-term damage.

In this procedure, the spatial random variables are adjusted depending on the measured data from the mid-term excavation phase. After that, the updated dependability metrics for subsequent phases are being estimated. The introduced method is applied on the finite element simulation of the twin tunnel project introduced in 2.3.5. The collected findings demonstrate how the reliability update concept may be used to determine the long-term viability of an initial geotechnical design for a mechanized tunneling project.

2.3.5.2 Random Field

In general, mechanized tunneling is often regarded of as a massive geotechnical project over a broad region. Almost all attributes of subsoil must be handled as heterogeneous materials owing to variation in lithological composition, stress history and sedimentation, weathering and erosion, probable faults and fractures. As a result, for every stochastic analysis, peculiarities of the spatial distribution of geological and geotechnical should be characterized and taken into consideration.

Regression analysis, geostatistics, and random field theory are three basic kinds of statistical approaches for estimating spatial variability that have been established. Regression techniques presume that all sample values within a medium have an equal and independent probability, i.e., that they are not autocorrelated, which contradicts field observations show that samples obtained closer together have a larger association than ones taken further apart. As a result, regression approaches are better suitable for preliminary analysis when just a small number of samples with wide distances between them are collected from the site [87]. However, the autocorrelation approach in geomaterials is taken into account in the other two categories.

Here, the Karhunen-Loève expansion method, which is extensively utilized in random field theory, is applied [29, 109]. The spectral decomposition of the covariance function is used in the Karhunen-Loève expansion, which may be written as

$$\hat{H}(x,\theta) = \mu_H(x) + \sigma_H(x) \sum_{i=1}^{M} \sqrt{\lambda_i \; \Phi_i(x) \; \xi_i(m)}. \tag{2.36}$$

The eigenvalues and eigenfunctions of a Fredholm integral equation, where the autocovariance function (i.e., autocorrelation function multiplied by the variance of the random field) is specified as a kernel, are λ_i and $\Phi_i(x)$, respectively. The mean and standard deviation are represented by $\mu_H(x)$ and $\sigma_H(x)$, respectively. M is the number of series terms in the equation, and $\xi_i(\theta)$ is a vector of uncorrelated random variables that represents the unknown parameters' randomness. This vector will be subjected to modifications in a Bayesian way later on in the model adaptation context. The further details regarding random discretisation can be found in [61, 63]. A random field discretisation example of Elastic modulus is shown in Fig. 2.30.
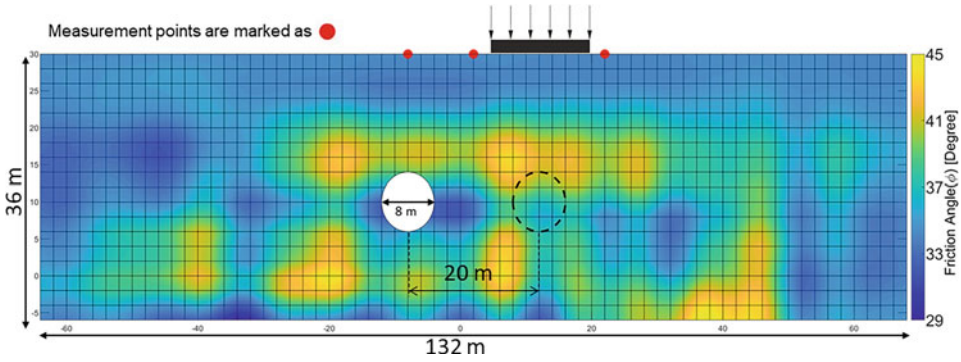
Fig. 2.30 Random field exemplar

2.3.5.3   Bayesian Back Analysis

With a given performance function G_x, the failure event is defined as

$$P_F = P[G_x \leq 0] = \int f_{(x)} \mathrm{dx}, \tag{2.37}$$

where $f_{(x)}$ is the joint probability density function of x, x being the vector of uncertain input variables.

Straub [106] presented the Bayesian back analysis approach, which is used here.

Employing the aforementioned Milan Metro tunnel in Sect. 2.3.5, Mahmoudi et al. [59], performed a reliability analysis at the end of the second tunnel excavation, merely considering the spatial uncertainty of material parameters. Afterwards, the Bayesian reliability updating concept is utilized to take into account the settlement recording at the end of first tube excavation. The ground measurement is assumed to be recorded equal to 12, 9 and 2 mm at the measurement point from left to right after the excavation of the first one is completed. These values are less than average amounts observed for the homogeneous cases. Figure 2.30 depicted a typical random field discretization generated by Karhunen-Loe've expansion. The spatial arrangement of random field will be changed after applying the Bayesian updating technique. The results show a particular change in the reliability measures prediction through considering the mid-term measurements. In addition, the effect of the arrangement and accuracy of the sensors on the reliability measures were investigated. Table 2.3 shows the change in the failure probability indices before and after Bayesian updating. Here the Mid-term measurement represent the monitored ground settlement at the middle of two tunnels. The considered error for the measurement is noted by σ_m, the updated reliability index and correlated probability of failure were shown by β and P_f, respectively. The reader is referred to [59] for detailed information about the applied techniques to obtain the reliability measures and updating them.

Table 2.3 Reliability measures updated by mid-term measurement

Mid-term Meas. (mm)	σ_m (mm)	β	P_f
Without Meas.	–	2.29	0.011
5	1	3.09	0.001
12	1	2.25	0.012
12	2	1.4	0.078
15	1	0.96	0.168

2.3.6 Pattern Recognition

Geotechnical construction has historically employed sensing technology for a variety of objectives, including identifying geological irregularities, health structure monitoring, and ensuring integrity. Using common instruments in geotechnics as e.g., strain gauges, load cells or piezometers, a vast amount of data in the form of time series will be provided, specifically, in large projects like tunneling. The high dimensionality and feature correlation of large time series databases, along with noises, is an evident challenge when studying them. This challenge can be overcome by using automated pattern recognition algorithms to time series for translating a dataset representation of an item or relationship to an output category. The data logs of pore water pressure and ground settlements recorded by a TBM during tunnel excavation are assessed in this work. Due to the different stress distribution in the soil domain as a result of different geological formation, the resultant vertical displacements and water pressure logs may vary substantially during tunneling. As a result, the changes in sensor data trend or motif may be identified and labeled across different geological conditions through supervised learning methods. Pattern recognition is referred to as a supervised learning process when a given pattern is assigned to one of the pre-defined classes using pre-labeled data to construct a model. A supervised machine learning (SML) algorithm can identify correlations and patterns in the fluctuation of observed data and correlate it to potential geological formation changes.

The Support Vector Method (SVM) [17], is used in this work as a well-known approach for conducting SML. Several scholars have used SVM in geotechnical engineering problems, tunnel excavation design, and reliability analysis [38]. Yao et al., [124] used SVM to forecast the displacement of the surrounding rock of a railway tunnel for tunnel safety estimation. Mahdevari et al. [58] used this technique as a nonlinear regression approach to forecast tunnel convergence after excavation. The results of performing SVM and K-Nearest Neighbor (KNN) analysis were presented by the authors in [60]. The learning process in human brains is the motivation for neural nets. A neural network is made up of a linked graph of perceptrons, each of which receives input from previous levels and passes output to subsequent ones. The weight supplied to each individual link, which is determined by the cost function and the optimizer, determines how each layer output becomes the input for the following layer. The ultimate findings of a classification task are really probabilities. The input dataset will be assigned with the label that received the highest probability. A neural network, on the other hand, has a lot of hyperparameters to

adjust. To successfully comprehend diverse datasets, multiple sets of hyperparameters are required. However, the enormous number of hyperparameters makes it difficult to identify their values to achieve an accurate prediction/classification results. Therefore, finding the appropriate settings of hyperparameters to create the model from a certain dataset requires hyperparameter tuning. For instance, the number of neurons, activation function, optimizer, learning rate, batch size, and epochs are the hyperparameters to be modified. Although, there are several techniques concentrating on optimizing the hyperparameter evaluation, the problem of determining the right combination of hyperparameters remains a challenge. In this study, a network for optimization using the stochastic gradient descent learning technique established in [89] is used. It includes five hyperparameters, namely, the number of neurons in hidden layers, epochs, learning rate, batch size, and lambda value. In order to tune these parameters a grid search is conducted.

In the following, the neural network concept as another supervised learning method, is applied to predict any geological distortion ahead of a TBM excavating a 8.5 m tunnel in the depth of 8.5 m. In order to train and validate the network, the gathered data from 10 ground settlement and ten pore water pressure sensors are employed. The details regarding the system configuration is explained by the authors in [88].

In order to measure the accuracy level of trained neural network, various indications can be used, namely accuracy, recall, precision and F1-score. They can be obtained as

$$\text{Accuracy} = \frac{T_P}{T_S}, \tag{2.38}$$

$$\text{Precision} = \frac{T_P}{T_P + F_P}, \tag{2.39}$$

$$\text{Recall} = \frac{T_P}{T_P + F_N}, \tag{2.40}$$

$$\text{F1-score} = 2\frac{1}{\frac{1}{\text{Precision}} + \frac{1}{\text{Recall}}}, \tag{2.41}$$

where T_P indicates the number of cases in which machine predicted the right class, and T_S is the number of all the validation test data. F_P and F_N denotes the false positive and false negative cases. Regarding multi-class cases as the present study, the precision and recall values are firstly calculated for all the classes, and finally use the mean value as a general metric.

The calculated metrics in various distance between the TBM face and the geological anomaly is represented in Table 2.4. In this neural network, 5% white error is assumed for the pore water and settlement gauges. The obtained results show acceptable accuracy level for all the cases, however, the prediction accuracy increased when the distance decreased.

The highest accuracy in classification, according to the data in [59], belongs to the combination of kriging and KNN, which improves recognition accuracy even when the excavation is taking place at a distance from the anomaly. However, the SVM and neural

Table 2.4 In-situ soil parameters according to [24]

Distance [m]	Accuracy	Recall	Precision	F1 Score
69	76.08	66.69	83.82	74.28
39	83.32	78.52	81.32	79.90
9	84.94	76.85	84.78	80.62
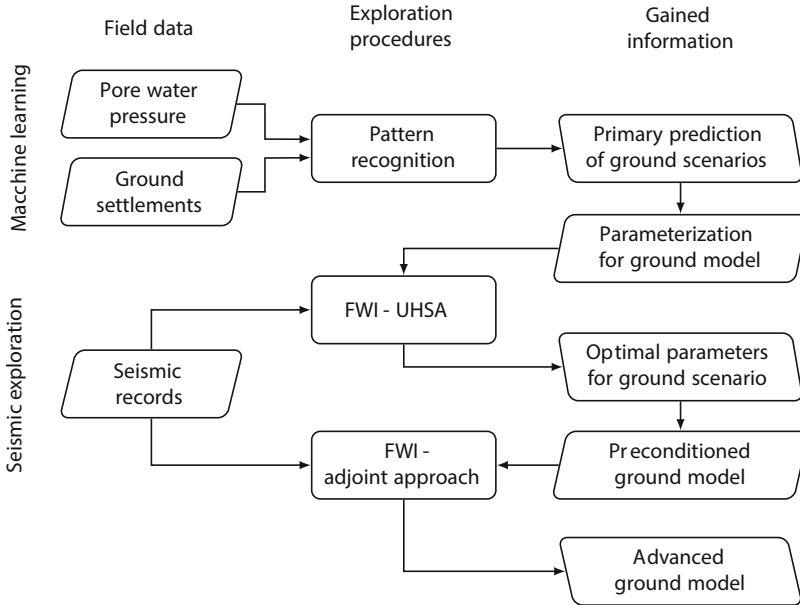
Fig. 2.31 Overview of the three-stage exploration approach. (Reproduced with permission from Elsevier from C. Riedel et al. "A hybrid exploration approach for the prediction of geological changes ahead of mechanized tunnel excavation". In: *Journal of Applied Geophysics*, 203, p. 104684 (2022))

network accuracy is sufficient for scenarios when the anomaly is predicted in the near field, despite the fact that it requires less computing work.

2.4 Three-Stage Concept

The previously explained methods of the current chapter can be combined into one hybrid method to improve the prediction of the subsoil properties as well as to reduce computational demand. In [88], a three-stage concept is presented which combines the pattern recognition approach (Sect. 2.3.6), UHSA (Sect. 2.2.3.1), and the adjoint approaches in time (Sect. 2.2.4) and frequency (Sect. 2.2.6) domain. The concept is shortly explained in the following, where an overview of the three-stage exploration approach is given in Fig. 2.31.

In the first stage, pore water pressures and ground settlements are continuously recorded while the tunnel is excavated. The acquired data is processed by the pattern

recognition approach in order to identify a potential anomaly. To do so, various machine learning algorithms are trained for different scenarios, e.g. a fully homogeneous model, an interlayer, a layer change or a boulder. The applied supervised methods, namely SVM and KNN shown high accuracy to classify the geological condition ahead of TBM, merely based on the monitored settlement and pore water pressure variation. If the SML approach successfully identifies an anomaly, the TBM is stopped in order to perform a seismic survey. Subsequently, the second stage is initiated, which is FWI with UHSA. Here, all available knowledge derived from the SML approach is processed, where the predicted scenario of the SML approach is used to implement a parametrization of the anomaly. UHSA might already bring a sufficient prediction; however, it is probable that some parts of the anomaly are not reconstructed in its entirety because the chosen parametrization might not be able to describe all features. Therefore, the third stage is executed in the form of adjoint FWI, where the final model of UHSA is used as the initial model. Both the time domain and the frequency domain approach can be used in order to finalize the prediction of the subsoil properties and to image further details. In [88], the three-stage concept is successfully tested with synthetic data, where the reference model contains a boulder. Each of the three stages can improve the image of the anomaly and on the basis of the final prediction, the location, shape and material properties of the boulder can be precisely estimated.

2.5 Soil-Shield Machine – Interactions

This chapter summarizes some result from a research focused on identification of ground conditions by analyzing machine data during excavation of shield driven tunnels in soils. The goal of this research is to utilize TBM machine data for estimating soil properties. Particularly data about movement of the cutting wheel and the shield with respect to subsoil conditions have been analyzed. Towards this goal, the geological and geotechnical properties of subsoil have been continuously evaluated and the raw machine data collected at a hydro-shield project. The raw data have been separated between active and passive parameters: Active parameters are set by the operator and include the cutting wheel rpm and pressure of thrust cylinders. Passive parameters (thrust force on cutting wheel, torque on cutting wheel, advance speed and rate of penetration) are the result of active parameters. The latter are termed excavation-specific data components which may serve as an indicator for the influence from the ground's resistance to excavation (ground conditions) and for the influence of the state of the cutting wheel (design of the wheel, state of tool wear and clogging), respectively.

2.5.1 Excavation-Specific Data Components

Table 2.5 distinguishes between excavation-specific and excavation-independent raw TBM data. Those data must be revised for arriving at meaningful interpretations of interactions between a TBM and the ground [22, 32]. For example, the total thrust force F_{Th} of the shield machine (raw data) must be stripped from excavation-independent data as shown in Fig. 2.50 to arrive at data of tool forces F_T to be compared with the soil condition. The detailed procedure is given in [22].

To connect machine data with soil conditions the following should be considered. The penetration rate Pen_{raw} is a target value in shield tunneling and requires a certain contact force F_{con} of the cutting wheel for soil with a given resistance to be excavated. Additionally, the torque at cutting wheel M_{raw} is a function of the specified penetration rate Pen_{raw} and the resistance of the soil to be excavated. It is defined accordingly

- specific torque $M_{spec} = M_{raw}/Pen_{raw}$,
- specific penetration $Pen_{spec} = Pen_{raw}/F_{con}$.

There are some general connections of the resistance of the soil with the specific torque moment and the specific penetration as shown in Table 2.6.

Table 2.5 Excavation-specific and excavation-independent components of machine raw-data

Machine raw-data			
Excavation-specific data components		Excavation-independent data components	
Influence from resistance to excavation	Influence from state of cutting wheel	Technical components	Human components
• Influence from ground conditions (e.g. soil density)	• Design of cutting wheel (diameter, grade of aperture, type of tools) • Actual state of tool wear and clogging	• Influence from friction forces • Influence from face support	• Operator's skills (adjustment of active parameters)

Table 2.6 Tendency of excavation resistance for the main soil types (SPT-values [67, 112])

Soil	Fine-grained soil (clay and silt)					Weak rock, claystone, siltstone
consistency	very soft	soft-medium	stiff	very stiff	hard	
SPT-value (N)	< 4	2–8	8–15	15–30	> 30	
Increase of excavation resistance (increase contact force, decrease specific penetration)						
Soil	Medium to coarse-grained soil (sand and gravel)					Weak rock, sandstone
Packing density	very loose	loose	compact	dense	very dense	
SPT-value (N)	< 4	4–10	10–30	30–50	> 50	
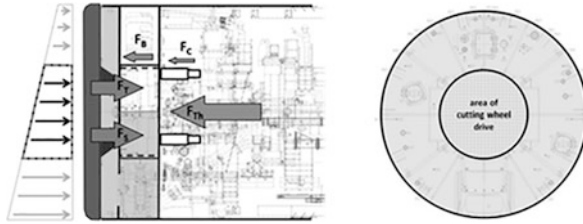
Fig. 2.32 Schematic presentation of forces acting on cutting wheel of a hydro-shield machine: F_T: tool forces; F_S: resulting force of face support pressure acting on area of cutting wheel drive; F_B: internal friction forces of main bearing; F_C: internal friction force of hydraulic cylinders; F_{Th}: thrust force on cutting wheel raw-data [21]

2.5.2 Case Study: Application to a Hydro Shield Project

A reference project, involved a 2.27 km long tunneling project of diameter 9.5 m driven through terraced rubble of the quaternary near the river Rhine is considered. Details about the project, the TBM and the geology and can be found in [21]. The soil consists of sand and gravel as shown in Fig. 2.33.

The raw TBM data were processed as described above and plotted in Fig. 2.34. The wide spread of the specific penetration can be attributed to different geological conditions at the face as shown in Fig. 2.35.

To compare different projects with different shield machines the specific contact force (SCF), which is contact force F_{con} divided by the area of the cutting wheel A_{CW}, is computed. The Force Index FI is introduced as

$$FI = Pen_{raw}/SCF, \tag{2.42}$$

and the Torque Index TI,

$$TI = M_{spec}/A_{CW}, \tag{2.43}$$

and show the plots in Fig. 2.35.
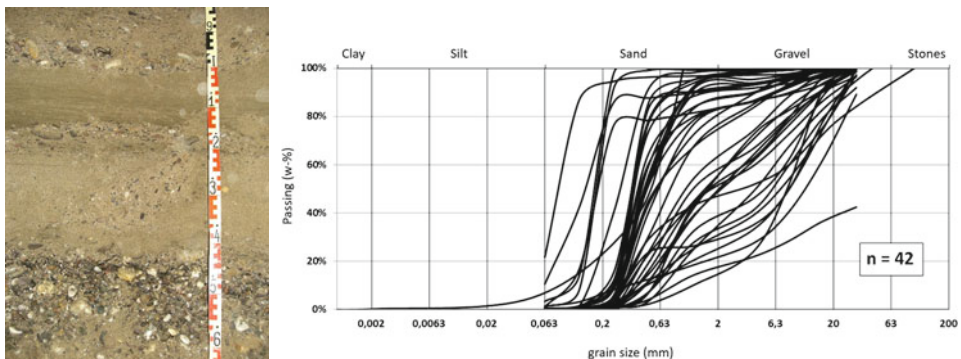
Fig. 2.33 Typical soil (left) and screenlines (right) at the hydro-shield drive [21]
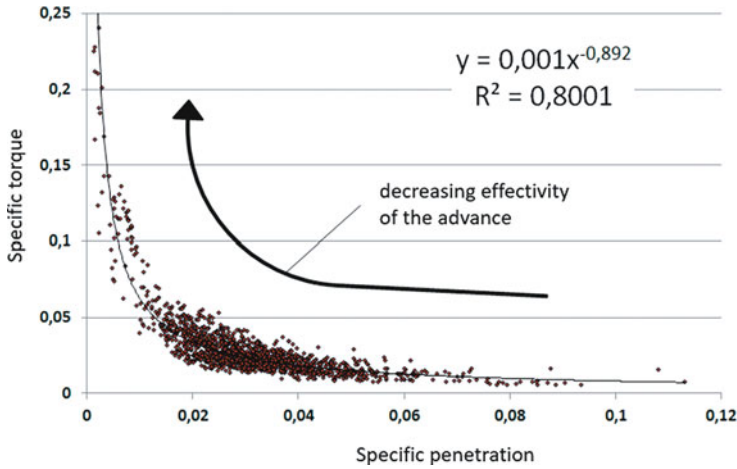
Fig. 2.34 Plot of specific torque vs. specific penetration at the hydro-shield project [21]
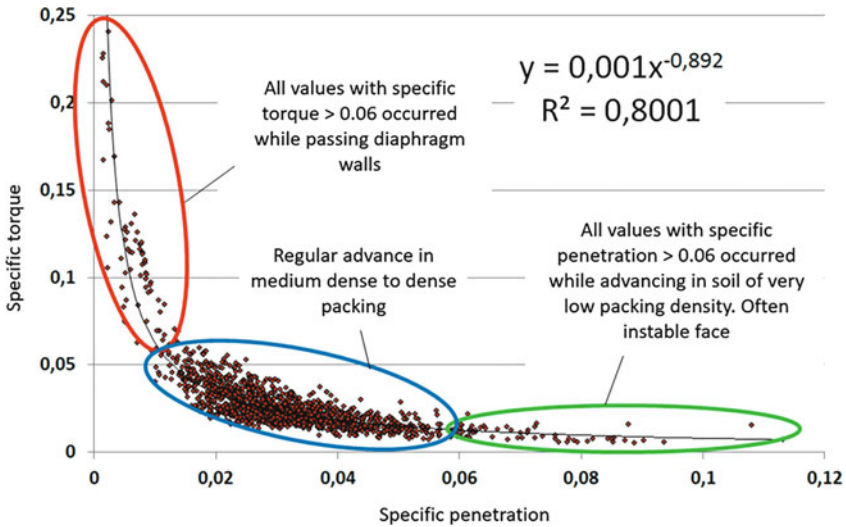
Fig. 2.35 Correlation of data with site conditions [21]

The different lines of the TI-FI plots reflect the different designs of the cutting wheel and TBM specifics. Analysis of the soil conditions at the various projects leads to Fig. 2.36. The torque of a shield TBM is mainly attributed to the shear strength of the soil and contact force is attributed to the packing density or consistency of soil.

For future studies it is possible to employ soil characteristics from site investigation to estimate the magnitudes of FI and TI, respectively. For a given penetration rate (the target parameter) the torque and the contact force of the cutting wheel may be tentatively estimated.
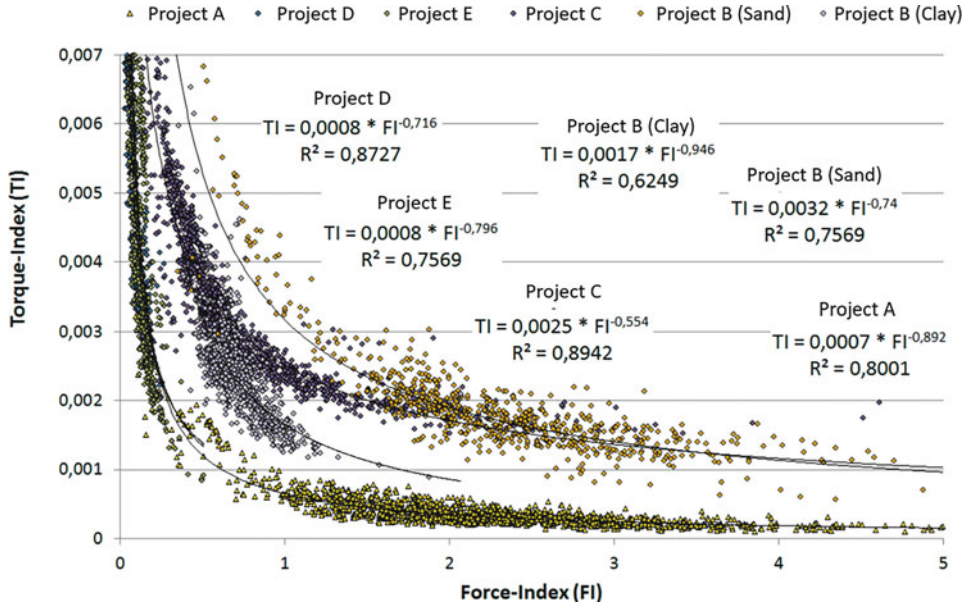
Fig. 2.36 Force-Index vs. Torque-Index plots for a wide range of case studies [21]
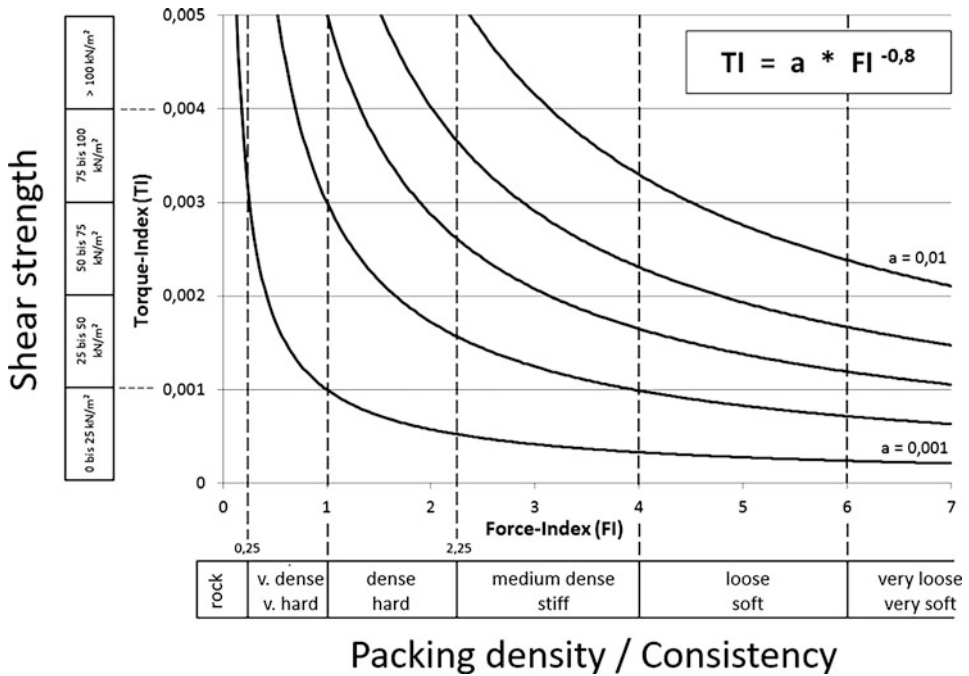
Fig. 2.37 Dependency of the torque index to the force index with respect to the shear strength and packing density [21]

2.6   Monitoring of Building Damages by Radar Interferometry

One important aspect of the settlement damage research was the monitoring of building damages using both traditional terrestrial- and advanced satellite-based monitoring techniques. Also, a combination of terrestrial and extra-terrestrial proved to be of valuable service to TBM operators. Of course, this presupposes proper damage assessment methods with validated mathematical and engineering theories are readily available.

2.6.1   On the Importance of Settlement Monitoring for the Management of Damage for Inner-City Tunnel Construction

The continuous increase in traffic volumes in metropolitan areas gives rise to further construction of underground transport facilities. Typical examples are road or subway tunnels usually driven by mechanized shield tunneling. This trend densifies the traffic facilities in the underground and consequently reduces the coverage of existent building structures [82].

With inner-urban tunneling projects reports on actual or potential damages due to settlements of existing structures often predominate in the press. Such reports unmistakably reflect the concerns of citizens and residents and let problems of acceptance arise that must be expected to extend the construction period already in advance. Thus, in particular the risk of damage to existent structures above-ground comes to the attention of developers and construction companies at an early stage [66].

A look into the past shows that this topic was already taken up in the 1950s when some rudimentary recommendations for the prediction of structural damage were first developed. However, significant influences from the settlement event itself, as well as the building materials and key properties of the structures, were not taken into account. It was not until the 1970s that Burland & Wroth [16] published their approach that is still current today, which made a semi-empirical prediction of potential damages to buildings due to tunneling-induced settlements possible.

Up to now published semi-empirical approaches to compute vertical settlements can be differentiated with reference to Fig. 2.38 into

- transversal 2D-approaches: Peck (1969), O'Reilly & New (1982), New & O'Reilly (1991), and Mair (1996);
- longitudinal 2D-approaches: Attewell & Woodman (1982) and
- 3D-approaches: Attewell (1982).

In addition to its stiffness, the effective displacement of the structure is of central importance in the evaluation of structural damage caused by tunneling-induced settlements. Due to (too) far-reaching simplifications, e.g. with regard to the often highly heterogeneous building stock, the approach according to Burland & Wroth shows deficits that

Fig. 2.38 Spatial extent of the settlement trough due to tunneling [95]
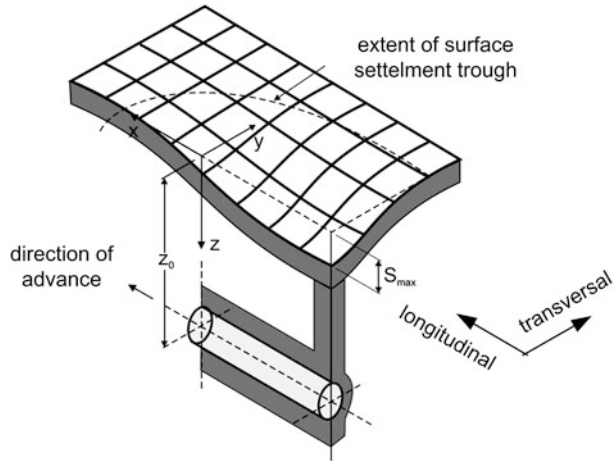
may lead to conservative but also to uncertain evaluation results. In tunneling practice, in particular (too) conservative evaluation results, intended to protect the structures, lead to expensive and time-consuming auxiliary measures (e.g. compensation injections).

2.6.2   Recent Methods of Damage Assessment Due to Tunneling Induced Settlements

Skempton & MacDonald [105] developed the first purely empirical approach to evaluate damages to above-ground structures due to settlements. The evaluation criterion for damages therein are the so-called angular distortions ρ/L or β, i.e., purely shear-based structural deformations. Limiting values of these distortions classify the extent of damage according to Table 2.7.

Burland & Wroth (1974) [16] and Burland et al. (1977) [15] recognized the deficits of a purely shear-based approach and published an enhanced semi-empirical approach to damage assessment, the Limiting Tensile Strain Method (LTSM). The basis of their approach is the transformation of the structure into an equivalent mass-less beam with a shear extension according to Timoshenko (1955) [113]. They recommend the evaluation

Table 2.7 Limits of angular distortions ρ/L or β according to [105]

Extent of damage	Limit for ρ/L or β
Cracks in structures	1/500
Limited cracks in vulnerable masonry structures (historical buildings)	1/1000
Structural damage of the facade	1/150
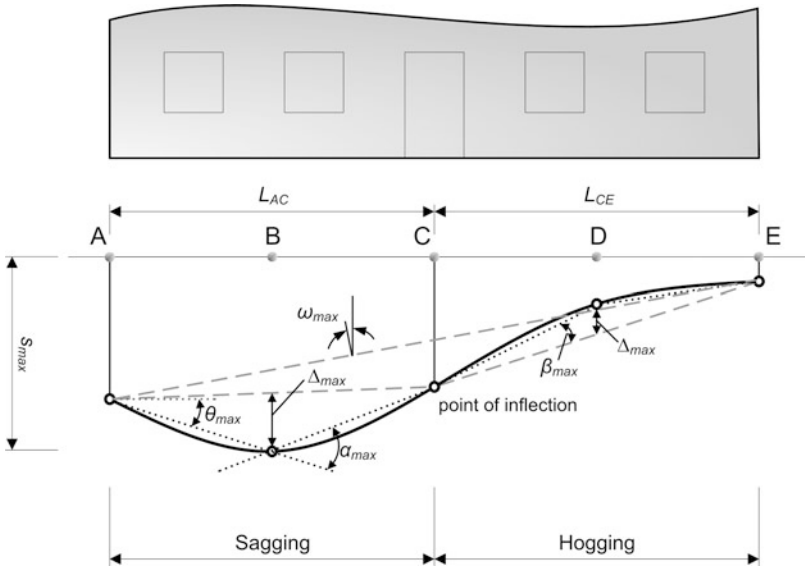
Fig. 2.39 Definition of structural rotation and translation: deflection ratio Δ/L, tilt ω, rotation θ, angular strain α and angular distortion β [95]

of damage by means of the limiting tensile strain $\varepsilon_{\mathrm{lim}}$, which indicates the onset of cracking and is defined as the ratio of the relative deflection Δ of the beam to its length L, the so called deflection ratio (cf. Fig. 2.39). Assuming the neutral axis at the center of gravity of the beam, they derived the analytical equations Eqs. 2.44 and 2.45. Thereby $\varepsilon_{b,\mathrm{max}}$ is the maximum bending strain due to direct tensile loading and $\varepsilon_{d,\mathrm{max}}$ is the maximum shear strain caused by diagonal tensile loading (cf. Fig. 2.40, middle).

$$\frac{\Delta}{L} = \left(0.167\frac{L}{H} + 0.25\frac{H}{L}\frac{E}{G}\right)\varepsilon_{b,\mathrm{max}}, \tag{2.44}$$

$$\frac{\Delta}{L} = \left(0.65\frac{L^2}{H^2}\frac{G}{E} + 1\right)\varepsilon_{d,\mathrm{max}}. \tag{2.45}$$

In Eq. 2.44 and Eq. 2.45, the stiffness of the structure is estimated by the moment of inertia of the equivalent substitute beam with length B, height H, shear modulus G, and Young's modulus E. The dimensions of the structure and the substitute beam are identical. Roof superstructures are not considered in the determination of H (Fig. 2.39). The influence of the estimated bending stiffness EI on the shape of the settlement trough is neglected in their approach, which makes the evaluation of the structural damage again conservative. The green-field settlement trough itself – as the damage-inducing event – can be determined using the approaches from Sec. 2.6.1 [97].
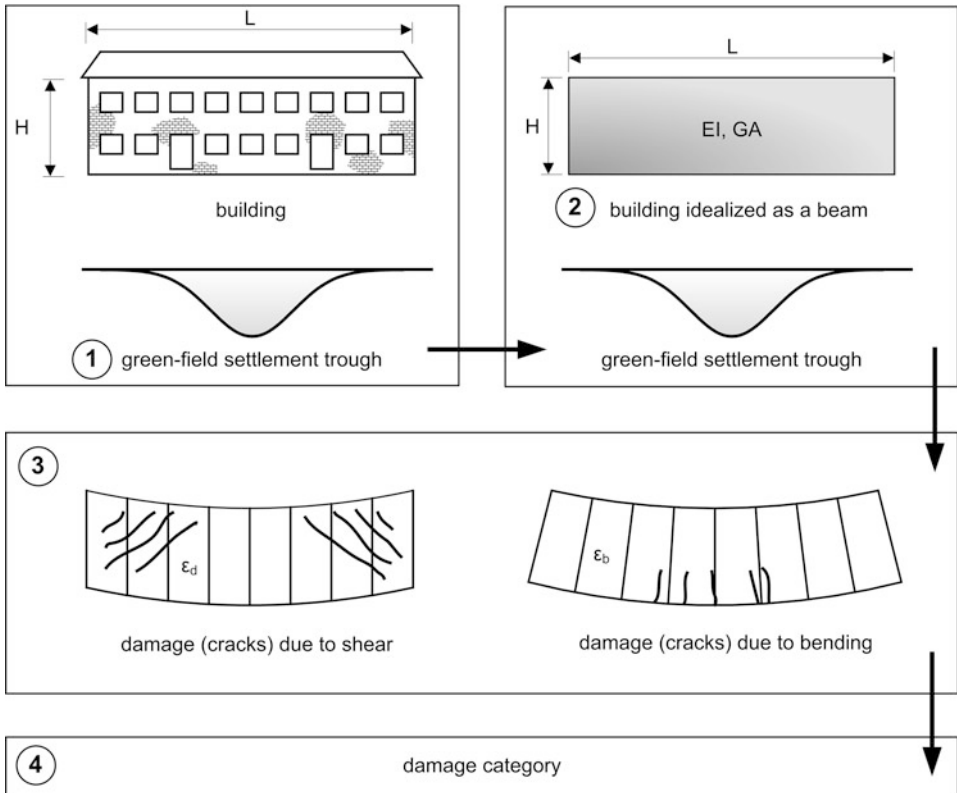
Fig. 2.40 Damage assessment scheme acc. to Burland and Boscardin [95]

The damage categorization proposed by Boscardin & Cording [11] finally relates Burland's limiting tensile strain ε_{lim} to the expected damage at a structure. Moreover, damaging contributions of horizontal strains could be integrated to the LTSM approach which practically comprises four steps (cf. Fig. 2.40):

1. predict the green-field settlement trough,
2. define the substitute beam and apply settlements in green-field conditions,
3. compute bending and shear strains and
4. match the relevant strains to a damage category.

To limit the settlement trough's region of influence, Mair et al. [64] proposed the 1 mm settlement line. For long structures that span several regions of the green-field settlement trough, only those parts within that boundary are to be considered.

2.6.3   Overview and Options for the Monitoring of Settlements

As mentioned above, the two most important approaches to settlement monitoring include traditional terrestrial monitoring and advanced satellite-based monitoring. A strategic combination of terrestrial and extra-terrestrial monitoring proved to be even more advantageous when the synergetic aspects of these methods were exploited.

2.6.3.1   Terrestrial Monitoring

Above all, the risk of damage can be more accurately assessed, controlled, and also predicted by monitoring or surveillance of above-ground structures. State of the art are terrestrial methods that record mainly vertical displacements of structures due to shield driving at the foundation or at the street level (e.g., barometric by tube water leveling). However, three-dimensional monitoring, i.e. the measurement of displacements in all coordinate axes including rotations, among others, with fully automatic total stations (Fig. 2.41), has already been proven suited several times. A recent example is the new metro crossing Amsterdam from north to south, where fully automatic measurement systems were used to monitor the facades of settlement-sensitive historic buildings. Regardless the devices used, all methods must

1. provide a sufficient short measuring cycle,
2. record data reliable over longer time periods and
3. should be highly accurate.

The accuracy of terrestrial methods is usually ± 0.2 mm per 100 m for total stations; leveling (e.g., barometric by tube water leveling) achieves less than 0.2 mm (per 100 m)
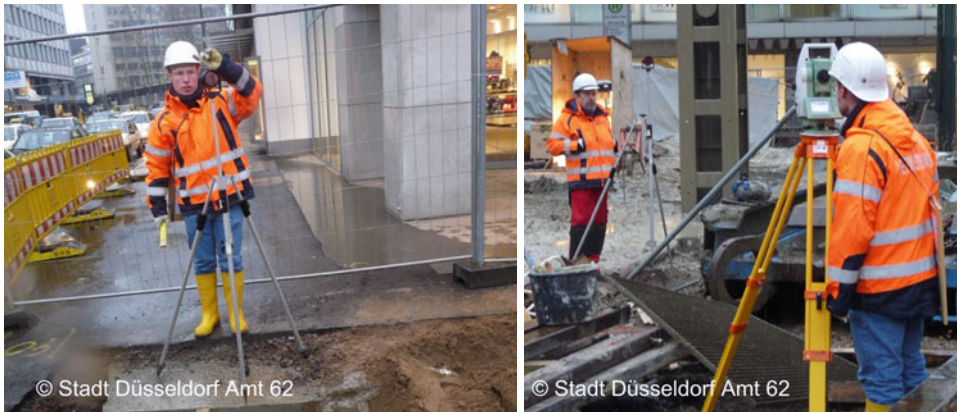
Fig. 2.41 Left: reflector applicable on tripods or an a facade, right: Measurement with tachymeter (total station) acc. to [95]

or up to 0.1 mm. Terrestrial settlement monitoring does not consist of individual measurements, but of the interaction of all (settlement) measurements before, during and after a tunnel construction measure. The boundary conditions and the scope of measurements, including the methods used, are defined in a so-called measurement program. This takes into account the expected settlement sensitivity (vulnerability) of individual structures [66, 82].

2.6.3.2 Satellite-Based Monitoring by Radar Interferometry (Synthetic Aperture Radar, SAR)

Since the launch of the German radar satellite TERRASAR-X, remote sensing systems for settlement monitoring in large urban areas have become competitive due to the increased geometric resolution of the radar system [5]. On-site installations, e.g. in buildings, are no longer required. The method records complex raw data signals (amplitude and phase information) of radar waves (electromagnetic waves) reflected at the Earth surface (Fig. 2.42). Suitable natural radar reflectors are metallic objects or parts of buildings, e.g. a window sill. These are visible as bright spots in the radar image (SAR image, Fig. 2.43). Water surfaces and vegetation in forests or open spaces reflect the radar waves poorly or even not at all and thus stay dark in radar images. Therefore, radar-interferometric settlement monitoring is particularly suited in urban areas. For open spaces, additional measures as installation of artificial reflectors becomes necessary.

The signals recorded by the radar sensor must be spatially and temporally stable to allow for superposition (interference) of two wave signals (coherent radar signals). By com-
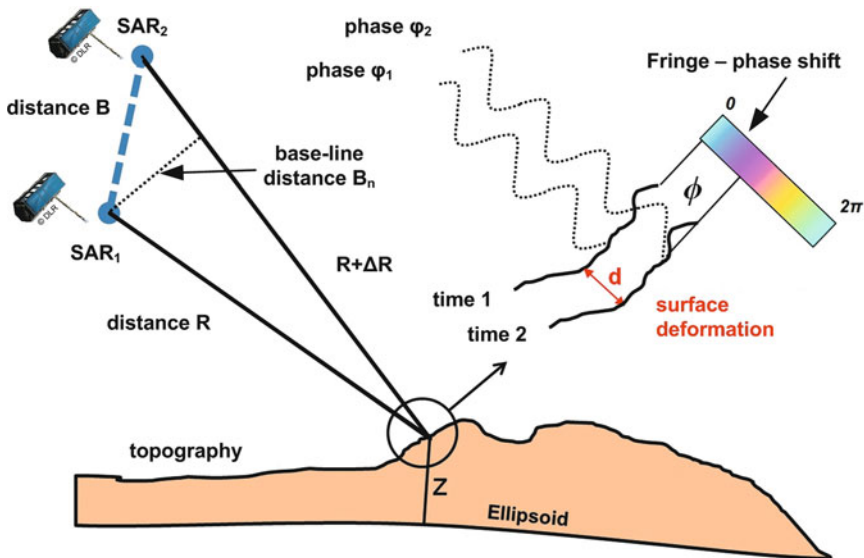
Fig. 2.42 Principle of radar interferometry (simplified) according to [19]

paring two phase positions ϕ_i recorded from slightly different satellite positions (SAR1
and SAR2) at the same position of an object, the interferometric phase ϕ,

$$\phi = \phi_{\text{flat\_Earth}} + \phi_{\text{topo}} + \phi_{\text{disp}} + \phi_{\text{path}} + \phi_{\text{noise}} + n2\pi, \tag{2.46}$$

can be calculated (phase shift). If the other components of the interferometric phase re-
main sufficiently stable, the phase fraction ϕ_{disp} can be used to infer the displacement, e.g.
of a natural radar reflector like a window sill. The displacement is then to be converted
from the satellite's "line of sight" into the sought components of the vertical settlement
or uplift. With the SAR method for acquisition and evaluation, the physically limited res-
olution in azimuth direction is increased by combining multiple images from different
satellite positions.

However, in general, the interferometric phase ϕ is composed of several components
that can have a significant impact on the accuracy of the method. Beside the target de-
formation ϕ_{disp} the further components are assigned to the impact of the Earth curvature
$\phi_{\text{flat\_Earth}}$ and to the height model of the Earth surface ϕ_{topo}. ϕ_{path} and ϕ_{noise} capture pertur-
bations from the atmosphere and noise. With the remaining so-called "phase-unwrapping"
term $n2\pi$ (with $n \geq 1$), portions that exceed a complete wavelength are regarded. If the
expected settlements are larger than the wavelength used, the evaluation becomes com-
plex and erroneous. Further details on the technique used and the procedures (D-InSAR,
PS-InSAR) for the evaluation of radar images can be found in the literature [3, 40].

Comprehensive analyses in [100] prove that an accuracy of less than 1.5 mm (stan-
dard deviation) can be reached with a sufficiently large sample. For the TERRASAR-X
radar satellite the maximum repetition rate today, i.e., the time interval between two sub-
sequent overflights, is 11 days. Thus, live monitoring of settlement data accompanying
the excavation process is not possible yet. But, future satellite missions are already sched-
uled that will reduce the repetition rate down to 4 days by combining several satellites.
The remarkable density of settlement information at so-called persistent scatterers (PS),
i.e. at long-term stable natural or artificial radar reflectors, amounts to approximately
$25{,}000\,\text{PS/km}^2$ in inner-city regions.
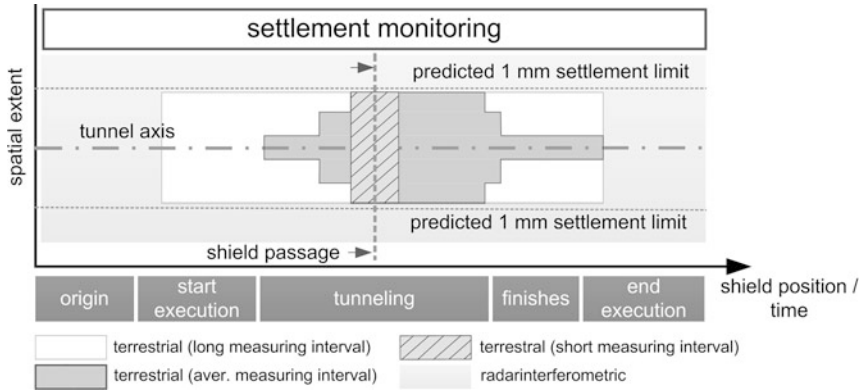
Fig. 2.44 conceptual combination of terrestrial and radar-interferometric techniques in tunneling and its spatial coverage acc. to [19]

2.6.3.3 Combination of Terrestrial and Extra-Terrestrial Techniques

If the advantages of both terrestrial and radar-interferometric methods are strategically combined, both performance and cost-effectiveness can be significantly increased. This also comprises the advantages of the satellite-based method in terms of gathering evidence. Without on-site installations, depending on the spatial resolution of the radar image on the ground, the monitoring region can be expanded almost at free will and without great additional expense. A potential combination of both methods is shown in Fig. 2.44.

The fundamental principle is the reduction of terrestrial measurements in favor of radar-interferometric settlement monitoring. In the close range of the tunnel axis, terrestrial measurements are still indispensable at the time of the shield passage, since short measurement intervals are urgently needed for checking the alarm or threshold values. This is different in the long-distance range in space as well as in time, areal satellite-based methods are preferred which require some time for stochastic evaluation of several overflights. The best division of regions for terrestrial and radar-interferometric methods finally depends on the topology, the geology, the damage risk of existent buildings and potential compensation measures [98].

2.6.4 Data Handling and Visualization Techniques

Besides the actual settlement monitoring, visualization plays a decisive role [30]. Visualized in space and time, critical conditions such as torsional deformations when underpassing structures in parallel are recognized easier. Then, countermeasures can be taken more quickly and in a targeted manner. Numerous commercial data management systems offer closed solutions for visualization. This holistic and visual settings allow settlements to be interpreted significantly easier. Visualization supports different perspectives, provides fading of additional information and various zooming options for detailed viewing.

Fig. 2.45 VR-Lab at the Ruhr-Universität Bochum, Germany

Time-related data such as settlement data can be animated which offers a high degree of interoperability between users. At best, a three-dimensional presentation of the results in a virtual reality (VR) environment supports the aforementioned analysis options (Fig. 2.45).

Virtual Reality offers the possibility of creating a realistic computer-generated three-dimensional and dynamic image of the reality. The generation takes place in real time and can be converted to the user's viewing angle. To perceive the 3D effect, tools such as shutter glasses are required. A so-called flystick enables navigation. Both components can be tracked to account for the current position and viewing direction of the user in the computation of the image and perspective (Fig. 2.45).

If data is not only to be visualized but also made available for further analyses, e.g. for FE computations, integral product models on a BIM (Building Information Modeling) and IFC (Industry Foundation Classes) basis are needed [96]. Figure 2.46 exemplifies the

Fig. 2.46 Integral product model for visualization of soil (bore holes), ground water level, tunnel, tunnel boring machine, above ground infrastructure and settlement data obtained from radar interferometry [96]
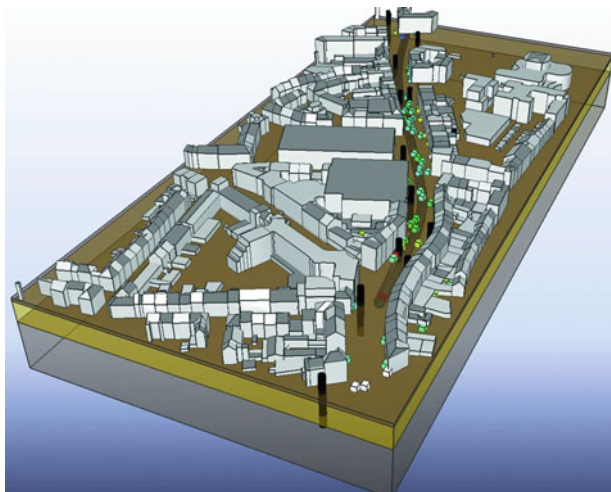
visualization of structures, tunneling, settlement data and the soil during construction of the Wehrhahn line in Dusseldorf, Germany [30].

2.6.5   Case Study: Wehrhahn line in Dusseldorf

The Earth-observation TERRASAR-X satellite of the German Aerospace Center (DLR) was launched in June 2007 to provide high-quality radar images from an altitude of 514 km. In the best available mode (Spotlight) the spatial resolution is about 1×1 m [28]. However, in the region of interest (Fig. 2.47), the tunnel construction site in Dusseldorf, Germany [30], another mode (Stripmap) with a resolution up to 3×3 m was used.

Results of displacements monitoring   To monitor displacements of existent infrastructures induced by tunneling a set of 16 TERRASAR-X images are evaluated, gaining already high density of persistent scatterers. A block of buildings near the starting shaft (Fig. 2.48 and 2.49) illustrates the settlement effects in a very clear way. It is especially appropriate, as the tunnel boring machine undergoes the buildings with only a small overburden between tunnel roof and existent foundations. Moreover, extended initial ground injections are arranged here to "prestress" the remaining ground and compensate subsequent settlements.

Results of uplift monitoring   To monitor the process of intended uplift by injections and the following settlements a conventional rubber tube leveling system was established at the foundations of the buildings close to the tunnel. The terrestrial data is used to verify and calibrate the satellite data in space and time. For this purpose terrestrial and PS measuring points are geo-referenced in identical coordinate systems and superimposed on the 3D terrestrial laser scan model of the intra-urban area (Fig. 2.49) including positions on roofs, facades and the ground surface.
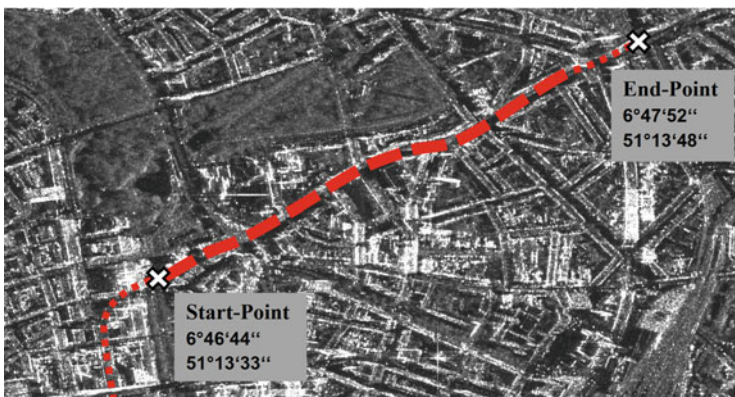
Fig. 2.47   Radar-Image and tunneling axis (Dusseldorf, Germany) [99]
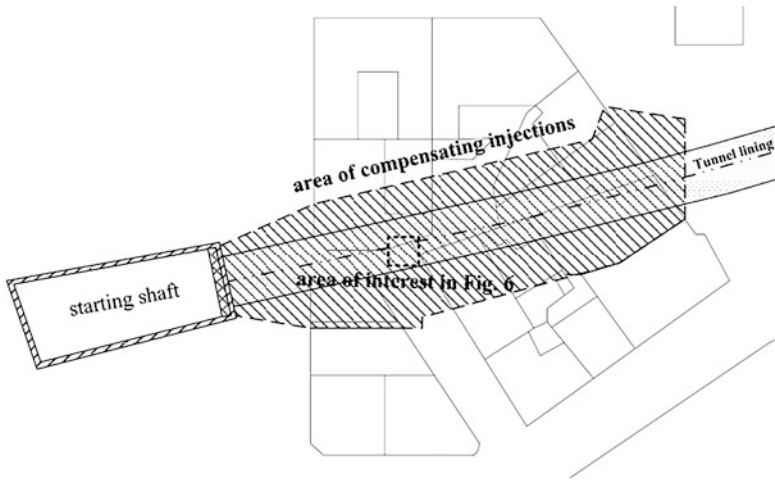
Fig. 2.48 Tunnel lining and region of compensating injections [99]
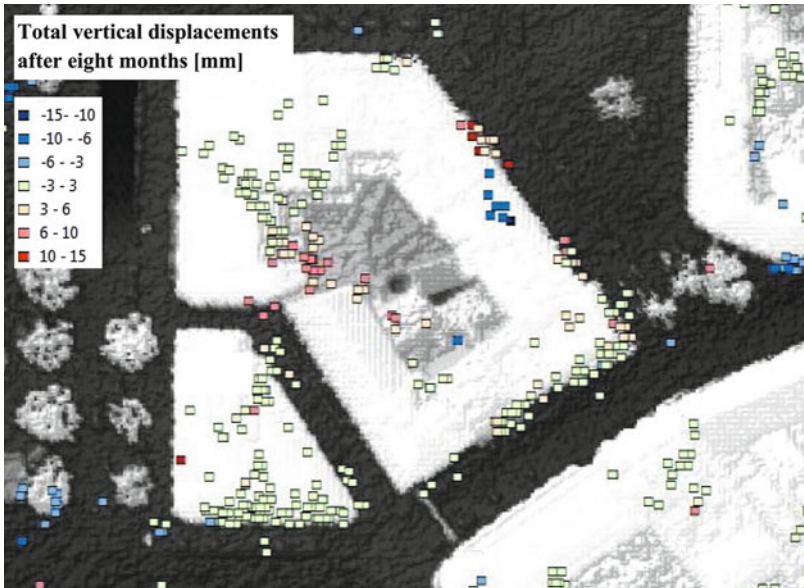
Fig. 2.49 Distribution of persistent scatterer along with displacements after eight months [99]

Figure 2.50 shows a representative time-series of displacements obtained from PS measurements compared to terrestrial values close to the PS points. All values are related to initial values prior to the tunneling workout to ensure an overall identical basis. The vertical ground movements derived from the PS-InSAR technique correspond very well to the terrestrial values. This especially holds true, if the very small extents of movements in
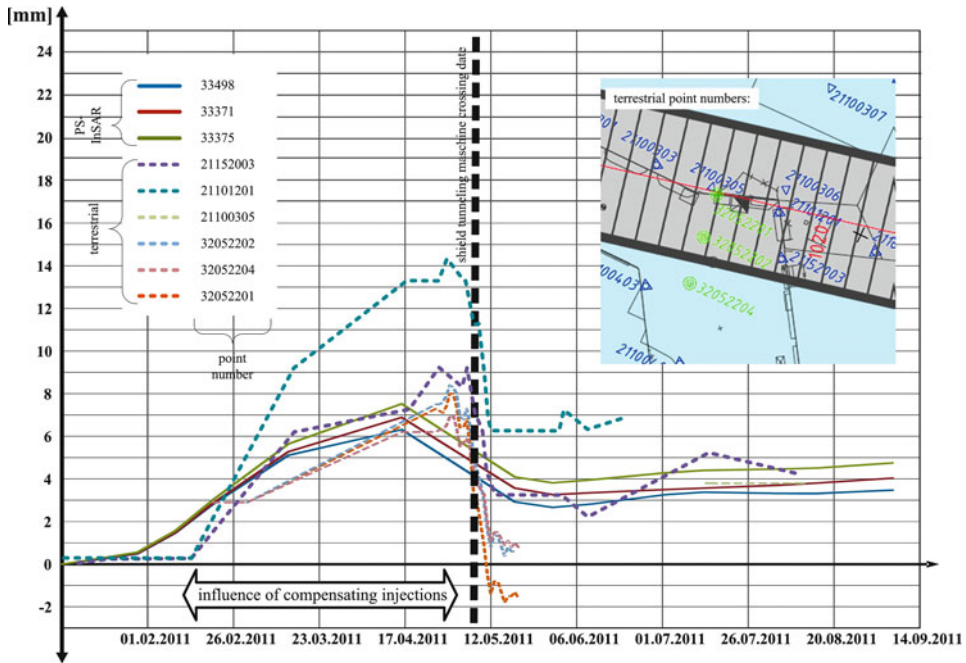
Fig. 2.50 Comparison of time-series of terrestrial determined displacements (solid lines) and satellite determined displacements (dashed lines) during compensating injections and shield tunneling crossing date [99]

a millimeter range are taken into account as well as certain inevitable local differences in the single points. Figure 2.50 clearly illustrates the intended initial uplift of the injections and its compensating effect on the subsequent settlements. Thus, an almost unaffected state of the buildings is fulfilled. It should be noted that the displacements measured by the satellite are given in line of sight (LOS). They have to be converted with the angle of incidence to end up with purely vertical displacements that are comparable to the terrestrial measurements on ground. However, an exact evaluation of error rates is still in progress.

References

1. J. B. Ajo-Franklin. "Frequency-domain Modeling Techniques for the Scalar Wave Equation: An Introduction". In: *Massachusetts Institute of Technology. Earth Resources Laboratory* (2005).
2. H. Akima. "A Method of Bivariate Interpolation and Smooth Surface Fitting for Irregularly Distributed Data Points". In: *ACM Transactions on Mathematical. Software* 4.2 (June 1978), pp. 148–159.

3. S. Arangio et al. "Assessment of structural damage due to ground settlements by using the DInSAR technique". In: *Life-Cycle and Sustainability of Civil Infrastructure Systems (IALCCE 2012)*. 2012, pp. 1897–1904.

4. S. Atamturktur et al. "Defining coverage of an operational domain using a modified nearest-neighbor metric". In: *Mechanical Systems and Signal Processing* 50-51 (2015), pp. 349–361.

5. R. Bamler, S. Hinz, and M. Eineder. "SAR-Interferometrie für geodätische Anwendungen". In: *Allgemeine Vermessungsnachrichten (AVN)*. 2008, pp. 243–252.

6. H. Bandemer and A. Bellmann. *Statistische Versuchsplanung*. Vol. 19. 2. 1979, pp. 1–116.

7. T. Bayes and R. Price. "An Essay towards solving a Problem in the Doctrine of Chances". In: *Philosophical Transactions of the Royal Society of London* 53 (1763), pp. 370–418.

8. T. Benz. "Small-Strain Stiffness of Soils and its Numerical Consequences". PhD thesis. Stuttgart, Germany: Universität Stuttgart, 2007.

9. J.-P. Berenger. "A perfectly matched layer for the absorption of electromagnetic waves". In: *Journal of Computational Physics* 114.2 (1994), pp. 185–200. ISSN: 0021-9991. https://doi.org/10.1006/jcph.1994.1159.

10. G. Bolzon and V. Buljak. "An effective computational tool for parametric studies and identification problems in materials mechanics". In: *Computational mechanics* 48.6 (2011), pp. 675–687.

11. M. D. Boscardin and E. J. Cording. "Building Response to Excavation–Induced Settlement". In: *Journal of Geotechnical Engineering* 115.1 (1989), pp. 1–21. ISSN: 0733-9410. https://doi.org/10.1061/(ASCE)0733-9410(1989)115:1(1).

12. R. Brossier. "Two-dimensional frequency-domain visco-elastic full waveform inversion: Parallel algorithms, optimization and performance". In: *Computers & Geosciences* 37.4 (2011), pp. 444–455.

13. R. Brossier, S. Operto, and J. Virieux. "Which data residual norm for robust elastic frequency-domain full waveform inversion?" In: *Geophysics* 75.3 (2010), R37–R46. https://doi.org/10.1190/1.3379323.

14. V. Buljak. "Proper orthogonal decomposition and radial basis functions algorithm for diagnostic procedure based on inverse analysis". In: *FME Transactions* 38.3 (2010), pp. 129–136.

15. J. B. Burland, B. B. Broms, and V. de Mello. "Behaviour of foundations and structures". In: *Proceedings of the 9th International Conference on Soil Mechanics and Foundation Engineering*. Tokyo, 1977, pp. 495–546.

16. J. B. Burland and C. P. Wroth. "Settlement of buildings and associated damage". In: *Prentech Press* (1974), pp. 611–654.

17. C. Cortes and V. Vapnik. "Support-vector networks". In: *Machine Learning* 20 (1995), pp. 273–297.

18. N. Cressie. "Spatial prediction and ordinary kriging". In: *Mathematical Geology* 20.4 (1988), pp. 405–421.

19. Deutsche Gesellschaft für Geotechnik e.V. *Taschenbuch für den Tunnelbau 2015*. Copyright Ernst u. Sohn GmbH. Reproduced with permission. 2015.

20. T. Dickmann and B. Sander. "Drivage concurrent tunnel seismic prediction". In: *Felsbau-rock and Soil Engineering* 14.1 (1996), pp. 406–411.

21. J. Düllmann. "Ingenieurgeologische Untersuchungen zur Optimierung von Leistungs-und Verschleissprognosen bei Hydroschildvortrieben im Lockergestein". Dissertation. Bochum: Ruhr-University Bochum, 2014.

22. J. Düllmann et al. "Analysis of Soil–Machine–Interactions (Part 1): Processing of TBM-Machine-Data and Extraction of Excavation-specific Data". In: *Proc. of EURO:TUN 2013, 3rd International Conference on Computational Methods in Tunneling and Subsurface Engineering, Bochum, Germany*. Apr. 2013, pp. 621–634.

23. V. Fargnoli, D. Boldini, and A. Amorosi. "Twin tunnel excavation in coarse grained soils: Observations and numerical back-predictions under free field conditions and in presence of a surface structure". In: *Tunnelling and Underground Space Technology* 49 (2015), pp. 454–469.

24. V. Fargnoli et al. "D numerical modelling of soil structure interaction during EPB tunnelling". In: *Géotechnique* 65.1 (2015), pp. 23–37.

25. G. Festa, E. Delavaud, and J.-P. Vilotte. "Interaction between surface waves and absorbing boundaries for wave propagation in geological basins: 2D numerical simulations". In: *Geophysical Research Letters* 32.20 (2005), p. L20306. https://doi.org/10.1029/2005GL024091.

26. A. Fichtner. *Full seismic waveform modelling and inversion*. English. Berlin; Heidelberg: Springer, 2011. ISBN: 9783642266072. https://doi.org/10.1007/978-3-642-15807-0.

27. R. Fisher. *The Design of Experiments*. Oliver and Boyd, Edinburgh, 1935.

28. T. Fritz and M. Eineder. *TerraSAR-X – Basic Product Specification Document*. Ed. by German Aerospace Center. 2010.

29. D. V. Griffiths and G. A. Fenton, eds. *Probabilistic Methods in Geotechnical Engineering*. Springer, 2007. ISBN: 978-3-211-73366-0.

30. F. Hegemann et al. "Integrated Data Processing and Simulation Platform for Mechanized Tunneling – Showcase Application on the "Wehrhahn-Linie" Project in Düsseldorf". In: *Proceedings of World Tunnel Congress 2014 – Tunnels for a better Life*. Foz do Iguacu, 2014.

31. J. S. Hesthaven and T. Warburton. *Nodal Discontinuous Galerkin Methods: Algorithms, Analysis, and Applications*. English. Vol. 54. Texts in Applied Mathematics. Springer, 2008. ISBN: 9780387720654. https://doi.org/10.1007/978-0-387-72067-8.

32. F. Hollmann et al. "Analysis of Soil-Machine-Interactions (Part 2): Influences on the Excavation-specific Data of TBM-Machine Data". In: *EURO:TUN 2013, 3rd International Conference on Computational Methods in Tunneling and Subsurface Engineering*. Apr. 2013, pp. 635–647.

33. R. Hölter. "Optimal Experimental Design in Geotechnical Engineering". PhD thesis. Bochum, Germany: Ruhr-Universität Bochum, 2021.

34. R. Hölter, E. Mahmoudi, and T. Schanz. "Optimal sensor Location for parameter identification in soft clay". In: *Application of Mathematics in Technical and Natural Sciences, Albena, Bulgaria*. Albena, Bulgaria, 2015, p. 030005.

35. R. Hölter et al. "Settlement prediction for an embankment on soft, structured clay using smeared soil-drain replacement technique and probabilistic analysis". In: *Embankment and Footing Prediction Symposium*. Ed. by S. W. Sloan and R. B. Kelly. Newcastle, Australia: ARC Centre of Excellence for Geotechnical Science and Engineering, 2016, CGSE EFPS–009.

36. R. Hölter et al. "Model validation using Bayesian optimal experimental design in urban mechanised tunnelling". In: *rd UNCECOMP 2019 ECCOMAS Thematic Conference on Uncertainty Quantification in Computational Sciences and Engineering*. Ed. by G. S. M. Papadrakakis V. Papadopoulos. Crete, Greece, 2019.

37. R. Hölter et al. "Optimal measurement design for parameter identification in mechanized tunneling". In: *Underground Space* 3.1 (2018), pp. 34–44.

38. S. Isam and Z. Wengang. "Use of soft computing techniques for tunneling optimization of tunnel boring machines". In: *Underground Space* (2020). ISSN: 2467-9674. https://doi.org/10.1016/j.undsp.2019.12.001.

39. S. J. Julier and J. K. Uhlmann. "Unscented filtering and nonlinear estimation". In: *Proceedings of the IEEE* 92.3 (2004), pp. 401–422.

40. B. M. Kampes. *Radar interferometry: Persistant Scatterer Technique*. 2006. https://doi.org/10.1007/978-1-4020-4723-7.

41. K. Karhunen. "Über Lineare Methoden in der Wahrscheinlichkeitsrechnung". In: *Annals of Academic Science Fennicae, Series A1 Mathematics and Physics* 37 (1946), pp. 3–79.

42. M. Käser and M. Dumbser. "An arbitrary high-order discontinuous Galerkin method for elastic waves on unstructured meshes – I. The two-dimensional isotropic case with external source terms". In: *Geophys. J. Int.* 166.2 (2006), pp. 855–877. https://doi.org/10.1111/j.1365-246X.2006.03051.x.

43. M. Käser et al. "An arbitrary high-order Discontinuous Galerkin method for elastic waves on unstructured meshes – III. Viscoelastic attenuation". In: *Geophys. J. Int.* 168.1 (2007), pp. 224–242. ISSN: 1365-246X. https://doi.org/10.1111/j.1365-246X.2006.03193.x.

44. J. Kennedy and R. Eberhart. "Particle Swarm Optimization". In: *Proceedings of IV. IEEE International Conference on Neural Networks*. Piscataway, New Jersey, 1995, pp. 1942–1948.

45. K. Khaledi et al. "Robust and Reliable Metamodels for Mechanized Tunnel Simulations". In: *Computer and Geotechnics* 61 (2014), pp. 1–12.

46. K. Khaledi et al. "Sensitivity analysis and parameter identification of a time dependent constitutive model for rock salt". In: *Journal of Computational and Applied Mathematics* 293 (2016), pp. 128–138.

47. S. Kirkpatrick, M. Vecchi, et al. "Optimization by simmulated annealing". In: *Science* 220.4598 (1983), pp. 671–680.

48. T. Knabe, H. F. Schweiger, and T. Schanz. "Calibration of constitutive parameters by inverse analysis for a geotechnical boundary problem". In: *Canadian Geotechnical Journal* 49.2 (2012), pp. 170–183.

49. G. Kneib, A. Kassel, and K. Lorenz. "Automatic seismic prediction ahead of the tunnel boring machine". In: *First Break* 18.7 (2000), pp. 295–302.

50. D. Komatitsch et al. *SPECFEM3D Cartesian v2.0.2 [software]*. Computational Infrastructure for Geodynamics, 2012. https://doi.org/http://doi.org/NoDOI.

51. T. Krishnamurthy. "Comparison of response surface construction methods for derivative estimation using moving least squares, kriging and radial basis functions". In: *Proceedings of the 46th AIAA / ASME / ASCE / AHS / ASC structures, structural dynamics and materials conference, AIAA-2005-1821*. 2005, pp. 18–21.

52. T. Lahmer. "Experimental design for nonlinear ill-posed problems applied to gravity dams". In: *Journal of Inverse Problems* 27.12 (2011).

53. L. Lambrecht. "Forward and inverse modeling of seismic waves for reconnaissance in mechanized tunneling". PhD thesis. Ruhr-Universität Bochum, Jan. 2015.

54. L. Lambrecht et al. "A nodal discontinuous Galerkin approach to 3-D viscoelastic wave propagation in complex geological media". In: *Geophysical Journal International* 212.3 (2018), pp. 1570–1587. https://doi.org/10.1093/gji/ggx494.

55. A. Lamert. "Tunnel Reconnaissance by Seismic Full Waveform Inversion". PhD thesis. Ruhr-Universität Bochum, 2019.

56. A. Lamert and W. Friederich. "Full Waveform Inversion for Advance Exploration of Ground Properties in Mechanized Tunneling". In: *International Journal of Civil Engineering* 17 (2019), pp. 19–32.

57. A. Lamert et al. "Imaging disturbance zones ahead of a tunnel by elastic full-waveform inversion: Adjoint gradient based inversion vs. parameter space reduction using a level-set method". In: *Underground Space* 3.1 (2018). Computational Methods in Mechanized Tunneling, pp. 21–33. ISSN: 2467-9674. https://doi.org/10.1016/j.undsp.2018.01.006.

58. S. Mahdevari, H. Shirzad Haghighat, and S. R. Torabi. "A dynamically approach based on SVM algorithm for prediction of tunnel convergence during excavation". In: *Tunnelling and Underground Space Technology* 38 (2013), pp. 59–68. ISSN: 0886-7798. https://doi.org/10.1016/j.tust.2013.05.002.

59. E. Mahmoudi and R. Hölter. "A model adaptation framework for mechanised tunnelling". In: *Modelling in geotechnical engineering*. Elsevier, AP, 2021, pp. 1–33.

60. E. Mahmoudi, R. Hölter, and C. Zhao. "A Pattern Recognition Approach to Evaluate the Uncertain Soil Stratum in Front of the Tunnel Face". In: *Proceedings of The Seventh Asian-Pacific Symposium on Structural Reliability and Its Applications (APSSRA2020)*. Ed. by T. Takada, I. Yoshida, and T. Itoi. 2020, pp. 351–355.

61. E. Mahmoudi, M. König, and T. Schanz. "Probabilistic analysis of a gas storage cavity mined in a spatially random rock salt medium". In: *Proceeding of VII International Conference on Computational Methods for Coupled Problems in Science and Engineering*. 2017.

62. E. Mahmoudi et al. "On the Global Sensitivity Analysis Methods in Geotechnical Engineering: A Comparative Study on a Rock Salt Energy Storage". In: *International Journal of Civil Engineering* 17 (2019), pp. 131–143.

63. E. Mahmoudi et al. "Stochastic field simulation of slope stability problems: Improvement and reduction of computational effort". In: *Computer Methods in Applied Mechanics and Engineering* 369 (2020), p. 113167. ISSN: 0045-7825.

64. R. J. Mair, R. N. Taylor, and J. B. Burland. "Prediction of ground movements and assessment of risk of building damage due to bored tunnelling". In: *Geotechnical aspects of underground construction in soft ground*. Rotterdam: Balkema, 1996, pp. 713–718. ISBN: 9054108568.

65. J. Meier et al. "Inverse Parameter identification technique using PSO algorithm applied to geotechnical Modelling". In: *Journal of Artificial Evolution and Applications* 2008 (2008), pp. 1–14.

66. G. Meschke et al. "Numerische Simulation maschineller Tunnelvortriebe in innerstädtischen Gebieten im Rahmen eines Tunnelinformationsmodells". In: *Bauingenieur* 89.11 (2014), pp. 457–466.

67. G. Meyerhof. "Penetration tests and bearing capacity of cohesionless soils". In: *Journal of the soil mechanics and foundation division. ASCE* 82.SM1 (1956), pp. 1-1–9.

68. S. Miro. "Calibration of Numerical Models Considering Uncertainties - Application to Mechanized Tunnel Simulations". PhD thesis. Bochum, Germany: Ruhr-Universität Bochum, 2016.

69. S. Miro, D. Hartmann, and T. Schanz. "Global Sensitivity Analysis for Subsoil Parameter Estimation in Mechanized Tunneling". In: *Computers and Geotechnics* 56 (2014), pp. 80–88.

70. S. Miro et al. "A probabilistic analysis of subsoil parameters uncertainty impacts on tunnel-induced ground movements with a back-analysis study". In: *Computers and Geotechnics* 68 (2015), pp. 38–53. ISSN: 0266-352X. https://doi.org/10.1016/j.compgeo.2015.03.012.

71. P. Mishra, P. Samui, and E. Mahmoudi. "Probabilistic Design of Retaining Wall Using Machine Learning Methods". In: *Applied Sciences* 11.12 (2021). ISSN: 2076-3417. https://doi.org/10.3390/app11125411.

72. T. Möller and W. Friederich. "Simulation of elastic wave propagation across fractures using a nodal discontinuous Galerkin method—theory, implementation and validation". In: *Geophysical Journal International* 219.3 (Sept. 2019), pp. 1900–1914. ISSN: 0956-540X. https://doi.org/10.1093/gji/ggz410.

73. V. Monteiller et al. "Three-dimensional full waveform inversion of short-period teleseismic wavefields based upon the SEM–DSM hybrid method". In: *Geophysical Journal International* 202.2 (2015), pp. 811–827.

74. T. Most and J. Will. "Meta-model of Optimal Prognosis – An automatic approach for variable reduction and optimal meta-model selection". In: *Proceedings of the Weimar Optimization and Stochastic Days 2008*. Weimar, Germany, 2008.

75. R. Mukherjee, U. M. Diwekar, and A. Vaseashta. "Optimal sensor placement with mitigation strategy for water network systems under uncertainty". In: *Computers and Chemical Engineering* 103 (2017), pp. 91–102. ISSN: 0098-1354.

76. A. A. Mullur and A. Messac. "Extended radial basis functions: more flexible and effective metamodeling". In: *AIAA journal* 43.6 (2005), pp. 1306–1315.

77. N. Müthing et al. "Settlement prediction for an embankment on soft clay". In: *Computers and Geotechnics* 93 (2018), pp. 87–103.

78. L. T. Nguyen. "Inference of ground condition in mechanized tunneling via inverse analysis using sequential Bayesian filtering". PhD thesis. Bochum, Germany: Ruhr-Universität Bochum, 2017.

79. L. T. Nguyen and T. Nestorović. "Reconstructing disturbance zones ahead of the tunnel face by elastic waveform inversion supported by a parametric level-set representation". In: *Soil Dynamics and Earthquake Engineering* 115 (2018), pp. 606–621.

80. L. T. Nguyen and T. Nestorović. "Unscented hybrid simulated annealing for fast inversion of tunnel seismic waves". In: *Computer Methods in Applied Mechanics and Engineering* 301 (2016), pp. 281–299.

81. J. Nocedal and S. Wright. *Numerical optimization*. 2nd ed. Springer Series in Operations Research and Financial Engineering. New York: Springer Science & Business Media, 2006. https://doi.org/10.1007/978-0-387-40065-5.

82. M. Obel et al. "Settlement Risk Assessment by Means of Categorized Surface Infrastructure". In: *Proceedings of the 10th International Conference on Structural Analysis of Historical Constructions*. Leuven, 2016. https://doi.org/10.1201/9781315616995-68.

83. R. G. Pratt. "Frequency-domain elastic wave modeling by finite differences: A tool for crosshole seismic imaging". In: *Geophysics* 55.5 (1990), pp. 626–632. https://doi.org/10.1190/1.1442874.

84. R. G. Pratt. "Seismic waveform inversion in the frequency domain; Part 1, Theory and verification in a physical scale model". In: *Geophysics* 64.3 (June 1999), pp. 888–901. ISSN: 0016-8033. https://doi.org/10.1190/1.1444597.

85. R. G. Pratt and R. M. Shipp. "Seismic waveform inversion in the frequency domain, Part 2: Fault delineation in sediments using crosshole data". In: *Geophysics* 64.3 (June 1999), pp. 902–914. ISSN: 0016-8033. https://doi.org/10.1190/1.1444598.

86. L. J. Pyrak-Nolte, L. R. Myer, and N. G. W. Cook. "Transmission of seismic waves across single natural fractures". English. In: *Journal of Geophysical Research: Solid Earth* 95.B6 (June 1990), pp. 8617–8638. https://doi.org/10.1029/JB095iB06p08617.

87. J.-M. Rendu. *An introduction to geostatistical methods of mineral evaluation*. Vol. 2. South African Institute of Mining and Metallurgy, 1978.

88. C. Riedel et al. "A hybrid exploration approach for the prediction of geological changes ahead of mechanized tunnel excavation". In: *Journal of Applied Geophysics* 203 (2022), p. 104684. ISSN: 0926-9851. https://doi.org/10.1016/j.jappgeo.2022.104684.

89. S. Ruder. "An overview of gradient descent optimization algorithms". In: *arXiv preprint arXiv:1609.04747* (2016).

90. S. Sakurai. "Lessons learned from field measurements in tunnelling". In: *Tunnelling and Underground Space Technology* 12.4 (1997), pp. 453–460. ISSN: 0886-7798. https://doi.org/10.1016/S0886-7798(98)00004-2.

91. A. Saltelli et al. *Global sensitivity analysis. The Primer*. John Wiley and Sons, 2008.

92. G. Sattel, P. Frey, and R. Amberg. "Prediction ahead of the tunnel face by seismic methods-pilot project in Centovalli Tunnel, Locarno, Switzerland". In: *First Break* 10.1 (1992), pp. 19–25.

93. T. Schanz et al. "Identification of constitutive parameters for numerical models via inverse approach". In: *Felsbau* 24.2 (2006), pp. 11–21.

94. R. Schenkendorf, A. Kremling, and M. Mangold. "Optimal experimental design with the sigma point method". In: *IET Systems Biology* 3.1 (2009), pp. 10–23.

95. S. Schindler. "Monitoringbasierte strukturmechanische Schadensanalyse von Bauwerken beim Tunnelbau". Dissertation. Bochum: Ruhr University Bochum, 2014.

96. S. Schindler and F. Hegemann. "Eine Interaktionsplatform für maschinelle Tunnelvortriebe: Anwendungen am Beispiel der Wehrhahn-Linie in Düsseldorf". In: *Geomechanics and Tunneling* 7.1 (2014). Copyright Ernst u. Sohn GmbH. Reproduced with permission.

97. S. Schindler and P. Mark. "Evaluation of Building Stiffness in the Risk-Assessment of Structures Affected by Settlements". In: *Proceedings of the 3rd International Conference on Computational Methods in Tunneling and Subsurface Enignering*. Ed. by G. Meschke et al. Freiburg, 2013.

98. S. Schindler and P. Mark. "Satellite-Based Radar Monitoring of Vertical Deformations Caused by Tunneling". In: *Cross Alpine Corridors (Brenner Congress 2015)*. Innsbruck, 2015, pp. 41–46.

99. S. Schindler et al. "Radar interferometric monitoring of vertical ground movements and imposed building deformations caused by tunneling". In: *Structures Congress*. Chicago, 2012, pp. 675–685. https://doi.org/10.1061/9780784412367.061.

100. S. Schindler et al. "Zur Genaugkeit der Radarinterferometrie im Setzungsmonitoring". In: *EI-Eisenbahningenieur* 1 (2014).

101. J. Schmitt, J. Gattermann, and J. Stahlmann. "Hohlraumerkundung im Tunnelbau". In: *Messen in der Geotechnik* (2004), pp. 173–200.

102. M. Schoen et al. "Application of optimal experiment design method to detect the optimal sensor positions: A case study of Milan metro line 5". In: ().

103. M. Schoen et al. "Numerical Model Calibration and Validation of Mechanized Tunnel Excavation of Milan Underground Line 5". In: *Challenges and Innovations in Geomechanics*. Ed. by M. Barla, A. Di Donna, and D. Sterpi. Cham: Springer International Publishing, 2021, pp. 215–222.

104. M. Schoenberg. "Elastic behavior across linear slip interfaces". English. In: *J. Acoust. Soc. Am.* 68.5 (Nov. 1980), pp. 1516–1521.

105. A. W. Skempton and D. H. MacDonald. "The Allowable Settlements of Buildings". In: *Proceedings of the Institute of Civil Engineering* 3.6 (1956), pp. 727–768. https://doi.org/10.1680/ipeds.1956.12202.

106. D. Straub. "Reliability updating with equality information". In: *Probabilistic Engineering Mechanics* 26.2 (2011), pp. 254–258. ISSN: 0266-8920. https://doi.org/10.1016/j.probengmech.2010.08.003.

107. W. Sun and Y.-X. Yuan. *Optimization theory and methods: nonlinear programming*. Vol. 1. Springer Science & Business Media, 2006.

108. B. Szabó, A. Düster, and E. Rank. "The p-version of the Finite Element Method". In: *Encyclopedia of Computational Mechanics*. Ed. by E. Stein, R. de Borst, and T. Hughes. Vol. 1. Volume 1: Fundamentals. John Wiley & Sons, 2004. Chap. 5, pp. 119–139. https://doi.org/10.1002/0470091355.ecm003g.

109. M. Tabarroki et al. "Determining the Factors of Safety of Spatially Variable Slopes Modeled by Random Fields". In: *Journal of Geotechnical and Geoenvironmental Engineering* 139.12 (2013), pp. 2082–2095.

110. A. Tarantola. "A strategy for nonlinear elastic inversion of seismic reflection data". In: *Geophysics* 51.10 (Oct. 1986), pp. 1893–1903. ISSN: 0016-8033. https://doi.org/10.1190/1.1442046.

111. A. Tarantola. "Inversion of seismic reflection data in the acoustic approximation". In: *Geophysics* 49.8 (Aug. 1984), pp. 1259–1266. ISSN: 0016-8033, 1942-2156. https://doi.org/10.1190/1.1441754.

112. K. Terzaghi and R. Peck. *Soil Mechanics in Engineering Practice*. John Wiley, 1967.

113. S. P. Timoshenko. *Strength of Materials – Part 1: Theory and Problems*. New York: D. Van Nostrand, 1955.

114. M. Trapp. "Bayesian full waveform inversion for exploration during mechanized tunneling". PhD thesis. Ruhr-Universität Bochum, Universitätsbibliothek, 2022. https://doi.org/10.13154/294-8994.

115. M. Trapp and T. Nestorović. "Non-gradient full waveform inversion approaches for exploration during mechanized tunneling applied to surrogate laboratory measurements". In: *Tunnelling and Underground Space Technology* (2021), p. 104252.

116. M. Trapp and T. Nestorović. "Reconstruction of structural anomalies out of seismic measurements by means of a non-deterministic full waveform inversion approach for application in mechanized tunneling". In: *Journal of Applied Geophysics* (2020), p. 104180. https://doi.org/10.1016/j.jappgeo.2020.104180.

117. M. Trapp et al. "Intelligent optimization and machine learning algorithms for structural anomaly detection using seismic signals". In: *Mechanical Systems and Signal Processing* 133 (2019), p. 106250. ISSN: 0888-3270. https://doi.org/10.1016/j.ymssp.2019.106250.

118. J. Tromp, D. Komatitsch, and Q. Liu. "Spectral-element and adjoint methods in seismology". In: *Communications in Computational Physics* 3.1 (2008), pp. 1–32.

119. J. Tromp, C. Tape, and Q. Liu. "Seismic tomography, adjoint methods, time reversal and banana-doughnut kernels". In: *Geophysical Journal International* 160.1 (2005), pp. 195–216.

120. D. Uciński. *Optimal Measurement Methods for Distributed Parameter System Identification*. CRC Press, Boca Raton, 2005.

121. J. Virieux and S. Operto. "An overview of full-waveform inversion in exploration geophysics". In: *Geophysics* 74.6 (2009), WCC1–WCC26.

122. G. G. Wang and S. Shan. "Review of metamodeling techniques in support of engineering design optimization". In: *Journal of Mechanical Design* 129.4 (2007), pp. 370–380.

123. O. Wolkenhauer et al. "Parameter estimation and optimal experimental design". In: *Essays in Biochemistry* 45 (Sept. 2008), pp. 195–210.

124. B. Z. Yao et al. "Applying Support Vector Machines to Predict Tunnel Surrounding Rock Displacement". In: *Applied Mechanics And Mechanical Engineering*. Vol. 29. Applied Mechanics and Materials. Trans Tech Publications Ltd, Sept. 2010, pp. 1717–1721. https://doi.org/10.4028/www.scientific.net/AMM.29-32.1717.

125. C. Zhao. "A Contribution to Modeling of Mechanized Tunnel Excavation". PhD thesis. Bochum, Germany: Ruhr-Universität Bochum, 2018.

126. C. Zhao et al. "A hybrid model for estimation of ground movements due to mechanized tunnel excavation". In: *Computer-Aided Civil and Infrastructure Engineering* 34.7 (2019), pp. 586–601.

127. C. Zhao et al. "Model validation and calibration via back analysis for mechanized tunnel simulations – The Western Scheldt tunnel case". In: *Computers and Geotechnics* 69 (2015), pp. 601–614.

128. H. Zhu et al. "Structure of the European upper mantle revealed by adjoint tomography". In: *Nature Geoscience* 5.7 (2012), pp. 493–498. https://doi.org/10.1038/ngeo1501.

Excavation Simulations and Cutting Tool Wear

<div style="text-align:right">**3**</div>

Lukas Brackmann , Arne Röttger, Hoang-Giang Bui , Sahir Butt ,
Golnaz Hoormazdi , Abdiel Ramon Leon Bal, Sebastian Priebe ,
Dennis Wingender, Hongwei Yang, Daniel Balzani , Klaus Hackl ,
Günther Meschke , Inka Mueller , and Jörg Renner

L. Brackmann (✉)
Materials Technology, Ruhr-Universität Bochum, Bochum, Germany
e-mail: lukas.brackmann@rub.de

A. Röttger
New Production Technologies and Materials, Bergische Universität Wuppertal, Wuppertal,
Germany
e-mail: roettger@uni-wuppertal.de

H.-G. Bui · G. Hoormazdi · K. Hackl
Mechanics of Materials, Ruhr-Universität Bochum, Bochum, Germany
e-mail: giang.bui@rub.de

G. Hoormazdi
e-mail: golnaz.hoormazdi@rub.de

K. Hackl
e-mail: klaus.hackl@rub.de

S. Butt · A. R. Leon Bal · S. Priebe · G. Meschke
Structural Mechanics, Ruhr-Universität Bochum, Bochum, Germany
e-mail: sahir.butt@rub.de

A. R. Leon Bal
e-mail: abdiel.leonBal@rub.de

S. Priebe
e-mail: Sebastian.Priebe@ruhr-uni-bochum.de

G. Meschke
e-mail: guenther.meschke@rub.de

Abstract

The mechanized tunnel construction is carried out by tunnel boring machines, in which the soil in front of the working face is removed, and the tunnel lining is carried out with shotcrete or the setting of segments and their back injection. Advancements in this field aim towards increase of the excavation efficiency and increase of the tool lifetime, especially in rock-dominated grounds. The latter is achieved by understanding the wear mechanisms abrasion and surface-fatigue, and by knowledge of the microstructure-property relation of the utilized materials. Improvements for tool concepts are derived, based on experiments and simulations. A key parameter towards efficient rock excavation is the shape of the cutting edge of the utilized disc cutters. Sharp cutting edges have proven to generate higher rock excavation rates compared to blunt ones. The compressive strength of the utilized steel has to be high, to inhibit plastic deformation and thereby to maintain sharp cutting edges. This requirement competes with the demand for toughness, which is necessary to avoid crack-growth in the case of cyclic loading. Solutions for this contradiction lie in specially designed multiphase microstructures, containing both hard particles and ductile microstructural constituents. Besides adapting the alloying concept, these required microstructures and the associated properties can be adjusted by specific heat-treatments.

D. Wingender · D. Balzani
Continuum Mechanics, Ruhr-Universität Bochum, Bochum, Germany
e-mail: dennis.wingender@rub.de

D. Balzani
e-mail: daniel.balzani@rub.de

H. Yang
School of Civil Engineering, Sun Yat-sen University, Guangzhou, China
e-mail: yanghw9@mail.sysu.edu.cn

I. Mueller
Technical Mechanics, Bochum University of Applied Sciences, Bochum, Germany
e-mail: inka.mueller@hs-bochum.de

J. Renner
Experimental Geophysics, Ruhr-Universität Bochum, Bochum, Germany
e-mail: joerg.renner@rub.de

3.1 Introduction

The excavation of soil and rock in mechanized tunneling is fundamentally different from that in other tunnel construction methods, such as open construction pits or blast excavation. In mechanized tunneling, tools are attached to a rotating shield, which also defines the tunnel's diameter. Thereby, the tools are selected taking into account the geological conditions. For example, chisels and scrapers are used in the case of non-cohesive soil, as they remove the geomaterial in a similar manner as a shovel. In contrast, disc cutters are employed in soft and hard rock, where material degradation occurs by crack initiation, crack propagation, and spalling of rock fragments. The profitability of tunnel construction is largely defined by the efficiency and speed of soil excavation. The excavation efficiency decreases due to the wear of the tools, so they have to be replaced upon reaching their wear limit. Precise knowledge of the tool wear and the associated excavation efficiency is essential for planning optimal tool change intervals and estimating construction costs. This chapter deals with excavation of soil and medium-strength rock, and the wear of the tools used for their excavation. It is important to understand both the soil-tool interaction to describe the degradation mechanisms and the tool wear on the microscale, thus deriving optimal material concepts for tunneling tools.

At the beginning of this chapter, the fundamental principles of soil and rock excavation are explained, and the results of recent advancements in the understanding of the rock excavation process are presented. The results of rock indentation tests and numerical simulations form the base for future design optimizations of tunneling tools, aiming towards improved excavation efficiency. Subsequently, the results of numerical simulations of the interaction between tunneling tools, such as disc cutters and chisel tools, and various soils and rocks are discussed with a focus on the determination of evolving cutting forces, especially at material interfaces, as is the case if tunneling occurs in heterogeneous ground conditions.

In the second part, the material concepts and wear mechanisms of tunneling tools are examined. Tool wear is discussed on macro- and micro-scale by explaining the interaction of the different tool microstructures and the abrasive particles in the ground to be excavated. In addition to abrasive wear, special emphasis is placed on the influence of cyclic mechanical loading and the connected wear mechanism of surface spalling. Several material concepts, such as hardfacing alloys and tool steels, are considered concerning their abrasive wear resistance and fatigue resistance. Furthermore, existing test methods for abrasiveness of soil and rock, as well as fatigue tests are described and critically evaluated. The numerical simulations investigate the previously introduced wear mechanisms on meso- and microscale. Mesoscale simulations address abrasive wear and focus on the interaction of abrasive particles with the tool surface during a scratching process. A bridge is built toward the scratch behavior of multiple particles, as well as particle mixtures from single-scratch simulations. The microscale simulations explore the material response of hard phase containing materials under static and cyclic loading conditions. The underlying computational methods are explained in detail, and the results of crack propagation sim-

ulations in different hard-phase containing materials are presented. Subsequently, novel techniques of in-situ monitoring of tool wear and damages using vibration analysis are presented. An experimentally based proof of concept for detecting damaged disc cutters is provided, after a short digress into the fundamental principles of wear detection and vibration analysis. A transfer of the gained results concludes the chapter with practical recommendations on increasing tunneling efficiency and improving tool lifetime.

3.2 Excavation of Geomaterials in Mechanized Tunneling: Experiments and Simulations on Failure Mechanisms

Mechanized tunneling relies on tunnel boring machines (TBMs) that have to be equipped with appropriate tools for the excavation of the material along the anticipated path. The terminology regarding the material "below our feet", for which we use the term "geomaterials" in an overarching sense, is unfortunately convoluted. Conventionally, the material below our feet is classified as either soil or rock. Appealingly simple, with only two groups, the classification and its use in different scientific communities bears complications. In geo-engineering, for example, the term "soil" is at times used synonymous with "ground," the latter meaning "solid material below us" in an objective way. Furthermore, either group is diverse in composition and mechanical behavior. Soils represent loose and unconsolidated sediments produced by the deposition of particles after their transport through air or water over vastly variable distances. A first subgroup of soil, the organic soils, with the adjective often dropped in agricultural context, is characterized by a substantial fraction of organic matter and forms the pedosphere. The introduction of the two further subgroups, granular and cohesive soils, rests on a mixture of structural and mechanical characteristics. For soils, cohesiveness, actually at conflict with the defining "loose," results from the presence of water that mediates and amplifies electrical forces between soil particles to the extent that they form aggregates with some shape stability, in cases associated with significant plasticity. While the mechanical property, cohesiveness, cannot be used alone to distinguish soils and rocks, the cause for the cohesion and its mechanical ramifications are strikingly different for them. The cohesiveness of rocks results from welding of grains, either by a "substance", the cement, acting as a glue leading to lithification of sediments or by the formation of "intact" grain boundaries (held together by interatomic forces as in metals or ceramics) during their genesis (crystallization from melts or recrystallization by solid-state reactions).

The overall success and the predictability of costs of excavation projects critically hinge on an (in the best of cases) a-priori knowledge or an experience-based principal understanding of the deformation behavior of the subsurface material to be penetrated. The selection of an appropriate excavation technique and associated tools requires at least a material classification, but the more is known about strength parameters the better. The excavation techniques and the activated failure processes shift from soil to rock. Cutting
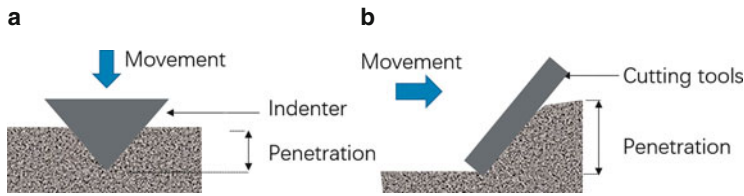
Fig. 3.1 Two basic processes in excavation: indentation (**a**) and cutting (**b**)

or scraping suffices to disintegrate soils, while indentation and fragmentation is required for rock (Fig. 3.1).

As a rule of thumb, the contents of organic matter decreases while the cohesiveness increases with depth. On an absolute scale, organic soils and cohesive soils exhibit compressive strengths as low as tens of kPa. The compressive strength of granular soils and highly porous sedimentary rocks overlap (1 to 10 MPa); crystalline rocks may exhibit strength up to a few hundreds of MPa. The significant changes in porosity during deformation and their effect on strength was first noted for soils; the related critical-state concept [38, 104] also has some applicability to porous rocks [22]. Likewise, the concept of effective stresses, introduced by Terzaghi for soils [93, 94], applies to rocks as well [71].

3.2.1 Excavation of Soft Soils

The mechanized excavation of soils by means of tunnel boring machines is characterized by the engagement of the scraper tools mounted on the cutting wheel with the ground. The TBM advancement actually leads to a strong and transient tool-soil interaction, during which the excavation tools penetrate the tunnel face and push the soil mass away, leading to destructuration and failure of the material that ultimately enters the excavation chamber. The excavation operation of soils involves the development of large displacements and deformations, as well as a strong coupling between skeleton deformation and pore pressure variations causing significant fluid flow in partially and fully saturated soils [63, 64]. The intrinsic complexity of mechanized excavation problems, associated to a great extent with the interaction between the excavation instrument and the penetrated soil, has stimulated experimental and numerical investigations [6–8, 52, 53] of tool-soil interaction processes. Here, we report on the development of an experimental device that allows for measuring the topology of the soil during the excavation and the evolution of the reaction forces on the tool when penetrating dry and partially saturated soils, and on the validation and application of single-phase [7, 8] and two-phase [53] numerical models based on the Particle Finite Element Method (PFEM) [68] coupled with a standard hypoplastic formulation for the modeling of granular materials [103].
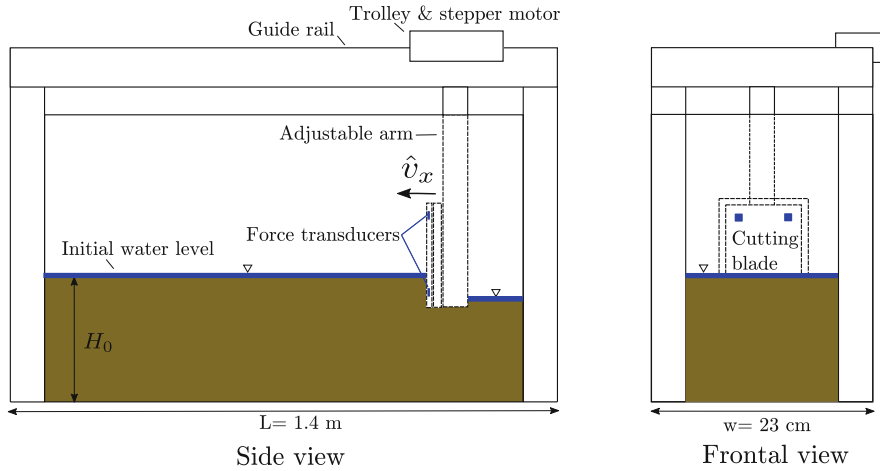
Fig. 3.2 Setup and main components of the developed excavation device (re-drawn after: [6])

3.2.1.1 RUB Excavation Device

The setup of the excavation device consists of a rectangular container filled in with sand and enclosed by four Plexiglass walls. The relevant dimensions are indicated in Fig. 3.2. The excavation tool is a rectangular Plexiglass panel with a height of 25 cm, displaced along the excavation container by a stepper motor and a trolley mounted on a dual linear guide rail system with sliding bearings. The excavation device permits adjusting the penetration depth of the cutting blade. Four force transducers, attached to the cutting blade, register reaction forces and torque during the experiment.

The excavation tests were carried out in dense Haltener Silbersand [76], a siliceous sand with rounded grains. The following conditions were considered in the experiments: initial height of sand in the container $H_0 = 30$ cm, penetration depth of the tool $d_p = 10$ cm, and horizontal velocity of the tool $\hat{v}_x = 1.2$ cm/s. After each test run, the sand was leveled to the same initial height (30 cm). Water-saturation is reached via a hose entering the container; water is added until a level is attained that slightly exceeds the soil surface.

3.2.1.2 Computational Analysis of Tool-Soil Interactions

The computational plane-strain and 3D PFEM simulations of tool-soil interactions for dry and water-saturated conditions, involving single and multiple cutting tool, used the configurations displayed in Fig. 3.3. Excavation analyses of dry soils were performed utilizing dimensions extracted from [20]: $L = 2.2$ m, width $w = 20$ cm, initial height of granular material $H_0 = 30$ cm, penetration depth of the tool $d_p = 20$ cm, height of the tool $H_{\text{tool}} = 25$ cm and its thickness $t_{\text{tool}} = 2.5$ cm. The tool moves with a prescribed horizontal velocity of $\hat{v}_x = 1.0$ cm/s. In simulations with multiple cutting tools, the horizontal velocity of the tools was $\hat{v}_x = 15$ cm/s. For simulation of the excavation of water-saturated soil, the model dimensions were: $L = 1.4$ m, $w = 23$ cm, $H_0 = 30$ cm, $d_p = 10$ cm, and $t_{\text{tool}} = 2.5$ cm.
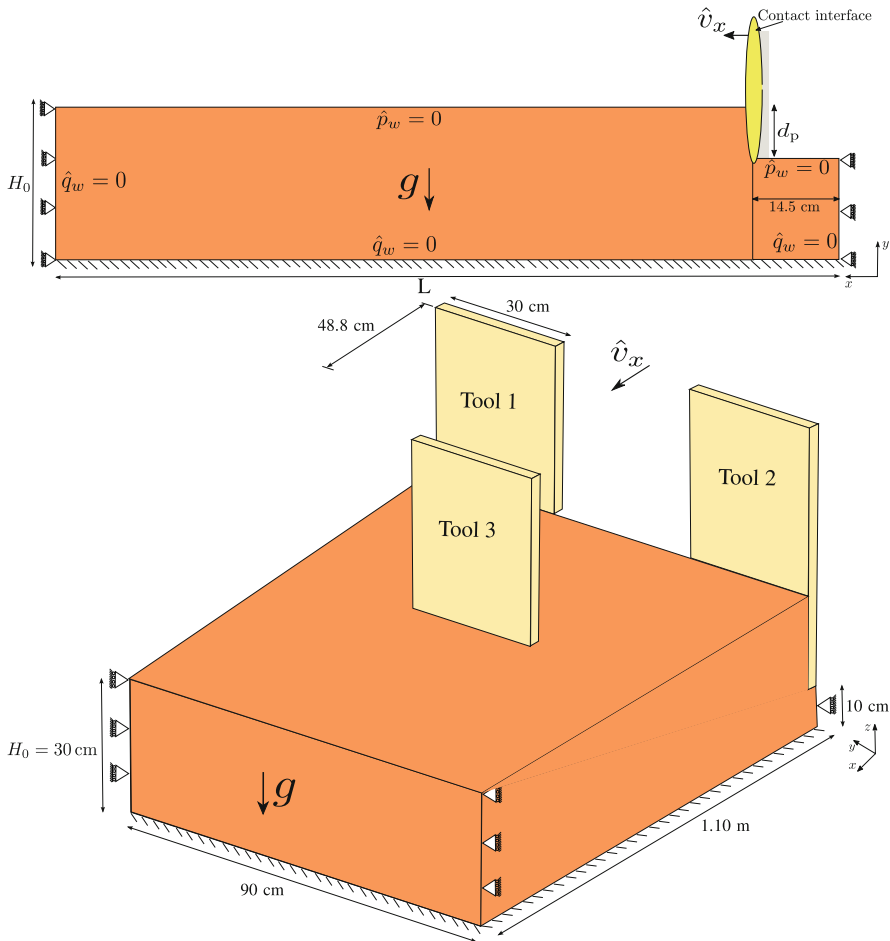
Fig. 3.3 Initial geometry, model setup and boundary conditions of the 2D (top, re-drawn after: [53]) and 3D (bottom, re-drawn after: [7]) PFEM excavation models

In this numerical model, the height of the tool is 5 cm larger than in the experiments (i.e. H_{tool} = 30 cm), to avoid soil over-passing the tool at the end. A horizontal tool velocity of 1.2 cm/s was applied. A frictional tool-soil interface discretized with triangular contact elements (shown as a red layer in Fig. 3.3, top, was considered in plane-strain excavation analyses, whereas a no-slip tool-soil interface was assumed for 3D simulations.

Excavation simulations for dry soil were performed assuming corn kernels [20]. The geotechnical and hypoplastic parameters adopted for corn can be found in [7]. The initial void ratio was set to $e_0 = 0.82$ (relative density of $I_d = 0.35$). Simulations of water-saturated soil, were carried out for Silbersand, assuming an initial void ratio of $e_0 = 0.66$ ($I_d = 0.70$). The hypoplastic parameters adopted for this sand are contained in [6, 53]. The constitutive model was initialized using at-rest later pressure conditions.
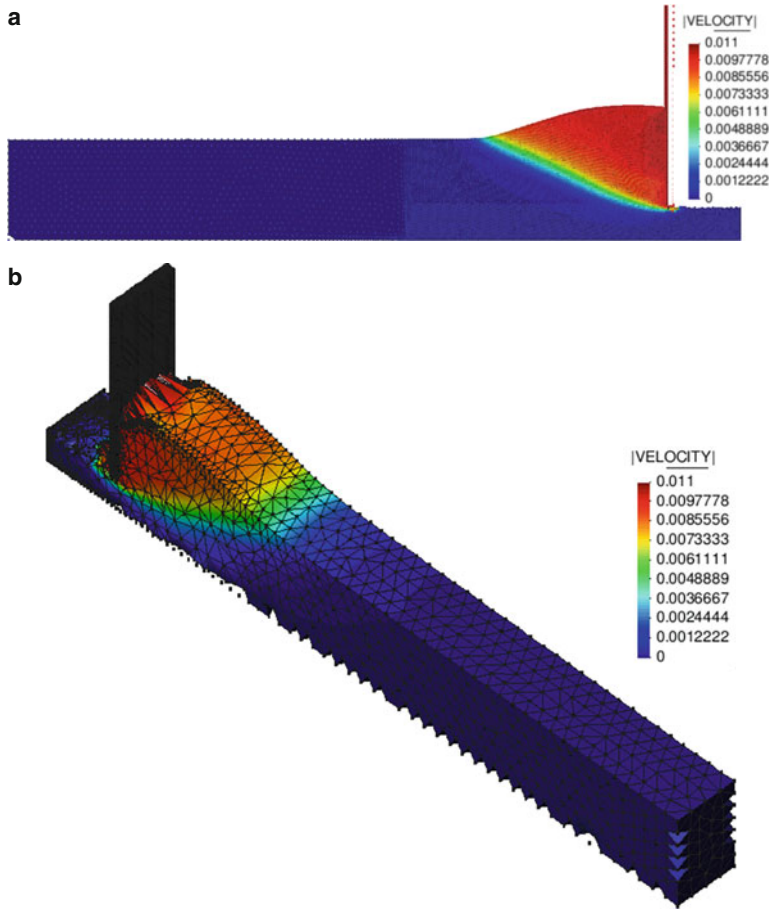
Fig. 3.4 Spatial distribution of the total velocities of the particles (in [m/s]) in the excavation according to the **a** 2D and **b** 3D excavation models, for a tool horizontal displacement of $S_x = 20$ cm

In both 2D and 3D numerical analyses assuming partially or fully saturated soil, the sides of the excavation models were impervious (Fig. 3.3), while the ground free surface was allowed to drain freely (i.e., $\hat{p}_w = 0$). In plane-strain simulations of partially saturated sand, the saturated hydraulic conductivity K_w^{sat} was estimated from the Kozeni-Carman permeability model [18]; the Soil-Water Characteristic Curve (SWRC) was defined via van Genuchten's model [97].

The spatial distributions of the total velocities of the particles in the deformed ground, according to the 2D and 3D excavation models (Fig. 3.4), show higher velocities near the cutting tool and within the heap of excavated material, than in the rest of the domain. The simulation results also show a shear slip plane in the velocity field, propagating from the bottom of the excavation tool towards the ground free surface.
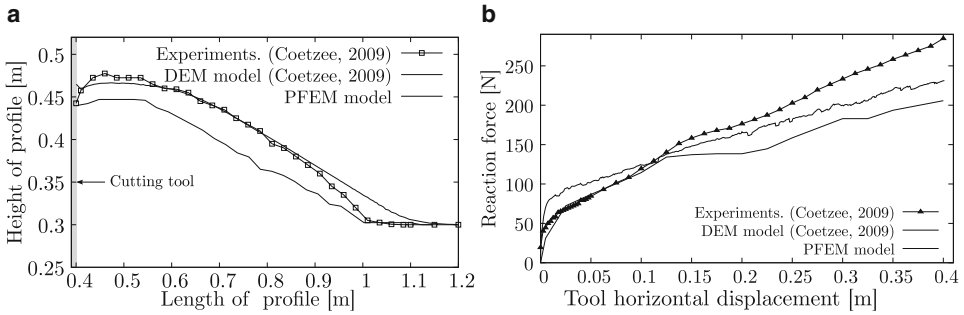
Fig. 3.5 **a** Profiles of the ground free surface for a tool horizontal displacement of $S_x = 40$ cm. **b** Evolution of the tool reaction forces, according to experiments and DEM simulations [20] as well as PFEM analyses [7] (re-drawn after: [7])

The profile of the ground free surface computed with the PFEM is compared with experimental and DEM results reported in [20] (Fig. 3.5a). In general, a very good correlation between laboratory results and numerical predictions from the hypoplastic PFEM model is observed for the assessed tool displacement. The evolution of the horizontal reaction force generated on the cutting tool vs. its horizontal displacement, displays an initial increase with a steep slope, where predictions obtained from PFEM analyses exceed DEM and laboratory results (Fig. 3.5b). As the excavation process continues, the reaction forces steadily increase due to the accumulation of granular material in front of the tool. For the evaluated horizontal displacement range of the tool, PFEM predictions [7] agree well with the results obtained from the DEM and the experiments presented in [20].

Tool-soil interaction analyses considering three cutting tools simultaneously excavating in soil are analyzed. The setup consists of one leading tool (tool 1) located ahead of the other two trailing tools (tool 2 and 3), which are positioned at the same level (Fig. 3.3, top). Similar to the PFEM results concerning excavations with a single tool (Fig. 3.4), distinctive shear slip lines emerge from the lower part of each cutting tool (Fig. 3.6a). The heaps in front of tools 1 and 2 exhibit a similar topology, characterized by an inclination towards the centerline of the container, while the heap in front of tool 3 resembles a semi-circular shape. Computed reaction forces on tools 1 (solid line) and 2 (dashed line) are very close, due to the similarity in the topologies of their associated excavation fronts, while for tool 3 (line with marks), higher reaction forces are calculated (Fig. 3.6b).

Excavation analyses in initially fully saturated Silbersand, are now considered. A staggered topology of the ground free surface occurs, i.e., bumps of soil develop ahead of the scrapper (Fig. 3.7a). In general, the computed and measured profiles of the free surface are in good agreement (Fig. 3.7b). For the assessed horizontal displacement of 35 cm, the maximum height attained by the heap of material in the test (denoted by $\hat{H}_{max}$) was nearly $\hat{H}_{max} = 20.26$ cm, at a horizontal distance of 11.03 cm from the tool. According to the PFEM simulations, the maximum height in the ground from the bottom of the tool (H_{max})
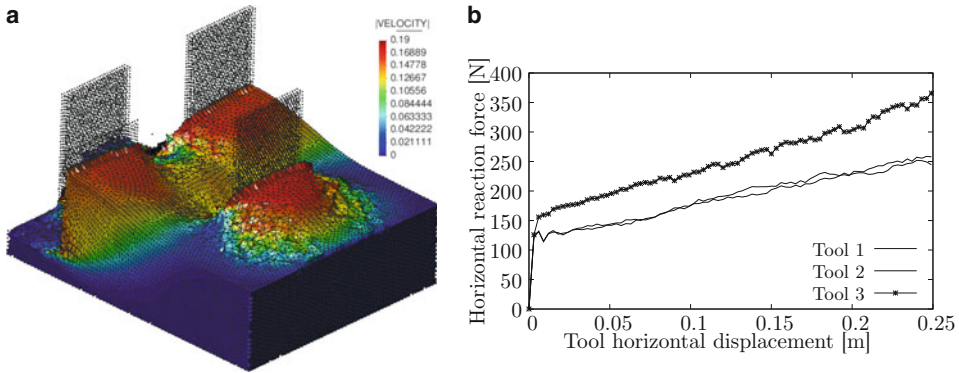
Fig. 3.6 **a** Spatial distribution of the total velocities of the particles (in [m/s]) for a horizontal displacement of the tools of $S_x = 20$ cm. **b** spatio-temporal evolution of the reaction forces in tools 1, 2 and 3 (re-drawn after: [7])
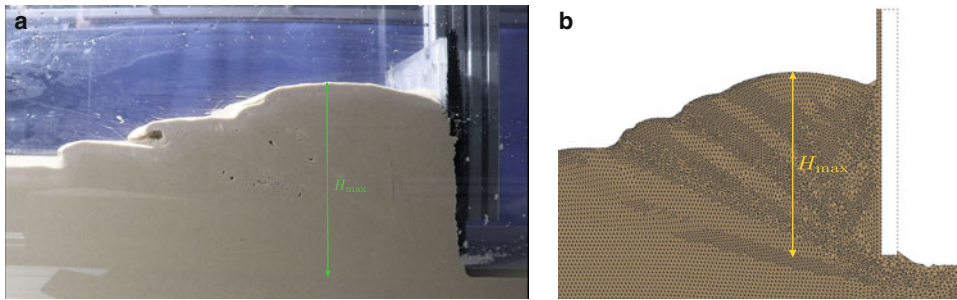
Fig. 3.7 **a** Measured and **b** computed profiles of the ground free surface for a tool horizontal displacement of $S_x = 35$ cm, in water-saturated excavations

is circa $H_{max} = 22.63$ cm computed at 10.29 cm ahead of the tool. It can also be observed a denser nodal distribution in shear deformation zones of the soil (i.e. shear bands) as compared to the rest of the excavation domain. This is achieved by means of an adaptive re-meshing procedure based on a soil dilation criterion, incorporated into the hypoplastic PFEM formulation for the improved capture of strain localization zones in the ground.

The capabilities of the proposed two-phase PFEM formulation are further assessed by means of the the computed and measured profiles of the ground free surface at selected tool displacements (Fig 3.8a). Experimental data (solid gray lines) show maximum heights of the excavation heap of ≈ 18.6 cm and 22.75 cm, for tool displacements of 25 cm and 45 cm, respectively. The maximum heights of the ground computed with the PFEM model (solid and dashed black lines), for corresponding tool displacements, are 18.9 cm and 25.5 cm. The computed and measured topology of the ground for the assessed tool displacements, are in good agreement.
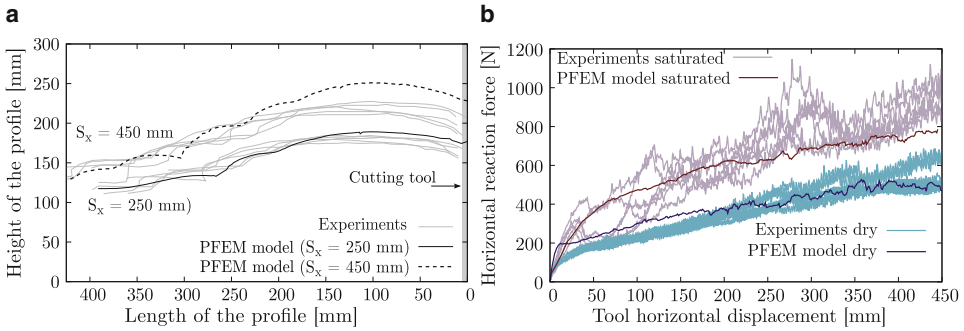
Fig. 3.8 Computed and measured **a** excavation profiles for tool horizontal displacements of $S_x = 25$ and $S_x = 45$ cm and **b** reaction force-tool displacement curves obtained from excavation analyses in dry and water-saturated sand (re-drawn after: [53])

We evaluate the tool reaction force-displacement curves generated during excavations in Silbersand (Fig. 3.8b). To complement the experiments performed in water-saturated sand, dry excavation tests were also carried out. Test results in initially fully saturated sand (red solid lines), show an initial increase of the reaction forces, followed by strong oscillations in the reaction forces, where a maximum reaction force of around 1100 N, at around 27.5 cm of tool displacement, is registered by the force transducers. Excavation experiments performed in dry conditions (aqua solid line), on the contrary, show a maximum reaction force of 490 N at the final displacement of the tool, corresponding to 45 cm. In this cases, no strong oscillations in the force plot are detected. Although the proposed model (results in dark red and dark aqua solid lines) is not able to fully reproduce the large oscillations observed in the reaction forces obtained from excavation tests in initially saturated sand, the numerical results lie within the experimental range.

Finally, 2D and 3D excavation analyses in fully saturated Silbersand, are presented. For these simulations, no-slip conditions at the tool-soil interface and a constant saturated hydraulic conductivity of $K_w^{\text{sat}} = 1 \times 10^{-4}$ m/s, are considered. Furthermore, the tool is horizontally displaced at constant velocity of 10 cm/s. The spatial distributions of pore water pressures in the deformed configuration of ground at a tool horizontal displacement of 36 cm, assuming initially loose i.e. $e_0 = 0.79$ ($I_d = 0.32$) and dense i.e. $e_0 = 0.70$ ($I_d = 0.58$) sands, are investigated (Figs. 3.9 and 3.10). For the evaluated tool displacement, pore pressures in the ground are mostly positive for initially loose sand, whereas for the denser specimen, negative pore pressures develop ahead of the excavation tool while the rest of the soil domain (e.g. near the left and bottom boundaries) undergoes positive pressures. Negative pore pressures are normally associated to the excavation [63] and strain localization phenomena [83] of dense, dilatant materials. Comparable distributions of pore pressures are computed with the 2D PFEM excavation model, for similar initial soil densities.
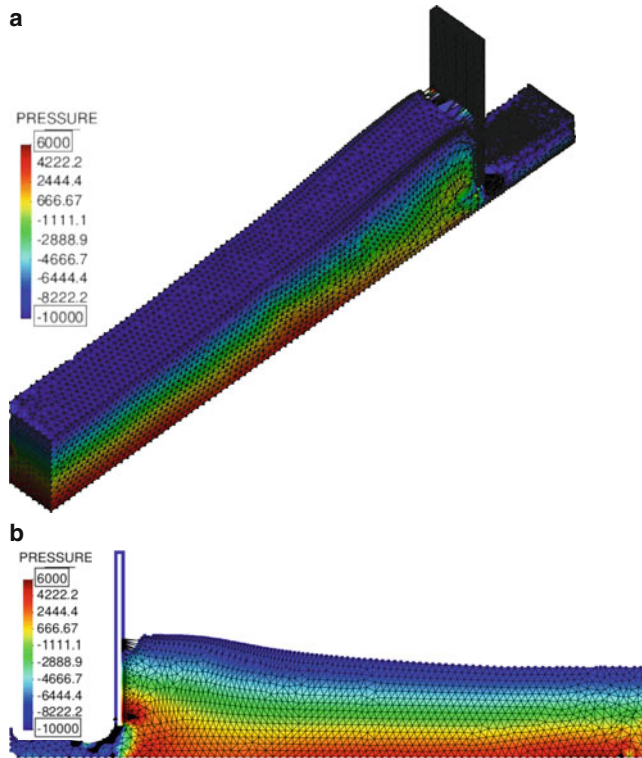
Fig. 3.9 **a** Three- and **b** two-dimensional spatial distributions of pore pressures (in [Pa]) in excavations performed on fully saturated loose sand ($e_0 = 0.79$) at a tool displacement of $S_x = 36$ cm

The topology of the ground free surface for a horizontal displacement of the tool of 36 cm, computed with both the 2D and 3D PFEM models, is analyzed (Fig. 3.11a). In general, slightly higher elevations of the free surface are observed in simulation results pertaining to dense sand (black solid line, blue dots), as compared to results involving loose sand. For loose sand, the 2D excavation model (red line) predicts a higher elevation of the ground free surface in comparison to its 3D counterpart (yellow dots). In the case of dense sand, the predicted curves remain close for the most part. Predictions obtained from the 2D and 3D PFEM models agree well. The computed evolution of tool reaction forces with respect to the horizontal displacement traveled by the tool, is assessed (Fig. 3.11b). Larger reaction forces are obtained for the tool-soil interaction carried out in the denser sand. For this set of simulations, the difference in the force levels between dense and loose sand is nearly sixfold at the end of the excavation process. For the selected soil parameters and tool displacement range, predictions from both versions of the excavation model, are in close agreement.
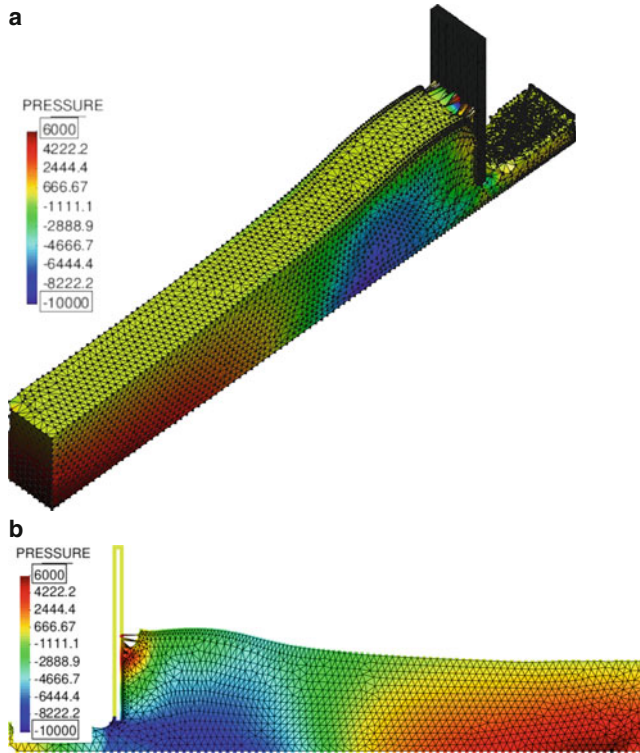
Fig. 3.10 **a** Three- and **b** two-dimensional spatial distributions of pore pressures (in [Pa]) in excavations performed fully saturated dense sand ($e_0 = 0.70$) at a tool displacement of $S_x = 36$ cm
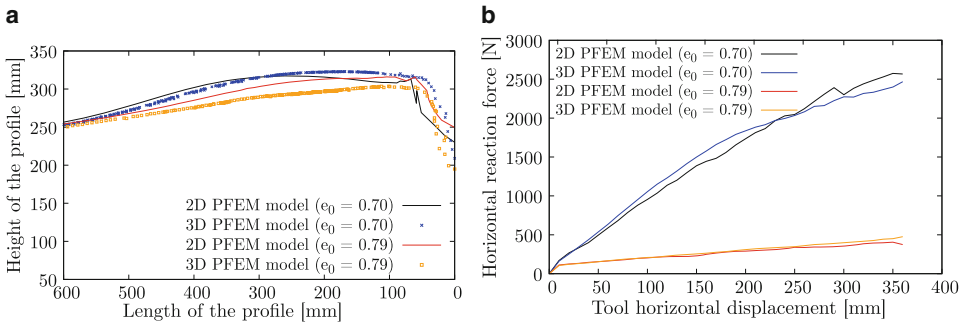
Fig. 3.11 **a** Computed free surface profiles of the ground for a tool horizontal displacement of $S_x = 36$ cm. **b** Reaction force-displacement curves computed during the tool-soil interactions performed with the 2D and 3D PFEM models, assuming dense and loose sands

3.2.2 Experimental and Simulation based Investigation of Rock Fragmentation

After briefly discussing the deformation characteristics of rocks, we present a suite of laboratory indentation test on a variety of intermediate-strength rock types. Finally, a peridynamic simulation model [13, 17] is presented that was used to simulate the indentation processes.

3.2.2.1 Deformation Characteristics of Rocks

Here, we briefly review the state of knowledge of the deformation characteristics of rocks focusing on aspects relevant for modeling purposes and intermediate-strength rocks. For modeling purposes, two questions are immanent: "How many parameter are needed to describe the deformation behavior? Where can the values of the relevant parameters be found?". We address the first one below and regarding the second we refer to data collections in [3, 86]. For further reading, we suggest the compact overview [59] and the extensive treatments [41, 71].

Rocks are aggregates of minerals, naturally occurring, in most cases crystalline compounds of elements. The chemical composition of the most common rock-forming minerals is actually restricted to a limited number of elements, i.e., Si, O, Ca, Mg, Fe, Al, Na, K, and H. The abrasiveness, the extent to which rock fragments scratch a (metallic) tool, is controlled by the hardness of the minerals, well known for the common rock-forming minerals and classified by Mohs (relative) scale. In contrast, fracturing of rocks, the elementary step of excavation, is controlled by the structure formed by the minerals. Planning as well as substantial modeling of an excavation project obviously requires a quantitative description of deformation behavior.

Elastic deformation of rocks is probably of subordinate relevance for their excavation. Elastic strains resulting from removal of material, the creation of openings, will remain well below 1% in most cases, because elastic moduli of rocks range from a few to a few tens of Gigapascal [34]. Elastic in-situ parameters are constrained by surveys using elastic waves. However, such dynamic parameters often significantly exceed the relevant static parameters [29]. This discrepancy originates from rock-mass heterogeneity associated with fractures and faults that also causes a scale dependence of elastic parameters. The arrival of elastic waves reflects the fastest paths associated with the least damaged rock sections, while static parameters represent bulk behavior dominated by the weakest sections. Non-linearity and inelasticity even for modest stress perturbations associated with excavation (typically orders of magnitude smaller than Young's moduli) are further consequences of the damage inventory.

As for any polycrystalline solid, the strength of rocks, i.e., a measure of the maximum stress they can bear in a specific loading configuration, depends on state variables, such as stress tensor components, temperature, and chemical milieu, and internal variables, such as grain size and porosity, including crack density. Under compression, the prevailing condition in the subsurface, geomaterials tend to fail on localized planes exhibiting obtuse

angles to the maximum principal (compressive) stress. This morphology and orientation relation led to address the failure planes as shear faults.

The presence of cracks and pores leads to the prominent dependence of compressive strength on mean stress. Failure of low porosity rocks in compression is accompanied by dilation, a relative increase in their volume, because failure results from nucleation, growth, and interaction of microfractures; therefore their strength increases with "confinement." The higher the porosity is the more shear-enhanced compaction may occur, counterbalancing the dilation. Porous rocks may develop localized compaction bands normal to the largest principal stress or deform in a ductile manner by non-localized cataclastic flow [96] at sufficiently high confinement. Pore collapse can even be induced by isostatic loading owing to the stress concentrations on grain contacts.

The faster the loading the stronger the rock appears; however, the effect of loading rate on strength is irrelevant for most technical applications since a change of one order of magnitude in strength requires more than 10 orders of magnitude change in strain rate. An increase in temperature tends to weaken rocks. With the potential exception of some carbonate rocks, evaporates, and claystones, the reduction stays well below an order of magnitude as long as temperatures stay below about 300 °C, the current limit for engineering subsurface projects. The limited number of data on samples of significantly different size indicates a reduction on strength with increasing size that likely reflects a scaling between the size of pre-existing flaws and sample size. The presence of water tends to have a weakening effect; the identification of the underlying physical and chemical processes has proven difficult.

Before representing descriptions of the failure of rocks, it seems mandated to emphasize that the user of such relations (and associated empirical parameters) has to answer the question what is to be modeled. The immediate interaction of a cutting tool and a rock is probably dominated by the strength as determined on rock samples that are intact before the experiment, in the sense that pre-existing interfaces do not completely dissect them. In-situ, the pre-existing inventory (size, density) of discontinuities (joints, faults) affect failure progression and the fragment size. Studies on rock properties distinguish (intact) rock and rock mass (including mesoscopic structure, joints, faults).

Frictional strength poses a lower limit for the compressive strength of rock masses. Frictional strength of interfaces in rocks varies significantly with their roughness and the acting normal stress. Frictional sliding is associated with local wear of asperities and thus strongly depends on deformation history. When described by a conventional linear relation between shear stress and normal stress, Amonton's law, the intercept, often addressed as cohesion, tends to increase with roughness. The slope, the coefficient of friction, converges to values between about 0.6 and 0.8 for many rocks, an empirical observation today known as Byerlee's law or, probably more appropriately, rule [11].

In contrast to metals, rocks -not unlike concrete- exhibit a uniaxial compressive strength C that is about an order of magnitude larger than their tensile strength T [59]. The determination of tensile strength is technically cumbersome and thus such experiments are seldom performed. In contrast, measurements of the mode I fracture toughness

K_{Ic}, the resistance of a material against propagation of a single tensile fracture, are simple and thus often performed. From a fracture mechanical perspective, tensile strength obeys

$$T = K_{Ic}/\sqrt{\pi c_{\text{ini}}} \tag{3.1}$$

and thus constitutes a measure of the size of the pre-existing crack c_{ini} that leads to the macroscopic failure.

Fracture criteria of rocks, surfaces in the three-dimensional space of principal stresses, have been extensively investigated for more than half a century [71]. The commonly used linear Mohr-Coulomb criterion postulates that failure occurs on a plane, for which a critical shear stress

$$|\tau| = S + \mu_{\text{int}}\sigma_n \tag{3.2}$$

is reached, where S denotes an intrinsic shear strength and μ_{int} the coefficient of internal friction. The shear strength is related to the uniaxial compressive strength as $S = C/\left[2\left(\sqrt{1 + \mu_{\text{int}}^2} + \mu_{\text{int}}\right)\right]$. Such a linear description is often acceptable for the limited range in normal stress relevant for technical applications. However, this formulation implies that the slope of the criterion μ_{int} and the orientation of the failure plane with respect to the least principal stress, β, are related by

$$\beta = \frac{\pi}{4} \pm \frac{\arctan\mu_{\text{int}}}{2}. \tag{3.3}$$

Experimental evidence does not support this assertion but documents an increase in the failure angle and a decrease in the coefficient of internal friction with increasing mean stress [59]. The non-linearity is reflected by the empirical Hoek-Brown criterion, in its most general form requiring the determination of three parameters [27]. Quite some effort has been spent on relating the parameters to rock-mass indices to allow for modeling of failure on the meter to decameter scale. Costamagna et al. [21] related failure to the Cardano condition for the existence of three real-valued eigenvalues of the characteristic equation of the stress tensor to arrive at linked friction and fracture criteria involving three parameters.

Murrell [67] extended the micromechanical Griffith concept of failure [37] to overall compressive stress states to arrive at a non-linear criterion with a single parameter,

$$\tau_{\text{oct}}^2 = 8T\sigma_{\text{oct}} = \frac{2}{3}C\sigma_{\text{oct}}, \tag{3.4}$$

where $\tau_{\text{oct}} = \sqrt{(\sigma_1 - \sigma_2)^2 + (\sigma_1 - \sigma_3)^2 + (\sigma_2 - \sigma_3)^2}/3$ and $\sigma_{\text{oct}} = (\sigma_1 + \sigma_2 + \sigma_3)/3$ denote octahedral shear and normal stress, the latter being identical to mean stress.

The second equality in Eq. 3.4 reflects the relation between tensile and uniaxial compressive strength $C = 12T$, inherent in the criterion, in good agreement with experimental

evidence. The fundamental criticism of fracture-mechanics based criteria as Eq. 3.4 addresses the notion that compressive failure is not caused by the propagation of a single critical defect. In contrast, compressive stresses eventually penalize growth [26] and the formation of the shear fault results from complex interaction and coalescence of multiple micro-cracks [58]. Subsequent fracture-mechanical treatments of compressive failure related the parameters of Mohr-Coulomb type linear criteria to the central parameters fracture toughness and initial crack length amended by a microscopic friction coefficient addressing the sliding of closed microfractures [5, 62, 89].

3.2.2.2 Laboratory Indentation Tests

Rock fragmentation in mechanized tunneling involves in general two basic processes: indentation and cutting (Fig. 3.1). In both processes, the fragmentation depends on the penetration depth of the used tool, though they differ in whether the tool travels normal (indentation) or parallel (cutting) to the rock surface. When penetration increases up to a critical depth, the rock behavior transits from non-localized deformation to localized deformation, i.e., fracturing, the latter of which is favorable for rock fragmentation. The simple, well-reproducible and accurate indentation test has long been utilized to measure different material properties, such as hardness [43], yield stress [91], and fracture toughness [85], though mostly for glasses and ceramics, and to assess rock properties, such as drillability and cuttability [90, 92]. The maximum indentation pressure p_{max} is a pivotal parameter in interpretation of indentation tests; it represents the specific energy for removing a unit rock volume in cutting experiments with a Non-Truncated Tip Indenter (NTTI) [92].

The indentation process can be continuously monitored using advanced experimental techniques, such as electron scanning microscopy [54], digital image correlation [107], acoustic emission [19, 106], infrared thermography [57], and electronic speckle interferometry [19]. Numerical simulations, based, for example, on the discrete element method [40] and the finite element method [56], have also been performed. These experimental and numerical studies revealed that rock indentation involves several operating processes including volumetric compaction, plastic deformation, and macro fracturing.

Many simplified models have been proposed to explain the stresses and the deformation under indenters in brittle solids, perhaps most notably in glasses, among which is the cavity expansion model (CEM) [42, 51]. Ever since its transfer to rock, a frictional geomaterial [19, 39], the model has gained popularity, but formulations were limited to the Non-Truncated Tip Indenter (NTTI). Such ideally sharp indenters suffer from severe wear due to the high stress concentration at their tips. The tool wear lowers the fragmentation efficiency as energy is invested in the deformation of the tools instead of in rock breakage, which motivates usage of cutting tools with truncated tips. The use of Truncated Tip Indenters (TTI) changes the failure mechanism; a phase of compressive failure below the flat indenter precedes the tensile splitting. Often, indentation tests conducted using a TTI were erroneously interpreted using relations developed for NTTI. The incorporation of tip truncation by [1] does not account for the ultimate fracturing. Recently, Yang et al.

[105] proposed a model based on the CEM for TTI that captures plastic deformation in compression and brittle tensile fracturing, and finite sample size. Here, we use the term "plastic" for macroscopically non-localized deformation irrespective of the deformation mechanisms on grain scale.

Mechanical and acoustic emission responses during indentation The investigations performed focused on intermediate-strength rocks, positioned between the two endmembers, soil and rock, either due to "weak" minerals (e.g., calcite, clays, halite) or "weak" structures (e.g., porous), because they pose particular problems regarding the "right" selection of excavation tools. We describe the general response of such intermediate-strength rocks to indentation using exemplary data from tests on a variety of sandstones, limestones, and tuffs with compressive strengths (UCS) from 11 to 140 MPa (Table 3.1). The damage progression and failure process was monitored during the indentation test using an acoustic-emission (AE) system (ASC Milne, Applied Seismology Consulting, UK). The uncertainty of locating AE hypocenters is around 8 ± 2 mm that is comparable to the size of the used AE sensors. Testing apparatus, procedures and specimen preparation are detailed in [105].

Typically, the force increases almost linearly to a distinct peak during the indentation process (Fig. 3.12); AE hypocenters gradually form a cluster beneath the indenter during the loading (Fig. 3.13). At the end of a test, the AE hypocenters trace the macroscopic fracture closely, indicating the validity of the AE technique for monitoring of the failure process. The indentation pressure typically exhibits a plateau-like maximum preceding the peak force, indicating that growth of the damage zone, where compressive failure conditions are reached, eventually proceeds at almost constant energy input until the tensile
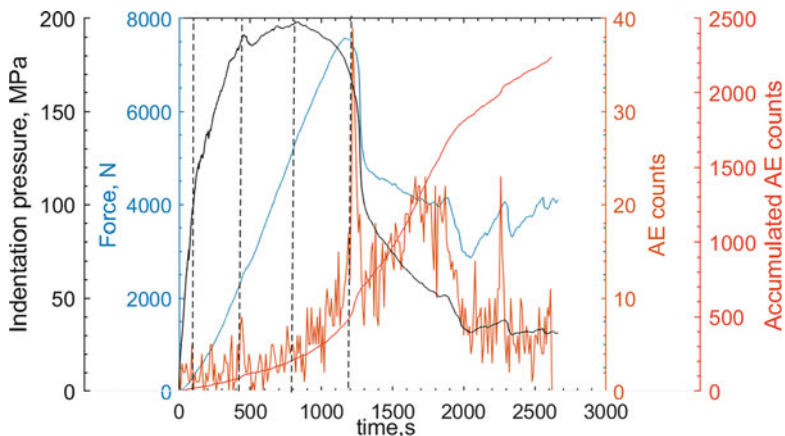
Fig. 3.12 Force, indentation pressure, number and total number of AE counts over an interval of 20 s as a function of time for a Gildehaus sandstone specimen of 84 mm diameter and 100 mm height. Tests performed in displacement control with a constant piston velocity of 0.05 mm/min

Table 3.1 Physical and strength parameters of eight rocks presented by mean values and their standard deviation, and the number of tested specimens in parentheses

Rock	Density kg/m³	Porosity %	$v_{p,dry}$ km/s	$v_{s,dry}$ km/s	$v_{p,sat}$ km/s	$v_{s,sat}$ km/s	E GPa	Poisson's ratio	K_{IC_dry} MN/m$^{1.5}$	K_{IC_sat} MN/m$^{1.5}$	UCS MPa	ϕ °	ψ °	p_{max_dry} MPa	d_{max_dry} mm	p_{max_sat} MPa	d_{max_sat} mm
Anroechter sst (AS)	2468 ±5(3)	8.9 ±0.5(3)	4.93 ±0.07(3)	2.97 ±0.02(3)	4.99 ±0.13(3)	2.61 ±0.10(3)	38.2 ±0.1(2)	0.16 ±0.04(2)	1.36 ±0.08(3)	1.18 ±0.04(2)	140	33	35	513 ±57(4)	0.28 ±0.05(4)	499 ±183(3)	0.19 ±0.02(3)
Stubener sst (ST)	2087 ±32(3)	16.5 ±3.3(3)	3.22 ±0.07(3)	1.98 ±0.05(3)	3.74 ±0.05(3)	1.91 ±0.04(3)	18.9 ±2.9(2)	0.21 ±0.11(2)	0.53 ±0.03(6)	0.41 ±0.03(4)	30	33	30	370 ±72(4)	0.15 ±0.04(4)	316 ±31(3)	0.14 ±0.02(3)
Leistaedter sst (LS)	2116 ±55(3)	16.6 ±5.5(3)	2.68 ±0.09(3)	1.80 ±0.04(3)	2.90 ±0(1)	1.00 ±0(1)	11.4 ±0.4(2)	0.21 ±0.02(2)	0.25 ±0.02(3)	0.13 ±0.05(4)	15	44	21	185 ±52(4)	0.23 ±0.02(4)	113 ±50(3)	0.30 ±0.17(3)
Ettringer Tuff (ET)	1594 ±15(3)	27.0 ±1.5(3)	2.95 ±0.01(3)	1.64 ±0.01(3)	3.27 ±0.09(3)	1.58 ±0.03(3)	7.5 ±0.4(2)	0.43 ±0.05(2)	0.32 ±0.05(3)	0.16 ±0.14(2)	22	0	113	125 ±50(4)	0.38 ±0.38(4)	0.21	±0.08(3)
Weiberner Tuff (WT)	1396 ±10(3)	39.8 ±1.0(3)	2.52 ±0(3)	1.44 ±0.03(3)	2.39 ±0.01(3)	1.30 ±0.04(3)	4.0 ±0.9(2)	0.15 ±0.04(2)	0.25 ±0.02(3)	0.24 ±0.01(2)	11	n.d.	n.d.	71 ±4(4)	0.50 ±0.08(4)	48 ±9(3)	0.49 ±0.21(3)
Gauinger Travertine (GT)	2203 ±31(3)	13.7 ±3.1(3)	4.93 ±0.11(3)	2.88 ±0.03(3)	5.18 ±0.14(3)	2.66 ±0.11(3)	28.5 ±1.7(2)	0.43 ±0(2)	0.84 ±0.14(3)	0.80 ±0.19(2)	50	n.d.	n.d.	486 ±159(4)	0.29 ±0.08(4)	534 ±162(3)	0.20 ±0.06(3)
Sellenberger shell limestone (SM)	2369 ±52(6)	9.0 ±5.2(6)	5.05 ±0.05(6)	2.77 ±0.03(6)	5.68 ±0.11(6)	2.65 ±0.01(6)	22.5 ±10.7(4)	0.44 ±0.01(4)	0.73 ±0.04(3)	0.48 ±0.03(2)	23	n.d.	n.d.	387 ±141(4)	0.16 ±0.03(4)	419 ±107(3)	0.14 ±0.06(3)
Gildehaus sst (GBS)	2010 ±20(18)	22.1 ±1.6(18)	2.56 ±0.06(34)	1.71 ±0.09(15)	3.20 ±0.09(15)	1.68 ±0.04(8)	9.5 ±1.2(3)	0.18 ±0.10(1)	0.30 ±0.03(9)	0.26 ±0.04(7)	57.0 ±4.5(3)	37	30	181 ±33(15)	0.58 ±0.22(15)	n.d.	n.d.

E: Young's Modulus; ϕ (= arctan μ_{int}): internal friction angle, (see Eq. 3.2); ψ: Dilation angle, i.e., parameter of non-associated flow rule; K_{IC}: Mode I fracture toughness determined from three-point bending tests on specimens of 10 mm diameter and 33 mm length; UCS: uniaxial compressive strength; p_{max}: peak indentation pressure determined from tests on specimens of 30 mm diameter and 50 mm height. Subscripts "dry" and "sat" indicate testing of dry or saturated specimens, respectively
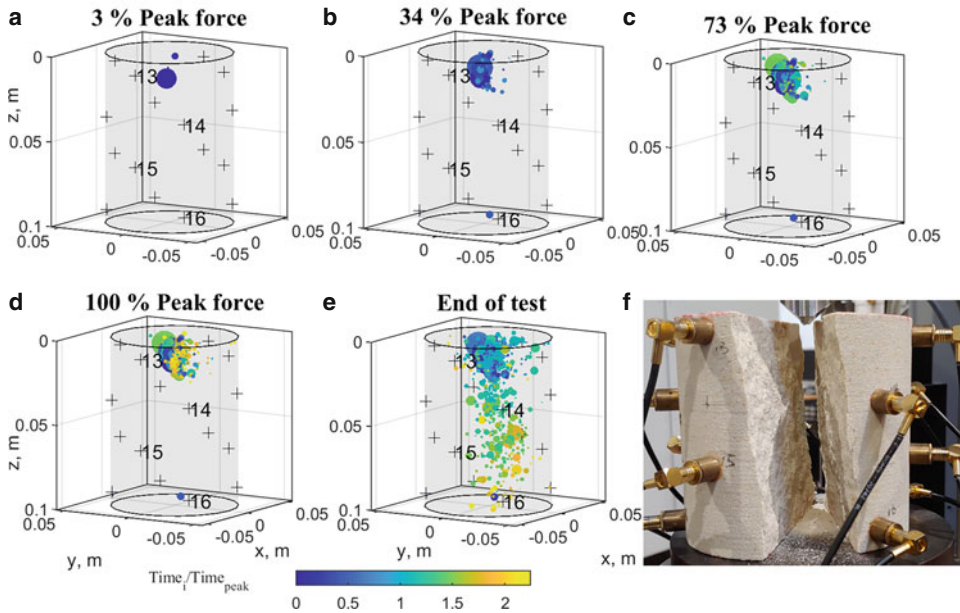
Fig. 3.13 Cumulative temporal-spatial distribution of AE hypocenters (circles) at different percentages of peak force (**a–d**) indicated in Fig. 3.12 by the vertical dashed lines, end of test (**e**) and photograph after indentation test (**f**). The marker size indicates the relative magnitude of AE energy. Crosses indicate sensor locations. The color bar indicates time relative to the one at peak force (with regard to [105])

tangential stress at the rim of this zone suffice to induce growth of a macroscopic tensile fracture that ultimately splits the specimen. When peak indentation pressure is surpassed, the cluster region representing the damage zone below the indenter does barely grow further (Fig. 3.13c, d), until growth of the macroscopic fracture becomes apparent.

The force-displacement curves for the "hard," Anröchter Sandstone (AS in Table 3.1), with the highest uniaxial compressive strength (140 MPa) among the tested rocks, differ from that for the "weak" to "intermediate-strength" (uniaxial compressive stress less than about 80 MPa) rocks regarding the post-peak stage of indentation. For the intermediate-strength rocks, indentation beyond peak force is associated with a drop to a finite load that is then maintained for a displacement of several tenths of millimeters, during which the median crack propagates towards the bottom of the specimen. For the hard rock, brittle fracturing after peak force is more violent and typically results in coeval splitting of the sample and total loss of load bearing capacity.

Analysis of the results of indentation tests   Analysis of the mechanical and acoustic-emission response indicates that the failure associated with rock indentation involves successively initial elastic deformation, punch-in of indenter into the specimen associated
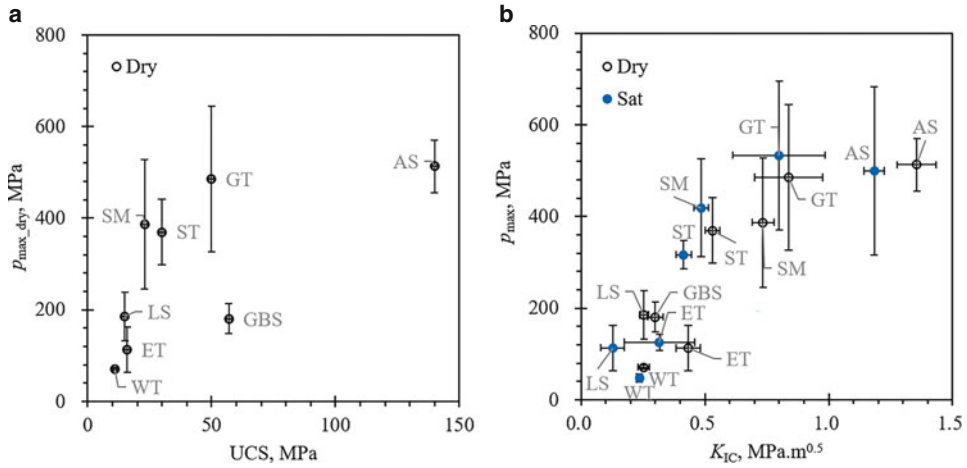
Fig. 3.14 Correlation between indentation characteristics and the two conventional strength parameters, unixial compressive strength (**a**) and fracture toughness (**b**). Uniaxial compressive strength (UCS) was only determined for dry samples. Indentation tests were not performed on saturated GBS samples. Error bars indicate standard deviations; a minimum of 3 tests were performed for each rock variety and saturation condition

with gradual formation of a crushed zone, formation of a damaged zone, and nucleation and growth of a macroscopic fracture that eventually splits the sample in half. We simplified sample failure due to indentation with a conceptual model as detailed in [105]. The model emphasizes the role of the peak-indentation pressure p_{max} that indicates the resistance of the tested rock to compressive failure in the damage zone, e.g., described by the Mohr-Coulomb failure law (Eq. 3.2), that precedes the initiation of macroscopic tensile fracturing.

The experimentally observed maximum indentation pressures correlate with fracture toughness for the eight investigated rocks (Table 3.1). While saturation of samples with water systematically reduced toughness, the sample-to-sample variability is too large to identify an effect of saturation on maximum indentation pressure (Fig. 3.14a). The correlation between p_{max} and uniaxial compressive strength (UCS) is also positive but the highly porous Gildehaus sandstone (GBS) seems to deviate from the general trend (Fig. 3.14b). The correlation of the maximum indentation pressure with the two strength parameters is consistent with our interpretation that it marks the transition from non-localized compressive failure in the damage zone to localized tensile fracturing at its boundary. The maximum indentation pressure increases with sample size, as evidenced by results for GBS specimens with a diameter from 30 mm to 84 mm.

For a specific rock variety, the sample-to-sample variability in maximum indentation pressure is not random, but we find an inverse correlation between p_{max} and the associated penetration depth d_{pmax} (Fig. 3.15a). The pairs (d_{pmax}, p_{max}) do however show no systematic relation for the suite of rocks.
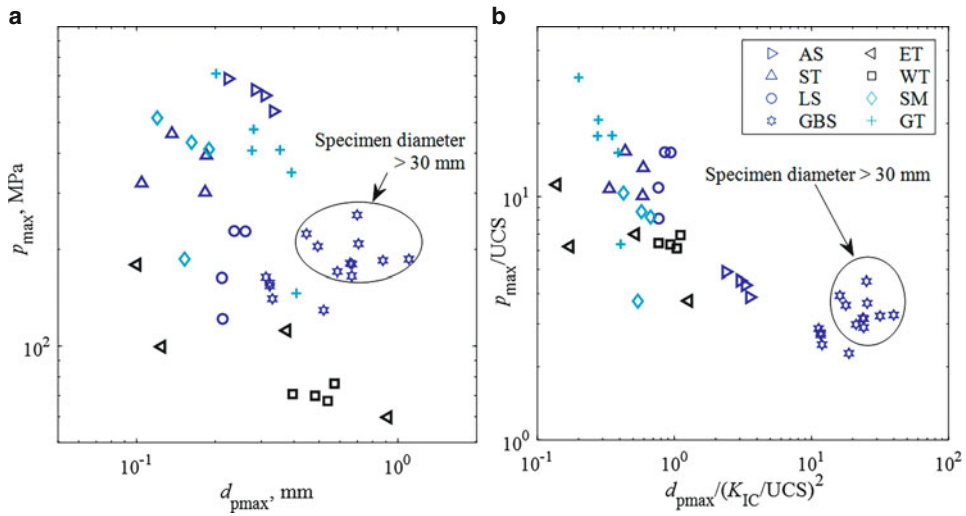
Fig. 3.15 Correlation between maximum indentation pressure and associated penetration depth in dimensional (**a**) and normalized form (**b**). Markers in blue, black and cyan indicate sandstone, tuff, and limestone, respectively. All but the encircled data points represent tests on samples with 30 mm diameter. The legend holds for (**a**) and (**b**)

To address material differences, the data is presented in normalized form, according to the theoretical analysis of [105]. Uniaxial compressive strength serves as a zero-order estimate of the stress corresponding to the yield conditions for the material in the damage zone, and we thus normalize maximum penetration pressure by it. The damage zone grows until its boundary reaches a pre-existing flaw, for which the tangential stress on the boundary corresponds to the critical stress concentration, the fracture toughness. For a given material, critical penetration depth and damage zone size correlate; damage zone size and the stresses in it–determined by compressive failure conditions–control the stress concentration on pre-existing flaws. The size of initial flaws scales approximately with $(K_{IC}/UCS)^2$ [5]; thus, we use this ratio to normalize critical penetration depth. As a result, there appears to be a general decreasing trend between the ratio of p_{max}/UCS and $d_{pmax}/(K_{IC}/UCS)^2$ (Fig. 3.15b); yet, some differences between the various tested rock types with compositional differences remain. A potential reason could be the material-dependence of the initial flaw-size relation beyond that accounted for by the two strength parameters. Furthermore, Zhu et al. [108] found that the initial-flaw size scaling involves a dependence on porosity beyond its effect on fracture toughness and uniaxial compressive strength.

3.2.2.3 Numerical Investigation of Rock Fragmentation

Simulation of rock excavation requires tools that can handle the discontinuities associated with fracturing leading to fragmentation. We developed a peridynamic model [87, 88]

providing a natural way of incorporating discontinuities in the simulation domain. All peridynamic simulations were carried out using an extended version of the open source software *Peridigm* [55, 70]. The interested reader is referred to [14, 16] for further details on the simulation model.

We performed two sets of simulations with respect to the kinematics of the disc. Simulations of indentation tests (see Sect. 3.2.2.2 and [105]) were performed to provide insight into the formation of the crushed zone at the tool-rock interface and of tensile fractures emanating from that zone. Linear Cutting Machine (LCM) tests [79, 80] were treated to estimate the cutting forces required in the excavation process as a function of penetration depth. Besides homogeneous materials, we also considered mixed or heterogeneous ground conditions, situations where two or more types of rock or soil with significantly different mechanical properties are exposed at the tunnel face, to assess the variability of loads on the cutting discs and associated wear (see also Sect. 3.3.5).

These analyses are motivated by the characterization of the impulse load exerted on the cutting disc when it traverses a material interface, as this can cause excess vibration in the cutter head and increased fluctuations in torque and thrust of TBM. These peak loads also complicate the extraction of damage sensitive features based on the force oscillations.

Simulation of indentation tests Our simulations of indentation tests cover a total of six specimen sizes, with a combination of three diameters 30, 50 and 84 mm and two heights 50 and 100 mm. The truncated-tip indenter used is the same for all simulations (Fig. 3.16). For validating the current model, we use the experimental data from indentation tests on Gildehaus Sandstone reported in [105]. A qualitative validation relates to the formation of the crushed zone, from which tensile cracks initiate, while a quantitative validation rests on comparing the force-penetration data obtained from the experiments and the simulations.

Fig. 3.16 Indenter geometry used in [105] (dimensions are given in millimeter)
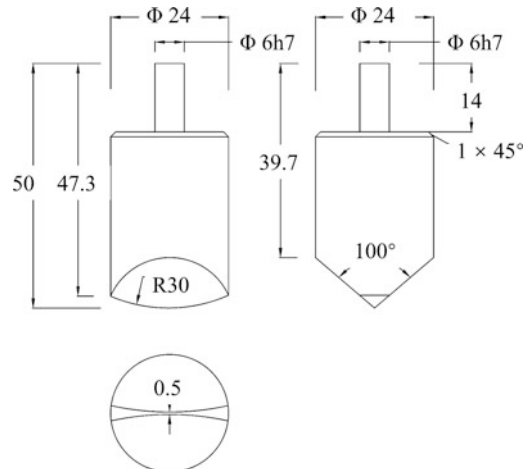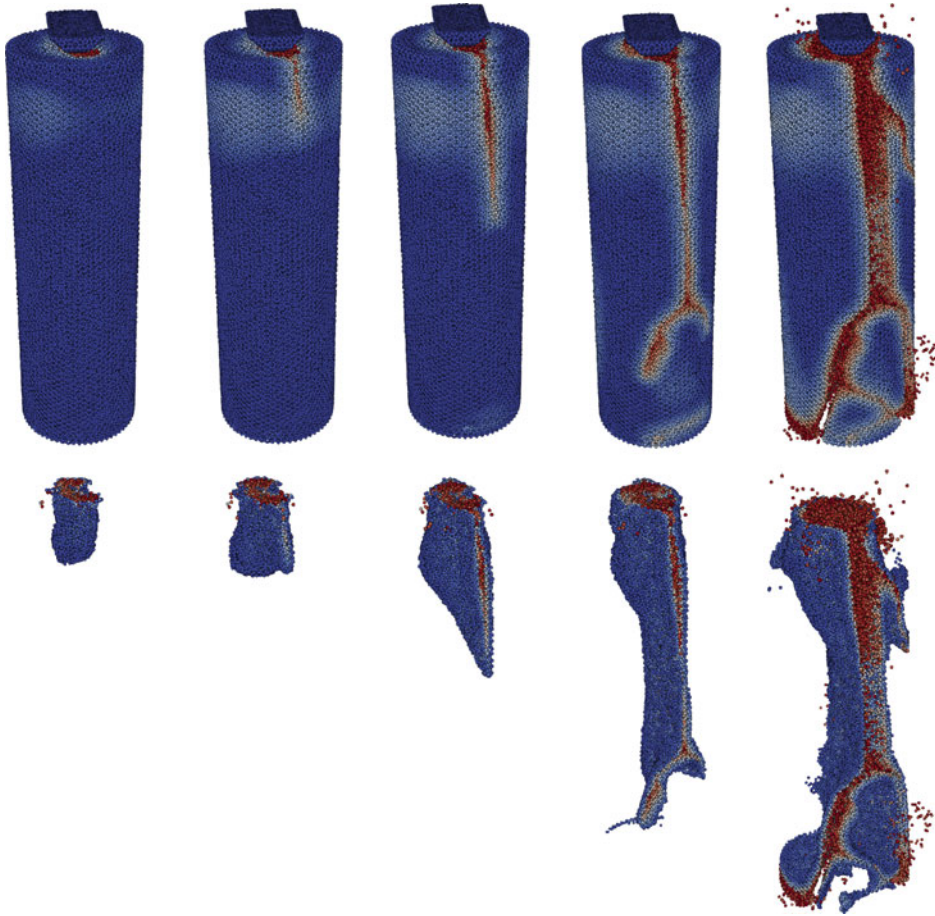
Fig. 3.17 Temporal evolution (left to right columns) of the fracture process during the indentation test (top row), the associated damaged and cracked regions are filtered out for visualization (bottom row)

The temporal evolution of fractures occurring due to the indentation load is presented in Fig. 3.17 for a specimen with 30 mm diameter and 100 mm height. The simulations capture the experimental observation of the successive formation of the crushed zone and the initiation of a central macroscopic tensile fracture splitting the sample in half. The interaction of the growing fracture with the sample's boundary leads to crack tip bifurcation [13, 15] and the crack branches. Finally, the specimen splits into two main and several small fragments. The loading stiffness as well as the peak load predicted by the simulation are in a good agreement with the experimental records (Fig. 3.18). However, the post-peak behavior differs slightly, which can be explained by the absence of damping in the simulations. As the main fracture starts propagating, the two large fragments move opposite to each other and separate faster than in the experiments, causing the indenter to

Fig. 3.18 Comparison of the force and penetration relationship measured in experiments and computed from the simulation model
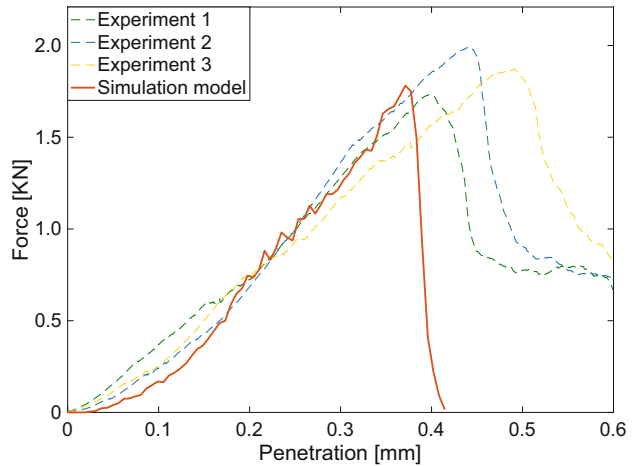
loose contact with the rock as soon as the specimen splits and thus the force at the indenter goes to zero. The progressing fracture opening can be can be observed qualitatively by comparing the last two columns of Fig. 3.17.

Simulation of rock excavation with cutting discs At the level of a single cutting disc, interactions between the rock and the cutting disc can be characterized by the reaction force, which is decomposed into normal, rolling and side forces. These forces need to be estimated for an individual disc to predict the performance of a TBM, i.e., the global torque and thrust requirements. In the LCM test [35, 78] developed at the Colorado School of Mines (CSM) to predict the performance of a single cutting tool, the cutting disc moves along the rock specimen at a known penetration level and the reaction forces are measured at the cutting disc. We use this test as a benchmark for our analysis model.

We performed peridynamic simulations of the LCM test with a cutting disc of constant cross-section and a diameter of 432 mm for four levels of fixed tool penetration. The dimensions of the specimen are 0.4 m × 0.4 m × 0.15 m in the simulations and we ascribed properties of an elastic-brittle constitutive relation corresponding to Colorado red granite (Young's modulus 41.0 GPa, Poisson's ratio 0.234, uniaxial compressive strength 158 MPa, fracture energy 85.7 J/m^2). The simulation results obtained from the rock cutting with a tool penetration depth of 7 mm (Fig. 3.19a) show an evolving damaged zone beneath the cutting disc; the temporal evolution of rolling, normal and side forces (Fig. 3.19b) are examined from 0.1 to 0.3 m to avoid the influence of the specimen boundaries. The average normal forces obtained from the peridynamic simulations [14] agree well with the experimental data from LCM tests [35] (Fig. 3.19c).

Simulations of excavation with cutting discs in mixed ground The excavation process in mixed ground conditions is analyzed using a scaled-down cutting disc. The analyses
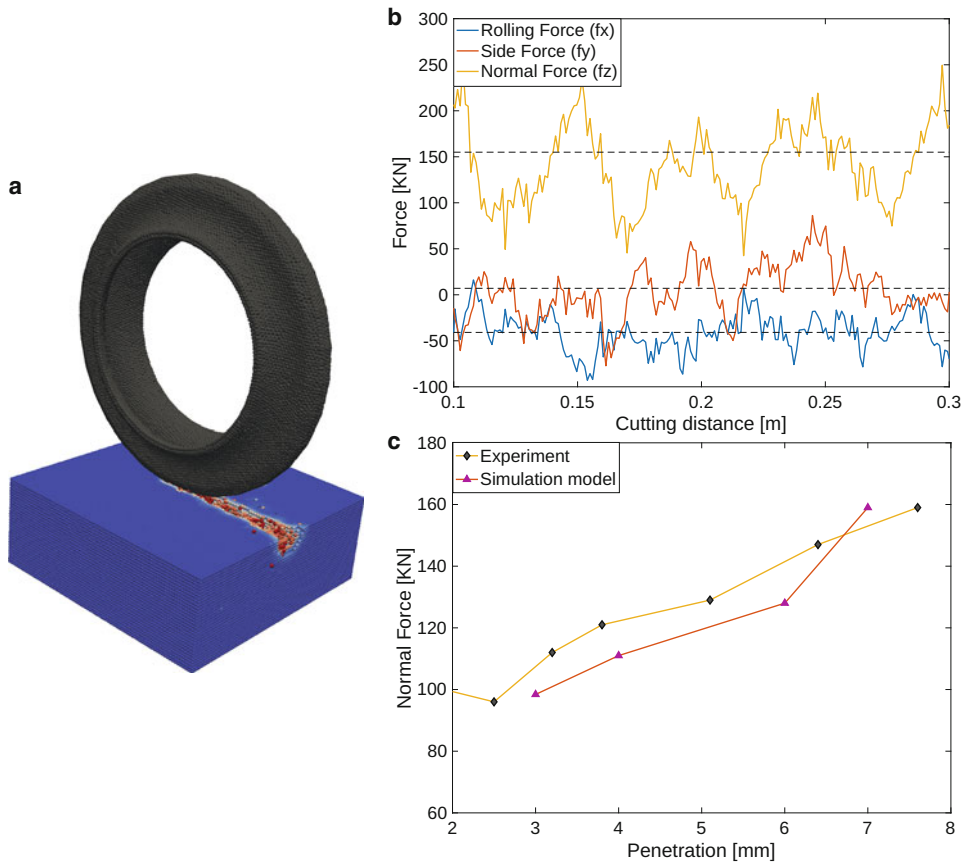
Fig. 3.19 Simulation of the LCM test showing the evolving fragmentation and crushing zone in the rock (**a**), evolution of cutting forces for a tool penetration of 7 mm (**b**) and average normal cutting forces for different tool penetrations compared against the results from the LCM experiment [35] (**c**)

consider a cutting disc moving from soft soil to hard rock medium. The soil material is modelled using an elastic-plastic constitutive relation and the rock material is modelled using an elastic-brittle constitutive relation. The soil's yield strength was 100 KPa and the rock's fracture energy $G_f = 23.7\,\text{J/m}^2$.

The simulated reaction forces at the cutting disc vary significantly with lateral displacement for the two penetration levels (Fig. 3.20b, d). The normal cutting forces are negligible (for the chosen yield strength) when the disc cutter is in the soil domain, but forces increase as it approaches the soil-rock interface (cutting length of 0.05 m) and when it thrusts through the rock domain. The peak in the cutting forces increases with an increase in tool penetration. Plastic deformations in the soil as well as the damage level in the rock also increase with increasing penetration levels (Fig. 3.20a, c).
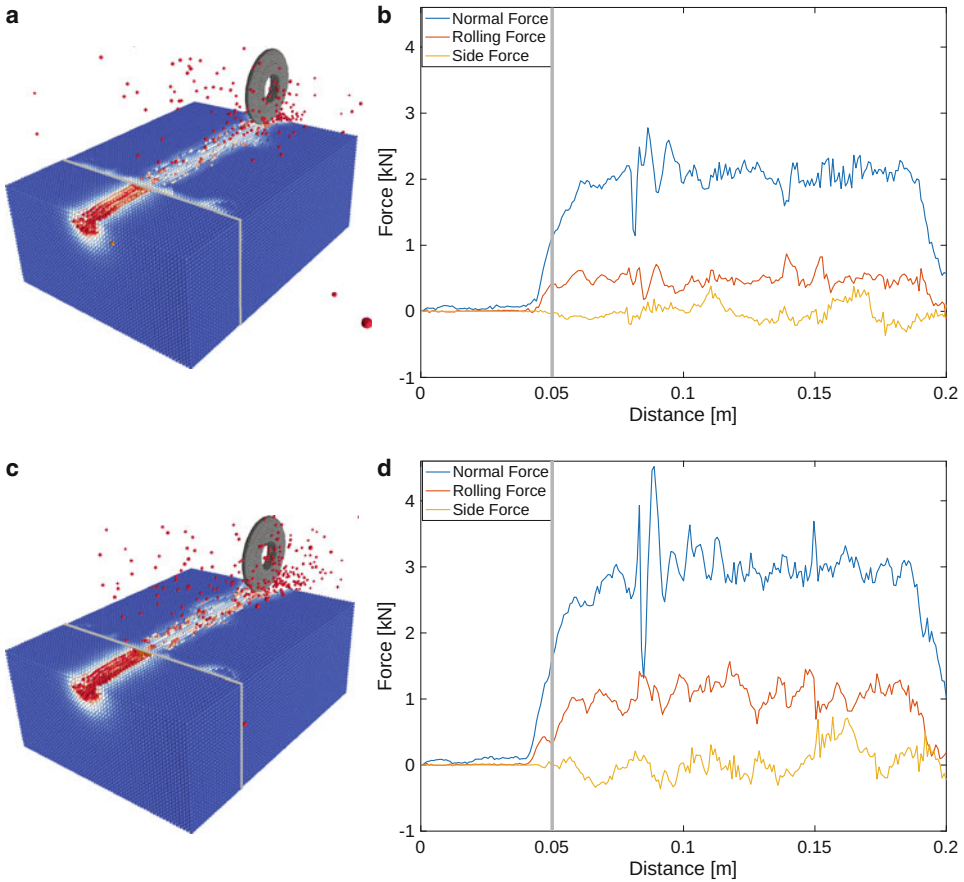
Fig. 3.20 Peridynamic simulation of a cutting disc working in mixed ground conditions (soft soil to hard rock domain) with a penetration of $p = 2$ mm and $p = 3$ mm. Plastic deformations and damage/fragmentation in hard rock is shown in **a** and **c** and the associated cutting forces acting on the disc are shown in **b** and **d**, respectively. (The vertical grey line represents the soil-rock interface)

3.2.3 Implications for Mechanized Tunneling and Outlook

Tool-soil interactions are a central component of mechanized tunneling excavations. The complexity of these interactions underlies the rapid evolution of the ground free surface and the development of large deformations, accompanied by the flow of the interstitial fluid in water-saturated soils. Laboratory tests performed on dry and water-saturated sand using a custom-made excavation device provided first-hand information regarding the topology of the material and the reaction forces generated on the tool during the excavation process. The presence of interstitial fluid and the development of shear bands strongly influences the reaction force-displacement curve. Presumably, this influence is associ-

ated with localized pore-pressure variations in the soil during the excavation. Numerical simulations of tool-soil interactions demonstrated that the proposed hypoplastic PFEM formulations were able to reproduce the main features of the mechanized excavation processes, including the soil deformations and the reaction forces on the tool. Furthermore, the presented models provided valuable insight into the spatial distribution of pore pressures in the ground and the effects of the initial density of the soil on the excavation process. Ongoing and future research concerning soil excavation include numerical simulations of mechanized excavations using an EPB cutting wheel model. Relevant boundary conditions, such as the required support pressure at the tunnel face, rotational speed and penetration rate of the wheel, will be considered. We will investigate the evolution of the torque generated at the wheel, the flow of excavated material at the face and the spatial distribution of pore pressures in the soil.

A crushed zone develops in rocks when the cutting discs installed on a rotating cutter head are hydraulically pressed against the tunnel face; as the disc continues to penetrate further, stresses around the crushed zone increase to the point that eventually macroscopic fractures are initiated. Fractures associated with neighboring discs coalesce leading to fragmentation and disintegration of the rock. Experimental investigation and analytical modeling of indentation tests identified the governing parameters for the involved mechanisms, non-localized damaging and localized brittle fracturing. The peak indentation pressure appears to indicate the transition from non-localized damaging below a truncated indenter to localized brittle fracturing, pre-requisite for the rock fragmentation that is aimed for in excavation procedures. Therefore, in practice, the tool has to exceed the penetration depth associated with the peak indentation pressure for efficient rock excavation. The corresponding thrust force may then be estimated through the established correlation between normalized peak indentation pressure and penetration. Thus, rock indentation tests performed in the laboratory provide relevant information on determination of operational parameters, such as thrust force and optimum penetration. In-situ, the rock fragmentation in mechanized tunneling is obviously complicated by many other factors, such as lithostatic stresses and the water-weakening effect, whose effects are poorly understood, and are therefore subject of ongoing research.

Numerical analyses performed using the framework of peridynamics theory have been proposed to predict the performance of a TBM in various scenarios. Results obtained from the indentation tests provided insight into the formation of the crushed zone from where the localized tensile fractures initiate leading to rock disintegration. Furthermore, the cutting forces obtained for a full-scale linear cutting test agree with the experimental recordings. Future work should account for different disc geometries, tool penetrations, tool spacings and cutting speeds. The cutting forces obtained from simulations of cutting discs moving from a soft ground domain to a strong rock layer yield a peak load at the soil-rock interface. The model was expanded to account for localized abrasive wear caused to the disc due to the cutting forces. Mechanized tunneling in mixed grounds results in highly variable loads on the cutting discs that may cause abnormal cutter wear leading to unexpected TBM stoppage.

3.3   Tool Wear in Mechanized Tunneling – Appearances, Mechanisms, and Countermeasures

Wear of tunneling tools causes downtimes of the TBM, both in a planned manner but more critically at unforeseen times if the wear rate of the tools exceeds preliminary wear predictions. It is crucial to understand the effective wear mechanisms that arise in the various geological conditions, to predict the rate of tool wear and its influence on the efficiency of the tunnel boring machine. Based on this assessment, the material concept for the tunneling tools can be adapted to minimize tool wear and reduce the risk of failure. This chapter illustrates the macroscopic appearance of the most important wear mechanisms, explains the underlying tribological micro-mechanisms, gives examples on how the wear behavior of materials can measured, and points out possible improvements for material concepts.

Tools in tunneling are subject to high mechanical impact loads that are caused by boulders and retaining walls, and abrasive wear. Both cause damage to the tools, which must be replaced in the case of mechanical overload (breakage by brittle fracture) or when the wear limit of the tool is reached. These tool replacements result in downtimes, which reduce the economic viability of the tunneling project [47]. To minimize downtimes for tool replacements, a large number of wear forecast models were developed in the past, which are mainly based on simple abrasiveness parameters of the soil to be removed, semi-empirical equations, or empirical values [45, 49, 60]. With the help of these wear forecast models, optimal tool replacement times can be determined in advance, supporting logistical planning of the tunneling project. Unfortunately, there are sometimes large deviations between the estimated and the actual tool wear occurring during operation. The reason can be traced back to the complexity of the description of tool wear. Wear does not only depend on the abrasiveness of the soil to be excavated, the tool concepts used, or the machine parameters, but wear is a system variable. To understand how wear of tunneling tools can be counteracted efficiently, we follow a top-down approach. After the description of the macroscopically visible wear, the tribological system of tunneling tools is illustrated and tooling concepts that derive from the tribological system explained. Then, the micromechanisms of wear are investigated, and finally laboratory experiments and test-rigs for wear-prediction and wear-investigation are presented. A subdivision into soils and rocks is made to cope with the variety of grounds and therefore utilized tunneling tools,

3.3.1   Soils: Excavation, Tooling Concepts and Wear Appearances

Excavation of non-cohesive soils is mainly carried out by scraping the soil surface to detach the loosely bound soil particles (Fig. 3.24a). The commonly used tools for this purpose are chisels and rippers [36]. The wedged shape of the chisels causes a peeling process within the soil when the rotating TBM shield is pressed against the soil surface.

Table 3.2 Classification of material groups with applications in mechanized tunneling

Material Group	Application	Microstructure	Hardness
construction steels	welded constructions	Ferritic-Pearlitic	lowest
Q+T Steels	chisel substrates	tempered martensite	medium
tool steels	cutting discs	tempered martensite + 5–15% carbides	medium-high
metal matrix composites	wear protective layers	Ni-based metal matrix + 50% WSC	high
cemented carbides	cutting edges	70–95% WC in Co-based matrix	highest

After being detached from the soil-corpus, the loose particles drop into the feed section of a transport screw at the bottom of the TBM-shield and are transported away from the tunnel face. Based on this excavation mechanism, chisel tools experience mainly abrasive wear. Due to the tool's motion relative to the soil particles, the tool surface is frequently scratched by the abrasive particles. To counteract abrasion, tools are locally protected with wear protection elements, such as inserts of cemented carbides and hardfacings produced by a built-up welding technique [47]. However, the material response to abrasive wear differs for the wear-protective elements and the substrate (Table 3.2). The wear-protective elements, such as the cutting edge, inlays, and welded wear-protective layers, are worn evenly at a low and steady rate. In contrast, the substrate can experience uneven abrasive wear that may have an increasing wear rate over time. For example, suppose a wear protective element is lost due to missing support of a worn substrate. In that case, the wear rate at the place of the missing wear-protective element will increase drastically, compared to other areas of the tool, which still possess their wear-protective elements (Fig. 3.21).
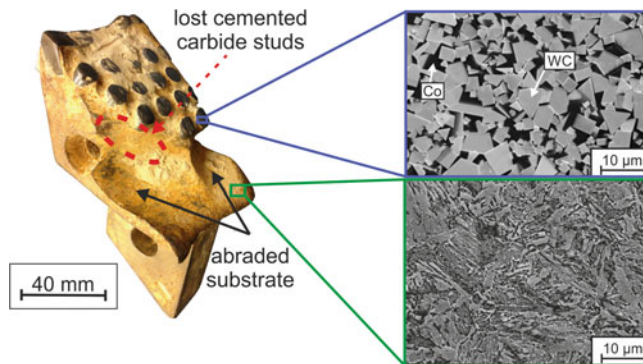
Fig. 3.21 Illustration of the graded build up of a chisel tool, consisting of a steel substrate and cemented carbide wear-protective elements

The abrasive attack on chisel tools is most pronounced at the cutting edge, which constantly encounters new soil layers and bears the highest cutting forces. Impacts, for example due to contact with large rock particle inclusions (e.g. pebbles) or layer interfaces, also act directly on the cutting edge; therefore, adequate toughness is necessary to avoid catastrophic fracture. The necessary combination of high resistance against abrasive wear and high fracture toughness renders the cutting edge the most demanding part of the tool. Cemented carbides of the type WC-Co have proven to be the only suitable group of materials, fulfilling the requirements for the cutting edge in practice. The microstructure of cemented carbides consists of 70-95 Ma% tungsten monocarbides WC, which are embedded in a cobalt-based binder phase [10].

To increase the fracture toughness, coarse grades with a Co-binder content of 15 Ma% or more are chosen for the cutting edge. At the same time, wear protective inserts on other places of the chisel tool may use a lower binder content to increase their wear resistance, as strong impact loads act less frequently on those parts. Other chisel parts, such as the backside, only experience wear due to excavated particles falling on them. In these cases, build-up welded wear-protective layers made of Ni-based metal matrices incorporating 30-50 Vol% Fused Tungsten Carbide (FTC) hard particles represent an easily applicable and cost effective solution to protect the steel substrate of the tool from abrasive wear. The substrate material forms the body of the tunneling tool and is the carrier of all functional elements, such as cutting edges and wear-protective elements. External forces acting on the tool are transmitted through these functional elements into the substrate, which must absorb and transmit the forces into the TBM superstructure. To avoid fracture because of mechanical overloads, the substrate has to be tough and must be able to dismantle critical stress peaks by means of small plastic deformations. Nevertheless, the substrate must also have the mechanical strength to bear the cutting forces during TBM operation and support the tool's functional elements. Quenched and tempered steels such as 42CrMo4 or 30CrNiMo8 are commonly employed as substrate materials for tunneling tools because of their high strength and sufficient toughness. A heat treatment of the forged base body enables the strength and toughness to be adapted to the needs in a wide range. Conventionally, quenched and tempered steels are hardened martensitically and tempered to a high degree to increase their toughness [9].

3.3.2   Rocks: Excavation, Tooling Concepts and Wear Appearances

Rocks cannot be excavated efficiently by scraping tools. Instead, cutting discs are used, which break down aggregates by induction of compressive stresses. The cutting discs roll over the rock surface in a circular path. Due to their direct contact with the rock and its fragments, cutting discs are exposed to abrasive wear, similar to chisel tools. However, their load collective is dominated by the high mechanical forces due to higher shear strength of rock compared to soil, as well as by a cyclic loading occurring upon repeated
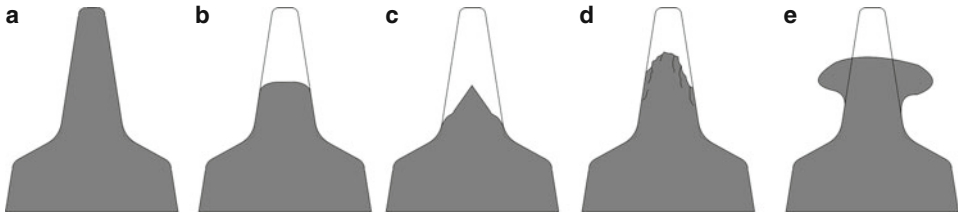
Fig. 3.22 Wear appearances on the cutting edge of cutting discs. **a** New cutting disc, **b** even abrasive wear, **c** flank wear, **d** surface fatigue, **e** plastic deformation

impact with the rock surface [47]. Therefore, cutting discs are typically not designed in a graded assembly of the substrate and dedicated wear-protection elements. Instead, the cutting disc is manufactured from forged tool steel with high strength and toughness and significantly higher hardness than the quenched and tempered steels used for substrates of chisel tools. In cases of extreme abrasive wear, cemented carbide studs may also be inserted into the cutting edge of cutting discs to increase the wear resistance.

The changes in geometry of the cutting edge during the use of the cutting disc depend on the activated wear mechanism (Fig. 3.22). Severe tapering of the edge as seen in Fig. 3.22c, for example, results from the different relative movements of soil particles to the cutting edge and the flanks of the cutting disc. While the contact of the cutting edge to the soil can be described as a rollover movement with ideally no relative movement, the flanks are in constant relative movement to soil particles. Especially the repeated movement of cutting discs in previously formed grooves can lead to flank wear.

Another form of uneven wear can be found on stuck or blocked cutting discs. If the cutting ring of the whole tool assembly is unable to rotate freely, one side is in constant contact with the soil and therefore worn out. This mechanism can occur especially in adhesive grounds or in case of a blocked roller bearing, for example, by infiltration of abrasive particles into the bearing assembly.

Surface fatigue mainly occurs on the surface of the wear-protective elements that are applied on tunneling tools. Worn tools show signs of spalling, as well as small cracks (Fig. 3.23).

The wear due to surface fatigue is concentrated to the parts of the tool that are regularly impacted by large abrasive particles. Due to the gradual sequence of the micro-processes of surface fatigue, the wear loss of the wear-protective elements can increase sharply after a particular time. Small fatigue cracks accumulate in the first stage of surface fatigue, but the actual wear loss only occurs in the last phase of spalling. Due to surface fatigue of the wear-protective elements, the soft substrate material underneath becomes exposed to the ground. As a result, the abrasive wear that has been prevented previously by the wear-protective elements increases and can lead to rapid unforeseen damage of the tunneling tools and even their support structures.
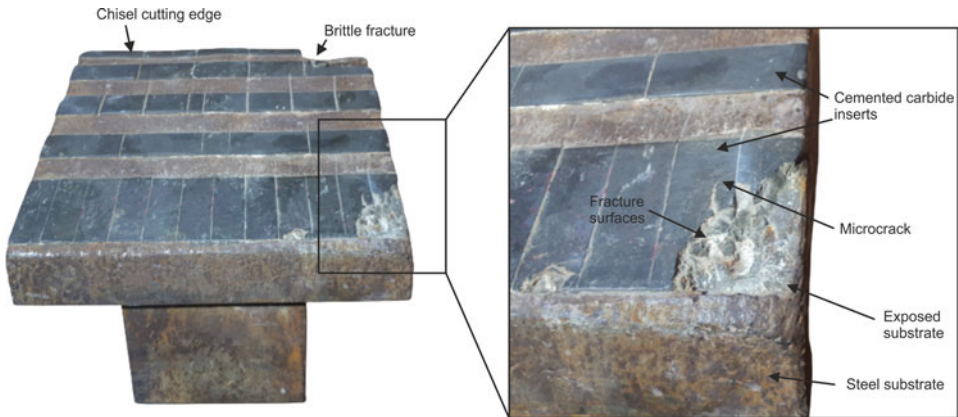
Fig. 3.23 Surface fatigue on the cemented carbide inserts of a chisel tool

3.3.3 Tool Wear Micromechanisms-Classification and Fundamental Concepts

The interaction of the tools with the ground can only be understood by developing a fundamental understanding of the tribological system. With this understanding, measures can be derived that improve the wear resistance of the tools and thus prolong their lifetime. The tribological system consists of the tool (base body), the wear-causing soil (counter body) and all other relevant variables such as the collective load (penetration, transferring forces), the surrounding medium (groundwater) and the intermediate medium (e.g. bentonite suspension) (Fig. 3.24) [23].

Four main wear mechanisms are distinguished, including abrasion caused by hard particles scratching the tool surface and surface disruption resulting from cyclical mechanical or impact stresses causing wear on TBM tools. Tribo-chemical reactions and adhesion have to be mentioned as well, however, they play a subordinate role in the wear damage to TBM tools. In reality, the main wear mechanisms overlap. For the derivation of suitable wear protection measures, the goal is to identify the dominant primary wear mechanism by developing a basic understanding of the tribological system. Because TBM tools are exposed to hard, abrasive particles and cyclical mechanical loads, both main wear mechanisms will be examined in more detail below. Once the dominant wear mechanism has been identified, it is essential to understand the interactions between the components in the material to be excavated and the individual structural components of the tool. With this knowledge, specific metallurgical measures can be derived that increase the tool life.

3.3.3.1 Abrasive Wear
Abrasive wear is the mass loss of a body due to scratching and/or grooving by a harder counter-body. In the case of mechanized tunneling, grains of quartz (SiO_2, ca. 1100–
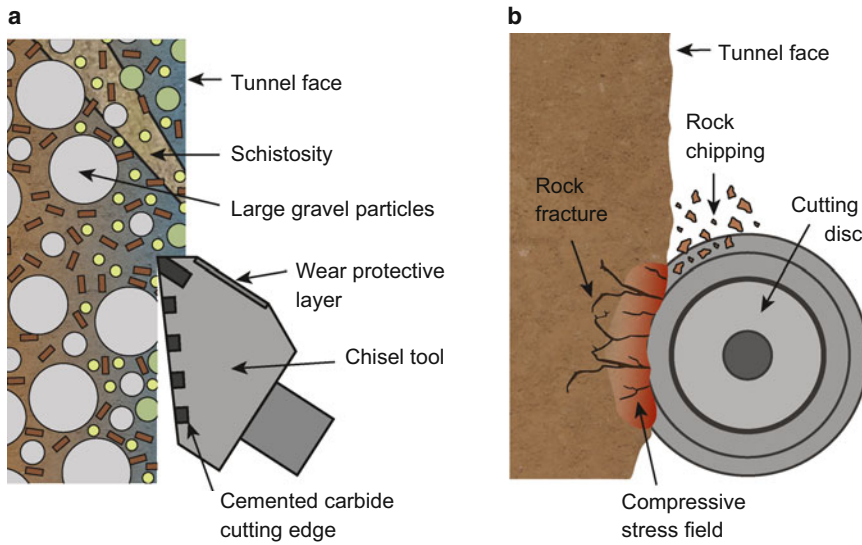
Fig. 3.24 Schematic illustration of the tribological system of **a** a chisel tool and **b** a disc cutter

1200 HV0.05) [81], corundum (Al$_2$O$_3$, ca. 2000–2200 HV0.05), or other hard non-metallic compounds represent the counter-body; they are regarded as abrasive particles because their hardness exceeds the hardness of the steels (max. 900 HV10) [10] used for the base construction of tunneling tools and the TBM itself, therefore causing abrasive wear.

Four distinct micro mechanisms of abrasive wear can be distinguished [33]: Micro ploughing, micro chipping, micro fatigue and micro cracking. Micro ploughing in its ideal form is not connected to mass loss, as the grooving of the base material by an abrasive particle is accomplished by severe plastic deformation to the sides of the formed groove. However, repeated ploughing of the material surface will lead to mass loss due to micro fatigue. Therefore, hardening mechanisms will embrittle the plastically deformed material and cause spalling at a future ploughing event. Micro chipping describes the removal of material in the form of a chip, which is ablated by an abrasive particle that scratches the surface of a body. Ideally, the volume of the chip matches the volume of the remaining groove. In a ledeburitic cold-work tool steel (Fig. 3.25b), the softer metal matrix is protected against abrasive wear by hard carbides. However, these reinforcement phases possess low fracture toughness due to their high hardness. Thus, ledeburitic cold work tool steels are susceptible to brittle failure induced by micro-breaking.

The dominant micro-mechanism of wear depends on the present tribological system. However, the main impact factors are the morphology and hardness of the abrasive particles, the hardness and microstructure of the scratched material, and the force and speed at which the abrasive particles interact with the abraded surface. The so called f_{ab} value helps to draw conclusions on the dominant micro-mechanism, integrating metallurgical
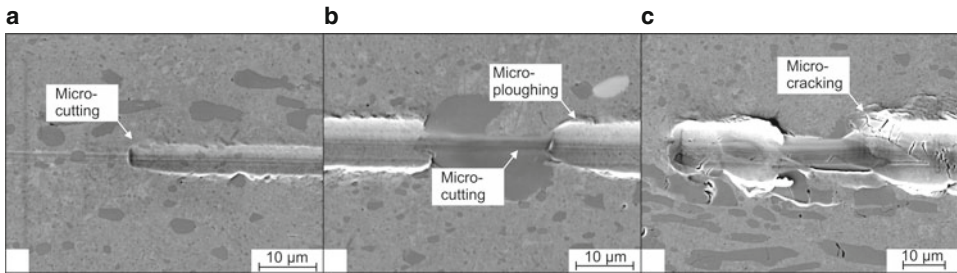
Fig. 3.25 **a** Micro cutting in a steel matrix, **b** micro ploughing of the steel matrix, **c** micro cracking of brittle carbides and the surrounding metal matrix due to severe plastic deformation

investigations and the characterization of the grooves resulting from the abrasive wear:

$$f_{ab} = \frac{A_g - A_s}{A_g},$$ (3.5)

where A_s describes the volume of material displaced laterally through plastic deformation by micro-plowing (positive value) or the volume removed laterally by the wear furrow through micro-breaking (negative value), and A_g represents the volume removed by an abrasive particle in a single scratch event. An f_{ab} value of 1 characterizes pure micro-chips, micro-breaking is preferably present in the case of $f_{ab} < 1$ and micro-ploughing in the case of $f_{ab} > 1$. The f_{ab} value describes abrasive wear between an abrasive particle and the constituents in the microstructure of the abrasively loaded material on the micro-scale. Deriving appropriate measures, micro-breaking can be counteracted, for example by increasing the material toughness. Otherwise, micro-ploughing can be reduced by increasing the hardness of the material. Thus a compromise has to be found for reducing the material removal due to wear because the material hardness and the toughness are inversely proportional to each other.

It is essential to understand that the cases of uneven wear presented in Sect. 3.3 are nevertheless based on the exact same micro-mechanisms, ploughing, chipping, cracking, and micro-fatigue, as evenly distributed abrasive wear and do not represent their own wear mechanisms. They are instead the result of certain parameter combinations in the tribological system.

3.3.3.2 Surface Fatigue

Surface fatigue is a wear mechanism, which is often insufficiently considered in the conceptualization of tooling and material concepts for mechanized tunneling. It is based on crack initiation and crack propagation at the tool surface due to cyclic mechanical loading. This type of loading occurs when the rotating tool hits larger soil particles such as rocks or gravel. However, also changing soil layers such as schistosities or slates, which cause a rapid change of the ground properties, can exert cyclic loading on the tunneling tools.
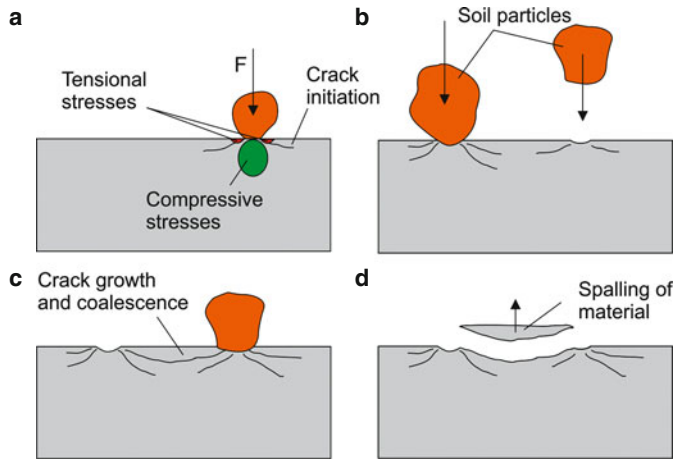
Fig. 3.26 **a** Stress distribution at the tool surface upon impact of soil particles and location of crack initiation, **b**, **c** repetitive impact of soil particles causes increase of the crack density and crack propagation, **d** material particles are spalled off the tool surface as cracks coalesce

Therefore, mixed grounds are especially capable of inducing cyclic loading, which has to be recognized and considered before choosing the tooling equipment. Surface fatigue must be distinguished from the micro fatigue mechanism of abrasive wear because surface fatigue requires no lateral movement of soil particles relative to the tunneling tool. Therefore, surface fatigue can also take place in hard rock excavation with cutting discs, which roll ideally over the rock surface whenever they get into contact. However, surface fatigue and abrasive wear often overlap to various extents, which hampers the determination of the dominant wear mechanism in practice. Awareness and understanding of the underlying wear mechanism are necessary to recognize the risks of wear due to surface fatigue and take appropriate action at an early stage. The wear mechanism surface fatigue can be subdivided into three stages crack initiation, crack propagation, and spalling (Fig. 3.26). Crack initiation can occur by either fracture or debonding of brittle phases, such as hard particles or non-metallic inclusions, inside the material when the forces of an external loading event cause internal stresses that exceed the strength of the brittle phase itself or it's interfacial bonding strength, respectively. The loading event that causes the crack initiation does not have to exceed the tensile strength by itself; it instead acts as a trigger of residual stresses due to accumulated lattice defects around the brittle phase.

Crack initiation can take place after several loading events, which by itself do neither exceed the material strength nor its yield strength. In many cases, however, crack initiation is bypassed due to internal defects such as micro cracks or pores originating from the manufacturing process. The following stage of subcritical crack growth is characterized by an incremental extension of the crack, whenever external mechanical loading is applied. The material's microstructure has a crucial role in the interaction with the crack, which is

growing by dislocation movement processes at the crack tip. In particular, the morphology, distribution, and volume content of brittle, hard particles define the crack path inside the material, as the fracture or debonding of the hard particles consumes less crack energy than growth inside a tough metal matrix. The metal matrix controls the crack-velocity, as the crack growth rate mainly depends on the propagation velocity between the brittle hard phases. In the last stage of surface fatigue, small particles are spalled from the surface, causing the actual wear loss. This stage occurs when the subcritical-cracks have grown to a length that reduces the load-bearing cross section of the material to such an extent that it cannot withstand external mechanical loads. Alternatively, multiple micro-cracks from different starting positions join below the material surface, leading to the spalling of a particle enclosed by the cracks [48].

3.3.4   Tool Wear Tests

Wear tests are a fundamental component in the design process of material concepts for tunneling tools. Their purpose is to compare and to quantify the wear behavior of different materials. Wear tests should aim towards accurate representation of the tribological system in which the materials will be used to be meaningful and precise.

3.3.4.1   Tool Wear Tests for Abrasive Wear

Several standardized lab tests to measure soil abrasivity have been developed to predict the service life of tunneling tools in abrasive grounds (Table 3.3). Results of LCPC-tests and the Cerchar test can be found in several soil property reports of tunneling projects describing soil abrasivity. These tests are based on the abrasion of test specimens with a standardized indentation hardness (LCPC: 60–75 HRB; Cerchar: 550–630 HV). While these tests are user-friendly, they do not necessarily permit prediction of the wear rate in tunneling due to the simple classification of complex soils with index-values (e.g., 0 = extremely abrasive; 10 = not abrasive) tools for several reasons. First, the standardization of the test samples based on their indentation hardness is insufficient, as different materials with the same indentation hardness can have different wear rates in the same soil, as

Table 3.3 Overview of the most commonly employed abrasivity tests, as well as notable tunneling test-rigs for investigating wear on non-cohesive soils

Wear test	Specimen design	Rock grain size (mm)	
LCPC-Test	Metal-propeller	6.3	[95]
Cerchar Abrasivity Test	Metal-pin	Solid-body	[72]
ASTM-G65	Metal plate	0.6	[2]
Soft ground abrasion tester (SGAT)	Steel-propeller	10	[24]
Penn State Soil Abrasivity Test (PSAI)	Steel-propeller	7	[77]
RUB-Tunneling Device (RUB-TD)	Pins on Metal-propeller	4	[50]

Fig. 3.27 Wear loss of various steels and wear resistant materials correlated to their hardness
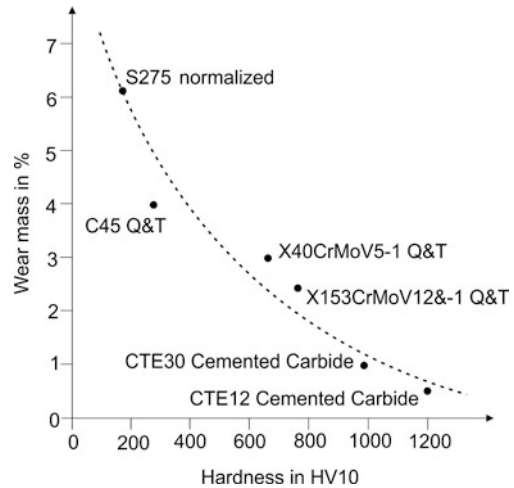
outlined on the example of the steels S275JR and C45 in soft-annealed condition, which both fulfill the hardness requirements of the LCPC-test but yield different wear rates when tested against the same abrasive (Fig. 3.27).

Reasons for the different wear resistance can be found in the microstructures of the steels, which both have a ferritic/pearlitic structure, but differ with regard to the size and distribution of the cementite lamellae of the pearlite and the overall pearlite content. The tempering steel C45 has a higher pearlite content than the construction steel S275JR, due to higher carbon content and more finely dispersed cementite lamellae [9]. The presence of the cementite lamellae (ca. 1100–1300 HV0.05) causes higher resistance against the grooving wear exerted by the abrasive particles in the LCPC-test, compared to the mostly ferritic microstructure of the steel S275JR.

Wear is a system property and has to be measured as such. Efforts have been made by several groups of researchers to recreate the tribological system of tunneling tools on a laboratory scale for wear testing (Table 3.3). The test rigs use a metal propeller, which rotates inside a conditioned soil sample, and acts as a carrier for wear specimens or the wear specimen itself. The wear-rate is determined by the mass-loss of the propeller, or the attached wear specimens. The TU Wien Abrasimeter [24], the SGAT, and the PSAI [77] have a vertical assembly of the rotating specimen in common, which is disadvantageous as it causes a time dependence of the wear test. The soil particles in contact with the rotating metal propeller are crushed over the course of the wear test, causing a steady decrease of the grain size and, therefore, a time-dependent change of the tribological system [46].

RUB-Tunneling Device   The RUB-Tunneling Device was designed with the idea to create an accurate replication of the tribological system of tunneling tools. For the investigation of abrasive wear it uses a metal propeller, which acts as a carrier for up to 12 wear-pin specimens. The main difference to previously described test-rigs is the horizon-

Fig. 3.28 Rub-Tunneling Device wear test-rig for experiments in non-cohesive soils

tal mounting of the metal propeller and a lateral movement of the soil-sample, relative to the wear-specimens. Both features are realized by the setup of the test-rig on a lathe, using the main spindle to rotate the metal propeller and the automatically driven support to move the soil-specimen (Fig. 3.28).

The wear-pins are constantly moved through fresh soil, which helps to keep the soil-properties as constant as possible over the whole test duration. Also, the replication of machine parameters such as penetration rate and rotational speed of the tools is possible. The soil-specimen can be conditioned with regard to grain-size, composition, and water-content before the experiment. In addition, further conditioning media such as bentonite suspension may be added through injection ports during the experiment. In the following, we present and discuss a selection of results that were obtained with the RUB-Tunneling Device.

Experiments on S275JR wear-pins show that the wear-rate increases with increasing penetration rate and is virtually independent from the rotational speed (Fig. 3.29a). This behavior can be explained with the increasing cutting forces, which are created at higher penetration rates due to a higher contact pressure between the tools and the soil. The increase of the cutting forces facilitates the indentation of abrasive particles into the material and therefore allows the formation of deeper wear scratches. A similar explanation applies to the observations made on the influence of the soil grain-size (Fig. 3.29b). Larger soil particles lead to a higher wear rate than small particles, as they create wider and deeper wear-grooves. In addition, coarse abrasive particles have the ability to extract small hard phases inside the tool material together with the surrounding matrix material. However, this effect does not apply to the steel S275JR that was tested in this study, as the material does not contain any hard phases.

Increasing non-uniformity of the soil causes an increase of wear (Fig. 3.29c), as the storage density of the soil can be increased when soil-particles with different sizes are present. Higher storage density leads to higher cutting forces, and therefore to increased wear. Dry soil has the lowest wear rate, as any presence of water increases the storage density of the soil and therefore increases the cutting forces (Fig. 3.29d). The peak of
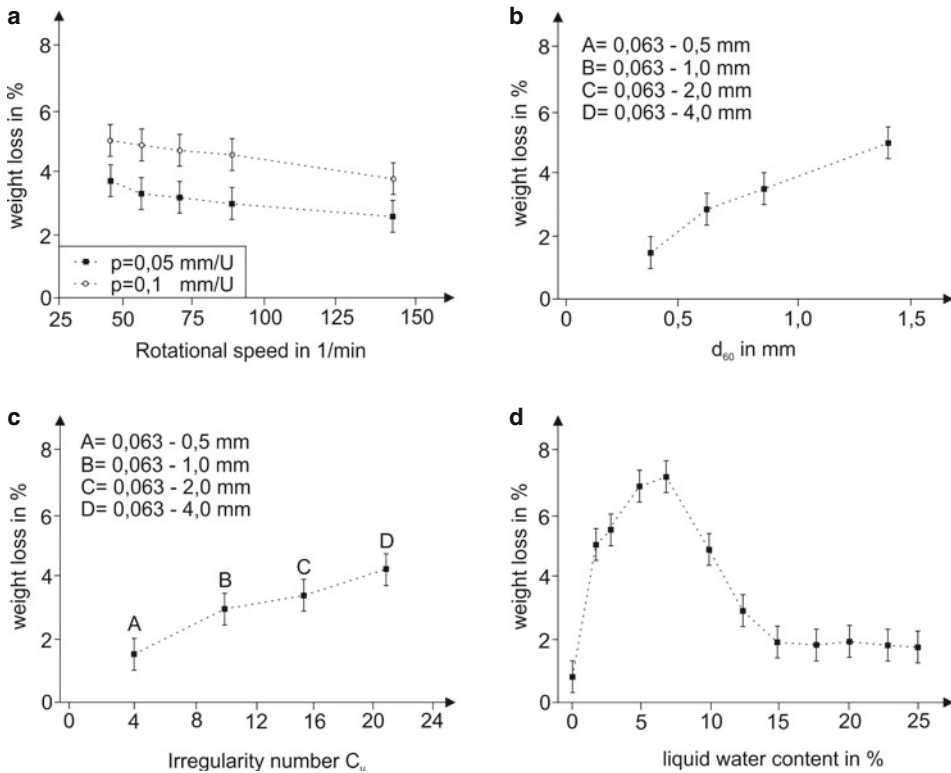
Fig. 3.29 Influence of the **a** rotational speed, **b** mean size of the abrasive particles, **c** irregularity number, **d** water content on the wear rate of S275 steel pins

the wear rate is found at a water content of 7.5%, followed by a decrease of the wear rate with higher water contents. The wear rate is highest when the pores between the soil particles are completely filled with water, leading to the maximum saturation of the soil, but simultaneously the water content is low enough to not significantly reduce the friction between the soil particles [50].

3.3.4.2 Tool Wear Tests for Surface Fatigue

Testing the resistance of materials against surface fatigue, requires to focus the attention on the underlying micromechanims of subcritical crack propagation. Often, internal defects such as pores or microcracks originate already from the manufacturing processes. Therefore, the stage of crack initiation can be considered as completed and the service lifetime of a tool is mainly dependent on the crack propagation. We developed a test-setup for the lab-scale investigation of subcritical crack growth. It is based on the setup first presented by Jones et al. [44] and uses a spherical ceramic indenter that cyclically loads a flat specimen with a constant load and frequency [48]. Hertzian contact stresses due to
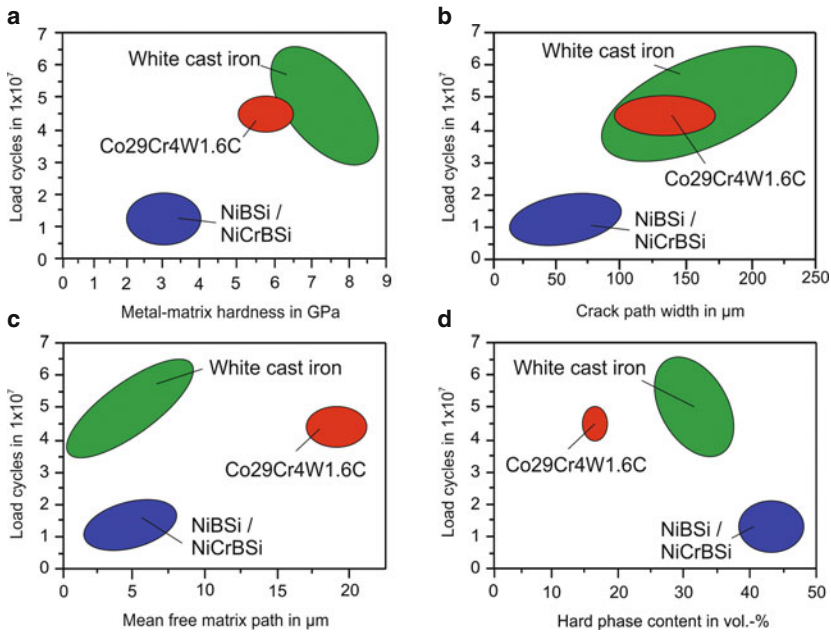
Fig. 3.30 Influence of the **a** metal matrix hardness, **b** mean width of the crack path, **c** mean free matrix length, **d** hard phase volume content on the fatigue life of various hard alloys (with regard to [12])

the cyclic loading cause the growth of a cylindrical crack around the contact area between the indenter and specimen [30]. As surface fatigue mainly occurs at the hard but brittle wear protective layers of the tunneling tools, these materials were the focus of attention.

Investigations on cemented carbides and several hard alloys on Fe, Ni, and Co-basis showed that the material's resistance against subcritical crack propagation depends on the content and morphology of metal matrix and hard phases, as well as on the mechanical properties of the respective phases (Fig. 3.30) [12]. In general, the metal matrix controls the crack propagation velocity due to its high toughness compared to the hard phases. High contents of the metal matrix and a microstructure with large metal matrix cells, creating large distances between adjacent hard phases are therefore beneficial to the crack propagation resistance. For the same reason, large hard phase sizes lead to a high crack propagation resistance, if materials with the same hard phase content but with different hard phase sizes are compared. In terms of mechanical properties, the strength of the individual microstructure constituents mainly determines the crack propagation resistance. As the subcritical crack propagation in the metal matrix originates from the gliding behavior of dislocations, strengthening of the metal matrix inhibits this mechanism and is therefore an effective method to increase the crack propagation resistance. Our investigations showed that martensitically hardened Fe-based metal matrices offer the highest

a **b**
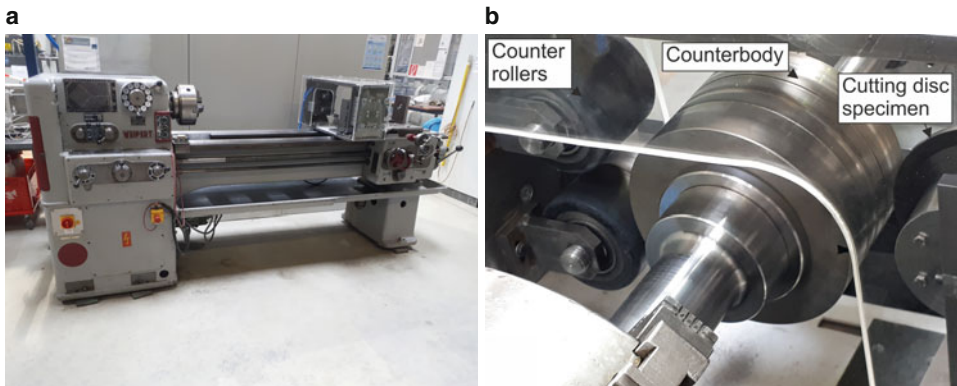
Fig. 3.31 Setup of the RUB-Tunneling device for testing the behavior of cutting discs under cyclic loading. **a** Overview of the test rig without built in counterbody, **b** close-up of the relative position of counterbody and cutting disc specimen

strength, followed by Co-based alloys. The Ni-based alloys that are commonly used for build-up welding have a weak metal matrix and therefore a low resistance against crack propagation. Cutting discs represent the second group of tools that is affected by surface fatigue. The RUB-Tunneling device wear-test rig was modified to accommodate miniature specimens of cutting discs (Fig. 3.31).

The specimens are pneumatically pressed against a counterbody, either made of rock or tool-steel, which is rotated by the main spindle of the lathe. Load cells in horizontal and vertical position enable measuring of the cutting forces, depending on the applied contact pressure, as well as on the rotational speed and type of the counterbody. To test the response of different tool-steels to cyclic loading, the cutting disc specimens roll over a metal counterbody with a weld seam, which exerts an impulse on the specimen on each rotation.

The tests were conducted over a duration of three hours (10,000 load cycles) with rotational speeds and estimated contact pressures that match the conditions reported from real tunneling projects. The strength of the metal matrix and the included hard phases have a significant impact on the behavior of the steels under cyclic loading; cracks are initiated at the surface of the cutting edge in most of the investigated steels and grow into the material (Fig. 3.32). Low metal matrix strength leads to severe plastic deformation of the cutting edge and fast crack initiation, due to facilitated mobility of dislocations. Large hard phases on the other hand act as barriers to the plastic deformation of the surrounding metal matrix, but the accumulated stresses at the matrix/hard phase boundary can lead to brittle fracture, as soon as the strength of the hard phase is surpassed. Therefore, sudden crack initiation and propagation are possible.

To gain more information about the high cycle fatigue behavior of the investigated steels, SN-curves were determined by the means of rotational bending tests (Fig. 3.33).
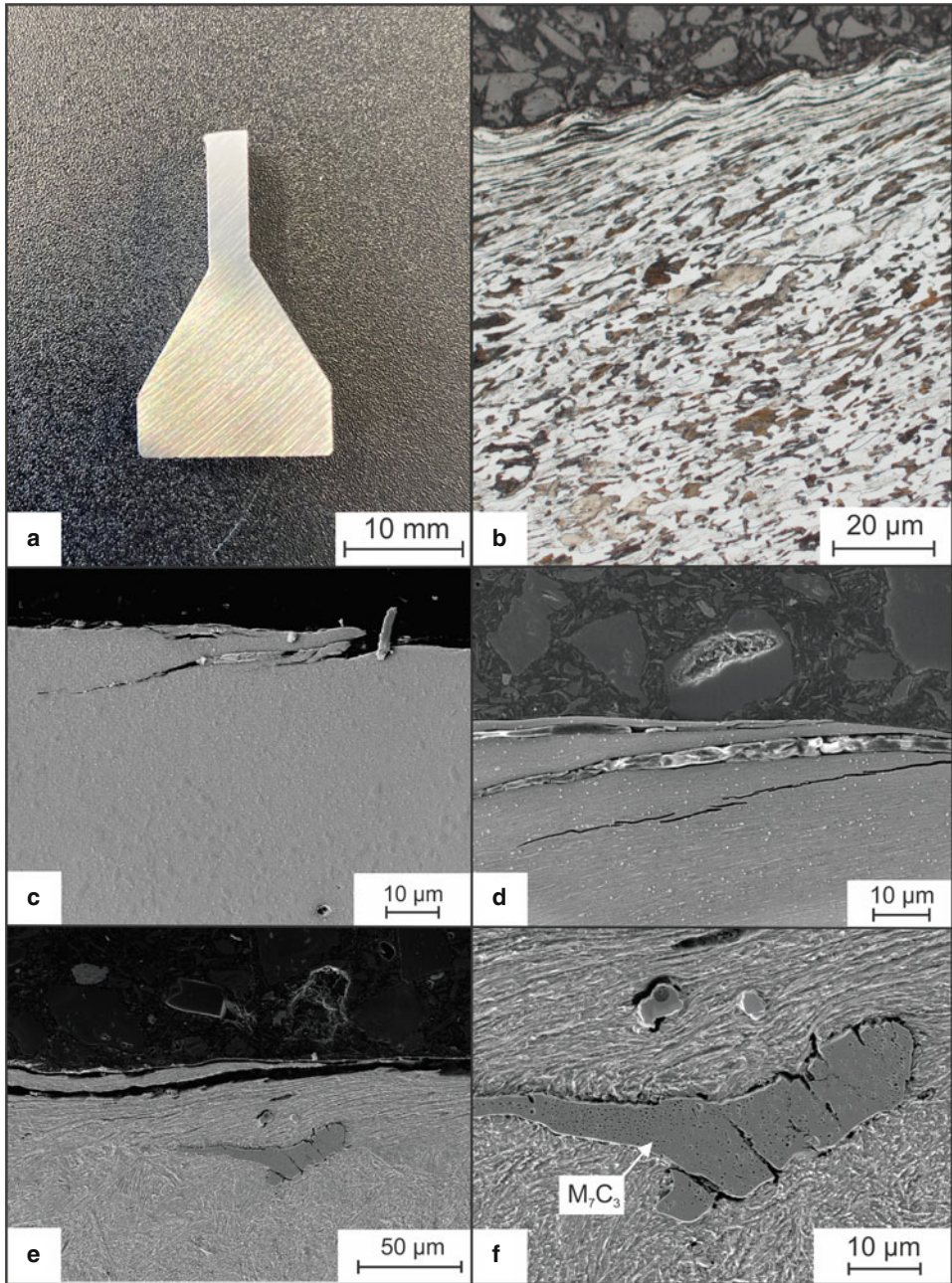
Fig. 3.32 **a** Cross section of a worn laboratory scale cutting disc, **b** cutting edge of construction steel S355, **c** cutting edge of cold work tool steel 90MnCrV8, **d** cutting edge of hot work tool steel X40CrMoV5-1, **e** cutting edge of cold work tool steel X153CrMoV12-1, **f** large carbides inhibit plastic deformation, due to their high Young's modulus and low plastic deformability
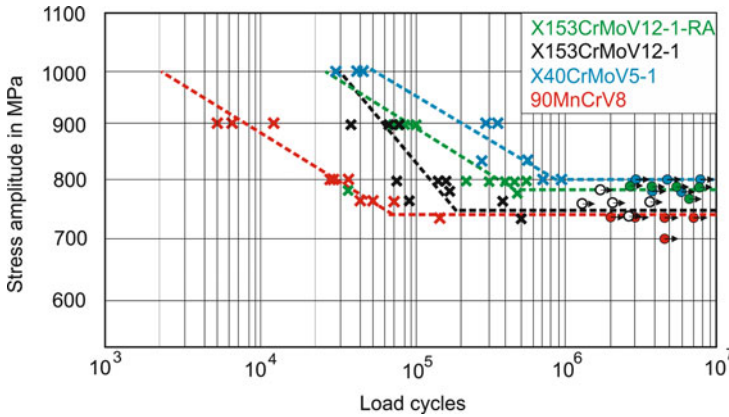
Fig. 3.33 Fatigue test results of different tool steels, obtained by rotary bending tests

The results indicate that the fatigue strength of carbide-rich cold work tool steels, such as X153CrMoV12-1, is lower compared to hot-work tool steels as X40CrMoV5-1, which contain no large eutectic carbides. However, by reconfiguring the heat-treatment, a content of about 10 vol% retained austenite could be implemented in the microstructure of the X153CrMoV12-1 steel. This led to an increase of the fatigue strength, due to stress induced transformation of the retained austenite and the subsequent formation of compressive residual stresses. A cold work tool steel with low carbon content that was also tested showed the worst fatigue properties. This behavior could be traced back to predominantly intergranular fracture of the grain boundaries, resulting in a brittle fracture behavior and low energy dissipation during crack propagation.

3.3.5 Abrasive Wear Modeling

Wear is related to sliding contact and abrasive wear occurs when a surface containing hard particles slides on another softer surface. The sliding causes the hard particles to dig into the softer surface and as the sliding motion continues, grooves are formed on the soft surface from where the material is removed. The volume lost due to abrasive wear can be quantified by considering the normal force between the two surfaces F_N, the abrasive wear coefficient k_{abr}, which depends on the average roughness of a surface, the hardness of the material to be abraded H, and the distance of sliding x in an *Archard* type wear model V_{wear} [4],

$$V_{wear} = k_{abr} \frac{F_N x}{H}. \tag{3.6}$$

The simulation model is verified using a sliding test for the abrasive wear. A steel block is resting under its body weight on a rock surface, it then slides on the rock specimen for
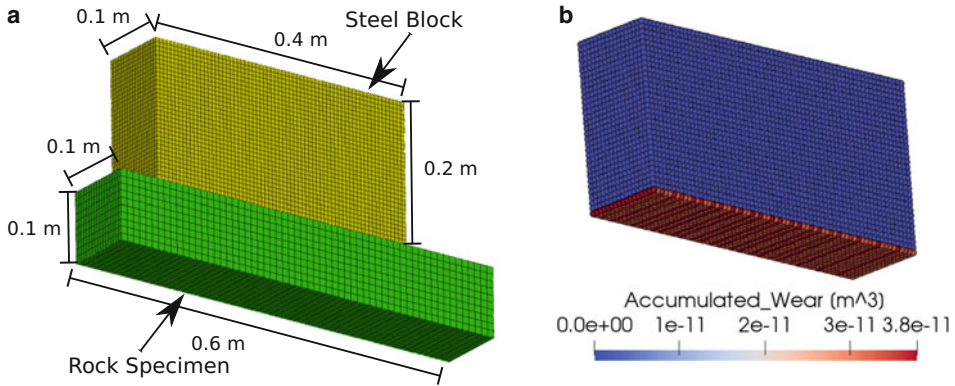
Fig. 3.34 Simulation setup and geometry of the steel and rock specimen for the wear test (**a**). Accumulated wear on the steel specimen surface after a sliding distance of 6.4 cm on Fell sandstone (**b**)

Fig. 3.35 Comparison of the theoretical total volume lost to abrasive wear with the peridynamic simulation model with respect to varying hardness of the rock surface
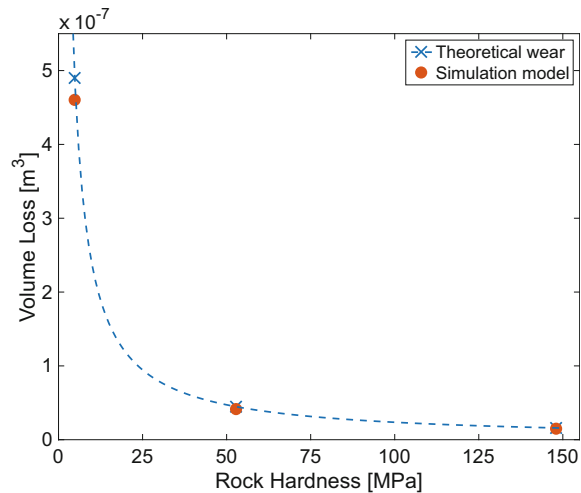
a known distance of 6.4 cm, as shown in Fig. 3.34a. The test is performed for three types of rocks with different hardness values: Sherwood sandstone ($H = 4.8 \times 10^6$ Pa), Fell sandstone ($H = 5.28 \times 10^7$ Pa) and Dealbeattie granite ($H = 1.48 \times 10^8$ Pa). Accumulated volume lost due to abrasive wear from Fell sandstone on the steel surface, computed using the peridynamic simulation model, is shown in Fig. 3.34b. Volume lost due to abrasive wear computed from the simulation model using rocks of varying hardness is compared with the theoretical values obtained from Eq. 3.6 in Fig. 3.35.

The verified model for abrasive wear can now be used to compute the volume lost on the cutting tools due to abrasion. The simulations performed for the LCM test in mixed ground conditions (Sect. 3.2.2.3) are used to investigate the abrasive wear on the cutting discs for two different penetration levels; $p = 2$ mm and $p = 4$ mm. Figure 3.36a shows the accumulated wear on the cutting disc at three stages, i.e. in the soil domain (left column),
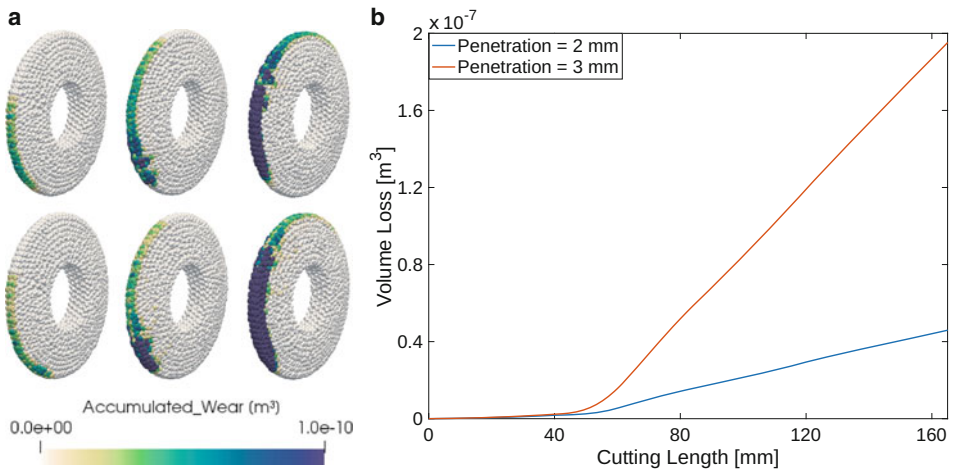
Fig. 3.36 Comparison of the abrasive wear on the cutting disc working in mixed ground conditions (Fig. 3.20) at two different penetration levels; $p = 2\,\text{mm}$ top row and $p = 3\,\text{mm}$ bottom row of **a**). Total volume lost on cutting disc due to abrasive wear over cutting length (**b**)

at the soil-rock interface (middle column) and in the rock domain (right column). It can be seen that the accumulated wear on the cutting disc increases significantly as the disc continues to move into the rock domain. Total volume lost due to abrasive wear at the cutting disc is plotted over the cutting length for both penetration levels in Fig. 3.36b.

3.3.6 Simulation of Abrasive Tool Wear on the Mesoscale

The interaction between tunneling tools and soil or rock causes abrasive wear in the tunneling process. Many different methods have been already used to describe the abrasive behavior of sand and rock, such as laboratory tests, field tests, and numerical simulations. The application of numerical analysis improves the design methodology and allows to achieve a more optimized shape for cutting tools. Numerical methods can be used to simulate the interaction between machine components and the ground. We introduce an efficient wear model for estimating the abrasive wear rate caused by a mixture of particles. Such a model can help the engineer to understand the wear mechanisms better, to determine the reasons for the cutting tool failure, and consequently to optimize the design of the tool components. The goal is to reduce the number of required laboratory tests in the design procedure of the TBMs, and thus to save costs.

Our wear model is based on the idea of extrapolating the behavior of a scratch caused by a single abrasive particle to the total wear rate of the particle mixture, employing relations resulting from 3D particle simulations. This objective is reached in two steps: in the first step, a single scratch test is modeled to investigate the cross-sectional geometry

of the resulting groove and to understand the dominant wear mechanism. In the second step, the results of single scratch tests are extended to the wear of the mixture by means of equations for the number of contact particles and normal contact forces obtained from particle simulations. Numerical methods used for these procedures are the Finite Element Method (FEM) for simulation of single scratch test and Distinct Element Method (DEM) for modeling of particle mixture. These steps are explained in detail in the following subsections.

3.3.6.1 Single Scratch Test

Abrasion can be numerically reproduced in a controlled way by simulating a single asperity scratch test where a pin or a conical indenter penetrates the surface of the specimen and slides over it. Scratch damage ranges from plastic grooving in ductile material to cracking and chipping in brittle material. The scratched surface is a result of the active micromechanisms of abrasion, namely, plowing, wedging, and cutting (see also Sect. 3.3).

A three-dimensional scratch process is modeled and simulated using a coupled damage-plasticity material model, implemented as a user subroutine (UMAT) in the finite element code Abaqus. The model consists of a rigid tip with a predefined radius and a flat deformable specimen (see Fig. 3.37). The specimen is fixed, and the tip slides over the surface in such a manner that a groove forms. The width and length of the specimen should be large enough to eliminate boundary effects. In the simulations, a displacement-controlled loading was applied in two steps:

- In the indentation step, a vertical displacement along the thickness of the specimen is applied to press the indenter down until it reaches the specified indentation depth.
- In the scratching step, a horizontal displacement is applied to slide the indenter in the z-direction at the constant indentation depth prescribed by the indentation step.

The contact area and the reaction forces were recorded during the process. The material properties of quartz (SiO_2), which is much harder than the steel of the specimen, are assigned to the tip. As a result, the tip does not wear during the scratching movement,

Fig. 3.37 Schematic representation of the scratch test in the initial undeformed configuration
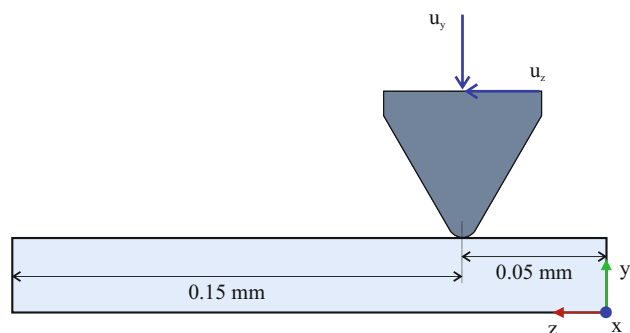
Table 3.4 Mechanical proper-
ties of the tested materials

Material	Quartz (SiO$_2$)	Steel (1.0570)
Young's modulus (GPa)	73	210
Poisson's ratio	0.17	0.33
Density (kg/m^3)	2200	7800
Hardness (GPa)	9.8	2

and can be considered rigid. We selected material properties of standard steel DIN 1.0570 $AISI1024$, which is commonly used in machine components, for the specimen to be scratched. Table 3.4 lists the mechanical properties of quartz and the steel used in the model.

The initial model for the tip and the specimen used in the numerical simulations with their discretization are depicted in Fig. 3.38. A very fine mesh or a uniform fine mesh for the specimen will drastically increase the computation time, especially in the three-dimensional models. However, a coarse mesh is not sufficient to capture the plastic deformation and the localization of damage. Therefore, we employed mesh refinement around the scratching zone to reduce the number of elements and consequently speed up the simulations and at the same time obtain sufficiently accurate results.

The single asperity test was performed for an indentation depth of 0.002 mm. A total sliding distance of 0.1 mm was realized by the tangential movement of the tip. An illustration of the simulation results with groove is depicted in Fig. 3.39. The influence of the abrasive particle size on the wear volume is typically studied for abrasive particles up to around 100 μm. Hence, the simulations were performed for three tip radii of 25, 50, and 100 μm with the cone angle of 60° (see Fig. 3.40). In these simulations, the indentation depth is constant and equal to 0.003 mm.

The smaller the tip radius is, the lower shoulders of the groove are obtained, and consequently more wear is caused (Fig. 3.41). Thus, the wear volume increases with decreasing tip size for constant indentation depth. In addition, the employed coupled
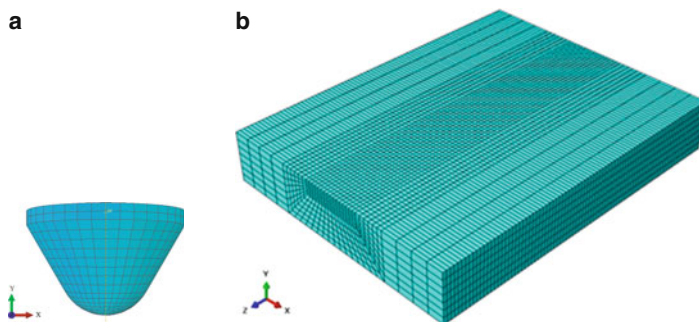
Fig. 3.38 **a** Spherical tip with a radius of $R = 50\,\mu$m, **b** mesh for the specimen used in the numerical simulations
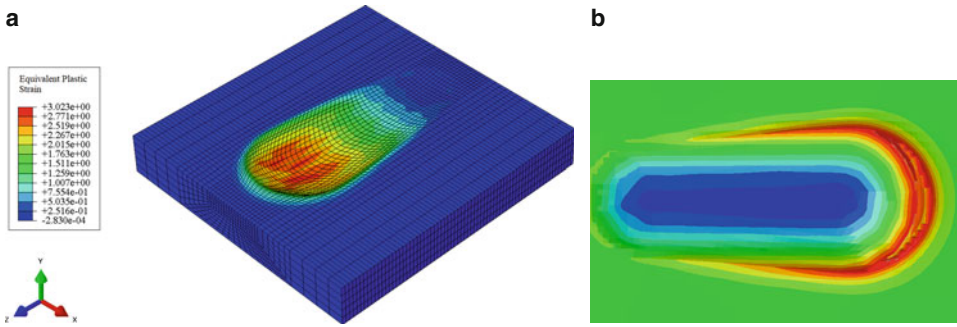
Fig. 3.39 A groove resulting from a single scratch test for $d = 0.002$ mm and $R = 50$ µm. **a** Distribution of equivalent plastic strain in 3D view and **b** result of a microscopic height profile measurement (blue is low and red is high)
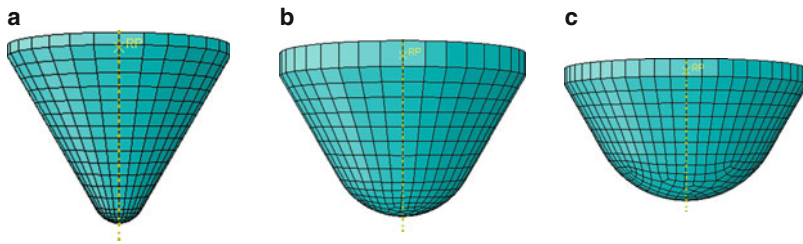
Fig. 3.40 Representation of the tips used in the simulations. **a** $R = 25$ µm, **b** $R = 50$ µm and **c** $R = 100$ µm

damage-plasticity model accounts for the damage induced on the specimen, which results in the volume loss of the surface. In experiments, the particle size effect is studied using a grid of particles or tips. For a grid of particles under constant pressure, the force per particle has a direct relation with its radius. Because the number of particles per unit area decreases for larger particles, it results in a larger amount of wear caused by every single particle. The cross-sectional geometry of the groove caused by a tip with a radius of 100 µm reveals a completely plastic deformation with large shoulders and no material removal. In contrast, for the scratch cross-section built by the tip with a radius of 25 µm almost no shoulders are observable, and a large wear volume is recorded. This effect is discussed in the following Sect. 3.3.6.2, where a grid of particles is simulated using DEM.

3.3.6.2 Total Abrasive Wear of a Mixture

Particle simulations permit extension of the prediction of abrasiveness of individual particles to the actual ground consisting of abrasive particles with different sizes and shapes. The simulation of a mixture of particles was performed using the distinct element method in PFC^{3D} software. The abrasive particles were simulated as quartz grains, as quartz is one of the most abrasive minerals in common soils.
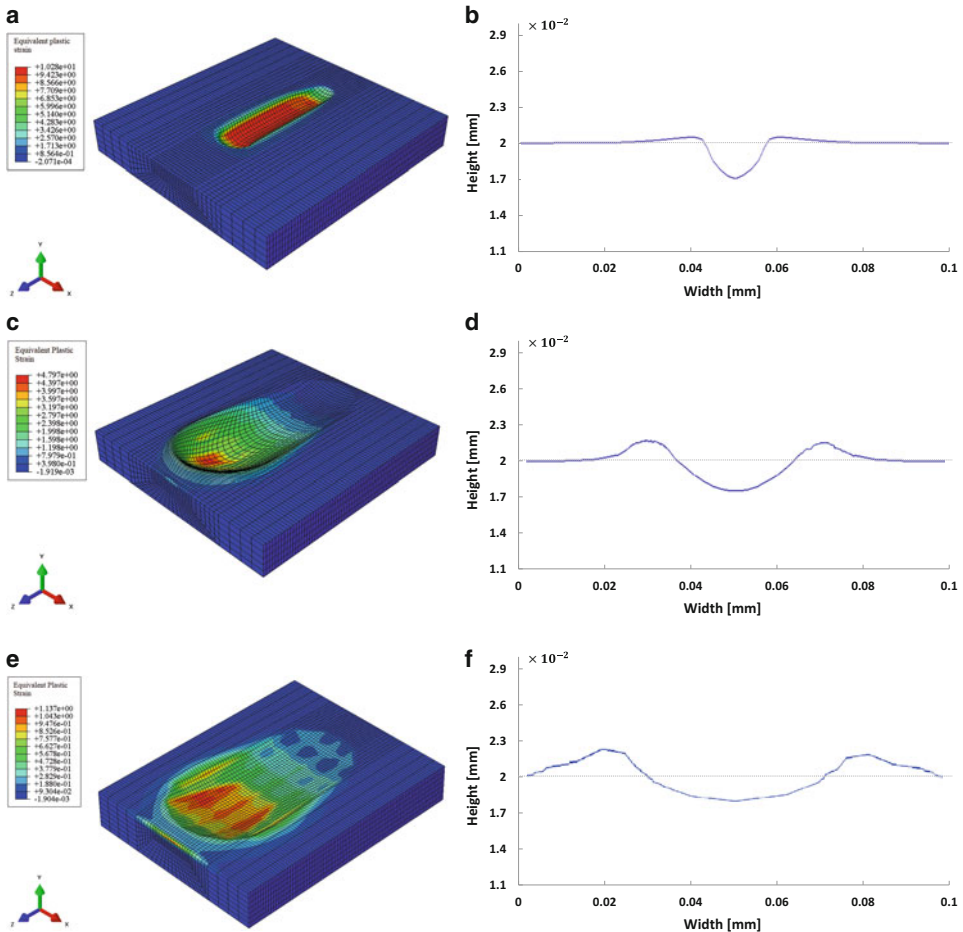
Fig. 3.41 Particle size effect (left) distribution of equivalent plastic strain for **a** $R = 25\,\mu m$, **c** $R = 50\,\mu m$ and **e** $R = 100\,\mu m$ and (right) cross-section of the groove for **b** $R = 25\,\mu m$, **d** $R = 50\,\mu m$ and **f** $R = 100\,\mu m$

The setup for the particle simulation consists of a box with unit dimensions filled with a mixture of particles with different radii. Two types of particles were assumed with the same mechanical properties, but different diameters, $D_A \geq D_B$, and a defined volume ratios θ_A and $\theta_B = 1 - \theta_A$. The particles are generated randomly inside the box and then settled down by applying gravity. Due to the small size of particles, the settling step takes a long time and is the most time-consuming step in the simulation. To have a satisfactory settlement prediction, the box is shaken in which a relative small velocity is applied to the side walls. A linear contact model is considered between the particles. The simulation results indicated that the inter-particle friction coefficient does not have a significant effect on the number of particles being in contact with the surface. Therefore, all wall and

Fig. 3.42 Relation between number of contacts and particle diameter for different volume ratios of **a** A-Particles and **b** B-Particles
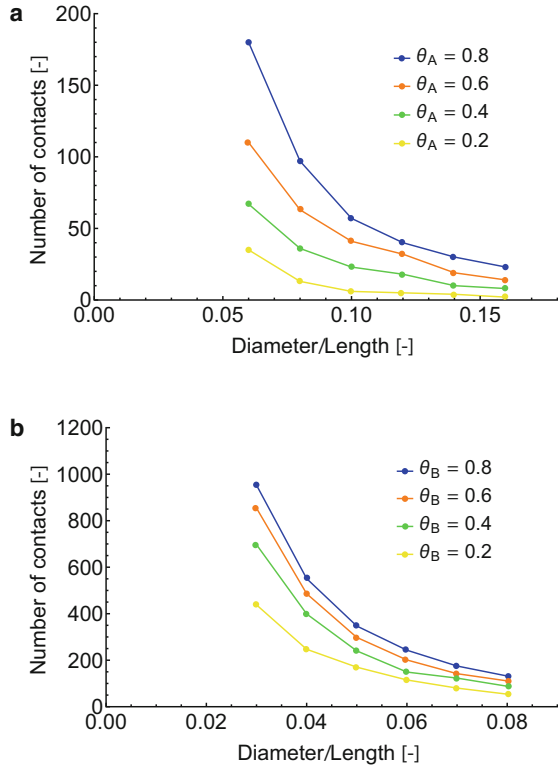
particle contacts are supposed to be free of friction. Pressure is applied to the top surface of the particles.

A parametric study was performed to derive a relation between the number of contacting particles as a function of particle size and volume ratio. By varying the diameter and volume ratio, a database is created for each particle type. Figure 3.42 presents the results for the number of contacts per unit area by A- and B-particles. Best curve fitting to these data points is performed using the MATLAB curve fitting tool. Finally, expressions for the number of contacting particles N_c are found as

$$N_{c,A} = 0.9\,\theta_A^{(2-1/r_{AB})}\,D_A^{-2}, \qquad N_{c,B} = 0.9\,\theta_B^{(1/r_{AB})}\,D_B^{-2}, \qquad (3.7)$$

in which $\theta_A + \theta_B = 1$ and r_{AB} as a ratio of D_A to D_B for $D_A \geq D_B$. These relations are used in the next section to estimate the total abrasive wear rate of the particle mixture.

The contribution of a particle to the total abrasive wear rate is defined by

$$\dot{v}_i = f_{ab}\,A_{g,i}\,v_t, \qquad (3.8)$$

where v_t indicates the tangential relative velocity between the abrasive particle and the tool. The average area of a groove caused by all particles of type i, $A_{g,i}$, is obtained from
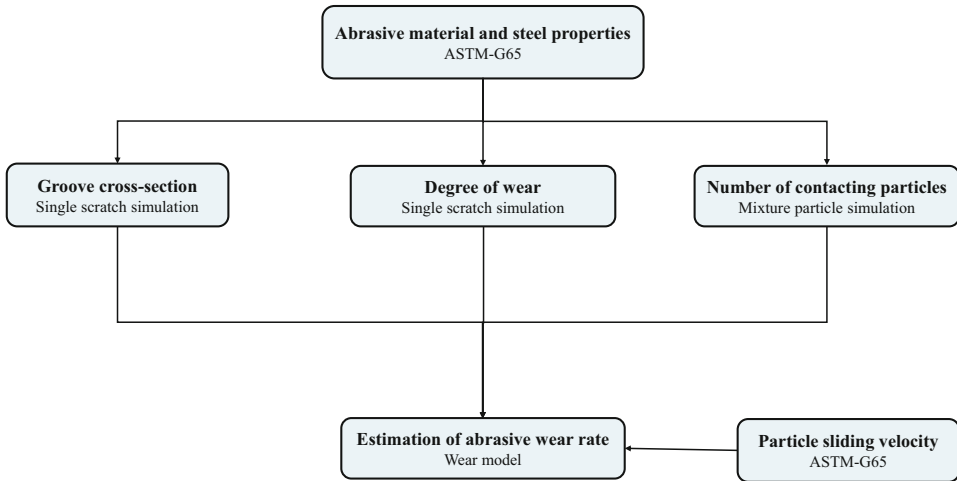
Fig. 3.43 Calculation procedure of abrasive wear model

the single scratch simulations. It is supposed to be a function of influencing parameters, i.e., the mean particle size and the normal contact force (or indentation depth).

The total wear rate $\dot{v}$ of a material is the summation of the wear rate for particles in contact with the tool surface,

$$\dot{v} = \sum_{i=1}^{n} N_{c,i}\, \dot{v}_i, \tag{3.9}$$

in which n is the number of particle types and $N_{c,i}$ is the number of contacts per unit area for particles of type i. The abrasive wear rate is determined using the calculation procedure illustrated as a flowchart in Fig. 3.43. The parameters influencing the abrasive behavior and the wear rate can be divided in three categories: abrasive medium characteristic, machinery component properties, and the contact mechanism.

The abrasivity of rocks can be deduced from their mineralogical composition, especially the fraction of hard minerals such as quartz. The important mechanical and geometrical properties of particles are size, shape, and hardness. Based on the literature, larger particles generate a higher contact force, remove the material surface faster, and create a harder texture. However, our observation in the single scratch test is opposite to the size effect reported in the literature. We found that smaller particles, with sharper tips, cause more wear in the form of material removal compared to the plastic deformation caused by larger particles. We speculate that, under a constant load, a smaller particle penetrates deeper into the material and creates a larger groove area.

In general, material removal rate is linearly related to particle hardness. Harder particles act as rigid indenters compared to softer particles and increase the surface roughness. However, for the occurrence of significant abrasion, the ratio between the hardness of the

particles and the surface is important. For a hardness difference higher than ∼1.2, the abrasive wear rate remains constant. In tunneling applications, the most abrasive particles are quartz, which is almost five times harder than steel surfaces, such as that of construction steel (see Table 3.4). Therefore, it is supposed that the possible variation in the hardness of sand particles does not influence the resulting abrasive rate.

3.3.7 Simulation of Tool Wear by Micro-Cracking

Wear-protective layers of tunneling tools, used to protect the soft substrates from abrasive wear, are subjected to surface fatigue. This wear mechanism is mainly governed by elasto-plastic deformations, crack initiation and crack propagation on the microscale (see Sect. 3.3.3.2). These effects may not be visible on the macroscale at first, but may lead to macroscopic cracks during the excavation process and ultimately to failure of the tool. For instance, if the cracks cluster, parts of the tool's surface break out. These phenomena are affected by the material's microstructural properties, namely the microstructure morphology and the material properties of the constituents. The surface layers of mining tools consist of metal matrix composites (MMC), which contain brittle carbide inclusions surrounded by a ductile metal matrix. The inclusions supply the resistance against abrasion whereas the properties of the ductile matrix provide crack resistance and thus, the necessary resistance against surface fatigue. Numerical simulations of crack propagation through microstructures can be carried out based on voxel data obtained from micro-CT scans. Basing the simulations on structure images enables the observation of the governing effects, even in complex three-dimensional structures. This property is beneficial, because imaging processes of real microstructures suffer from the problem that the measurement of crack surfaces in three-dimensional bodies, especially for the crack propagation over time, is extremely costly if not partially impossible. Additionally, the mechanical fields, such as the plastic deformations and the stress distributions, can be visualized and investigated in the numerical simulations. Furthermore, the simulations enable comparative studies of different microstructures promising to improve those regarding crack growth resistance and thus wear by design and material choice.

3.3.7.1 Simulation Framework for Ductile Crack Propagation on the Microscale

We developed a numerical method for the efficient simulation of ductile crack propagation at finite strains based on voxel data cf. [101], which enables robust and mesh-independent simulations and is capable of simulating crack propagation along a priori unknown crack paths through brittle as well as ductile materials. Its starting point is the so called Eigenerosion approach for crack propagation as introduced in [84] and implemented into the Finite Element Method in [69]. This approach was extended to ductile fractures at finite strains in [100].
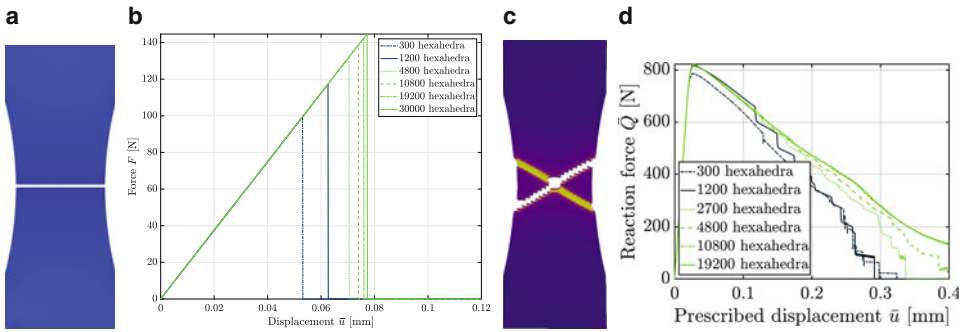
Fig. 3.44 Simulated tension test of **a** a brittle plate, which is loaded vertically with an over time linearly increasing displacements, **b** its resulting reaction force for different numbers of elements and **c** the specimen and **d** reaction force of a plate of ductile material, taken from [100]

The developed algorithm leads to plausible results as demonstrated for the example of a simple tension test (Fig. 3.44). A brittle plate fractures into two parts along a crack perpendicular to the load direction. A shear zone develops at an obtuse angle to the pulling direction. The mesh convergence of the brittle as well as the ductile specimen is demonstrated in the reaction forces. Previously, this algorithm was shown to be capable of simulating subcritical crack propagation under cyclic loading in [102]. For the efficient simulation based on voxel data, the approach is combined with the Finite Cell Method in a new algorithmic framework [101]. Thereby, the problem of meshing the complex microstructures is circumvented because therein, the mesh is generated independently from the inner material boundaries. The material boundaries are imposed by decomposing the elements, the so called "finite cells", into subcells. These subcells are constructed conformingly according to the material interfaces allowing for a suitable integration of the material coefficient jumps inside the finite elements. A special discretization technique, which ensures efficiency on the one hand and a certain accuracy and numerical stability on the other hand, is applied. In order to maintain accuracy of the crack propagation, the mesh is adaptively refined at the crack tip by splitting the finite cells into separate finite elements whenever the crack enters a finite cell.

We demonstrated the concept of the proposed algorithm and its efficiency using an artificial microstructure as an example (Fig. 3.45). It consists of a spherical tungsten carbide inclusion that is surrounded by an η-carbide layer and a ductile nickel matrix, is simulated with the boundary conditions in Fig. 3.45d to show the concept of the proposed algorithm and its efficiency. Hereby, a tetrahedral mesh, a semi-regular hexahedral mesh with hanging nodes and the proposed algorithm is applied. As shown in Fig. 3.45b, e, the crack path is independent of the chosen discretization type. Furthermore, the semi-regular hexahedral FE mesh and the proposed algorithm lead to a very similar reaction force, cf. Fig. 3.45c. In Fig. 3.45f, the computational efficiency of the proposed approach is demonstrated by comparing the number of equations, that are solved in each Newton-Raphson iteration.
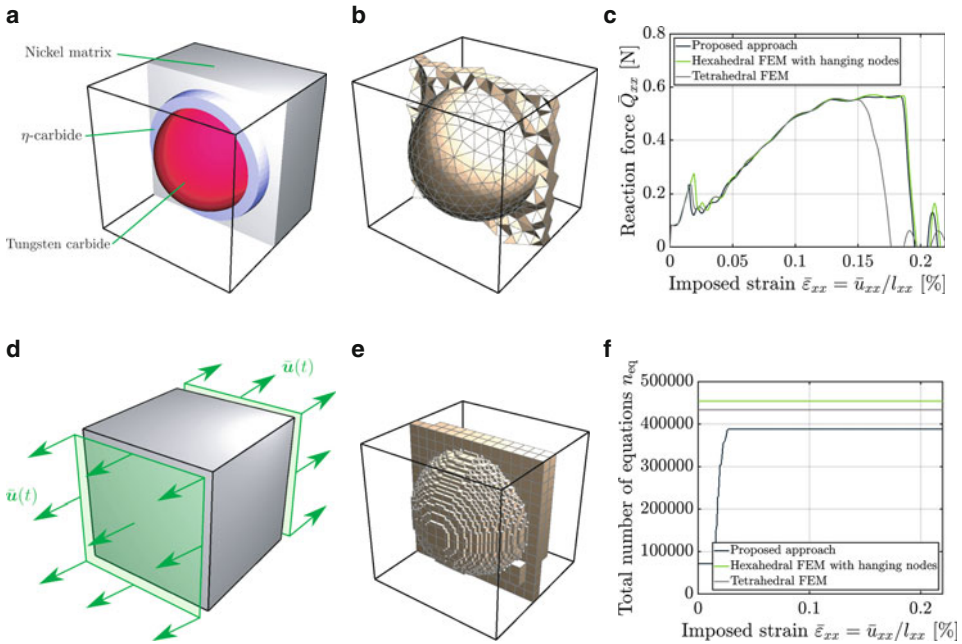
Fig. 3.45 Simulation on an artificial microstructure in **a** and boundary conditions in **d** resulting in the final crack paths for **b** a tetrahedral mesh and **e** a hexahedral mesh. In **c**, the resulting reaction forces and, in **f** the number of equations in each Newton step are shown, cf. [101]

Especially, in the beginning of the simulation of the proposed approach, the number of equations is reduced by a factor of 5 compared to the semi-regular hexahedral FE mesh. However, this academic example was constructed with the purpose of examining the accuracy rather than efficiency. Since all elements in the material interface are fractured in the end, no significant gain in the computational costs can be reached by the proposed method. This circumstance will change when considering real microstructures with only a small fraction of ruptured material interfaces.

3.3.7.2 Voxel-Based Analysis of Crack Propagation Through MMC

We performed simulations on the microstructure obtained from micro-CT scans to examine crack propagation in MMC used as wear-protective layer on tunneling tools. A typical micro-CT scan of the metal matrix composite Ferrotitanite (Fig. 3.46) consists of grey-scale values that represent the density of the specimen and is obtained by measuring the X-rays, which are emitted by an X-ray tube and which penetrate the specimen. The brighter the value, the higher the intensity of the measured X-rays and thus the lower the density of the investigated voxel. For the application, the resulting grey-scale values are processed to erase noise and artifacts. Afterwards, they are binarized by application of a threshold value to identify the distribution of the two composites, here the brittle and
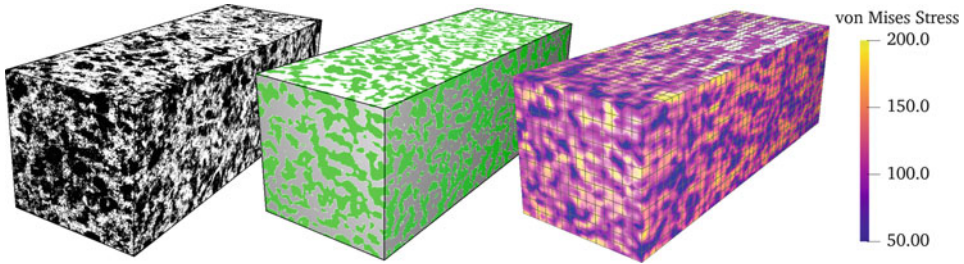
Fig. 3.46 Voxel data as grey-scale values obtained from a micro-CT scan, which is cleaned and binarized into the inclusion (green) and iron matrix phase (silver) and contour plot of the von Mises stress under one dimensional tension in axial direction

stiff titanium carbide inclusions and the ductile iron matrix. Even though the resulting microstructure is of a high complexity, it is discretized without high computational effort by the FCM. Based on this, efficient simulations are carried out on these data. As an example, the result of a one dimensional tension test without the assumption of crack propagation is shown in Fig. 3.46. The material properties of the inclusions are obtained from the literature whereas the material parameters of the iron matrix are fitted to tension tests to accurately represent the behavior in the plastic regime. The von Mises stress is high in the inclusion phase compared to the stress in the ductile matrix (Fig. 3.46). Hence, loads applied on the Ferrotitanite are primarily carried by the stiff inclusions.

A representative section is selected from the whole scan, under linearly increasing deformation in one direction and symmetry boundary conditions in lateral direction, cf. Fig. 3.47a, for the simulation of crack propagation through the microstructure. The crack is initialized as shown in Fig. 3.47b, c by assuming eroded elements at the beginning of the simulation, because the numerical framework only considers crack propagation and not crack initiation. The numerical parameters for the crack propagation, namely the Griffith-type energy release rate G_c and a regularization parameter ϵ, are obtained by fitting them so that the results of a specimen of a tension test breaks into two parts under the correct tensile stress. The overall material behavior is elastic even though one of the constituents, here the metal matrix, behaves elasto-plastically. Furthermore, the crack propagates in steps instead of breaking the material into two parts at once. The resulting crack surface propagates in general straight through the microstructure in agreement with observations from the experimental results.

3.3.7.3 Influence of Different Inclusion Shapes on Crack Propagation

The crack propagation through different microstructure morphologies is investigated, to improve the material microstructure of the layers applied to the mining tools regarding surface fatigue. Therefore, simulations are carried out under the assumption of simplified inclusion shapes.
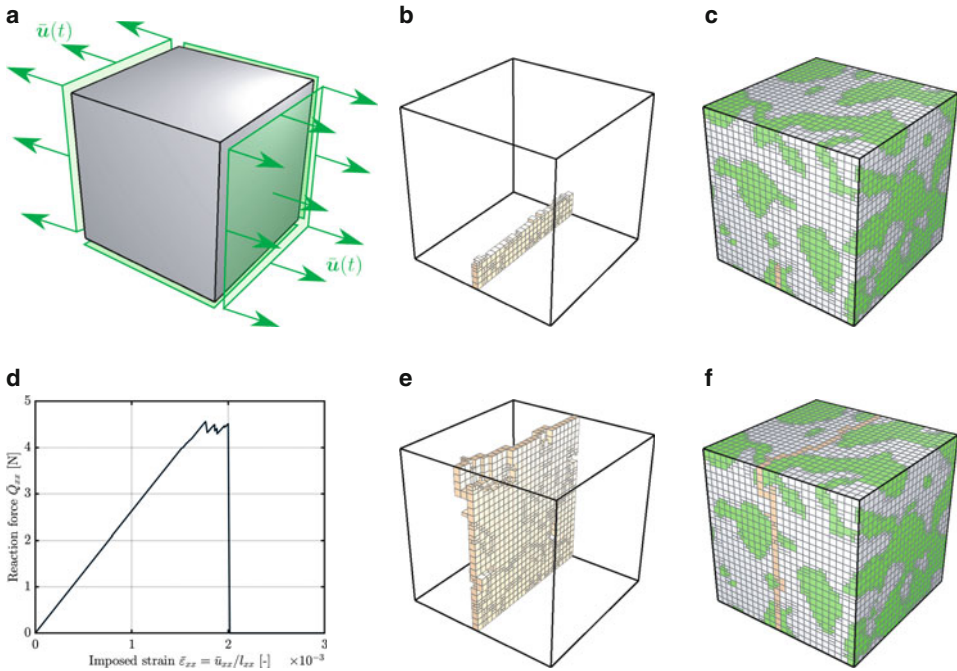
Fig. 3.47 **a** Boundary conditions of a one-dimensional tension test on MMC microstructure with **b** initial crack and microstructure, **c** consisting of titanium carbide inclusions (green) and iron matrix (silver) resulting in the reaction force in **d** and the crack path in **d** and **e**, cf. [101]

The inclusion shape depends on the production process of the material. The simplified microstructure of a cold-work steel, produced by hot-isostatic pressing (HIP), is characterized by spherical chromium carbide inclusions embedded in the ductile steel matrix (Fig. 3.48). In contrast, the inclusions are shaped as ellipsoids in Fig. 3.48d, which is typical for hot-rolled steels. Symmetry boundary conditions with an externally applied deformation (Fig. 3.47) are applied, which increases linearly over time. In the resulting crack paths of the cold work tool steel microstructure containing the spherical carbides (Fig. 3.48b, e), the crack primarily propagates around the inclusions whereas the crack in the microstructure containing ellipsoids propagates straight through the inclusion phase. This effect occurs because the crack propagates along the energetically most favorable path. Different from the case with ellipsoids, now the path around the spherical inclusions is energetically more favorable than the one intersecting them. The same effects are observed in experiments. For instance, the crack in Fig. 3.48c through a real microstructure which inherits rather spherical inclusions avoids propagation through the chromium carbides. However, cracks propagate through the ellipsoidal inclusions as well (Figure 3.48f), as also observed in the simulations.
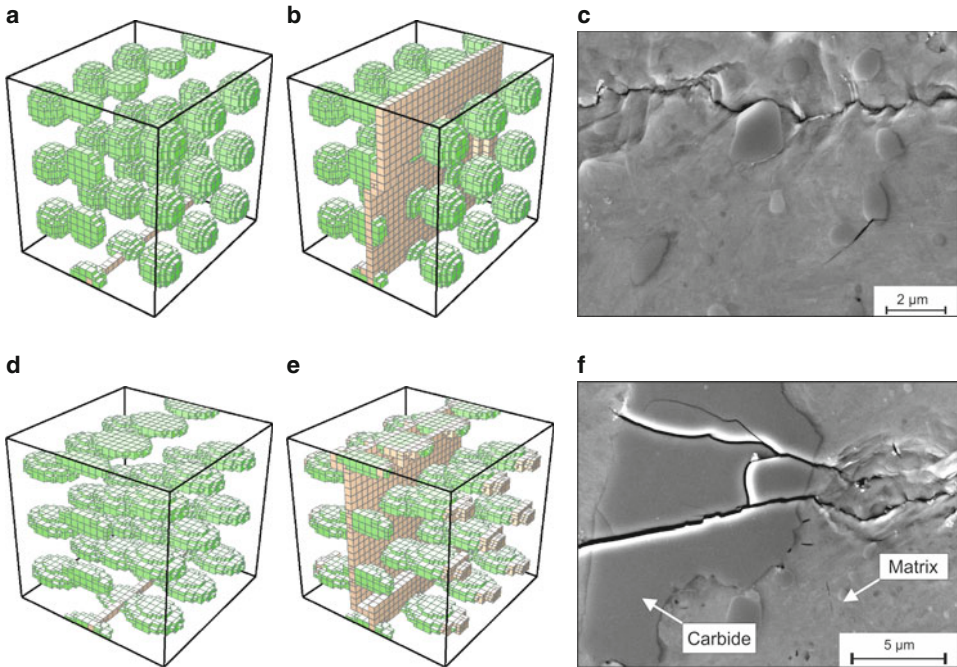
Fig. 3.48 Microstructure consisting of **a** spherical and **d** ellipsoidal chromium carbide inclusions (green) within ductile steel matrix and **b**, **e** the resulting crack paths (gold) that occur under the boundary conditions in Fig. 3.47a. **c** and **f** show the microstructure of comparable experiments

Fig. 3.49 Reaction force of one-dimensional tensile test with boundary conditions in Fig. 3.47a of the cold work steel microstructures in Fig. 3.48a, c
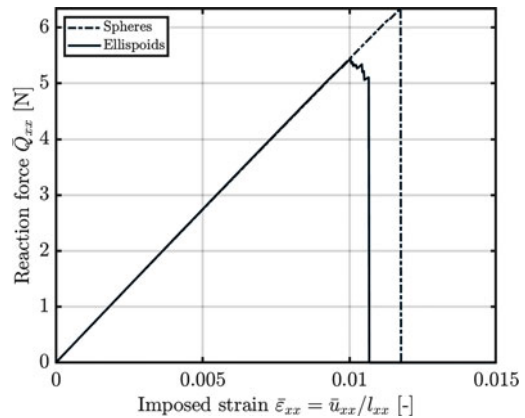
The maximum forces and displacements are extracted from the force-displacement curves, to decide, which morphology leads to a higher resistance against crack propagation and thus surface fatigue. The cold work tool steel microstructure with spheres (Fig. 3.49) is capable of enduring a higher force and larger imposed mechanical energy than the microstructure which includes ellipsoids. Therefore, it is expected that the unrolled material

inherits a higher resistance against surface fatigue than the rolled material. In general, the simulation of crack propagation for the investigation of the crack resistance can also be applied on different forms of microstructures, e.g., ones which result from other production processes, like casting. Furthermore, microstructures with different inclusion sizes and microscopic material properties can be analyzed. Improvements can be suggested regarding the choices of microstructures of the metal matrix composite layers on the tunneling tools by comparing the results of these simulations.

3.3.8   Monitoring of tool wear and damages

We investigated the possibility of monitoring the cutting tools of a TBM in real time to ultimately reduce maintenance and downtimes. While performance and other parameters of TBMs are routinely monitored [65], monitoring the cutting tools directly has to overcome many challenges. In civil structures and rotary machinery, such as jet engines, wind turbines and trains, where monitoring systems are already in use, the conditions are often assumed to be quasi static. During operation, the different phases of an operational cycle of a machine, are considered as a whole. They are therefore static, as the machine just repeats the same cycle. However, for a TBM this assumption is taken to a different magnitude compared to other machines. Factors that influence the "cycle" of a TBM are the amount of overburden, cavities and excavated materials leading to the shield partially not being in contact to the tunnel face as well as water content, shield force/head pressure and most importantly the type of rock or soil.

We introduced the general principles of machine monitoring and damage detection before discussing possible sensor technologies and where these can be applied regarding TBM. To address the possibility of monitoring a TBM, we used vibration-based experimental data from the RTD (Sect. 3.3.4.1) as a small scale model of the disc cutters. Then strategies and methods will be explained, and finally we conclude with a proof of concept using artificial damages.

3.3.8.1   Principle of wear and damage detection

The fundamental concepts of detecting damage in machine parts and structural components come from condition monitoring (CM) and structural health monitoring (SHM), respectively, and are highly application specific (e.g., [32]). The damages that should be detected need to be defined to build a monitoring system. Furthermore, the operational and environmental conditions should be determined to evaluate limitations of the data acquisition. The acquisition requires selecting the type, number, and location of sensors. It is important to normalize data, to separate damage relevant information from other influences. After that, feature extraction and information condensation take place. Finally, the extracted features need to be statistically analyzed and classified into damaged and undamaged cases. This last step is called statistical model development and can be performed involving one of three common methods: supervised learning, unsupervised learning or

novelty detection. The first and second are neural-network based methods, while the second and third method do not require a priori knowledge of the damaged case [28].

The economical aspects of a monitoring system are to be considered, in particular in the planning and testing phases. With more knowledge about the quality and characteristics of collected data and specifics of the monitored machine/structure, analysis methods become more robust and data acquisition can be reduced, lowering monitoring costs.

Our research concentrated on the most common damages of disc cutters and their bearings, using vibration-based feature extraction. For disc cutters these damages are wear, impact damage, split ring loss or blockage due to seal failure of the bearings [31] and for bearings these are single-point defects and generalized roughness faults [109]. While bearings are well investigated regarding monitoring [25, 61, 99], monitoring of disc cutters is in its infancies [82, 98] and until today rarely been used on actual TBMs [66]. Currently, the prediction of wear is based on many parameters of TBMs, which are already monitored, like cutter head revolutions per minute (RPM), cutter head torque, axial force and displacement of thrust jacks [65]. We explored the use of acceleration (model 333B30–PCB Synotech) and force (KM40–ME-Systeme) sensors in a small scale model of a TBM.

3.3.8.2 Vibration-based monitoring

Every machine that carries out physical work generates vibrations. These vibrations fundamentally depend on the properties of each machine component, i.e., geometry, material parameters, velocity, etc. While the machine is running, all of its components experience wear, which changes their properties and therefore the characteristics of the generated vibrations. The basic idea of monitoring is to determine how these vibrations change over time and distinguish between an operational state and a damaged one.

Most of the time, machines have components, like gears, bearings, and shafts, that generate repetitive signals, i.e., with systematic frequencies. These signals can be classified into stationary and non-stationary, meaning that statistical properties do not change over time, continuous or transient, and random or deterministic. The classification is important for a selection of an appropriate signal processing method, like Fourier transform, Hilbert transform, digital filters, and demodulation.

The greatest advantages of using vibrations for monitoring are the immediate response of vibrations to changes and the ability to identify the actual faulty component. Oil analysis, for example, can take days for wear to be detectable based on the accumulation of metal chips and even then it is unclear from which part these originate [75].

3.3.8.3 Proof of concept

To demonstrate that damages can be detected with the RTD, we use data from experiments and two models. Each of these datasets contains data for an undamaged and damaged case. Two different methods for damage detection, namely the Hilbert transform and a complex demodulation algorithm, were used to investigate the capability of damage detection [73]. We extracted the same feature with both envelope generating methods and compared them.

The data show that for the different datasets the Hilbert transform,

$$E_x = F^{-1}(F(x_i)\,2U) = x_i + iH(x_i)\,,\tag{3.10}$$

with the discrete time series x_i, the Fourier transform F, the Heaviside step function U, the Hilbert transform H and the resulting Envelope of the data E_x, extracts damage relevant feature more efficiently.

Based on the results from [73], we conducted a larger study with purely experimental data to correlate the initial findings with an increasing, albeit artificially introduced, damage state of disc cutters [74]. We performed 65 experiments with three individual disc cutters of same geometry and material and up to four different damage states. The experiments were done using the RTD described in Sect. 3.3.4.1. However, the conditions the disc cutters were performing at can be described as rather ideal. Rocks were not used at this stage, instead the disc cutters rolled on a steel surface. We removed low frequency components from the recorded data using a moving average filter

$$\bar{x}_i = x_i - \frac{1}{2n+1} \sum_{k=i-n}^{i+n} x_k\,.\tag{3.11}$$

Here, $2n + 1 = 21$ is the size of the used box car window of the filter. After this step, only high frequency noise and the interaction of the damage of the disc cutter, which happens exactly once every rotation, is left. Figure 3.50a shows an example of the raw data obtained from these experiments. Here, the disc cutter had a damage of roughly 2 mm
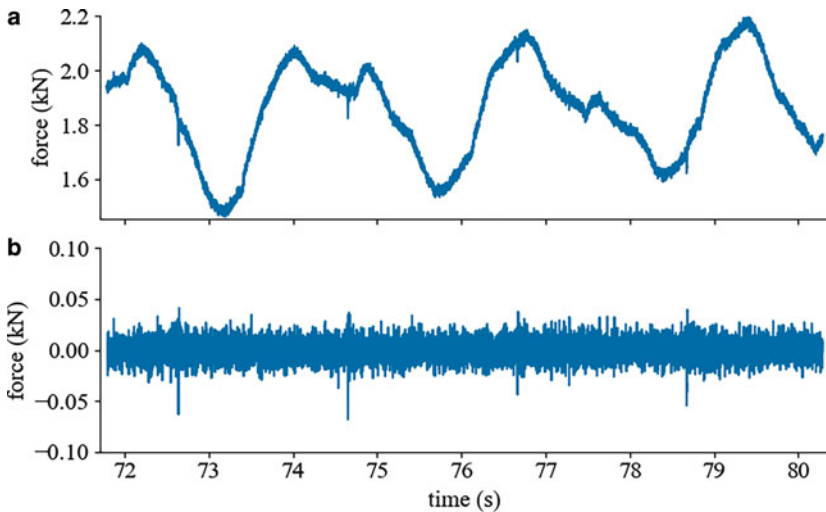
Fig. 3.50 **a** Exemplary time domain data of a disc with a damage interacting every two seconds. **b** The same data with the moving average removed from it, still showing the damage interaction

in size. Figure 3.50b shows the results of the filtering method. In this short example, the interaction can be seen four times with an interval of two seconds in between.

After the data is cleansed, the envelope is calculated according to Eq. 3.10 and transformed to the frequency domain, where the feature, called damage indicator (DI) from here on, is extracted. The DI we chose is the maximum value of the envelope between 0.45 and 0.55 Hz, as the frequency of the interaction of the damage is expected to be roughly 0.5 Hz. This expectation is based on the a priori knowledge of the speed of the RTD and the ratio of diameters of the parts involved. In an attempt to further improve the correlation between DI and damage size, the DI is normalized by the total energy of the signal

$$E_{\mathrm{T}} = \frac{1}{N} \sum_{k=0}^{N-1} \| F_k \|^2 \,, \tag{3.12}$$

with the total number of discrete samples N in the frequency domain.

The results for disc cutters A and B show a correlation between DI and damage size for both considered disc cutters (Fig. 3.51). DI from disc cutter A benefit from the normalization, while the same is not true for disc cutter B. Results for the third disc cutter were not conclusive and are not considered here. An extended analysis of these results revealed that the operational conditions have greater impact than expected [74].
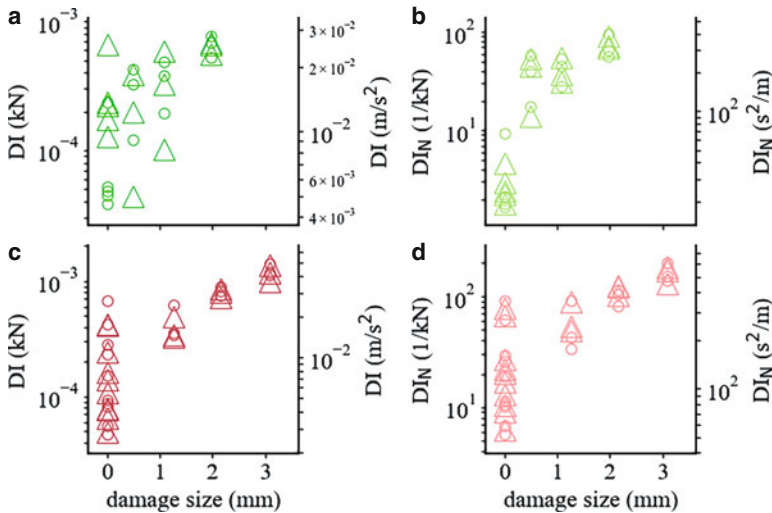
Fig. 3.51 The left column of plots, **a** and **c**, shows the damage indicator (DI) without normalization and the right column, **b** and **d**, show the DI with normalization. In the first row, only data of disc cutter A, green color, and in the second row data of disc cutter B, red color, is shown. Each of the four figures shows data from a force sensor on the left y-axis, represented by circles, and the right y-axis shows data from an acceleration sensor, represented by triangles

3.3.8.4 Outlook

In the future, we will expand our investigations towards disc cutters used on Anröchter sandstone, a rock with moderate anisotropy and low porosity (see Sect. 3.2.2.2. Exploratory tests showed that the rock is initially free of fractures. Specimens are drilled from blocks with a core drill. To define a baseline, data with mainly damage free discs and bearings will be collected. The baseline will then be used for statistical analysis to discriminate among damage sensitive and insensitive features. The monitoring will be improved by using high frequency sensors and video footage of the experiments. We plan to improve on the currently used sensors to enable modal analysis. Video footage will be used to correlate as many parts of the data as possible to different non-damage-related events, such as rock fracturing. Improvements of the data analysis will consider fitting algorithms, methods as well as using neural networks for direct disc cutter monitoring.

3.4 Influence of Tool Wear on the Effectiveness of Excavation

The material concept for tunneling tools is based on two main aims. A long and well predictable service lifetime helps to keep maintenance interruptions short and a high tunneling efficiency allows for fast penetration rates of the TBM. Based on the results of our laboratory testing and numerical modeling of tool wear, several recommendations can be derived to improve material concepts for tunneling tools and thus the excavation process.

Counteracting the dominant wear mechanism, which depends on the properties of the excavated ground, is the key to increase the tool's lifetime. Selection of the optimal material or an optimal tool design is based on suitable wear tests and in-depth analysis of the tribological system during the planning stage of the tunneling project. For granular soils, which will mainly be excavated by scraping tools, the hardness of the soil particles, their size and morphology have to be considered for the material choice of wear protective layers and inserts on chisels, reamers, and scrapers to inhibit abrasive wear. Furthermore, the presence of boulders, schistosities and other soil-inhomogeneities should be assessed to evaluate the extent of cyclic mechanical loading that is to be expected. If severe cyclic loading is predicted, it is advisable to choose materials with a low content of hard-phases for wear-protective layers or inserts to increase their content of the crack-resistant metal matrix. Küpferle [46] showed for cemented carbides that the fatigue strength of a 15 vol%-Co grade is increased by about 80 %, compared to a 6 vol%-Co grade under cyclic compressive loading. Thus optimizing Co-content bears the potential for significant improvement potential for wear protective inserts, that wear out due to fatigue micro-spalling under the repetitive impact of abrasive particles.

Apart from the hard-phase volume content, the behavior of the metal matrix in wear-resistant composite materials was identified as the decisive factor to promote a high fatigue strength. The commonly used Ni-based metal-matrix composites of NiBSi or NiCrBSi, reinforced with fused tungsten carbide hard particles, are susceptible to fatigue cracking due to their comparably low strength Ni-metal matrix, which promotes premature crack

initiation at a low number of loading cycles. In contrast, Fe-based and Co-based hard alloys offer significant fatigue strength, due to their metal matrices, which exhibit a higher strength than Ni-based metal matrices (Fig. 3.30). Despite the challenges connected with the use of Fe-based hard alloys, such as higher processing temperatures and restricted availability of well-established hard phases, they represent a promising material concept. Possible applications that allow for the replacement of fused tungsten carbide with soft carbides of the type M_7C_3, comprise soils with a hardness of the soil particles below 1000 HV (e.g. Flint), or soils with severe cyclic load potential due to large particle sizes and thus high impact energies during contact to the tool.

Regarding disc cutters, tool lifetimes can especially be improved for tunneling in soft-rock with a low amount of inhomogeneities. Then, the disc cutters are only rarely subjected to severe mechanical loads and the main wear mechanism is abrasion, as the disc cutters are dragged through the ground with a large relative movement. In these cases, carbide-containing cold-work tool steels like X153CrMoV12-1 or 90MnCrV8 may replace the currently used hot work-tool steels (X50CrMoV5-1) with a low content of hard-phases to achieve high abrasion resistance. Adjusted heat treatments can be applied to form low (< 15 vol%) amounts of the tough phase retained austenite to increase the fatigue strength and fracture toughness of these cold-work tool steels (Fig. 3.33). This metastable phase can transform to the hard phase martensite, featuring a higher resistance against abrasive wear. In addition, subcritical crack growth is stopped due to the residual compressive stresses that are created as a result of the lattice transformation. For excavation of hard rocks or heterogeneous soils, the hot-work tool steels remain the superior choice due to their overall high fatigue resistance. To guarantee the desired material behavior, tool manufacturers and suppliers must pay attention to the chemical purity of the utilized steel and to the heat-treatment. Especially the contents of sulfur, phosphor, and oxygen have to be kept to the lowest possible level, as these elements form non-metallic inclusions, which promote crack initiation under cyclic loading. Refinement processes such as electro-slag remelting can reduce the content of these unwanted elements and can increase the overall homogeneity of the steel, which improves the mechanical properties.

3.4.0.1 Implications for Tunneling Efficiency

To realize the predetermined advancement rates of the TBM, the tunneling tools must be capable of excavating a certain amount of ground-volume in a fixed timespan. The excavation process includes the release of soil particles from the tunnel-face and the removal of the material from the excavation chamber. The excavation process of rock by the means of disc cutters involves introducing compressive stresses and subsequent crack propagation inside the rock, which eventually leads to chipping. To achieve high efficiency of this excavation mechanism, the applied external force has to be converted into the newly created crack surface, which encloses a maximum rock volume. The energetic assessment implies a positive impact of large single cracks in the rock on the tunneling efficiency, in comparison to a high number of small cracks that take up the same amount of fracture work than one large crack. Therefore, rock excavation should aim for large fragment sizes of the released material.

Fig. 3.52 **a** Experimental setup of uniaxial rock indentation testing, **b** calculated energy consumption of various system components in the indentation test, **c** blunting of a soft indenter over several cycles of use
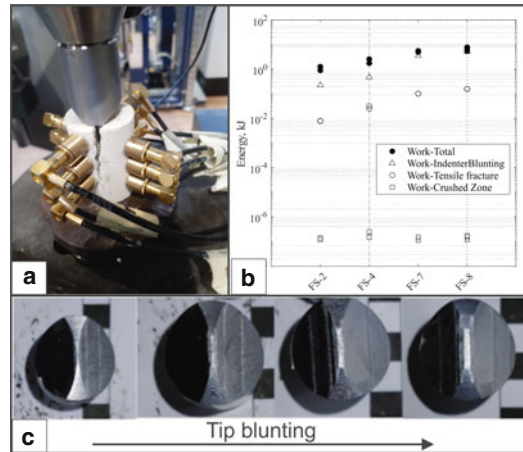
Uniaxial indentation tests on several rock types (see Fig. 3.52a), as well as rock excavation experiments at the RUB-Tunneling Device were conducted, to investigate the interaction of different tool geometries with rocks. The most significant finding of the indentation experiments was that indenters with a sharp tip, which produces a small contact area and therefore high stresses in the contact area, facilitate the propagation of a large median crack, in contrast to blunt indenters. Blunt indenters cause the formation of a large pseudo-plastic zone at the rock surface, which is characterized by pore collapse and propagation of a high number of microcracks and therefore dissipates energy but will not lead to the desired fragmentation (see Fig. 3.52b). In addition, the plastic deformation of the indenter itself takes up a significant amount of the externally applied work. For these reasons, blunt indenters and correspondingly blunt cutting edge geometries of disc cutters appear unfavorable concerning the tunneling efficiency. Based on this result, geometry changes of the cutting edge during the tunneling process, which are caused by plastic deformation or other wear phenomena, must be critically assessed. Indentation tests with an indenter made of soft steel (300 HV30) on Fontainebleau sandstone revealed successive blunting of the indenter tip after several tests (see Fig. 3.52c). In correlation, the necessary indentation forces to fracture the rock specimen increased significantly. Excavation experiments on Anröchter sandstone with a pristine disc cutter (2.8 mm cutting edge width) and a worn disc cutter with blunted cutting edge (4.0 mm cutting edge width) demonstrated the impact of the tool geometry change on the tunneling efficiency. At the same contact pressure, the new disc cutters excavation performance was much better, compared to the blunted disc cutter (see Fig. 3.53). The large difference can be traced back to the rock fracture behavior that is caused by the disc cutters. While the new disc cutter caused fracture of large rock particles, the blunted disc cutter only generated rock dusting by releasing single rock grains and small chips. This experimental investigation confirms the previously presented theoretical analysis and emphasizes the importance of cutting edge retention of the disc cutters for the tunneling efficiency during rock excavation.

Fig. 3.53 Comparison of the excavation capability of a disc cutter with small edge width (2.8 mm cutting edge width) and a disc cutter (4.0 mm cutting edge width), measured on Anröchter sandstone
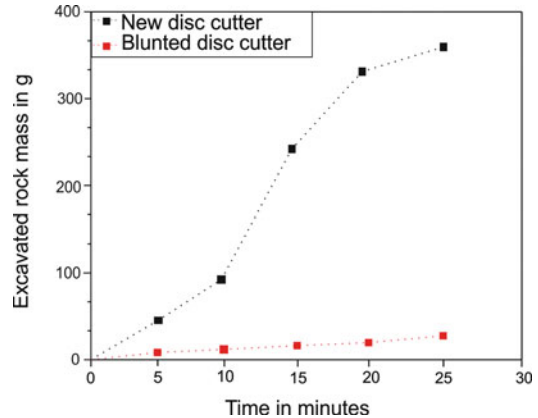
References

1. H. Alehossein, E. Detournay, and H. Huang. "An analytical model for the indentation of rocks by blunt tools". In: *Rock Mechanics and Rock Engineering* 33.4 (2000), pp. 267–284. ISSN: 1434-453X. https://doi.org/10.1007/s006030070003.

2. American Society of Testing and Materials. *Standard Test Method for Measuring Abrasion Using the Dry Sand/Rubber Wheel Apparatus*. norm. 1985.

3. G. Angenheister, ed. *Zahlenwerte und Funktionen aus Naturwissenschaft und Technik*. Vol. Neue Serie, Gruppe 5. Landolt-Börnstein. Berlin: Springer, 1982.

4. J. Archard. "Contact and rubbing of flat surfaces". In: *Journal of applied physics* 24.8 (1953), pp. 981–988.

5. M. Ashby and C. Sammis. "The damage mechanics of brittle solids in compression". In: *Pure and applied geophysics* 133.3 (1990), pp. 489–521.

6. A. L. Bal and G. Meschke. "Adaptive two-phase Particle Finite Element model for soft soil excavations in partially saturated soils". In: *th edition of the International Conference on Computational Methods for Coupled Problems in Science and Engineering (COUPLED PROBLEMS 2021)*. 2021.

7. A. R. L. Bal, T. S. Dang, and G. Meschke. "A 3D particle finite element model for the simulation of soft soil excavation using hypoplasticity". In: *Computational Particle Mechanics* 7.1 (2020), pp. 151–172.

8. A. R. L. Bal et al. "Hypoplastic particle finite element model for cutting tool-soil interaction simulations: Numerical analysis and experimental validation". In: *Underground Space* 3.1 (2018), pp. 61–71.

9. H. Berns and W. Theisen. *Eisenwerkstoffe: Stahl und Gusseisen*. Springer-Verlag, 2008.

10. H. Berns and W. Theisen. *Hartlegierungen und Hartverbundwerkstoffe: Gefüge, Eigenschaften, Bearbeitung, Anwendung*. Springer-Verlag, 1998.

11. W. Brace and D. Kohlstedt. "Limits on lithospheric stress imposed by laboratory experiments". In: *Journal of Geophysical Research: Solid Earth* 85.B11 (1980), pp. 6248–6252.

12. L. Brackmann et al. "Subcritical crack growth in hard alloys under cyclic loading". In: *Fatigue and Fracture of Engineering Materials and Structures* 2 (2021), pp. 349–365.

13. S. N. Butt and G. Meschke. "Peridynamic analysis of dynamic fracture: influence of peridynamic horizon, dimensionality and specimen size". In: *Computational Mechanics* 67.6 (June 2021), pp. 1719–1745. ISSN: 1432-0924. https://doi.org/10.1007/s00466-021-02017-1.

14. S. Butt and G. Meschke. "A 3D peridynamic model of rock cutting with TBM disc cutters". In: *Proceedings of the 7th GACM Colloquium on Computational Mechanics for Young Scientists from Academia and Industry*. Ed. by M. von Scheven, M. Keip, and N. Karajan. Stuttgart, Germany: Institute for Structural Mechanics, University of Stuttgart, 2017, pp. 752–755.

15. S. Butt and G. Meschke. "A rate-dependent damage model for prediction of high-speed cracks". In: *Proceedings in Applied Mathematics and Mechanics (PAMM)* (2018). https://doi.org/10.1002/pamm.201800330.

16. S. Butt and G. Meschke. "Interaction of cutting disc with heterogeneous ground". In: *Proceedings of Applied Mathematics and Mechanics* 20 (2021), 20: e202000060. https://doi.org/10.1002/pamm.202000060.

17. S. N. Butt, J. J. Timothy, and G. Meschke. "Wave dispersion and propagation in state-based peridynamics". In: *Computational Mechanics* 60.5 (2017), pp. 725–738.

18. R. P. Chapuis and M. Aubertin. *Predicting the coefficient of permeability of soils using the Kozeny-Carman equation*. Tech. rep. 2500 Chemin de Polytechnique, Montreal, QC H3T 1J4 Canada: Polytechnique Montréal, 2003.

19. L. H. Chen and J. F. Labuz. "Indentation of rock by wedge-shaped tools". In: *International Journal of Rock Mechanics and Mining Sciences* 43.7 (2006), pp. 1023–1033. ISSN: 1365-1609. https://doi.org/10.1016/j.ijrmms.2006.03.005.

20. C. Coetzee and D. Els. "Calibration of granular material parameters for DEM modelling and numerical verification by blade–granular material interaction". In: *Journal of Terramechanics* 46.1 (2009), pp. 15–26. ISSN: 0022-4898.

21. R. Costamagna, J. Renner, and O. T. Bruhns. "Relationship between fracture and friction for brittle rocks". In: *Mechanics of Materials* 39.4 (2007), pp. 291–301. https://doi.org/10.1016/j.mechmat.2006.06.001.

22. R. J. Cuss, E. H. Rutter, and R. F. Holloway. "The application of critical state soil mechanics to the mechanical behaviour of porous sandstones". In: *International Journal of Rock Mechanics and Mining Sciences* 40 (2003), pp. 847–862.

23. H. Czichos. *Tribologie-Handbuch: Tribometrie, Tribomaterialien, Tribotechnik*. Vieweg + Teubner, 2010.

24. P. Drucker. "Abrasivity of soil and tool wear in ground engineering and tunnelling". In: 156 (2011), pp. 1–7.

25. Z. Duan et al. "Development and trend of condition monitoring and fault diagnosis of multi-sensors information fusion for rolling bearings: a review". In: *The International Journal of Advanced Manufacturing Technology* 96.1-4 (Jan. 2018), pp. 803–819. https://doi.org/10.1007/s00170-017-1474-8.

26. A. V. Dyskin, L. N. Germanovich, and K. B. Ustinov. "A 3-D model of wing crack growth and interaction". In: *Engineering Fracture Mechanics* 63.1 (1999), pp. 81–110.

27. E. Eberhardt. "The Hoek–Brown failure criterion". In: *The ISRM Suggested Methods for Rock Characterization, Testing and Monitoring: 2007-2014*. Springer, 2012, pp. 233–240.

28. C. R. Farrar and K. Worden. "An introduction to structural health monitoring". In: *Philosophical Transactions of the Royal Society A: Mathematical, Physical and Engineering Sciences* 365.1851 (Dec. 2006), pp. 303–315. https://doi.org/10.1098/rsta.2006.1928.

29. E. Fjaer. "Relations between static and dynamic moduli of sedimentary rocks". In: *Geophysical Prospecting* 67.1 (2019), pp. 128–139. https://doi.org/10.1111/1365-2478.12711.

30. F. Frank and L. B. "On the theory of Hertzian fracture". In: *Proceedings of the Royal Society of London A: Mathematical, Physical and Engineering Sciences* 299 (1967), pp. 291–306.

31. C. Frenzel, H. Käsling, and K. Thuro. "Factors Influencing Disc Cutter Wear". In: *Geomechanik und Tunnelbau* 1.1 (Feb. 2008), pp. 55–60. https://doi.org/10.1002/geot.200800006.

32. H. Friedmann and P. Kraemer. "Vibration-based condition monitoring, structural health monitoring, population monitoring–Approach to a definition of the different concepts by means of practical examples from the field of wind energy". In: *Proceedings of the 8th European Workshop on Structural Health Monitoring (EWSHM 2016), Bilbao, Spain*. 2016, pp. 5–8.

33. K.-H. Gahr. "Wear by hard particles". In: *Tribology International* 31 (1998), pp. 587–596.

34. H. Gebrande. "Elastic wave velocities and constants of rocks and rock forming minerals". In: ed. by G. Angenheister. Vol. 1b. Zahlenwerte und Funktionen aus Naturwissenschaft und Technik, Landolt-Börnstein, Neue Serie, Gruppe 5. Berlin: Springer, 1982, pp. 1–34.

35. R. Gertsch, L. Gertsch, and J. Rostami. "Disc cutting tests in Colorado Red Granite: Implications for TBM performance prediction". In: *International Journal of rock mechanics and mining sciences* 44.2 (2007), pp. 238–246.

36. C. Gonzalez, M. Arroyo, and A. Gens. "Wear and abrasivity: observations from EPB drives in mixed soft-rock sections". In: *Geomechanics and Tunnelling* 3 (2015), pp. 258–264.

37. A. Griffith. "Theory of rupture". In: ed. by C. Biezeno and J. Burgers. First International Congress Applied Mechanics. 1924, pp. 55–63.

38. G. Gudehus. *Physical Soil Mechanics*. Advances in Geophysical and Environmental Mechanics and Mathematics. Springer, 2011, p. 840. https://doi.org/10.1007/978-3-540-36354-5.

39. H. Huang, B. Damjanac, and E. Detournay. "Normal wedge indentation in rocks with lateral confinement". In: *Rock Mechanics and Rock Engineering* 31.2 (1998), pp. 81–94. ISSN: 1434-453X. https://doi.org/10.1007/s006030050010.

40. H. Huang and E. Detournay. "Discrete element modeling of tool-rock interaction II: rock indentation". In: *International Journal for Numerical and Analytical Methods in Geomechanics* 37.13 (2013), pp. 1930–1947. ISSN: 0363-9061.

41. J. C. Jaeger, N. G. Cook, and R. Zimmerman. *Fundamentals of rock mechanics*. John Wiley & Sons, 2009.

42. K. L. Johnson. "The correlation of indentation experiments". In: *Journal of the Mechanics and Physics of Solids* 18.2 (1970), pp. 115–126. ISSN: 0022-5096. https://doi.org/10.1016/0022-5096(70)90029-3.

43. K. L. Johnson and K. L. Johnson. *Contact mechanics*. Cambridge university press, 1987. ISBN: 0521347963.

44. H. Jones et al. *Test Methods For High Rate Impact Loading Of Hardmetals*. EURO PM2012, 2012.

45. F. Köppl. *Abbauwerkzeugverschleiß und empirische Verschleißprognose beim Vortrieb mit Hydroschild TVM in Lockergesteinen*. TU München, 2014.

46. J. Küpferle et al. "Influence of the slurry-stabilized tunnel face on shield TBM tool wear regarding the soil mechanical changes – Experimental evidence of changes in the tribological system". In: *Tunnelling and Underground Space Technology* 74 (2018), pp. 206–216. https://doi.org/10.1016/j.tust.2018.01.011.

47. J. Küpferle, A. Röttger, and W. Theisen. "Excavation tool concepts for TBMs – Understanding the material-dependent response to abrasive wear". In: *Tunnelling and Underground Space Technology* 68 (2017), pp. 22–31.

48. J. Küpferle, A. Röttger, and W. Theisen. "Fatigue and surface spalling of cemented carbides under cyclic impact loading – Evaluation of the mechanical properties with respect to microstructural processes". In: *Wear* 390–391 (2017), pp. 33–40.

49. J. Küpferle et al. "Assessment of the LCPC abrasiveness test from the view of material science / Bewertung des LCPC-Abrasivitätstests aus werkstofftechnischer Sicht". In: *Geomechanics and Tunnelling* 3 (2015), pp. 211–220.

50. J. Küpferle et al. "The RUB Tunneling Device – A newly developed test method to analyze and determine the wear of excavation tools in soils". In: *Tunnelling and Underground Space Technology* 59 (2016), pp. 1–6.

51. B. R. Lawn, A. G. Evans, and D. B. Marshall. "Elastic/Plastic Indentation Damage in Ceramics: The Median/Radial Crack System". In: *Journal of the American Ceramic Society* 63.9-10 (1980), pp. 574–581. ISSN: 0002-7820. https://doi.org/10.1111/j.1151-2916.1980.tb10768.x.

52. A. R. Leon, T. S. Dang, and G. Meschke. "Computational Excavation Analysis of a Single Cutting Tool using a Hypoplastic Constitutive Model". In: *PAMM* 16.1 (2016), pp. 369–370. ISSN: 1617-7061.

53. A. R. Leon and G. Meschke. "Two-phase Particle Finite Element model for the coupled analysis of cutting tool-soil interaction in partially saturated soft soils". In: *International Journal for Numerical and Analytical Methods in Geomechanics* (2022). Submitted.

54. P. A. Lindqvist, H. H. Lai, and O. Alm. "Indentation fracture development in rock continuously observed with a scanning electron microscope". In: *International Journal of Rock Mechanics and Mining Sciences & Geomechanics Abstracts* 21.4 (1984), pp. 165–182. ISSN: 0148-9062. https://doi.org/10.1016/0148-9062(84)90794-0.

55. D. J. Littlewood. "Roadmap for peridynamic software implementation". In: *SAND Report, Sandia National Laboratories, Albuquerque, NM and Livermore, CA* (2015).

56. H. Y. Liu et al. "Numerical simulation of the rock fragmentation process induced by indenters". In: *International Journal of Rock Mechanics and Mining Sciences* 39.4 (2002), pp. 491–505. ISSN: 1365-1609. https://doi.org/10.1016/S1365-1609(02)00043-6.

57. Q. Liu et al. "Experimental study on rock indentation using infrared thermography and acoustic emission techniques". In: *Journal of Geophysics and Engineering* 15.5 (2018), pp. 1864–1877. ISSN: 1742-2132. https://doi.org/10.1088/1742-2140/aac096.

58. D. Lockner. "The role of acoustic emission in the study of rock fracture". In: *International Journal of Rock Mechanics and Mining Sciences & Geomechanics Abstracts* 30.7 (1993), pp. 883–899. https://doi.org/10.1016/0148-9062(93)90041-B.

59. D. A. Lockner. "Rock failure". In: *Rock physics and phase relations: A handbook of physical constants*. Ed. by T. J. Ahrens. Vol. 3. AGU Reference Shelf. American Geophysical Union, 1995, pp. 127–147.

60. J. Macias. *Hard Rock Tunnel Boring – Performance Predictions and Cutter Life Assessments*. Trondheim: NTNU, 2016.

61. C. Malla and I. Panigrahi. "Review of Condition Monitoring of Rolling Element Bearing Using Vibration Analysis and Other Techniques". In: *Journal of Vibration Engineering & Technologies* 7.4 (May 2019), pp. 407–414. https://doi.org/10.1007/s42417-019-00119-y.

62. F. McClintock. "Friction on Griffith cracks in rocks under pressure". In: *Proc. 4th US Nat. Congr. Appl. Mech.* Vol. 2. 1962, pp. 1015–1022.

63. S. Miedema. "The cutting of densely compacted sand under water". In: *Terra et Aqua* 28 (1984), pp. 4–10.

64. S. Miedema. "The cutting of water saturated sand, the final solution". In: *WEDAXXV & TAMU37, New Orleans, USA* (2005).

65. M. A. Mooney, B. Walter, and C. Frenzel. "Real-time tunnel boring machine monitoring: A state of the art review". In: *North American Tunnelling, 2012 proceedings* (2012), pp. 73–81.

66. K. Mosavat. "A smart disc cutter monitoring system using cutter instrumentation technology". In: *RETC Proceedings*. 2017.

67. S. A. F. Murrell. "A criterion for brittle fracture of rocks and concrete under triaxial stress and the effect of pore pressure on the criterion". In: *Rock mechanics* (1963), pp. 563–577.

68. E. Oñate et al. "The particle finite element method. An overview". In: *International Journal of Computational Methods* 1.02 (2004), pp. 267–307.

69. A. Pandolfi, B. Li, and M. Ortiz. "Modeling failure of brittle materials with eigenerosion". In: *Computational Modelling of Concrete Structures* 1 (2013), pp. 9–21. https://doi.org/10.1007/s10704-012-9788-x.

70. M. L. Parks et al. *Peridigm Users' Guide v1. 0.0*. Tech. rep. Sandia National Laboratories, 2012.

71. M. S. Paterson and T.-F. Wong. *Experimental rock deformation-the brittle field*. Springer Science & Business Media, 2005.

72. R. Plinninger et al. "Testing conditions and geomechanical properties influencing the CERCHAR abrasiveness index (CAI) value". In: *International Journal of Rock Mechanics and Mining Sciences* 40 (2003), pp. 259–263.

73. S. Priebe et al. "Comparison of Hilbert Transform and Complex Demodulation for Defect Identification in Cutting Discs using Vibration-Based Feature Extraction". In: *European Workshop on Structural Health Monitoring*. Springer. 2020, pp. 564–572.

74. S. Priebe et al. "Vibration-Based Feature Extraction for Artificial Damages in Small Scale Cutting Discs of Tunnel Boring Machines". In: *The e-Journal of Nondestructive Testing* 26.12 (Dec. 2021).

75. R. B. Randall. *Vibration-based Condition Monitoring*. WILEY, July 2021. 448 pp. ISBN: 1119477557.

76. L. Röchter. *Systeme paralleler Scherbänder unter Extension im ebenen Verformungszustand*. Lehrstuhl für Grundbau, Boden-und Felsmechanik, 2011.

77. J. Rostami. "Development of soil abrasivity testing for soft ground tunneling using shield machines". In: *Tunneling and Underground Space Technology* 28 (2012), pp. 245–256.

78. J. Rostami. *Development of a force estimation model for rock fragmentation with disc cutters through theoretical modeling and physical measurement of crushed zone pressure*. Colorado School of Mines, Golden, CO, USA, 1997.

79. J. Rostami and L. Ozdemir. "A new model for performance prediction of hard rock TBMs". In: 1993.

80. J. Rostami, L. Ozdemir, and B. Nilson. "Comparison between CSM and NTH hard rock TBM performance prediction models". In:

81. A. Röttger et al. *Abrasion in Tunneling and Mining*. ICSCM, 2015.

82. U. K. Sahinoglu and U. Ozer. "The prediction of cutter wear from temperature measurements on TBM discs and cutting face". In: *Arabian Journal of Geosciences* 13.5 (Feb. 2020). https://doi.org/10.1007/s12517-020-5188-0.

83. L. Sanavia, B. Schrefler, and P. Steinmann. "A formulation for an unsaturated porous medium undergoing large inelastic strains". In: *Computational Mechanics* 28.2 (2002), pp. 137–151.

84. B. Schmidt, F. Fraternali, and M. Ortiz. "Eigenfracture: an eigendeformation approach to variational fracture". In: *Multiscale Modeling & Simulation* 7.3 (2009), pp. 1237–1266. https://doi.org/10.1137/080712568.

85. T. Scholz et al. "Fracture toughness from submicron derived indentation cracks". In: *Applied physics letters* 84.16 (2004), pp. 3055–3057. ISSN: 0003-6951.

86. J. H. Schön. *Physical properties of rocks: Fundamentals and principles of petrophysics*. Elsevier, 2015.

87. S. A. Silling. "Reformulation of elasticity theory for discontinuities and long-range forces". In: *Journal of the Mechanics and Physics of Solids* 48.1 (2000), pp. 175–209.

88. S. A. Silling et al. "Peridynamic states and constitutive modeling". In: *Journal of Elasticity* 88.2 (2007), pp. 151–184.

89. G. Singh and R. W. Zimmerman. "Modification of Griffith–McClintock–Walsh model for crack growth under compression to incorporate stick-slip along the crack faces". In: *International Journal of Rock Mechanics and Mining Sciences* 72 (2014), pp. 311–318. https://doi.org/10.1016/j.ijrmms.2014.09.020.

90. T. Szwedzicki. "Indentation hardness testing of rock". In: *International Journal of Rock Mechanics and Mining Sciences* 35.6 (1998), pp. 825–829. ISSN: 1365-1609. https://doi.org/10.1016/S0148-9062(97)00334-3.

91. D. Tabor. "Indentation Hardness and Its Measurement: Some Cautionary Comments". In: *Microindentation Techniques in Materials Science and Engineering: A Symposium Sponsored by ASTM Committee E-4 on Metallography and by the International Metallographic Society, Philadelphia, PA,* ASTM International, p. 129. ISBN: 0803104413.

92. R. Teale. "The concept of specific energy in rock drilling". In: *International Journal of Rock Mechanics and Mining Sciences & Geomechanics Abstracts* 3.1 (1965), pp. 57–73. ISSN: 0148-9062. https://doi.org/10.1016/0148-9062(65)90022-7.

93. K. Terzaghi. "Die Berechnung der Durchlässigkeitsziffer des Tones aus dem Verlauf der hydromechanischen Spannungserscheinungen". In: *Sitzungsberichte der Akademie der Wissenschaften in Wien, mathematisch-naturwissenschaftliche Klasse* 132 (1923), pp. 125–138.

94. K. Terzaghi. *Theoretical soil mechanics*. Wiley, New York, 1943.

95. K. Thuro et al. "Soil Abrasivity Assessment Using the LCPC Testing Device". In: *Felsbau* 24 (2006), pp. 37–45.

96. V. Vajdova, P. Baud, and T.-f. Wong. "Compaction, dilatancy, and failure in porous carbonate rocks". In: *Journal of Geophysical Research: Solid Earth* 109.B5 (2004).

97. M. T. Van Genuchten. "A closed-form equation for predicting the hydraulic conductivity of unsaturated soils". In: *Soil Science Society of America Journal* 44.5 (1980), pp. 892–898.

98. F. Wang et al. "Optimum Design and Application Research of Eddy Current Sensor for Measurement of TBM Disc Cutter Wear". In: *Sensors* 19.19 (Sept. 2019), p. 4230. https://doi.org/10.3390/s19194230.

99. H. Wang et al. "Research on rolling bearing state health monitoring and life prediction based on PCA and Internet of things with multi-sensor". In: *Measurement* 157 (June 2020), p. 107657. https://doi.org/10.1016/j.measurement.2020.107657.

100. D. Wingender and D. Balzani. "Simulation of crack propagation based on eigenerosion in brittle and ductile materials subject to finite strains". In: *Archive of Applied Mechanics* (2022), pp. 1199–1221. https://doi.org/10.1007/s00419-021-02101-1.

101. D. Wingender and D. Balzani. "Simulation of crack propagation through voxel-based, heterogeneous structures based on eigenerosion and finite cells". In: *Computational Mechanics* (2022), pp. 1–22. https://doi.org/10.1007/s00466-022-02172-z.

102. D. Wingender et al. "Simulation of ductile crack propagation in metal matrix composites – Comparison with cyclic experiments". In: *PAMM* 21.1 (2021), e202100113. https://doi.org/10.1002/pamm.202100113.

103. P.-A. von Wolffersdorff. "A hypoplastic relation for granular materials with a predefined limit state surface". In: *Mechanics of Cohesive-frictional Materials* 1.3 (1996), pp. 251–271. ISSN: 1099-1484.

104. D. M. Wood. *Soil Mechanics: A One-Dimensional Introduction*. Cambridge University Press, 2009. https://doi.org/10.1017/CBO9780511815553.

105. H. Yang et al. "Normal indentation of rock specimens with a blunt tool: role of specimen size and indenter geometry". In: *Rock Mechanics and Rock Engineering* (2022).

106. L. J. Yin et al. "Use of indentation tests to study the influence of confining stress on rock fragmentation by a TBM cutter". In: *International Journal of Rock Mechanics and Mining*

Sciences 72 (2014), pp. 261–276. ISSN: 1365-1609. https://doi.org/10.1016/j.ijrmms.2014.07.022.

107. H. Zhang et al. "Experimental investigation of deformation and failure mechanisms in rock under indentation by digital image correlation". In: *Engineering Fracture Mechanics* 96 (2012), pp. 667–675. ISSN: 0013-7944. https://doi.org/10.1016/j.engfracmech.2012.09.012.

108. W. Zhu, P. Baud, and T.-F. Wong. "Micromechanics of cataclastic pore collapse in limestone". In: *Journal of Geophysical Research: Solid Earth* 115.B04405 (2010), B04405. ISSN: 0148-0227. https://doi.org/10.1029/2009JB006610.

109. H. Zoubek, S. Villwock, and M. Pacas. "Frequency Response Analysis for Rolling-Bearing Damage Diagnosis". In: *IEEE Transactions on Industrial Electronics* 55.12 (2008), pp. 4270–4276. https://doi.org/10.1109/TIE.2008.2005020.

Face Support, Soil Conditioning and Material Transport in Earth-Pressure-Balance and Hydro Shield Machines

4

Britta Schößer ⓘ, Arash Alimardani Lavasan ⓘ, Wiebke Baille ⓘ,
Thomas Barciaga, Sascha Freimann, Mario Galli, Sebastian Kube ⓘ,
Peyman Mianji, Poria Saberi, Marius Schröer, Markus Thewes ⓘ,
Andreas Vogel ⓘ, Chenyang Zhao, and Zdenek Zizka ⓘ

B. Schößer (✉) · S. Kube · M. Schröer · M. Thewes
Tunneling and Construction Management, Ruhr-Universität Bochum, Bochum, Germany
e-mail: britta.schoesser@rub.de

S. Kube
e-mail: sebastian.kube@rub.de

M. Schröer
e-mail: marius.schroeer@rub.de

M. Thewes
e-mail: markus.thewes@rub.de

A. A. Lavasan · W. Baille · P. Mianji
Soil Mechanics, Foundation Engineering and Environmental Geotechnics, Ruhr-Universität
Bochum, Bochum, Germany
e-mail: arash.alimardanilavasan@rub.de

W. Baille
e-mail: wiebke.baille@rub.de

P. Mianji
e-mail: peyman.mianji@rub.de

T. Barciaga
Dr. Spang Ingenieurgesellschaft für Bauwesen, Geologie und Umwelttechnik GmbH, Witten,
Germany
e-mail: Thomas.Barciaga@rub.de

Abstract

The excavation process in mechanised tunnelling consists of various technical components whose interaction enables safe tunnel driving. In reference to the existing geological and hydrogeological conditions, different types of face support principles are applied. In case of fine-grained cohesive soils, the face support is provided by Earth Pressure Balanced (EPB) machines, while the Slurry Shield (SLS) technology is adapted in medium-grained to coarse grained non-cohesive soils even under high groundwater pressure. For both machine techniques, the support medium (the excavated and conditioned soil (EPB) or the bentonite suspension (SLS)) needs to be adapted for the specific application. Within this chapter, the theoretical, experimental and numerical developments and results are presented concerning the fundamentals of face support in EPB and SLS tunnelling including the rheology of the support medium, the material transport and mixing process of the excavated soil and the added conditioning agent in the excavation chamber of an EPB shield machine as well as the constitutive models for investigations of the near field interactions between surrounding soil and advancing shield machine.

S. Freimann · M. Galli
Vössing Ingenieurgesellschaft mbH, Düsseldorf, Germany
e-mail: sascha.freimann@voessing.de

M. Galli
e-mail: mario.galli@voessing.de

P. Saberi · A. Vogel
High Performance Computing, Ruhr-Universität Bochum, Bochum, Germany
e-mail: seyed.saberi@rub.de

A. Vogel
e-mail: a.vogel@rub.de

C. Zhao
School of Civil Engineering, Sun Yat-sen University, Guangzhou, China
e-mail: zhaochy28@mail.sysu.edu.cn

Z. Zizka
METROPROJEKT PRAHA, Prague, Czech Republic
e-mail: zdenek.zizka@metroprojekt.cz

4.1   Fundamentals of Face Support in Mechanized Tunneling Adapting Conditioned Soil and Bentonite Suspensions as Support Media

Two important variants of pressurized face tunnel boring machines include TBMs with Slurry Shields SLS and Earth Pressure Balance (EPB) machines. In the following sections, background information will be given to show how the experimental investigations and models of soil structure can be used to analyze and improve the excavation process.

4.1.1   Face Support in EPB Tunneling

In mechanized tunneling with Earth Pressure Balance Shields (EPB Shields), the machine uses the excavated soil to stabilize the tunnel face against earth and possibly existing water pressures and thus to generate a static equilibrium. For this purpose, the excavated soil is compressed in the excavation chamber until a state of stress is reached that corresponds to the required support pressure. Fluctuations and a constantly required adjustment of the support pressure during excavation significantly show the influence of the changing material properties of the mostly heterogeneous construction ground on the tunnel face support. For controlled support pressure transfer and safe advance, the support medium, i.e. the excavated soil, must have various material properties. The required properties include sufficient workability and flow behavior of the supporting medium. If the excavated ground does not provide the required muck behavior in its natural state, it is necessary to award it such properties. These properties of the soil can be changed and positively influenced for tunneling with earth pressure shields by soil conditioning.

Shield excavation can be divided into two discontinuous phases: excavation and the assembly of segment lining. Figure 4.1 schematically shows the structure of an EPB shield. By rotating the cutting wheel (2) and simultaneously extending the hydraulic jacking presses (10), the machine penetrates the ground. For this purpose, the jacking presses use the last segment ring built as a thrust bearing and press the cutting wheel against the working face (1) via the pressure bulkhead (4). If the excavation chamber (3) is completely filled, a supporting pressure can be built up via the extension speed of the jacking presses (10) as well as the speed of the screw conveyor (6) or transferred via the thrust plate (4) to the soil mixture located in the excavation chamber (3).

The workability and the flow behavior of the soil mixture in the excavation chamber (3) is essential for reliable support pressure transmission. For this purpose, stators or rotors (5) are arranged on the thrust plate (4) as well as on the cutting wheel back (1) to mix the excavated soil. In the protection of the shield (12), the segments of the tunnel lining (11) are assembled to a circular profile. For this, a vacuum is created between the segment stone and the vacuum plate of the erector. Meanwhile, the segments are held in their position and orientation by the extension and pressing of the hydraulic jacks (10). The

Fig. 4.1 Schematic illustration of an EPB shield [94]

cavity created thus receives its final securing immediately after driving and is therefore capable of absorbing the forces and resulting stresses that occur during ring closure. The excavated material transported by the auger conveyor (6) is transported out of the tunnel using conveyor belts (8) or wagons (not shown here). In case of need, e.g. an increased groundwater infiltration, the screw conveyor (6) can be retracted and the opening closed with a sliding gate (7).

Support pressure transfer The steering and control of the support pressure in EPB tunneling depends primarily on the soil and, if applicable, on its degree of conditioning. Furthermore, machine-related factors such as the direction of rotation, the rotational speed of the cutting wheel and the position of the screw conveyor influence the support pressure control. [11, 16, 62]

The density of the supporting medium is changed by the addition of conditioning agents, in particular by the addition of foam, water or polymers. The conditioning agent is injected into the soil during tunneling through injection nozzles in the cutting wheel and the excavation chamber. As the added amount of foam increases, the density of the supporting medium decreases. Due to the inherent weight of the supporting medium, the density of the material is of great importance for the build-up of a supporting pressure and its control. The support pressure is measured by pressure sensors which are installed over the entire surface of the pressure wall. Due to the relatively inert behavior of the support medium, support pressure fluctuations between +/- 0.3 bar must be considered during tunneling [11, 16–18].

Figure 4.2 shows a simplified schematic of the interaction between the support pressure and the earth and water pressure.

Fig. 4.2 Pressure interaction between the EPB-TBM and the tunnel face

Application range for EPB machines and experimental investigations According to Maidl (1995) [62], the supporting medium should have plastic properties, viscoplastic deformation behavior and sufficient flow behavior. These properties can be summarised in the term workability. The ideal consistency of the supporting medium is often described as pasty. In cohesive soils with sufficient plasticity, a very soft to soft consistency should be aimed for [16, 62]. Using the term workability, for cohesive soils, both possible clogging risks must be excluded, and a homogeneous support pressure transfer must be ensured. Since a cohesionless, in-situ soil often does not have the necessary properties for sufficient workability, this is realised by adding conditioning agents, including foam, water or bentonite suspension. Figure 4.3 shows the extended application range for the use of earth pressure shields according to Maidl (1995) [62].

To investigate and measure workability and rheology of soil, various experimental procedures were analysed and further developed within the Collaborative Research Center 837. These experiments are described in the sections below, and their essential evaluation methodology is outlined.
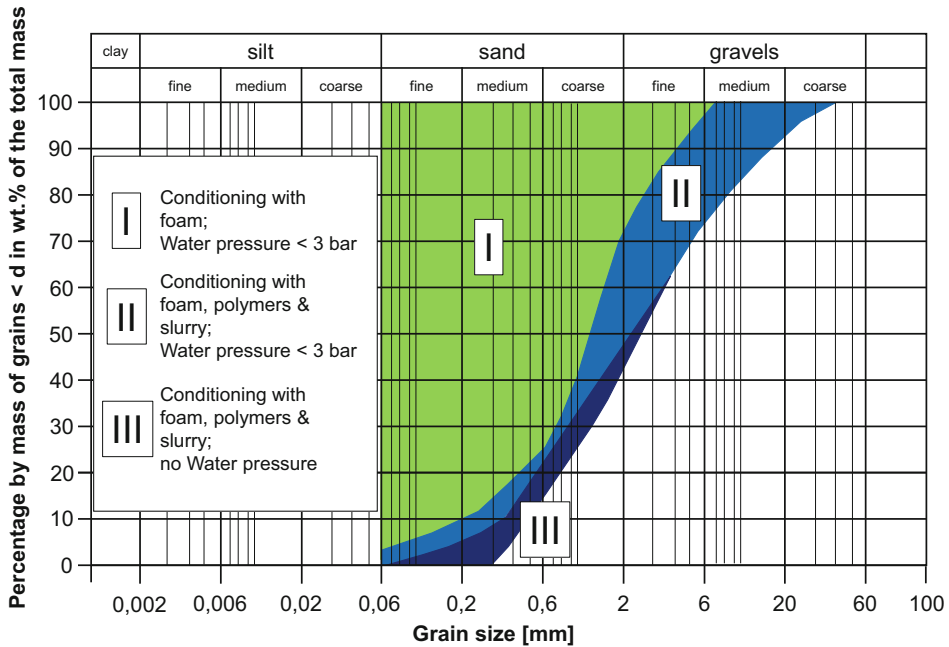
Fig. 4.3 Extended application range for the use of EPB shields after [16]

4.1.2   Face Support in Slurry Shield Tunneling

In tunnel boring machines (TBM) with fluid support (Slurry Shield machine, SLS), active support of the working face is provided by a pressurized fluid, usually a bentonite suspension. The required pressure is applied via an air cushion in the working chamber, which is separated from the excavation chamber by a submerged wall (Fig. 4.4). In addition to the advantage of active face support and thus protection against soil and water inflow, fluid support is particularly suitable for the support of challenging ground conditions with sensitive control of the support pressure [28].

Support pressure transfer   The supporting effect in slurry-shield tunneling is achieved by the bentonite suspension creating an excess pressure compared to the surrounding earth and water pressures and penetrating into the pores of the existing soil [39, 53, 78]. The origin of this principle as well as prevailing theories lie in diaphragm wall technology and are transferred to tunnel construction [61]. The penetration behavior is significantly influenced by the yield point of the suspension and the ratio of bentonite particle size and pore space. A distinction is made between three penetration processes of the bentonite suspension into the soil [78]:
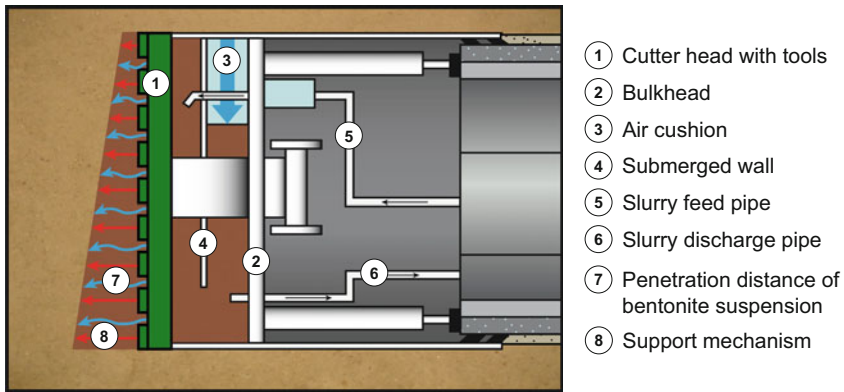
Fig. 4.4 System Layout SLS after [28]

- formation of an outer filter cake (Fig. 4.5a),
- pure penetration of the bentonite suspension into the soil (Fig. 4.5b),
- formation of an inner filter cake (Fig. 4.5c).

The formation of an external filter cake (see Fig. 4.5a) occurs when the pore size of the soil is smaller than the dispersed particles in the bentonite suspension. In this case, the suspension does not penetrate into the soil but a filtering of bentonite particles takes place at the surface of the supported soil. The bentonite particles lying flat on top of each other and act as a sealing membrane [39]. Among other things, this is important in tunneling when the excavation is stopped in order to prevent the tunnel face from collapsing [39]. The ability of the filter cake formation as well as its thickness and the filtrate water release can be determined by the filter press test according to API RP 13B-2 [3].

If the bentonite particles within the suspension are smaller than the smallest pore diameters in the soil, the suspension including the bentonite particles can penetrate far into the soil (see Fig. 4.5b). The suspension causes a supporting flow force, which is transferred into the soil via the grain structure and prevents grains from falling out and thus the soil to be supported from collapsing [39, 53]. During penetration, shear stresses occur on the grain surfaces due to the yield point of the suspension, which lead to stagnation of the suspension after a defined depth. This seals the pores and prevents further flow of the suspension [52].

If the particle size of the bentonite dispersed in the suspension lies between the minimum and maximum pore diameter, the suspension with contained bentonite particles can penetrate into the soil, but at pore constrictions the solid particles are filtered from the suspension, as they are too large to pass through the pore channels. Due to the successively increasing deposition of bentonite particles in front of the pores, the pores become clogged over time. An internal filter cake is formed (see Fig. 4.5c) [78].
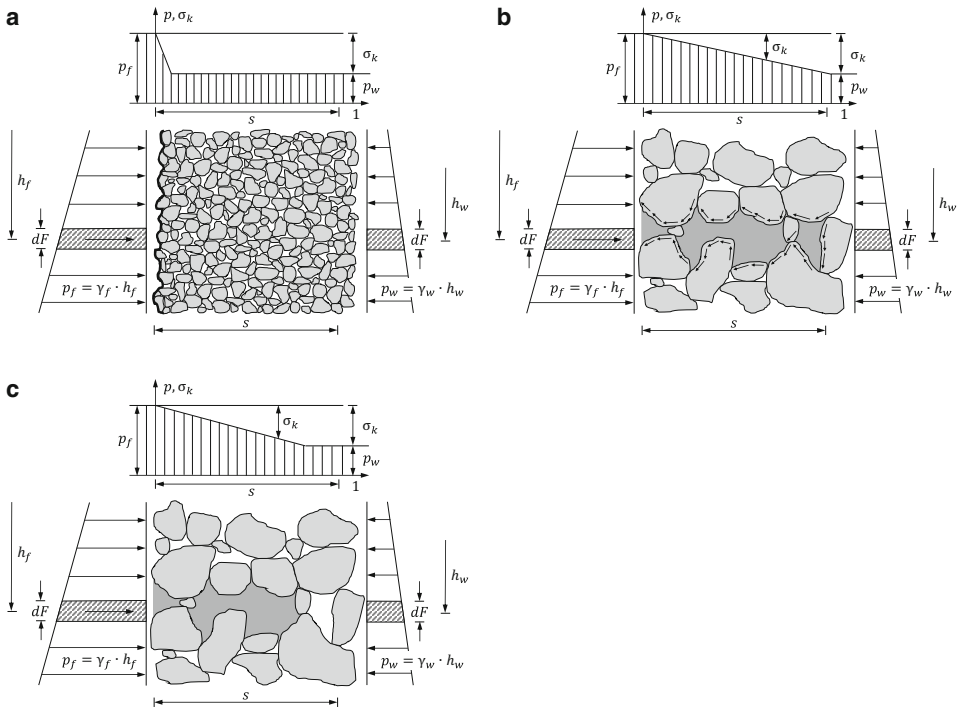
Fig. 4.5 Mechanisms of support pressure transfer. **a** filter cake formation, **b** penetration, **c** internal filter cake after [28]

4.2 Experimental Investigations of the Workability of Cohesive and Non-Cohesive Soils

Experiments to investigate the workability of both cohesive and non-cohesive soils include the slump test, the ball measuring system, the COSMA large-scale testing device and a displacement-controlled penetration testing device, among others. A novel new device to detect the penetration depth of bentonite suspension in non-cohesive soils will also be introduced.

4.2.1 Slump Test

To investigate the flow behavior of cohesionless soils, the slump test has become widely accepted both in laboratories and in tunneling practice. This test method, initially used for concrete technology and anchored in DIN EN 12350-2:2019 [30], provides index values for the workability of conditioned soils or excavated material. This means that the flow behavior of conditioned soils cannot be measured directly but can be determined indirectly
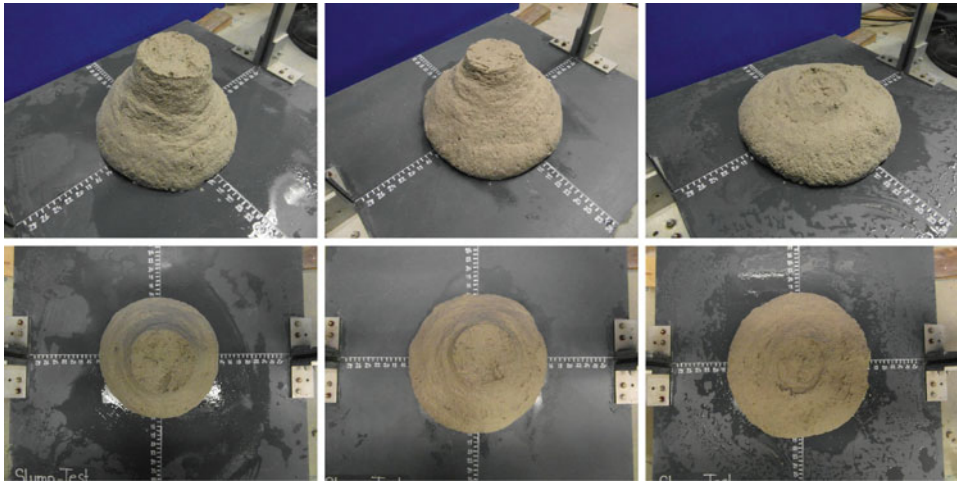
Fig. 4.6 Photo study on the influence of the FIR on the slump and slump yield determined in the slump test. Successive increase of FIR in 5 vol.% steps from left to the right [94]

via the slump and slump flow. An increasing Foam Injection Ratio (FIR) increases the slump and slump flow rate. Figure 4.6 shows an example of the influence of FIR on slump and slump flow based on slump tests carried out on sandy soil. While coarser soils react much more sensitively to a change in the FIR in the slump test, an increase of between 5 vol.% and 10 vol.% is necessary for fine sands in order to determine clear differences regarding the slump. In this research, the range of workability of cohesionless unconsolidated soils–determined in the slump test–is defined according to [16] for a slump between 10 cm and 20 cm.

There is no standardised test procedure among the various authors, which shows a severe weakness concerning the comparison and reproducibility of test results. In addition, this test method fails with fine-grained cohesive soils. Which reveals a further disadvantage with regard to the field of application of the slump test. Furthermore, the determination of rheological parameters such as viscosity or yield point with the slump test is only possible indirectly. For this reason, existing test methods were further developed into a new test method within the context of the Collaborative Research Centre 837, with which a wide range of soils can be investigated with regard to workability.

4.2.2   Ball Measuring System And cosma

To determine rheological parameters of foam conditioned fine sand Galli (2016) [40] and Freimann (2021) [36] used the Rheolab QC rheometer and the associated ball measuring systems from Anton Paar (see Fig. 4.7).
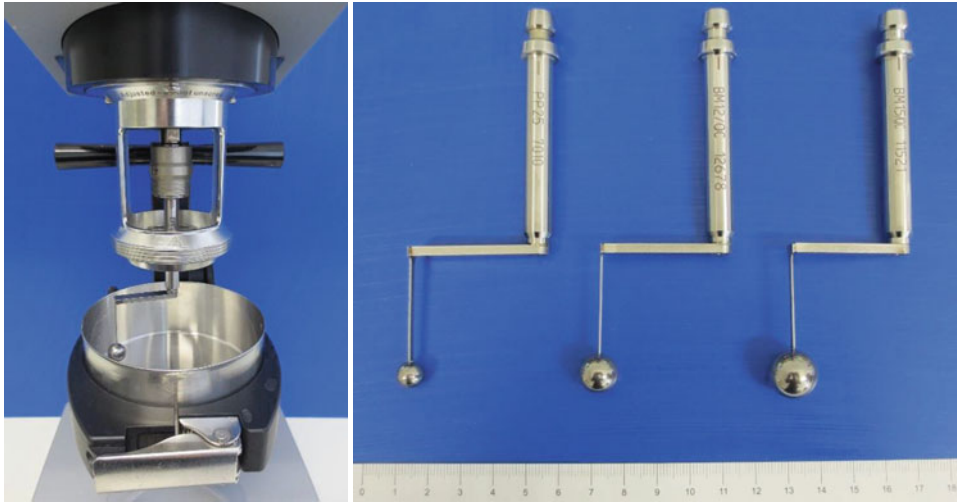
Fig. 4.7 Rheolab QC rheometer from Anton Paar (left) and different ball bearing attachments (right) [40]
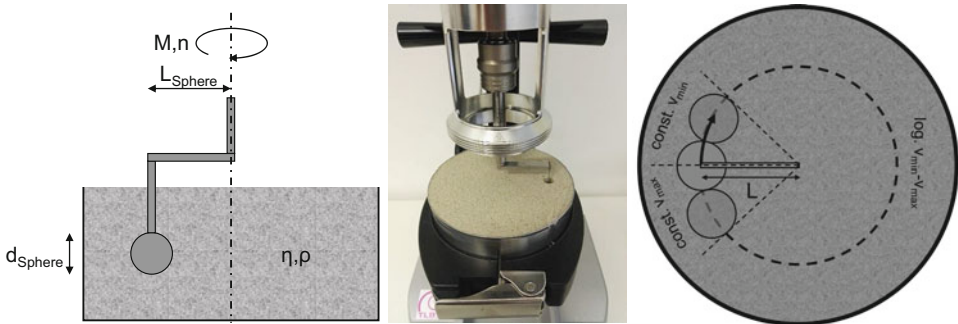
Fig. 4.8 Experiment with soil-foam mixture in the ball rheometer (middle); schematic sketch (left & right)

During the rheometric investigation, the sphere moves rotationally around the measuring system axis with radius L through the sample at a predefined speed n, thereby generating a displacement flow. The vertical mounting strut of the sphere has a very small thickness in the direction of movement in order to reduce the disturbing influences. The experimental setup is shown in Fig. 4.8.

The recorded torque M can be formulated as a function of the rotational speed n. The choice of the measurement profile for generating rheological material quantities is of decisive importance, as it defines the rotational speed of the ball as a function of time. The measurement profile Galli (2016) [40]) developed, contains a total of six revolutions of the sphere. A complete revolution includes 360°, avoiding measurements in the zone

close to the point of immersion of the ball in the sample to avoid possible interferences in the measurement. This zone is defined as one ball diameter before and after the point of immersion. During the measurement, the speed increases logarithmically and the torque is recorded using 31 measuring points (see Fig. 4.8, right). To determine the rheological material quantities from the known geometric and physical data, the conversion factors C_{SS} (Conversion Shear Strength) for calculating the shear stress and C_{SR} (Conversion Shear Rate) for calculating the shear rate according to Galli (2016) [40] are used in the Rheoplus software. These conversion factors were determined based on calibration tests with different fluids for the measurement system used in this research so that the shear stress τ and the shear rate γ can be calculated as

$$\tau = C_{SS} \times M,\tag{4.1}$$

and

$$\gamma = C_{SR} \times \eta,\tag{4.2}$$

with shear stress conversion factor C_{SS}, torque M, shear rate conversion factor C_{SR} and speed η.

4.2.3   COSMA – Conditioning of Soil in Mechanized Tunneling Using Additives

The COSMA large-scale testing device, as shown in Fig. 4.9, was designed to test conditioned sands under pressure conditions, such as those encountered with EPB shield machines during tunneling. The test device consists of a cylindrical container ($h = 0.7$ m; $D_i = 1$ m; $v = 550\,\ell$) with an agitator installed in the centre and is mounted so that it can be tilted by approx. 100°. Within the Collaborative Research Centre 837, the first investigations under atmospheric pressure conditions were carried out and analysed in the large-scale test device with the ball rheometer in order to be able to evaluate the use of a ball rheometer in the excavation chamber.

To determine the rheological properties of the conditioned loose rock in the large-scale test rig, a spherical rheometer was installed at the bottom of the sample container. The ball rheometer consists of a ball with a diameter of 80 mm, which is connected to the drive shaft via a rod ($d = 40$ mm, $h = 95$ mm) that is eccentrically arranged by 55 mm. Thus, it is possible to examine samples with a maximum grain size of 16 mm, taking into account. The drive shaft is driven by a hydraulic swivel motor. Thus, the ball is moved by a differential pressure in the hydraulic hoses of the drive between the end bearings on a circular path with an angle of 338° at a constant speed. Due to the installed components, in contrast to the small-scale rheometer tests, it is not possible to vary the rotational speed of the ball rheometer during a test. The oil pressure of the hydraulic unit can be measured, recorded and evaluated with two pressure sensors from HBM. The speed of the ball

Fig. 4.9 COSMA large-scale test stand and installation position of the ball rheometer [36]

rheometer can be adjusted depending on the speed of the hydraulic unit of the drive shaft. The differential pressure, which is set according to the set speed, is software recorded at a frequency of 1 Hz for the entire duration of the test.

4.2.4 Load-Controlled Penetration Test Device

Freimann (2021) [36] adapted the test principle from the falling cone test [31], which originates from geotechnics, and the Kelly ball test [4], which are used to test the fresh concrete. Furthermore, Hansbo (1957) [46] and Merrit (2004) [65] provided important insights into the design of the test rig as well as the evaluation of the data. To investigate the workability of conditioned cohesionless soil, [36] conducted a parameter study with different penetration body geometries as well as different ballasting. The measured values were correlated with slump test results from the same soil-foam mixture. The force-controlled test consists of a sample cylinder, into which the medium to be tested is filled, and a steel frame construction, which guides the penetration body or shaft via a sliding bearing, (Fig. 4.10).

The cones used have a width of 15 or 21 cm and a height of 13 or 18.5 cm. They weigh 800 g (small cone) and 890 g (large cone). The bullet mould used in the preliminary investigations is 18.5 cm high, 15 cm wide and weighs 4500 g. The steel shaft, to which a thread attaches the penetration bodies, has a diameter of 1.5 cm and a length of 100 cm (weight 1160.5 g). Freimann (2021) [36] selected the large cone shape and a penetration weight of 2050 g by evaluating penetration tests as well as slump tests and shear strength tests carried out in parallel. This test setup made it possible to map the most extensive
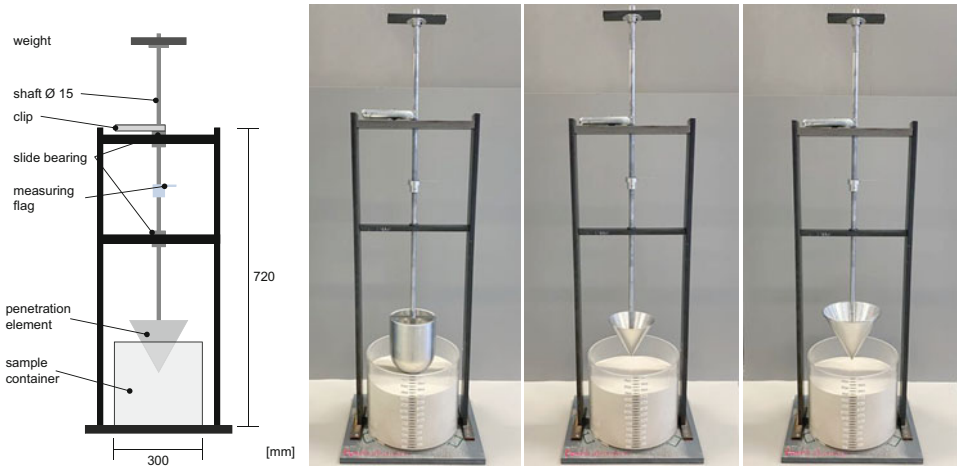
Fig. 4.10 Construction of the load-controlled penetration test device [36, 94]

realizable penetration range between the slump limits of 10 cm and 20 cm (acc. to Budach (2012) [16]) in the penetration test. The resolution of the force-controlled penetration test was greatest with these design parameters for foam-conditioned loose rock. To carry out the experiment, the penetration element is positioned directly above the soil sample and the clamp on the upper part of the shaft is loosened. Then the penetration depth is read off via a scale and the measuring flag.

Calculation of the shear strength using the load-controlled penetration test device
To determine the undrained cone shear strength C_{urfc}, an equation established by Freimann (2021) based on DIN EN ISO 17892-6, 2017-07 is

$$C_{\mathrm{urfc}} = 0.27 \times g \times \frac{m}{i^2}, \tag{4.3}$$

with gravitational acceleration g, penetration mass m and penetration depth i.

In addition, the shear stress acting on the surface of the cone results from the input parameters fall weight W, penetration depth i and the opening angle of the penetration cone. Figure 4.11 shows the forces and stresses acting during the test. The evaluation of the shear stresses acting on the cone has already been studied in the experiments by Abd Elaty et al. (2016) [1] and Perrot et al. (2018) [77] for fresh concrete and grout. After completion of the penetration process, a state of equilibrium is established between the penetration force W of the falling cone and the opposing force resulting from the shear force F_{sh} and the normal force F_n acting perpendicular to the cone surface. The shear stress τ acting on the wetted cone surface can be calculated with the help of the penetration
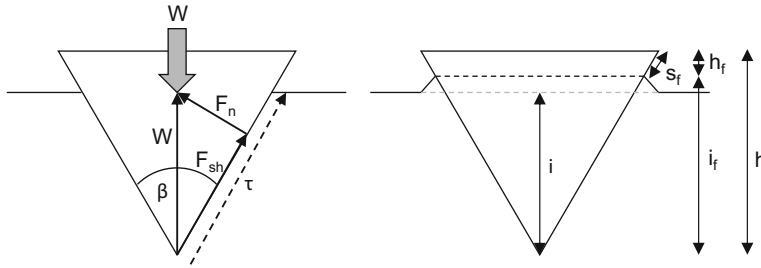
Fig. 4.11 Force interaction at the penetration cone during the penetration test with W (penetration force), F_{sh} (shear force resulting of W), F_n (normal force resulting of W) and τ (shear force at cone surface) (left). Dimensions at the penetration cone to determine the fictive penetration depth i_f, with h_f (free height of the cone) s_f (free length of the cone) and h (total height of the cone) (right) [36]

force W, the opening angle of the drop cone β and the wetted cone surface A,

$$\tau = \frac{w \times \cos \frac{\beta}{2}}{A}.$$ (4.4)

The wetted cone surface A results from the measured penetration depth.

4.2.5 Displacement-Controlled Penetration Test Device

An important material parameter when driving with earth pressure shields (EPB shields) in cohesive unconsolidated rock is the consistency of the soil. It determines the flow behavior of the excavated material or the support medium in the excavation chamber and the auger. Furthermore, depending on the consistency and other material parameters, e.g. the plasticity index, sticking phenomena can occur on the cutting wheel during tunneling, which can cause high costs due to power losses, cleaning measures and possibly also increased wear. The experimental identification of a critical consistency of the excavated material during the excavation process and an appropriately adjusted conditioning of the soil can help to make EPB excavations safer, more cost-efficient and easier to plan in the future. Based on the findings from Freimann (2019) [38] and Freimann (2021) [36], the load-controlled penetration test was further developed into a displacement-controlled version. The displacement-controlled version takes up the principle of penetration into flowable and displaceable media, while differs from the force-controlled version from Freimann (2021) [36] with regard to the control and the induced impulse. The test results, i.e. penetration depth and penetration resistance, are digitally measured and logged. The new test device (Fig. 4.12) can measure flow behavior for both cohesionless and cohesive soils using different correlations. In particular, cohesive soils cannot be investigated with the previously presented slump test. This limitation in the field of application is entirely eliminated by the displacement-controlled penetration test due to the new test procedure.
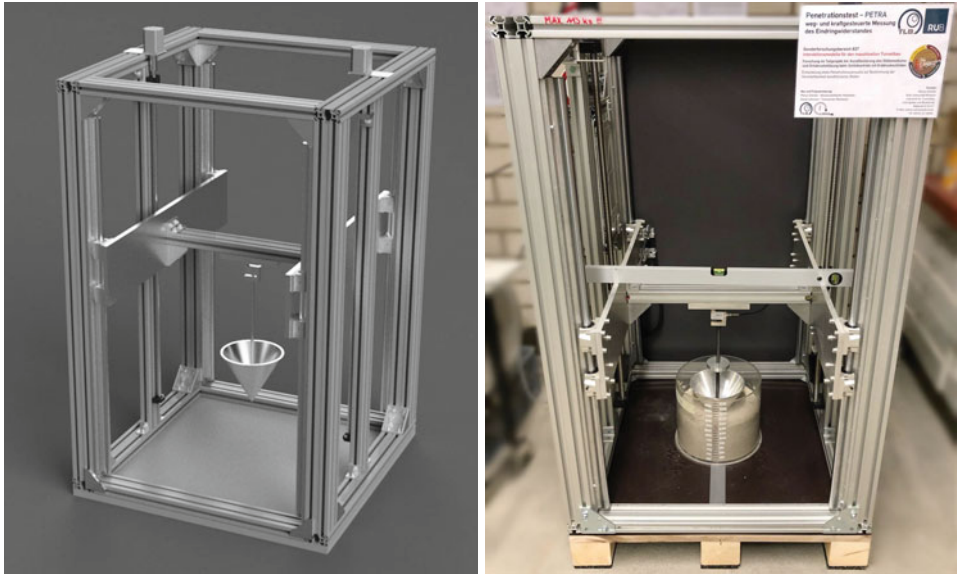
Fig. 4.12 Construction of the displacement-controlled penetration test device [94]

4.3   Experimental and Numerical Investigations on the Support Pressure Transfer of Slurry Shields SLS in Non-Cohesive Soil

Detailed investigations on the stability of the tunnel face have been carried out using raw data gained from on-site measurements. Based on the insight gain during these analyses, a new device was developed based on the electric resistance measured in real time.

4.3.1   Investigations on the Tunnel Face Stability in Mechanized Tunneling with Fluid Support

The interactions between excavation tools and ground are particularly relevant for the consideration of face stability in mechanized tunneling with fluid support. For a better understanding of the interactions between machine and ground, also with regard to the tunnel face support, construction process data from tunneling projects were analysed. For this purpose, tunneling data from three reference projects with comparable machine diameters were used. For tunneling in soil, scrapers and reamers were identified as relevant tunneling tools. For each cutting wheel, homogeneous cutting zones were defined, each with a constant number of excavation tools within a cutting track. Figure 4.13 shows the subdivision of the three cutting wheels into three, four and five cutting zones. The aim was
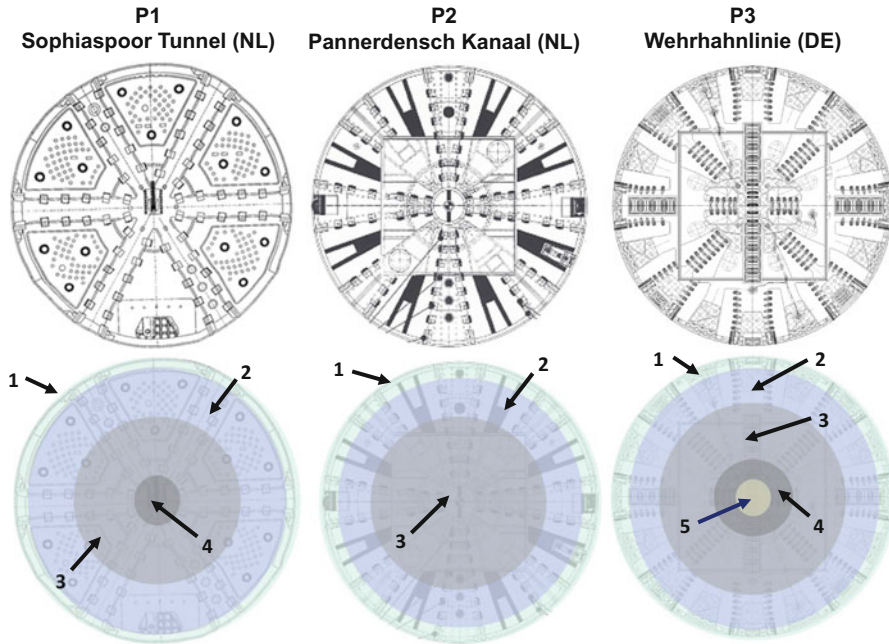
Fig. 4.13 Cutting wheels of projects P1, P2 and P3 (top row) and the division into cutting zones (bottom row) after [104]

to determine characteristic mean values for the sequential passage of the mining tools at a local point of the working face [104].

To observe the transient processes during tunneling, excavation data are necessary. Raw data such as revolutions of the cutting wheel per minute (RPM) and advance rate (AR) are recorded directly and the penetration depth of the cutting wheel per revolution is calculated from this. The recording is done as actual or average values per ring. To take a closer look at the interaction between cutting tool and ground it is necessary to adapt the data to a single cutting tool. A cutting tool moves forward and in a rotational motion at the same time, it follows a spatial spiral. Each tool of a cutting track excavates only a part of the soil at the tunnel face of a complete wheel rotation. The penetration depth of a tool therefore depends on the number of tools on a cutting track (n), this results in an average penetration depth per tool. The time spans (t_{tool}) between two successive tools can be determined from the cutting wheel revolutions per minute (RPM) as

$$t_{tool} = \frac{1}{n \times RPM} \tag{4.5}$$

according to the same principle. In this time span, the pressure transfer mechanism can form without being disturbed [104].
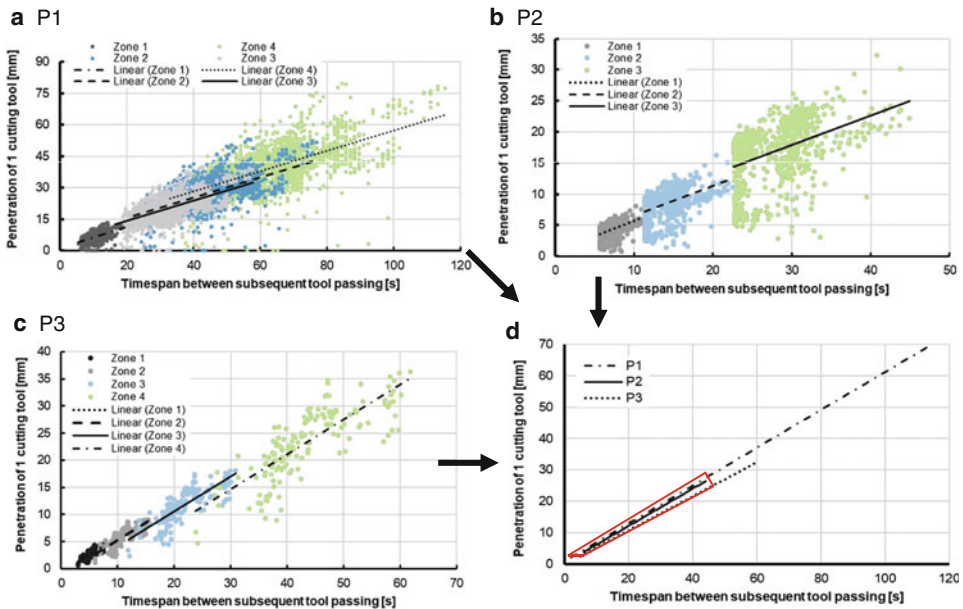
Fig. 4.14 Correlation of penetration of one cutting tool with timespan between subsequent tools after [104]

The evaluation of the penetration depth of a cutting tool during one pass with the time span between the pass of subsequent tools is shown in Fig 4.14a–c. Homogeneous cutting zones are considered separately and are color coded. Furthermore, linear trend lines are shown in each diagram, which have the same slope with a slight offset within a project. The same trend was observed in all three projects with regard to the excavation sequence. The penetration depth of a cutting tool increases with increasing time between two tools. The reason for this phenomenon lies in the distance between the tools and the centre of the cutting wheel. The greater the distance, the more tools are in a cutting track and the lower the penetration depth of each cutting tool. The trend lines shown in Fig. 4.14d characterise all homogeneous cutting zones of the three projects. Marked in red is the typical cyclic time interval and the typical penetration depth d of the tools in a fluid-assisted advance [104].

The interaction between the pressure transfer mechanism and the cutting tools can be described at the local level with two general situations. The first case (Case A) occurs when a passing tool at a local tunnel face location removes the entire infiltrated zone with bentonite suspension. Due to the abrupt removal, it may result in increased pore water pressures in front of the tunnel face caused by the flow of slurry. This is in contrast to case B, where only a part of the infiltrated zone is removed over which the pressure transfer takes place. Both cases are compared in Fig. 4.15 [121].
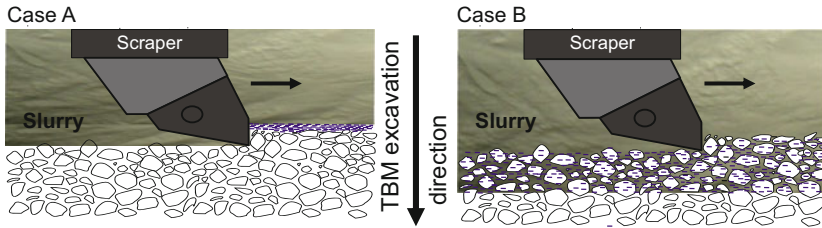
Fig. 4.15 Definition of case A and B of the interaction at the tunnel face during excavation after [122]

Since in Case B only a part of the pressure transfer mechanism is removed, it is necessary to describe it in more detail. After partial removal, immediate "re-penetration" of bentonite suspension takes place each time a cutting tool passes through. That means, bentonite suspension penetrates in an area of the soil skeleton where there are already deposited bentonite particles from the previous suspension pass. Due to only partial removal of the pressure transfer mechanism, occurring changes in pore water pressure and effective stresses are less abrupt compared to Case A [120].

The stagnation gradient f_{s0} is

$$f_{s0} = \frac{a\,\tau_f}{d_{10}}, \tag{4.6}$$

with a as an empirical factor from the experiments, $a = 2$ or 3.5; τ_f the yield point of the supporting fluid (ball harp or pendulum device) and d_{10} as the characteristic grain size of soil (10% passage in sieve analysis).

In numerical simulations, Zizka [119] shows for Case A that the existing pressure gradient during excavation is much lower than the stagnation gradient of the slurry during primary penetration in steady state (ring building phase). The stagnation gradient describes the pressure drop across the penetration depth of the slurry and is an important parameter in DIN 4126 [29] for the support pressure transfer mechanism. The stagnation gradient f_{so} is calculated according to Eq. (4.6). In Case A, as a result of the local damage of the supporting pressure transfer mechanism, the pore water pressure increases globally outside the penetrated zone (see Fig. 4.16a) [123]. The build up of the pressure transfer mechanism is heterogeneous during excavation and can be transferred according to one of the following modes (compare mechanisms described in Talmon et al. [100]):

- Flow pressure–in areas where the soil including pressure transfer mechanism is freshly cut, comparable to pressure transfer suggested by [9];
- pressure drop over the partially formed pressure transfer mechanism and flow pressure– in areas where the pressure transfer mechanism is still forming and has not yet been completely formed, comparable to pressure transfer suggested by [14];
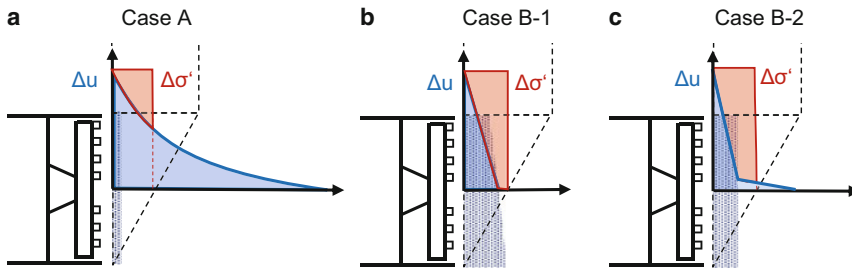
Fig. 4.16 Efficiency of the pressure transfer mechanism for different interaction t the tunnel face during excavation stage, illustrated for the elevation at the tunnel axis after [124]

- pressure drop over the fully formed pressure transfer mechanism–in areas where the mechanism is almost completely developed, corresponds to the transfer suggested by Kilchert and Karstedt [52].

Case B implies that after the partial excavation of the pressure transfer mechanism, only this part needs to be rebuilt during re-penetration. For a more detailed consideration of case B, it is necessary to distinguish between Case B-1 and Case B-2. Figs. 4.16a and b the differences on the basis of existing stresses and their distribution are shown [123].

Case B-1 is characterised by no increasing pore water pressure outside the penetrated zone (Fig. 4.16b). Experiments have shown that the pore pressure distribution is linear and decreases to zero within the penetrated zone [119]. This case is characterised by a higher pressure gradient during excavation relative to the stagnation gradient at steady state. Anagnostou and Kovari [2] already proposed this hypothesis, which was proven in the experiments. The fraction of the suspension overpressure that is converted into effective stresses in the soil skeleton depends only on the penetration depth of the bentonite suspension. This implies that the ratio of the transferred pressure to the applied pressure is well predictable. The application of the approaches described in DIN 4126 [29] for the calculation and consideration of the stagnation gradient can be safely applied for Case B-1 [123].

Compared to Case B-1, Case B-2 is characterised by a non-linear pore pressure distribution during primary slurry penetration (Fig. 4.16c). The existing pressure gradient during excavation is lower than the stagnation gradient f_{s0} according to DIN 4126 [29] in the steady state. Since increased pore water pressures also occur outside the sliding wedge to be supported, the efficiency of the support is lower than in Case B-1 and it is more difficult to be predicted. The application of the approaches from DIN 4126 [29] can therefore lead to uncertain results [123].

For the required Case B-1, Fig. 4.17 was developed to substantiate the recommendation for a minimum stagnation gradient according to DIN 4126 for Slurry Shields [29]. With Fig. 4.17 it is possible to receive the minimum stagnation gradient, which implies an efficient support of the tunnel face and avoids pressure losses due to escalating penetration.
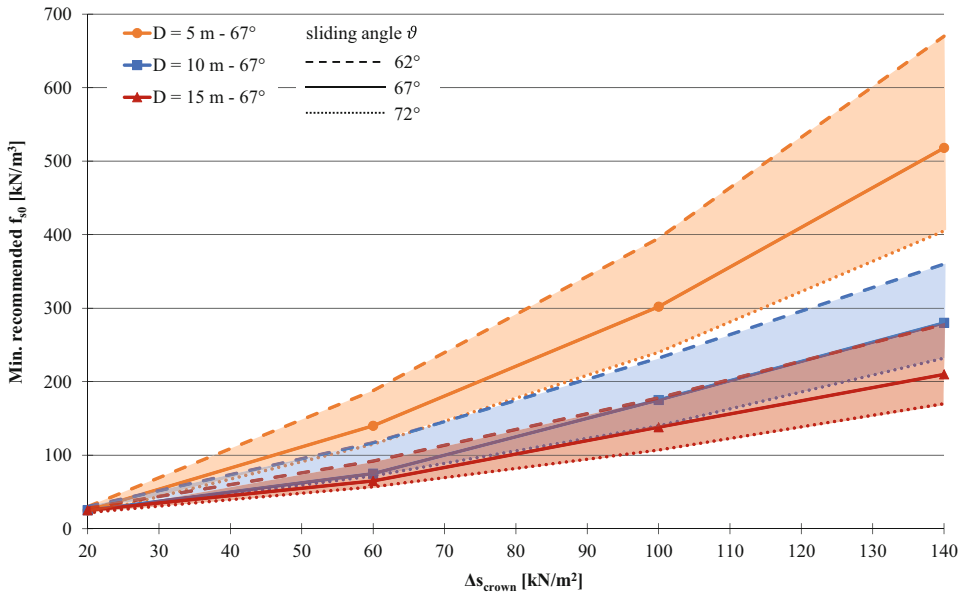
Fig. 4.17 Minimum recommended stagnation gradient of slurry $f_{s0,min}$ to avoid a loss of efficient face support due to deep slurry penetration after [119]

The diagram does not take into account the additional increase of the existing pressure gradient during excavation for case B-1.

Figure 4.17 is based on four fixed values for the slurry overpressure Δs_{crown} (20, 60, 100 and 140 kN/m^2) under variation of the tunnel diameter D and the sliding angle of the wedge φ. The sliding angles used for the calculation are typical for cohesionless soils. The unit weight of the suspension is assumed to be 12 kN/m^3 and it is thus on the safe side, in contrast to the unit weight of fresh slurry. To calculate the minimum stagnation gradient, the areas of total penetration and penetration within the sliding wedge are overlaid (see Fig. 4.18). When the maximum decrease in efficient slurry overpressure transfer averages exactly 5 kPa over the entire tunnel face, the recommended minimum stagnation gradient is achieved [123].

For tunneling practice, it is important to aim for case B at the tunnel face without a very deep penetration of the slurry to ensure sufficient efficiency. The minimum stagnation gradient f_{s0} for this case can be determined according to Fig. 4.17. In this context, it is important to emphasise that increasing the slurry concentration does not necessarily improve the efficiency of the support, as it may lead to Case A. The results shown here apply to fresh suspension, which is why the penetration depth of the suspension is higher than that of loaded slurry [80]. The efficiency of pressure transfer in tunneling practice can be influenced in several other scenarios. Broere [14, 15] already investigated excavation through a semi-confined aquifer. This excavation situation can be characterised as
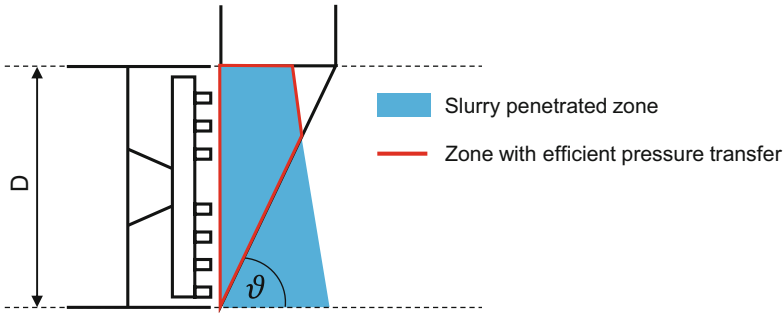
Fig. 4.18 Stagnation of supporting fluid inside the soil skeleton with $0 < f_{s0} < \infty$ after [119]

excavation through a permeable soil layer with limited dimensions in vertical direction, as the permeable soil layer is confined in two impermeable layers. The direction of flow is thus limited for the slurry and the efficiency of pressure transfer is reduced and especially true for Case A. Similar problem can occur in excavations between artificial structures, e.g. diaphragm and pile walls, where the flow field is also limited [119]. In addition to the tunnel face environment or boundaries, there may be a heterogeneous working face where, for example, Case A occurs in the lower half and Case B in the upper half. This situation is shown in Fig. 4.19a. Coarse grained soil with a higher permeability favours Case B and leads to the dissipation of the increased pressure from the finer soil. The efficiency of pressure transfer is increased with Case A compared to the entire face. Figure 4.19b shows a possible case with simultaneous presence of Cases A and B, which can be triggered by different homogeneous cutting zones at the working face. The presence of case A here can also reduce the coverage with Case B. Compared to the heterogeneous working face, the difference here lies in areas with the same permeability. Therefore, it can be assumed that the distribution of the increased pore pressure is dominated by the presence of Case A in the part of the tunnel wall [119].
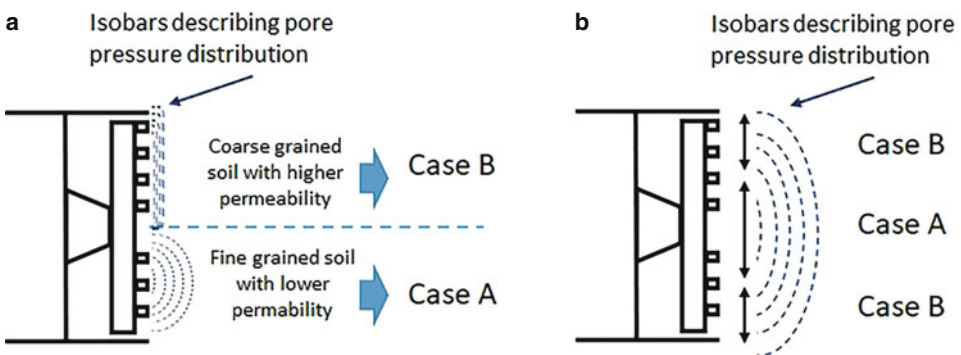
Fig. 4.19 **a** Heterogeneous tunnel face, **b** homogeneous tunnel face with simultaneous presence of Case A and B at the tunnel face within homogeneous soil conditions after [119]

With specified soil conditions and cutter wheel design, it is possible to adjust factors such as suspension concentration and excavation settings to achieve Case B across the entire tunnel face. The following measures can be taken [119]:

- Decrease the yield point of the slurry – note, that the criterion for the local stability of the tunnel face after DIN 4126 [29] still have to be fulfilled, furthermore, minimally recommended slurry stagnation gradient to avoid efficiency decrease (Fig. 4.17) is to be achieved.
- Increase slurry excess pressure to obtain deeper slurry penetration–note that this measure is efficient only in coarse soils.

As soon as Case B has been confirmed experimentally with adjusted parameters, the minimum required support pressure can be designed easily by standard approach described for instance in DAUB recommendation for face support.

4.3.2 Development of a New Device for the Detection of the Penetration Depth of Bentonite Suspension in Non-Cohesive Soil

The penetration depth of bentonite slurry into saturated soil is usually determined in column tests. Information on the penetration depth is provided either by visual inspection through the usually transparent cylinders or by the distribution of the pore water pressure within the soil sample. Up to now, however, there has been no way to measure the mechanisms by which bentonite particles are deposited in the pore structure of the soil.

A total of three measuring cylinders are developed on the basis of geoelectric resistance measurements. In the first preliminary test stage, the aim is to differentiate between various materials relevant to tunnel construction on the basis of their electrical resistance. A cylinder with eight measuring electrodes forms the basis for these investigations. A low voltage (5 volts) is introduced into a sample (water, bentonite suspension, water-saturated soil or soil-suspension mixtures) via the measuring electrodes and the resulting current intensity is measured. This results in a total of four electrical resistances, which are derived from the eight measuring electrodes and provide information about the electrical resistance at different points within the sample. Very good results are already achieved in this first step [55].

In a second series of experiments, a new measuring cylinder is designed on the basis of the previously described cylinder and the number of measuring sections was tripled. The materials of the cell, the installation methodology and the input voltage are retained. The conversion to electrical resistance is done digitally and recorded by a measurement program. Figure 4.20a shows the experimental setup, Table 4.1 the material compositions of the three selected experiments. Figure 4.20b shows an example of the evaluation of the three tests (Table 4.1) of the soil 0.5 to 1.0 mm with varying pore fluid. The aim of these tests is to find out whether the electrical resistances of different material compositions can
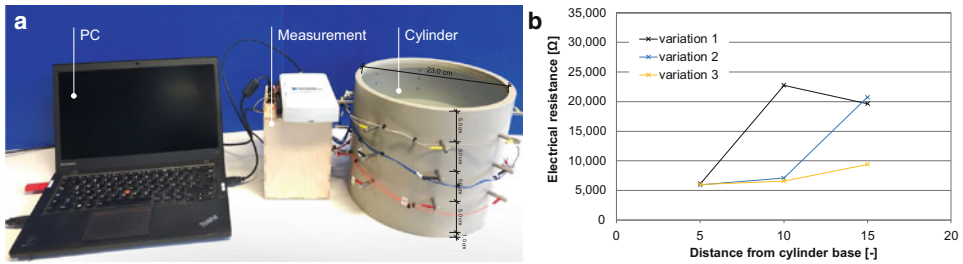
Fig. 4.20 a Experimental setup of the scaled experiments, **b** electrical resistance measurement of varying material compositions after [55]

Table 4.1 Material compositions after [55]

Variation	0.5–1.0 mm and B1 6%	0.5–1.0 mm saturated	0.5–1.0 mm and B1 3%	Pictogram
(1)	0 to 75 mm	75 mm to 200 mm	–	
(2)	0 to 125 mm	125 mm to 200 mm	–	
(3)	0 to 125 mm	–	125 mm to 200 mm	

be detected in the measuring cylinder. It is found that both the saturated soil from the soil-suspension mixture with high solids content and different soil-suspension mixtures within the measuring cylinder can be distinguished from each other on the basis of electrical resistance [55].

The finding of being able to measure different resistance zones within a soil sample forms the basis for penetration tests on a larger scale. Figure 4.21a shows a schematic diagram of the test setup, Fig. 4.21b shows the test setup in the laboratory. 24 electrodes (6 levels of 4 electrodes each) are embedded in the penetration cylinder. For the recording of the resistances to the second, a measuring program is developed, which makes it possible to set all necessary parameters (measuring time, waiting time, number of measuring cycles) and to carry out the measurement automatically as well as to display it in real time. In addition to the penetration cylinder, two other cylinders (suspension and filtrate water reservoir) are required to carry out a test [55].

A measurement cycle starts below the soil sample (−2 cm) and ends above the soil sample (53 cm). When the suspension stagnates and the resistance values stabilize, the measurement is stopped. Figure 4.22 shows an example of the results of three penetration tests (a to c). Bentonite product B1 was used fot the penetrating slurry. In the input plane
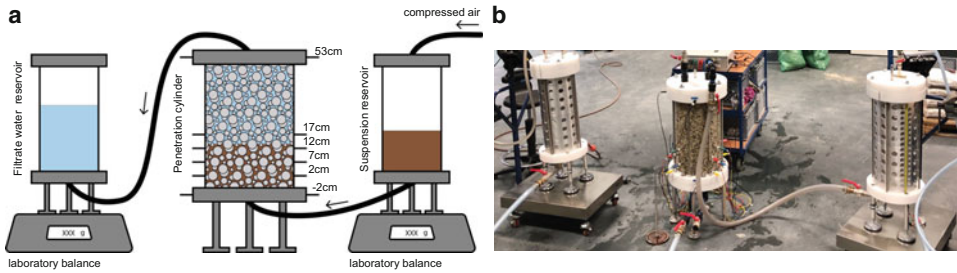
Fig. 4.21 **a** Schematic test setup, **b** test setup in the laboratory after [56]
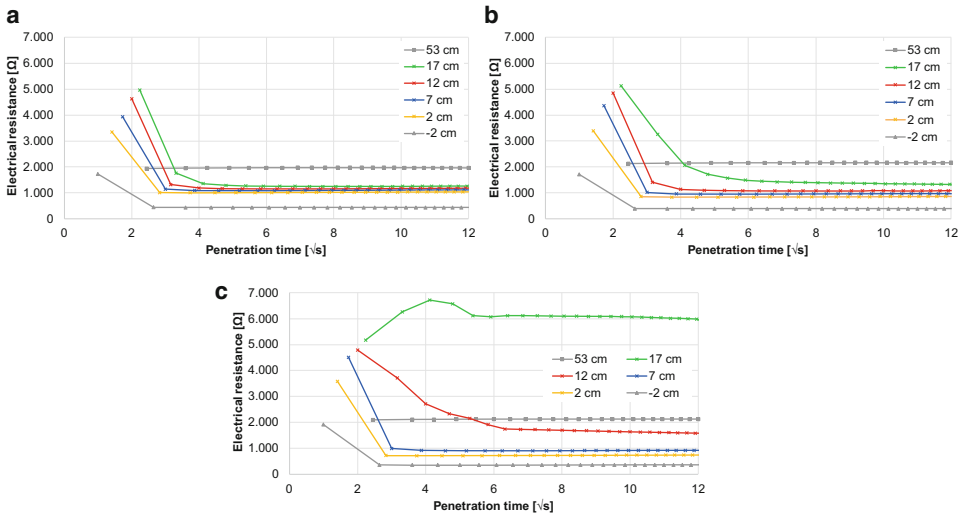
Fig. 4.22 Electrical Resistance measurements during bentonite penetration (0.5–1.0 mm, 0.30 bar).
a B1 4%, **b** B1 5%, **c** B1 6% [56]

(-2 cm), the electrical resistance decreases as the solid content of the suspension increases.
The same phenomenon can still be seen in the first measuring level in the soil body (2 cm).
The electrical resistance then increases with increasing penetration depth. Based on the
development of the electrical resistance of each individual measuring level, conclusions
can be drawn about the penetration depth of the suspension; a stagnation of the measuring
value here indicates that a measuring level has been reached. The penetration depth can
be estimated to within 5 cm due to the vertical electrode resistance. Furthermore, it can be
seen from the evaluations that the electrical resistance decreases more quickly at low solid
concentrations and reaches a stagnant measured value earlier [55].

The electrical resistance data shown in Fig. 4.22 form the basis for further evaluation
possibilities. By looking at the last measured value and the graphical evaluation via the
penetration depth (Fig. 4.23), it is possible to obtain information about the deposition of
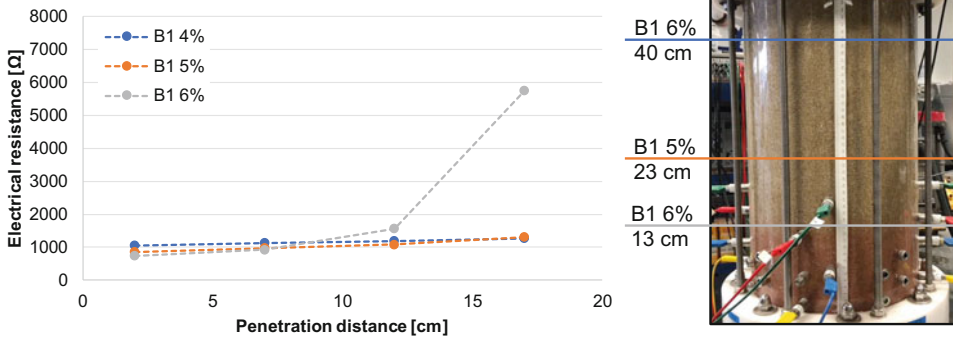
Fig. 4.23 Evaluation of the electrical resistance over penetration depth after 180 s of penetration [56]
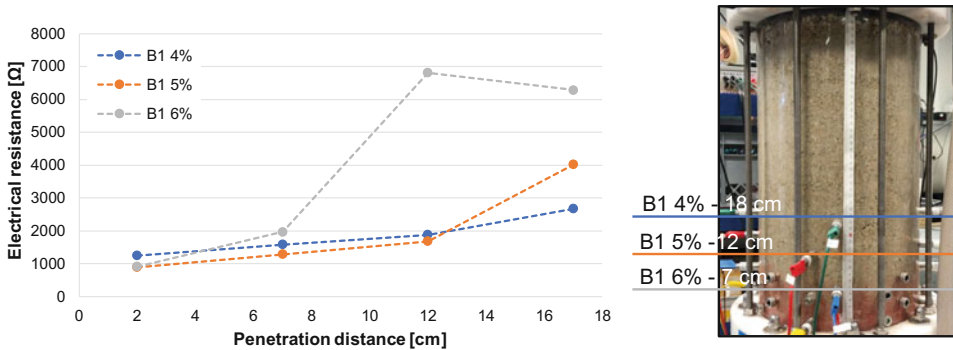
Fig. 4.24 Evaluation of the electrical resistance over penetration depth after 180 s of penetration [54]

bentonite particles. Figure 4.23 shows the evaluation of a sand with 0.5–1.0 mm grain diameter and the corresponding penetration depths of bentonite suspensions with three different solid contents (4%, 5% and 6%). Based on the electrical resistances and the optically assessed penetration depths, it can be concluded that with the 4% and 5% suspensions all measurement levels (2 cm to 17 cm) were reached. This is not the case with the 6% penetration. Based on the respective gradients between two measuring points, deposited bentonite particles in the grain structure can be visualized.

The electrical resistance of the penetrated soil is directly related to the content of bentonite particles. When the soil is changed (Fig. 4.24) to a grain size of 0.063–4.0 mm, the filtration mechanisms become even clearer. The gradients increase and the penetration depths decrease in the same course. Here, too, measurement levels that have not been
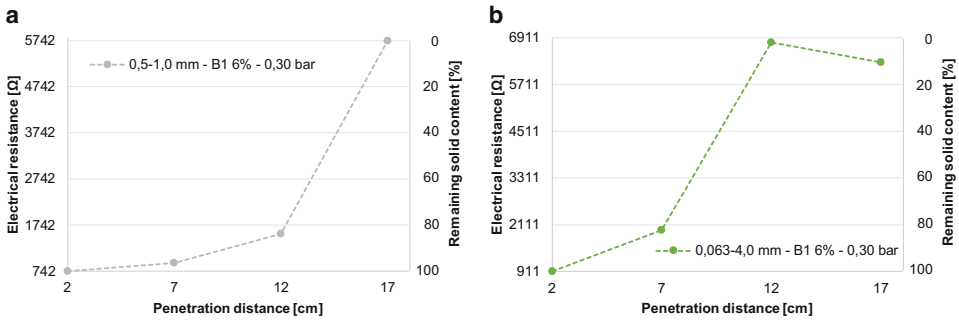
Fig. 4.25 Resulting percentage solids content of the pore fluid at different penetration depths [54]
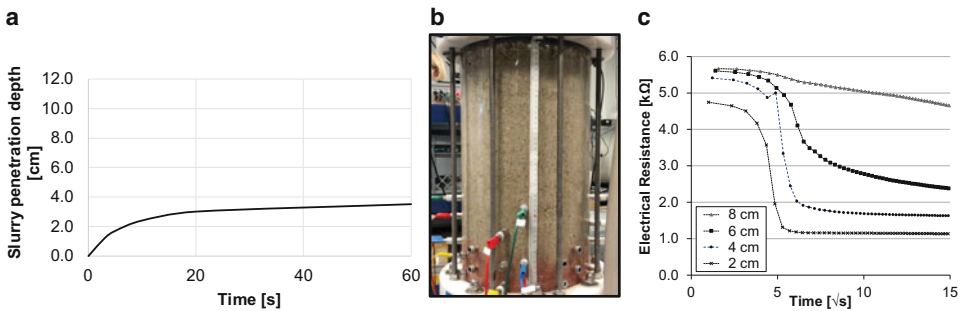
Fig. 4.26 **a** Temporal development of slurry penetration depth [119] of B1 6% into 0.063–4.0 mm, **b** soil cylinder after penetration of B1 6% into 0.063–4.0 mm, **c** temporal development of electrical resistance [54] of B1 6% into 0.063–4.0 mm

reached can be recognized by a clearly steeper gradient of the connecting lines. Furthermore, the difference in electrical resistance within a graph indicates a clear change in particle content.

Figure 4.25 provides a correlation to the remaining solid content within the pore fluid. The lowest measured resistance in the first measurement plane (2 cm) is set to 100% solids content, the highest value to 0% solids content (= pure water). In a direct comparison it becomes clear that the soil 0.063–4.0 mm filters more particles over a shorter distance under the same experimental boundary conditions and therefore leads to a faster increase of the electrical resistance. In [54], further penetration tests will be analysed and a direct reference to supporting pressure calculations will be made.

Figure 4.26a, c shows investigations on the penetration behavior of a bentonite suspension with 6% solids content into a soil with 0.063–4.0 mm. Figure 4.26a shows the results of Zizka [119] based on the evaluation of the displaced filtrate water. Figure 4.26c shows the evolution of the electrical resistances over time for the same soil-suspension combination. Based on the filtrate water analysis, a penetration depth of about 3.5 cm can be derived. Kube [54] determines that the bentonite particles penetrate more than 6 cm into

the soil, which can be seen in the development of the electrical resistance in the different measurement levels. The measuring planes 2 cm and 4 cm are reached completely, 6 cm almost completely and 8 cm reach only a few particles, which lower the electrical resistance. Penetration studies with measurement of the electrical resistance at different levels can therefore not only provide information about the pure penetration depth but also about the distribution of bentonite particles in the soil body.

4.4   Analysis of the Soil Structure and Particle Storage – Determination of the Phase Composition in Soils

In Sect. 4.1.2, the three different infiltration procedures and resulting mechanisms of support pressure transfer were introduced. In the present section, the effect of bentonite slurry infiltration on shear strength and on microstructural changes in the bentonite slurry will be discussed. In the first part of the section, the materials used and the methodological experimental approach are presented. This includes a method for the measurement of particle storage of bentonite solids, thus, bentonite concentration as function of penetration length at the end of the infiltration process.

4.4.1   Material and Methods

Three sands with different grain size distributions (0.1 to 0.5 mm, 0.5 to 1 mm, 1 to 2 mm) are used to mimic the support mechanisms in the experiments. The initial bentonite concentration is identical in most of the tests performed and was chosen to be 6%, which resulted in the formation of an external filter cake for the finest sand (0.1–0.5 mm) (see Fig. 4.5a), whereas the use of sands with grain sizes of 0.5–1 mm and 1–2 mm led to the internal filter cake formation (Fig. 4.5c) and pure penetration (Fig. 4.5b), respectively. The grain size distributions of the sands used are provided in Fig. 4.27a. A common commercially available sodium-activated bentonite powder with high plasticity properties and swelling capacity is used for slurry preparation. The bentonite has a liquid limit of $w_L = 317\%$ and a plasticity index of $I_P = 253\%$. The slurry is prepared through mixing bentonite powder with tap water with the mixing ratio 60 g/l for 10 minutes. Subsequently, the slurry is kept 16 to 18 hours at rest in a temperature-controlled room before being used for the experiments. The flow behavior of the B60 slurry obtained from rheometer (at 20 °C) is shown in Fig. 4.27b. An infiltration column, shown in Fig. 4.28, is used to perform infiltration tests and the preparation of samples for the element tests. The column itself is equipped with 16 pore pressure sensors radially distributed along the height, which measure the pore water pressures during bentonite slurry infiltration over time. One fluid reservoir containing about 30 l bentonite slurry is connected to the inflow (bottom) side of the column, and a second fluid reservoir is connected to collect the slurry or water at the outflow side. The mass contained in both reservoirs is continuously monitored. A hy-
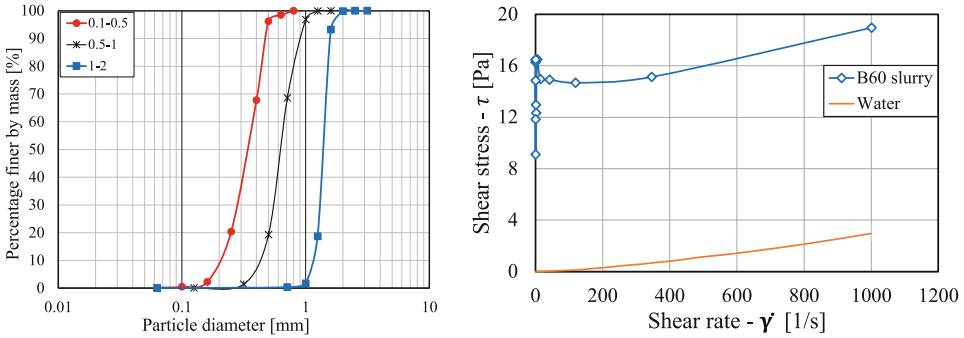
Fig. 4.27 Soil and slurry classification data

Column test setup   Mold arrangements
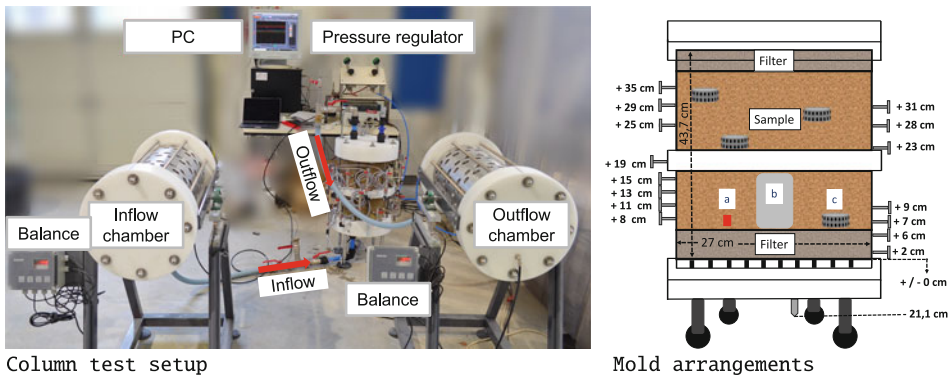
Fig. 4.28 Laboratory setup for infiltration tests and sample preparation for element tests

draulic gradient of $\Delta_p = 50$ kPa was applied through respective air pressures of 90 and 40 kPa on the fluid in the inflow and outflow containers, respectively. All infiltration tests, except for the samples prepared for microstructural investigation, are performed with an upward flow. The test duration was about 45 min. However, in case of sand 1–2 mm showing pure penetration mechanism, the test has to be stopped after approximately 3 min since the inflow reservoir discharges very fast.

The given sand is filled into the column by air-pluviation method. The density achieved is controlled by measuring layer wise the mass of the sand filled for a given layer thickness. Subsequently, CO_2 is flushed through the sand filled column for 1 hour replacing the pore air. The sample is saturated by de-aired water. Permeability tests performed after the saturation phase together with the precise measurements of density ensured the control of initial soil conditions and reproducibility of test results. The time-dependent slurry penetration data is then calculated using the balance measurements assuming one-dimensional fluid displacement with a uniform infiltration front over the cross-sectional area of the column. The samples for the planned tests (measurement of bentonite concentration and rheology, triaxial tests, microstructural investigation) are taken after the infiltration test

from the column. For this purpose, moulds of different sizes and geometries are designed and produced. The moulds were installed inside the column prior to and during the air-pluviation of the host sand. They were acquired at the end of the experiment through dismantling of the column in a segment wise manner. The arrangement of the moulds inside the column is schematically shown in Fig. 4.28, where a) is the sample mould for the microstructural investigation, b) is the triaxial split mould, and c) are the perforated hollow cylinders to entrap the infiltrated slurry at target heights.

4.4.2   Particle-Storage and During Bentonite Slurry Infiltration

A method to directly measure the locally distributed bentonite concentration after the end of the infiltration tests was developed. The concept consist in entrapping the infiltrated pore fluid at different distances from the infiltration front, thus, at different heights in the column. For this, 16 flat aluminum cylinders with dimensions 2 cm in height and 6 cm in diameter providing an inner volume of about 30 cm^3 were produced and perforated with multiple 5 mm diameter holes at top and bottom surfaces. The perforated cylinders were placed during air-pluviation at the target heights h_i. In order to avoid reciprocal effects during one-dimensional flow between neighbor cylinders, the cylinders at height h_{i+1} were shifted also radially with respect to the preceding lower cylinder. After the end of infiltration and pressure release, the overlaying soil was extracted carefully until reaching the top of the cylinder. The fluid volume of about 30 cm entrapped in the cylinder was collected from the container using a pipette and filled into glasses. The collected fluid samples tested regarding their bulk rheological properties using a rheometer. A second sample from the same height was used to measure the solid content by oven drying. By this method, an correlation between solid content and bulk rheological properties is established. Further, the method of direct measurement of concentration can be used to calibrate the indirect measurements using geoeelectric methods as presented in Sect. 4.3.2.

In Fig. 4.29, the concentration profile obtained by the direct method for the sands resulting in the three different infiltration mechanisms is shown. For sand 1–2 mm, no change in the slurry concentration is observed, which indicates the pure penetration of the slurry. However, for the other two sands, where formation of an external filter cake and internal filtration is expected, a sharp decrease in measured bentonite solid content can be observed. In case of the finest sand (Fig. 4.29a), the concentration decrease occurs over the first 10 cm from the infiltration front from $c_0 = 50$ g/l to $c = 2$ g/l. For the medium-coarse sand (Fig. 4.29b), an initial penetration of the slurry without any bentonite filtration and a constant concentration of about 50 g/l followed by a sudden drop of concentration down to a concentration of $c \approx 2$ g/l occurs over 6 cm distance.

It was shown that the developed direct measurement of locally distributed final bentonite solid content reflects well the interaction of the sand skeleton with the infiltrated slurry and provides an insight into the quantitative filtration of bentonite solids inside the grain skeleton. Further, the results will be used for the calibration of model parameters

Fig. 4.29 Particle storage in terms of bentonite concentration vs. height for the different infiltration mechanisms: formation of external filter cake (**a**), internal filter cake (**b**), pure penetration (**c**)
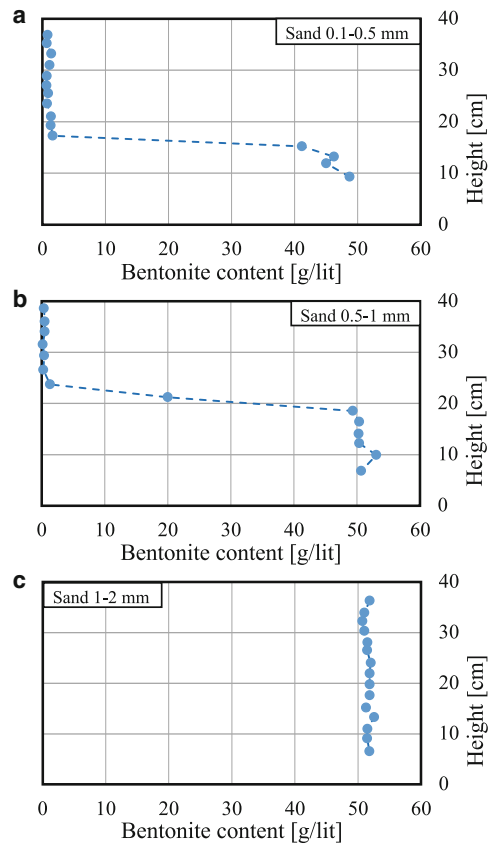
for the implementation of the continuum model of [89] for the simulation of filtration process of bentonite slurry into grain skeleton and the resulting change in porosity and permeability. Details of this work are published in [68].

4.4.3 Shear Strength of the Bentonite-Infiltrated Sand

The following paragraphs deal with the effect of bentonite slurry penetration on the shear strength of the granular soil. This investigation is motivated by two reasons. Firstly, depending on the properties of the granular soil and the bentonite slurry, different infiltration mechanisms and pressure transfer mechanisms occur. As a result, the zone where the bentonite slurry has penetrated into the pores can partly extend over the potential slip surface of the active earth pressure wedge (see Fig. 4.15). Further, bentonite penetration and filtration induce a decrease in permeability, resulting in a concentration of pore water pressures at the working face [115] due to the reduced drainage. This can in turn lead to a decrease in effective stress and a resulting change in shear strength. Secondly, the shear strength

of the soil matrix is one of the main components controlling the cutting tool wear and subsequently the excavation process [113].

In order to study the effect of bentonite penetration on the shear strength of sand, consolidated undrained monotonic triaxial tests were performed on a sample of clean sand (grain size 1–2 mm) and a bentonite-infiltrated sample of the same sand. In both tests, the initial relative density was very similar with ID = 71% and ID = 67% for the clean sand sample and the infiltrated sample, respectively. Both values refer to density of the sand grain skeleton (without the bentonite solid content of the infiltrated sample). Both samples were taken as undisturbed samples from the column test. For this, the triaxial mold in the form of a split mold equipped with a latex membrane is placed inside the column at the respective height close to the infiltration front (Fig. 4.28).

Subsequently, the sand is filled into the column. It is to be noted that a vacuum is applied to the split mold during filling the column with sand in order to ensure a good contact between the inner surface of the split mold and the latex membrane, and thus, to ensure a defined volume and shape of the sand sample inside the split mold. Prior to the bentonite infiltration, the soil column is saturated with water. The bentonite slurry was infiltrated into the sand by applying a hydraulic gradient of 50 kPa between the inflow and outflow sides of the column. After the end of bentonite infiltration, vacuum is applied again to the split mold to avoid any deformation of the sample due to stress release during dismantling of the column and removal of the overlaying soil. The split mold together with the bentonite-infiltrated sample is carefully extracted and sealed by lids at top and bottom. The sampling procedure for the clean sand sample is similar, except that the excavation of the mold takes place after saturation with water. The mold with either the clean sand or the bentonite-infiltrated sand sample is transferred to the triaxial device and mounted into the triaxial device. The drainage system is saturated with de-aired water. After ensuring the appropriate B-values greater than 0.95, the sample is consolidated at 100 kPa effective stress, with a cell pressure of 700 kPa and a back-pressure of 600 kPa. After consolidation, the samples were monotonically sheared at undrained condition. The results for both a clean sand as compared to and a bentonite-infiltrated sand sample are shown in Fig. 4.30a–c.

As shown in the prior section (see Fig. 4.29), the combination of sand grain size of 1–2 mm with bentonite slurry with initial 60 g/l solid content results in pure penetration mechanism, where no bentonite particles are filtrated out of the slurry. The solid content of the bentonite slurry remains unchanged over the penetration length. The bentonite concentration is therefore homogeneous inside the infiltrated triaxial sample and equal to the initial value of 60 g/l. The results indicate that the qualitative behavior of the clean sand and the infiltrated sample is similar. They show an increase of deviator stress q (as measure of the shear stress) until they reach a maximum value at about 15 % axial strain, followed by a subsequent decrease in deviator stress (see Fig. 4.30a). With further increase in axial strain, the samples tend towards a stationary condition, known as *critical state*, in which shearing can continue without further changes in effective stress or volume. The difference in peak deviator stress between the clean sand and the bentonite-infiltrated sample

Fig. 4.30 Results of mono-
tonic undrained triaxial tests
on clean sand (grain diameter
1–2 mm) and bentonite-
infiltrated sand (grain diameter
1–2 mm, bentonite concen-
tration of used slurry 60 g/l):
deviatoric stress vs. axial
strain (**a**), pore pressure vs.
axial strain (**b**), stress path as
deviatoric stress q vs. mean
effective stress p', with (**c**)
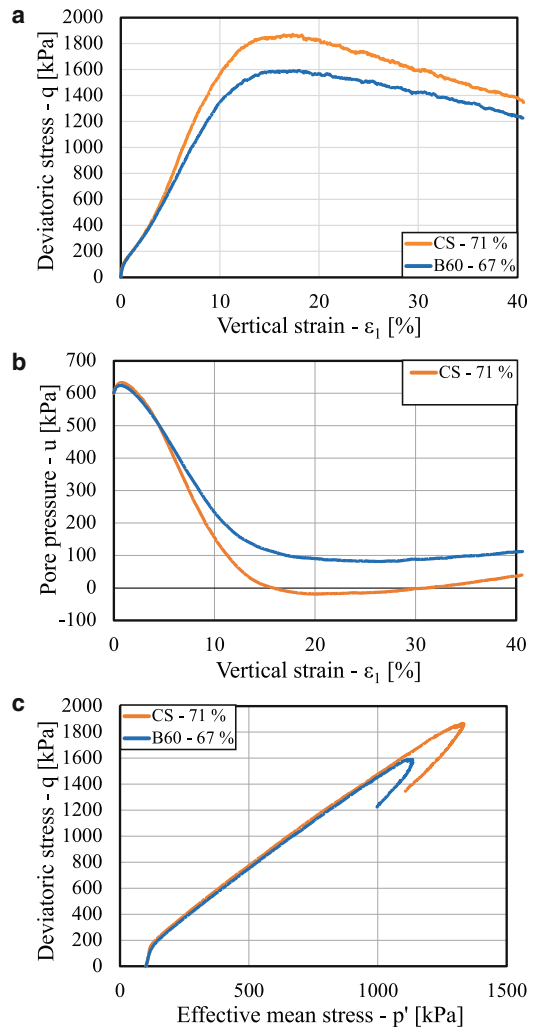
was found to be 10 to 15 %, with smaller peak deviator stress for the latter. Accordingly, in Fig. 4.30b, the pore pressure decrease after the slight initial pore pressure increase corresponds to dilative behavior for both sample conditions. The less steep decrease in pore pressure for the infiltrated sample indicates a smaller rate of dilation for the infiltrated sample than for the clean sand. Again, from the stress path shown in Fig. 4.30c, a smaller peak deviator stress for the bentonite-infiltrated sample is visible. According to [101], peak strength is the result of both the rate of dilation and the steady friction (at critical state) inside the soil. Considering the critical state friction as dominated by the grain skeleton, and therefore being identical for the clean sand and the bentonite-infiltrated sand, it is presumed that the rheological properties of the bentonite suspension reduces the contribution of dilatancy to the peak friction.

4.4.4 Microstructural Investigation of Bentonite Slurry and Bentonite-Sand Contact Zone

In the following, the microstructural investigation of the bentonite slurry at initial state and after being subjected for 16 h to 100 kPa applied pressure in contact with the host sand (0.1–0.5 mm grain size) is presented. In both cases, the microstructure was investigated using the Cryo-BIB-SEM technology (Broad Ion Beam polishing and Scanning Electron Microscopy under cryogenic conditions) as presented by [91], building on the first prototype established by [27]. Cryo-BIB-SEM is a suitable technique to image pore-fluid distribution in porous media [90]. For the investigation of the pure slurry at initial state, the bentonite slurry was prepared with a water content w corresponding to 1.1 times the liquid limit water content of the bentonite ($w = 1.1w_L = 349\%$). Few drops of the slurry were placed in a small container and rapidly frozen in slushy Nitrogen. About 1 mm^2 large, flat, and damage-free cross-sections were cut into the samples using Cryo-BIB (Leica TIC3x), following exactly the protocol of [91] (see Fig. 1 in [91]), except for the water phase in the samples having been sublimated under controlled conditions in the SEM (Zeiss Supra 55 equipped with Leica VCT100) prior to sputter coating with Tungsten. The sample cross-sections were investigated and imaged with high magnification across large areas using simultaneously the SE2, BSE, and EDS detectors (SE2: Secondary Electrons, BSE: Backscattered Electrons, and EDS: Energy Dispersive Spectroscopy).

For investigation of the bentonite-sand contact zone, five specially designed sampling molds with dimensions 8 mm (length) × 3 mm (width) × 12 mm (height) were embedded with ca. half of their height into a sand-filled column. The molds were distributed equally over the area of the sand-filled column. Subsequently, the slurry was carefully poured onto the sand surface, thus, also into the half-embedded sampling moulds. By this manner, the bentonite-sand interface was captured inside the sampling mould. After completing filling the slurry volume on top of the sand, an air pressure of 100 kPa was applied for about 16 h. After the end of the test, the slurry was carefully removed until reaching the sampling moulds. They were carefully excavated, then the sampling molds were opened and the small samples were directly frozen in slushy nitrogen. The subsequent procedure (Broad Ion Beam polishing) was the same as for the pure bentonite slurry.

Figures 4.31 and 4.32 show the resulting images for the bentonite slurry (B60), and the sand-bentonite contact zone, respectively.

In Fig. 4.31 (left), the white and light grey zones indicate the solid phase, which is mainly constituted by the highly porous bentonite matrix and contains few other components like feldspar (green particle in the center) or carbonates (few small orange particles). The matrix is divided into sub-areas separated by larger elongated pores of arbitrary orientation. The bentonite solids inside the matrix are forming a network, in which distinct particles cannot be distinguished. Similar results were reported in [5] for a Calcium-bentonite slurry. The bentonite solids arrange themselves in a manner to form the walls of the pores of about 0.5 to 5 μm in average diameter. The arrangement resembles a honey-
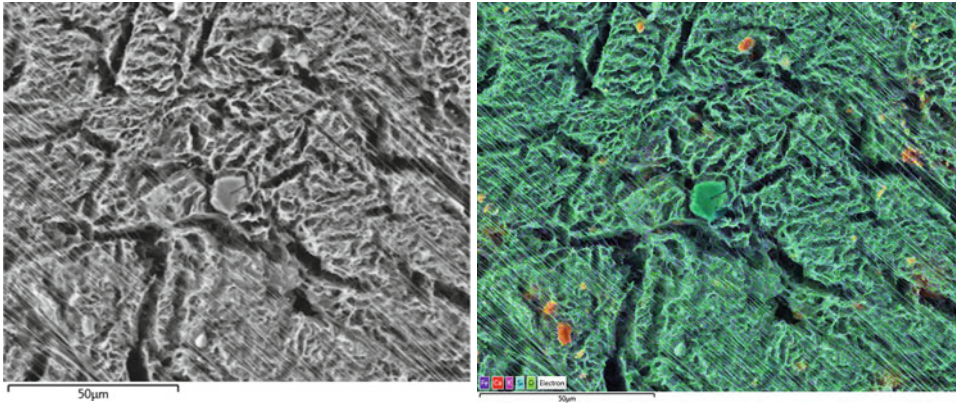
Fig. 4.31 Cryo-BIB-SEM images of the pure bentonite slurry with $w = 1.1w_L$: SE-image with bentonite solid phase in white/light grey and sublimated pore space in dark grey/black color (left), and EDS-image indicating chemical main elements of the solid phase (right)
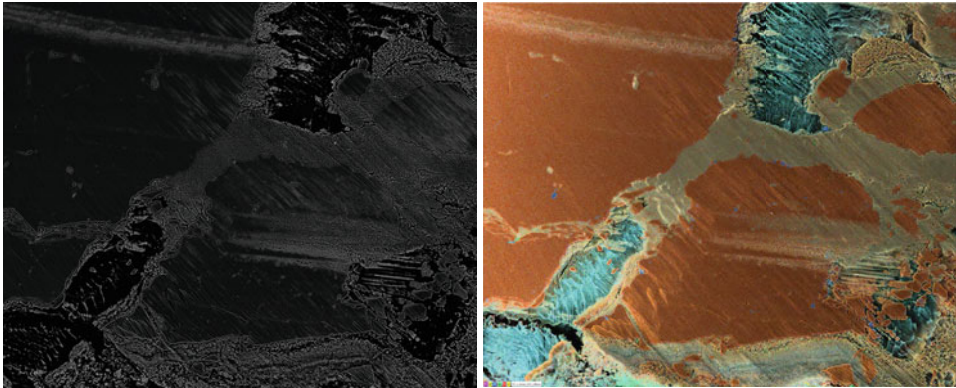
Fig. 4.32 Cryo-BIB-SEM images of the contact zone of coarse sand 1–2 mm with bentonite slurry (4% bentonite content) uploaded with 10 g/l fine sand 0.1–0.5 mm: BSE-image (left), and EDS-image (right); picture width 1.3 mm

comb structure, however, with much less regular geometrical arrangement in the case of the bentonite slurry.

The Cryo-BIB-SEM images of the bentonite-sand contact zone (Fig. 4.32) reveal three different phases. Firstly, the large (1–2 mm) and small (0.1–0.5 mm) quartz sand grains are shwon in orange in the EDS-image and in dark grey in the corresponding BSE-image. The bentonite solids in the pore space between the sand grains are shown in turquoise in the EDS-image, whereas the elongated bentonite solids are visible in white in between the black sublimated pore space. The image reveals that the bentonite particles are oriented parallel and perpendicular to the circumference of the sand grains. The zones in beige color (and a medium grey scale) indicate the existence of a third phase. However, it is

also possible that the beige zones indicate a layer of saw dust prevailing during the BIB-SEM procedure and hindering the view on the bentonite slurry in the pore throats. The microstructural study indicated that the initial irregular fabric of the bentonite slurry was affected by the pressure conditions and the contact with the sand grains and changed to a more parallel arrangement with an orientation perpendicular to the sand grain surface.

4.5 Material Transport in the Excavation Chamber of Hydro and Earth-Pressure-Balance Shields

The simulation of material transport processes require the development of specific numerical methods, each having their own particular numerical challenges. Also, the constitutive models for inflow, mixing and interactions at the cutting wheel and in the excavation chamber can be derived with some care from these numerical methods.

In Sects. 4.5.1–4.5.3, a computational fluid mechanics model for the material transport in EPB shield machines, developed by Dang and Meschke [25, 26] is presented. The respective findings and results from applications of the numerical model to an EPB shield machine are contained in Sect. 4.5.4 (see [26] for more details).

4.5.1 Introduction

The excavated soil in front of the cutterhead of earth pressure balance (EPB) shield tunnel boring machines (TBM) is typically modified by means of conditioning agents such as water and conditioning foams, forming a soil paste in the pressure chamber [105]. The cutterhead and the pressure chamber in the EPB-shield machine are shown in Fig. 4.33.
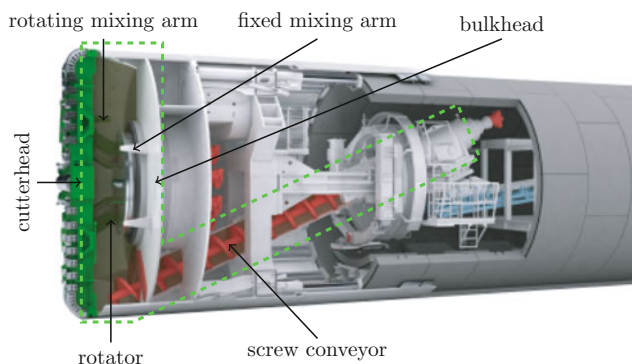
Fig. 4.33 Earth-pressure balance (EPB) shield tunnel boring machine. The cutterhead, pressure chamber and screw conveyor are marked by the dotted green line [25]

The transport and mixing processes inside the pressure chamber have an overarching influence on face stability and steering of the machine and more broadly on the entire excavation process as the soil paste is used as the support medium for the tunnel face in order to avoid ground surface displacement and the flow of water into the chamber [61]. Gaining insight into such processes is therefore undoubtedly of interest to the practicing engineer on one hand and poses several challenges to the researcher on the other. A recurring obstacle in the way of studying the processes inside the pressure chamber, for instance, is the fact that such processes are often not empirically accessible using sensory mechanisms. The pressure distribution in the chamber is a prominent example of such limitation, where the pressure gauges on the bulkhead and the cutterhead can only provide a partial picture of the actual distribution inside the chamber. Numerical simulations have proven to be valuable tools in complementing this lack in empirical data, and many studies have attempted to use numerical methods for the simulation of various aspects of the transport and mixing processes in TBMs [25, 26]. In addition to obtaining a fuller picture of the pressure distribution, numerical methods can be used as frameworks to study ways in which the transport and mixing processes can be manipulated to bring about desirable effects. For instance, numerical simulations can be used as cheaper alternatives to experiments for the optimization of the configuration of the mixing arms in order to maximize mixing efficiency inside the chamber.

The mixture of soil and conditioning agents in the pressure chamber is typically considered as a viscoplastic fluid [44, 64]. The Bingham model [13] and the Herschel-Bulkley model [22] are popular choices to model such viscoplastic fluids, see also [74]. Given that the rotation of the cutterhead and consequently the soil mixture inside the chamber are relatively slow, the Stokes equations, see, e.g., [35] often provide a good approximation for the fluid flow. Nevertheless, the nonlinear term in the Navier-Stokes equations are not dominant for low-velocity fluid flows, and the extension to the Navier-Stokes equations normally does not pose significant numerical challenges for such flows. It is moreover often necessary to include, at least weak, compressibility to capture an accurate description of the flow because of the presence of the air component in the soil mixture.

The strong form of the Navier-Stokes equations are given by

$$
\begin{aligned}
\rho\left(\frac{\partial \mathbf{u}}{\partial t} + \mathbf{u} \cdot \nabla \mathbf{u}\right) - \nabla \cdot \boldsymbol{\tau} + \nabla p &= \rho \mathbf{f} \quad \text{in } \Omega \times [T_0, T], \\
\frac{\partial \rho}{\partial t} + \nabla \cdot \rho \mathbf{u} &= 0 \quad \text{in } \Omega \times [T_0, T],
\end{aligned}
\tag{4.7}
$$

where $\mathbf{u}$ is a vector-valued function representing the velocity of the fluid, p is a scalar function representing the pressure of the fluid, t denotes time and Ω is the domain. T_0 and T denote the start and end time, respectively. ρ is the fluid density and $\mathbf{f}$ is a body force function. The stress tensor $\boldsymbol{\tau}$ is a function of the rate of strain tensor $\mathbf{D}(\mathbf{u})$, which is defined as the symmetric gradient of velocity $\mathbf{D}(\mathbf{u}) := \frac{1}{2}(\nabla \mathbf{u} + \nabla \mathbf{u}^\top)$.

Introducing the isothermal compressibility coefficient χ_Θ,

$$\chi_\Theta := \frac{1}{\rho}\frac{\partial \rho}{\partial p}, \tag{4.8}$$

and expanding the continuity equation, the strong form becomes

$$\rho\left(\frac{\partial \mathbf{u}}{\partial t} + \mathbf{u}\cdot\nabla\mathbf{u}\right) - \nabla\cdot\boldsymbol{\tau} + \nabla p = \rho\mathbf{f} \quad \text{in } \Omega \times [T_0, T],$$
$$\chi_\Theta\left(\frac{\partial p}{\partial t} + \mathbf{u}\cdot\nabla p\right) + \nabla\cdot\mathbf{u} = 0 \quad \text{in } \Omega \times [T_0, T]. \tag{4.9}$$

The density-pressure relations for the soil mixture are described as follows (see also [26]),

$$\rho = \frac{\rho_0}{\Phi_0^a f_a^{-1}(p) + \Phi_0^{\text{sw}}}, \tag{4.10}$$

$$\frac{d\rho}{dp} = \frac{\rho_0}{(\Phi_0^a f_a^{-1}(p) + \Phi_0^{\text{sw}})^2}\left[\Phi_0^a \frac{f_a'(p)}{f_a^2(p)}\right], \tag{4.11}$$

where ρ_0 is the initial mixture density and Φ_0^a and Φ_0^{sw} are the initial volume fractions of air and solid-water, respectively, at atmospheric condition. $f_a(p)$ is air density as a function of pressure. The air volume fraction can be calculated as

$$\Phi_0^a = \frac{\text{FIR}}{1 + \text{FIR}}\left(1 - \frac{1}{\text{FER}}\right), \tag{4.12}$$

where FIR and FER are the foam injection ratio and the foam expansion ratio, respectively [34]. We use a regularized Bingham model as the constitutive model. The standard Bingham model for compressible fluids with Stokes' hypothesis, i.e., zero bulk viscosity, can be written as

$$\begin{cases} \boldsymbol{\tau} = 2\mu\mathbf{D}(\mathbf{u}) + \frac{\mathbf{D}(\mathbf{u})}{\|\mathbf{D}(\mathbf{u})\|}\tau_y - \frac{2}{3}\mu(\nabla\cdot\mathbf{u})\mathbf{I} & \text{if } \|\boldsymbol{\tau}\| > \tau_y, \\ \mathbf{D}(\mathbf{u}) = \mathbf{0} & \text{if } \|\boldsymbol{\tau}\| \le \tau_y, \end{cases} \tag{4.13}$$

where μ denotes the constant plastic viscosity and τ_y denotes the yield stress. The Bingham model can alternatively be written as

$$\begin{cases} \boldsymbol{\tau} = 2\mu_e\mathbf{D}(\mathbf{u}) - \frac{2}{3}\mu(\nabla\cdot\mathbf{u})\mathbf{I} & \text{if } \|\boldsymbol{\tau}\| > \tau_y, \\ \mathbf{D}(\mathbf{u}) = \mathbf{0} & \text{if } \|\boldsymbol{\tau}\| \le \tau_y, \end{cases} \tag{4.14}$$

where the equivalent plastic viscosity μ_e is defined as $\mu_e := \mu + \frac{\tau_y}{2\|\mathbf{D}(\mathbf{u})\|}$. The regularization function in [75] is employed, which can be written as

$$\mu_{e,\varepsilon} := \mu + \frac{\tau_y}{2\|\mathbf{D}(\mathbf{u})\|}(1 - e^{\frac{-2\|\mathbf{D}(\mathbf{u})\|}{\varepsilon}}), \tag{4.15}$$

where ε is a numerical parameter introduced to smooth out the exact Bingham formulation in Eq. 4.14. The plastic viscosity and yield stress of the soil mixture are considered as functions of pressure, see Sect. 4.5.5.

The solution to the flow problem in the pressure chamber of TBMs is a challenging task, and special numerical methods are often necessary for such simulations. Some of these challenges are outlined in Sect. 4.5.2. Furthermore, the theoretical aspects of two numerical approaches are discussed. The first approach in Sect. 4.5.3 is based on the shear-slip mesh update method and the immersed boundary method, and the second approach in Sect. 4.5.4 is based on the finite cell method. In addition, adaptive geometric multigrid methods as well as parallelization strategies and scalability from the perspective of high-performance computing for the solution of large-scale problems are discussed in Sect. 4.5.4. A numerical model for the pressure chamber of EPB-shield TBMs is presented in Sect. 4.5.5, and the numerical results with focus on the pressure distribution in the chamber are discussed.

4.5.2 Numerical Challenges

The adequate definition of the geometry of the problem involves a sufficiently detailed description of the computational domain with consideration for the essential components of the cutterhead and pressure chamber such as the cutterhead rotators, the agitator and the fixed mixing arms, see Fig. 4.34 on one hand and the sufficient resolution of the discretized domain for numerical computation on the other.

A variety of CAD formats, such as boundary representation (B-rep) [98] and constructive solid geometry (CSG) [81] are often employed for the former. The vastly different requirements for the CAD representation of TBM components in the design stage, where the majority of the CAD data is often produced compared to the requirements for such data for numerical computation manifests itself as a myriad of deficiencies and errors in the

Fig. 4.34 The geometrical components of the cutterhead and pressure chamber of EPB-shield TBMs: the cutterhead rotators, the fixed and rotating mixing arms and the screw conveyor [25]
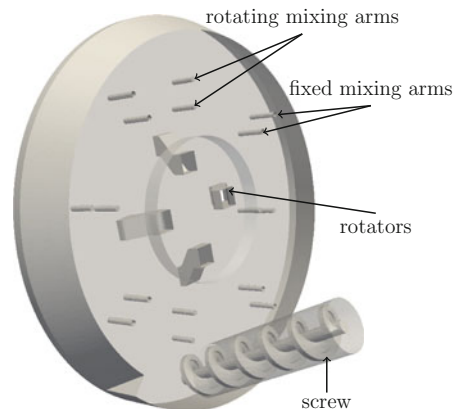
available CAD data from the perspective of numerical tools that in turn requires laborious, often manual, corrections before numerical simulations can be carried out. Many numerical methods such as iso-geometric analysis (IGA) [47] that aim to integrate CAD and numerical analysis for instance rely on nonuniform rational B-spline (NURB) patches in the CAD data being non-overlapping, which is not necessarily satisfied during the creation of the CAD data. On the other hand, the sufficient resolution of the discretized computational domain requires the solution of large-scale numerical problems, especially in 3D, with problems ranging up to millions of degrees of freedom (DoF), motivating the use of parallelization methods and high-performance computing (HPC) algorithms and hardware in order to obtain scalable solutions.

Furthermore, the rotating components of the geometry, namely the cutterhead and the screw conveyor introduce additional numerical challenges. For instance, the finite element method, which is one of the most popular numerical tools for the solution of the flow equations described above does not immediately allow for the extreme distortions in the discretized domain that result from the rotation of the geometry, and further considerations are often necessary. The combination of the shear-slip mesh update method and the immersed boundary method and the finite cell method are discussed in Sects. 4.5.3 and 4.5.4, respectively.

4.5.3   Shear-Slip Mesh Update – Immersed Boundary Finite Element Method

In this section, a combination of two numerical methods, namely the shear-slip mesh update (SSMU) method [102] and the immersed boundary (IB) method [69, 97] are described for the simulation of the pressure chamber and the screw conveyor. More specifically, the IB method is used for the treatment of the screw conveyor and the SSMU method is used for a number of rotating objects, including the cutterhead rotators and the mixing arms.

The shear-slip mesh update method is an FEM-based method, optimized for the simulation of rotating objects in a fluid domain. The computational domain is partitioned into fixed and rotating zones, in which Eulerian and arbitrary Eulerian-Lagransian (ALE) formulations are used, respectively. A thin mesh layer, called the shear-slip zone is inserted between every rotating zone and the adjacent fixed zone. The division of the domain into different zones is shown in Fig. 4.35.

While the mesh in the fixed and rotating zones remains untouched during the simulation, the shear-slip zone must be re-meshed at every simulation step as it borders a non-moving boundary in the fixed zone and a moving boundary in the rotating zone, see the Black points in Fig. 4.35. Note that the rotating zone undergoes a rigid body motion, and therefore its mesh is not distorted during the rotation. An advantage of the SSMU method in comparison with conventional ALE methods is the limitation of the zone where re-meshing is necessary to a relatively small part of the domain, namely the shear-slip
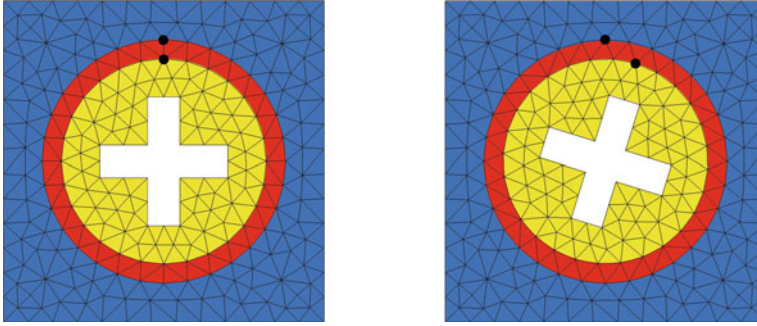
Fig. 4.35 Illustration of the different zones in the SSMU method. The fixed and rotating zones are designated by blue and yellow colors, respectively. The shear-slip layer, designated by red color, connects the fixed and rotating zones. The nodes in the shear-slip zone are connected to a fixed on one side and a rotating mesh on the other, see the black nodes [26]

zone(s). The ALE formulation of Eq. 4.7 takes the following form

$$
\begin{aligned}
\rho \frac{\partial \mathbf{u}}{\partial t} + \rho (\mathbf{u} - \mathbf{u}_m) \cdot \nabla \mathbf{u} - \nabla \cdot \boldsymbol{\tau} + \nabla p &= \rho \mathbf{f} \quad \text{in } \Omega \times [T_0, T], \\
\frac{\partial \rho}{\partial t} + (\mathbf{u} - \mathbf{u}_m) \nabla \cdot \rho + \rho \nabla \cdot \mathbf{u} &= 0 \quad \text{in } \Omega \times [T_0, T],
\end{aligned}
\tag{4.16}
$$

where $\mathbf{u}_m$ is the velocity of the mesh, which only appears in the convective terms. See [25] for a more detailed description of the SSMU formulation.

The immersed boundary method is another technique for the simulation of moving boundaries in a fluid domain. While the SSMU method is practically limited to objects that undergo rotation, the IB method can handle general movements and provides a more flexible approach to such simulations. The solid object is allowed to move freely in the fluid domain in the IB method without requiring the computational mesh to conform to the boundary of the solid object, thereby bypassing the necessity for re-meshing as the solid object moves in the fluid domain, see Fig. 4.36.

To this end, the nodes in the computational domain are divided into three categories: solid nodes, which are covered by the solid object, adjacent nodes, which are those nodes in the fluid domain that belong to elements cut by the solid object and fluid nodes, which compose the rest of the domain, see Fig. 4.36. The movement of the solid object is taken into account by imposing either an appropriate body force or an appropriate Dirichlet boundary condition on the solid and adjacent nodes, see [25] for a detailed description of the technical aspects.

The SSMU method for the simulation of the cutterhead rotators and the mixing arms in the chamber and the IB method for the simulation of the screw conveyor are used in this section. It should be noted that the SSMU method can also be used to model the screw conveyor; however, the small gap between the screw surface and the conveyor wall on the one hand and between the screw head and the mixing arms on the other as well as the
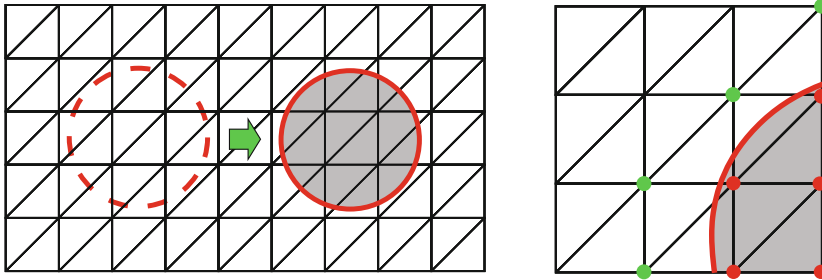
Fig. 4.36 A moving boundary within a fluid domain in the immersed boundary method (left). Note that the mesh does not conform to the boundary of the moving object. And the different types of nodes in the IB method (right). The solid and adjacent nodes are designated by red and green colors, respectively. The fluid nodes constitute the remaining nodes in the mesh [25]

inclination of the screw would make the pre-processing steps, i.e., the preparation of the fixed, rotating and shear-slip mesh zones rather complex in comparison. Therefore, the IB method is used for the screw conveyor. Similarly, the IB method can be used for the simulation of the cutterhead rotators and the mixing arms. The SSMU method, however, is more computationally efficient for rotating objects and provides a more straightforward way for the application of boundary conditions as well as post-processing the results as the mesh conforms to the boundaries of the solid objects. The technical aspects of the coupling between SSMU and IB methods is described in [25].

4.5.4   Finite Cell Method with Adaptive Geometric Multigrid

The generation of boundary-conforming meshes for complex geometries is often a time-intensive and error-prone process and marks a standing challenge in analysis using conventional numerical methods such as the finite element method that rely on the existence of such discretization of the domain. A variety of techniques such as the cut finite element method (Cut-FeM) [19], the extended finite element method (XFEM) [8], the immersed boundary method [69, 97], see also Sect. 4.5.3 and the finite cell method (FCM) [32, 76] attempt to avoid the need for a boundary-conforming mesh to address this issue.

The finite cell method is a fictitious domain method that employs adaptive integration for the resolution of the arbitrary physical domain, while a structured background mesh is used as the computational domain as shown in Fig. 4.37 where a rotating solid object is embedded in a fluid domain, also compare with the SSMU method in Fig. 4.35.

Essentially, the need for a boundary-conforming tessellation of the physical domain is circumvented by postponing the resolution of the physical domain to the integration stage. Adaptive integration is widely used in order to ensure sufficiently accurate numerical integration in the finite cell method. We use space-tree data structures, see, e.g., [20] for the discretization of the background mesh [85]. Space trees allow for adaptive mesh
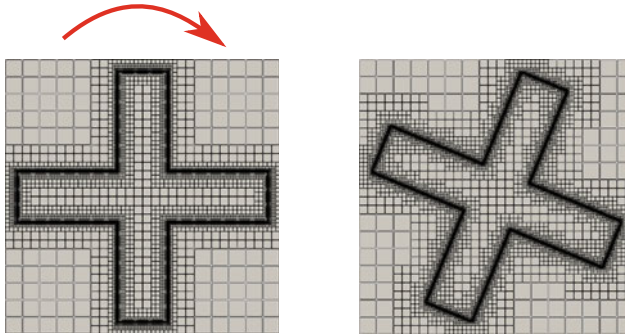
Fig. 4.37 An arbitrary rotating solid object, namely a cross-shaped rotating arm is embedded in a fluid domain (physical domain). A structured background mesh is used in the finite cell method. Note that adaptive mesh refinement is used in addition to adaptive integration in order to better resolve the boundaries of the solid structure
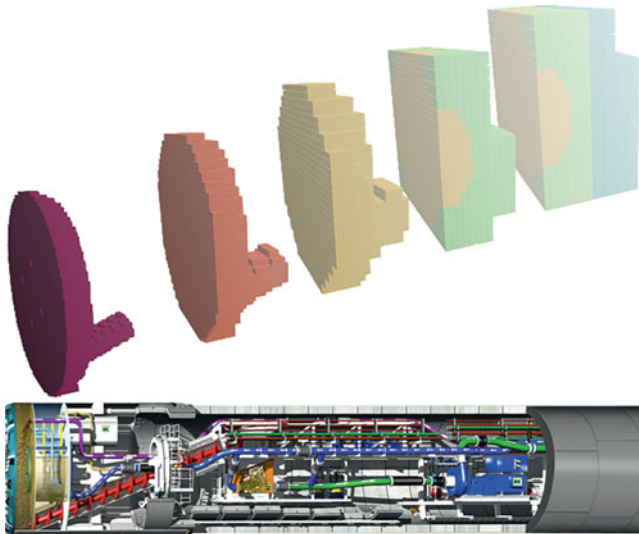
Fig. 4.38 Resolution of the TBM pressure chamber and cutterhead through adaptive refinement in the finite cell method

refinement (AMR) as well as the efficient handling of large computational domains on distributed-memory systems with a low memory footprint. In addition to adaptive integration, AMR is employed as an extra layer for the resolution of the physical domain, as shown Fig. 4.37. The resolution of the pressure chamber and cutterhead of the TBM is illustration in Fig. 4.38.

The mixed finite cell formulation of the Navier-Stokes problem described in 4.5.1 follows the general steps of the finite element method [86]. The strong form is multiplied by appropriate test functions from the left and integration by parts is used to transfer deriva-

tives from the trial functions to the shape functions. However, unlike the finite element formulation, the boundary terms in the weak form on the Dirichlet part of the physical boundary Γ_D do not vanish because the solution space of the finite cell method in general does not conform to the physical domain. The Nitsche's method [73] for the weak imposition of the boundary conditions is used, which leads to a consistent weak form and does not introduce additional degrees of freedom in the global system. In addition to the considerations for the imposition of essential boundary conditions, volume integrals are multiplied by a function $\alpha(\mathbf{x})$ that penalizes the fictitious parts of the domain. As model problem, incompressible Newtonian fluids are considered in this section for illustration. The strong form of the incompressible Navier-Stokes equations for Newtonian fluids are obtained by replacing $\boldsymbol{\tau} = 2\mu \mathbf{D}(\mathbf{u})$, where μ is the constant viscosity, and assuming density to be constant,

$$\rho\left(\frac{\partial \mathbf{u}}{\partial t} + \mathbf{u} \cdot \nabla \mathbf{u}\right) - \mu \nabla^2 \mathbf{u} + \nabla p = \rho \mathbf{f} \quad \text{in } \Omega \times [T_0, T],$$
$$\nabla \cdot \mathbf{u} = 0 \quad \text{in } \Omega \times [T_0, T], \tag{4.17}$$

which in addition to the boundary conditions

$$\mathbf{u} = \mathbf{w} \text{ on } \Gamma_D \subset \partial\Omega,$$
$$\mu \frac{\partial \mathbf{u}}{\partial \mathbf{n}} - \mathbf{n} p = \mathbf{h} \text{ on } \Gamma_N := \partial\Omega \setminus \Gamma_D, \tag{4.18}$$

form the Navier-Stokes boundary value problem. Γ_D and Γ_N are the Dirichlet and Neumann parts of the boundary, respectively. $\mathbf{w}$ and $\mathbf{h}$ are prescribed functions and $\mathbf{n}$ denotes the normal vector to the boundary with unit length.

The weak form of the mixed FCM formulation of the Navier-Stokes problem for incompressible Newtonian fluids, following the procedure described above, is obtained as

Find $(\mathbf{u}, p) \in (\mathbf{V}_e, Q_e)$ such that

$$(\mathbf{v}, \rho \frac{\partial \mathbf{u}}{\partial t})_{\Omega_e} + (\nabla \mathbf{v}, \alpha\mu\nabla\mathbf{u})_{\Omega_e} - (\mathbf{v}, \mathbf{n} \cdot \mu\nabla\mathbf{u})_{\Gamma_D} - (\mathbf{n} \cdot \mu\nabla\mathbf{v}, \mathbf{u})_{\Gamma_D} + (\mathbf{v}, \lambda\mathbf{u})_{\Gamma_D}$$
$$+ (\mathbf{v}, \rho\mathbf{u} \cdot \nabla\mathbf{u})_{\Omega_e} - (\nabla \cdot \mathbf{v}, \alpha p)_{\Omega_e} + (\mathbf{v}, \mathbf{n}p)_{\Gamma_D} + (\mathbf{n}q, \mathbf{u})_{\Gamma_D} - (q, \alpha\nabla \cdot \mathbf{u})_{\Omega_e} \tag{4.19}$$
$$- (\mathbf{v}, \alpha\rho\mathbf{f})_{\Omega_e} - (\mathbf{v}, \mathbf{h})_{\Gamma_N} + (\mathbf{n} \cdot \mu\nabla\mathbf{v}, \mathbf{w})_{\Gamma_D} - (\mathbf{v}, \lambda\mathbf{w})_{\Gamma_D} - (\mathbf{n}q, \mathbf{w})_{\Gamma_D} = 0,$$
$$\forall(\mathbf{v}, q) \in (\mathbf{V}_e, Q_e),$$

where $(\mathbf{v}, q)$ are the infinite-dimensional vector-valued velocity and scalar pressure test functions, respectively. Ω_e is the extended domain, in which the physical domain Ω is embedded. λ is the scalar stabilization parameter in Nitsche's method, which is typically computed using a generalized eigenvalue problem. The penalization function $\alpha = \alpha(\mathbf{x})$ is defined as

$$\begin{cases} \alpha = 1 & \text{in } \Omega, \\ \alpha = 0 & \text{in } \Omega_e \setminus \Omega. \end{cases} \tag{4.20}$$

In practice, $\alpha \ll 1$ is used outside of the physical domain in order to avoid severe ill conditioning of the system.

Aside from additions described above, the solution process remains relatively similar to the finite element method. Given the uniformity of the computational steps, the structured background mesh and the availability of appropriate data structures such as space trees, the finite cell simulation pipeline provides ample opportunities for massive parallelization and the use of high-performance computing hardware. Nevertheless, the scalable solution of the resultant linear system is a potential bottleneck. In this regard, iterative solvers are the natural choice as direct solvers typically have high complexity on the one hand and low concurrency for parallelization on the other, see, e.g., [83]. The convergence of virtually all iterative solvers however depends on the conditioning of the linear system, making the use of iterative solvers for the finite cell method a challenging task as the resultant system is usually severely ill conditioned, especially when small cut fractions between the physical domain and the background mesh are present. Therefore, development of tailored iterative methods for the finite cell is essential to scalable simulations, see, e.g., [49, 50, 79, 85, 86].

We focus on adaptive geometric multigrid (GMG) methods. GMG methods are among the most efficient linear solvers as they can lead to optimal convergence, where the iteration count of the solver is independent of the problem size, see [45]. Geometric multigrid methods are based on the idea that the problem on the fine grid can be solved using a hierarchy of coarser grids. Broadly, the highly oscillatory frequencies of the error are smoothed on the fine grid, while the smooth frequencies are projected onto the coarse grid. The smoothing operator constitutes an integral part of the multigrid methods, and the convergence and effectiveness of the solver heavily depends on the suitability of the smoother to the problem at hand. We develop a restricted additive Vanka-type smoother for the solution of the finite element formulation of the Stokes problem in [84]. The restricted additive smoother is shown to be competitive with the multiplicative smoother in terms of convergence and provides more favorable properties in terms of complexity and parallelization.

In the context of the finite cell method, special smoothers which consider the ill-conditioning of the system matrix are necessary for multigrid methods to converge [85, 86]. In [85], a hybrid multiplicative-additive Schwarz smoother for the solution of the finite cell formulation of the Poisson equation with adaptive geometric multigrid methods is used. It is shown that the proper treatment of cutcells in the finite cell system plays a crucial role in the performance of the geometric multigrid method. Strong and weak scaling of the finite cell method with adaptive geometric multigrid for the Poisson equation for problems with up to 1.1 billion degrees of freedom on distributed-memory clusters is shown in [85], see also Figs. 4.39 and 4.40. Two smoothers for the finite cell formulation of the Navier-Stokes equations are proposed in [86]. It is similarly shown that the treatment of cutcells is an important aspect of the smoother operator. Results indicate that adaptive geometric multigrid with appropriate smoothers can be a scalable solver for the finite cell method.
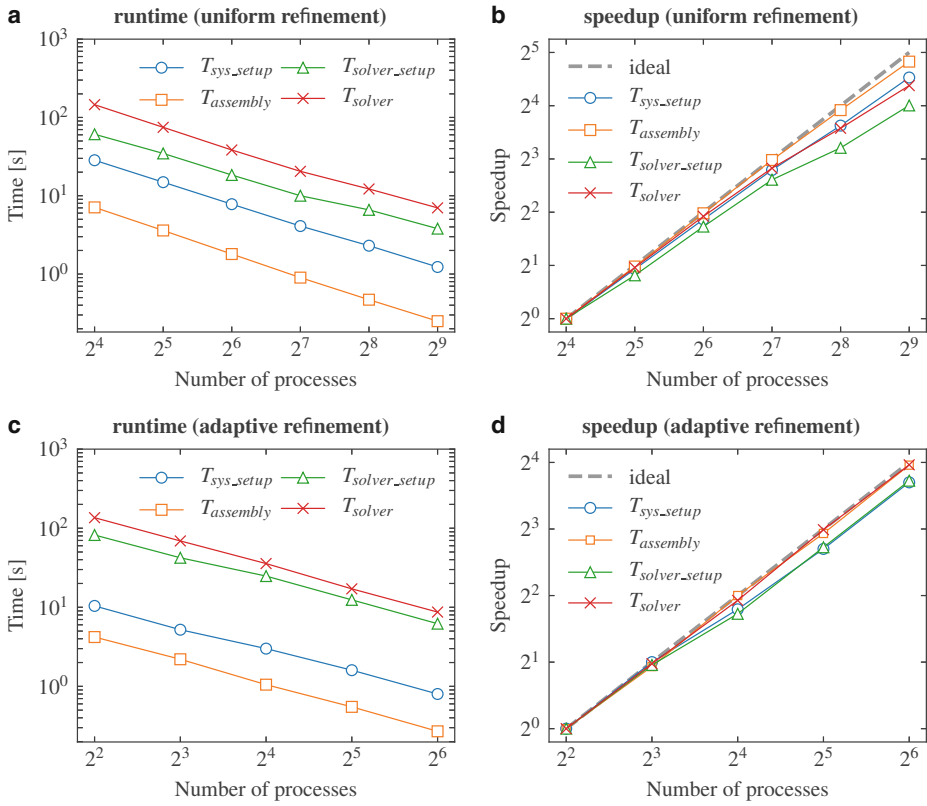
Fig. 4.39 The strong scaling of the finite cell method for the Poisson problem on a benchmark with 268 468 225 degrees of freedom in **a** and **b**, and 16 859 129 degrees of freedom in **c** and **d** [85]
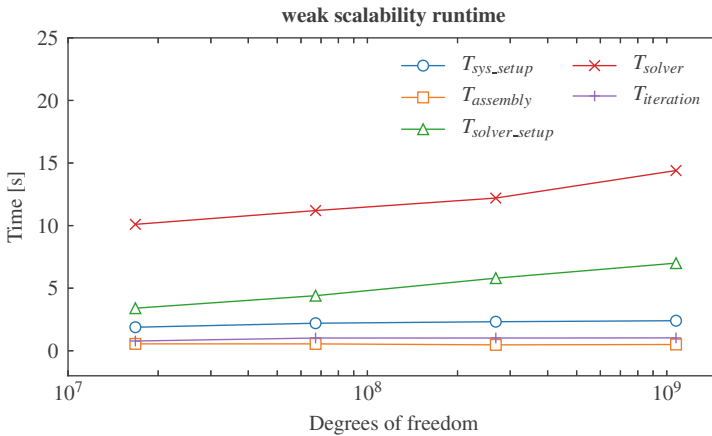
Fig. 4.40 The weak scaling of the finite cell method for the Poisson problem on a benchmark with up to 1.1 billion degrees of freedom [85]

4.5.5 Numerical Results

A 3D model of the pressure chamber is presented in this section and focus on the pressure distribution inside the chamber. The model and the results presented in this Subsection have been presented by Dang and Meschke in more detail in [26]. As mentioned, the pressure distribution is relevant for the determination of the tunnel face stability. While sensors provide a discrete picture of the distribution and the average pressure in the chamber can easily be estimated, insight into the actual distribution of pressure in the chamber is not well studied and is important for the design of the chamber and the determination of safe operational parameters. The model is based on the SSMU-IB approach described in Sect. 4.5.3. The model includes the rotators and two sets of mixing arms connected to the cutterhead, two sets of mixing arms connected to the bulkhead and the screw conveyor, see Fig. 4.34. Note that the length of the screw conveyor is shortened in order to reduce the computational effort as the transport process is not the focus of the model. The chamber has a diameter of 7 m, a width of 0.61 m at the center and an outer width of 0.92 m. Although the geometry of the cutterhead is simplified, see Fig. 4.34, the openings where the excavated soil enters the chamber and the closed parts are represented. Inflow boundary conditions are imposed on the openings of the cutterhead, where the inflow velocity is calculated as the normal component of velocity as

$$\mathbf{u}_n = \frac{\mathbf{u}_{\text{tbm}}}{\varepsilon_{\text{opening}}},$$ (4.21)

where $\mathbf{u}_{\text{tbm}}$ is the advance velocity of the TMB and $\varepsilon_{\text{opening}}$ is the opening ratio of the cutterhead. A zero-pressure boundary condition is applied at the exit of the screw conveyor. Partial slip boundary conditions are imposed on the surface of the chamber and the rotators. The advance speed of the machine is $\mathbf{u}_{\text{tbm}} = 1.5$ mm/s. The cutterhead has a velocity of 0.3 rad/s in the counter-clockwise direction when looked at from the tunnel, and the screw conveyor has a velocity of 2 rad/s in the clockwise direction when looked at from the outlet. The parameters of the model are described in more detail in [25].

The soil-water-foam paste inside the chamber is assumed to be homogeneous, whose pressure-dependent plastic viscosity and yield stress are chosen according to those of foam-conditioned sand as follows (see [64]),

$$\tau_y = 1500 + 0.017p,$$ (4.22)
$$\mu = 6700 + 0.032p.$$ (4.23)

The cutterhead rotators and the two sets of rotating mixing arms modeled using the SSMU method. Therefore, a total of three rotating zones and three shear-slip zones are necessary as shown in Fig. 4.41 (left). On the other hand, the screw conveyor is modeled using the IB method. An auxiliary mesh for the conveyor is used to keep track of the solid boundary within the fluid domain as shown in Fig. 4.41 (right).

Figure 4.42 shows the pressure contours in the chamber at three time steps. The pressure at sensor locations on the bulkhead is shown in Fig. 4.42. The pressure along the symmetry axis of the chamber on the cutterhead and the bulkhead is shown in Fig. 4.42.
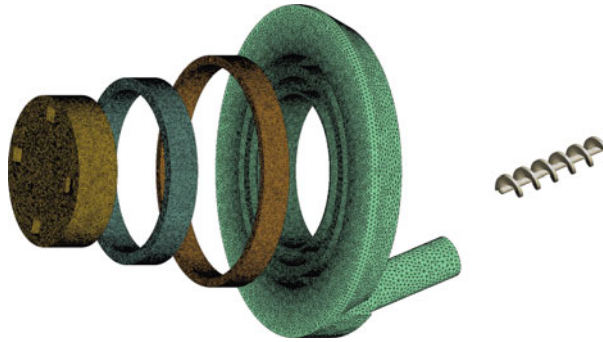
Fig. 4.41 Illustration of the computational mesh of the pressure chamber and screw conveyor. The fixed and rotating mesh layers for the cutterhead rotators and the mixing arms are shown on the left. There is a thin shear-slip mesh layer between every rotating layer and the fixed mesh, which are not shown to increase clarity. The auxiliary mesh of the screw conveyor is shown on the right [25]

The following observations can be made

- The pressure distribution in the chamber evolves in time.
- An increase in pressure can be seen from the left to right direction in the middle and bottom of the chamber, while the pressure is almost constant from left to right at the top of the chamber, as shown in Fig. 4.43. This observation is consistent with field measurements, see, e.g., [12].
- Although the fluid pressure is close to the hydrostatic pressure along a significant portion of the axis, local pressure fluctuations, e.g., a pressure drop the vicinity of the screw conveyor and local variations near the rotators and mixing arms can be seen. Furthermore, the effect of the screw conveyor on the pressure contours in Fig. 4.42 is easily noticeable.
- The pressure is observed to be the same on the cutterhead and on the bulkhead, which agrees with monitoring data, see, e.g., [105].

The influence of the design of the chamber, the material properties of the soil paste and the operational parameters of the TBM on the pressure distribution in the chamber can

Fig. 4.42 Pressure contours in the chamber at 25 s, 27 s and 29 s, from left to right [25]
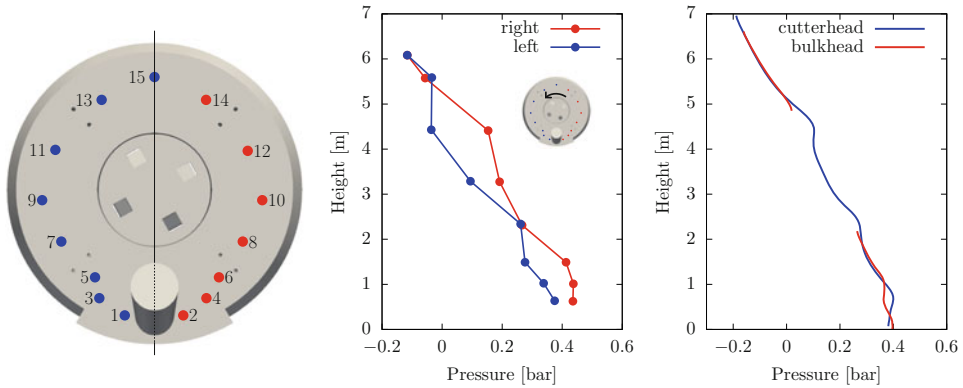
Fig. 4.43 Pressure distribution at discrete sensor locations at 27 s. The symmetric axis of the bulkhead and the locations of the pressure sensors on the bulkhead are shown on the left. The sensors to the left and right of the symmetric axis are denoted by the blue and red colors, respectively. The computed pressure at the sensor locations on the bulkhead are shown in the middle. The pressure profile on the symmetric axis on the bulkhead and the cutterhead are shown on the right [25]

also be studied using the numerical model. In [26], two chamber designs with multiple variations of the compressibility and rheological parameters of the soil paste are studied. It is seen that more compressible and more viscous soil pastes can lead to an increase in the pressure unbalance in the chamber. Furthermore, pressure fluctuations are observed to heavily depend on the design and size of the chamber. The readers are referred to [26] for a detailed discussion of the findings.

The results seem to point that the assumption of a linear pressure distribution along the vertical axis of the chamber, which is common in the design of TBMs is not strictly valid. Furthermore, fluctuations in the pressure distribution are in general undesirable as they could potentially deteriorate the stability of the tunnel face. The drop in pressure near the conveyor is especially critical, as it could lead to a loss of support in front of the cutterhead. The presented computational models can therefore be valuable tools to provide a more accurate picture of the pressure distribution inside the chamber on one hand and to allow the investigation of the influence of chamber design, material properties as well as operational parameters on the pressure distribution on the other hand.

4.6 Determination and Modification of the Flow Behavior of Soils for Tunneling with Earth Pressure Shields

The determination and the modification of the flow behavior of soils specifically found at TBMs with earth pressure shields has been extensively investigated. In particular, new evaluation methods, new test devices and novel conditioning agents were developed as a result of detailed research carried out within the project.

4.6.1   Correlation of Slump Tests and Rheometrically Determined Parameters

Galli (2016) [40] investigated the relationships between slump, slump flow and conditioning parameters of fine sand and sand. Both soils could be conditioned to the recommended range of suitable workability according to Budach (2012) [16] with the examined water contents (2 to 12 wt.%). With increasing foam and/or water content, the slump and slump flow increases. The grain-to-grain contact is successively eliminated, and the flow behavior of the sample becomes more dominant. The relationship can be established by approximating the data (Fig. 4.44, left), which results in

$$SF(S) = 20 + 0.039 \times S^2, \tag{4.24}$$

with slump flow SF [cm] and slump S [cm].

However, the flow motion is a non-static phenomenon in its origin and cannot be expressed by a single parameter resulting from a state of equilibrium at rest. Galli, 2016 [40] investigated the slump regime and spread regime models with own experimental test results. By correlating the slump test results with the results from the rheological investigations by means of a ball rheometer using the Bingham yield curve model, the final conversion model between slump yield stress and BMS yield stress is expressed as

$$\tau_0(S) = (220.26 \times S^2 - 11916.06 \times S + 164643.75)^{0.5}, \tag{4.25}$$

with yield point $\tau_0(S)$ and slump S.
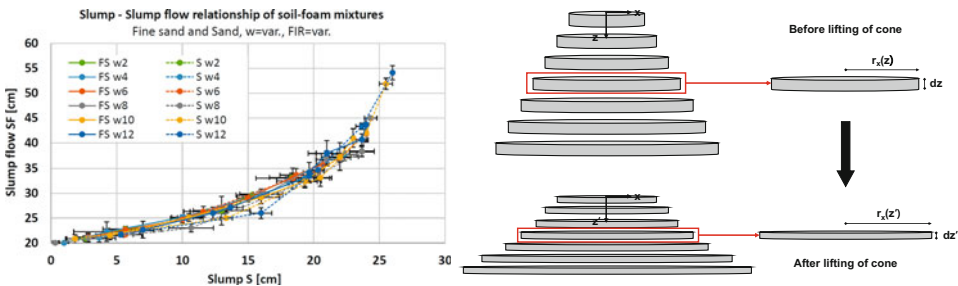
Fig. 4.44 Mean slump flow values SF over corresponding mean slump values S and standard deviations from experiments on different soil foam mixtures; dashed lines represent Slump/Slump flow relationship according to Eq. 4.24 (left). Sliced slumping behavior: mass conservation before and after lifting of the cone due to assumed incompressibility (right). [40]

4.6.2 Empirical Analytical Approach to Estimating the FIR During EPB Tunneling

There are no general models for predicting the amount of foam used in EPB tunneling, as both the residual water content after the addition of foam and the ground itself play a decisive role. EFNARC [33] gives recommended foam injection rates for different soils, but only takes the porosity of the soil into account. Due to the numerous test runs of the slump test with the cohesionless soils fine sand, sand and fine gravelly sand, Freimann, 2021 [36] developed a prediction model for the estimation of the foam injection rate. A decisive factor influencing soil conditioning is the granulometry of the soil. The results show that the soil parameter best estimates the foam injection rate and recommends Eq. 4.26 ($R^2 = 0.94$) for the calculation.

$$\text{FIR}_S = 0.897 \times S - 2.433 \times w - 72.842 \times d_{50} + 69.649 \qquad (4.26)$$

with foam injection rate FIR_S [vol.%], water content w [wt.%], slump S and grain size at 50 wt.% sieve passage.

The regression model used has an adjusted coefficient of determination of 0.94, which indicates an excellent approximation. Qualitatively, the conclusion can be made that the higher the coefficient for the slump, the higher the estimated foam injection rate. Furthermore, the value of the FIR increases with reduced coefficients for the water content and the grain diameter d_{50}. In Fig. 4.45, the estimated settling dimensions are shown graphically by applying Eq. 4.26 as a function of the actual foam injection rate. The different colors indicate the three soils investigated. The linear regression function is described by the black line and shows the very good approximation.

Fig. 4.45 Correlation of the estimated FIR using the empirical analytical approach and the actual FIR [36]. Soil: Fine sand, sand and fine gravelly sand, $w = 4$–12 wt.
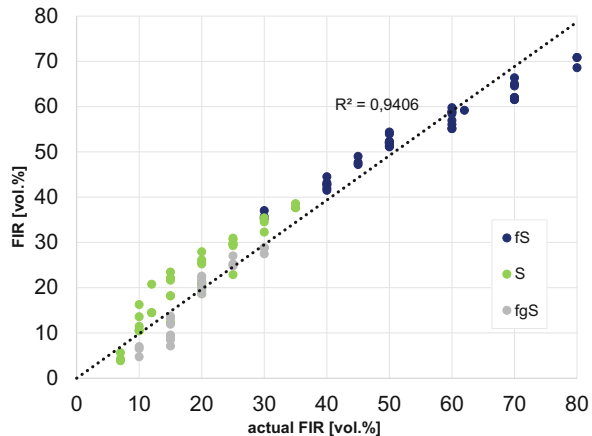
4.6.3 Analysis of the Workability of Conditioned Soils and Test Results by the Correlation Between Slump Test and Penetration Test Results and BMS

The analysis of the workability of conditioned soils can be done with a penetration test and compared with other investigation methods that characterize the flow of soil-foam mixtures typically found in TBMs.

4.6.3.1 Analysis of the Workability of Conditioned Soils with the Penetration Test

The results of the penetration tests show a similar material behavior to that as when performing the slump tests and the rheometer tests. The fluidity of the sample increases with increasing water content or FIR. Thereby the measured penetration depth increases, which causes the shear strength and shear stress values to decrease. All soil-foam mixtures could be investigated over the range of sufficient workability defined by the slump test. The evaluation of the measured values from the penetration tests clearly shows the influence of the water content and the amount of foam added to the investigated soil-foam mixtures. The achieved penetration depths were between 3 and 14 cm. Figure 4.46 shows the average penetration depth as a function of FIR for fine sand. In addition, the maximum and minimum penetration depths are indicated by the water content and the FIR.
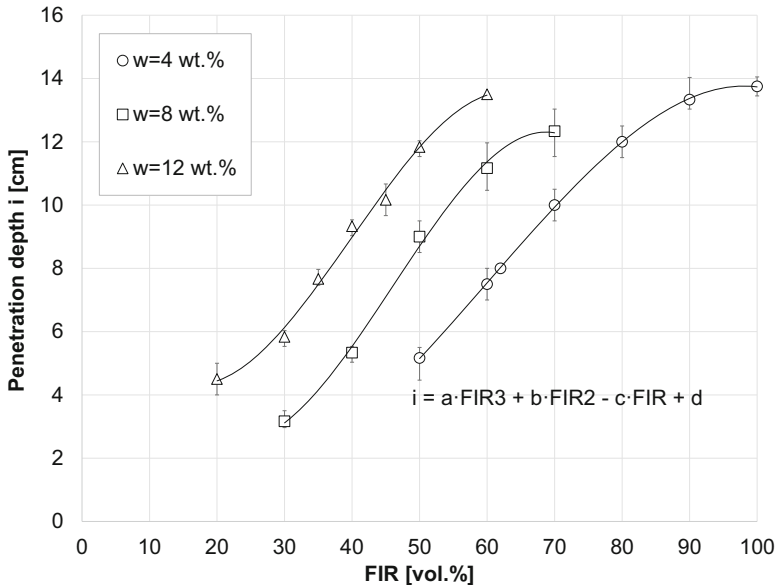
Fig. 4.46 Mean penetration depth values and maximum and minimum values from experiments on fine sand-foam mixtures [36]
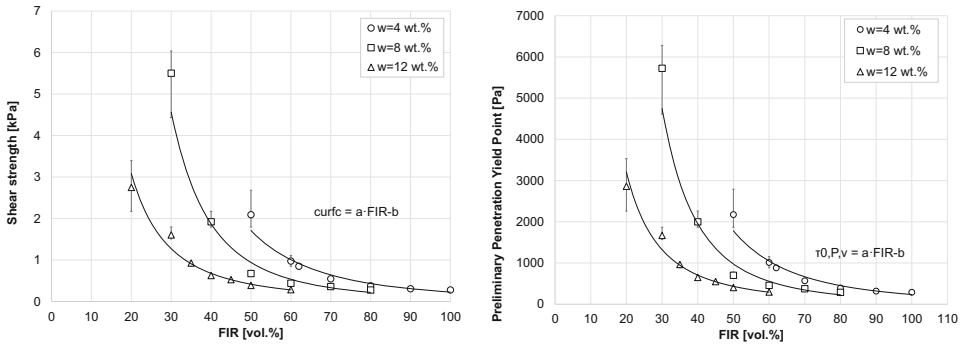
Fig. 4.47 Mean shear strength values c_{urfc} of fine sand-foam mixture determined with the Penetration test and maximum and minimum value. Regression with power function (left). Mean preliminary yield point values $\tau_{0,P,v}$ of fine sand-foam mixture determined with the Penetration test and maximum and minimum value. Regression with power function (right) [36]. Soil: Fine sand, w = var.; FER = 15; FIR = var.; cone 60°

Figure 4.47 shows the results of the penetration tests performed concerning the averaged undrained shear strength c_{urfc} and the maximum and minimum values of the shear strength exemplarily for fine sand. The calculated shear strengths of the samples range from 0.258 kPa to 6.036 kPa. As already expected, due to the increasing penetration depth over the FIR, the value of the undrained shear strength decreases with increasing FIR. The influence of the FIR on the undrained shear strength decreases with increasing FIR. The trend of the data can be approximated using a power function for all soil-foam mixtures investigated. In addition, the results show that the scatter of the values increases with increasing foam injection rate and water content which is caused by the influence of low penetration depth in the regression function. To determine the preliminary penetration yield point, the displaced soil-foam mixture's accumulation at the penetration cone must be considered. This observation is shown schematically in Fig. 4.47 (right). Therefore, the preliminary penetration yield point is calculated through fictitious penetration depth if resulting from the free cone side sf. The trend of the measured values for the preliminary penetration yield point shows an almost identical course with values of almost 200 to 6000 Pa.

The experimental results of the penetration tests with different soils and conditioning parameters have shown that information about the workability or the soil conditioning is possible due to the penetration depth. The penetration behavior of the samples reacts sensitively to the varying conditioning parameters of water content FIR. Using the 60° cone, it was possible to determine the shear strength and the preliminary yield point. The comparison of the initial penetration yield point with the penetration depth shows an excellent approximation using a power function, independent of the soil and conditioning

parameters. The preliminary penetration yield point $\tau_{0,P,v}$ can thus be calculated as

$$\tau_{0,P,v} = 60723 \times i^{-2.033}, \tag{4.27}$$

with penetration depth i and the preliminary yield point determined with the penetration test $\tau_{0,P,v}$.

4.6.3.2 Comparative Analysis of the Applied Investigation Methods for the Flow Characterization of Soil-Foam Mixtures

Both the slump test and the penetration test are static tests, i. e. the result of the tests stems from the determination of values after the flow or test movement of the material has ended. Figure 4.48 shows all averaged results of the force-controlled penetration test of the individual test series with the associated maximum and minimum penetration depths over the respective slump dimensions. Referring to the limits of the slump dimension recommended in the literature for the workability of conditioned soils, the measured values result in a penetration range for adequate workability between approx. 8.0 and 11.5 cm. However, a large scatter range of the penetration depth can be seen in the range between the slump dimensions 10 cm and 20 cm. Due to this scattering of the data, it is not possible to define strict limit values of the penetration depth for suitable workability for all investigated soil types.

The grey dashed lines represent the scatter range of penetration depths resulting from the measured data. From the intersections of these lines with the limit value for sufficient workability from the slump test (10 and 20 cm), an overlapping range between I = 9.5 and 11.0 cm is obtained. Following, the grey area indicates a reliable penetration range

$$i = 0.0014 \cdot S3 - 0.0546 \cdot S2 + 0.903 \cdot S + 3.8389$$
$$R^2 = 0.9352$$
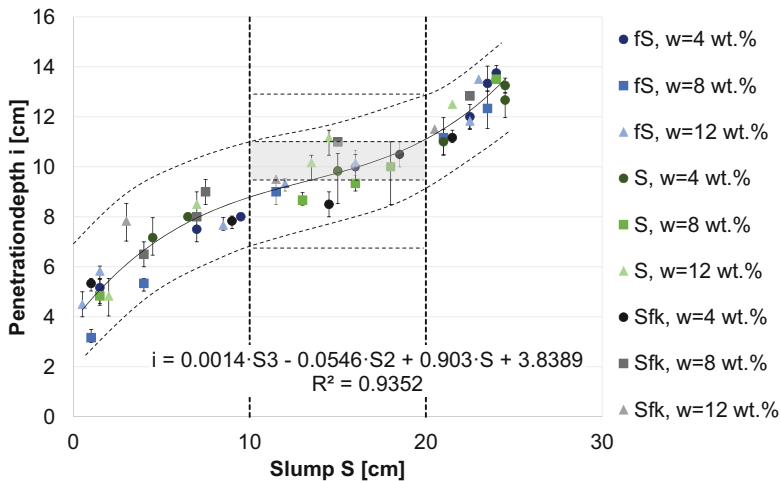
Fig. 4.48 Mean penetration depth as a function of the determined slump S from the slump test for all investigated soil-foam mixtures [36]. Soil: var.; w = var.; FER = 15; FIR = var.; cone 60°
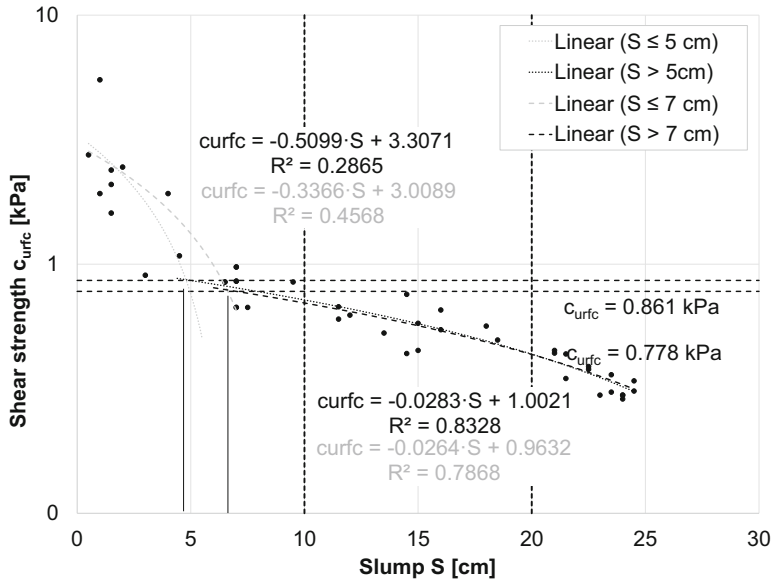
Fig. 4.49 Mean penetration shear strength c_{urfc} as a function of the determined slump S for all investigated soil-foam mixtures [36]. Soil: var.; w = var.; FER = 15; FIR = var.; cone 60°

for soil-foam mixtures with sufficient workability. The measured values from the tests show that the data in this penetration range exclusively exhibit slump values 11.5 and 18.0 cm. Based on the experimental results, the values of penetration depth for sufficient workability amounts to a ratio of 1/4 for an initial sample height of 14.0 cm. Thus, the range for adequate workability is somewhat larger for the slump test with a ratio of 1/3. The penetration test must have a higher sensitivity to allow the same significance of the test results. The detectable increase in penetration depth from a slump of about 22.0 cm is due to the physical limitations of the slump test.

Figure 4.49 shows the mean shear strength values determined from the penetration tests for all investigated soil-foam mixtures, correlated to the corresponding slump dimensions. The shear strengths determined from the penetration test have values ranging from 0.44 to 0.76 kPa within the slump value range for adequate workability. In previous research, wing shear tests were used to determine shear strengths of 0.3 to 1.5 kPa for conditioned cohesionless soils with a settlement dimension of 10 to 20 cm [16].

The values of undrained shear strength determined by penetration testing are within these values and thus within an equivalent range of scales. The trend of the data points indicates that within the slump dimension range between approx. 5 cm and 7 cm, a change in the material behavior occurs. Using multilinear regressions with intersection points at a slump of 5 or 7 cm, an exemplary range of values for shear strength can be identified as a change in the material properties from stiff to flowable. The gradient of the linear regression function for the corresponding shear strength values from a settling dimension
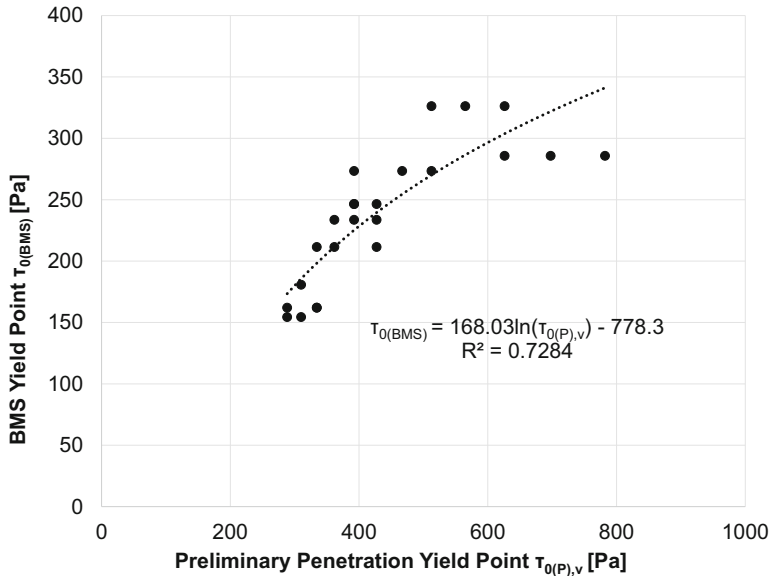
Fig. 4.50 BMS yield point as a function of preliminary penetration yield point for foam-conditioned fine sand [36]. Soil: Fine sand; w = var.; FER = 15; FIR = var.; BMS12; 60°cone

of 5 or 7 cm indicates a more flowable test medium than for soil-foam mixtures with a slump dimension of less than 5 or 7 cm.

The reliability of the rheological parameters from the penetration tests can only be confirmed using the results from the rheometer tests as a calibration standard. Figure 4.50 shows the BMS yield points from the ball measuring system using the Herschel-Bulkley model over the preliminary yield points from the penetration test for foam-conditioned fine sand. The data do not show a linear relationship. The magnitude of the yield points from the penetration test shows values nearly twice as high as the yield stresses from the ball rheometer tests. Using Eq. 4.28, the course of the data can be shown in the best possible way.

$$\tau_{0(BMS)} = 160.03 \times \ln(\tau_{0(P),v}) - 778.3, \tag{4.28}$$

with yield point $\tau_{0(BMS)}$ determined with BMS and preliminary yield point $\tau_{0(P),v}$ determined with the penetration test.

Substituting Eq. 4.27 into Eq. 4.29, the flow limits for the penetration test corrected based on the results from the BMS can be determined. Using the corrected yield points from the penetration test, a correction factor for the penetration yield point can be calculated on the one hand via the ratio of $\tau_{0(P),corr}$ to $\tau_{0(P),v}$. This correction factor is 0.54 on average. Thus,

$$\tau_{0(P),corr} = 160.03 \times \ln(52116 \times i^{-1.983}) - 778.3, \tag{4.29}$$

with corrected yield point $\tau_{0(P),corr}$ determined from penetration test and penetration depth i.

By considering the correction factor in Eq. 4.29, Eq. 4.30 can be defined to determine the yield point of soil-foam mixtures based on penetration depth. Taking into account the correction factor, yield point limits of 231 to 477 Pa can be determined for the penetration depth limits for adequate workability of soil-foam mixtures,

$$\tau_{0(P)} = 0.54 \times \frac{W \times \frac{\beta}{2}}{A}, \tag{4.30}$$

with penetration yield point $\tau_{0(P)}$, penetration force W, point angle of the cone β and moistened surface of the cone A.

Conclusion   Soil-foam mixtures represent a complex multiphase system, making it difficult to quantify workability or flow behavior. The material may exhibit different physical states depending on the degree of conditioning. The higher the water content or FIR, the more the sample exhibits fluid-like behavior. Dry or low-conditioned soil material, on the other hand, exhibits solid-like behavior.

One of the most important material properties of the support medium in EPB tunneling is the workability or flow behavior, which is influenced by soil conditioning and is used as a basis for the development of conditioning concepts. A fundamental factor for the optimal investigation of the workability of soil-foam mixtures is homogeneous material or shear conditions. These conditions are very difficult to achieve due to drainage effects of the test medium, heterogeneous flow conditions in rheometer tests or wall effects in the slump tests or penetration tests. The results from the laboratory tests are consequently subject to a certain degree of uncertainty since it is not possible to exclude all of these systematic sources of error. Figure 4.51 shows the test methods used in this research are assigned to the different material behaviors based on the findings from the test results.
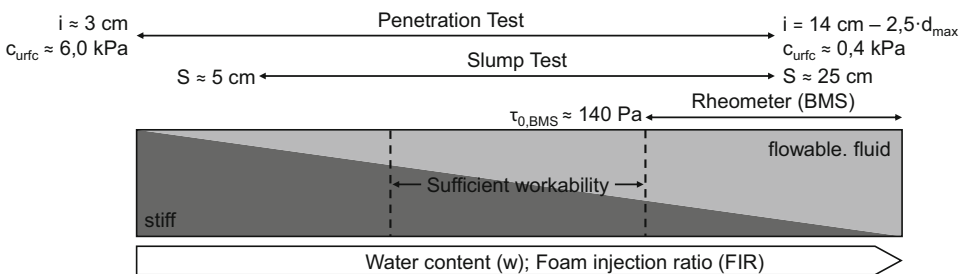
Fig. 4.51 Classification of the analyzed investigation methods based on the different material state forms of the soil-foam mixture [36]

4.6.4   Analysis of the Flow Behavior of Conditioned Soils

Various rheological parameters influence the flow behavior of the conditioned soil in the excavation chamber. Two essential parameters are viscosity and yield stress. Considering the results of the Slump Tests, the corresponding results of the rheological tests with BMS can be reflected. Since there are generally accepted limits for workability for the Slump Test with a slump between 10 and 20 cm, the results of the rheological investigations were examined with the corresponding slump results to determine a yield stress range for the soils examined. Figure 4.52 shows an example of the yield stress range for fine sand, considering the ball diameters used. The results of the Slump Tests were only evaluated for a slump of 10 and 20 cm without consideration of the conditioning parameters (w, FER and FIR). The horizontal lines show the mean value of the corresponding BMS yield stresses for these slumps independent of the ball diameter. The average values are 250 Pa for a slump of 10 cm and 130 Pa for a slump of 20 cm and indicate a range of yield stresses for optimum conditioning of the fine sand [37, 40–43].

The results for the other soils show that the yield stress range can vary depending on the soil, whereby medium sand and coarse sand could not be conditioned with foam alone for a slump of 10 cm. Table 4.2 represents the mean values of the yield stresses for all examined conditioned soils with foam, which represent the desired slump.
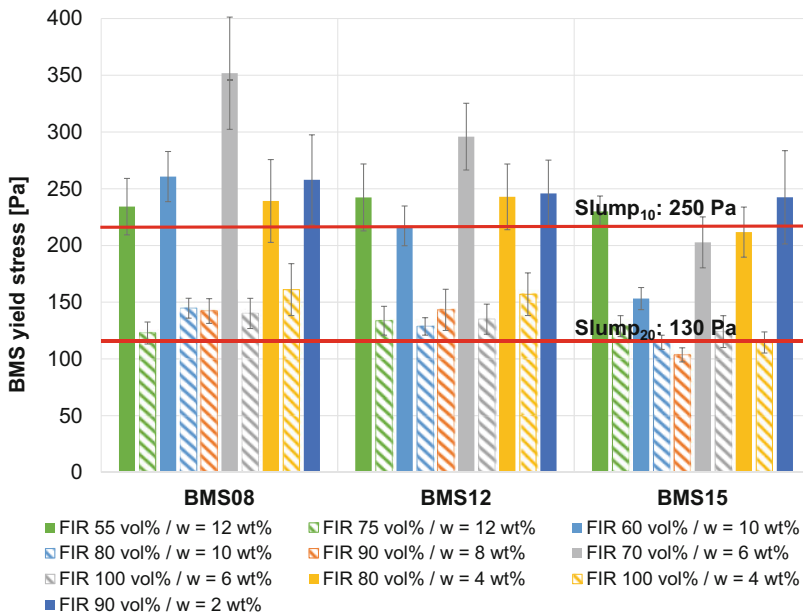
Fig. 4.52 Average BMS yield stresses and standard deviations corresponding to the Slump results (10 and 20 cm) of fine sand-foam mixtures [40]

Table 4.2 Average yield
stresses for slump range
d_{BMS12} with $c_f = 3\%$ [42]

Soil	yield stress Slump$_{10}$ (Pa)	yield stress Slump$_{20}$ (Pa)
Fine Sand	250	130
Fine sandy medium sand	310	190
Medium sand	270	190
Sand	250	130
Medium sandy coarse sand	–	130
Coarse sand	–	100

Further studies with Herschel-Bulkley model   The flow curves obtained by means of rheological laboratory tests with the BMS are exemplarily shown in Fig. 4.53 (left) for fine sand with a water content of 12 wt.% and illustrate the shear stress as a function of an increasing shear rate. The flow curves were approximated by applying the Herschel-Bulkley flow curve model. Based on the observed, measured values in the tests, the shear-thinning flow curve model, according to Herschel-Bulkley, is used for the evaluation of the rheological tests utilizing the BMS.

The measured data are shown as data points in the graph and represent the average of the six rounds of the rheometer. The standard deviation is also shown based on the individual measured values. The different colors indicate the increasing FIR. With increasing shear rate, a slight increase in shear stress can be seen depending on the conditioning parameters. The higher the foam injection rate of the samples, the more significant this effect. The influence of the water content and the FIR have a significant effect on shear stress. The higher the water content and the higher the foam injection rate, the lower the determined shear stresses. The results of the BMS yield point determination show the expected trend that the BMS yield point decreases with increasing FIR and water content (Fig. 4.53, right). However, the BMS yield point is not to be defined as a sharp value since
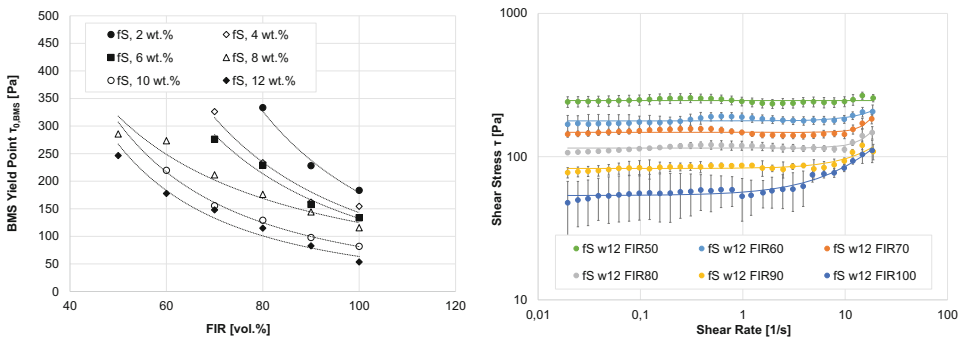
Fig. 4.53 Average flow curve data of fine sand-foam mixtures with water content w = 12 wt.% and increasing foam content (BMS12); curve fitting with Herschel-Bulkley Model (left). Development of BMS yield point of fine sand-foam mixtures (right) [36]

the material behavior in the range of shear rate = 0 can only be determined via the Model functions. Winnefeld (2001) [111] refers to this range of the yield point also as yield zone.

4.6.5 Implementation of a Ball Measuring System in the Large-Scale Test Device cosma to Investigate the Flow Behavior of Soil-Foam Mixtures

For the full scaling of the rheometric experiments, the suitability of the rheometer for the rheological investigation of conditioned soils under atmospheric pressure conditions should first be tested in a first series of experiments with the COSMA large-scale test rig. This makes it possible to test the possibility of using several rheometers at different installation heights on the pressure wall in the excavation chamber of an EPB shield machine to generate data on the flow behavior of the supporting medium during tunneling. To determine the influence of the conditioning grade on the torque of the ball rheometer in COSMA, three different soil-foam mixtures were investigated (see Fig. 4.54). These are the phase- and extreme value-adjusted torque curves over the test time for the investigated soil-foam mixtures exemplarily shown for a speed of 8 rpm. The different colors of the curves indicate the different conditioning parameters. The red dashed line represents the torque of the rheometer at no load.
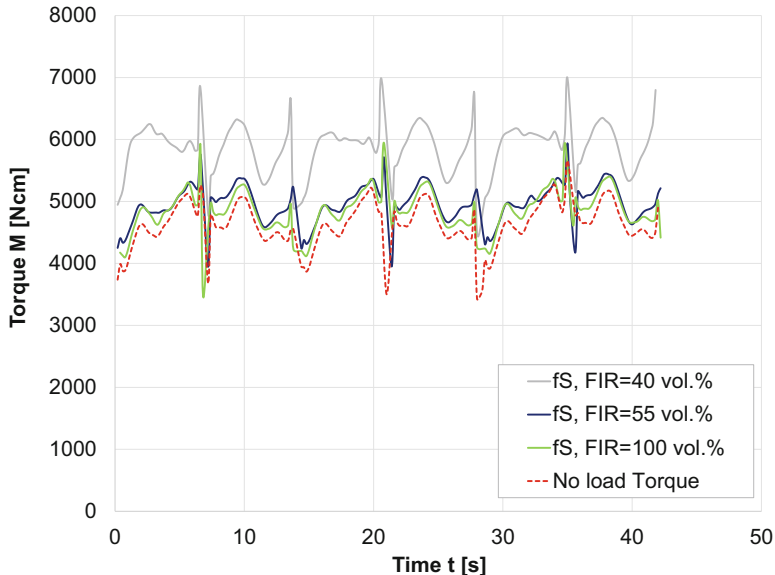
Fig. 4.54 Comparison of the torque curves of the ball rheometer in COSMA for the investigated soil-foam mixtures for a speed of 8 rpm [36]. Soil: Fine sand; $w =8$ wt.%; FER $= 15$; FIR $=$ var

It can be clearly seen that the torque of the ball rheometer decreases with increasing foam addition quantity. Differentiation between the individual soil-foam mixtures with different conditioning parameters is possible in principle, but the measuring range is very small. For a soil-foam mixture with a settling dimension of $S=10$ cm, torques of approx. 5000 - 6200 Ncm could be recorded in the large-scale rheometer tests. The torque curves for a soil-foam mixture with a settling dimension of $S=20$ cm (approx. 4200 - 5300 Ncm) and an overconditioned soil-foam mixture with a settling dimension of $S = 25$ cm (approx. 4100–5200 Ncm) show almost identical values of the torque at certain test times. Furthermore, the torque curves of these two tests show only slightly higher torque values than those recorded when the rheometer is idle (approx. 4000 - 5100 Ncm), which can be attributed to the excessive power of the drive of the ball rheometer. Thus, it can be seen that the sensitivity of the ball rheometer with the described test setup has weaknesses in the area of the limit of workability ($S = 20$ cm) but allows a rough comparison of the curve progressions. The aim of rheometer tests is to determine the rheological parameters of the test medium based on flow curves or the recording of shear stresses via the shear rate. The shear stresses are determined via the resistance moment of the rheometer and the shear rate via the speed of the rheometer. For the large-scale rheometer tests with the COSMA large-scale trainer, representative torque values were therefore calculated for the respective speed of the rheometer. For this purpose, the difference between the measurement data of a respective conditioned sample and the no-load torques for the individual speeds is determined.

In Table 4.3 and Fig. 4.55, the median of the individual data is shown and supplemented with the 1st and 3rd quartile value to show the range of the measured representative torque values of a specific soil-foam mixture. Figure 4.55, left, shows the median of the differential torque from the rheological tests with soil-foam mixtures and the median of the torque values at idle. It is clear that the torque of the ball rheometer decreases with increasing foam addition. The different colors represent the three different foam injection rates. The data points of the median values are only connected for better illustration. The spread of the values (Fig. 4.55, right) decreases the higher the foam injection rate so that a mean spread of the torque values for an FIR of 40 vol.% of approx. 500 Ncm and for an FIR of 100 vol.% of approx. 150 to 100 Ncm could be determined. The torque values determined show the highest values in each case for a speed of 2 rpm.

Table 4.3 Results of the analysis of the large-scale rheological investigations with three selected soil-foam mixtures

soil	w	c_f	FER	FIR	Δ Torque (N cm)			
	(wt.%)	(vol.%)	(–)	(vol.%)	2 rpm	4 rpm	6 rpm	8 rpm
fine sand	8	3.0	15	40	1526	1187	1257	1274
fine sand	8	3.0	15	55	536	374	409	424
fine sand	8	3.0	15	100	196	93	83	201
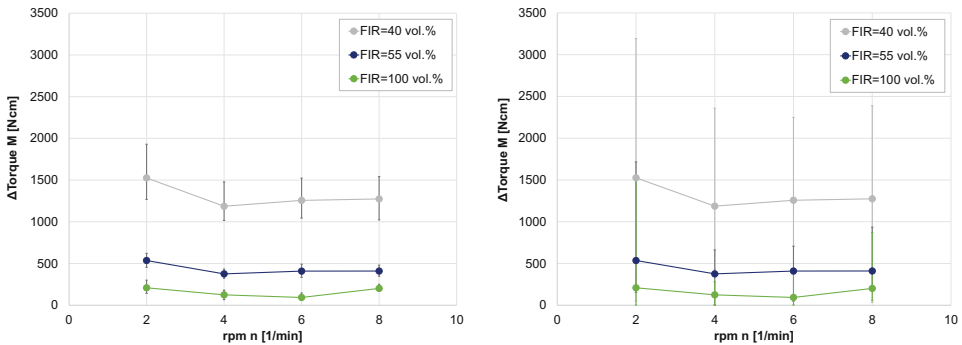
Fig. 4.55 Representation of the median and the 1st and 3rd quartile of the measured torques over the speed of the ball rheometer in the COSMA large-scale test rig (left) and representation of the scatter range of the measured values of the differential torque (right). [36]

To generate rheological flow curves with the ball rheometer in the COSMA large-scale test facility and thus also determine the yield point of conditioned samples, a complex calibration of the ball rheometer is required, e.g. according to the procedures of Galli (2016) [40] with a rheologically defined calibration medium.

Overall, the large-scale rheological investigations show that a rough qualitative assessment of the degree of conditioning is possible with the experimental setup used, but that the system has weaknesses regarding the sensitivity of the measurements and in control. Figure 4.55, right, shows the scatter of the measured values from the minimum value to the maximum value of the differential torque. The overlap of the individual scatter ranges for the respective speeds is clearly visible so that, for example, a differential torque of 1000 Ncm at a speed of 2 rpm can be covered in all three measurement series. To generate torque curves over the speed or flow curves, a great deal of effort is required in the preparation and execution of the tests as well as in the test evaluation. By using an electric motor, a more sensitive data recording could be achieved. In addition, by installing an electric motor, the complete rotation of the rheometer of 360° can be realised.

4.6.6   Displacement-Controlled Penetration Test Device – Results

Similar to the Kelly-Ball Test [4] or the Fall Cone Test [31] the test results, conducted with the new penetration test, show that the correlation between penetration resistance and consistency of cohesive soils is possible. Consistency and the resulting indentation resistance have a non-linear relationship. Depending on the consistency, the expected penetration stresses on the test cylinder can be approximated via an exponential function (Fig. 4.56, left). Penetration tests under pressure conditions have also shown that the external pressure has no qualitative influence on the measurement results. Only the penetration stresses are increased by a factor of 1.5 on average (Fig. 4.56, right and Fig. 4.57).
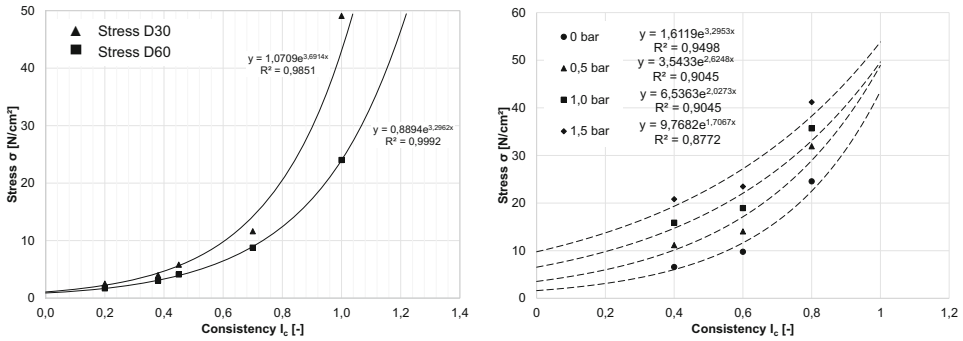
Fig. 4.56 Stress as a function of consistency using two different sized cylinders (D30, D60) (left), Stress as a function of consistency as well as external pressure (right) [94]
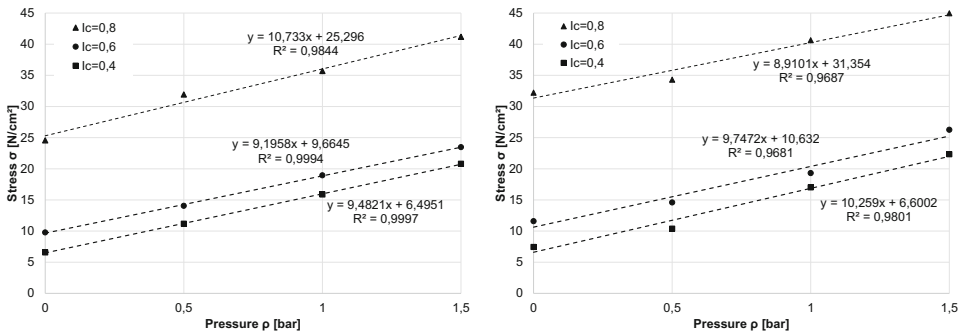
Fig. 4.57 Stress as a function of external pressure and consistency, Soil: Clay/Marl (left), Clay (right). Change of material properties [94]

By evaluating and analysing the test results, further correlations between plasticity and the corresponding measured penetration stress can be established (Fig. 4.56, right). By interpreting the measured data, the change in material properties from a non-flowable to a more flowable excavated material that may no longer be prone to sticking can be recognized. This is shown both by the results as a function of consistency and by the results as a function of plasticity, see (Fig. 4.57).

4.6.7 Development of New Conditioning Agents – Soil Conditioning Using High-Density Foam

Another study deals with the expansion of the application range of EPB tunnel boring machines through the development of a new conditioning agent or the procedural production of a foamed suspension. The test results obtained were compared with different conditioning methods, including a non foamed high density slurry (HDS) with a density
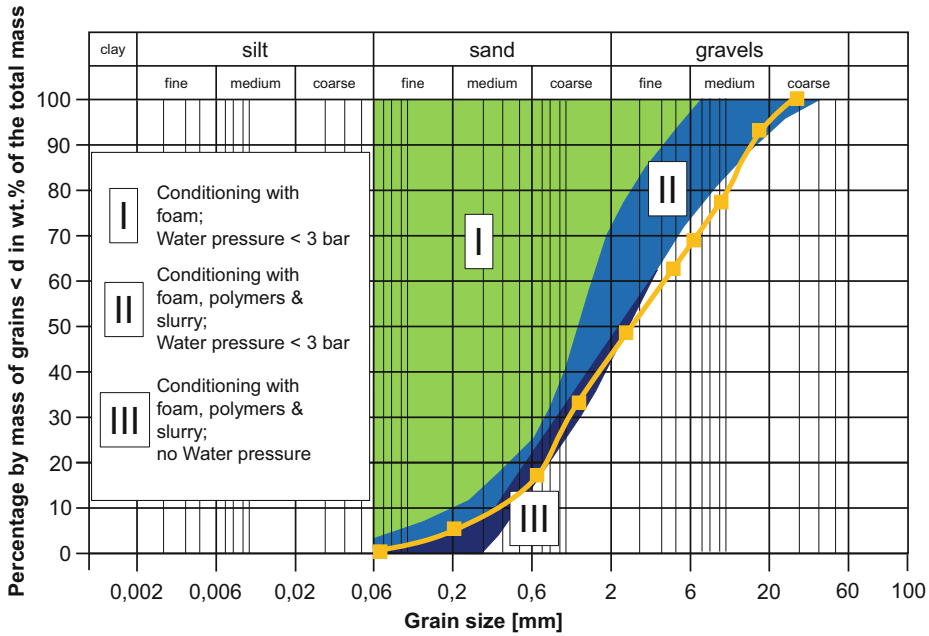
Fig. 4.58 Grain size distribution of the examined soil added in the application range according to [16]
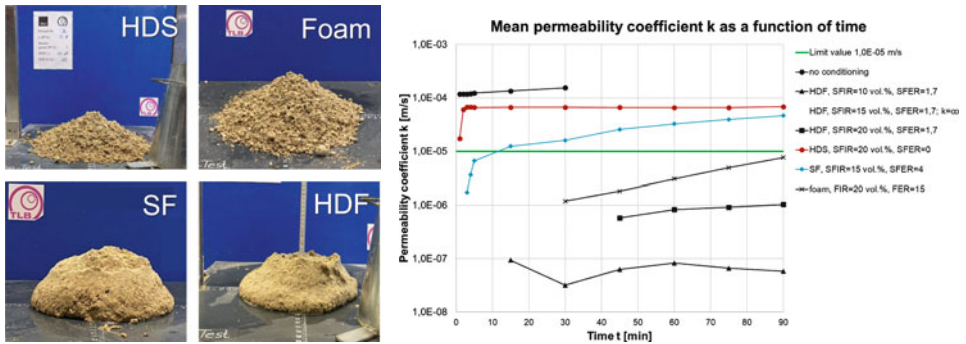
Fig. 4.59 Slump test for the conditioning methods investigated (left), water permeability for the conditioning methods investigated (right)

of $\rho = 1.7$ g/cm^3, foam and slurry foam (SF). The aim was to condition, i.e. ensure workability and reduce water permeability of, a soil on the edge of the application range of EPB shields with soil conditioning. Figure 4.58 shows the grain size distribution as well as the range of application of EPB shields according to Budach (2012) [16]. Figure 4.59 shows on the left selected photos of the different conditioning methods and on the right the results of the permeability tests.

Table 4.4 Recommendation matrix for the use of Foam, Slurry Foam, High Density Foam and High Density Slurry as conditioning agents for coarse soils while ensuring workability and compliance with permeability limits

Conditioning/ Criterion	none	High Density Slurry (HDS)	Foam	Slurry Foam (SF)	High Density Foam (HDF)
workability		×	(✓)	(✓)	✓
permability	×	×	(✓)	×	✓

×: not fulfilled; (✓): fulfilled with restrictions; ✓: completely fulfilled

In the tests, the conditioning of coarse and highly permeable soils with a foamed high-density suspension was able to fulfil both the criteria regarding workability and the limit values for water permeability (see Table 4.4). In particular, large reserves could be created in the reduction of water permeability, which can be particularly useful in the case of unplanned shutdowns of the TBM and high water pressures.

4.7   Determination of the Transient Rheological Parameters of Bentonite Suspensions

Bentonite suspensions are the supporting medium for stabilising the tunnel face during soil excavation in slurry shield tunneling. Their rheological properties are largely determined by the solid content of dispersed bentonite particles in the carrier medium water. The support mechanism is based on an equilibrium principle in that the suspension is pressed into the pore space of the soil under an adapted hydrostatic support pressure. This reliably counterbalances the acting groundwater pressure and earth pressure [78].

Support pressure transfer occurs via various mechanisms on the microscale, which lead to changes in the soil mechanical and hydromechanical parameters of the ground and the rheological parameters of the support medium (macroscale). The application of the supporting pressure provokes various reactions: With pressure-induced suspension penetration, a flow of the existing pore fluid is generated in the pore space. Due to the suspensions yield point, shear stresses are transferred to the grain surfaces, which act against the direction of flow. At the same time, bentonite particles from the suspension are deposited on the inlet surface to the grain structure and at pore throats. As a result, the permeability of the soil within the penetration zone decreases and the flow velocity reduces until the suspension finally stagnates in the pore space. The support pressure is transferred to the tunnel face as a reaction from the combination of flow pressure, grain-to-grain pressure and fluid pressure. As tunneling continues, the respective proportions change cyclically in the course of soil excavation at the tunnel face [78].

The incorporation of bentonite particles in the pore space is the result of filtering these particles out of the suspension. As the flow through the pore space progresses, the solid content of dispersed particles in the suspension decreases continuously. Since the rheology

of the suspensions is determined by the bentonite content, the flow behavior changes fundamentally with this decrease. If the solid content in the suspension falls below a certain value, the bentonite suspension with non-Newtonian flow behavior changes into a fluid with Newtonian properties. In this case, the special rheological properties of yield point and thixotropy would be lost.

Bentonite suspensions are non-Newtonian fluids with yield point and structurally viscous, thixotropic flow behavior. Structural viscosity describes the decrease in viscosity with increasing shear rate. Time-dependent thixotropic behavior shows an increase in viscosity with decreasing shear rate. This behavior is reversible and determined by the intensity and duration of an induced shear rate. The decrease in viscosity arises from a structural change in the fluid, which ensures that the individual fluid particles slide past each other more easily. In non-Newtonian fluids, the viscosity is not constant [78].

The traditional predominant models for describing the flow behavior of bentonite suspensions include the Bingham and the Herschel-Bulkley model. However, none of these models is able to represent the full spectrum of bentonite suspensions, as either aspects of shear-thinning behavior are omitted or the determination of the yield point is inaccurate. These errors are exacerbated by the fact that the measuring techniques and equipment used do not fully account for the thixotropic effect of the suspensions [63].

For Newtonian fluids (viscous, no yield point, no thixotropy), there is a linear relationship between the shear stress τ and the shear rate $\dot{\gamma}$ via the constant proportionality factor viscosity η [67],

$$\tau = \eta \cdot \dot{\gamma}. \tag{4.31}$$

The shear stress is the force referred to a surface whose direction is parallel to the surface of attack. The shear rate is the shear velocity in a rectilinear layer flow [106].

According to DIN 1342-3 [107], the Herschel-Bulkley model is used to describe non-Newtonian flow behavior. This describes flow curves with yield point and variable viscosity, whereby the time dependence or thixotropy is not recorded. The Herschel-Bulkley model assumes that the viscosity does not remain constant after the yield point of the suspension has been exceeded in relation to the shear rate and shear stress. The model is composed of three nonlinear parameters,

$$\tau = \tau_0 + k \cdot \dot{\gamma}^n, \tag{4.32}$$

with τ as shear stress, τ_0 as flow index, k as "consistency index" [Pa s^n], $\dot{\gamma}$ as shear rate and n as flow index.

Thixotropy and yield point are usually considered as separate phenomena, although they show a tendency to occur in the same fluid. There is general consensus that they are caused by the same basic physics. Accordingly, thixotropy is attributed to the same microstructure that exists in a fluid and resists large rearrangements (for which the yield point is responsible) until it is broken by flow. Although the yield point, viscosity and
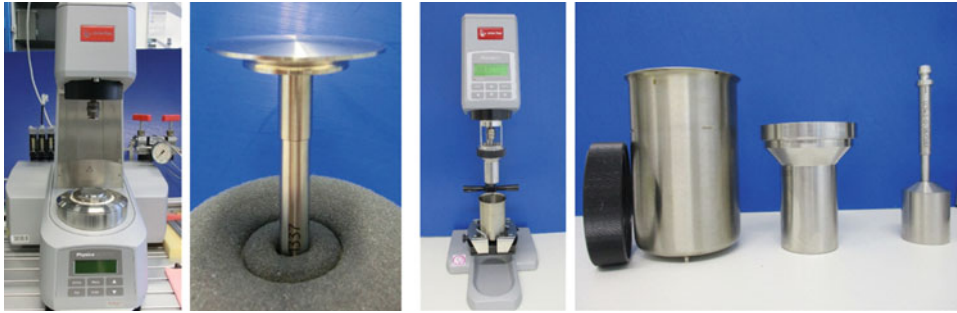
Fig. 4.60 Rotational and oscillatory rheometers with incorporated measuring geometry

thixotropy parameters are determined separately, they influence each other in their characteristics [66, 70].

The rheological properties of the bentonite suspensions used in the column test (Section 4.3.2) were determined with rotational and oscillatory rheometers (Fig. 4.60). The solid concentration of the suspensions was systematically changed. In the rotational test, a concentric cylinder geometry according to the Couette system was used, and in the oscillatory test, a cone-plate geometry was used [72, 93].

For the experimental investigations, various measurement programs were developed that are capable of mapping the rheological properties of the suspensions and their changes with decreasing solids content. The aim was to detect the transition from non-Newtonian to Newtonian flow:

- Flow behavior by means of a standard flow curve via specification of the mechanically induced shear rates: The flow curve is described by an up-sweep region with increasing shear rate and a subsequent down-sweep region with decreasing shear rate. A discernible loop between the up-sweep and down-sweep regions characterizes the thixotropy effect present.
- Thixotropy test: shear jump with recovery: At an initially low shear rate, the viscosity value in the fluid at rest is determined. This is destroyed by the subsequent high shear rate input and rebuilt in the subsequent quiescent mode. The basic ability to rebuild the internal structure and the time required can be evaluated.
- Determination of elastic and viscous modulus by amplitude sweep test: The oscillation test investigates the development of the storage modulus G' and the loss modulus G'' with simultaneous acquisition of the shear stress τ. The storage modulus G' describes the elastic behavior and the loss modulus G'' the viscous behavior of the test sample. In addition, the yield point of the suspension can be determined at the transition point between elastic and plastic behavior [51, 60].

The combination of these three methods allows an in-depth analysis of the transient rheological properties of the suspensions.
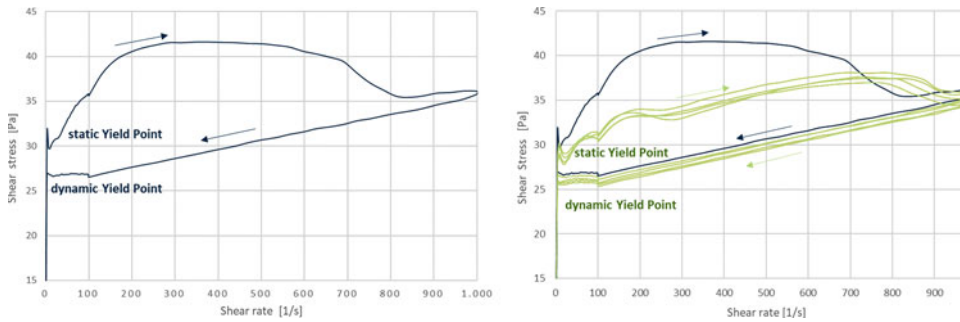
Fig. 4.61 Flow curves of a bentonite suspension with solid content 60 kg/m^3: (left) first up-sweep and down-sweep measurement (cycle 1 – blue), (right) subsequent cycles 2, 3, 4, 5 (green) with identical shear rate range (up-sweep and down-sweep) as repeated measurements

Flow curve: A particular challenge in determining the rheological properties of bentonite suspensions is the markedly time-dependent flow behavior. Thixotropic solidification is defined as the increase in the yield point of a thixotropic liquid during the rest period after completion of a flow movement. It is therefore reversible [63]. The yield point has its minimum value, the dynamic yield point, at the end of the flow movement and approaches its maximum limit value, the static yield point, asymptotically during the rest period. The limit values and the course of the curve are basically temperature-dependent. Figure 4.61 shows the differences in the level of the measurable yield stresses (static and dynamic) over different measuring cycles.

The objective of this measurement program is to investigate the flow behavior of the bentonite suspensions at very low and very high shear rates. The bentonite suspension is sheared from low to high shear rate linearly increasing for the upward curve. Starting from the high shear rate, the suspension is sheared linearly decreasing to the low shear rate for the downward curve. With the aid of the flow curve, it is possible to analyze the flow behavior of the suspension over the entire shear process using various flow and viscosity models.

In Fig. 4.62 (right), the logarithmic axis view reveals the irritations of the suspension 20 kg/m^3 for the shear stress curve and viscosity curve (up-sweep region), slight irritations are visible for 30 kg/m^3 for the viscosity.

Thixotropy test: For carrying out a thixotropic test, the method shear jump with recovery was chosen as a rotational test with specification of the shear rate [67]. The measuring program consists of three sections. The first reference section is characterized by resting shear stress at a low shear rate. A constant viscosity value is aimed for, which will later be adopted as a reference value during structural reconstruction. In the loading section, a high shear stress is introduced into the suspension. The gel character of the suspension from the resting phase is converted into the sol character by changing the internal structure. This results in a constant equilibrium state between the shear force and the flow resistance of
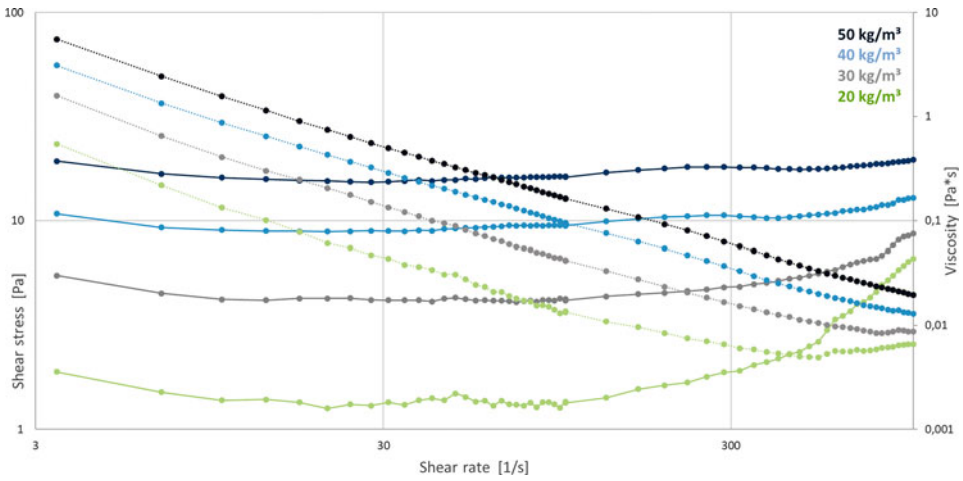
Fig. 4.62 Results of measuring program in logarithmic scale: flow curve (continuous lines), viscosity curve (dotted lines)

the sample. Finally, the structure recovery section is performed, which is again characterized by a low shear stress. The aim of the measurement program is to determine the time required for a suspension to fully regenerate–or whether a thixotropy effect is measurable.

This thixotropy test evaluates the proportional regeneration of the suspension during a specified time of the recovery phase. The viscosity value read is compared to the resting viscosity from the reference phase, which represents the 100 percent viscosity values. Figure 4.63 shows the structure recovery evaluation. At time t_1, the curve shows a viscosity value η_1, which corresponds to 100 percent structure reconstruction. The viscosity value η_2 corresponds to the percentage structure reconstruction at time t_3, at the end of the recovery phase. The objective of this evaluation is to determine the time of structure reconstruction at the end of the recovery phase. In the positive case, the tested fluid shows a thixotropic reconstruction.

Amplitude sweep method: Within oscillation tests, the upper cone geometry oscillates while the lower plate geometry remains rigid. Doing so, the test sample is subjected to sinusoidal deformation with small amplitude. In the amplitude sweep method, the deformation of the suspension is determined by measuring the shear stress τ, the storage modulus G' and the loss modulus G''.

The storage modulus G' is a measure of the deformation energy stored in the sample material during the shear process. According to [67], fluids that fully store deformation energy exhibit fully reversible deformation behavior. They are present in unchanged form after a load/unload cycle. The storage modulus G' represents the elastic behavior of a specimen.

The loss modulus G'' is a measure of the deformation energy consumed in the specimen material during the shear process and lost to the test specimen afterwards. Mezger [67]
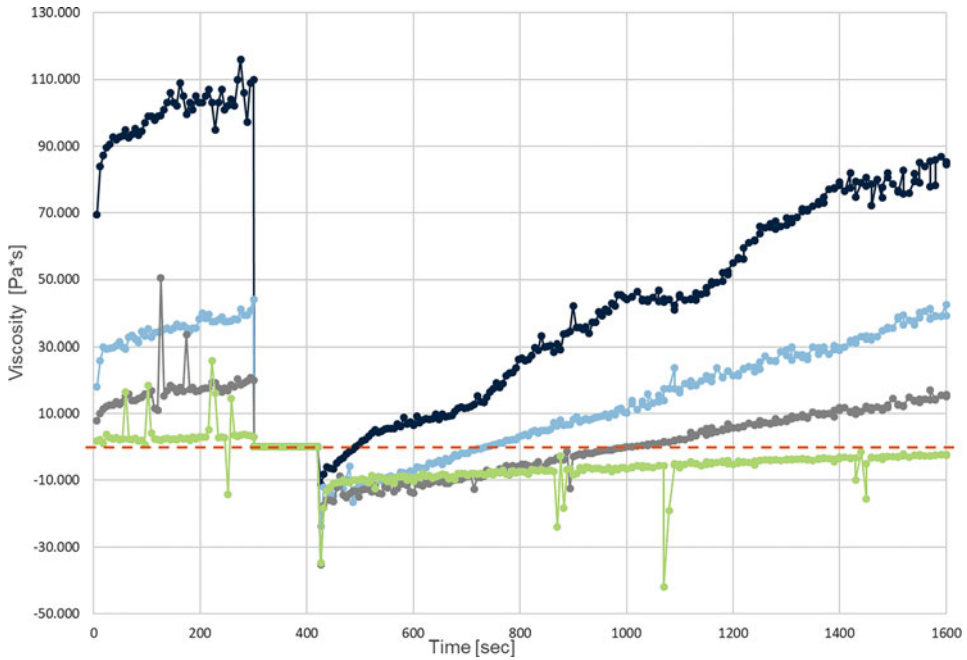
Fig. 4.63 Results of measuring program shear jump with recovery

describes fluids that lose energy during the shear process exhibit irreversible deformation behavior. They are present in altered form after a load/unload cycle. The loss modulus G'' represents the viscous behavior of a sample. Loss factor $\tan \delta$ is the quotient of the lost and stored deformation energy and gives the ratio between the viscous and the elastic part of the viscoelastic deformation behavior [67]. We have

$$0 \leq \tan \delta \leq \infty, \tag{4.33}$$

$$\text{with} \quad 0 \leq \delta \leq 90°, \tag{4.34}$$

$$\tan \delta = \frac{G''}{G'}. \tag{4.35}$$

It is valid that

- $\tan \delta > 1$ (with $G'' > G'$) for a fluid state of the sample,
- $\tan \delta < 1$ (with $G'' < G'$) for a solid state of the sample and
- $\tan \delta = 1$ (with $G'' = G'$) at the transition point of solid-to-fluid state of the sample.

The storage modulus and loss modulus are adapted to evaluate the yield and yield point. A solid state must be present in the linear viscoelastic range to determine the yield point. At the transition pint, the aggregate state of the sample changes from the solid state to the fluid state. This shear stress value corresponds to the true yield point of the sample (see Fig. 4.64).
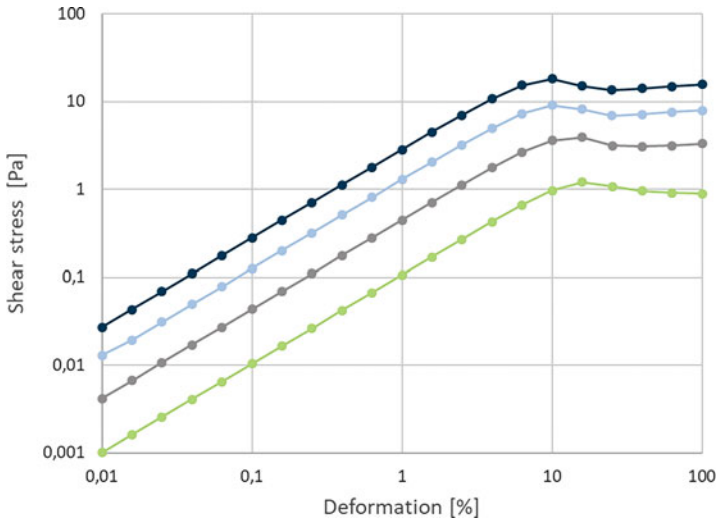
Fig. 4.64 Results of the measurement amplitudes sweep curve: Shear stress over deformation

4.8 TBM-subsoil Interactions Considering the Influence of Subsystems

The process of tunnel excavation and the corresponding hydro-mechanical coupled interactions between TBM, tunnel structure and soil impose complex stress patterns, pore pressure evolution and flow regimes in the vicinity of tunnel (e.g. near-field). In case of mechanized tunneling, these interactions are mainly induced by the subsystems such as overcut, shield conicity, face pressure and tail void grouting in the near-field of the tunnel. For instance, the pore pressure contour in the vicinity of the TBM obtained from a finite element simulation of mechanized tunnel excavation in a fine-grained soil with low hydraulic conductivity (e.g. 1×10^{-9} m/s) as shown in Fig. 4.65 shows a significant evolution of the pore pressure ahead of the Tunnel as well as around the shield tail.

Such evolution of the pore-pressure, as shown in Fig. 4.65, has been observed through various in-situ measurements and monitoring data. For instance, the field measurements carried out by [9, 10, 48] have shown the stresses and pore pressures around the TBM evolve non-monotonously. The main reason for such observation is the stepwise TBM advance that lead to the variation of hydro-mechanical (HM) interactions around the TBM upon evolution of the arching mechanism by TBM advance, distinct moving and stationary pressure transfer mechanisms to the soil during drilling and standstill phases, filter cake formation in front of the cutting head by the slurry shield tunneling and infiltration at the shield tail due to the deposition of the grout fine particles at the annular gap. In order to properly simulate these complex coupled interaction in the tunnel near-field, it is essential to conduct a coupled HM analysis in conjunction with an adequate constitutive
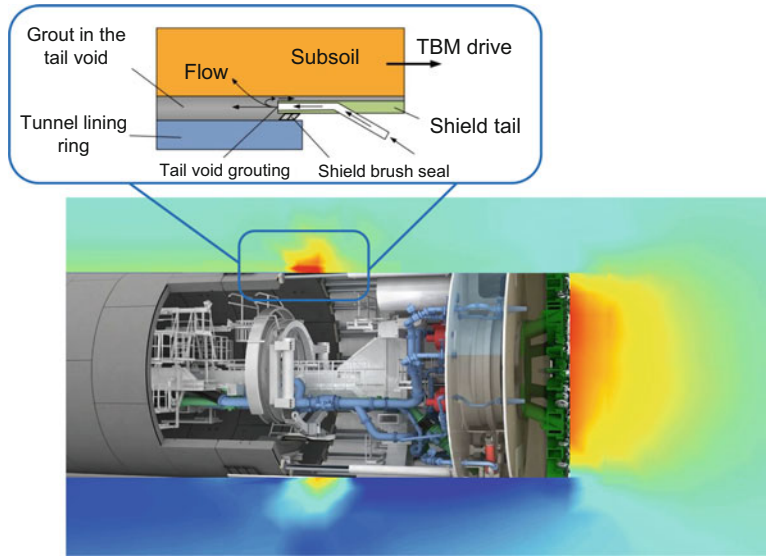
Fig. 4.65 Evolution of pore pressure field in vicinity of TBM in a low permeable ground

model that is capable of accounting for the soil behavior under the complex effective stress path. However, on one hand, the use of advanced soil models is crucial for enabling an accurate prediction of system response; on the other hand, use of an advanced constitutive model often entails exact knowledge about enormous constitutive parameters, where some parameters are difficult to obtain due to the complex and costly in-situ or laboratory tests. For instance, previous studies showed that calibration of advanced constitutive models to model the Western Scheldt tunnel in the Netherlands [118] as well as the Milan metro line 5 [92] requires comprehensive investigations that could not be achieved without monitoring data. In order to overcome this challenge, development of hierarchical constitutive model families that consist of models with different features and levels of sophistication can allow activation of particular features in a specific subdomain without a need to re-calibrate the model parameters can significantly reduce the computational cost and improve the prediction quality.

4.8.1   Hierarchical Constitutive Modeling

The level of the sophistication of a constitutive model can significantly affect the complication in the calibration of the model parameters. Commonly, the basic constitutive models include a few number of parameters that can be calibrated trough standard laboratory tests. Moreover, various investigations are available in the literature in which the possible range of the parameters for different types of the soils and even empirical corre-

lations to the field tests are provided. Therefore, the model parameters can be calibrated with a high degree of certainty, however, the basic models are often unable to realistically represent the behavior of the system. In contrast, advanced constitutive models are capable of predicting the soil behavior specially under complex hydro-mechanical boundary conditions, while the calibration of their enormous parameters require advanced laboratory testing procedure. Additionally, the lack of literature about the model parameters which sometimes have no physical definition lead to high degree of uncertainty in the parameters and correspondingly in the model predictions. To overcome this obstacle, adaptive constitutive modeling is an effective approach to apply advanced models only to the near-field of the tunnel with complex stress path while the rest of the model (i.e. far-field) is modelled by adopting a simple model. In order to facilitate the constitutive model exchange and the corresponding internal variable evolution during the TBM movement, development of hierarchical constitutive model families that consist of consistent models with different features is an essential choice.

In case of mechanized tunneling in granular subsoils, several studies [112, 117] have indicated that the hierarchical model family including the Mohr-Coulomb model as the basic one, hardening soil model as the intermediate one and the hardening soil model with the small strain stiffness as the advanced model in this family can be considered as an adequate hierarchical model in which several soil features such as soil damping and shear modulus degradation upon shear straining, stress dependency of soil stiffness, gradual mobilization of friction and dilation angles with stress evolution, distinct stiffness for primary loading, oedometric loading and un-/re-loading can be taken into consideration. Nevertheless, these features can be deactivated by employing the Mohr-Coulomb model through the basic model in this family.

The behavior of natural clays is strongly affected by effects of anisotropy and structure. The anisotropy due to the fabric of a clay (i.e. spatial arrangement of the particles or aggregates) implicates that the mechanical behavior of the clay depends on the loading direction. The natural structure of the clay due to the inter-particle bonding leads to an increase in stiffness and strength, which may partially or fully eliminate due to destructuration upon straining [21]. The behavior of such natural structured clays becomes even more complicated when subjected to non-monotonic that may lead to inelastic and nonlinear response even at small load increments.

To address the complex constitutive behavior of natural clays, a constitutive model family based on the critical state theory was implemented in a hierarchical framework. This model family is represented at its simplest end by the Modified Cam-Clay model (MCC) [82] in the frame of conventional elastoplasticity (stress dependent elasticity, isotropic hardening/softening upon volumetric plastic staining). As the second member of this family, SANICLAY [23, 24] model is that additionally accounts for intrinsic and stress-induced anisotropy by incorporating rotational and distortional hardening rules (MCC + anisotropy). The SANICLAY-D [99] that is capable of addressing the destructuration upon degradation of inter-particle bonding due to volumetric and deviatoric plastic strain (SANICLAY + destructuration). As the most sophisticate member of this
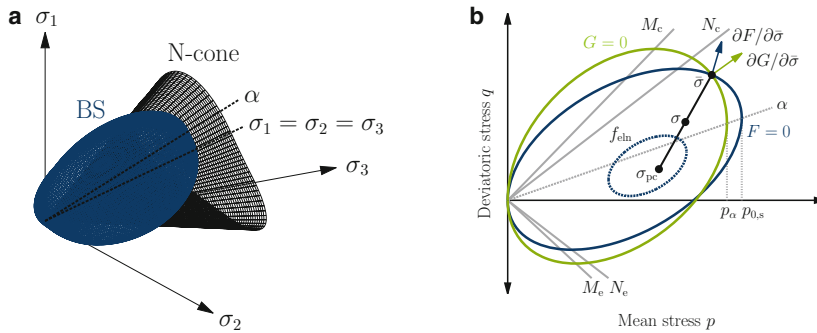
Fig. 4.66 Schematic view of **a** anisotropic bounding surface (BS) and Lode angle dependent N-cone in principal stress space, **b** rotated bounding surface (F), plastic potential surface (G) and elastic nucleus (f_{eln}) in p, q-stress space

family, the SANICLAY-B-D [7, 95] is developed in the frame of bounding surface plasticity (BSP) to address the degradation of the stiffness and accumulation of the strain upon to non-monotonous loading (SANICLAY-D + Bounding surface plasticity). In the most advanced SANICLAY-D-BSP model of this family, an elastic nucleus is incorporated to allow simulation of elastic behavior, while the size of elastic nucleus is controlled through a model parameter.

In the collaborative research center 837, this hierarchical constitutive model family is efficiently and robustly implemented in a three-dimensional finite element software. Additionally, to enable computationally stable numerical simulations of the mechanized tunneling process, an Euler algorithm with automatic subdivision of the size of the strain increments (substepping) and automatic error control [96] was used for the explicit time integration of the constitutive laws of the bounding surface model. Moreover, the Lode angle θ dependency of the bounding surface F, plastic potential surface G and critical stress rations M and N were incorporated to the model while the implementation was carried out in a hierarchical framework, including a family of constitutive models with different features and level of sophistication. The development of such hierarchical model family enabled (a) systematic calibration of the based on different laboratory tests as presented in [7], and (b) activation and deactivation of the model features without a need for further calibration or parameter adjustment. Figure 4.66 shows the shape of the bounding surface, N-Cone (Lode angle dependent critical state surface) and plastic potential surface for the enhanced model.

The parameters of the model family were calibrated for a well-studied natural structured Onsøy clay from Norway on the basis of a systematic protocol for the hierarchical calibration of the enhanced model as shown in Fig. 4.67. By considering the calibration protocol, the essential laboratory tests (e.g. oedometer test, monotonic anisotropically consolidated undrained triaxial tests under compression and extension and cyclic undrained triaxial tests) and the sampling types (e.g. disturbed or intact) required for the calibration

Features of soil behavior	Constitutive model parameters	Laboratory tests	Soil condition
Critical state concept	**Stiffness** κ, λ	**Isotropic** or **1D consolidation** test *(including unloading & reloading path)*	reconstituted
	Poisson's ratio ν	K_0 **consolidation and unloading**	reconstituted
	Critical state M_c, M_e	**Undrained triaxial** tests *(compression & extension)*	structured
	Yield / Bounding surface N, $p_{0,s}$, α_0	**Drained triaxial** tests *(compression & extension)*	structured
Anisotropy	**Rotational hardening** c, x μ_W, β_W c, s, z α_{cs}, c, m, n, μ	**Triaxial** tests *where significant rotation appears*	structured
Structure	**Destructuration** S_{i0}, k_i, A	**Isotropic** or **1D consolidation** test	structured & reconstituted
Non-monotonous response	**Elastic nucleus** s_{eln}	**Triaxial** test *(including unloading & reloading path)*	structured
	BSP - hardening & damage h_0, a_{dam}	**Cyclic** oedometer or triaxial tests	structured

Fig. 4.67 Systematic protocol for the hierarchical calibration of the enhanced bounding surface plasticity model family

of the model features are defined. For this purpose, the laboratory tests on natural Onsøy clay from the Ruhr-Universität Bochum, Norwegian Geotechnical Institute and Karlsruhe Institute of Technology (KIT) [6, 59, 71, 109, 110] were taken into consideration. The constitutive parameters obtained from the calibration of SANICLAY model family for Onsøy clay are listed in Table 4.5.

In this hierarchical model family, deactivation of the any model feature that corresponds to the values listed in the bracket in Table 4.5 would reduce the number of required experiments.

Figure 4.68 show the comparison between the numerical and experimental results for a cyclic undrained triaxial test on Onsøy clay after model calibration based on various types of loading on reconstituted and intact samples. Additionally, to gain a better insight into the large number of constitutive parameters and their possible correlations with respect to the model response at the loading, unloading and reloading states, a global sensitivity analysis carried out based on [87] for small, intermediate and large stress ranges. The results shown in Fig. 4.69 reveal that the stress level and loading condition (e.g. loading and un/reloading) significantly affect the impact of the parameters on the model response.

To assess the influence of the model features on the numerical estimation of ground settlement, a synthetic model of a shallow tunnel with a diameter of $D = 10\,\mathrm{m}$ and $1D$ overburden depth in a homogeneous Onsøy clay under drained conditions along with the

Table 4.5 Parameters of SANICLAY model family calibrated against different types of laboratory tests on structured Onsøy clay (values in the parentheses used to inactivate particular features of the model)

Type	Parameter	Unit	Value	Description
Critical state soil mechanics MCC	κ	–	0.012	Elastic swelling parameter
	ν	–	0.3	Elastic Poisson's ratio
	λ	–	0.164	Elastoplastic compression parameter
	M_c	–	1.44	Critical stress ratio in compression
	M_e	–	0.83	Critical stress ratio in extension
Non-associated flow rule	N_c	–	1.2	Defining shape of BS in compression
	N_e	–	0.7	Defining shape of BS in extension
Initial conditions	e_0	–	varies for each test	Initial void ratio
	K_0	–	0.5	Coefficient of earth pressure at rest
	$p_{0,s,\text{init}}$	kPa	80	Defining initial size of BS
	YSR	–	1.0	Yield stress ratio
Anistropy and rotational hardening	α_0	–	0.24 (0)	Defining initial rotation
	c_α	–	100 (0)	Controlling rate of rotation
	$s_\alpha = z_\alpha$	–	5.7 (0)	Controlling bounding attractor
Structure and destructuration	$S_{i,0}$	–	8 (1)	Defining initial structure
	k_i	–	1 (0)	Controlling rate of destruction
	A	–	0.5	Controlling fraction of plastic strains
Bounding surface plasticity	s_{eln}	–	1.1 (100)	Defining size of elastic nucleus
	h_0	–	250 (10,000)	Defining initial shape hardening stiffness
	a_{dam}	–	25 (0)	Controlling rate of stiffness degradation
Additional parameters	γ	kN/m³	16.35	Density
	γ'	kN/m³	6.35	Density below the groundwater table
	k_f	m/s	1×10^{-9}	Permeability

previously calibrated parameters was developed. The length of the TBM and tubing rings are assumed to be equal to 10 m and 2 m, respectively. The conicity of the shield is modelled with a contraction factor which develops from 0% at the tunnel face to 0.5% at the shield tail. The face support pressure at the tunnel crown s_{crown} and invert s_{invert} are assumed to be 85 kN/m² and 248.5 kN/m², respectively. In this model, the backfill grouting pressure is applied as a normal surface pressure equal to 135 kN/m² in the tunnel crown and 255 kN/m² in the tunnel invert in the shield tail. The ground water table is assumed to be 2 m below the ground surface. To assess the impact of overconsolidation ratio (OCR), two scenarios were considered as the normally consolidated (NC) or slightly overconsolidated (OC) subsoil with OCR=1.0 and 1.3, respectively.

The comparison of the settlement trough in the tunnel longitudinal and transversal directions shown in Fig. 4.70. As seen, the MCC model incorporating isotropic hardening resulted in the least ground settlements with $u_{\text{v,max MCC}} = 6.6$ cm for the assumed condition (i.e. horizontally oriented tunnel in a homogeneous stratum). In this idealized condition,
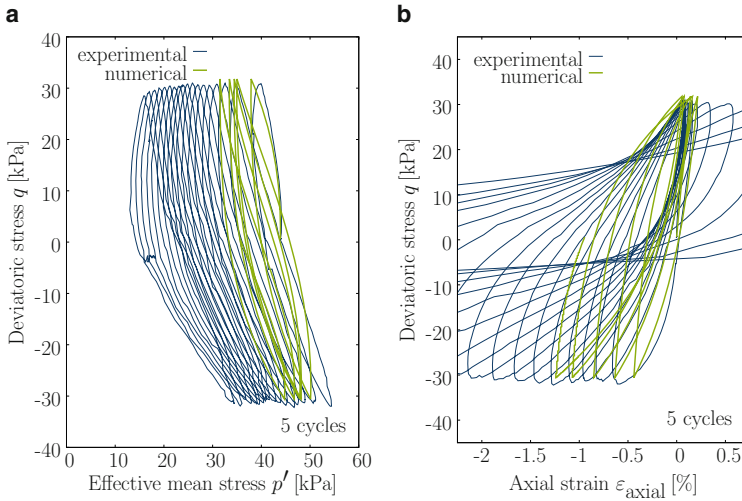
Fig. 4.68 Cyclic undrained triaxial test on Onsøy clay. **a** Effective stress path, **b** stress-strain behavior

Fig. 4.69 Sensitivity of vertical strain to model parameters in an oedometer test
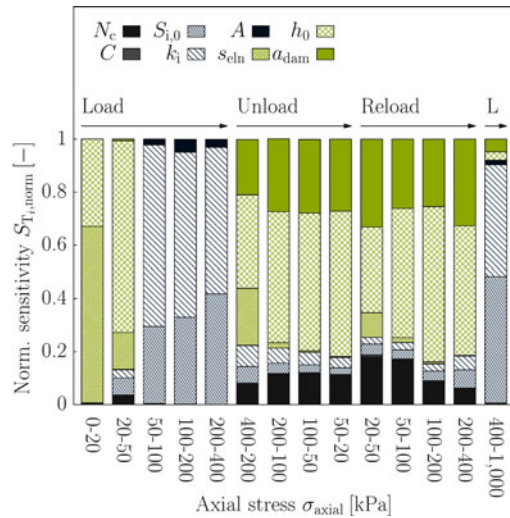
the anisotropy of the soil has a minor influence on the surface settlements. However, the consideration of destructuration seems to be essential for a realistic prediction of the surface settlements because significantly larger deformations have been observed at the soil surface when these features have been accounted. Since the generation and dissipation of the excess pore pressure has not been considered in these drained analyses (i.e. no consolidation), the influence of bounding surface plasticity is found to be relatively small; however, the bounding surface plasticity feature of the model led to considerably larger settlements in case of slightly OC natural Onsøy clay.
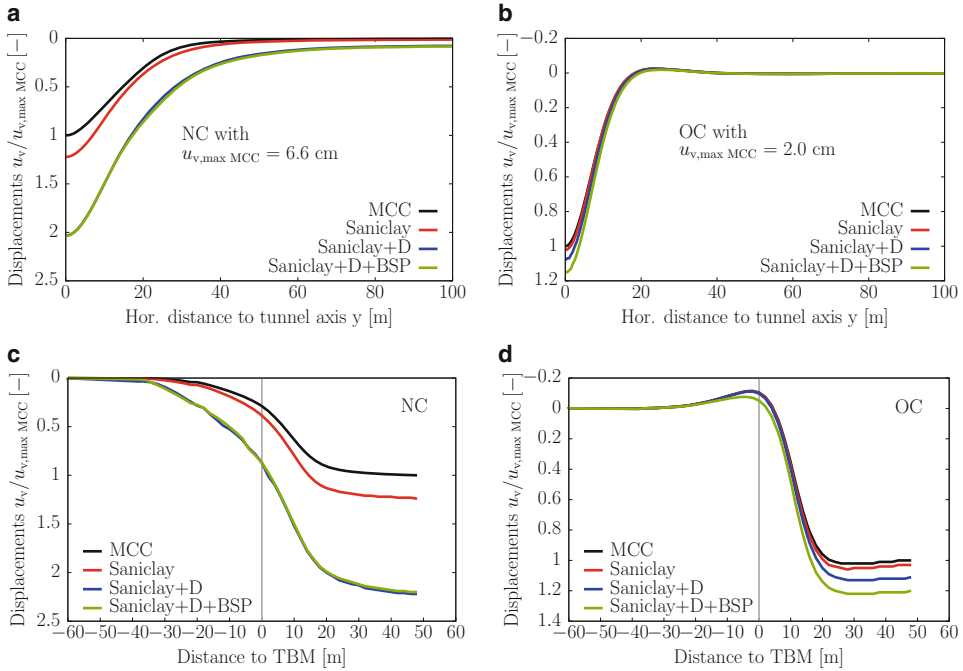
Fig. 4.70 Numerical estimation of surface settlement in a homogeneous Onsøy clay layer [103]. **a** Transversal direction OCR = 1.0, **b** transversal direction OCR = 1.3, **c** longitudinal direction OCR = 1.0, **d** longitudinal direction OCR = 1.3

4.8.2 Constitutive Model Adaption for Mechanized Tunneling

The novel concept of constitutive model adaption for mechanized tunneling was proposed by [57], who applied the Hardening Soil model family (HSsmall, HS and MC) to shallow and deep tunnels. The main objective in this concept was to develop a framework that allows progressive exchange between basic and advanced constitutive models and vice versa in the model upon TBM advance. Results of this study showed that the numerical model can predict the system behavior in terms of tunnel deformation, surface settlement, and stress redistribution in the vicinity of the TBM when the advanced model (i.e. HSsmall model) is employed in the near-field of the tunnel with an approximate size of 2–3D, where D states the diameter of the tunnel. Figure 4.71 illustrates the distribution of the plastic strain components in the soil for a shallow and deep tunnel with depth of 1D and 5D ($D = 8.5$ m) in a typical granular soil with a friction angle of 35 degrees where the advanced model is assigned to the entire domain. As seen, the excavation of the tunnel leads to a significant plastic strain evolution in the near-field of the tunnel while the rest of the model remains almost uninfluenced. Therefore, the use of the more sophisticated model can be advantageous in the TBM near-field because most of the advanced features of the sophisticated models get activated upon plastic straining while the rest of the model can be adequately simulated by adopting the basic constitutive model.
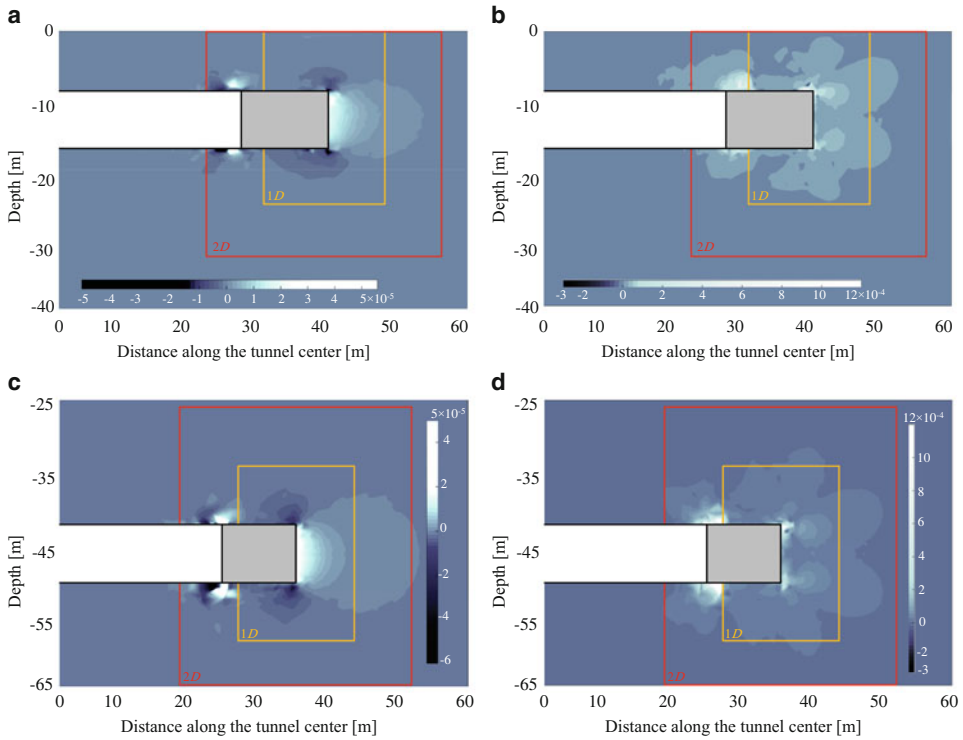
Fig. 4.71 Plastic strain distribution during TBM excavation [57]. **a** volumetric strain in shallow tunnel, **b** deviatoric strain in shallow tunnel, **c** volumetric tunnel in deep tunnel, **d** deviatroic strain in deep tunnel

Additionally, [57] indicated that considering adaptive constitutive modeling approach in mechanized tunneling can also reduce the uncertainty in the numerical predictions due to uncertain constitutive parameters. This observation is attributed to the fact that the advanced constitutive models, despite their capabilities to better estimate soil behavior under complex stress path, have more constitutive parameters that have to be determined through complex experimental tests. Accordingly, the uncertainty or error in the calibration of these parameters can be directly propagated into the tunnel simulation results. In contrast, basic models such as Mohr-Coulomb (MC) and Modified Cam-Clay (MCC), despite inability to offer reliable stress-strain soil behavior under complex load conditions, have fewer parameters which can be directly determined from standard laboratory tests with high level of certainty. To study this phenomena, a series of numerical analyses carried out for a shallow tunnel with an embedment depth of $1D$ (D=8.5 m) by assuming three different numerical scenarios as: (a) basic MC model in the entire domain, (b) advanced HSsmall in the entire model, and (c) advanced HSsmall model adopted to $2D$ around the TBM (i.e. near-field) and basic soil model in the TBM far-field. In these analyses, a normal distribution is considered to highlight the uncertainty of the parameters. For both basic and

advanced constitutive models, the stiffness and shear strength parameters are defined with 10% coefficient of variation (COV) whilst a larger COV of 20% is assumed for the G_0^{ref} and $\gamma_{0.7}$ because of complex experiments needed to determine these parameters. Results showed that the model adaption approach improves the error in settlement prognosis reduced from 45% for basic model to 4% for model adaption while the uncertainty of model prediction reduced from 39.7% for the advanced model to 30.2% for model adaption. On the basis of these findings, [114] proposed a novel methodology of applying submodeling technique in the numerical modeling of mechanized tunneling, where submodel is a smaller scale cut out of the full scale model in which the more in detail simulations along with higher degree of precision are conducted. In this approach, the submodel represents the near-field around the TBM as considered in adaptive constitutive modeling. In order to analyze the submodel, the nodal displacements are derived from a global model (i.e. full tunnel model with a simple constitutive model) and applied to the boundaries of the submodel. This approach was later enhanced to a so called "hybrid model" in which only the submodel was simulated in a detailed model while the boundary conditions were defined through a surrogate model [116]. As shown in [114, 116], the submodeling approach in the significantly reduces the computational costs and provides realistic prediction of the deformations in the system and lining forces.

4.8.3   Hydro-Mechanical Interactions and Material Property Evolution Around the TBM

The overcut, annular gap and the conicity of the TBM shield cause a volume loss in the soil due to ground movements and effective stress redistributions that leads to ground surface settlements. Additionally, the field observations and monitoring data obtained from in-situ measurements have shown the pore pressure evolution around the TBM in case of mechanized tunneling not only in cohesive soils with low permeability but also in saturated fine grained non-cohesive soils. The main reason for such observation is the stepwise TBM advance and variation of the hydro-mechanical interactions around the TBM (i.e. arching effect, differing moving and stationary pressure transfer mechanism to the soil during TBM drilling and standstill, infiltration and filter cake formation in front of cutting head and at the shield tail). The measurement of pore pressure in font on cutting head and on a segmental lining ring equipped with multitude of pressure sensors during TBM advance in Sophia Rail Tunnel [9, 10] excavated in fine sand and the Crossrail tunnel [108] in clay indicated an apparent pore pressure evolution and correspondingly effective stress variation due to the face support and tail grout pressure ahead and around the TBM. In addition to this phenomena, the hydration of the cementitious annular gap grout as well as transport of fine particles of grout into the surrounding soil (e.g. infiltration) induce time-dependent changes in the permeability of the surrounding soil and the stiffness of the annular gap grout. For a realistic prediction of the system behavior of a tunnel in water-saturated ground conditions, a hydro-mechanically coupled numerical model that accounts
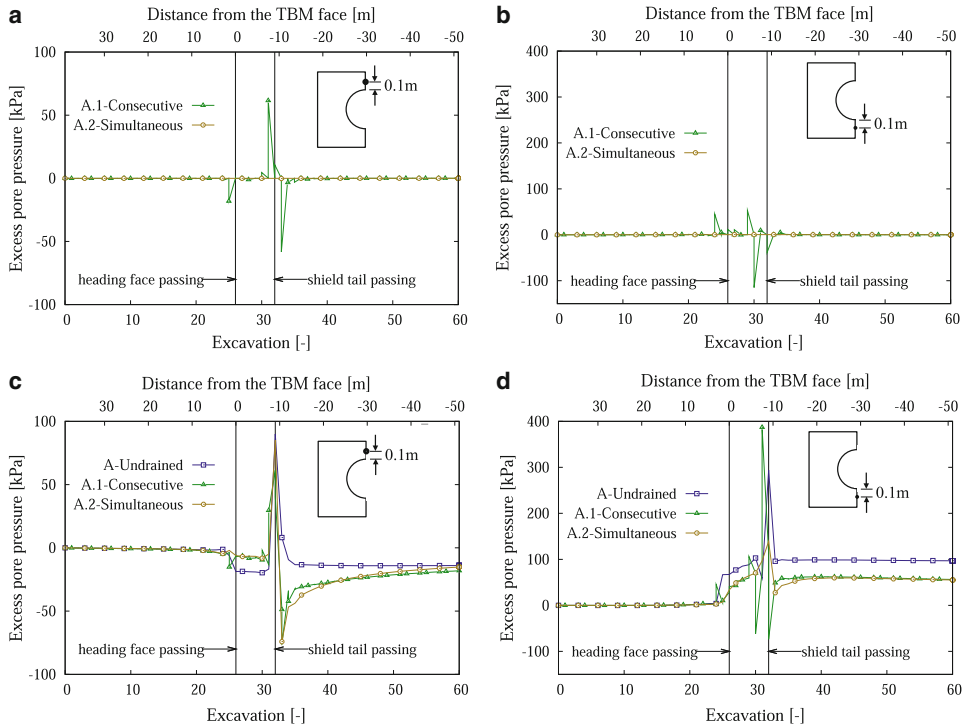
Fig. 4.72 Variation of the excess pore pressure (suction is positive and compression is negative) due to backfill grouting simulated as pore pressure [58]. **a** soil with high hydraulic conductivity 10^{-5} m/sec, **b** soil with low hydraulic conductivity 10^{-9} m/sec

for such phenomena is essential not to only consider the the consolidation process in soil but also to address the parameter evolution in the near field of tunnel [58]. To study the pore pressure evolution and dissipation around the TBM, two consolidation approaches were proposed in [58], where in the consecutive consolidation approach A.1, each excavation step was divided into two numerical calculation phases, an undrained phase for simulation of the drilling step and pore pressure buildup and a subsequent consolidation phase representing the standstill step in which the pore water pressure can dissipate over a specified period of time under constant boundary conditions. In the simultaneous consolidation approach A.2, the drilling and standstill period were each modeled in separate HM coupled numerical calculation phases to enable the consolidation of the soil to take place simultaneously with TBM drilling. In these analyses, the grouting pressure is simulated as predefined hydraulic pore pressure in the annular gap [58]. Results obtained from these consolidation schemes in subsoil with low and high hydraulic conductivity with the primary and oedometric stiffness of $E_{50}^{ref} = E_{oed}^{ref} = 35$ MPa, unloading/reloading stiffness of $E_{ur}^{ref} = 100$ MPa at a reference pressure of $p_{ref} = 100$ kPa and an effective friction angle of $25°$ is shown in Fig. 4.72.
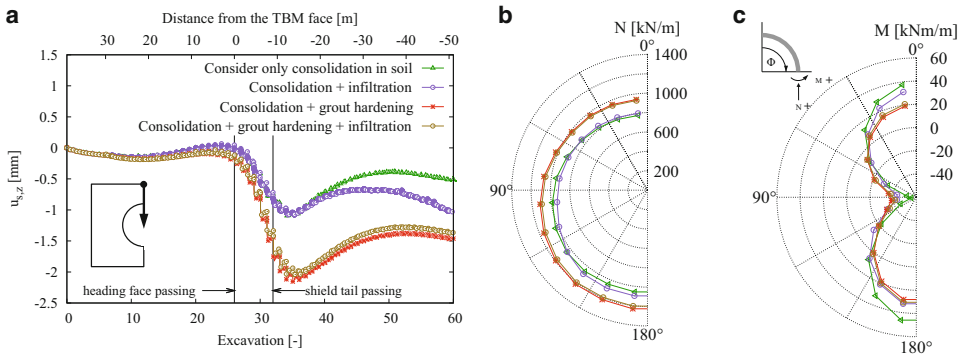
Fig. 4.73 Influence of considering the HM interactions and the corresponding material parameters evolution on the model responses [58]. **a** ground surface settlement along the tunnel, **b** axial forces in the lining, **c** bending moments in the tunnel lining

Although simultaneous consolidation scheme is the most realistic way of simulating a HM process, it is unable to capture the instant generation of excess pore pressure during tunneling in soil with higher permeability for large time step while the TBM advance process has to be divided into significantly small time steps. Due to the computational costs, the alternative consecutive consolidation scheme enables simulation of excavation process with less computational effort in soils with high permeability. Therefore, the consecutive consolidation approach A.1 was chosen for the HM coupled analysis of TBM excavation in non-cohesive granular soil with a hydraulic conductivity of 10^{-5} m/sec. In this model, the time-dependent gap grout hardening process and corresponding stiffness evolution was considered by adopting the mechanical model developed by [88] assuming a final stiffness of $E_{(28\ days)} = 500$ MPa while 65% of the stiffness was obtained in 1 day. The evolution of the time-dependent hydraulic conductivity in the region close to the annular void is simulated by introducing a mesoscopic four-phase continuum model [89] which interacts with the macroscopic model for mechanized tunneling process only through the evolution of hydraulic conductivity [58] and the results are illustrated in Fig. 4.73.

As seen in Fig. 4.73, considering the parameter evolution around the TBM as the consequence of hydro-mechanical interactions between different materials, namely backfill grout and soil is essential to allow realistic estimation of the system behavior.

References

1. M. A. Abd Elaty and M. F. Ghazy. "Evaluation of consistency properties of freshly mixed concrete by cone penetration test". In: *Housing and Building National Research Center (HBRC Journal)* 12 (2016), pp. 1–12.
2. G. Anagnostou and K. Kovári. "The Face Stability of Slurry-shield-driven Tunnels". In: *Tunnelling and Underground Space Technology* 9.2 (1994), pp. 165–174. ISSN: 08867798. https://doi.org/10.1016/0886-7798(94)90028-0.

3. API RP 13B-2. *Recommended Practice for Field Testing Water-based Drilling Fluids*. Dallas, Texas, 2014.

4. ASTM C360-92. *Test Method for Ball Penetration in Freshly Mixed Hydraulic Cement Concrete: Withdrawn 1999*. 1999.

5. W. Baille. "Hydro-Mechanical Behaviour of Clays – Significance of Mineralogy". PhD Thesis. Bochum, Germany: Ruhr University Bochum, 2014.

6. L. Bamberg. "The influence of oedometer cell diameter in testing of soft clays". Masters Thesis. Oslo, Norway: Norwegian Geotechnical Institute, 2009.

7. T. Barciaga et al. "Cyclic response of natural Onsøy clay – Part II: Constitutive Modeling". In: *Lecture Notes in Applied and Computational Mechanics*. Vol. 82. 2017, pp. 275–296.

8. T. Belytschko et al. "Arbitrary discontinuities in finite elements". In: *International Journal for Numerical Methods in Engineering* 50.4 (2001), pp. 993–1013.

9. A. Bezuijen, J. P. Pruiksma, and H. H. van Meerten. "Pore Pressures in front of tunnel, measurements, calculations and consequences for stability of tunnel face". In: *Modern Tunneling Science and Technology: Proceedings of the International Symposium, Kyoto, Japan* (2001), pp. 27–33.

10. A. Bezuijen et al. "Field measurements of grout pressures during tunneling of the Sophia Rail tunnel". In: *Soils and Foundations* 44.1 (2004), pp. 41–50.

11. A. Bezuijen et al. "Pressure Gradients and Muck Properties at the Face of an EPB". In: *Tunneling. A Decade of Progress. GeoDElft 1995-2005* (2006), pp. 43–49.

12. A. Bezuijen et al. "Pressure gradients at the tunnel face of an Earth Pressure Balance shield". In: *Proc. ITA* (2005).

13. E. C. Bingham. *Fluidity and plasticity*. Vol. 2. McGraw-Hill, 1922.

14. W. Broere and A. F. van Tol. "Influence of infiltration and groundwater flow on tunnel stability". In: *Geotechnical Aspects of Underground Construction in Soft Ground, Tokyo, Japan* (2000), pp. 339–344.

15. W. Broere and A. F. van Tol. "Time-dependant infiltration and groundwater flow in a face stability analysis". In: *Modern Tunneling Science and Technology* (2001), pp. 629–634.

16. C. Budach. *Untersuchungen zum erweiterten Einsatz von Erddruckschilden in grobkörnigem Lockergestein: Dissertation, Ruhr-Universität Bochum, Fakultät für Bau- und Umweltingenieurwissenschaften, Lehrstuhl für Tunnelbau, Leitungsbau und Baubetrieb*. Schriftenreihe des Instituts für Konstruktiven Ingenieurbau. Bochum: Shaker-Verlag, 2012. ISBN: 9783844008456.

17. C. Budach and M. Thewes. "Application ranges of EPB shields in coarse ground based on laboratory research". In: *Tunnelling and Underground Space Technology* 50 (2015). https://doi.org/10.1016/j.tust.2015.08.006.

18. C. Budach and M. Thewes. "Erweiterte Einsatzbereiche von EPB-Schilden". In: *Geotechnik* 36.2 (2013), pp. 96–103. https://doi.org/10.1002/gete.201200012.

19. E. Burman et al. "CutFEM: discretizing geometry and partial differential equations". In: *International Journal for Numerical Methods in Engineering* 104.7 (2015), pp. 472–501.

20. C. Burstedde, L. Wilcox, and O. Ghattas. "p4est: Scalable Algorithms for Parallel Adaptive Mesh Refinement on Forests of Octrees". In: *SIAM Journal on Scientific Computing* 33.3 (2011), pp. 1103–1133. ISSN: 1064-8275.

21. R. Chandler. "Stiff sedimentary clays: geological origins and engineering properties". In: *Géotechnique* 60.12 (2010), pp. 891–902.

22. R. P. Chhabra. "Non-Newtonian fluids: an introduction". In: *Rheology of complex fluids*. Springer, 2010, pp. 3–34.

23. Y. Dafalias, M. Manzari, and M. Akaishi. "A simple anisotropic clay plasticity model". In: *Mechanics Research Communications* 29.6 (2002), pp. 241–245.

24. Y. Dafalias, M. Manzari, and A. Papadimitriou. "SANICLAY: simple anisotropic clay plasticity model". In: *International Journal for Numerical and Analytical Methods in Geomechanics* 30.12 (2006), pp. 1231–1257.

25. T. Dang and G. Meschke. "A Shear-Slip Mesh Update – Immersed Boundary Finite Element Model for Computational Simulations of Material Transport in EPB Tunnel Boring Machines". In: *Finite Element in Analysis and Design* 142 (Mar. 2018), pp. 1–16. https://doi.org/10.1016/j.finel.2017.12.008.

26. T. Dang and G. Meschke. "Influence of muck properties and chamber design on pressure distribution in EPB pressure chambers – Insights from computational flow simulations". In: *Tunneling and Underground Space Technology* 99.103333 (2020), pp. 1–14. https://doi.org/10.1016/j.tust.2020.103333.

27. G. Desbois et al. "Argon broad ion beam tomography in a cryogenic scanning electron microscope: a novel tool for the investigation of representative microstructures in sedimentary rocks containing pore fluid". In: *Journal of Microscopy* 249 (2013), pp. 215–235.

28. Deutscher Ausschuss für unterirdisches Bauen e. V. *Recommendations for the Selection of Tunnel Boring Machines*. 2022.

29. DIN 4126. *Nachweis der Standsicherheit von Schlitzwänden*. Berlin, 2013.

30. DIN EN 12350-2. *Prüfung von Frischbeton: Teil 2: Setzmaß; Deutsche Fassung EN 12350-2:2019*. Berlin, Sept. 2019.

31. DIN EN ISO 17892-6. *Geotechnische Erkundung und Untersuchung – Laborversuche an Bodenproben: Teil 6: Fallkegelversuch (ISO 17892-6:2017); Deutsche Fassung EN ISO 17892-6:2017*. Berlin, July 2017.

32. A. Düster et al. "The finite cell method for three-dimensional problems of solid mechanics". In: *Computer methods in applied mechanics and engineering* 197.45-48 (2008), pp. 3768–3782.

33. EFNARC. *Specification and Guidelines for the use of specialist products for Soft Ground Tunnelling*.

34. A. EFNARC. "Specifications and Guidelines for the use of specialist products for Mechanized Tunnelling (TBM) in Soft Ground and Hard Rock". In: *Recommendation of European Federation of Producers and Contractors of Specialist Products for Structures* (2005).

35. H. C. Elman, D. J. Silvester, and A. J. Wathen. *Finite elements and fast iterative solvers: with applications in incompressible fluid dynamics*. Oxford University Press, USA, 2014.

36. S. Freimann. *Untersuchung der Verarbeitbarkeit von konditionierten Lockergesteinsböden für den EPB-Schildvortrieb: Dissertation, Ruhr-Universität Bochum, Fakultät für Bau- und Umweltingenieurwissenschaften, Lehrstuhl für Tunnelbau, Leitungsbau und Baubetrieb*. Schriftenreihe des Instituts für Konstruktiven Ingenieurbau. Bochum: Shaker, 2021.

37. S. Freimann, M. Galli, and M. Thewes. "Rheological Characterization of Foam-conditioned Sands in EPB Tunneling". In: *EURO:TUN 2017 Innsbruck University, Austria* (2017).

38. S. Freimann, M. Schröer, and M. Thewes. "Experimental investigation of the flow behaviour of conditioned soils for EPB tunnelling in closed mode". In: *Proceedings of WTC2019: Tunnels and Underground Cities: Engineering and Innovation meet Archeology, Architecture and Art* (2019).

39. P. Fritz, R. Hermanns Stengele, and A. Heinz. *Modified Bentonite Slurries for Slurry Shields in Highly Permeable Soils*. Zürich, 2002.

40. M. Galli. *Rheological Characterisation of Earth-Pressure-Balance (EPB) Support Medium composed of non-cohesive Soils and Foam: Dissertation, Ruhr-Universität Bochum, Lehrstuhl für Tunnelbau, Leitungsbau und Baubetrieb*. Schriftenreihe des Instituts für Konstruktiven Ingenieurbau. Bochum: Shaker, 2016. ISBN: 9783844047042.

41. M. Galli and M. Thewes. "Influence of Soil Conditioning on the Flow Behaviour of EPB Face Support Medium". In: *Proceedings WTC 2018 - ITA World Tunnel Congress, Dubai, UAE* (2018), pp. 2863–2877.

42. M. Galli and M. Thewes. "Rheological Characterisation of Foam-Conditioned Sands in EPB Tunneling". In: *International Journal of Civil Engineering* (2018). https://doi.org/10.1007/s40999-018-0316-x.

43. M. Galli, M. Thewes, and S. Freimann. "Material Flow in EPB Tunnelling – Characterisation and Importance". In: *TAC/NASTT-NW Tunnelling and Trenchless Conference – TT2018, Edmonton* (2018).

44. M. Galli. "Rheological characterisation of earth-pressure-balance (EPB) support medium composed of non-cohesive soils and foam". In: (2016).

45. W. Hackbusch. "Multi-grid methods and applications". In: *Springer Series in Computational Mathematics* 4 (1985).

46. S. Hansbo. "A New Approach to the Determination of the Shear Strength of Clay by the Fall-Cone Test". In: *Royal Swedish Geotechnical Institute Proceedings No. 14* (1957).

47. T. J. Hughes, J. A. Cottrell, and Y. Bazilevs. "Isogeometric analysis: CAD, finite elements, NURBS, exact geometry and mesh refinement". In: *Computer methods in applied mechanics and engineering* 194.39-41 (2005), pp. 4135–4195.

48. E. S. Ieronymaki, A. J. Whittle, and D. S. Sureda. "Interpretation of free-field ground movements caused by mechanized tunnel construction". In: *Journal of Geotechnical and Geoenvironmental Engineering* 143.4 (2017), p. 04016114.

49. J. N. Jomo et al. "Parallelization of the multi-level hp-adaptive finite cell method". In: *Computers & Mathematics with Applications* 74.1 (2017), pp. 126–142.

50. J. N. Jomo et al. "Robust and parallel scalable iterative solutions for large-scale finite cell analyses". In: *Finite Elements in Analysis and Design* 163 (2019), pp. 14–30.

51. D. de Kee and R. P. Chhabra. "Elastic modulus and yield stress of suspensions". In: *Rheola Acta* 33.3 (1994), pp. 238–240. https://doi.org/10.1007/BF00437308.

52. M. Kilchert and J. Karstedt. *Standsicherheitsberechnung von Schlitzwaenden nach DIN 4126*. Vol. 2. Wiesbaden, Berlin, Köln: Bauverlag GmbH and Beuth Verlag GmbH, 1984.

53. D. Kolymbas. *Geotechnik: Bodenmechanik, Grundbau und Tunnelbau*. 5. Berlin, Heidelberg: Springer Vieweg, 2019. ISBN: 978-3-662-58472-9.

54. S. Kube. "Eindringverhalten von Bentonitsuspensionen in kohäsionsloses Lockergestein". Dissertation. Bochum: Ruhr University Bochum, 2023.

55. S. Kube. "Elektrische Widerstandsmessungen zur Beschreibung der Partikeleinlagerung während der Penetration von Bentonit in kohäsionsloses Lockergestein". In: *Forschung + Praxis 56, Vorträge der STUVA-Tagung 2021* (2021), pp. 133–139.

56. S. Kube, B. Schoesser, and M. Thewes. "Electrical resistance measurements of materials relevant in tunnelling to detect porosity and particle deposits in non-cohesive soil". In: *Proceedings of the WTC Kopenhagen - Underground solutions for a world in change* (2022).

57. A. A. Lavasan, C. Zhao, and T. Schanz. "Adaptive constitutive soil modeling concept in mechanized tunneling simulation". In: *International Journal of Geomechanic* 18.9 (2018). https://doi.org/10.1061/(ASCE)GM.1943-5622.0001219.

58. A. Lavasan et al. "Numerical investigation of tunneling in saturated soil: the role of construction and operation periods". In: *Acta Geotechnica* 13 (2018), pp. 671–691.

59. W. Lieske. "Compression behaviour of a natural and remoulded clay". Masters Thesis. Bochum, Germany: Ruhr University Bochum, 2015.

60. F. Mahaut et al. "Yield stress and elastic modulus of suspensions of noncolloidal particles in yield stress fluids". In: *Journal of Rheology* 52.1 (2008), pp. 287–313. ISSN: 0148-6055. https://doi.org/10.1122/1.2798234.

61. B. Maidl. *Mechanised shield tunnelling*. Berlin: Ernst & Sohn, 2012. ɪsʙɴ: 978-3-433-02995-4.

62. U. Maidl. *Erweiterung der Einsatzbereiche der Erddruckschilde durch Bodenkonditionierung mit Schaum: Dissertation, Ruhr-Universität Bochum, AG Leitungsbau und Leitungsinstandhaltung*. Technisch-wissenschaftliche Mitteilungen des Instituts für Konstruktiven Ingenieurbau. Bochum, 1995.

63. J. Maxey. "Thixotropy and yield stress behaviour in drilling fluids". In: *Proceedings of American Association of Drilling Engineers (ADDE) National Technical Conference and Exhibition, Houston, Texas* (2007).

64. Q. Meng, F. Qu, and S. Li. "Experimental investigation on viscoplastic parameters of conditioned sands in earth pressure balance shield tunneling". In: *Journal of mechanical science and technology* 25.9 (2011), pp. 2259–2266.

65. A. S. Merritt. *Conditioning of clay soils for tunnelling machine screw conveyors: St. John's College, University of Cambridge, Department of Engineering*. United Kingdom, 2004.

66. J. Mewis and N. J. Wagner. "Thixotropy". In: *Advances in colloid and interface science* 147–148 (2009), pp. 214–227. https://doi.org/10.1016/j.cis.2008.09.005.

67. T. G. Mezger. *The Rheology Handbook*. Hannover, Germany: Vincentz Network, 2012. ɪsʙɴ: 9783748600367. https://doi.org/10.1515/9783748600367.

68. P. Mianji. "Hydromechanical properties of bentonite-infiltrated sand". PhD Thesis. Bochum, Germany: Ruhr University Bochum, 2023.

69. R. Mittal and G. Iaccarino. "Immersed boundary methods". In: *Annu. Rev. Fluid Mech.* 37 (2005), pp. 239–261.

70. P. C. F. Møller, J. Mewis, and D. Bonn. "Yield stress and thixotropy: on the difficulty of measuring yield stresses in practice". In: *Soft matter* 2.4 (2006), pp. 274–283. https://doi.org/10.1039/b517840a.

71. N. Müthing. "On the consolidation behaviour of fine-grained soils under". PhD Thesis. Bochum, Germany: Ruhr University Bochum, 2017.

72. Q. D. Nguyen and D. V. Boger. "Characterization of yield stress fluids with concentric cylinder viscometers". In: *Rheologica Acta* 26.6 (1987), pp. 508–515. https://doi.org/10.1007/BF01333734.

73. J. Nitsche. "Über ein Variationsprinzip zur Lösung von Dirichlet-Problemen bei Verwendung von Teilräumen, die keinen Randbedingungen unterworfen sind". In: *Abhandlungen aus dem mathematischen Seminar der Universität Hamburg*. Vol. 36. 1. Springer. 1971, pp. 9–15.

74. G. Ovarlez and S. Hormozi. *Lectures on Visco-Plastic Fluid Mechanics*. Springer, 2019.

75. T. C. Papanastasiou. "Flows of materials with yield". In: *Journal of rheology* 31.5 (1987), pp. 385–404.

76. J. Parvizian, A. Düster, and E. Rank. "Finite cell method". In: *Computational Mechanics* 41.1 (2007), pp. 121–133.

77. A. Perrot, D. Rangeard, and T. Lecompte. "Field-oriented tests to evaluate the workability of cob and adobe". In: *Materials and Structures* (2018).

78. S. Praetorius and B. Schößer. *Bentonithandbuch: Ringspaltschmierung für den Rohrvortrieb*. Bauingenieur-Praxis. Berlin: Ernst & Sohn, 2016. ɪsʙɴ: 9783433031360. https://doi.org/10.1002/9783433606568.

79. F. de Prenter et al. "Multigrid solvers for immersed finite element methods and immersed isogeometric analysis". In: *Computational Mechanics* (2019), pp. 1–32.

80. M. Pulsfort and C. Thienert. "Neue Erkenntnisse zur Stützdruckübertragung beim Tunnelvortrieb mit flüssigkeitsgestützter Ortsbrust". In: *Forschung + Praxis, Vorträge der STUVA-Tagung 2013* (2013).

81. A. A. Requicha and H. B. Voelcker. "Constructive solid geometry". In: (1977).

82. K. Roscoe and J. Burland. "On the generalized stress-strain behaviour of wet clays". In: *Engineering plasticity*. Ed. by J. Heyman and F. Leckie. Cambridge University Press, 1968, pp. 535–609.

83. Y. Saad. *Iterative methods for sparse linear systems*. Vol. 82. siam, 2003.

84. S. Saberi, G. Meschke, and A. Vogel. "A restricted additive Vanka smoother for geometric multigrid". In: *Journal of Computational Physics* 459 (2022), p. 111123. https://doi.org/10.1016/j.jcp.2022.111123.

85. S. Saberi, A. Vogel, and G. Meschke. "Parallel finite cell method with adaptive geometric multigrid". In: *Lecture Notes in Computer Science* (2020).

86. S. Saberi, G. Meschke, and A. Vogel. "Adaptive geometric multigrid for the mixed finite cell formulation of Stokes and Navier-Stokes equations". In: *arXiv preprint arXiv:2103.10151* (2021).

87. A. Saltelli et al. *Global sensitivity analysis. The Primer*. John Wiley and Sons, 2008.

88. B. Schaedlich, T. Schweiger H.F.and Marcher, and E. Saurer. "Application of a novel constitutive shotcrete model to tunnelling". In: *Rock Engineering and Rock Mechanics: Structures in and on Rock Masses*. 2014.

89. A. Schaufler, C. Becker, and H. Steeb. "Simulation of the backfilling process with annular gap grouting mortar". In: *Proceedings of the third international conference on computational methods in tunneling and subsurface engineering*. 2013, pp. 587–597.

90. J. Schmatz, J. Urai, and S. Berg. "Nanoscale imaging of Pore-Scale Fluid-Fluid-Solid Contacts in Sandstone". In: *Geophysical Research Letters* 42.7 (2015), pp. 2189–2195.

91. J. Schmatz et al. "Nanoscale morphology of brine/oil/mineral contacts in connected pores of carbonate reservoirs: Insights on wettability from cryo-bib-sem". In: *SPE J.* 22.5 (2017), pp. 1374–1384.

92. M. Schoen et al. "Application of optimal experiment design method to detect the optimal sensor positions: A case study of Milan metro line 5". en. In: *Tunneling and Underground Space Technology* (). Accepted.

93. G. Schramm. *Einführung in Rheologie und Rheometrie*. Karlsruhe: Haake, 1995.

94. M. Schröer. *Neue Untersuchungsmethoden und Erweiterung der Anwendungsbereiche von konditionierten Böden beim maschinellen Tunnelvortrieb mit Erddruckstützung: Dissertation, Ruhr-Universität Bochum, Fakultät für Bau- und Umweltingenieurwissenschaften, Lehrstuhl für Tunnelbau, Leitungsbau und Baubetrieb*. Schriftenreihe des Instituts für Konstruktiven Ingenieurbau. Bochum: Shaker, 2023.

95. G. Seidalinov and M. Taiebat. "Bounding surface SANICLAY plasticity model for cyclic clay behavior". In: *International Journal for Numerical and Analytical Methods in Geomechanics* 38.7 (2014), pp. 702–724.

96. S. Sloan, A. Abbo, and D. Sheng. "Refined explicit integration of elastoplastic models with automatic error control". In: *Engineering Computations* 18 (2001), pp. 121–194. https://doi.org/10.1108/02644400110365842.

97. F. Sotiropoulos and X. Yang. "Immersed boundary methods for simulating fluid–structure interaction". In: *Progress in Aerospace Sciences* 65 (2014), pp. 1–21.

98. I. Stroud. *Boundary representation modelling techniques*. Springer Science & Business Media, 2006.

99. M. Taiebat, Y. Dafalias, and R. Peek. "A destructuration theory and its application to SANICLAY model". In: *International Journal for Numerical and Analytical Methods in Geomechanics* 34.10 (2010), pp. 1009–1040.

100. A. M. Talmon, D. R. Mastbergen, and M. Huisman. "Invasion of pressurized clay suspensions into granular soil". In: *Journal of Porous Media* 16.4 (2013), pp. 351–365. https://doi.org/10.1615/JPorMedia.v16.i4.70.

101. D. W. Taylor. *Fundamentals of soil mechanics*. New York: John Wiley & Sons, 1948.

102. T. Tezduyar et al. "Flow simulation and high performance computing". In: *Computational Mechanics* 18.6 (1996), pp. 397–412.

103. E. Thele. "Numerical analysis of mechanized tunneling in natural clay – the influence of soil's structure". Masters Thesis. Bochum, Germany: Chair of Soil Mechanics, Foundation Engineering and Environmental Geotechnics, Ruhr University Bochum, 2020.

104. M. Thewes, B. Schösser, and Z. Zizka. "Transient face support in slurry shield tunnelling due to different time scales for penetration time of support fluid and for excavation sequence of cutting tools". In: *ITA-AITES World Tunnel Congress and International Tunnelling and Underground Space Association and Society for Mining, Metallurgy, and Exploration. San Francisco, California.* (2016).

105. M. Thewes, C. Budach, and A. Bezuijen. "Foam conditioning in EPB tunnelling". In: *Geotechnical Aspects of Underground Construction in Soft Ground* 127 (2012).

106. *DIN 1342: Viskosität: Teil 2: Newtonsche Flüssigkeiten*. Berlin, 2003. https://doi.org/10.31030/9502319.

107. *DIN 1342: Viskosität: Teil 3: Nicht newtonsche Flüssigkeiten*. Berlin, 2003. https://doi.org/10.31030/9502320.

108. M. Wan et al. "Pore Water Pressure and Total Horizontal Stress Response to EPBM Tunnelling in London Clay". In: *Géotechnique* 69.5 (2019), pp. 434–457.

109. T. Wichtmann. "Soil behaviour under cyclic loading – experimental observations, constitutive description and applications". Habilitation Thesis. Karlsruher, Germany: Karlsruher Institute of Technology, 2016.

110. T. Wichtmann et al. "Cyclic tests on high-quality undisturbed block samples of soft marine Norwegian clay". In: *Geotechnical Journal* 50.4 (2013), pp. 400–412.

111. F. Winnefeld. "Rheologische Eigenschaften von Mörteln und Betonen: neuartiges System für Messungen". In: *tec21* 127.40 (2001).

112. C. Zhao. "A Contribution to Modeling of Mechanized Tunnel Excavation". PhD thesis. Bochum, Germany: Ruhr-Universität Bochum, 2018.

113. Küpferle, J., Zizka, Z., Schoesser, B., Röttger, A., Alber, M., Thewes, M., and Theisen, W. "Influence of the slurry-stabilized tunnel face on shield TBM tool wear regarding the soil mechanical changes – Experimental evidence of changes in the tribological system". In: Tunnelling and Underground Space Technology 74 (2018), pp. 206–216.

114. C. Zhao, A. Lavasan, and T. Schanz. "Application of submodeling technique in numerical modeling of mechanized tunnel excavation". In: *International Journal of Civil Engineering* 17 (2019), pp. 75–89.

115. C. Zhao et al. "Support pressure transfer at a slurry supported tunnel face due to time dependent decrease of soil permeability". In: *Proc. of the Tenth Int. Symposium on Geotechnical Aspects of Underground Construction in Soft Ground, IS-Cambridge 2022, UK, 27-29 June 2022*. Ed. by M. Elshafie, G. Viggiani, and R. Mair. Cambridge, UK: CRC press/Balkema, 2022, pp. 451–458.

116. C. Zhao et al. "A hybrid model for estimation of ground movements due to mechanized tunnel excavation". en. In: *Computer-aided Civil and Infrastructure Engineering* 34.7 (July 2019), pp. 586–601.

117. C. Zhao et al. "Mechanized tunneling induced ground movement and its dependency on the tunnel volume loss and soil properties". en. In: *International Journal for Numerical and Analytical Methods in Geomechanics* 43.4 (Mar. 2019), pp. 781–800.

118. C. Zhao et al. "Model validation and calibration via back analysis for mechanized tunnel simulations – The Western Scheldt tunnel case". en. In: *Computers and Geotechnics* 69 (Sept. 2015), pp. 601–614.

119. Z. Zizka. "Stability of slurry supported tunnel face considering the transient support mechanism during excavation in non-cohesive soil". Dissertation. Bochum: Ruhr University Bochum, 2019.

120. Z. Zizka, B. Schoesser, and M. Thewes. "Investigations on the transient support pressure transfer at the tunnel face during slurry shield drive Part 2: Case B – Deep slurry penetration exceeds tool cutting depth". In: *Tunnelling and Underground Space Technology* 118.104169 (2021). ISSN: 08867798. https://doi.org/10.1016/j.tust.2021.104169.

121. Z. Zizka, B. Schoesser, and M. Thewes. "Investigations on transient support pressure transfer at the tunnel face during slurry shield drive part 1: Case A – Tool cutting depth exceeds shallow slurry penetration depth". In: *Tunnelling and Underground Space Technology* 118.104168 (2021). ISSN: 08867798. https://doi.org/10.1016/j.tust.2021.104168.

122. Z. Zizka, B. Schoesser, I. Popovic, and M. Thewes. "Excess pore pressures in front of the tunnel face during slurry shield excavations due to different time scales for excavation sequence of cutting tools and penetration time of support fluid". In: *Proceedings of EUTO:TUN 2017, Innsbruck* (2017).

123. Z. Zizka, S. Kube, B. Schoesser, and M. Thewes. "Influence of stagnation gradient for face support calculation in Slurry Shield Tunnelling". In: *Geomechanics and Tunnelling* 13.4 (2020), pp. 372–381. ISSN: 18657362. https://doi.org/10.1002/geot.202000009.

124. Z. Zizka, B. Schoesser, M. Thewes, and T. Schanz. "Slurry Shield Tunneling: New Methodology for Simplified Prediction of Increased Pore Pressures Resulting from Slurry Infiltration at the Tunnel Face Under Cyclic Excavation Processes". In: *International Journal of Civil Engineering* 17.1 (2019), pp. 113–130. https://doi.org/10.1007/s40999-018-0303-2.

Tunnel Linings

5

Gerrit Emanuel Neu ⓘ, Florian Christ ⓘ, Tagir Iskhakov ⓘ,
Christina Krikelis, Diego Nicolás Petraroia ⓘ, Sven Plückelmann,
Maximilian Schoen ⓘ, Rolf Breitenbücher ⓘ,
Arash Alimardani Lavasan ⓘ, Peter Mark ⓘ, Günther Meschke ⓘ, and
Jithender J. Timothy ⓘ

G. E. Neu (✉) · T. Iskhakov · G. Meschke
Structural Mechanics, Ruhr-Universität Bochum, Bochum, Germany
e-mail: gerrit.neu@rub.de

T. Iskhakov
e-mail: tagir.iskhakov@rub.de

G. Meschke
e-mail: guenther.meschke@rub.de

F. Christ · M. Schoen · A. A. Lavasan
Soil Mechanics, Foundation Engineering and Environmental Geotechnics, Ruhr-Universität
Bochum, Bochum, Germany
e-mail: florian.christ@rub.de

M. Schoen
e-mail: maximilian.schoen@rub.de

A. A. Lavasan
e-mail: arash.alimardanilavasan@rub.de

C. Krikelis · S. Plückelmann · R. Breitenbücher
Building Materials, Ruhr-Universität Bochum, Bochum, Germany
e-mail: christina.krikelis@rub.de

S. Plückelmann
e-mail: sven.plueckelmann@rub.de

R. Breitenbücher
e-mail: rolf.breitenbuecher@rub.de

D. N. Petraroia · P. Mark
Concrete Structures, Ruhr-Universität Bochum, Bochum, Germany
e-mail: diego.petraroia@rub.de

P. Mark
e-mail: peter.mark@rub.de

J. J. Timothy
Centre for Building Materials, TU Munich, Munich, Germany
e-mail: jithender.timothy@tum.de

Abstract

In this chapter, important research results for the development of a robust and damage-tolerant multimaterial tunnel lining are presented. This includes the production, design and optimization of fiber-reinforced hybrid segmental lining systems based on numerical models and experimental investigations under tunneling loads. In addition, novel tail void grouting materials are developed and optimized regarding their infiltration and hardening behavior while taking the interaction with the surrounding ground into account. In order to expand the applicability of mechanized tunneling regarding soils characterized by significant swelling potential due to water uptake by clay minerals, a deformable segmental lining system is presented. The risk of damage due to high localized loads is reduced by the integration of additional radial protective layers on the lining segments and a compressible annular gap grout, which protect the tunnel structure by undergoing high deformations after reaching a certain yielding load. However, the deformability of such support systems affects the distribution of the stresses around the tunnel which governs the magnitude and buildup of the swelling pressure in the soil. Therefore, the development of damage tolerant lining systems requires a material and structural design which ensures an optimal soil-structure interaction through a synergy of computational and experimental techniques.

5.1 Introduction

Segmental linings form the load-bearing ring of mechanically excavated tunnels. Most commonly, they are divided into 5 to 10 segments per ring and joined together with direct concrete to concrete contact at the longitudinal and ring joints. Typically, segmental linings are prefabricated in serial production with hundreds or thousands of repetitions [41]. As reinforced concrete (RC) members they are made of higher-strength normal concretes and detailed with classic reinforcing steel. Regarding the design, the regions of load introduction at the longitudinal joints and at the jacks, the coupling joints for the shear load transfer from ring to ring [64] as well as the ring cross-section itself with compressive axial force and moderate eccentricities [29, 36] are essentially relevant. In addition, high geometric accuracy must be met in contact at the longitudinal and ring joints. Otherwise damage due to cracking and spalling can occur.

Analytical methods, beam-spring, and continuum models have become established for the analysis of internal forces [75, 102]. They usually consider only the final state of the finished tunnel and take into account the interaction between soil and structure in a conservative and simple way. This interaction however, plays a crucial role [13]. It is already activated by the annular gap grouting in the construction state of the tunnel and is decisive especially in case of one-sided loading–e.g., from buildings–and swelling soils. Since a stiff ring can hardly compensate for axial deformation, only compensation with lateral displacement into the soil bedding remains possible.

The research findings outlined in the remainder introduce a holistic optimization of the coupled tunnel system comprising the concrete segments, the annular gap grouting and the surrounding bedding soil [26, 63]. It is both experimental and numerical in nature. The segments are formed with hybrid reinforcement consisting of reinforcing steel bars and steel fibers [88], whereas the regions of load application subject to partial area loading are locally reinforced. At that, different concretes and precast elements are combined employing "fresh to fresh" or "fresh to solid" casting technologies. The steel fibers are aligned in a tailored way in direction of the tensile stresses exploiting the wall effect of temporary formworks during casting. As a result, load-bearing capacities, especially for biaxial load transfer at the longitudinal joints [67, 74], increase significantly. In the sense of an optimization-aided design [23, 73], this results in segments with uniform stress utilization across the ring. The segments get significantly more material-efficient and adapt to the variable loading and stress conditions along a tunnel. In addition, the robustness against spalling, unintended deformations or offsets, variations in load scenarios, or non-uniform ground conditions greatly increases.

The grout for the annular gap is developed as a single or a multi-component material – depending on the demands of the individual soil-structure interaction and the process of grouting [7]. Experimentally this is performed from small scale up to real scale level in a novel prototype testing facility [70].

For swelling soils, a deformation-tolerant segmental lining is developed. It consists of two components. The first one is a compressible annular gap mortar that deforms nearly plastic at defined pressures [89]. The second component is a hybrid segment of high-strength concrete with reduced thickness which is supplemented by a soft and deformable mortar layer at the outside. Thus, two layers protect the sensitive lining. The development proceeds in interaction and captures the locally concentrated soil deformations [9], which are derived from numerical simulation accounting for specific swelling scenarios activated by the tunnel construction [103]. Experimental implementations are treated up to full scale proving true bearing capacities of the segments as well as the deformation capacities of the soft layers [60].

5.2 Steel Fiber Reinforced Concrete (SFRC) for Tunnel Linings

Experiments have been conducted to examine the behavior of fiber pullout, considering fiber shape, dimensions and inclination angles, among others. Also, the following sections introduce the experiments along with the corresponding numerical models that were set up to adequately describe steel fiber reinforced concrete for tunnel linings.

5.2.1 Fiber Pullout

For the analysis, design and optimization of robust and damage-tolerant tunnel linings made of SFRC, it is essential to first understand the mechanical behavior of the material

at a structural level. As is well known, the mechanical behavior of SFRC is related to the bridging effect across a crack opening, which is governed by the total contribution of all the fibers intercepting the crack. Since the bridging efficiency of each individual fiber depends largely on the fiber-matrix bond characteristics, the pullout behavior of single steel fibers embedded in a concrete matrix was systematically investigated by means of laboratory tests and analytical models. The results provide the basis for the numerical modeling of the mechanical processes in SFRC (Sect. 5.2.3), and on the other hand, they are the basis for further specific investigations on the use of SFRC in lining segments, such as investigations on the behavior under partial-area loading (Sect. 5.2.2).

5.2.1.1 Experiments on Fiber Pullout

The bond mechanisms of steel fibers in a concrete matrix were experimentally investigated by performing pullout tests on single steel fibers. The test program included the variation of relevant parameters influencing the pullout behavior, such as fiber shape, fiber dimensions, fiber tensile strength, inclination angle and concrete strength. A detailed description of the properties of the investigated fibers and the concrete mixes used as the pullout matrix is given in [11, 77, 79].

For the pullout tests, cylindrical specimens with dimensions of 60 mm × 60 mm (Fig. 5.1, left) were prepared. The fibers were fixed and embedded in the concrete as described in [11, 77, 79]. The test setup used for the pullout tests is shown in Fig. 5.1, right.

The pullout behavior was analyzed focusing on the correlation between the pullout force and the fiber displacement. Moreover, the failure mode of fibers and concrete matrix were taken into account. The key findings of the experimental investigations on the pullout behavior are presented in the following. Further results and more detailed analyses can be found in [11, 63, 77, 79]
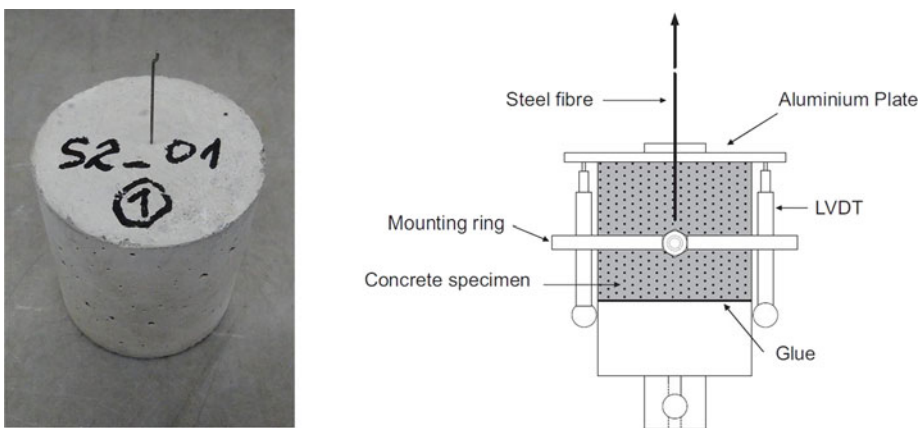
Fig. 5.1 Concrete specimen with embedded steel fiber [11, 79] (left) and pullout test setup [11, 77] (right)

5.2.1.2   Fiber Shape and Dimensions

In Fig. 5.2, left, the influence of fiber shape (straight, crimped, hook-ended and twin-coned) on the pullout response is illustrated for fibers with embedded length of $L_f = 20$ mm and inclination angle of $\theta = 0°$ in a high-strength concrete matrix ($f_c = 84$ MPa). As shown in Fig. 5.2, left, the pullout responses differed significantly from each other depending on the fiber shape. In the case of straight fibers, the bond between fiber and matrix is only provided by interfacial friction. As a result, complete debonding occurred at an almost very low pullout load, which was accompanied by a sudden drop of the load. In contrast, due to the mechanical anchorage of deformed fibers, the pullout loads continued to increase after debonding. Thus, deformed fibers provided significantly higher resistance against pullout than straight fibers. As a consequence of the strong anchorage in the high-strength concrete matrix, both crimped and twin-coned fibers failed in all tests by rupture shortly after the ultimate load was exceeded. However, to achieve ductile material behavior, fiber rupture at small pullout displacements should be avoided. Beneficial pullout behavior was observed for the hook-ended fibers. For these fibers, the hook tended to be progressively mobilized and straightened, which caused a decrease of the pullout force and a further increase of the pullout displacement.

Figure 5.2, right, shows the effects of fiber dimensions by comparing hook-ended fibers with $l/d = 60/0.75$ mm/mm and $l/d = 35/0.55$ mm/mm under otherwise identical testing conditions. As can be seen, the load-displacement curves of the two fibers were similar and almost parallel to each other. However, the fibers with larger dimensions exhibited a considerably higher ultimate pullout load ($+77.0\%$). With increasing diameter and hook size, respectively, the bending stiffness of the fiber and the contact area between fiber and matrix increases, which led to an increase in the energy required for plastic deformation of the hook. However, by comparing the two fibers in terms of the ratio between ultimate pullout load and fiber strength, it was shown that the efficiency of the fibers differed only marginally (60.1% and 61.0%) [11].
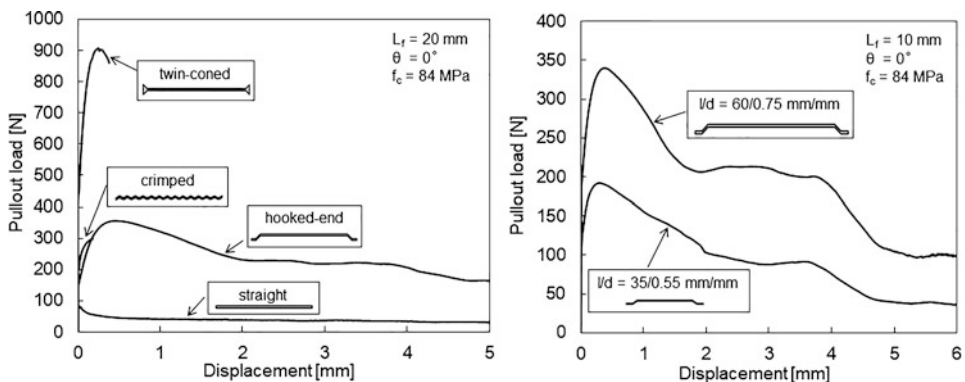
Fig. 5.2 Influence of fiber shape [11, 77] (left) and fiber dimensions [79] (right) on pullout response

For concretes with the same fiber content, the number of shorter/thinner fibers is several times higher than that for longer/thicker fibers. As a result, for smaller/thinner fibers, the number of fibers intercepting potential cracks is also comparatively higher. Therefore, although the results showed a higher pullout resistance for longer/thicker fibers compared to smaller/thinner fibers, poorer load-bearing behavior must not be expected for the latter in general. Rather, a positive synergy effect can be concluded from the results. In fiber cocktails the advantages of fibers with different dimensions (longer/thicker and shorter/thinner fibers) can be used in combination. In particular, such fiber cocktails could have a positive effect in edge areas of linings segments to prevent cracking and spalling.

5.2.1.3 Fiber and Concrete Strength

The influence of fiber strength ($f_t = 1225$ MPa, 2600 MPa) and concrete strength ($f_c = 44$ MPa, 84 MPa) are depicted in Fig. 5.3. For both concrete strengths, the pullout resistance up to the frictional sliding stage was almost twice as high for the high-strength fibers as for the normal-strength fibers. As expected, fibres embedded in high-strength concrete exhibited a comparatively higher pullout load than those in normal-strength concrete. However, this effect was much more pronounced for high-strength fibers.

While the load-displacement curves of high-strength fibers differed significantly for both concretes tested, normal-strength fibers showed similar load-displacement behavior regardless of the concrete strength. The curves of high-strength fibers in normal-strength concrete dropped relatively slowly after the ultimate pullout load was reached. This indicates that the mechanical anchorage of the hook was only utilized to a low level due to the low concrete strength. Hence, the fiber efficiency for high-strength fibers tested in normal-strength concrete was comparatively low (42.7%). However, it should be noted that these fibers had a remarkably higher efficiency in high-strength concrete (61.6%), as shown in [79]. Therefore, to achieve an optimal fiber efficiency, the properties of steel fibers in terms of tensile strength should be adjusted to the concrete strength.

Fig. 5.3 Influence of fiber and concrete strength on pullout response [79]
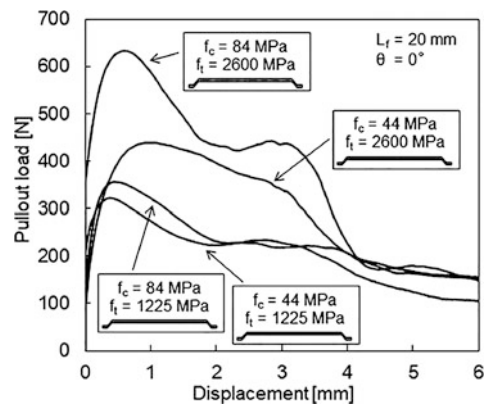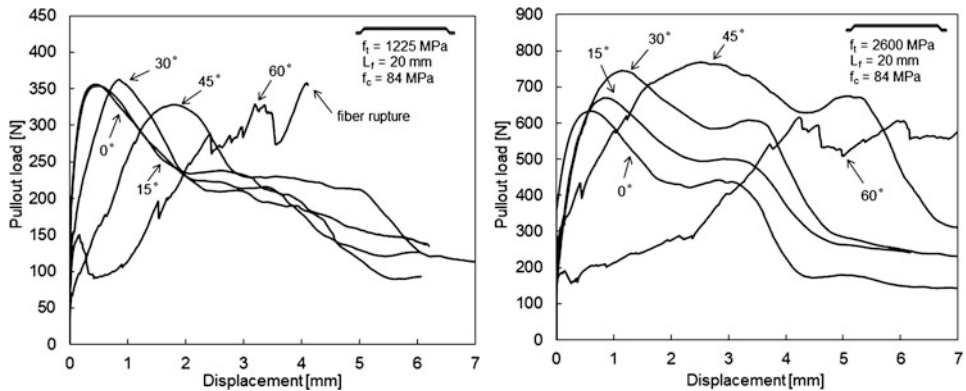
Fig. 5.4 Influence of fiber inclination angle on pullout response: normal-strength fiber (left) and high-strength fiber (right) embedded in high-strength concrete [11, 77, 79]

5.2.1.4 Fiber Inclination Angle

Results of pullout tests on normal-strength and high-strength hooked-end fibers embedded with different inclinations angles (0°, 15°, 30°, 45° and 60°) in high-strength concrete are shown in Fig. 5.4. As expected, the high-strength fibers exhibited significantly higher ultimate pullout loads for all inclination angles considered. In the case of normal-strength fibers pulled out without rupture, the ultimate pullout loads were very similar independent from the inclination angle (Fig. 5.4, left). In contrast, high-strength fibers showed a remarkable increase in the ultimate pullout load at inclination angles between 30° and 45° (Fig. 5.4, right).

In general, the pullout displacement at ultimate load increased and the slope of the pre-peak branch decreased as the inclination angle rose, particularly for inclination angles greater than 30°. With the increase of the inclination angle, also an increase of matrix crushing and spalling at the exit point of the fiber was observed. This phenomenon was more pronounced in the case of high-strength fibers. Furthermore, fiber rupture occurred more frequently as the inclination angle increased, especially for normal-strength fibers [79].

5.2.2 SFRC Under Partial-Area Loading

As mentioned in the introduction, lining segments are subjected to high concentrated loads (i.e. partial area loadings) during both, the construction and final stage. The resulting splitting tensile stresses are usually decisive for the design and must be resisted by appropriate reinforcement. Among other advantages, the use of steel fiber reinforcement can increase the load-bearing capacity and positively affect the fracture behavior under such concentrated loading situations. In order to realize an optimized use of SFRC especially for lining segments, the bearing and fracture behavior of SFRC under partial-area loading was systematically investigated through experimental and numerical approaches.
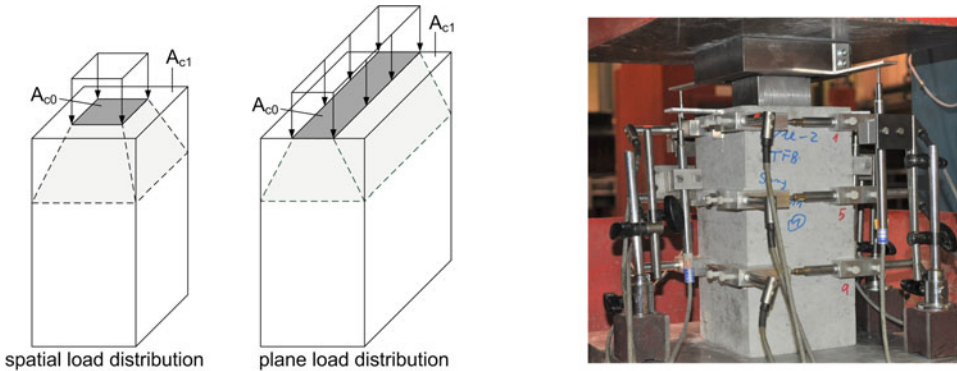
Fig. 5.5 Schematic illustration of partial-area loading with spatial and plane load distribution (left) and test setup for partial-area loading with spatial load distribution [62, 78] (right)

5.2.2.1 Experiments on SFRC Under Partial-Area Loading

To characterize the bearing and fracture behavior of SFRC under partial-area loading, a comprehensive experimental program containing the variation of both non-fiber-related and fiber-related parameters has been conducted. The non-fiber-related variables included concrete strength, specimen dimensions, area ratio and eccentricity of load. Furthermore, taking into account the two relevant concentrated loading scenarios that occur in the ring and longitudinal joints of lining segments, partial-area loadings with spatial (i.e. point loading) and plane load distribution (i.e. strip loading) were considered (Fig. 5.5, left). The fiber-related factors included fiber properties (e.g. strength, dimensions, geometry and aspect ratio), fiber content and orientation as well as the combination of different fiber types (i.e. fiber cocktails).

The base mix designs of the investigated concretes corresponded to those typically used for lining segments. Detailed information regarding the mix designs and the various fiber reinforcements as well as the production and preparation of specimens can be found in [62, 78].

Figure 5.5, right, shows the test-setup as an example for partial-area loading with spatial load distribution on a specimen with dimensions of $150 \, \text{mm} \times 150 \, \text{mm} \times 300 \, \text{mm}$. Further details on the test-setup are given in [62, 78].

The effects of the various parameters on the load-bearing and fracture behavior were studied by analyzing the ultimate local compressive stress (i.e. ultimate bearing capacity), the stress-displacement response as well as the failure and cracking characteristics. In the following, some of the main results and key findings are presented. A more detailed description of the experiments and the results obtained is published in [8, 10, 55, 62, 78, 80].

5.2.2.2 Area Ratio and Fiber Addition

In Fig. 5.6, left, the effects of area ratio ($\delta = A_{c1}/A_{c0} = 2.25, 4, 9$ and 16) and fiber addition ($60 \, \text{kg/m}^3$ of hooked-end steel fibers) on the local compressive stress versus longitudinal
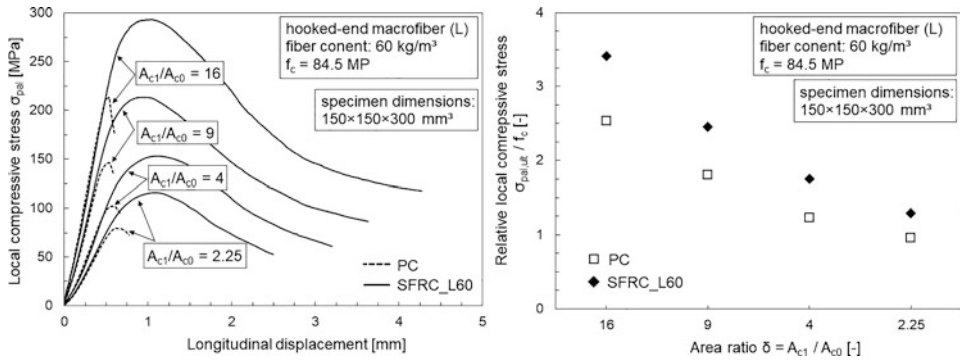
Fig. 5.6 Influence of area ratio and fiber addition on the stress-displacement response (left) and on the stress ratio ($\sigma_{\text{pal,ult}}/f_c$) (right) for high-strength concrete under partial-area loading [8, 78]

displacement response are presented for high-strength concrete ($f_c = 84.5$ MPa) under centric partial-area loading with spatial load distribution. Note that in the following, local compressive stress σ_{pal} is defined as the applied load divided through the loaded area A_{c0}. As can be seen from the stress-displacement curves, the addition of fibers to the plain concrete (PC) led to a strong increase in the ultimate local compressive stress $\sigma_{\text{pal,ult}}$ (up to 47%). In Fig. 5.6, right, the ratios between ultimate local compressive stress and concrete strength ($\sigma_{\text{pal,ult}}/f_c$) are depicted for each area ratio. Comparing PC and SFRC, it can be seen that the difference of these values is larger at higher area ratios. Therefore, is obvious that the influence of the fibers on the load-bearing capacity is more pronounced at higher area ratios.

As expected, ultimate local compressive stress was also significantly enhanced with increasing area ratio for both PC and SFRC due to the confinement effect of the surrounding concrete. In the case of partial-area loading with spatial load distribution, a proportionality between the ultimate local compressive stress and the square root of the area ratio could clearly be ascertained [78]. Due to the incomplete confinement in the case of partial-area loading with plane load distribution, the increase in the ultimate local compressive stress was comparatively lower. In this case, a proportionality to the cubic root of the area ratio was found [62]. These correlations provided the basis for an analytical approach to calculate the bearable local stress of high-strength SFRC, which is presented in [55, 62].

Shortly after reaching the maximum stress, the stress-displacement curves of PCs were characterized by a sharp drop (Fig. 5.6, left), indicating a sudden failure of the specimens during the test. In contrast, SFRCs exhibited a gradual reduction in stresses with continuously increasing displacement, corresponding to a ductile fracture behavior. In the case of partial-area loading with plane load distribution, this effect was less pronounced due to the incomplete confinement [62].

Representative fracture patterns of high-strength PC and SFRC specimens are presented in Fig. 5.7, matching the respective stress-displacement curves shown in Fig. 5.6,
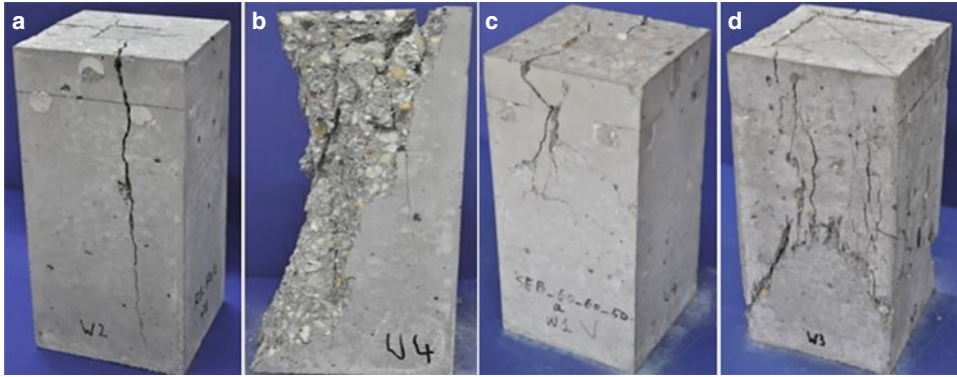
Fig. 5.7 Fracture patterns of high-strength PC (**a**, **b**) and SFRC (60 kg/m^3 hooked-end macrofiber) (**c**, **d**) loaded with area-ratios 9 (**a**, **c**) and 2.25 (**b**, **d**) [78]

left. In general, for both PC and SFRC, no visible cracking or spalling was observed until shortly before reaching the ultimate load. Soon afterwards, all PC specimens failed in a more or less explosive manner, in particular in the case of high-strength concrete, accompanied by the sharp drop of the load-displacement curves shown in Fig. 5.6, left. While for large area ratios single major splitting cracks developed and spread across the testing and lateral surfaces to the bottom (Fig. 5.7a), PC specimens tested with small area ratios completely collapsed (Fig. 5.7b). In contrast, all SFRC specimens retained their integrity until the end of testing and exhibited a multiple cracking pattern. At large area ratios, cracking in conjunction with minor concrete spalling occurred mainly on the upper half of SFRC specimens (Fig. 5.7c). With decreasing area ratio, the cracks and spalling tended to increasingly develop also in the lower half (Fig. 5.7d).

5.2.2.3 Fiber Type and Cocktails

As can already be assumed from the studies on the pullout behavior of steel fibers (Sect. 5.2.1), the properties of fibers also had a significant influence on the bearing and fracture behavior of SFRC under partial-area loading. Figure 5.8, left, shows the ultimate local compressive stress of high-strength SFRC produced with various types of steel fibers at a fiber content of 60 kg/m^3 (spatial load distribution, $\delta = 9$). Compared to PC, the increase in the ultimate local compressive stress was between 28% and 51%. As expected, the high-strength hook-ended macrofibers (Lh60) appeared to be most effective in enhancing the ultimate bearing capacity. However, it was found that SFRC with high-strength macrofibers had only an increment of 15% in its ultimate bearing capacity compared to SFRC produced with normal-strength macrofibers (L60), although the results of the pullout tests showed that the ultimate pullout load was almost twice as high for the high-strengths fibers (cf. Fig. 5.3).

For SFRC produced with fiber cocktails, a positive synergy effect could be observed for certain combinations of fiber types. For high-strength concrete, however, this effect was
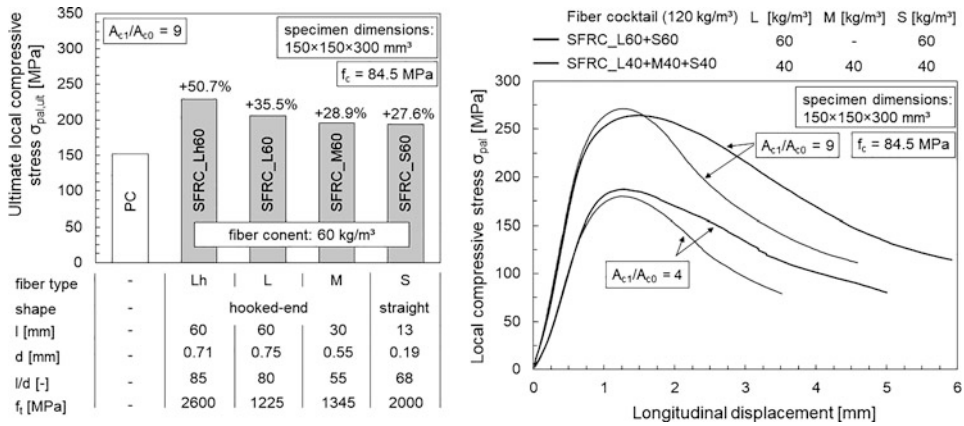
Fig. 5.8 Influence of fiber type on ultimate local compressive stress of high-strength SFRC (left) and stress-displacement response of high-strength SFRC with different fiber cocktails under partial-area loading [78] (right)

only clearly visible at relatively high fiber contents ($> 80\text{–}100\,\text{kg/m}^3$) [78]. Investigations on different fiber cocktails in [55, 62, 78] showed that under such loading conditions the combination of hooked-end macrofibers and straight microfibers proved to be most advantageous. Even though the ultimate local compressive stresses of the two fiber cocktails compared in Fig. 5.8, right, were almost identical, it can be seen that SFRC with 50% macrofibers and 50% microfibers (SFRC L60+S60) was characterized by a much more ductile behavior in the post-cracking stage (compared to SFRC L40+M40+S40). A positive influence on the load-bearing and fracture behavior due to the reinforcement with fiber cocktails was particularly evident in the case of partial-area loading with eccentric load introduction [78].

5.2.2.4 Fiber Orientation

As is well known, fibers aligned to the acting direction of tensile stresses have the best crack-bridging capacity. In the case of partial-area loading, the resulting splitting tensile stresses perpendicular to the loading direction usually limit the bearable local compressive stress and dominate the failure mode [39, 78, 90]. Accordingly, it has to be expected that the fiber orientation has a significant influence on the bearing and fracture behavior of SFRC under partial-area loading. In order to study this influence, partial-area loading tests were performed on SFRC in which the fiber orientation was intentionally manipulated through varying the casting direction in the production of specimens in standing and lying formworks.

In Fig. 5.9, left, the fiber orientation (measured by means of an electromagnetic device described in [78]) with respect to the loading direction is depicted by percentage in the three spatial directions (x, y, z) for SFRC specimens ($60\,\text{kg/m}^3$ hook-ended macrofibers) cast in both standing and lying formworks ($150\,\text{mm} \times 150\,\text{mm} \times 300\,\text{mm}$). For specimens
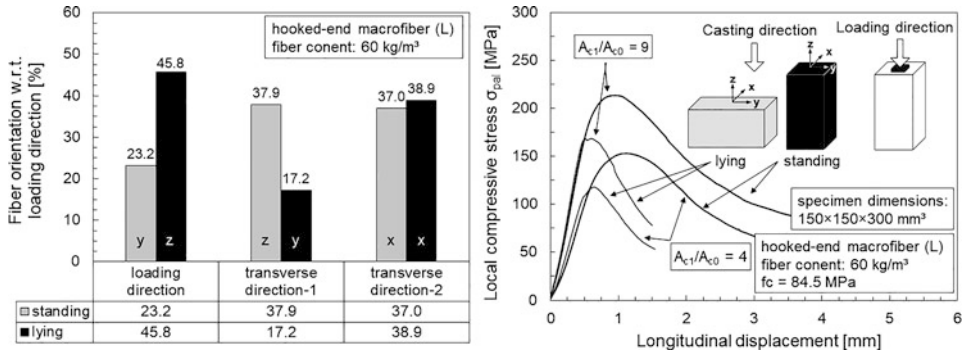
Fig. 5.9 Influence of the casting direction on the fiber orientation in SFRC specimens with respect to loading direction (left) and influence of the casting direction on the stress-displacement response of high-strength SFRC (right) [8, 10, 78]

produced in lying formworks, about 46% of the fibers were oriented towards the loading direction. Consequently, compared with specimens cast in standing formworks, fewer fibers were oriented in the two directions perpendicular to the loading direction, which correspond to the directions of principle tensile stresses (in the case of partial-area loading with spatial load distribution). As a results, the specimens produced in lying formworks exhibited considerably lower values of ultimate local compressive stress (stress drop up to 23%, Fig. 5.9, right). Furthermore, after reaching ulimate local compressive stress, the stress-displacement curves were characterized by a comparatively abrupt stress drop, indicating a less ductile fracture behavior. As can be seen in Fig. 5.9, right, this effect was clearly proven independent of the area ratio.

The effects of a preferred fiber orientation depending on the casting direction (standing/lying formwork) were even more significant for partial-area loading with plane load distribution, since in this case the principle tensile stresses act predominantly in only one transverse directions (perpendicular to the load direction) compared to partial-area loading with spatial load distribution [55, 62].

5.2.3 Numerical Modeling of SFRC

An integral part for the design and optimization of damage-tolerant tunnel linings is the development of a virtual-lab to analyze fiber reinforced concrete structures. Through the interaction of experiment and simulation, the developed models are validated and together novel segment designs are developed. In order to analyze the post-cracking behavior of arbitrary combinations of fiber type, concrete strength and optional bar reinforcement, the numerical models have to capture the major physical behavior of SFRC and RC subjected to tunneling related loading.

5.2.3.1 Multi-Level SFRC Model

Steel fibers provide a residual strength after onset of cracking depending on the type, content and orientation of the fibers. Available guidelines (i.e. [44]) characterize the residual strength of SFRC based on bending tests and derive uniaxial stress-strain relationships for Ultimate Limit State (ULS) and Service Limit State (SLS) design. In the framework of the Collaborative Research Center SFB 837 *Interaction modeling in mechanized tunneling*, a multi-level SFRC model has been developed (see [100] for more details), which allows to directly assess the influence of the individual fiber type, content, and orientation on the structural response. In contrast to the guideline approaches, the explicit modeling of important SFRC design parameters allows for their consideration as material uncertainties in the model based design of SFRC structures.

As illustrated in Fig. 5.10, the proposed multi-level model consists of submodels related to three different scales involved in the numerical analyses of SFRC structures:

- **Fiber Scale:** At the level of the individual fibers and the matrix, the pullout behavior of a single fiber is controlled by the interface conditions, the fiber shape and the fiber inclination with respect to a crack. A semi-analytical model predicting the pullout force-displacement relation of single fibers $F(w, \theta, \tilde{x})$, which depends on the position of the centroid $\tilde{x}$ and the inclination θ of the fiber with respect to the crack plane (Fig. 5.10, top center), has been developed in [99]. The model is capable of capturing the major mechanisms (straightening of the hooked-end, concrete spalling and fiber rupture) activated during the pullout of a single steel fiber embedded in a concrete matrix, accounting for different configurations of fiber type and strength, concrete strength, fiber inclination and embedment length (see Fig. 5.10, top).
- **Crack Scale:** At the level of an opening crack within the fiber-concrete composite, the fibers crossing the crack are activated and ensure a residual post-cracking strength depending on the fiber content and the fiber orientation. In the multi-level SFRC model, the post cracking response is approximated by a traction-separation law which is derived via the integration of the pullout force-displacement relations $F(w, \theta, \tilde{x})$ of all single fibers intercepting the crack and taking an anisotropic orientation of fibers into consideration [100].
- **Structural Scale:** At the structural level, the post-cracking behavior is captured by a discrete crack model based on cohesive interface elements [50, 100]. Between the regular finite elements (bulk elements), interface elements are inserted (Fig. 5.10, bottom), which allow a discrete mapping of cracks and provide direct information on the crack widths. The behavior of the interface elements is governed by the traction separation law derived on the crack scale with the multi-level SFRC model. In order to account for reinforcement bars if present, a mesh independent contact-based tying algorithm for the discrete representation of steel reinforcement was developed [24]. The rebars are modeled as truss elements and are coupled with the concrete matrix using a constraint condition between control points located on the rebar elements and their respective projection points within the solid elements in which they are embedded (see
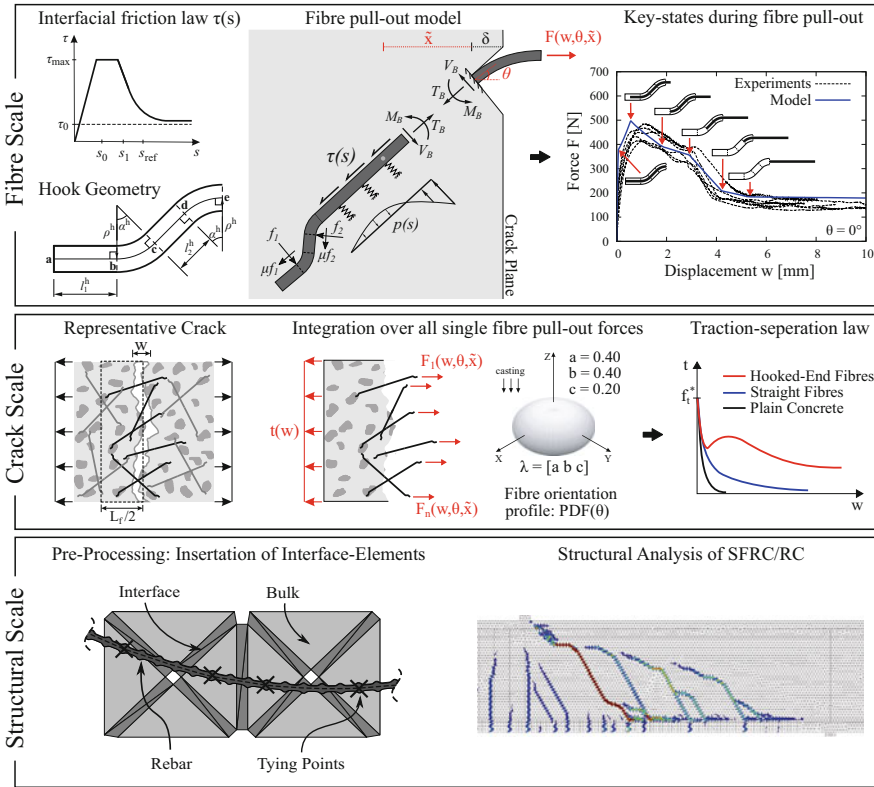
Fig. 5.10 Multi-level modeling of SFRC: Semi-analytical model for single fiber pullout considering various "key states" during elongation, plastification and concrete spalling of hooked-end fibers (Fiber Scale); Integration of the pullout response of all fibers crossing a representative crack and considering their orientation to calculate the traction-separation law (Crack Scale); Modeling of discrete cracks via interface elements inserted between the regular bulk elements and consideration of conventional reinforcement (Structural Scale)

Fig. 5.10, bottom). The constraint condition includes the bond-slip mechanism as provided in [44] and the steel behavior itself is considered with an elastoplastic v. Mises yield surface with linear hardening.

5.2.3.2 Validation for Fiber Pullout

The laboratory tests published in [11, 77, 79] (see also Sect. 5.2.1) are also used for the validation of the semi-analytical fiber pullout model incorporated in the multi-level SFRC model (Sect. 5.2.3.1). Beside the aforementioned material parameters of the concrete and the fiber, the explicit fiber geometry (length $L_f = 60$ mm, diameter $d_f = 0.75$ mm and hooked-end geometry described by $l_1^h = 1.8$ mm, $l_2^h = 1.3$ mm, $\alpha^h = 45°$, $\rho^h = 1.4$ mm) and the fiber-concrete bond characteristics ($\tau_{max} = 1.70$ MPa, $\tau_0 = 0.42$ MPa, $s_{ref} = 0.38$ mm
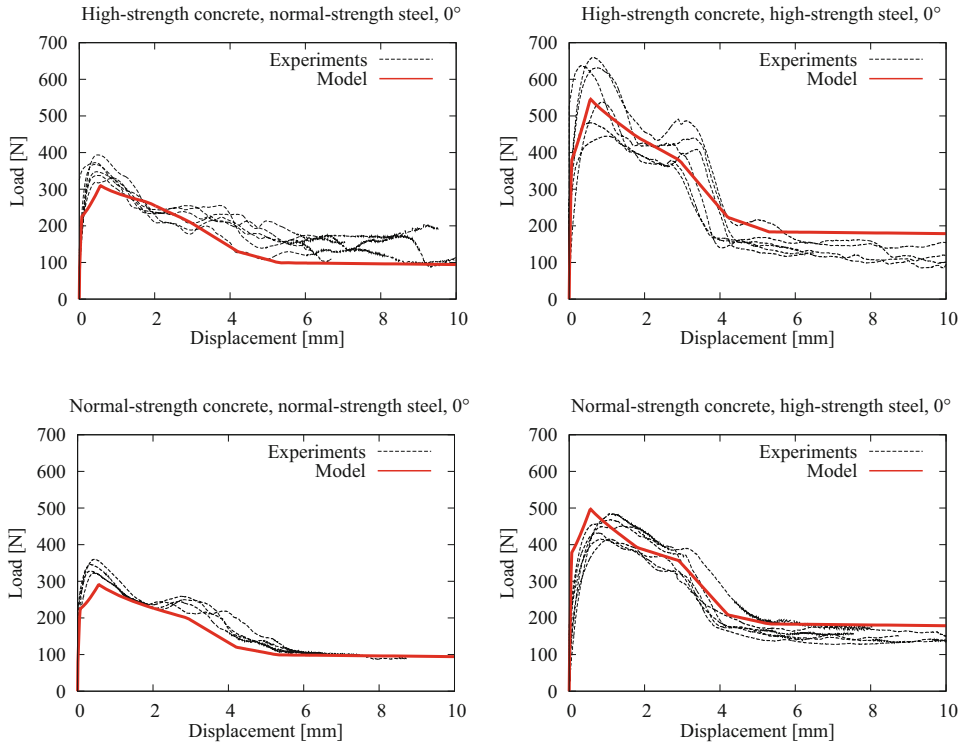
Fig. 5.11 Model validation for hooked-end fiber pullout without inclination (0°): Model results vs. experimental results for different combinations of concrete and fiber strength [101]

and the friction coefficient $\mu = 0.3$) are used as model input. The model predictions for the different concrete and fiber strengths are compared to the experimental results in Fig. 5.11.

A remarkably good correlation is observed in all cases. In each diagram, the first nearly vertical ascending branch corresponds to the elastic state of the hooked-end. The further ascent of the curve leads to the pullout force peak which is reached when both of the arcs of the hook become fully plastic and the hooked-end starts to enter the straight part of the fiber channel. Afterwards the pullout force decreases, accompanied with the progressive straightening and sliding of the segments of the hooked-end. Finally, the whole hook is straightened and a residual pullout force remains corresponding to the frictional sliding in the fiber channel.

In addition, the pullout tests on inclined fibers (Sect. 5.2.1.4) are used for the validation of the semi-analytical fiber pullout model (Sect. 5.2.3.1). All the model results and the respective test results are plotted in Fig. 5.12.

A good agreement between the model predictions and the experimental results can be observed. While the pullout response for fibers with an inclination of $\theta = 15°$ is similar to non-inclined fibers (see Fig. 5.11), the pullout characteristics change considerably when
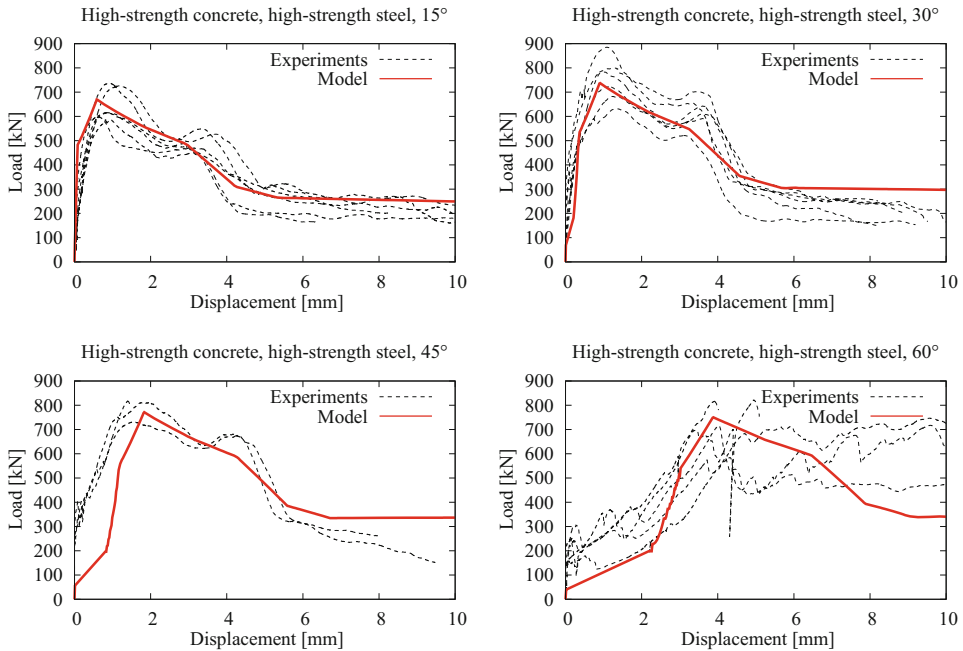
Fig. 5.12 Model validation for the pullout of hooked-end fibers embedded in high-strength concrete: Model results vs. experimental results of the load-displacement relation for different inclination angles [101]

the inclination angle is increased from 30° to 60°. Particularly, in the case of 60°, instead of a steep ascending branch prior to the peak force, the pullout force continuously increases and reaches its maximum at a rather high level of pullout displacement due to matrix spalling.

5.2.3.3 Validation for Partial Area Loading

For the validation of the multi-level SFRC model, the partial area loading experiments with a plane load distribution and an area ratio of $\delta = A_{c1}/A_{c0} = 4$ are used [62] (Sect. 5.2.2). All available experimentally obtained material parameters and the explicit fiber geometry (Fig. 5.13, left) are used as a direct model input. A detailed description of the model input can be found in [47]. With these parameters, first the single fiber pullout responses $F(w, \theta, \tilde{x})$ of arbitrary inclined fibers with homogeneous distributed embedment lengths (see Fig. 5.10, top) are calculated, and then the crack bridging behavior is predicted (see Fig. 5.10, middle). The derived traction separation laws are validated for mode I fracture by re-analyzing the experimental 4-point bending tests. A comparison between the experimentally and numerically obtained nominal stress-midspan-deflection curves are presented in Fig. 5.13, right.
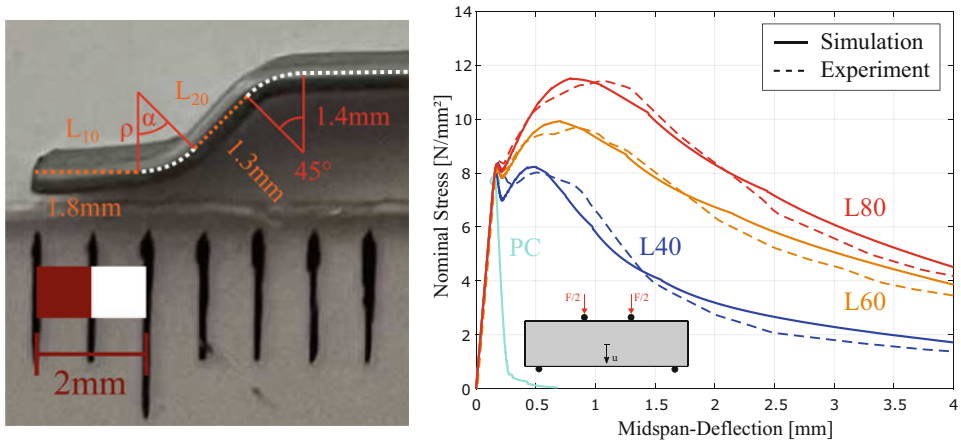
Fig. 5.13 Measurement of Dramix 3D 80/60 hooked-end geometry (left); Strength characterization of SFRC with different fiber contents by 4-point bending tests based on the DAfStb guideline [82] (right) [47]
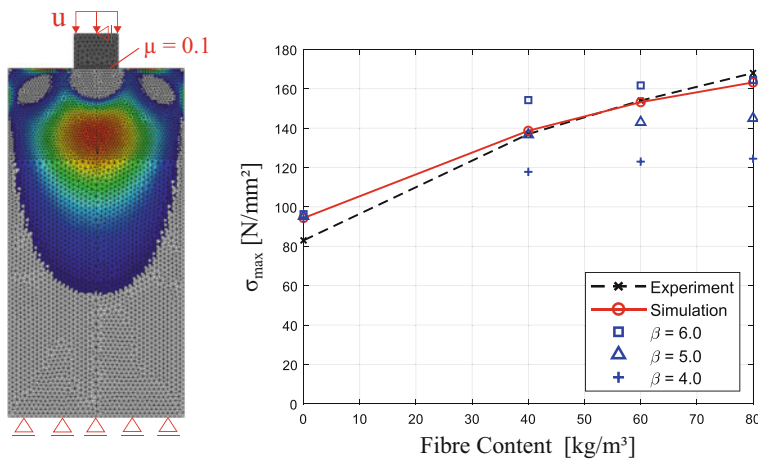
Fig. 5.14 Numerical model used for the re-analysis of the strip loading experiments with the distribution of the principal tensile stresses in the elastic regime (left); Comparison of the experimental and predicted peak load with different values for the shear strength parameter β (right) [47]

In general, a good agreement between the numerically obtained stress-deflection-curves and the experimental results is observed. The flexural strength, the post-cracking peak and the qualitative response is captured for all investigated fiber contents.

For the re-analysis of the strip loading tests, a plane stress model with an unstructured mesh and an element size between 4 mm up to 10 mm is used (see Fig. 5.14, left). To consider the influence of friction between the load plate and the specimen to the structural response, the load plate is explicitly modeled, and contact elements are inserted between

the plate and the specimen. Due to the high uncertainty regarding the shear strength, different values of the model parameter β controlling the shear strength are investigated in the re-analysis of the strip loading experiments. In Fig. 5.14, the numerically and experimentally obtained maximum load of the PC and the SFRC specimens are shown for different values of β (blue).

It can be observed, that the load bearing capacity for the plain concrete specimen (i.e. for zero fiber content) is mainly influenced by the tensile strength, whereas for the fiber reinforced specimens, the shear strength governs the failure load. Furthermore, depending on the fiber content, an increased shear strength (β values between 5.0 and 6.0) is required to capture the experimentally obtained failure loads. Employing the empirical formulas for estimating the shear strength [47, 76] a reasonably good agreement between experimental results and numerical predictions can be observed (see red line in Fig. 5.14).

5.2.3.4   Casting Simulation of SFRC Structural Members

A major source of uncertainty involved in the mechanical properties of SFRC is the orientation and distribution of the fibers in the concrete matrix, which is influenced by the casting process and the geometry of the mold. If scale bridging material models are employed for the simulation of SFRC structures (see Sect. 5.2.3.1), assumptions regarding the orientation and distribution of fibers are required to predict the crack bridging behavior of the SFRC in the hardened state.

In order to simulate the casting process of SFRC and taking the formwork geometry into account, a numerical model based on Smooth Particle Hydromechanics (SPH) was developed and implemented in the open-source Code DualSPHysics [16]. The fiber orientation during the casting process is described by the Folgar-Tucker model [1, 22] in combination with the weakly compressible SPH method and allows the determination
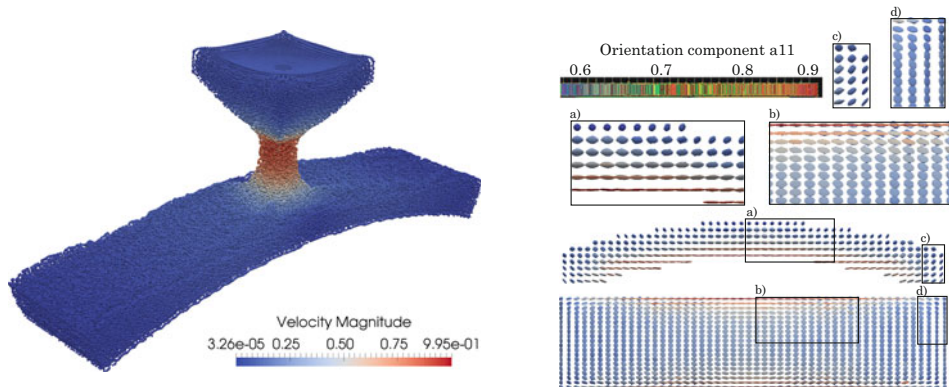
Fig. 5.15 SPH flow model to predict the fiber orientation resulting from the casting of a tunnel lining segment (left). Fiber orientation visualized by ellipsoids, where the orientation component a_{11} shows the probability of fibers aligned towards the horizontal direction (right) [32]

of the spatially as well as temporally varying probability density function of the fiber orientation. The flowable cement matrix is modeled as a viscous, regularized Bingham-Papanastasiou fluid, where the influence of the fiber content on the flow behavior is taken into account by the micromechanical model of Ghanbari and Karihaloo [30]. Finally, the orientation tensors can be easily visualized by ellipsoidal surfaces, where the eigenvalues denote radii, and the eigenvectors the axes orientations. The resulting fiber orientation after casting of a tunnel lining segment is shown in Figure 5.15. A detailed description and validation of the model can be found in [32].

5.3 Hybrid Segmental Tunnel Linings

The peripheral zones of lining segments (i.e. corners, edges, joints) are usually exposed to significantly higher forces than the interior regions due to various complex loading scenarios (e.g. concentrated load introduction, bending moments and shear force transmission) and are also particularly vulnerable to damages, such as concrete spalling. The risk of such damages is particularly high when lining segments are conventionally reinforced with steel bars, since such type of reinforcement cannot cover the edge areas due to the requirement of minimum concrete cover. A potential improvement of this problem could be achieved by the use of SFRC. Due to the small dimensions of steel fibers and their homogeneous distribution in the concrete, lining segments made of SFRC are more robust than conventionally reinforced lining segments, especially with regard to corner and edge spalling. However, the steel fiber content of conventional SFRC for lining segments usually ranges between 30 and 50 kg/m^3. The reinforcement efficiency of SFRC with such low (subcritical) fiber content is limited, so that the reinforcement exclusively with steel fibers is not expedient in the case of high loadings. SFRC with a supercritical fiber content (approximately > 100 kg/m^3), which is necessary for an adequate reinforcement efficiency as well as for achieving the intended crack distribution and crack width limitation, is no reasonable alternative for the use in lining segments, especially from an economic point of view.

A robust, damage-tolerant as well as economical efficient solution is provided by the concept of hybrid lining segments. The basic idea of the hybrid concept is to use high-performance steel fiber reinforced concretes (HPSFRC) with a high fiber content (> 100 kg/m^3) – even in combination with conventional rebars – only locally in the highly stressed and vulnerable zones of the segment, while in less stressed interior regions a conventional lining concrete (LC) with reduced steel bar reinforcement or a moderate steel fiber content is used, respectively. In addition, the segment cross-section can be significantly reduced by an optimized hybrid design (Sect. 5.3.5). This leads to a smaller excavation cross-section and lower material consumption, resulting in both economic and ecological benefits.

The development of the hybrid concept was based on a multi-level approach, which included the tunnel lining system, the individual segments and details in terms of material

and contact areas. For an optimization-based design, the developed numerical models and methods for the modeling of hybrid SFRC components at the structural level were used. On the one hand, the focus was on the design, taking into account aspects of robustness and an experimental validation of the methodology, and on the other hand, the development of adequate production methods and suitable joint and material concepts.

5.3.1 Production Methods

For the production of hybrid lining segments two main concepts were pursued, resulting in different production methods and casting techniques, respectively [58, 61]. The first concept ("wet-on-solid") aims to use geometrically tailored built-in components made of HPSFRC, which are pre-fabricated in a separate production process. The hardened precast components are installed at the critical zones (i.e. corners, edges, joints) in the conventional segment formwork, followed by the placing of a wet mixed conventional lining concrete. In this way, the precast components are integrated into the lining segment "wet-on-solid" (Fig. 5.16, left). In the case of precast components with additional re-bars, appropriate connection reinforcement must be provided. Apart from this, only minor modifications compared to the conventional production process are necessary. However, to ensure a sufficient bond between the precast components and the subsequently added lining concrete, appropriate measures are required (cf. Sect. 5.3.2.1).

The second concept ("wet-on-wet") is characterized by a simultaneous casting of the two concretes (HPSFRC/LC) in a standing segment formwork (Fig. 5.16, right). The concretes are initially separated from each other by a temporary interior formwork (i.e. moveable partition plates). During compaction, this interior formwork is continuously lifted up so that the two concretes get into contact "wet-on-wet", without getting mixed. This production method was first successfully tested on small-scale. It was shown that
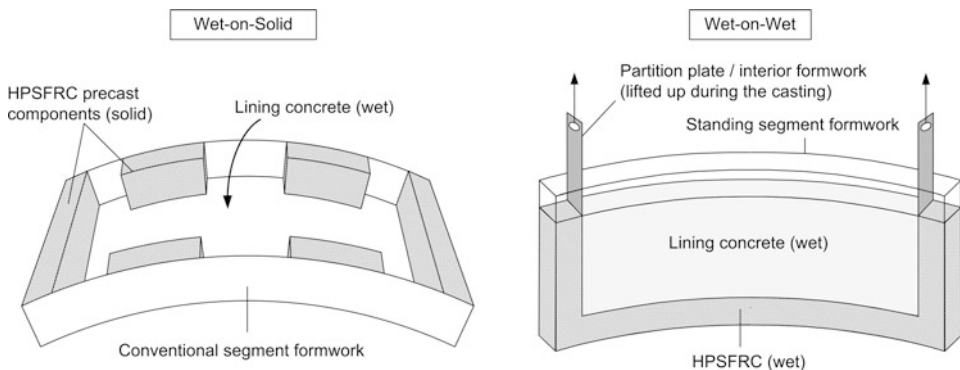
Fig. 5.16 Schematic illustration of production methods for hybrid lining segments: "wet-on-solid" (left), "wet-on-wet" (right)

Fig. 5.17 Standing wooden formwork for the "wet-on-wet" production of hybrid specimens (top left), cutting surface through a hybrid specimen (bottom left) and standing segment formwork for the "wet-on-wet" production of hybrind lining segments in real scale (right)

in a standing formwork, the HPSFRC can be precisely installed in horizontal but also in vertical thin layers together with an adjacent lining concrete (Fig. 5.17, left). Samples taken from such hybrid specimens consistently showed a monolithic bond between the two concretes.

In order to investigate this production method on the real scale, a standing segment formwork was used, which was designed and manufactured exclusively for this purpose by Herrenknecht Formwork. This formwork allows to cast rectangular segments with an external ring diameter of 7.80 m, a thickness of 0.40 m and a width/height (length of segment in longitudinal direction of the tunnel) of 1.00 m. The production of hybrid segments in this formwork (Fig. 5.17, right) has demonstrated that the "wet-on-wet" production method can be successfully realized on real scale.

For the "wet-on-wet" production of hybrid lining segments with additional rebars in the zones close to the longitudinal joints, alternative systems were also investigated for the use as an interior formwork, instead of monolithic steel plates. On the one hand, slotted steel plates were used, which could also be pulled during compaction, and on the other hand, steel mesh was used, which remained permanently in the segment. The latter solution, however, led to a significant weakening of the bond between the two concretes and is therefore not appropriate.

Moreover, it should be mentioned that in the case of the "wet-in-wet" production method additional production steps are required compared to the production in a conventional segment formwork. For example, in order to comply with the dimensional tolerances for lining segments and to install the circumferential sealing properly, mechanical finishing of the longitudinal joint is necessary, which is the unmolded surface in the standing segment formwork.

5.3.2 Experimental Investigations on Hybrid SFRC Systems

As the following sections demonstrate, investigations on the bonding behavior between precast components and the added lining show that a so-called hybrid SFRC system can substantially improve the overall system behavior, in particular when considering partial-area loading.

5.3.2.1 Investigations on the Bonding Behavior ("wet-on-solid")

The weak point of the "wet-on-solid" concept is the bond between the precast components and the subsequently added lining concrete. In order to ensure a durable tensile and shear resistant bond between the two concretes, the bonding surfaces of the precast components must have a certain macro and micro roughness. If necessary, also an additional mechanical connection with appropriate connection reinforcement may even be required. To investigate the pure bond behavior (i.e. without reinforcement) between the precast components and the lining concrete, experimental tests were carried out [59, 61]. To this end, plate-like precast components (50 cm $\times$ 30 cm $\times$ 5 cm) made of HPSFRC ($f_c = 120$ MPa, 120 kg/m^3 steel fibers) were first produced. By means of various measures [59, 61] (e.g. use of formliner with a specific geometrical structure, surface "washing" with high-pressure water jets), the roughness of the bonding surface of the precast components was varied in the range from tenths of a millimeter (micro roughness) to several centimeters (meso roughness). The hardened precast components were then positioned and fixed in a formwork (50 cm $\times$ 30 cm $\times$ 25 cm), followed by the placing of a wet mixed lining concrete ($f_c = 70$ MPa, 50 kg/m^3 steel fibers). The so produced hybrid specimens represent sub-segments of a hybrid lining segment. Drilling cores were taken from these hybrid specimens to investigate the bonding behavior under shear and tensile loading (Fig. 5.18, left, middle).

In the case of a bonding zone with a pyramid or frustum of pyramid shaped structure in combination with surface roughening trough "washing" with high-pressure water jets
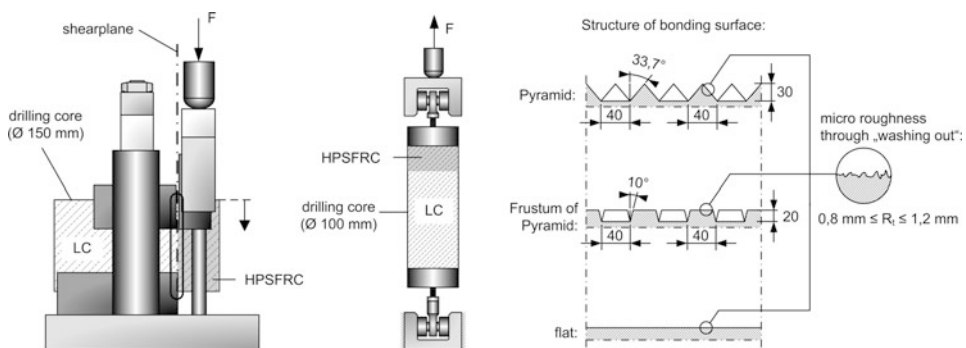
Fig. 5.18 Test setup for investigations on the bonding behavior under shear (left) and tensile loading (middle) [61]; structure of the bonding surface of precast components (right)
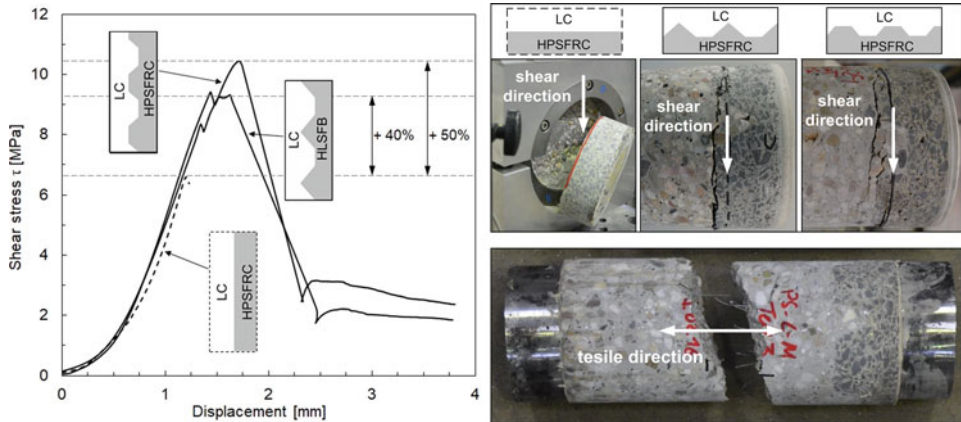
Fig. 5.19 Influence of the structure of the bonding zone on the stress-displacement response under shear loading (left); characteristic failure patterns of hybrid specimens under shear (top right) and tensile loading (bottom right) [61]

(Fig. 5.18, right), the ultimate bearable shear stress was enhanced by 40% to 50% compared to a flat bonding zone (Fig. 5.19, left). Specimens with a flat bonding zone showed an abrupt and brittle failure immediately after reaching the ultimate shear stress. The failure occurred trough a complete shear-off of the HPSFC layer along the flat bonding zone (Fig. 5.18, top right). In contrast, specimens with a specific structure of the bonding zone (pyramid, frustum of pyramid) clearly showed a more robust fracture behavior [59, 61]. In these cases, a significant load increase was observed after first cracks appeared. After reaching the ultimate shear stress, the stress-displacement curves were characterized by a sharp drop. However, a residual load-capacity was observed (Fig. 5.18, left) and no complete shear-off failure has occurred until the end of testing (Fig. 5.18, top right). Under tensile loading the fracture always occurred in the lining concrete (Fig. 5.18, bottom right), irrespective of the structure of the bonding zone [59, 61]. Therefore, a sufficient bond under tensile loading could be proven.

5.3.2.2 Hybrid SFRC Systems Under Partial-Area Loading

As the investigations on pure SFRC under partial-area loading (Sect. 5.2.2) clearly demonstrate, the use of steel fiber reinforcement can significantly increase the bearable local compressive stress and positively influence the fracture behavior. However, with regard to the stress distribution prevailing in concrete elements subjected to partial-area loading, it is known that critical tensile stresses develop predominantly in the load propagation zone (i.e. St. Venant disturbance zone) and vary as a function of the distance to the loaded area [39, 78, 90]. Therefore, following the basic idea of the hybrid concept, it is not necessarily appropriate to reinforce the entire concrete element with steel fibers, rather only those zones where (critical) tensile stresses are expected. To experimentally verify the hybrid concept on the material level, partial-area loading tests were performed analogue
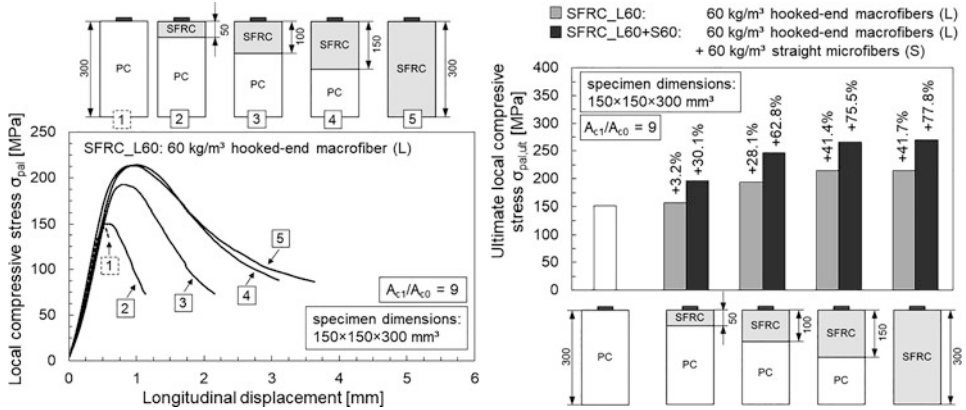
Fig. 5.20 Influence of the reinforcement layer thickness on the stress-displacement response (left) and on the ultimate local compressive stresses (right) of hybrid specimens under partial-area loading [78]

to Sect. 5.2.2, however, on hybrid specimens. Instead of a full range fiber reinforcement, the hybrid specimens were partially strengthened with steel fibers just in the St. Venant disturbance zone. To this end, the hybrid specimens were produced with both PC and SFRC using the "wet-on-wet" production method. In [56–58, 78, 81] the experimental investigations on hybrid SFRC elements under partail-area loading are presented in detail.

In Fig. 5.20, left, the stress-displacement response of PC specimens is compared to those of SFRC and hybrid specimens with L60 fiber reinforcement ($60\,kg/m^3$ hooked-end macrofibers) tested under partial-area loading (spatial load distribution, $\delta = 9$). For hybrid specimens, the thickness of the fiber reinforcement layer was 50, 100 and 150 mm (total specimen height: 300 mm). Figure 5.20, right, shows the corresponding ultimate local compressive stresses. In addition, Fig. 5.20, right, also shows the ultimate compressive stresses for SFRC and hybrid specimens produced with L60+S60 fiber reinforcement ($120\,kg/m^3$ fiber cocktail).

For all hybrid specimens, a considerable increase in the ultimate bearing capacity was observed with increasing thickness of fiber reinforcement compared to PC specimen, especially for those reinforced with fiber cocktails (up to 41% for L60 and 76% for L60+S60, Fig. 5.20, right). In the case of fiber cocktail reinforcement, by incorporating an only 50 mm thick reinforcement layer (1/6 of the total specimen height), an increase of 30% in ultimate bearing capacity was recorded. With increasing thickness of fiber reinforcement, hybrid specimens exhibited not only an increase in the ultimate bearing capacity, but also showed a considerable improvement in their ductility (Fig. 5.20, left). However, hybrid specimens with a 150 mm thick layer of fiber reinforcement (1/2 of the specimen height) exhibited, besides an almost identical bearing capacity, also nearly the same ductile behavior as SFRC specimens. This clearly shows, that a full range fiber reinforcement is not necessary.

In the case of partial-area loading with plane load distribution (Fig. 5.21, left), it was also found that the installation of a relatively thin layer with fiber cocktail reinforcement
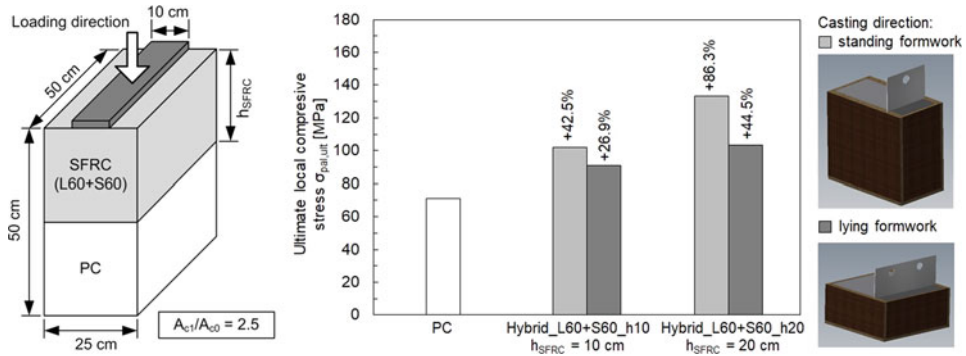
Fig. 5.21 Dimensions of PC and hybrid specimens tested under partial-area loading with plane load distribution (left); influence of the reinforcement layer thickness and casting direction on the ultimate local compressive stress of hybrid specimens (right) [58]

($120 \, kg/m^3$ L60+S60) in the load propagation zone already leads to a significant improvement in the ultimate bearing capacity (Fig. 5.21, right). Analogous to specimens with a full range fiber reinforcement, the casting direction (standing/lying formwork) had a remarkable influence on the ultimate bearing capacity, in both plane and spatial cases of partial-area loading. In the plane case, hybrid specimens produced in standing formworks exhibited an up to 30% higher bearing capacity compared to hybrid specimens produced in lying formworks, depending on the thickness of the reinforcement layer (Fig. 5.21, right). Thus, it could be shown that the production in a standing formwork, as in the case of the "wet-on-wet" production method for hybrid lining segments, can have a positive effect with regard to the fiber orientation.

Although ductile fracture behavior was less pronounced for hybrid specimens under partial-area loading with plane load distribution due to the incomplete confinement, the high content of steel fibers in the reinforcement layer nevertheless caused a considerable slower crack propagation and prevented complete splitting, as in the case of unreinforced specimens (Fig. 5.22). Moreover, concrete spalling was prevented by the fibers and was only present in the unreinforced areas of the specimens. Above a certain reinforcement layer thickness (here: 20 cm), the fracture behavior could even be changed to the effect that no cracking or spalling occurred in the peripheral zones close to the loaded area.

5.3.3 Reinforcement Layout by Topology Optimization

Topology optimization gives the opportunity to distribute a limited amount of material in a geometrical domain Ω, so that the structural stiffness K is maximized or the weight is minimized [71]. From a mathematical point of view, this is a minimization problem steered by the principles of elasticity. The design space is discretized with finite elements. Iteration and variation of the material distribution therein yields the optimal relation be-
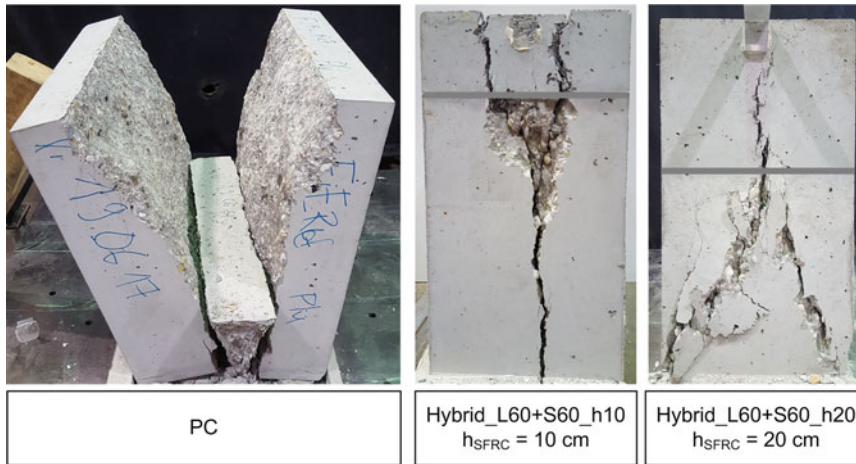
Fig. 5.22 Fracture of PC (left) and hybrid specimens (middle, right) under partial-area loading with plane load distribution [58]
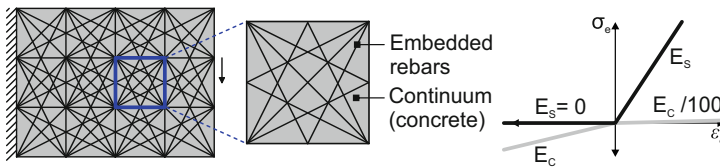
Fig. 5.23 Left: Mesh and material definition in hybrid truss-continuum optimization. Right: stress-strain relationship employed for concrete and steel. Modified with reference to [74]

tween the load F and the displacements u [34]. Among the three established methods of structural optimization – sizing, shape and topology optimization – topology optimization is the most suitable one for this purpose. In the past, it has been shown a valuable design tool especially for structures with complex stress states. In certain conditions employing distinct parameters, it automatically gives distributions of materials in structural elements comparable to strut-and-ties models (STM) [23].

Topology optimization is commonly applied to continuous or truss structures. Then, the objective is to find the optimal distribution of material in terms of densities ρ or cross-section areas A among the elements e that constitute the design space. In this context, reinforced concrete poses a special challenge as a composite of two materials–concrete and steel reinforcement–whose behavior is strongly nonlinear. In the past, especially the hybrid truss-continuum optimization (HTCO, e.g. [4, 27, 74, 92]) has provided good solutions for reinforced concrete. Different to the classical approach, the design space (geometrical domain) is filled with continuous volume (Ω_c) and truss elements (Ω_t) simultaneously. Compressive (σ_c) and tensile (σ_t) stresses result from the applied loads F
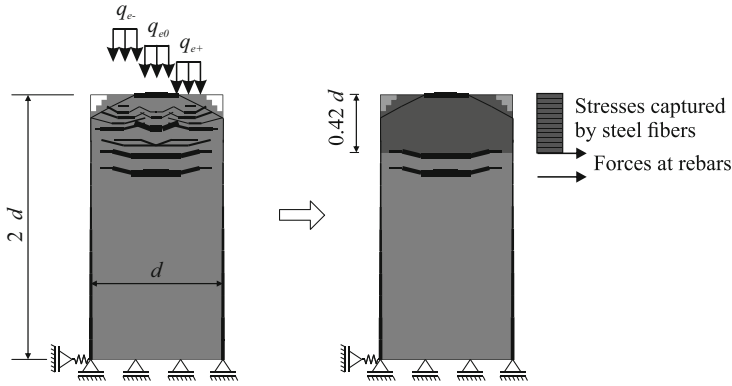
Fig. 5.24 Left: Hybrid optimization of an isolated longitudinal joint subjected to multiple (centric and eccentric) loads. Rebars represented as black truss elements. Right: Design simplification after replacement of smeared trusses by steel fibers. Modified with reference to [74]

and steer the use of both materials (Fig. 5.23). That way, it helps designers to identify suitable STMs for complex cases. Thereby, HTCO provides an objective – non subjectively biased – computational solution that suggests rebars in direction of the principal tensile stresses. Just the task to choose suitable diameters remains to the designer. The constrained optimization problem is formulated in terms of the vector of densities ρ and cross-section areas $\mathbf{A}$ according to [27, 74]:

$$\min_{\rho, \mathbf{A}} \quad c = \mathbf{F}^\top \mathbf{u} \tag{5.1a}$$

$$\text{such that} \quad \mathbf{K}(\rho, \mathbf{A}, \sigma_t, \sigma_c)\mathbf{u} = \mathbf{F}, \tag{5.1b}$$

$$\sum_{e_c \in \Omega_c} \rho_e V_e + \sum_{e_s \in \Omega_s} A_e L_e \leq \beta \, V_0, \tag{5.1c}$$

$$\rho_{\min} \leq \rho_e \leq 1, \ \forall \rho_e \in \Omega_c \,, \tag{5.1d}$$

$$A_{\min} \leq A_e \leq A_{\max}, \ \forall A_e \in \Omega_t \,. \tag{5.1e}$$

Therein the total compliance c is computed from the sum of the continuum and truss contributions. The total volume is restricted to a fraction β of the initial volume V_0. Further constrains limit the design variables. Usually ρ takes values between 0 and 1 to represent void or full material at each element. Minima for A_e and ρ_e avoid numerical singularities when solving the central FEM equation (Eq. 5.1b) to obtain $\mathbf{u}$, whereas A_{max} keeps the design feasible, limiting the diameter of rebars to those available on the market.

This scheme was applied to an idealized longitudinal joint of a segmental lining of width d and depth $2d$ – in order to fully capture the discontinuity region – subjected to single and multiple loads (q_{e-}, q_{e0} and q_{e+}) in Fig. 5.24 [74]. In practice, the ring loads can be introduced at the longitudinal joint not only centered, but also eccentrically. As
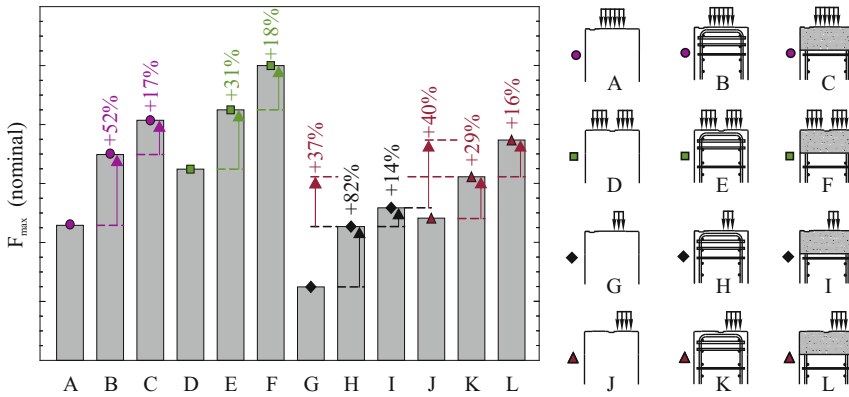
Fig. 5.25 Bearing capacity of the tested specimens. Modified with reference to [74]

expected, tensile stresses below the load introduction appear and the algorithm places suitable ties. Directly below load introduction, up to a depth of $0.42d$, a region of small trusses is identified. This motivates the replacement of rebars by steel fibers in this region to cover the smeared tensile forces and simplify the design. Conventional reinforcement still takes over the larger tensile stresses below that region (Fig. 5.24, right). Such a design bears potential to save material and manufacturing time as discussed in Sect. 5.3.2.2.

These results motivated the extension of the experimental campaign to hybrid SFRC systems. In the experiments not only SFRC was employed for the strengthening of the longitudinal joint, but also conventional rebars. Below load introduction, a layer of HPS-FRC with a depth of $0.42d$ was cast wet-on-wet [58, 74] to the normal strength concrete of the specimen. To quantify the performance of the strengthened joints, geometrically equivalent specimens with and without conventional reinforcement were cast for testing. Also the impact of relocating the gasket to the center was investigated. In this configuration, even higher bending moments are bearable by the same thickness and the splitting forces are reduced. In total, this leads to less reinforcement [74].

The bearing capacities reached by all alternative configurations tested are summarized in Fig. 5.25. Longitudinal joints with hybrid reinforcements have up to 18% more bearing capacity than those reinforced with rebars only. The relocation of the gasket to the center provides an increase of 37% with respect to the classical location at the edge and bar reinforcement, whereas for hybrid reinforcement, an increase of 40% was registered [74].

New reinforcement concepts derived from topology optimization proved to be more efficient in terms of bearing capacity of longitudinal joints. Strengthening the region below load introduction, and the relocation of the gasket to the center of the segment, leads to a considerable increase of the bearing capacity of longitudinal joints. That way, longitudinal joints are no longer decisive for the design and segments get a more homogeneous material utilization throughout [74].

5.3.4 Numerical Investigations of RC, SFRC and Hybrid Segmental Lining Designs

In order to investigate the performance of hybrid reinforced segmental linings on the tunnel scale and compare it to conventional RC segment designs, the structural responses of different reinforced segmental linings is analyzed using a detailed 2D model consisting of the grout layer and the individual tunnel lining segments, respectively (Fig. 5.26, left). For this purpose, a reference tunnel project is defined (overburden 20 m, sandy soil, lateral earth pressure coefficient of 0.5), where the loading acts on the lining (at steady state) is determined by the process-oriented tunnel simulation as described in Sect. 6.4.1.

The focus of the analyses is on the durability, quantified by means of the maximum crack opening exceeding the tolerated width of 0.2 mm. A RC segment with minimum reinforcement ($\varnothing$ 10–10 + additional rebars in high stressed regions), a SFRC segment with 60 kg/m^3 of 60 mm normal-strength hooked-end fibers (see Sect. 5.2) and a hybrid reinforced segment are analyzed (125 mm SFRC band and 200 mm long SFRC cap). The total steel mass of the SFRC and RC segment is similar ($\approx$260 kg/segment), whereas the steel amount in the hybrid segment is reduced by 65% (92 kg/segment). The simulations are carried out using a C40/50 concrete with a design tensile strength of 2.5 N/mm^2. For the designs containing SFRC an isotropic fiber orientation is assumed. A comparison of fiber and conventionally reinforced segments and different safety concepts in non-linear FE analysis can be found in [45].
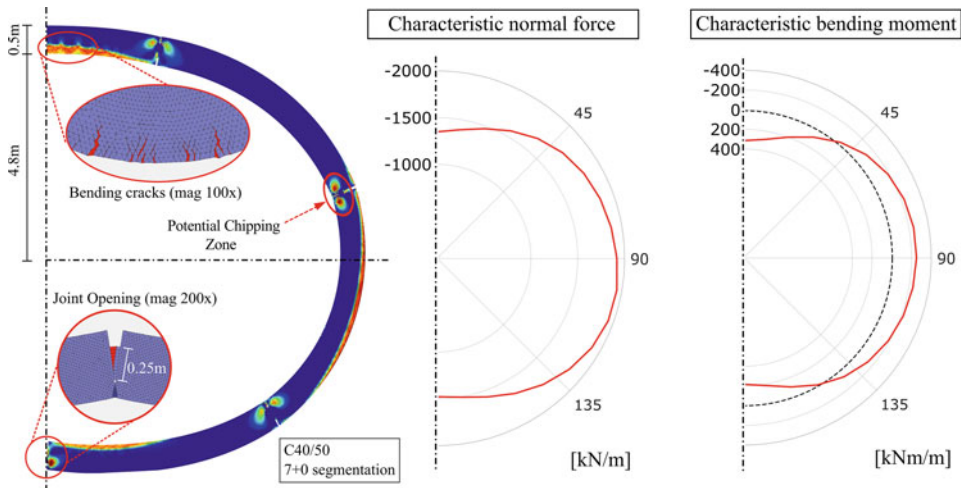
Fig. 5.26 Left: Dimension of the ring and the longitudinal joint contact and maximum principal stresses in the segmental lining model and indication of potential failure mechanisms.; Right: Characteristic normal force and bending moment distribution around the ring from a linear elastic analysis

The resulting maximum principal stresses and stress resultants are shown in Fig. 5.26. Under the characteristic loading, no large cracks occur in the plain concrete segmental lining. However, two potential failure modes are indicated: At the crown segment, the lowest normal force (-1375 kN/m) in conjunction with the highest bending moment (329 kNm/m) can be observed, potentially resulting in bending cracks. Around the longitudinal joint at $78°$, the largest tensile stresses occur due to a normal force of -1943 kN/m and a bending moment of -217 kNm/m. This could lead to a potential chipping of the segment corner (Fig. 5.26, left). Based on these observations, two loading cases are created for design purposes. For the design of the crown segment subjected to bending, the loads are modified such that the resulting bending moment is increased by a factor of 1.5 and the normal force is reduced by a factor of 0.5. For the design of the area around the longitudinal joint, where chipping could occur, the normal force and bending moment are increased by a factor of 1.5 to increase the stress transmission and maintain the joint rotation.

5.3.4.1 Load Case: Bending

The responses of all lining designs, or rather, reinforcement schemes, to the bending load case are shown in Fig. 5.27. Only the bending response at the crown segment is shown, as this is the area in which maximum cracking is observed. Further, only the crack width is shown. The lining system does not fail and continues to function as a load bearing structure. Therefore, the only limiting factor controlling the choice of any of these scenarios is the predicted crack width, which may not exceed the project dependent requirements for the SLS (around 0.2 mm).

As expected the plain concrete lining ring (PC), exhibits the largest bending cracks, with the dominant crack occurring at the inner edge of the tunnel lining at the crown, which is where the maximum bending moment is predicted. What is of note, is that the PC case exhibits multiple cracking behavior (due to the compressive normal force), rather than a single monolithic crack which leads to segment failure. The RC segment exhibits a similar response to that of the PC segment, with the primary difference being that the crack pattern is much more regular. Rather than predicting a crack size that more or less corresponds to the moment applied at a point, as is the case in the PC segment, the cracks that are observed in the RC segment are more or less all of similar size, indicating that the reinforcement bar effectively normalizes the cracking response along the length of the rebar. The maximum cack width predicted by the RC segment is 0.158 mm, which is within a tolerable range of below 0.2 mm as prescribed by the serviceability limits. Interestingly, the SFRC segments are the most effective in reducing crack width along the length of the segment. Both reinforcement schemes lead to cracks that are significantly below the serviceability limit and therefore represent valid reinforcement designs. In the case of the hybrid reinforcement scheme, the bending performance of a full SFRC segment is only slightly better (0.112 mm vs. 0.142 mm). This equals an increase in crack width of approximately 25% relative to a total decrease of SFRC of 75%.
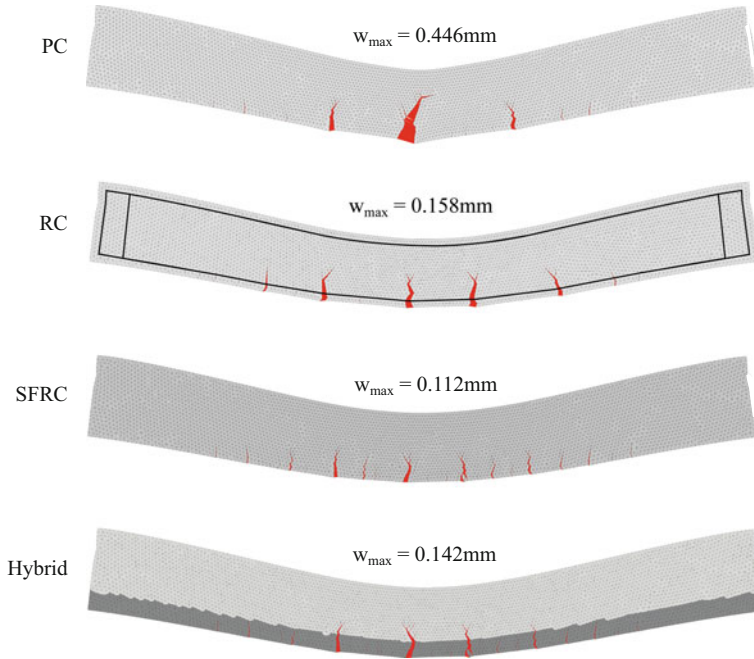
Fig. 5.27 Crack patterns at the crown segment for a plain concrete (PC), a conventional reinforced (RC), a steel fiber reinforced (SFRC) and a hybrid reinforced (Hybrid) segment design (magnification of 300×) [25]

5.3.4.2 Load Case: Chipping at the Longitudinal Joint

The responses of all lining designs, or rather, reinforcement schemes, subjected to the chipping load case are shown in Fig. 5.28. The maximum chipping cracks occur at the longitudinal joint located 78° away from the tunnel crown, as measured clockwise from the top of the ring.

Generally, the trend in predicted maximum crack width is similar to that as of the bending variants as shown in Fig. 5.27 and discussed above. However, in the case of chipping, the SFRC proves to be significantly more effective in reducing crack widths. Significantly, the minimum reinforcement provided against splitting stresses in the RC design is not sufficient to inhibit the formation of cracks in exceedance of the tolerance. This indicates that SFRC is much better suited to resist chipping cracks than RC. While the performance of the hybrid reinforcement scheme is better than the conventional RC design and below the serviceability limit, it's effectiveness can be increased by using a higher SFRC cap length. The splitting crack is initiated outside the SFRC layer and therefore the SFRC cap can only limit further crack development. In order to estimate an optimal SFRC cap length, optimization algorithms can be applied (see Sect. 5.3.5).
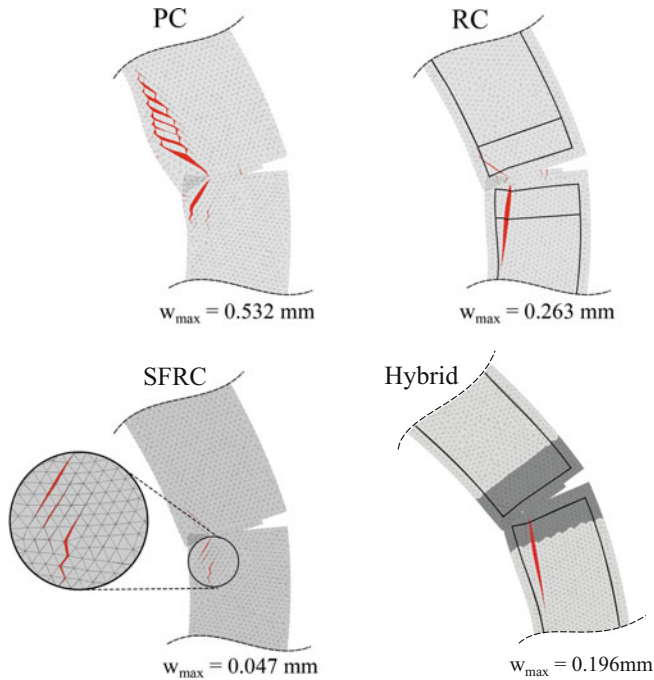
Fig. 5.28 Crack patterns at the longitudinal joint located at 78° for a plain concrete (PC), a conventional reinforced (RC), a steel fiber reinforced (SFRC) and a hybrid reinforced (Hybrid) segment design (magnification of 100x) [25]

5.3.5 Optimization Based Design for Hybrid SFRC Linings

A robust segment design in tunneling projects, going along with the reduction of the risk of damage, also needs to satisfy the economic feasibility. As shown in the previous sections, SFRC segments provide a sufficient load bearing capacity and an increased serviceability performance compared to conventional RC segments. If a proper hybrid reinforcement is chosen, a similar performance to a SFRC reinforcement scheme can be achieved while the steel content is further reduced. In this section, hybrid SFRC segment designs are derived by using optimization algorithms in conjunction with complex numerical models and by taking material uncertainties into account [68]. Due to the high computational effort of solving optimization tasks under uncertainty, the structural models are replaced by Artificial Neural Networks (for more details i.e. [47]).

5.3.5.1 Robust Optimization Earth Pressure Loadings
In Sect. 5.3.2.2 as well as in Sect. 5.3.4 it was shown that hybrid segments are capable to prevent critical cracking around the longitudinal joint and to simultaneously reduce the amount of steel. Here, a robust optimization [6, 98], with the design parameters sum-
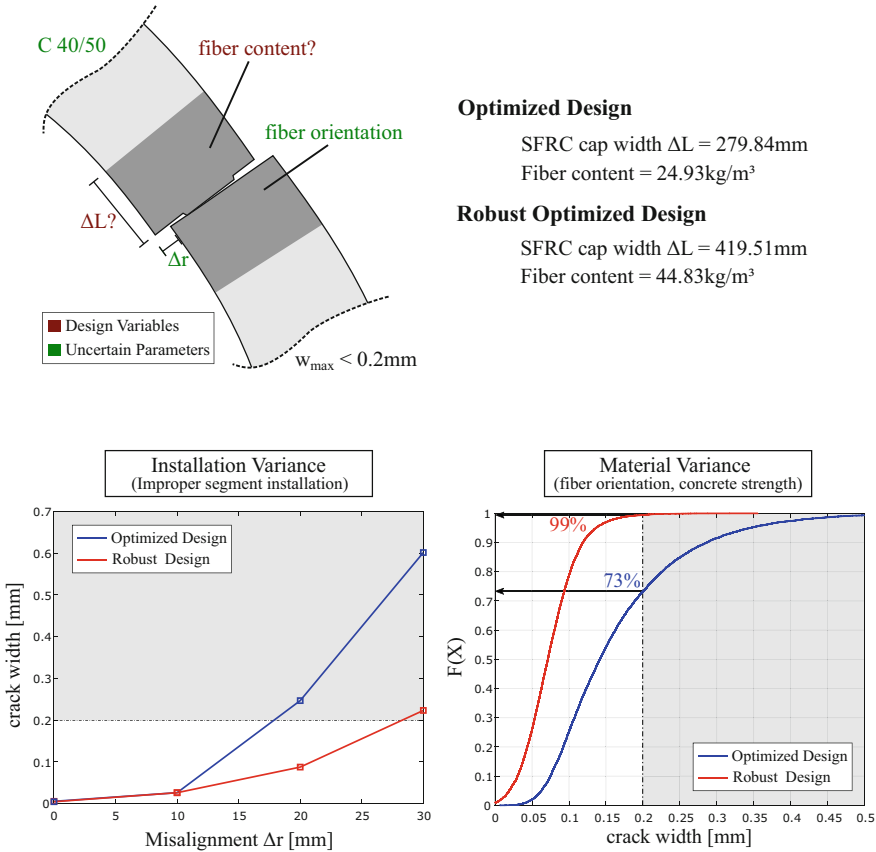
Fig. 5.29 Optimized design vs. robust optimization of longitudinal joints. Specification of the optimization tasks and resulting width of the SFRC cap and fiber content (top). Comparison between an optimized and robust optimized segment design in terms of installation as well as material variance (bottom) [43]

marized in Fig. 5.29 (top) and using the numerical model described in Sect. 5.3.4, is performed to determine a robust hybrid segment design with a minimal SFRC material usage (see also [43, 46]). In addition, conventional optimization is performed to minimize the SFRC cap width and the required fiber content. Besides the savings on material costs, the minimization of the fiber amount reduces the likelihood of fiber clumping and therefore contributes to a more consistent performance. A maximum tolerable crack width of 0.2 mm is employed as constraint. In case of the robust optimization, also the variance of the maximum crack width due to uncertain material properties is included as an objective function. The tensile strength of the C40/50 concrete is modeled as Gaussian distribution ($\mu = 3.5\,\text{N/mm}^2$, $\sigma = 1.0\,\text{N/mm}^2$) and also the fiber orientation is considered as interval representing favorable to unfavorable orientations. The optimization task is solved by the particle swarm optimization [37].

The optimized design leads to a 280 mm long SFRC cap with 25 kg/m³ of fibers, while the robust optimized design leads to a 420 mm SFRC cap with 45 kg/m³ fibers. In order to evaluate the vulnerability of both designs, their performance in case of an improper segment installation, resulting in a misalignment Δr between adjoining segments (Fig. 5.29, bottom left), and their reliability regarding variances in the concrete strength as well as in the fiber orientation (Fig. 5.29, bottom right) are investigated. In terms of installation variances, both designs are damage tolerant with respect to small misalignment, but only the robust optimized design prevents the development of critical cracks at larger misalignment. In addition, the robust optimized design provides a consistent performance in the full range of possible material properties. Considering the material variance, unfavorable realizations of concrete strength and fiber orientation, results in a probability of 27% that the maximum tolerable crack width of 0.2 mm is exceeded when using the optimized design.

5.3.5.2 Reliability Based Optimization of Thrust Jack Forces

Beside the earth as well as the water pressure loads acting on the tunnel structure, the thrust jack forces during TBM advancement are often decisive for the chosen segment thickness. Therefore, the same reference tunnel project as described in Sect. 5.3.4 is used as an example, where the maximum thrust jack force of the tunnel boring machine F_{design} is specified to 5600 kN. Here, a hybrid fiber reinforced segment consisting of two SFRC layers (A and B) is designed, whose required thickness d and the fiber content c_F as well as the width ΔL of the strengthening SFRC layer B (see Fig. 5.30) is determined by solving an optimization task under consideration of uncertainties (for more details see [47]). Through the consideration of material parameter uncertainties (fiber orientation λ_F as interval, concrete tensile strength f_t as log-normal distribution) as well as construction
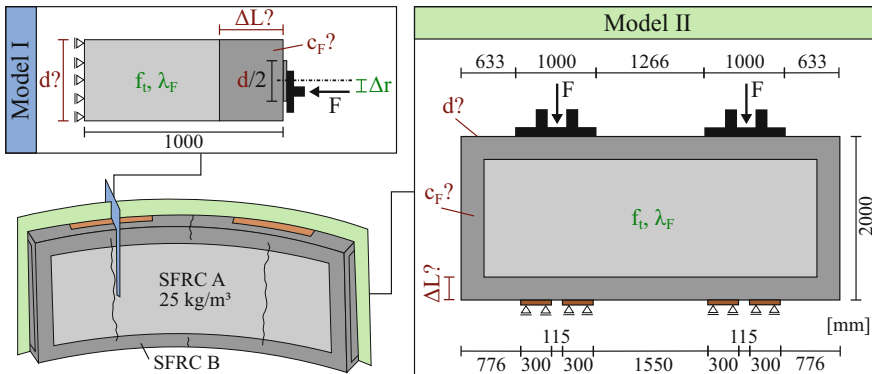
Fig. 5.30 Design variables (red), the jack eccentricity and material uncertainties as uncertain a priori parameter (green) considered in two structural models used for the optimization task to generate a robust hybrid lining design. The potential cracks due to the thrust jack loading are indicated in the illustration of the segment at the bottom left [47]
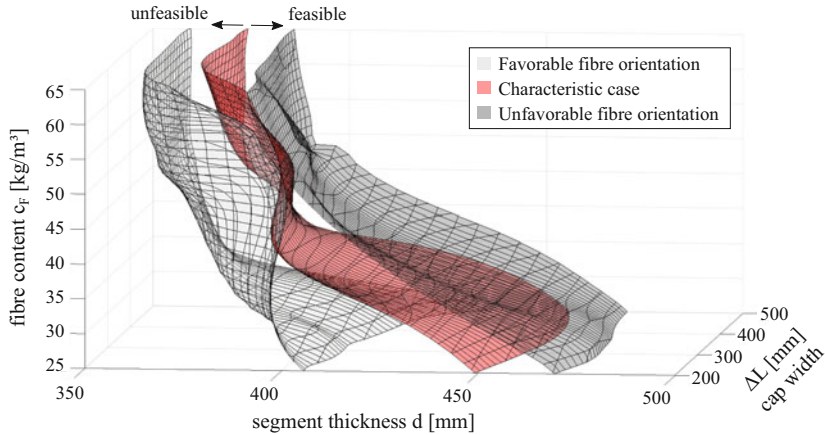
Fig. 5.31 Constraint limit states for the characteristic case and the realizations of a favorable as well as an unfavorable fiber orientation [47]

tolerances resulting in an eccentric placement of the thrust jacks Δr and considering accepted failure probabilities as constraints in the optimization procedure, a cost-effective as well as durable hybrid fiber reinforcement segmental lining design can be derived. In order to design the lining segment subjected to thrust jack forces, two plane FE models, labeled as *Model I* (plane strain) and *Model II* (plane stress), are used analogous to the design models in engineering practice (Fig. 5.30). In accordance with the design models for the bursting stresses due to partial area loading, *Model I* is decisive for the load bearing capacity of a segment subjected to thrust jack loading. The main objective of *Model II* is to examine, if the serviceability requirements in terms of critical crack widths are fulfilled. Therefore, a plane stress model of the segmental lining is employed to check, if the derived design can prevent the occurrence of critical cracks between the two thrust jack pads.

The inner part of the segment is reinforced by 25 kg/m³ of Dramix 3D 65/60 hooked-end steel fibers (minimum fiber content according to [82]), whereas a SFRC cap with a higher content of fibers c_F and a width ΔL (both to be optimized) is placed at the outer part (see Fig. 5.30). The post-cracking behavior depending on the fiber type, content and the orientation is calculated by the multi-level SFRC model described in Sect. 5.2.3.1, which was systematically validated for the Dramix 3D 65/60 hooked-end steel fibers in [33].

Figure 5.31 illustrates the constraint limit state from the reliability based optimization in the design space expanded by the fiber content, the segment thickness and the width of the layer cap. The constraint limit state divides the design space into a feasible and an unfeasible region. As can be seen in Fig. 5.31, the segment thickness d and the fiber content c_f are dominating the shape of the constraint limit state for each case, whereas the cap width ΔL has only a minor influence. With the minimum fiber content of 25 kg/m³, a segment thickness of $d \approx 460$ mm (characteristic case) will still lead to a feasible de-

sign. An increase of the fiber content up to $40\,kg/m^3$ enables a reduction of the segment thickness to $d \approx 400\,mm$ for the characteristic case, but by further increasing the fiber content, only small reductions of the segment thickness can be achieved. The width of the SFRC cap ΔL is the least sensitive design variable. If a certain width is provided (tensile stresses occur within the outer SFRC layer), only small improvements with increasing cap width ΔL can be obtained (see characteristic case at higher fiber contents c_F in Fig. 5.31). A reduction of the segment thickness up to $d \approx 375\,mm$ can be achieved. Furthermore, the characteristic case is investigated for an unfavorable fiber orientation ($\lambda_F = 0.3$) and for a more favorable fiber orientation ($\lambda_F = 0.45$) according to [86]. It can be seen in Fig. 5.31, the fiber orientation has a high impact on the performance of the constraint limit state, which can either result in a further reduction of the segment thickness d by $\approx 17\,mm$ or to an increase by $\approx 13\,mm$ for the characteristic case.

For this reason, the first set of weights adopted in the multi-objective optimization problem prioritize the reduction of the thickness over the minimization of the remaining design variables and results in a $402\,mm$ thick segment with a $200\,mm$ wide SFRC cap containing $41\,kg/m^3$ of fibers for the characteristic case. When compared to the RC reference segment design, the steel content is reduced by 59% (106 vs. $260\,kg/segment$) and the concrete volume is reduced by 20% (3.61 vs. $4.53\,m^3/segment$).

5.4 Full-Scale Tester for Segmental Linings Subjected to Conditions in Real Tunnels

5.4.1 Experimental investigation

The knowledge gained on isolated longitudinal joints (Sects. 5.2.2 and 5.3.3 had to be transferred and extended to large-scale experiments on full lining segments. To this end, a testing rig capable to introduce up to 5 MN in horizontal and vertical direction was developed (Fig. 5.32). It has the advantage that the resources of the testing facility can be concentrated on a single segment. Nevertheless, it preserves the boundary conditions in real tunnels [9, 53]. The vertical load V is introduced by means of a vertical steel frame that distributes it on eight contact points of the segment extrados. The transition between steel profile and curved specimen is realized with elastomeric bearings which, simultaneously, considerably reduce the transmission of shear stresses. Thus, the load introduction is radial, properly reflecting surrounding ground and water pressure conditions. The presence of adjacent segments is simulated by steel wedges that copy the geometry of the longitudinal joints, where the compressive load of the ring is introduced, following the static scheme of an arc. The load introduction mimics the conditions in real tunnels, i.e., the effects of partial area loading are taken into account simultaneously by compression with variable eccentricity. An experiment on a conventional segment showed that for an eccentricity $e \approx 0.14 \cdot h$ (being h the segmental width) the longitudinal joint becomes decisive, showing brittle failure. Further details can be taken from [53].
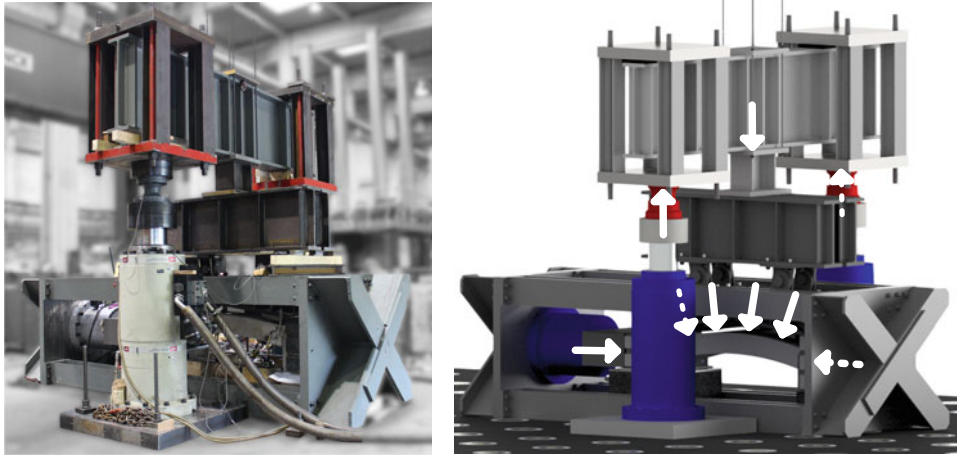
Fig. 5.32 Test setup (left) and load concept (right). Modified with reference to [9]
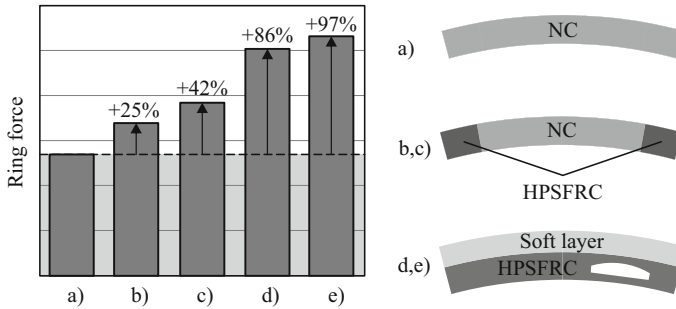
Fig. 5.33 Bearing capacities of conventional and hybrid linings. NC: normal concrete. HPSFRC: high-performance steel fiber reinforced concrete

The experimental campaign was then extended to two segments employing hybrid reinforcement concepts, i.e., casting normal concrete at the central region (reinforced with conventional rebars), and high performance steel fiber reinforced concrete at the longitudinal joints, which constituted a strengthening of that region. Both were manufactured employing the methods described in Sect. 5.3.1. Strengthening the longitudinal joints led to an improvement in the capacity of 25.5% and 42.1% in the two specimens, respectively (Fig. 5.33b, c). The difference observed between both results is directly related to the compressive strength of the concretes cast in the central region of the segments, which the experiments showed to be the decisive factor for failure. In this case, however, a ductile failure due to compression with low eccentricity in the central region was found, which enables thickness reduction, and thus concrete and excavation savings.

The use of high-performance materials was even exploited to a further extent. Next, the complete body of two segments with hollows were cast that increased the material savings

by 20% with respect to a conventional design. The geometry of the hollows was set to create an arc effect, given that the strut above is subjected to local bending due to external loading. A highly deformable mortar was cast on top to allow large plastic deformations (see Sect. 5.6.2) and better distribute the radial loads over the bearing part of the segment. In the segment (d), the load was introduced at the longitudinal joint in a conventional way, which corresponds to an outer gasket location. In another segment (e), the gasket was moved to the middle as learned from the simplified isolated specimens, investigated in Sect. 5.3.2.2. The eccentricity was increased by 10 mm to match the load level at failure with the capacity of the testing device. All bearing capacities are compared in Fig. 5.33.

5.4.2   Validation and Numerical Exploration of Novel Segment Designs

In order to explore arbitrary combinations of reinforcements schemes in a virtual-lab, the numerical simulation platform described in Sect. 5.2.3 is used to replicate the presented real-scale segment test device.

After the model was validated for SFRC structures in Sect. 5.2.3, the predictive capability for conventional RC segments is checked by re-analysis of the experimental investigated reference segment. The material properties are determined on the basis of the experimentally obtained compressive strength ($f_{cm} = 42.8$ MPa) using [44] and [18]. The
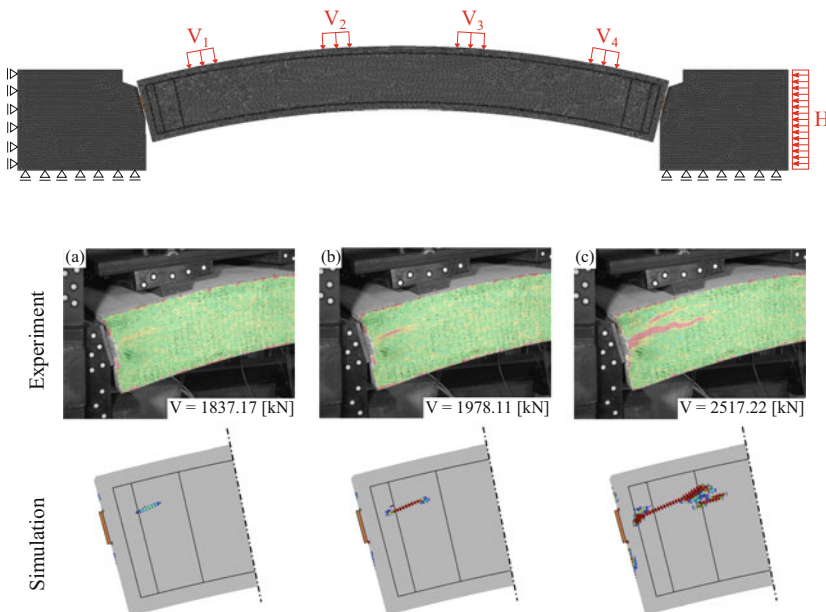
Fig. 5.34 FE model (top) and comparison of the DIC measurement with Aramis (GOM GmbH) and the damage predicted by the numerical model (down). Modified with reference to [52]

tensile strength of the concrete is calculated to be $f_{ctm} = 3.7$ MPa and the modulus of elasticity to $E_{cm} = 29\,658.7$ MPa, assuming a mode I fracture energy of $G_{F,I} = 0.1$ Nmm. The material behavior of the B500B rebars is assumed to be perfectly plastic (yield strength $f_y = 500$ MPa, $E_s = 200\,000$ MPa) and the bond-slip relationship from [44] is used. The plane FE model, representing a single layer of reinforcement, and an comparison between the numerically obtained crack pattern and the DIC measurement are presented in Fig. 5.34.

A good agreement between the experimental and numerical predicted load bearing capacity (2519.8 vs. 2503.5 kN) as well as the crack development (Fig. 5.34, bottom) can be observed.

After the validation of the numerical model, different novel segment designs (from pure SFRC over combinations of SFRC and RC to segments with hollows) are investigated. For the SFRC, a post-cracking behavior is assumed, which was derived within the framework of a systematic validation campaign [33] for concrete reinforced with 57 kg/m^3 Dramix 3D 65/60 steel fibers. The load bearing capacity of the investigated variants and the crack patterns for the segmental designs containing hollows are shown in Fig. 5.35.

A pure SFRC segment can carry a similar load as the experimentally investigated conventionally reinforced segment, whereas a combination of bar and fiber reinforcement (SFRC/RC) increases the load bearing capacity by 25.6% (Fig. 5.35, left). If two hollows (479 x 65/125 mm) are placed, the concrete volume per segment can be reduced by 23.8%. When the reinforcement layout is adopted from the experiment of the reference segment, critical cracking occurs in the corner areas of the hollows (Fig. 5.35, top right) and results in a by 65.9% reduced load bearing capacity. By adding steel fibers, even a slightly increased load bearing capacity can be achieved compared to the reference segment tested experimentally. Adopting the reinforcement layout by placing additional reinforcements around the hollows, the performance of conventional segments can be improved (see Fig. 5.33).
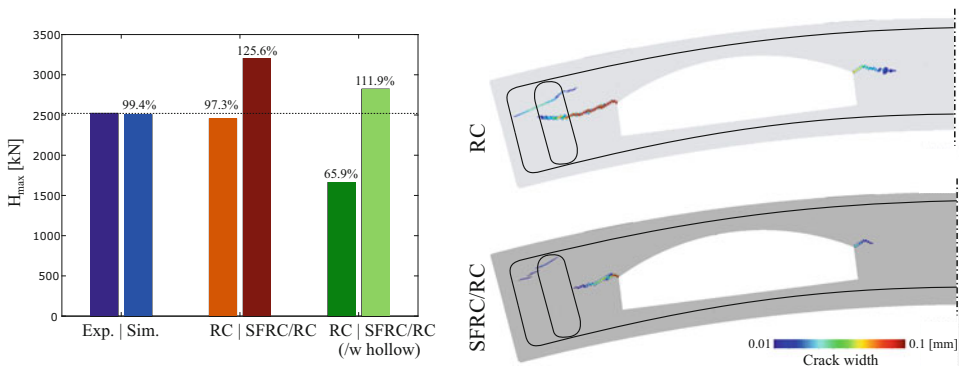
Fig. 5.35 Comparison of the maximum vertical forces of the investigated segmental designs (left) and the numerical crack patterns of the segments with hollows for two reinforcement schemes (right). Modified with reference to [52]

5.5   Annular Gap Grouts in Mechanized Tunneling

During tunnel driving a gap remains between the segment lining and the surrounding ground with a thickness of about 10 to 20 cm, the so-called annular gap. This gap must be backfilled with a suitable grouting material [7]. The state of the art is to inject the grouting material under pressure in order to completely backfill the annular gap and to stabilize the tunnel lining soon after mounting of the segment rings. Simultaneously, settlements of the ground surface shall be minimized. The main material-specific requirements on annular gap grouting materials are optimal workability and sedimentation stability until grouting as well as, immediate strength development soon after grouting. Thereby, the grouting materials have to be defined considering the respective (hydro-)geological and constructional boundary conditions. While one-component grouts are usually used in permeable soils, two-component grouts are applied in cohesive, impermeable soils. The hardening or rather stiffening of one-component grouts is primarily achieved through dewatering under pressure into the surrounding soil and thus consolidating the grout. In contrast, the strength development of two-component grouts is based on a chemical reaction usually between cement and accelerator.

5.5.1   One-Component Grouts – Experimental Investigations on the Material Characteristics

One-component grouts are mixed before being pumped to form a final annular gap grout and are used in both unconsolidated and solid rock. The annular gap grouting is usually carried out by pilaster strips in the shield tail (Fig. 5.36).
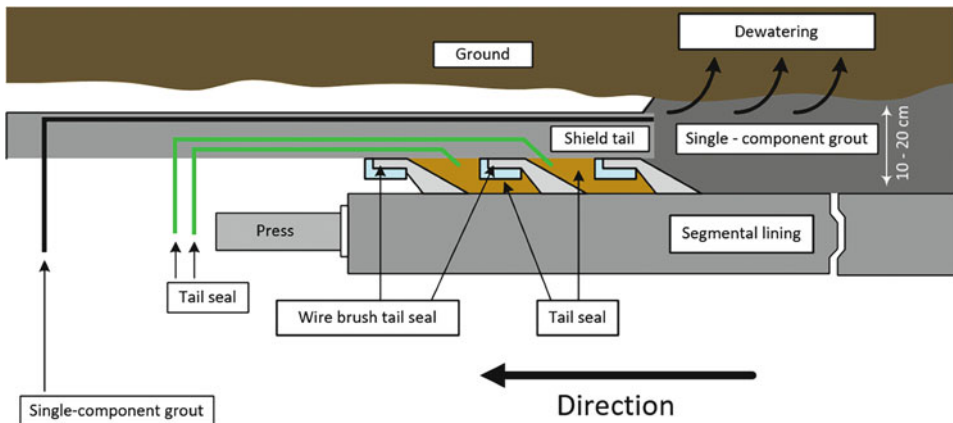
Fig. 5.36 Schematic illustration of the annular gap grouting with one-component grout

Table 5.1 Reference formulations of one-component grouts (kg/m^3)

Components	A-194	SI-120	SI-120	I-0
Cement	194	120	60	0
Sand 0–1 mm	169	169	169	169
Sand 0–2 mm	674	674	674	674
Gravel 2–8 mm	454	454	454	454
Bentonite	153	183	166	183
Water	207	177	164	135

According to the current state of the art, one-component grouts can be classified according to their binder content [17, 84]:

- Active grouts (Portland cement (OPC) > 200 kg/m^3)
- Semi-inert or reduced-active grouts (50 kg/m^3 < OPC < 200 kg/m^3)
- inert or inactive grouts (OPC < 50 kg/m^3)

The focus of the laboratory tests under varying material- and construction-specific parameters was on the decisive properties of a one-component grout namely workability/consistency, sedimentation stability, dewatering behavior and stiffness development. Through variations of the constituents and composition of the grout mixes the dewatering and thus the consolidation behavior of the annular gap grout can be influenced significantly. This affects the further dewatering process of the grout. Table 5.1 shows example mix designs of one-component grouts, which were already used in practice. The grout designation contains information the grout type and cement content, for example, "SI-120" is a semi-inert grout with a cement content of 120 kg/m^3.

These grout mix designs served as base mixes for the material-specific variations of binder composition (type, ratio) and aggregate (type, grading curve). Besides the original binder components (cement and fly ash) additives such as fine limestone powder, quartz powder and granulated blast-furnace slag were also used. A detailed list of the various compositions can be found in [94].

5.5.1.1 Workability and Sedimentation Stability

In the laboratory tests sufficient sedimentation stability was given for all reference mixes throughout testing. Furthermore, the investigated reference mixes exhibited a sufficient flowability (as a characteristic value for the workability) at a target spread flow diameter of 15 ± 5 cm after 6 to 8 h [84] after mixing. A correlation between the granulometry of the fine material and the consistency could be determined. A high specific surface area ($S_{m,b}$ – area of grains per unit weight) and thus an increased fineness of the initial materials results in a reduced flowability of the grout. This effect could be identified both for the binder fineness and for grading curves with smaller grain size fractions and was probably due to the 20% higher water demand of the fines. Also the surface texture and the grain shape have an effect on the consistency. While angular, rough surfaces impeded the optimum

sliding of the solids in the grout, smooth, round grain particles positively influenced the flowability.

Furthermore, the binder type had a decisive influence on the consistency of the grout. While active and semi-inert grout compositions stiffened faster due to the initial hydration reactions of cement, inactive or cement-free compositions showed a significantly higher flowability over a longer period of time (> 8 h after mixing).

5.5.1.2 Dewatering Behavior by Means of a Modified Filter Press Test

In order to investigate the dewatering behavior of one-component grouts more realistically than previously possible, a specially modified filter press (cf. [94]) was developed (Fig. 5.37, left). Thereby, typical steering parameters (grouting pressure p = 2.5 ± 0.25 bar, driving speed/dewatering duration t = 30 min) of a tunnel driving with segment lining (segment length of 2.00 m) were applied on grout samples with a layer thickness of about 17 cm. The total amounts of filtrate water f_{30} of the reference mixes with different binder combinations showed significant differences in the results (Fig. 5.37, right). With a linear regression analysis, a correlation between the total amount of filtrate water and the specific surface of the binder could be calculated, shown as trend lines at a mortar age t_M of 0 h and 6 h, respectively. Only with increasing age ($t_M = 6$ h) a downward trend of the total amount of filtrate water f_{30} could be observed (Fig. 5.37, right, grey highlighted area). Apparently, the progressive hydration of cement led to a decrease of the amount of filtrate water. This effect could be clearly seen at mortars, containing ordinary Portland cement (OPC) and fly ash (FA). With an equal substitute amount of FA ($S_{m,b} = 6.130$ to $8.910 \, cm^2/g$) with OPC ($S_{m,b} = 6.070 \, cm^2/g$) the amount of filtrate water was reduced by approx. 25%. Whereas, cement-free grouts ($S_{m,b} = 5.580 \, cm^2/g$) with identical initial water content exhibited an approx. 48% higher amount of filtrate water, which is attributed to the smaller specific surface ($S_{m,b} = 5.580 \, cm^2/g$) and thus smaller water demand of
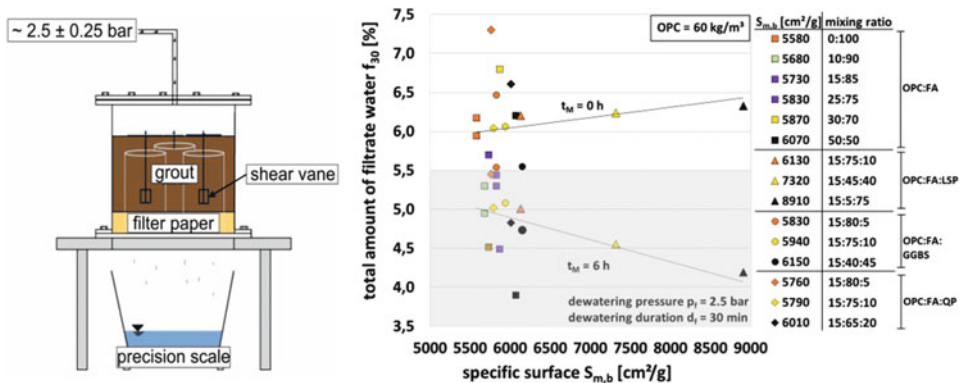
Fig. 5.37 Complete test setup of the "modified filter press" (left) [97]. Total amount of filtrate water f_{30} of grout mixes depending on the specific surface of the binder $S_{m,b}$ at the age t_M of 0 h and 6 h (grey highlighted area) (right) [93]
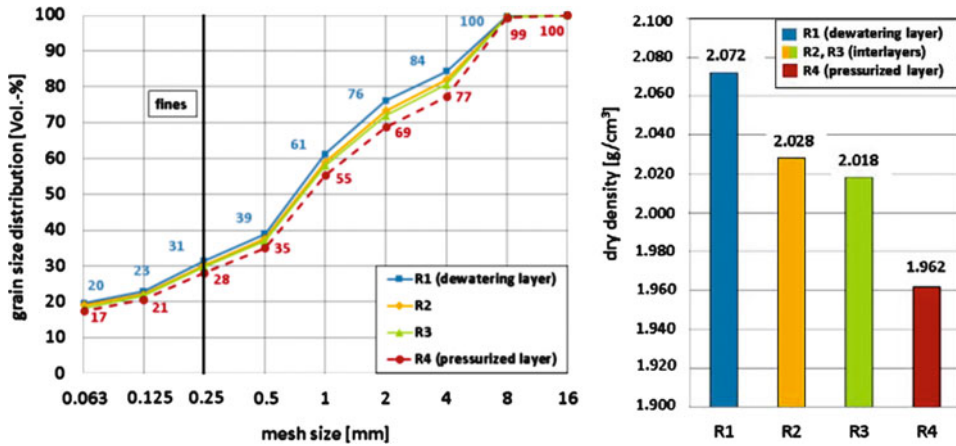
Fig. 5.38 Grain size distribution of individual layers of a dewatered one-component-grout (semi-inert grout "SI-60") (left). Dry density of individual layers (right) [95]

FA. A substitution of FA with limestone powder (LSP) and quartz powder (QP) demonstrated that the total amounts of filtrate water f_{30} decreased significantly through a high amount of the respective fine (LSP: 75% by mass, $f_{30} = 4.2\%$ by mass, QP: 20% by mass, $f_{30} = 4.7\%$ by mass). Whereas, a high substitute amount of FA with ground granulated blast-furnace slag (GGBS: 45% by mass) resulted in approx. 22% more filtrate water f_{30}. What can be deduced from this is that beside the specific surface of the binder $S_{m,b}$ also the fineness of the respective fines contributes to the dewatering potential of the mortar [93].

Through dewatering under pressurization the grout consolidates, leading to an internal compaction of the grain system through a re-distribution of the fine particles. On the basis of the particle size distribution and the dry density, it could be demonstrated that fine and ultra-fine particles (< 0/0.25 mm) are rearranged from the pressurized side to the dewatering side. In the present case (Fig. 5.38, left, exemplary shown for a semi-inert grout), the coarse grain content (> 4 mm) was about 20% by volume before pressurization. At the end of the dewatering test the dewatered grout sample exhibited a grain content about 23% by volume on the pressurized side and only 16% by volume on the opposite side (towards the water release). This is reflected through the dry densities of the grout sample. Higher densities were determined at the dewatering side than at the pressurized side (Fig. 5.38, right). Accordingly, a more intense compaction occurred, resulting not only from the re-distribution of the fine particles but also from the increased water release at the pressurized side.

5.5.1.3 Shear Strength Development

In order to measure the development of shear strength at different ages and depths of the dewatered grout compositions, shear blades were already installed before pressurization into the fresh grout [94]. All investigated grout compositions consistently achieved the
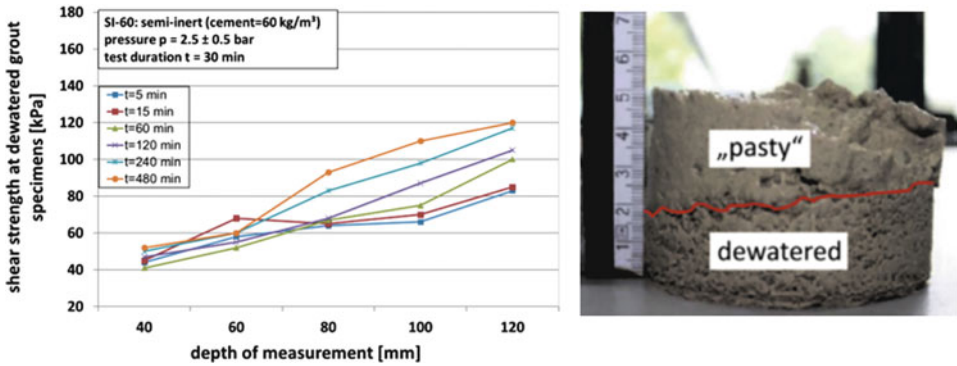
Fig. 5.39 Development of shear strength at dewatered specimens of semi-inert mixes "SI-60" depending on the grout depth (left). Formation of different dewatered layers (dewatering gradient) (right) [96]

required minimum shear strength of $\tau \geq 2.0\,\text{kN/m}^2$ after 30 min [84]. Overall, a positive effect on the shear strength was observed with an increase in binder fines, use of coarse-grained aggregate, higher drainage pressures, and at greater depths of placement. Significantly higher shear strengths were obtained when initial components with a high specific surface area were used and inert materials were substituted by finer cement particles. In addition to the granulometry effect and the associated physical filler effect of the fines, this was a result of the progressive hydration development of the cement. The development of shear strength correlated with the amount of filtrate water of the respective grout compositions. In the pressurized zones less consolidation could be observed due to the relatively soft consistency of the grout. In contrast, in deeper layers (towards the water release), an approximately complete dewatering and as a result of the continuous increase in the packing density of this layer, the highest shear strength values were determined (Fig. 5.39, right). Accordingly, it can be stated that due to the re-distribution of fines, the transportation routes for further dewatering successively decrease (Fig. 5.39, left).

5.5.2 Two-Component Grouts – Experimental Investigations on the Material Characteristics

As an alternative to one-component grouts, two-component grouts have steadily become more relevant in practice. Such systems are indispensable in soils with very low permeability. In two-component grouts, an activating component B is added to the actual grout (component A) immediately before or during grouting in the annular gap. This causes an instantaneous stiffening/consolidation of the grout system. Therefor both physical effects (internal dewatering, e.g. via superabsorbent polymers, cf. Sect. 5.5.4) and chemical reactions (e.g. alkaline activation by water glasses) can be considered.

Table 5.2 Reference formulation and practical orientated minima and maxima of the corresponding source materials in kg/m^3

Components	Min.	M0	Max.
Cement	85	250	482
Bentonite	25	30	60
Water	730	836	870
Retarder	0.2	2.5	5.2
Accelerator (Sodium water glass)	53	90	140

Currently, two-component grouts are formulated on a purely empirical basis. Component A usually consists of cement, bentonite, possibly pozzolanic/inert additives and a high water content (approx. 70% to 80% by volume) [65, 87]. To achieve sufficient workability retarders can be added. Accelerators, usually alkali silicates (water glass), are used as the activating component B. The performance of practice-established grouts was determined on a reference grout (designation: M0). The focus was on investigating characteristic properties of two-component grouts such as workability/consistency, sedimentation stability and strength development (gel phase, early strength and final strength). In addition to the reference grout, used in practice minima and maxima of every source material are listed in Table 5.2.

Various modifications especially with regard to type and quantity (cement and bentonite content, ratio of cement to accelerator, retarder) were investigated, based on grouts used in practice. A detailed description of the respective grout mix designs (also cementless mixes) as well as an overview of typical requirements and reference values for two-component grouts can be found in [69].

5.5.2.1   Workability an Sedimentation Stability

The required processing time depends on the logistical conditions of the respective tunnel construction project. In this context the workability of component A is commonly determined by the Marsh time [83] as its use in several completed projects shows [69]. Sufficient workability and, consequently, pumpability of the two-component grout is considered at a Marsh time between 30 and 45 sec for 72 h [51]. The workability of the reference grout M0 was within the target range of the Marsh time from 30 to 45 sec up to approx. 60 h after production. Subsequently, a marked increase of the Marsh time can be observed with an excess of the target range of approx. 10%. Furthermore, with a higher content of granulated blast-furnace slag in the total binder, a reduced Marsh time was observed within the first 24 h. Thereby an increased flowability of the grout was a result of the cement substitution. After 48 h, the Marsh times of the considered grouts were approximately at the same level, which can be explained by the beginning hydration of the binder.

With regard to the sedimentation stability of the reference grout, the amount of bleeding water was determined to be below the limit value of 3% [51] after 3 h. The guideline value of 4% after 24 h [51], however, was exceeded by approx. 1.5 M.-%. With increasing time up to 48 h after mixing, the amount of bleeding water did not increase significantly.

5.5.2.2 Strength Development

The consideration of the strength development of a two-component grout can be divided into three phases:

- Gel phase up to 0.5 h,
- early strength from 0.5 up to 24 h,
- final strength.

The essential phase for the immediate bedding of the installed segments is the transition of the gel phase to early strength. Assuming an advance rate of 50 mm/min, a segment width of 1.5 m and a construction time of 30 min, the annular gap is grouted within 30 min by simultaneous grouting. After the grouting, the drift presses are released from the last and now freshly inserted segment ring. At this point, the lifting forces are decisive and the grouting material needs to be solidified so far that the segment ring remains stable in its position.

A previously developed test method was used to determine the gel time. For this purpose, the activation of the two-component grout takes place in a vertically arranged mixing device (Fig. 5.40, left). Components A and B are both filled separately into sealed cells. The cells are opened by valves and the components collide/homogenize in the static mixer arranged below. The two-component grouts, which is thus completely mixed, enters a funnel with a defined geometry and discharge opening (diameter: 6 mm). The time from the collision of the components to the break-off point of the volume flow is measured.
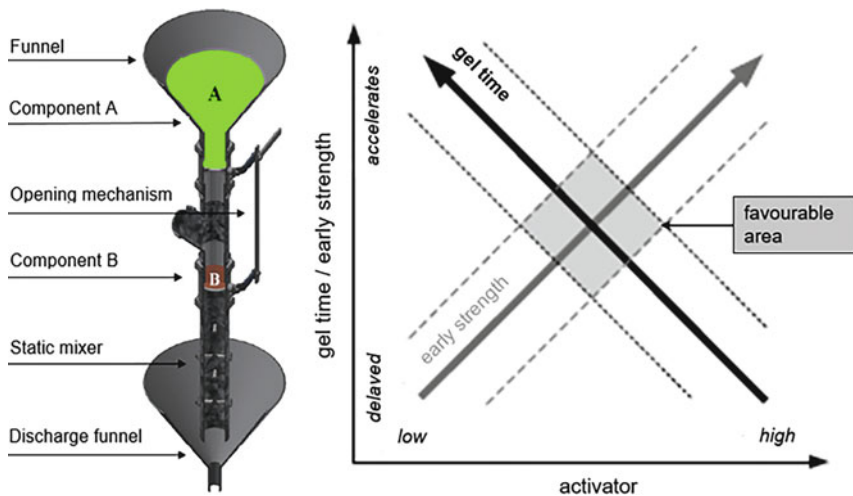
Fig. 5.40 Test method for determining the gel time of two-component grouts and visualizing of the mixing process of mortar (component A: green) and activator (component B: red) (left). Schematic illustration of the dependence between gel time and early strength with variable activator content (right) [69]
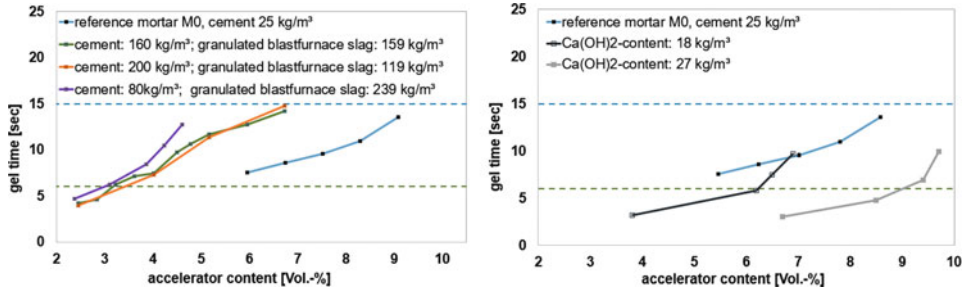
Fig. 5.41 Gel times alkaline activated two-component grout containing granulated blast-furnace slag with variable content of Portland cement (left) and cementless compositions with calcium hydroxide as solidification medium (right) [69]

The gel times of the reference grout M0 ranged from 6–15 sec at an accelerator content of 70 to 120 kg/m³ and thus are within the frame of reference of 5–30 sec known from literature [51, 72]. Furthermore, a dependence between the accelerator content and the gel time was found. In this framework, contrary to expectations, an increase in the accelerator content lead to an increase in gel time. While a gel time of about 7.5 sec was determined with an accelerator content of 80 kg/m³ (6.1% by volume), the gel time with an accelerator content of 120 kg/m³ (9.8% by volume) was about 12 sec. (Fig. 5.41, left).

In addition, the gel time and early strength interact directly with each other and can be controlled by the accelerator content if the binder content is kept steady. A high accelerator content is required for rapid development of the early strength. In contrast, the gel time is prolonged with an increased accelerator content. This reciprocal relationship is shown in Fig. 5.40, right.

The extent to which alkaline activation supports cement substitution and thus the use of latent-hydraulic and/or pozzolanic materials was further investigated. Through coordination of accelerator and binder, such additives can be stimulated and form their strengthening structures accordingly. Compared to the reference grout, the addition of granulated blast-furnace slag depending on an appropriate sodium/potassium water glass dosage reduced the cement content by up to 170 kg/m³ (approx. 68%) (Fig. 5.41, left). In addition, sodium-water glass leads to a faster strength development in cement, whereas potassium-water glass supports a faster strength development if blast-furnace slag is used.

Besides, the gel time for a cementless composition could be determined. The grout was modified by adding a calcium hydroxide $(Ca(OH)^2)$ suspension as a solidification medium together with blast-furnace slag. As seen in Fig. 5.41, right, the test results prove that the requirements for the gel time could be achieved with at a calcium hydroxide content of approx. 18 kg/m³ and an accelerator content of 90 kg/m³ (6.8% by volume). The actual long-term strength was subsequently due to the reaction of the blast-furnace slag. The material-technological decoupling of the gel and strength phases consequently allows the employment of different binder compositions of latent-hydraulic and/or pozzolanic materials.
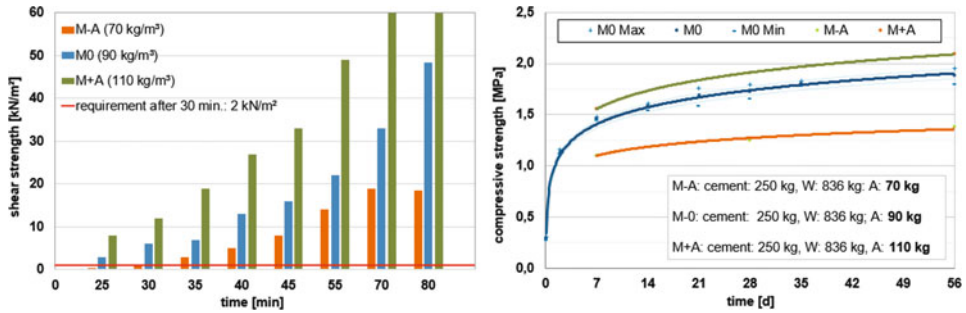
Fig. 5.42 Development of the shear strengths (left) and the compressive strength (right) of the reference grout M0 with different accelerator contents [69]

The development of the shear strengths is the decisive characteristic for the stabilization of the segments. A shear vane (according to [49]) was used to determine the shear strength over a period of 25 to 80 min after preparation. The shear strength requirements ($2\,kN/m^2$ after 30 min) were achieved with an accelerator content of $90\,kg/m^3$ (Fig. 5.42, left). Similarly, a rapid development of the compressive strength also occurred (Fig. 5.42, right). After only 2 h, the grout with an activator content of $90\,kg/m^3$ had a compressive strength of approx. 0.3 MPa. The usual requirement of 0.5 MPa of compressive strength after 24 h [85] is thus already achieved immediately after grouting.

5.5.3 Test Setup for the Simulation of the Annular Gap Grouting

A special test device was developed to simulate annular gap grouting under realistic conditions. The relevant control variables were included in the design: Grouting volume, advance rate, grouting pressure and the grouting nozzles. With the test setup, the distribution of the material in the annular gap, and the homogeneity of the grout can be recorded during the grouting process.

5.5.3.1 Constructive Design
The grouting device can be separated into six assemblies: bucket (1, soil), slide (2, simulated tunnel boring machine or its shield tail), the annular gap (3), the nozzle (4, mixing of component A and B), the hydraulic system including the abutment (5) and the cover (6). The internal dimension of the simulated annular gap are $1500\,mm \times 600\,mm \times 150\,mm$. In Fig. 5.43 is a schematic overall view (left) and a photograph of the experimental setup (right). Further detailed information can be found in [70].

5.5.3.2 One-Component Grout
To verify the pressure distribution in the annular gap during a grouting test, the comparison between the set pressure (approx. 0.5 bar) at the grout pump and the measured pressure

Fig. 5.43 Overall view of the test setup for annular gap grouts (left). Recording of the experimental setup (right) [70]

Fig. 5.44 Pressure measurement in the annular gap in the plane of the mortar opening during a grouting process of a one-component grout (grouting pressure: 0.5 bar, advance rate: 60 mm/min) [69]

with the ceramic sensors (nominal pressure range: 0–4 bar) was investigated. The results of the pressure measurement are presented in Fig. 5.44.

The set pressure of approx. 0.5 bar was reached within 90 sec after filling the first section. This value was kept constant during the entire test. Based on the individual curves of the pressure sensors (Fig. 5.44, right), it can be determined that the pressure and the measured fluctuations of the respective curves developed in parallel. This indicates constant pressure distribution in the annular gap over the height and width. Thus, it is ensured that there is an equal pressure at every point of the grouted annular gap and homogeneous material is obtained for subsequent tests.

During groutability verification of a semi inert one-component grout (cf. [69]), grouting pressures of about 0.5, 1.0 and 1.5 bar were applied. In order to evaluate the flow behavior, the grout was pigmented (Fig. 5.45). The color gradient reveals a ring-shaped distribution of the grout. In addition, the homogeneous distribution of the one-component grout confirmed the applicability of the material.

Fig. 5.45 Pressed one-component grout (left). Flow behavior of the grout (right) [70]

5.5.3.3 Two-Component Grout

In the course of the grouting tests, the two-component grout M0 (cf. Table 5.2) was also investigated with regard to the flow properties after activation and subsequent strength development. The tests were realized without pressure and an advance rate of 90 mm/min. The filling process or the expansion of the activated grout was observed directly upon entry into the annulus (Fig. 5.46).

The grouted material was demolded after approx. 30 min. (dimensionally stable at every point) and homogeneous or evenly gelled (Fig. 5.47, top). On the exposed activated material, the shear strength development was determined with a shear vane according to [49] (Fig. 5.47, bottom left/center). The results of the shear strength tests are shown in Fig. 5.47 (bottom right) and compared with the shear strength development of the same grout produced separately in the laboratory, by hand.

The results reveal a higher shear strength of the grouted material compared to the laboratory specimens, especially up to 40 min after activation, which may be due to a more intensive mixing of the two components in the mixing unit. From a period of 80 min, the shear strengths were at approximately the same level, with the laboratory specimens showing a larger increase in strength.

Fig. 5.46 Filling of the annular gap with a two-component grout commonly used in practice (reference grout M0, activator content: $90 \, kg/m^3$, gel time: approx. 9 sec.) [69]
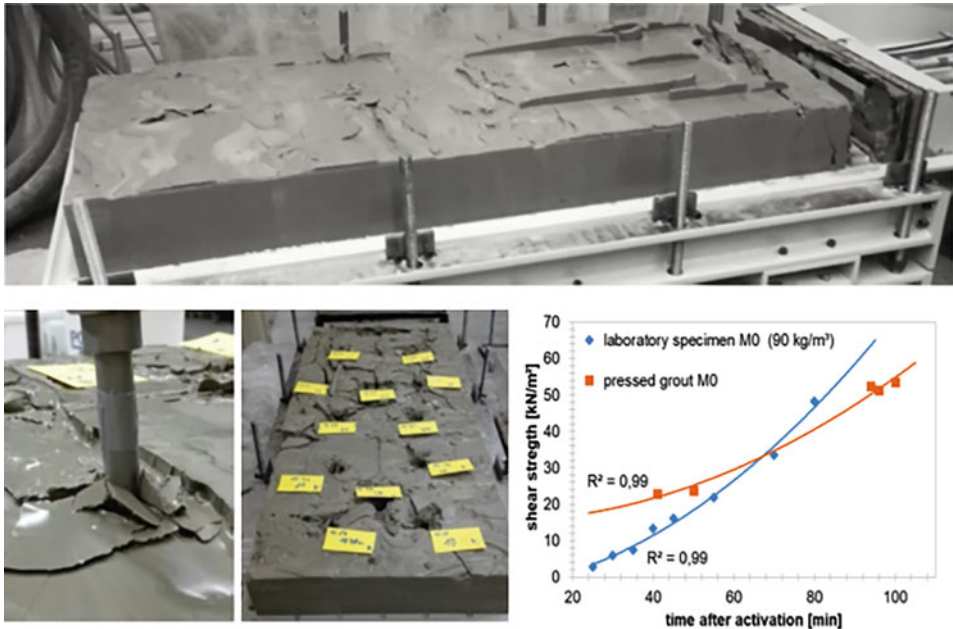
Fig. 5.47 Demolded reference grout M0 (Age of the sample: 30 min., activator: 90 kg/m^3, gel time: 9 sec.) (top). Procedure for determining the shear strengths (bottom, left/center). Comparison of the shear strengths of the reference grout M0 with the results on laboratory test specimens (bottom, right) [69]

5.5.4 Multiscale Simulation for the Strength Development of Two-Component Grouts

In order to provide reliable stiffness development for two-component grouts, physically acting superabsorbent polymers (SAP) could be considered as component B. The polymers bind an extensive amount of fluid within a very short time and thus contribute to the stiffening of the grout. Therefore, experimental tests with regards to the water absorption of SAPs under conditions close to the final application have been carried out in accordance to [48]. In parallel, a thermodynamically consistent model based on the Theory of Porous Media (TPM) was developed to account for the internal mass transfer between the pore fluid and the SAP particles in a two-component grout mix [66]. Finally, the parameters of the experimental results were used to generate the constitutive law for the mass transfer in the numerical model. In [66], the derivation for calibration of the multiphase multi-species model, using defined properties, balance equations, and the specific model description, is presented.

Based on the water absorption capacity of SAP for different environmental solutions (tap water, different NaCl concentration), a drastic increase in water absorption with higher NaCl concentration could be observed. In the case of using tap water, the poten-
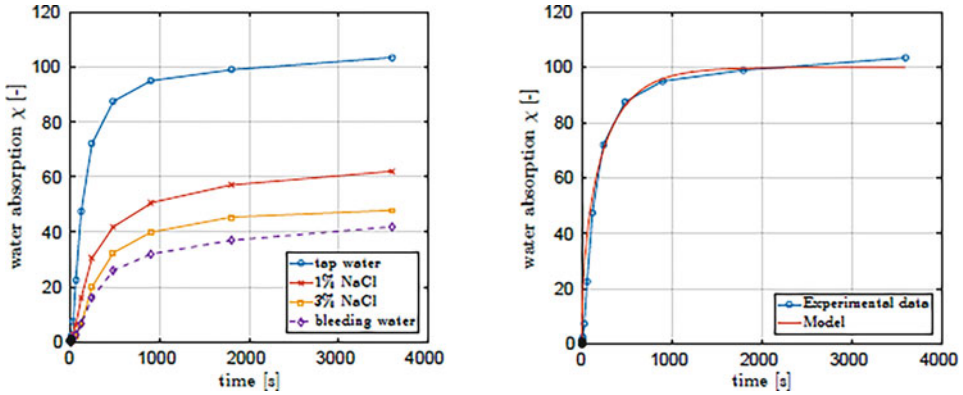
Fig. 5.48 Experimental water absorption tests of SAP with different environmental solutions (left). Fitted model parameter to experimental data (right) [66]

tial of water uptake continued to increase by up to 60% (Fig. 5.48, left). Accordingly, a particular salt concentration was assigned to the tap water in the numerical model. The comparison of the simulated model with the results from the experimental investigations is shown in Fig. 5.48, right, [66].

A resulting simplified volume balance was used to describe the absorption kinetics [66],

$$\partial_t(\chi) = \frac{n^B}{n_0^B} = \frac{1}{\tau_W}\left(\frac{a_1}{\chi} - a_2\chi\right). \tag{5.2}$$

The function $\chi = n^B/n_0^B$ relates the absorbed water and the initial volume of the SAPs, while the partial derivative $\partial_t(\chi)$ represents the time. The first term in the function accounts for the addition of water due to a difference in salt concentration, while the second term simulates the development of a restoring force of the polymer network during swelling. Similar approaches can also be found in literature [12]. In this model, a_1 and a_2 are associated with the charges attached to the polymer chains and the elasticity of the network, respectively. Accordingly, τ_W scales the driving force and can be related to the friction between the polymer chains. Applying a least-squares fit to the parameters in Eq. 5.2, results to absorption curves that correspond to the experimental studies (Fig. 5.48, right) [66].

5.6 Deformation Tolerant Tunnel Lining

The stress redistribution and dilation due to the excavation in clay shale results in a so called Excavation Damaged Zone (EDZ) in the nearfield of tunnel. Taking into account the inhomogeneous structure of clay shales that consists of inherent cracks, joints and
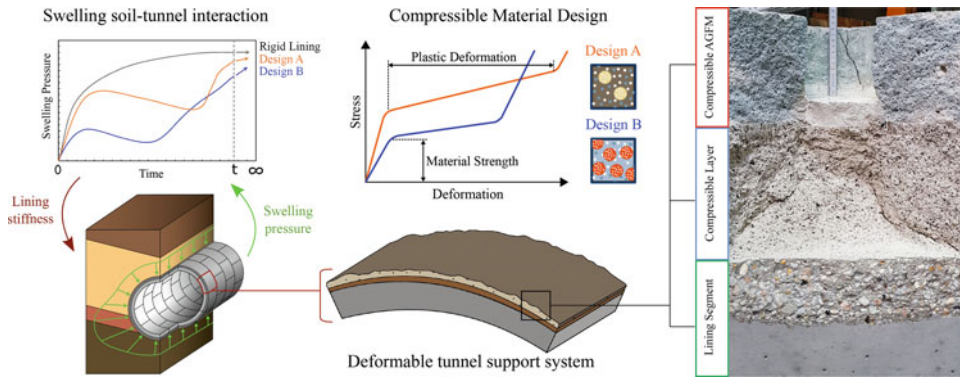
Fig. 5.49 The concept of deformation tolerant tunnel lining in swelling clay rocks which includes deformable cementitious layer and deformable annular gap grout around the lining segments. Typical mechanical behavior of the compressible material is characterized by 3 stages: elastic, plateau and densification [9]

discontinuities, development of EDZ results in a reduction of shear strength while the increases in hydraulic conductivity forms a preferential flow path at the vicinity of the tunnel. In case of tunneling in shales with the potential of swelling, the water transport through the EDZ results in swelling of the clay rock that build up significant pressure at the tunnel support system. Apparently, development of a deformation tolerant lining can avoid extreme pressure evolution at the tunnel structure, however, the deformation of the tunnel support may lead to further development of the EDZ. In this context, proper prediction of the tunnel behavior requires adequate knowledge about the (a) swelling behavior of the host rock, (b) size and shape of the EDZ, and (c) load-deformation behavior of the tunnel support. Figure 5.49 indicates the coupled interactions between swelling pressure evolution and the deformability of the tunnel support system.

5.6.1 Swelling Behavior of Clay Shales Under Tunneling Relevant Boundary Conditions

The swellable clay shales exhibit a significant volume or pressure increase upon hydration respectively in free or volume constant conditions, where the innercrystalline and osmotic swelling are the main mechanisms involved. The negative charge of smectite layers is compensated by interlayer cations which hydrate when getting in contact with water. This hydration is called innercrystalline swelling and results in swelling pressures larger than common overburden pressures in tunneling practice [20, 40, 42] which take place in the geological life of the formation. Therefore, innercrystalline swelling does not play a significant role in tunneling whereas the osmotic swelling occurs when the unloaded swellable clay shale adsorbs additional water. In this mechanism, the ions in the pore wa-
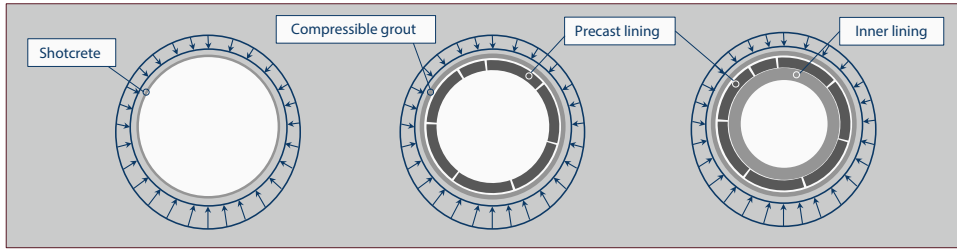
Fig. 5.50 Tunneling relevant boundary conditions for swelling test

ter form a diffuse double layer at the surface of negatively charged clay particles. The repulsion of such diffuse double layers is called osmotic swelling [40] that plays a role in tunneling practice. Dilation due to tunneling in the EDZ decreases the degree of saturation around the tunnel and initiates a suction-induced osmotic flux in radial direction towards the tunnel whilst, the higher hydraulic conductivity of the EDZ can trigger fluid water flow along the tunnel. This can result in swelling of clayey soils, if the three-sheet layered silicate smectite is present.

To study the swelling behavior of a shale, it is important to consider the appropriate boundary conditions of the application in the test set-up. In the context of mechanized tunneling, these are explicitly the saturation modi and volumetric deformations due to the tunnel support reaction. As shown in Fig. 5.50, depending on the tunnel support condition, various volumetric deformation conditions can be adopted in the laboratory testing. For instance, free swelling, controlled-volume swelling and volume constant swelling tests represent unsupported tunnels as well as tunnels with flexible and rigid support structure, respectively. In terms of hydraulic boundary conditions, the advective flux in preferential flow paths in EDZ along the tunnel can be represented by hydration of sample with water fluid (i.e. single step hydration) and the diffusive flux in radial direction towards the tunnel due to a dilation induced suction increase can be reproduced by vapor saturation (i.e. multi step hydration). For this purpose, a novel multi-purpose swelling pressure device for tunneling relevant boundary conditions was designed and constructed (Fig. 5.51) in which free as well as controlled and constant volume tests are possible to be carried out. Water saturation from bottom inlets (single step) or by vapor saturation with a peristaltic pump, gas washing bottle and the cell's top and bottom inlets/outlets (multi step) are enabled. The gas washing bottle is filled with an oversaturated salt solution which controls the relative humidity of the vapor and can be combined with a temperature to a suction via the Kelvin equation,

$$\psi_{\text{tot}} = -\frac{RT}{v_{w0}\omega_v} \ln(RH), \tag{5.3}$$

where ψ_{tot} is the total suction, R is the universal gas constant, T is the absolute temperature, v_{w0} is the specific volume of water, ω_v is the molecular mass of water vapour and RH is the relative humidity.

Fig. 5.51 Newly developed swelling pressure cell for tunneling relevant boundary conditions [9]

For clay shales, also the sample preparation plays a significant role, since the undisturbed structure and fabric of the material has a substantial impact on the mechanical, hydraulic and hydro-mechanical behavior. Additionally, clay shales are usually strongly anisotropic due to their geological formation process (e.g., the approximately 170 million years old marine sediment Opalinus clay shale (OPA) [19]). Samples have to be prepared carefully regarding their bedding plane orientation (Fig. 5.52b). Considering the significant inhomogeneities like microfossiles, pyrite or quartz lenses in the intact samples that often complicate sample preparation and test results interpretation [21], it may be reasonable to destroy the fabric and structure to generate reconstituted powder samples for certain applications. In this frame a series of swelling tests on reconstituted shale samples have been carried out as well.

In the present study, the hydro-mechanical behavior of clay shales was investigated on OPA shale, since the New Belchen Tunnel (NBT) in Northern Switzerland was partly driven through this clay shale and the project was considered as the reference project. Samples were obtained from the construction site and total pressure sensors around the tunnel lining installed for long-term in-situ measurements. Results of swelling pressure tests showed a pronounced influence of anisotropy. The swelling pressure perpendicular to bedding planes (1.2–2 MPa) was 5 to 20 times larger than parallel to bedding planes (0.1–0.25 MPa), average swelling pressure curves of intact OPA in both directions are presented in Fig. 5.53a). Such a strong anisotropy is important to consider for the dimensioning of the tunnel lining, since the load on the individual lining segments can vary significantly regarding the bedding plane orientation of the surrounding soil which may vary along
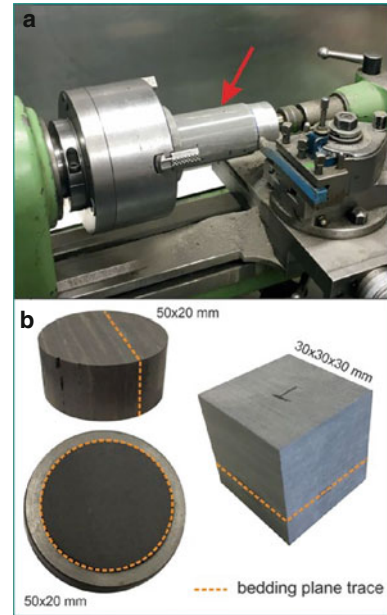
the tunnel. Discrepancies in test results with the same orientation exist due to naturally varying clay contents or inhomogeneities like pyrite and quartz lenses. The rate of saturation, and thus the increase in swelling pressure, depends on the hydraulic conductivity of the material. Considering volumetric deformations, minor strains of the material (less than 1%) resulted in approximately 50% reduction in swelling pressure. Due to structure and texture of the material the volumetric swelling of the material is significantly limited. Volumetric deformations can be used to upgrade the decreasing dry density of the material and derive a dry density-swelling pressure curve, which usually shows a logarithmic increase of swelling pressure with increasing dry density. For bentonites it is common to conduct swelling pressure tests with different initial dry densities to determine this unique correlation for its swelling potential. However, deriving this correlation at an intact clay shale due to stepwise strain release mimicking unloading and dilation of the material due to mechanized tunneling is a novelty.

In tunneling practice the newly developed deformation tolerant tunnel lining will allow volumetric deformations of the surrounding swellable clay shale in a controlled manner and therefore reduces the acting loads on the lining system. First results of sandwich tests, with samples composed of 2 cm OPA and 1 cm compressible grout, confirmed the effectiveness of this design. Test results of OPA powder with an initial dry density of 2.0 g/cm^3 and OPA powder plus grout are presented in Fig. 5.53a) and show a reduction of 80% in swelling pressure. A compacted sample in the sample ring is shown in Fig. 5.53b) and the setup of a sandwich test in Fig. 5.53c).
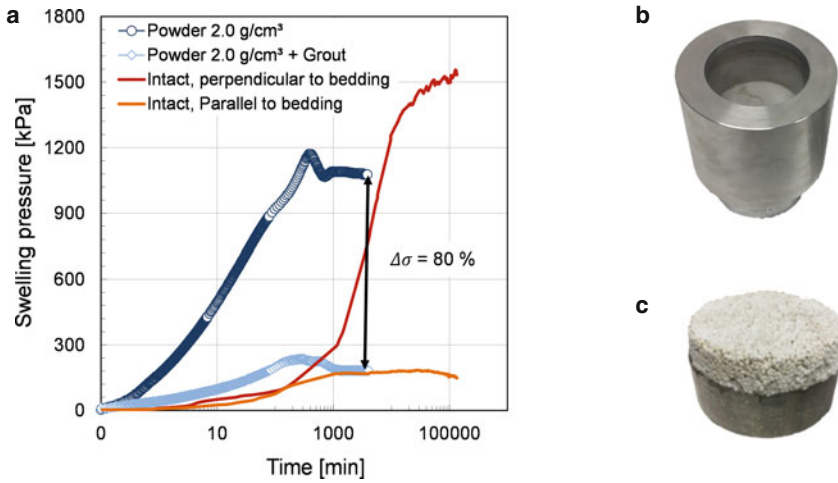
Fig. 5.53 Experimental results of tests on intact OPA and powder with and without grout (**a**), sample ring (**b**) and test setup of the sandwich test (**c**)

5.6.1.1   Numerical Assessment of the Excavation Damaged Zones in Tunneling

Concerning the coupled interaction between the size and shape of the EDZ and swelling process in shale, assessment of the time dependent development of EDZ is very crucial. In the literature, different approaches have been proposed to model the fractures such as discrete element method, damage models or simulation of shearband localization using the finite element method. To enable simulation of not only the fracture development but also the swelling process, the approach involving finite element modeling was adopted. In this frame, the shear band localization approach in conjunction with a regularization technique can be successfully applied to model the EDZ without mesh dependency issues. In order to overcome the mesh dependence of strain localization in classical finite elements, it is essential to adopt an advanced model to properly address the post peak behavior as well as the localization aspect. Among different models, the second gradient model proposed by [14] is used as a regularization method where the continuum model kinematics includes macro- and micro-kinematics.

To study the influence of tunneling parameters on the EDZ shape and size in partially saturated Opalinus shale, a 2-dimensional multi-phase model in conjunction with a the second gradient localization model was developed. The model is based on the model presented in [5]. To simulate the stress evolutions due to tunneling in the 2D model, a stress-release method was applied (Fig. 5.54). By this approach, stress reduction in front of the TBM as well as overcut and shield conicity (A-B), pressure increase due to grouting (B-D) and pressure drop upon TBM passing (D-E) are considered.

Figure 5.55 shows that the EDZ develops less during faster tunnel excavation. This can be explained by quicker support of the semi-unsupported excavation zone in case of faster
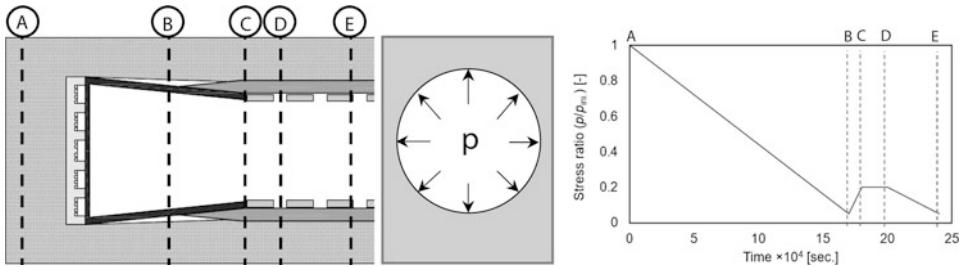
Fig. 5.54 Details of numerical modeling of the EDZ shape
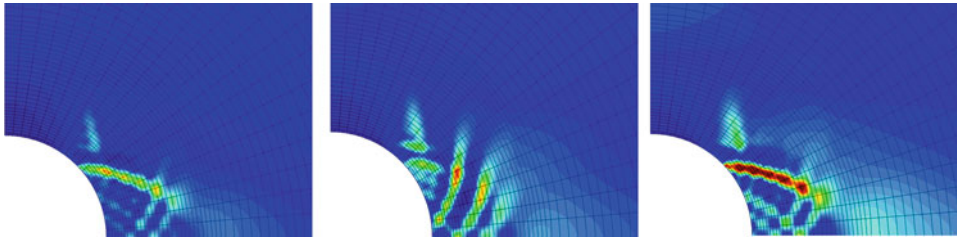
Fig. 5.55 Variation of the shape of EDZ by the TBM advance speed: 10% faster (left), reference case as Fig. 5.54 (middle), 10% slower (right)

TBM advance. In this condition, less time for EDZ development is available before the clay rock gets supported by the tail grouting pressure.

5.6.1.2 Swelling Laws

For tunnel excavation in swelling clay rock, modeling of the swelling process in conjunction with an appropriate swelling law is essential. In the literature, various types of simplified analytical models like [31, 38, 54] and fully coupled swelling laws like the one of Wittke or the Barcelona Basic Model (BBM) [2] have been proposed. The analytical models generally provide a relationship between the swelling pressure and the swelling-induced volume increase on the basis of Huder and Amberg swelling tests. Referring to the complexity of coupled interactions due to mechanized tunneling, simplified analytical models are not sufficient. Therefore, Wittke developed a coupled semi-logarithmic swelling law according to [31]. Since the model parameters are calibrated only on the basis of Huder Amberg swelling tests, the model cannot be used to model the volume constant (e.g. rigid tunnel lining) boundary conditions.

The Barcelona Basic Model [2] is an extension of the modified Cam-Clay model that considers the stress-strain behavior of clays in partially saturated conditions. According to [28], the BBM is unable to reproduce large swelling strains, but only small reversible swelling in the elastic zone. Therefore, it is not suitable for so-called expansive soils where large volumetric strains upon saturation is expected. Therefore, [3, 28] extended the BBM with micro-structure effects to model large swelling strains; however, this approach is par-
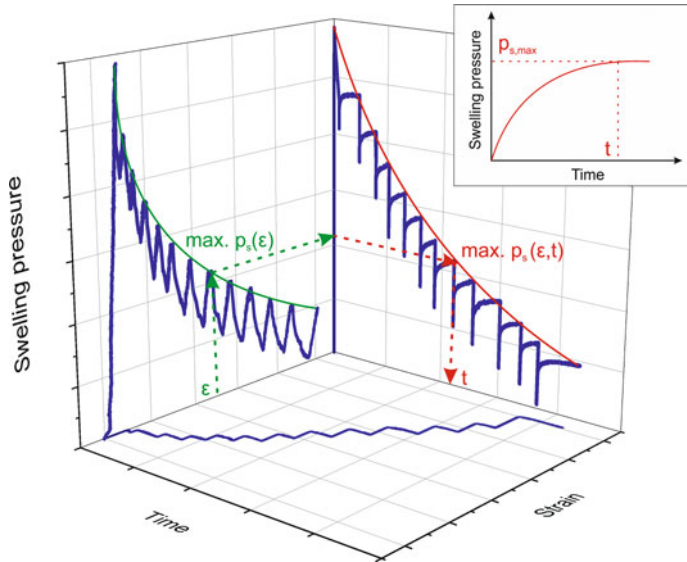
Fig. 5.56 Exemplary correlation between swelling pressure, strain and time

ticularly relevant for double-porosity clay shales (e.g. micro- and macro-pores). Therefore, to study the swelling behavior of single-pore OPA shale, swelling tests have been carried out using the device shown in Fig. 5.51. In these experiments, each test consisted of multitude of volume constant and deformation release steps to consider the impact of tunnel deformations in the swelling behavior. Figure 5.56 illustrates graphically a mechanized-tunneling relevant swelling law that represents the correlation of swelling pressure, strain and time determined in the swelling pressure cells for tunneling relevant boundary conditions. A first peak in swelling pressure is reached for volume constant boundary conditions with a specific initial dry density. Each deformation release resulted in a drop of swelling pressure with a subsequent increase, where the water is absorbed in newly available pore space (i.e. desaturation upon unloading). As seen, an equilibrium swelling pressure can be assigned to any strain and additionally time by projecting the swelling pressure to the swelling pressure over time plane. In this frame, not only the maximum swelling pressure but also the trend of the swelling pressure evolution in time can be defined for each strain level using this swelling law.

5.6.2 Deformable Cementitious Materials

To realize a deformation compensating tunnel lining, compressible cementitious materials were developed, which can be arranged as annular gap grout or as an additional compressible layer at the exterior of the lining (Fig. 5.49). The functional principle of the materials
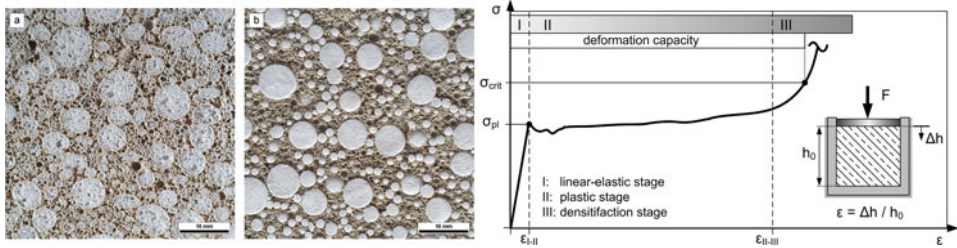
Fig. 5.57 Left: Compressible cementitious materials produced with a highly porous cement matrix and expanded glass (**a**) and expanded polystyrene (**b**); right: Qualitative illustration of the stress-deformation behavior of compressible cementitious materials under axial compression with transverse strain constraint [60]

is the same in both cases. By using highly porous additives (e.g. lightweight aggregates, expanded polystyrene) and highly air-entraining admixtures (foaming agents), the cementitious materials are characterized by a very high porosity. As an example, Fig. 5.57, left, shows the structure of two developed materials produced with a highly porous cement matrix (air void content of approx. 30% by volume) and different additives (expanded glass/expanded polystyrene). The high porosity of the materials enables a high degree of volume compressibility and thus a high plastic deformation capacity even for complete transverse strain constraint, as is more or less the case on the exterior of the tunnel lining.

The material behavior is characterized by a stress-deformation behavior shown qualitatively in Fig. 5.57, right. Under axial compression, a linear elastic behavior is initially present (stage I). This corresponds to the typical stress-deformation behavior of mortar and concrete, whereby the slope of the curve in this stage is indicating the initial material stiffness. When a certain stress (σ_{pl}) is reached, which is in the range of the compressive strength of the material, the material behavior changes from linear elastic to plastic (stage II). Optimally, in this stage a more or less constant stress level is maintained over a large range of deformation. With increasing plastic deformation, the volume compression gradually leads to a densification of the material (stage III). This stage is characterized by a huge increase of stresses. Total deformation capacity of the material is ultimately limited by this densification process.

With regard to the design of compressible materials, the stress-deformation behavior must be individually adjusted to the project-specific conditions. On the one hand, in order to avoid overloading of the segmental lining, the primary target value for the material design is a critical stress σ_{crit} (Fig. 5.57, right), which must not be exceeded as a result of the densification process until a defined deformation is reached. On the other hand, to avoid early plastic deformation due to lower scheduled loadings (e.g. grouting pressure, water pressure), sufficient minimum strength also has to be ensured.

In an extensive test program, compression tests were carried out to experimentally investigate the developed materials in terms of their stress-deformation behavior. Through variations of material composition (e.g. type of additives, air content, volume fractions,
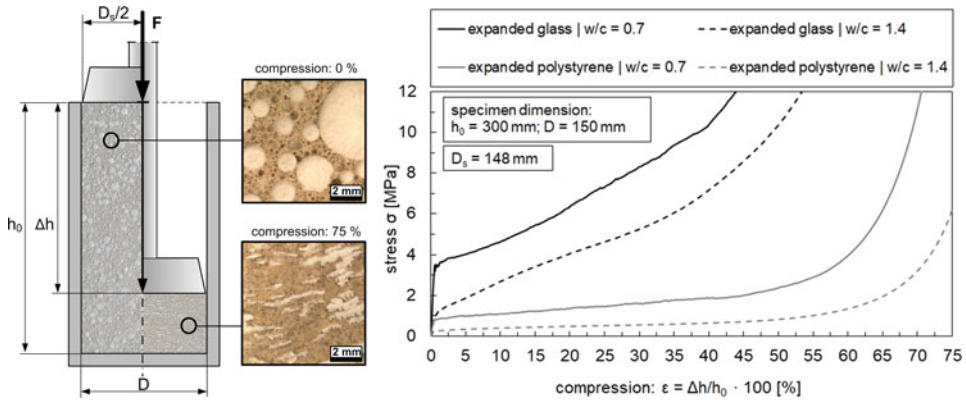
Fig. 5.58 Schematic illustration of a compression test and structure of the material before/after compression (left); influence of water-cement ratio and different additives on the stress-compression behavior (right) [9]

water-cement ratio) and test-related parameters (e.g. with/without lateral confinement, specimen geometry and dimensions, loaded area), essential influencing factors on the compressive behavior were identified, which can be used as control parameters for the design and optimization of the materials with regard to project-specific conditions.

Figure 5.58, left, schematically shows the compression tests performed on cylindrical specimens ($h_0 = 300$ mm, $D = 150$ mm) with lateral confinement (i.e. complete transverse strain constraint) in a fully-enclosed, rigid specimen holder. As an example, Fig. 5.58, left, shows the structure of the material before and after compression.

In Fig. 5.58, right, the stress-deformation behavior of selected materials is presented, which have been compressed over the full cross-sectional area ($D_s = 148$ mm), indicating the influence of the water-cement ratio ($w/c = 0.7$, 1.4) and different additives (expanded glass, expanded polystyrene). Both variations clearly showed an influence on the stress σ_{pl}, which defines the transition from the linear-elastic to the plastic deformation stage. A lower water-cement ratio led to a higher matrix strength and thus to a higher value of σ_{pl}. The multiple higher strength of expanded glass in comparison to expanded polystyrene also led to an increase in σ_{pl}. The slope of the curves in the plastic stage was mainly influenced by the properties of the used additives. As can be seen, the stress-deformation curves of the materials with expanded glass were significantly steeper than those of the materials with expanded polystyrene in this stage. In contrast, the matrix strength had a comparatively small influence on the slope of the curves in the plastic deformation stage.

Under realistic conditions, it has to be assumed that deformations due to swelling pressures do not occur uniformly over the entire circumference of the tunnel, but rather locally. Against this background, also compression tests were carried out in which the load or deformation, respectively, was applied over a partial area (Fig. 5.59, left). As can be seen in Fig. 5.59, right, on the one hand, an increase in σ_{pl} was observed with decreasing of the
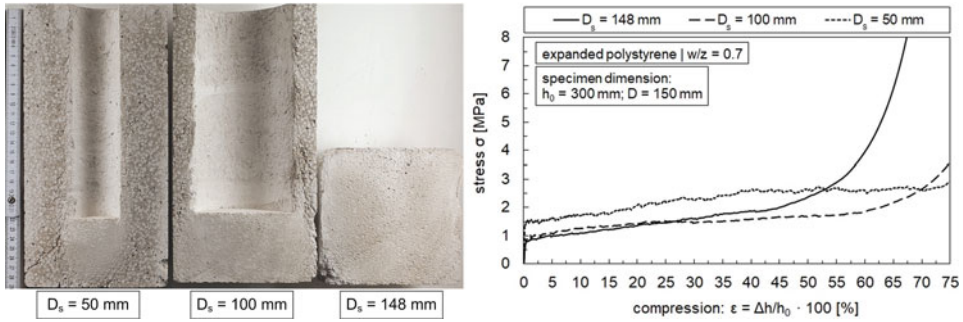
Fig. 5.59 Section images of compressed specimens with different loaded areas (left) and influence of the loaded area on the stress-compression behavior (right) [60]

loaded area. This increase can be mainly attributed to the shear resistance of the material, which was activated by the penetration of the loading punch into the specimen [60]. On the other hand, the effect of the densification process leading to a steeper increase in the stress-deformation curve, occurred with increasing loaded area at smaller deformations.

In addition to the fundamental investigations into compressive behavior, specific process and manufacturing aspects were also considered in the material design. For example, as the annular gap grout is pressed into the resulting gap between the outside of the segment and the surrounding soil, supplementary requirements have to be considered: sufficient flowability, pumpability, complete filling of the gap, none precompression of the highly porous additives due to the grouting pressure.

While the fundamental deformation behavior is the same for the annular gap grout and the compression layer, the formulation of the materials differ in order to satisfy the respective general requirements. The annular gap grout contains ingredients such as bentonite (to ensure sedimentation stability), retarders (to ensure a sufficiently long flowability) and a considerably higher water content, thus leads to a reduced strength of the mortar in contrast to the compressible layer.

In order to simulate the grouting and to take into account all the above needs, the test setup developed for evaluating the process qualification of annular gap grouts (Sect. 5.5.3) was modified and adapted to the compressive material (Fig. 5.60). For this purpose, an extended prototype of the static mixer was first developed, which could be considered for field-oriented projects. The static mixer contains alternating spiral-shaped sections, each of the elements being at a 90° angle to the following element and providing the required mixing effects by the radial mixing process forming, the rotational circulation as well as by the flow section. In enhancement, a magnetic inductive flow meter could be introduced into the circuit for the grouting test in order to record the volume of the grouted material and compare it with the calculationally necessary material requirement. This provides a direct indication of whether compression of the material is already occurring during the grouting process as a result of excessively high grouting pressures. Premature compression
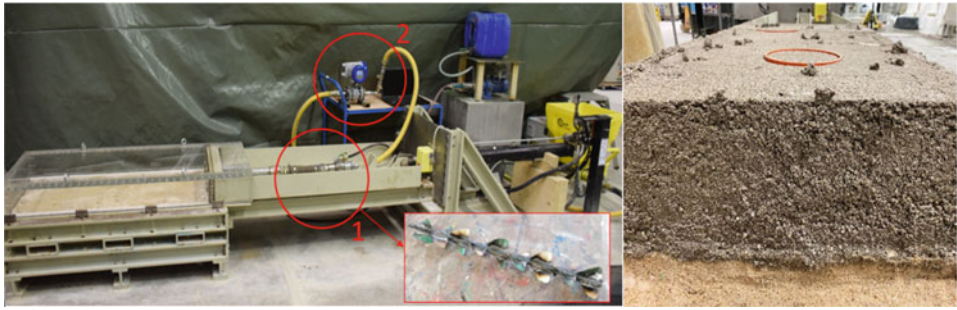
Fig. 5.60 Design of the modified test set-up with adapted static mixer (1) and flow meter (2) for investigating the process qualification of compressible annular gap grouts (left). Detailed view of a cut surface on a two-component grout with expanded polystyrene as compressible additive (set pressure of approx. 1.0 bar) (right)
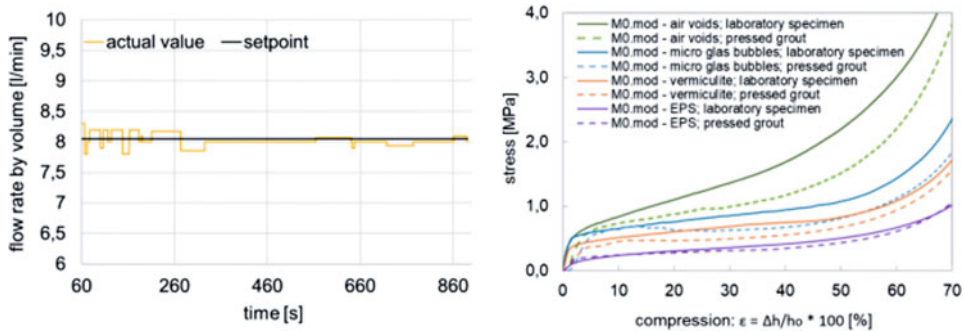
Fig. 5.61 Volume flow measurement during a grouting test (left). Comparison of the stress-compression behavior of manually produced reference specimens to grouted two-component mortar taken from the test setup (with varying porous additives) (right)

of the material could lead to a decrease in the subsequent compression potential. Based on the reference mix M0 (cf. Table 5.2), compressible two-component grouts (M0.mod) with varying porous additives (e.g. high air void ratio, micro glass bubbles, expanded polystyrene and vermiculite), were developed and subjected to a grouting test with set pressure of approx. 1.0 bar. Figure 5.60 includes the modified test setup with adapted static mixer and flow meter as well as a cut surface of a grouted two-component mortar with expanded polystyrene as porous additive.

As seen in Fig. 5.61, left, the flow measurement during a grouting test demonstrated, with a relatively constant flow rate of approx. 8 l/min, that the calculated volume of 135 l was reached within the scheduled time of approx. 17 minutes at an advance rate of 90 mm/min. Thus, it can be ensured that no additional material was grouted as a result of an early compression of the grout. Furthermore, no significant decrease in deformation potential was observed for the grout. Figure 5.61, right, compares the stress-deformation
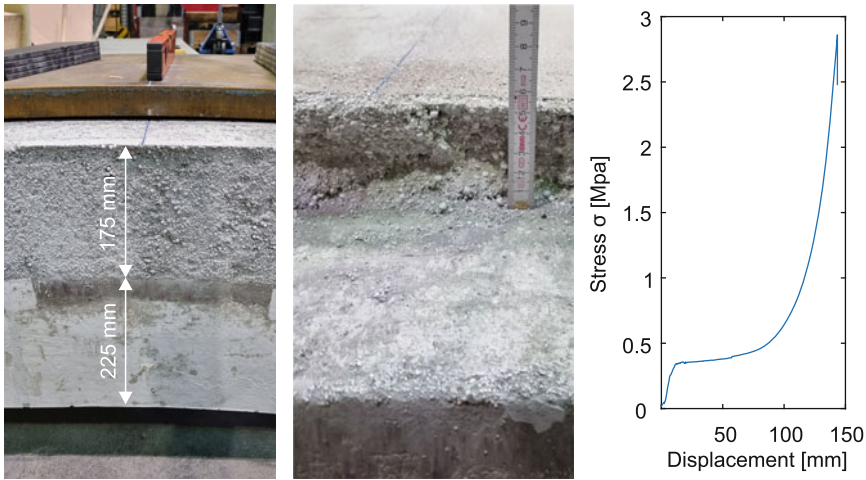
Fig. 5.62 Compressible cementitious layer before (left) and after testing (middle); stress-displacement response in radial direction of a tested lining segment with compressible layer (right)

behavior (of different mortars with various compressible additives) of the laboratory specimens prepared by hand and the samples of the grouted material taken from the test setup. Relative to the manually prepared reference specimens, the grouted mortar specimens showed a low slope in the linear-elastic range. Accordingly, the laboratory specimens indicated a minor increase in stiffness.

The knowledge gained in compressible cementitious materials was applied in form of a compressible layer on top of the lining segments tested in large scale, introduced in Sect. 5.4.1. As an example, Fig. 5.62 shows the stress-displacement response in radial direction of a lining segment with compressible layer in one of the experiments. The plastic behavior allowed for high deformations (> 100 mm for a compressible layer thickness of 175 mm) at a load level considerably lower than the ultimate load attained by the lining segment. As a result the lining segment was initially subjected to low utilization ratios.

5.6.3 Model Based Design of Deformable Materials

The choice of a suitable deformable cementitious layer with the required deformation characteristics for certain geological conditions can be supported by performing computational simulations. The computational model should account for the material properties of the individual composite components, the geometry of the constituents, their volume and spatial distribution, in order to replicate the three stages characterizing overall behavior of compressible composites (an elastic stage, a plateau and a densification stage).

To this end, two different strategies for numerical description of highly compressible cementitious composites have been developed and analyzed: 1) a numerical strategy using

the Discrete Element Method and 2) a multiscale approach based on continuum microme-
chanics.

5.6.3.1 Discrete Element Method

Simulations using the Discrete Element Method (DEM) can be used to model the un-
derlying physical mechanisms such as a pore collapse occurring on the microscale of
cementitious composites subject to compression.

In DEM models, the material is described as an assembly of discrete particles which
interact and exert forces on each other. The dynamics of these DEM particles is governed
by the second law of Newton. Within the DEM framework, cementitious materials are
modeled as packing of discrete particles linked together by cohesive frictional forces.
The induced forces are transmitted via a network of contacts between these particles.
The current DEM formulation is based on the soft-sphere approach, where a contact is
characterized by an interaction between overlapping spherical particles. The elastic bond
between two discrete particles is characterized by a normal and tangential stiffness moduli.
The interaction of two discrete particles in normal direction under tension is governed
by a damage softening law, which enables one to replicate the behavior of cementitious
materials in tension. The normal compression regime is characterized by an elasto-plastic
constitutive law. Shear behavior is defined by a modified Mohr-Coulomb frictional law.
Within this DEM framework, a highly porous cementitious composite material has been
generated (Fig. 5.63, left) [89].

The DEM model has been calibrated for a cementitious mix of certain volume frac-
tion of soft inclusions and validated for mixes of different inclusion volume fractions

Slice of numerical   Cut surface of
DEM specimen: grout specimen in
packing with   the experimental
distributed voids   program

DEM sample
mix B
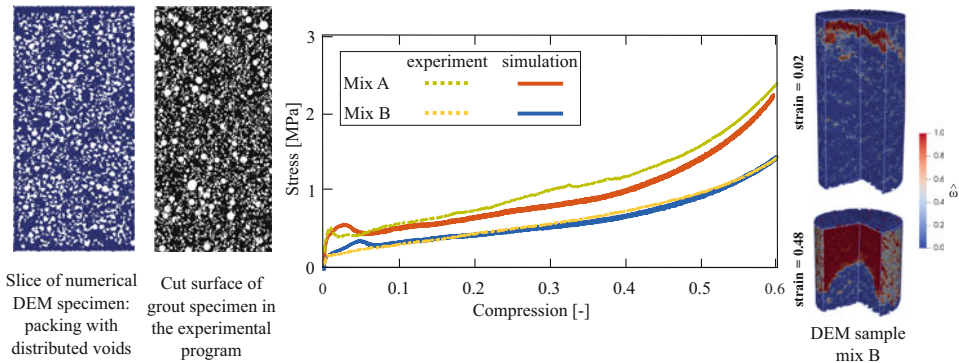
Fig. 5.63 Left: Comparison of the cut surface of the experimental sample with the generated numer-
ical DEM model. Middle: Comparison of simulation results with experimentally obtained behavior
in confined compression test. The experimental curve (green dotted line) has been used for cali-
bration of the modeled behavior (red line). The behavior of another mix (yellow dotted line) has
been used to validate the model prediction (blue line). Right: Damage distribution in a numerical
specimen at two stages of compressive loading [89]

(Fig. 5.63, middle) [89]. According to the computational model, diffuse cracking occurs initially within the whole specimen arbitrarily. Damage initiation occurs at the top part of the sample where a compression band, characterized by compaction, is formed as well. Consequently a material compaction gradient can be clearly observed in Fig. 5.63, right. Simulation shows that most pores collapse "layer by layer". When all contacts of a discrete particle are "broken", it starts dynamically interacting with the other particles by means of newly created interaction ("collision" of particles). The particles thus rearrange and fill the voids. This mechanism manifests itself at the specimen scale as a plateau behavior of the stress-strain curve also observed in the experiments. After all voids have experienced collapse, a densification process, characterized by a regain in stiffness, starts, which agrees with the laboratory observations.

DEM modeling enables one to capture the main physical mechanisms associated with compaction processes occurring in the cemenitious composite specimens. However, the composite microstructure of the investigated cementitious compositions is characterized by inclusions (pores, air voids, and EPS beads) at multiple scales. Thus, it requires a tremendous amount of very small discrete particles to resolve the topology of the small inclusions. Therefore, the prediction of the stiffness for materials characterized by inclusions at multiple scales is difficult. This issue can be solved by applying a multiscale approach based on continuum micromechanics.

5.6.4 Multiscale Model

Continuum micromechanics (as opposed to the numerical strategy using DEM) can resolve the complete range of inclusions and is computationally cheaper. A multiscale voxel model based on continuum micromechanics has been developed, where an individual voxel representing a particular volume of the material can compact (i.e. undergo irreversible deformation due to a pore collapse). The multiscale appoach includes three observation scales: the scale of the specimen (i.e. the dm scale), the scale of an individual voxel (i.e. the cm scale) and an analytical RVE (Representative Volume Element) scale (i.e. the mm scale) shown in Fig. 5.64, left.

Each voxel is characterized at the lower scale by an RVE of cement paste matrix with embedded inclusions of zero stiffness. The RVE defines the strength and stiffness of the voxel. The voxel compacts when the strength of the corresponding RVE is reached. The strength is characterized by a damage initiation in the cement paste around the inclusion. Hexahedral finite elements are used to model the voxels, whereas the analytical framework of continuum micromechanics is used for description of the RVE and the processes occuring in it.

The RVE strength is defined by the stress field $\sigma_m(\mathbf{x})$ in the cement paste matrix in the vicinity of the inclusion, which can be determined by localization. As soon as at any point $\mathbf{x}$ around the inclusion, the stress reaches the tensile strength of the cement paste f_t, damage is assumed to initiate and the voxel compacts. The elasticity parameters of the
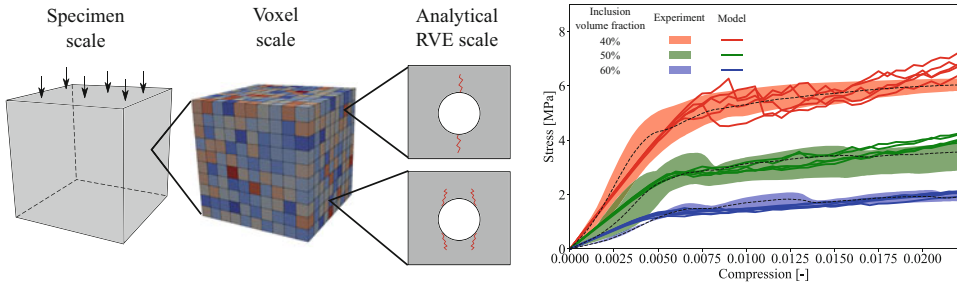
Fig. 5.64 Left: The continuum micromechanics based multiscale strategy with three observation scales: the scale of specimen (i.e. the dm scale), the scale of an individual voxel (i.e. the cm scale) and an analytical Representative Volume Element scale (i.e. the mm scale). Right: Comparison of the model predictions with the experimental stress-deformation behavior of a set of compressible cementitious materials studied in Sect. 5.6.2

cement matrix and the microscopic tensile strength of the cement paste f_t are assumed to be equal for all voxels. The inclusion volume fraction differs from voxel to voxel. It is obtained from a normal distribution among all voxels (Fig. 5.64, left).

Given the volume fraction of the soft inclusions and the properties of the cement paste matrix (determined within the experimental program), the multiscale approach enables one to predict the stiffness and the transitional stress $\sigma_{\rm pl}$ of the cementitious composite material. Figure 5.64, right, provides comparison of the model predictions with the experimental stress-deformation behavior of a set of compressible cementitious materials studied in Sect. 5.6.2.

5.6.5   FE Simulations on Structural Scale

The choice of the deformable material for the protective layer around the tunnel lining is analyzed on the structural scale. Figure 5.65 presents the tunnel geometry, the boundary conditions together with the loading scenario and the mechanical properties of the Opalinus Clay [15] used in the simulation. Earth pressure is applied first and followed by the swelling pressure of 2 MPa (see Sect. 5.6.1) uniformly distributed on the tunnel.

The figure presents the normal force in the concrete lining at the crown. The black curve denotes the reference case without compressible layer around the tunnel. The green, red and blue curves denote the cases with compressible layer. The effect of three different compressible materials around the tunnel is analyzed. The materials have different stiffness and the transitional stress $\sigma_{\rm pl}$ (see Sect. 5.6.2). It can be observed that the use of the compressible layer can reduce the normal force. The strength of the compressible material governs when the compressible layer yields, which leads to a reduction of the normal force in the tunnel lining. The yielding of the compressible material can be observed for the mix B (red line) in Fig. 5.65, right bottom, which depicts the hydrostatic stress in the
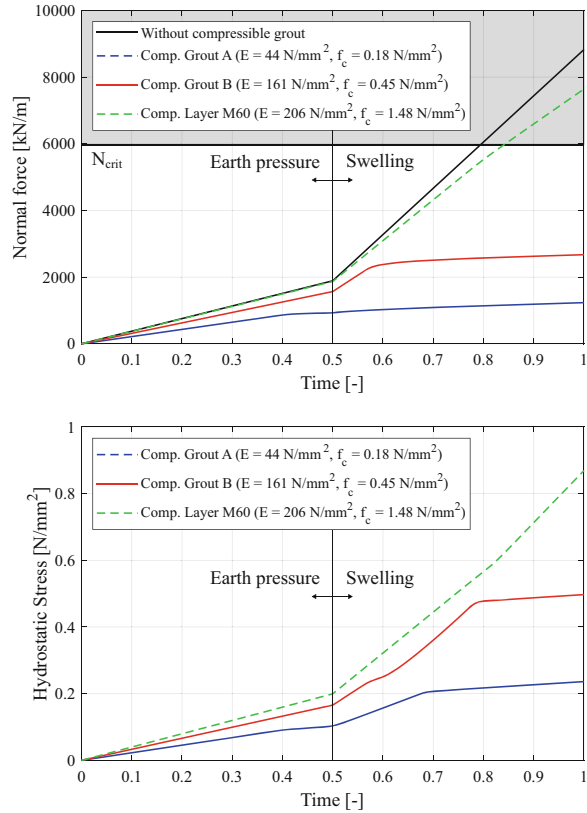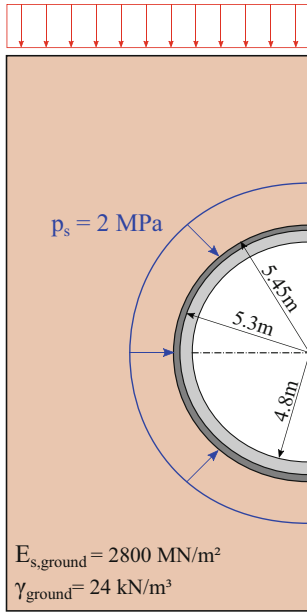
Fig. 5.65 Left: Tunnel geometry, boundary conditions and the mechanical properties of Opalinus Clay. Scenario of swelling pressure uniformly distributed on the tunnel lining is presented. Right: Evolution of normal force in concrete lining and hydrostatic stress in compressible layer. The values are evaluated at the tunnel crown

compressible layer at the crown. The corresponding change in rate of the growth of normal force in the concrete lining at the crown can be observed in Fig. 5.65, right top. The choice of a too soft compressible material with low σ_{pl} may not provide a sufficient tunnel support due to low normal forces in concrete lining (blue line in Fig. 5.65). In contrast, too stiff compressible material with high σ_{pl} may not reach the yielding point which leads to high normal forces in the concrete lining (green dashed line in Fig. 5.65).

Figure 5.66 presents the second loading scenario where the swelling pressure is locally distributed on the tunnel lining. As compared to the case of the uniformly distributed swelling pressure, the locally applied load induces lower normal forces. That can be observed in the plot of normal force evolution at the invert of concrete lining (see Fig. 5.66, top right). The locally applied pressure induces, however, high bending moment in the concrete lining at the tunnel invert (see Fig. 5.66, bottom right). Simulations show that this bending moment can be reduced by using the compressible layer.
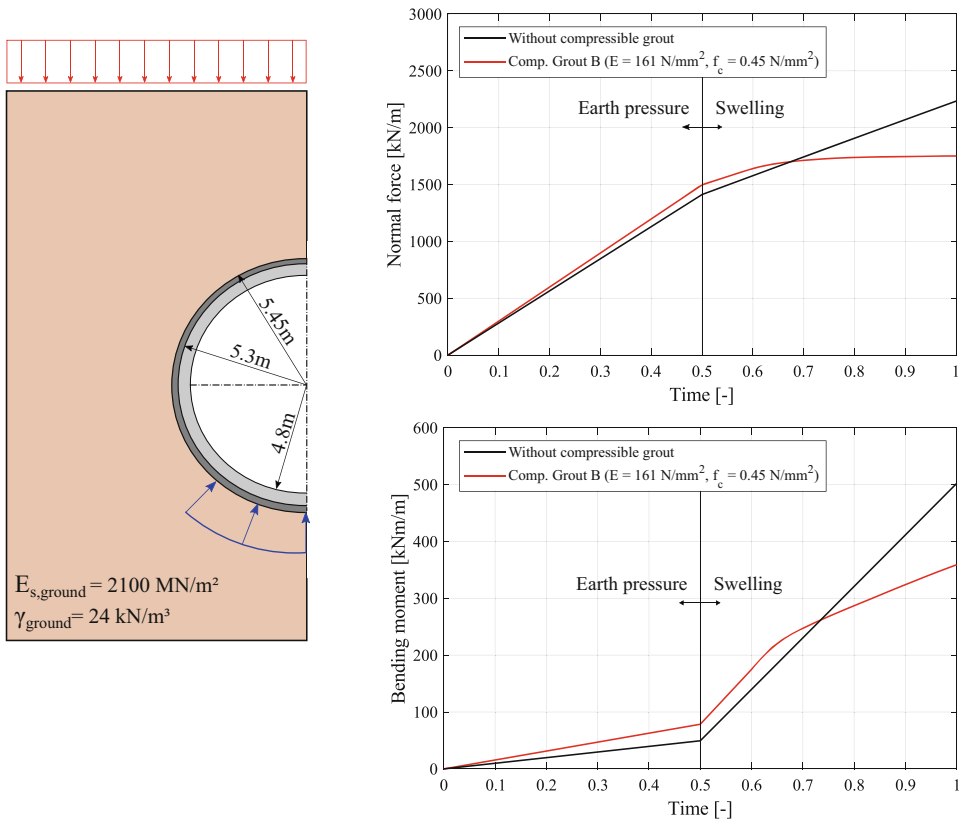
Fig. 5.66 Left: Tunnel geometry and boundary conditions. Scenario of a swelling pressure locally distributed on the tunnel lining is presented. Right: Evolution of normal force and bending moment in concrete lining at the tunnel invert

References

1. S. Advani and C. Tucker. "The use of tensors to describe and predict fiber orientation in short fiber composites". In: *Journal of Rheology* 31 (1987), pp. 751–784.
2. E. E. Alonso, A. Gens, and A. Josa. "A constitutive model for partially saturated soils". en. In: *Géotechnique* 40.3 (Sept. 1990), pp. 405–430. ISSN: 0016-8505, 1751-7656. https://doi.org/10.1680/geot.1990.40.3.405.
3. E. Alonso, J. Vaunat, and A. Gens. "Modelling the mechanical behaviour of expansive clays". In: *Engineering geology* 54.1-2 (1999), pp. 173–183.
4. O. Amir and O. Sigmund. "Reinforcement layout design for concrete structures based on continuum damage and truss topology optimization". In: *Structural and Multidisciplinary Optimization* 47.2 (2013), pp. 157–174. https://doi.org/10.1007/s00158-012-0817-1.
5. F. Bertrand and F. Collin. "Anisotropic modelling of Opalinus Clay behaviour: From triaxial tests to gallery excavation application". In: *Journal of Rock Mechanics and Geotechnical En-

gineering 9.3 (2017), pp. 435–448. ISSN: 1674-7755. https://doi.org/10.1016/j.jrmge.2016.12.005.

6. H.-G. Beyer and B. Sendhoff. "Robust optimization — A comprehensive survey". In: *Computer Methods in Applied Mechanics and Engineering* 196.33 (2007), pp. 3190–3218.

7. R. Breitenbücher. "Beton-Kalender 2014: Unterirdisches Bauen, Grundbau, Eurocode 7". In: ed. by K. Bergmeister, F. Fingerloos, and J.-D. Wörner. Vol. 31. Ernst & Sohn, 2014. Chap. Spezielle Anforderungen an Beton im Tunnelbau, pp. 391–422.

8. R. Breitenbücher and F. Song. "Festschrift zum 60. Geburtstag von Josef Hegger: Massivbau im Wandel". In: 2014. Chap. Verhalten von Stahlfaserbeton unter Teilflächenbelastung, pp. 207–2017.

9. R. Breitenbücher et al. "Deformation-Tolerant Tunnel Linings in Swelling Soils (Verformungsfähiger Tunnelausbau in quellfähigen Böden)". In: *Tunnel* 4 (2021), pp. 50–54.

10. R. Breitenbücher et al. "Experimental and numerical study on the load-bearing behavior of steel fiber reinforced concrete for precast tunnel lining segments under concentrated load". In: *Proceedings of FRC 2014 Joint ACI-fib International Workshop*. 2012, pp. 431–443.

11. R. Breitenbücher et al. "Experimental, analytical and numerical analysis of the pullout behaviour of steel fibres considering different fibre types, inclinations and concrete strengths". In: *Structural Concrete* 15 (2014), pp. 126–135. https://doi.org/10.1002/suco.201300058.

12. S. I. Budtova T. "Swelling behaviour of a polyelectrolyte network under load". In: 38 (1997).

13. B. T. Cao et al. "Artificial neural network surrogate modelling for real-time predictions and control of building damage during mechanised tunnelling". In: *Advances in Engineering Software* 149.102869 (2020), pp. 1–14. https://doi.org/10.1016/j.advengsoft.2020.102869.

14. R. Chambon, D. Caillerie, and N. El Hassan. "One-dimensional localisation studied with a second grade model". en. In: *European Journal of Mechanics – A/Solids* 17.4 (July 1998), pp. 637–656.

15. *Characteristics of the Opalinus Clay at Mont Terri*. Tech. rep. Mont Terri Rock Laboratory, 2008.

16. A. J. Crespo et al. "DualSPHysics: Open-source parallel CFD solver based on Smoothed Particle Hydrodynamics (SPH)". In: *Computer Physics Communications* 187 (2015), pp. 204–216.

17. EFNARC. *Specification and guidelines for the use of specialist products for Mechanised Tunneling (TBM) in soft ground and hard rock*. Tech. rep. 2005.

18. *EN 1992 – Eurocode 2: Design of concrete structures*. European Comittee for Standardisation. 2005.

19. V. Favero, A. Ferrari, and L. Laloui. "On the hydro-mechanical behaviour of remoulded and natural Opalinus Clay shale". In: *Engineering geology* 208 (2016), pp. 128–135.

20. E. Ferrage. "Investigation of the interlayer organization of water and ions in smectite from the combined use of diffraction experiments and molecular simulations. A review of methodology, applications, and perspective". In: *Clays and Clay Minerals* 64 (2016), pp. 348–373.

21. A. Ferrari et al. "Microstructural characterization of Opalinus shale". In: *th US Rock Mechanics/Geomechanics Symposium, Houston, Texas, USA* (2016).

22. F. Folgar and C. Tucker. "Orientation behavior of fibers in concentrated suspensions". In: *Journal of Reinforced Plastics and Composites* 3 (1984), pp. 98–119.

23. G. Gaganelis, P. Mark, and P. Forman. *Optimization Aided Design - Reinforced Concrete*. 1st. Berlin: Ernst & Sohn, 2022. ISBN: 978-3-433-03337-1.

24. V. E. Gall et al. "An embedded rebar model for computational analysis of reinforced concrete structures with applications to longitudinal joints in precast tunnel lining segments". In: *Computational Modelling of Concrete Structures (EURO-C 2018)*. Ed. by G. Meschke, B. Pichler, and J. G. Rots. CRC press, 2018, pp. 705–714.

25. V. Gall. "Numerical Investigation of Hybrid Segmental Lining Response to Mechanized Tunneling Induced Loadings". PhD thesis. Ruhr University Bochum, 2018.

26. V. E. Gall et al. "A holistic approach for the investigation of lining response to mechanized tunneling induced construction loadings". In: *Underground Space* 3.1 (2018), pp. 45–60. https://doi.org/10.1016/j.undsp.2018.01.001.

27. A. T. Gaynor, J. K. Guest, and C. D. Moen. "Reinforced Concrete Force Visualization and Design Using Bilinear Truss-Continuum Topology Optimization". In: *Journal of Structural Engineering* 139.4 (2013), pp. 607–618. https://doi.org/10.1061/(asce)st.1943-541x.0000692.

28. A. Gens and E. E. Alonso. "A framework for the behaviour of unsaturated expansive clays". In: *Canadian Geotechnical Journal* 29.6 (1992), pp. 1013–1032.

29. German Tunnelling Committee (DAUB). *Recommendations for the design, production and installation of segmental rings*. Tech. rep. Deutscher Ausschuss für unterirdisches Bauen e. V. (DAUB), 2013.

30. A. Ghanbari and B. L. Karihaloo. "Prediction of the plastic viscosity of self-compacting steel fibre reinforced concrete". In: *Cement and Concrete Research* 39.12 (2009), pp. 1209–1216.

31. H. Grob. "Schwelldruck im Belchentunnel". In: *Proc. Int. Symp. für untertagebau, luzern*. 1972, pp. 99–119.

32. V. Gudzulic, T. Dang, and G. Meschke. "Computational modeling of fiber flow during casting of fresh concrete". In: *Computational Mechanics* 63(6) (2018), pp. 1111–1129. https://doi.org/10.1007/s00466-018-1639-9.

33. V. Gudzulic et al. "Numerisches Mehrebenen-Modell für Stahlfaserbeton: Von der Faser- zur Strukturebene". In: *Beton und Stahlbetonbau* 115 (2020), pp. 146–157. https://doi.org/10.1002/best.201900067.

34. L. Harzheim. *Strukturoptimierung: Grundlagen und Anwendungen*. First. Frankfurt am Main: Harri Deutsch, 2008. ISBN: 9783817118090.

35. J. Huder and G. Amberg. "Quellung in Mergel, Opalinuston und Anhydrit". In: (1970).

36. International Tunnelling and Underground Space Association. *ITA Report n°22: Guidelines for the Design of Segmental Tunnel Linings*. Tech. rep. Avignon, 2019.

37. J. Kennedy and R. C. Eberhart. "Particle swarm optimization". In: *Proceedings of the IEEE International Conference on Neural Networks*. Ed. by I. Press. Piscataway, NJ, USA, 1995, pp. 1942–1948.

38. D. Kirschke. "Neue Versuchstechniken und Erkenntnisse zum Anhydritschwellen". In: *Taschenbuch für den Tunnelbau, Verlag Glückauf GmbH, Essen* (1996), pp. 203–225.

39. F. Leonhardt and E. Mönning. *Vorlesungen über Massivbau: Teil 2 - Sonderfälle der Bemessung im Stahlbetonbau*. 3rd. Berlin Heidelberg: Springer, 1986. ISBN: 978-3-642-61643-3.

40. F. T. Madsen and M. Müller-Vonmoos. "The Swelling Behaviour of Clays". In: *Applied Clay Science* 4 (1989), pp. 143–156.

41. P. Mark et al. "Vom Handwerk zur individualisierten Serienfertigung: Schwerpunkt adaptive Modulbauweisen mit Fließfertigungsmethoden". In: *Bautechnik* 98.3 (2021), pp. 243–256. https://doi.org/10.1002/bate.202000110.

42. L. Massat et al. "Swelling pressure development and inter-aggregate porosity evolution upon hydration of a compacted swelling clay". In: *Applied Clay Science* 124-125 (2016), pp. 197–210.

43. G. Meschke, G. Neu, and A. Marwan. "Robust Segmental Lining Design - Potentials of advanced numerical simulations for the design of TBM driven tunnels". In: *Geomechanics and Tunneling* 12.10 (2019), pp. 484–490. https://doi.org/10.1002/geot.201900032.

44. fib Model Code for Concrete Structures 2010. *Fédération internationale du béton (fib)*. Ernst & Sohn, 2013. https://doi.org/10.1002/9783433604090.

45. G. E. Neu, V. Gudzulic, and G. Meschke. "Design of steel fiber reinforced concrete tunnel lining segments by nonlinear finite-element analysis with different safety formats". In: *Computational Modelling of Concrete and Concrete Structures (EURO-C 2022)*. Ed. by G. Meschke, B. Pichler, and J. G. Rots. 2022.

46. G. E. Neu et al. "Robust Design of hybrid steel fiber reinforced concrete tunnel lining segments". In: *Computational Modelling of Concrete Structures (EURO-C 2018)*. Ed. by G. Meschke, B. Pichler, and J. G. Rots. Taylor & Francis, 2018, pp. 715–724.

47. G. Neu et al. "Reliability based optimization of steel-fibre segmental tunnel linings subjected to thrust jack loading". In: *Engineering Structures* (2022).

48. D. 1.-0. D. I. für Normung e. V. *Soil, testing procedures and testing equipment – determination of water absorption*. Tech. rep. 2012.

49. D. 4.-4.-0. D. I. für Normung e. V. *Zusatzmittel für Beton, Mörtel und Einpressmörtel – Prüfverfahren: Teil 4: Bestimmung der Wasserabsonderung des Betons (Bluten)*. Tech. rep. 2005.

50. M. Ortiz and A. Pandolfi. "Finite-deformation irreversible cohesive elements for three-dimensional crack-propagation analysis". In: *International Journal for Numerical Methods in Engineering* 44.9 (1999), pp. 1267–1282. https://doi.org/10.1002/(SICI)1097-0207(19990330)44:9<1267::AID-NME486>3.0.CO;2-7.

51. P. P. Pellegrini L. "Sao Paulo Metro Project – Control of Settlements In Variable Soil Conditions Through EPB Pressure And Bicomponent Backfill Grout". In: 2009.

52. D. N. Petraroia et al. "Versuchsstand für simulations- und experimentell gestützte Untersuchungen von Tunnelsegmenten unter Realbedingungen". In: *Forschung + Praxis 56, U-Verkehr und unterirdisches Bauen, STUVA (Ed.)* 2021, pp. 152–157. ISBN: 978-3-00-070615-8.

53. D. N. Petraroia and P. Mark. "Variable, full-scale tester for tunnel linings". In: *Structural Concrete* 22.6 (2021), pp. 3353–3367.

54. E. Pimentel. *A laboratory testing technique and a model for the swelling behavior of anhydritic rock*. Vol. All Days. ISRM congress. July 2007.

55. S. Plückelmann and R. Breitenbücher. "Bearable Local Stress of High-Strength SFRC". In: *BEFIB 2020 – RILEM Bookseries 30*. Ed. by S. et. al. 2020, pp. 176–188.

56. S. Plückelmann and R. Breitenbücher. "Experimental Investigation of Hybrid Concrete Elements with Varying Fiber Reinforcement under Concentrated Load". In: *FIB BULLETIN No. 95: Fibre Reinforced Concrete: From Design to Structural Applications. Proceedings of the ACI-fib-RILEM International Workshop – FRC 2018*. 2018, pp. 422–431. ISBN: 978-2-88394-142-7.

57. S. Plückelmann and R. Breitenbücher. "Hybrid Concrete Elements with Splitting Fiber Reinforcement under Two-Dimensional Partial-Area Loading". In: *Proceedings of the fib Symposium 2017 – High Tech Concrete: Where Technology and Engineering Meet*. 2017, pp. 347–355.

58. S. Plückelmann and R. Breitenbücher. "Hybrid lining segments – bearing and fracture behavior of longitudinal joints". In: *Tunnels and Underground Cities: Engineering and Innovation meet Archaeology, Architecture and Art- Proceedings of the WTC 2019 ITA-AITES World Tunnel Congress*. 2019, pp. 2881–2890. ISBN: 9781138388659.

59. S. Plückelmann and R. Breitenbücher. "Untersuchungen zum Trag- und Bruchverhalten von hybriden Betonelementen". In: . *Forschungskolloquium des DAfStb (2017)*. 2017, pp. 34–45.

60. S. Plückelmann and R. Breitenbücher. "Verformungsverhalten von Betonen mit ausgeprägtem plastischen Stauchvermögen". In: *Beton- und Stahlbetonbau* 115.12 (2020), pp. 994–1005. https://doi.org/10.1002/best.202000033.

61. S. Plückelmann, F. Song, and R. Breitenbücher. "Load-Bearing and Bonding Behavior of Hybrid Concrete Tunnel Lining Segments". In: *Proceedings of the ITA-AITES World Tunnel Congress – Surface challanges – Unterground solutions*. 2017, pp. 1311–1318.

62. S. Plückelmann et al. "Aufnehmbare Teilflächenspannung von hochfestem Stahlfaserbeton". In: *Beton- und Stahlbetonbau* 114.9 (2019), pp. 653–662. https://doi.org/10.1002/best.201900015.

63. T. Putke et al. "Entwicklung von hybriden Stahlfaserbetontübbings - Experimentelle und numerische Analysen von der Material- bis zur Bauwerksebene". In: *Bauingenieur* 89 (2014), pp. 447–456.

64. T. Putke, R. Bohun, and P. Mark. "Experimental analyses of an optimized shear load transfer in the circumferential joints of concrete segmental linings". In: *Structural Concrete* 16.4 (2015), pp. 572–582. https://doi.org/10.1002/suco.201500013.

65. S. Pelizza, D. Peila, L. Borio, E. Dal Negro, R. Schulkins, A. and Boscaro. "Analysis of the Performance of Two Component Back-filling Grout in Tunnel Boring Machines Operating under Face Pressure". In: *ITA-AITES World Tunnel Congress 2010, Vancouver (CA), 14 to 20 May, 2010*. 2010.

66. M. Sauerwein et al. "Applicability of superabsorbent polymers for the consolidation and strength development of two-component mortars for the annular gap". In: ed. by 2. ECCOMAS Thematic Conference EURO:TUN 2017 Innsbruck University. Hofstetter, G.; Bergmeister, K.; Eberhardsteiner, J.; Meschke, G.; Schweiger, H.F., 2019.

67. G. Schmidt-Thrö et al. "Experimental analysis of concrete elements under partial area strip loading". In: *Civil Engineering Design* 1 (2019), pp. 28–38. https://doi.org/10.1002/cend.201900001.

68. G. Schuëller and H. Jensen. "Computational methods in optimization considering uncertainties — An overview". In: *Computer Methods in Applied Mechanics and Engineering* 198.1 (2008), pp. 2–13.

69. C. Schulte-Schrepping. "Materialkonzepte zur Aktivierung von Ringspaltverfüllmaterialien im maschinellen Tunnelbau". PhD thesis. Ruhr-University Bochum, 2020.

70. C. Schulte-Schrepping and R. Breitenbücher. "Development of a test setup for the simulation of the annular gap grouting on a semi technical scale". In: 2019.

71. A. Schumacher. 2013, p. 314. ISBN: 9783642346996.

72. R. Shah. "A numerical study on backfilling of the tail void with two-component grout based on laboratory tests". PhD thesis. Politecnico di Torino, 2017.

73. M. Smarslik, M. A. Ahrens, and P. Mark. "Toward holistic tension- or compression-biased structural designs using topology optimization". In: *Engineering Structures* 199.109632 (2019). https://doi.org/10.1016/j.engstruct.2019.109632.

74. M. Smarslik and P. Mark. "Hybrid reinforcement design of longitudinal joints for segmental concrete linings". In: *Structural Concrete* 20 (2019), pp. 1926–1940. https://doi.org/10.1002/suco.201900081.

75. M. Smarslik et al. "Berechnungsmodelle für Bau- und Endzustände von Tübbingtunneln". In: *Taschenbuch für den Tunnelbau 2018*. Ed. by Deutsche Gesellschaft für Geotechnik e.V. Berlin: Ernst & Sohn, 2018. Chap. 2, pp. 111–146. ISBN: 978-3-433-03217-6.

76. T. Soetens and S. Matthys. "Shear-stress transfer across a crack in steel fibre-reinforced concrete". In: *Cement and Concrete Composites* 82 (2017). https://doi.org/10.1016/j.cemconcomp.2017.05.010, pp. 1–13.

77. F. Song. "Effect of fibre properties and embedment conditions on fibre pullout behavior from concrete matrix". In: *Proceedings of the 9th International PhD Symposium in Civil Engineering*. 2012, pp. 597–602.

78. F. Song. "Steel fiber reinforced concrete under concentrated load". PhD thesis. Ruhr-University Bochum, 2017.

79. F. Song and R. Breitenbücher. "Experimentelle Untersuchungen zum Auszugverhalten von Stahlfasern in höherfesten Betonen". In: *Beton- und Stahlbetonbau* 109.1 (2014), pp. 43–52. https://doi.org/10.1002/best.201300049.

80. F. Song and R. Breitenbücher. "Study on the load-bearing behavior of steel fiber reinforced concrete (SFRC) under localized compression". In: *Proceedings of TU Seoul 2013*. 2013, pp. 336–339.

81. F. Song and R. Breitenbücher. "Untersuchungen zum Trag- und Bruchverhalten von Stahlfaserbeton speziell für Tübbinge unter Teilflächenbelastung". In: *Proceedings of the 19th International Conference of Building Materials*. 2015, pp. 1258–1265.

82. D. A. für Stahlbetonbau. *DAfStb Richtlinie Stahlfaserbeton*. Tech. rep. Deutscher Ausschuss für Stahlbetonbau e.V. – DAfStb, 2012.

83. A. S. for Testing and Materials. *ASTM C185-20. Standard Test Method for Air Content of Hydraulic Cement Mortar*. Tech. rep. ASTM International, West Conshohocken, PA.

84. M. Thewes and C. Budach. "Grouting of the annular gap in shield tunnelling – an important factor for minimisation of settlements and production performance". In: *Safe tunnelling for the city and for the environment, 23-28 May 2009, Budapest, Hungary*. Ed. by P. Kocsonya. 2009.

85. M. Thewes and C. Budach. "Mörtel im Tunnelbau – Stand der Technik und aktuelle Entwicklungen zur Verfüllung des Ringspalts bei Tunnelvortriebsmaschinen". In: *BauPortal 2009, Heft 12* (2009).

86. G. Tiberti et al. "An overview of the flexural post-cracking behavior of steel fiber reinforced concrete". In: *Structural Concrete* 19.3 (2018), pp. 695–718. https://doi.org/10.1002/suco.201700068.

87. C. Todaro et al. "Two-component grout in tunnelling applications". In: (2021). Ed. by E. Sohn.

88. I. Trabucchi et al. "A hybrid solution proposal for precast tunnel segments". In: *Structural Concrete* 22.3 (2021), pp. 1534–1548. https://doi.org/10.1002/suco.202000629.

89. G. Vu et al. "Cementitious Composites with High Compaction Potential: Modeling and Calibration". In: *Materials* 13.21 (2020).

90. M. Wichers. "Bemessung von bewehrten Betonbauteilen bei Teilflächenbelastung unter Berücksichtigung der Rissbildung". PhD thesis. Technical University of Braunschweig, 2013.

91. M. Wittke. "Begrenzung der Quelldrücke durch Selbstabdichtung beim Tunnelbau im anhydritführenden Gebirge". In: *Geotechnik in Forschung und Praxis: Wbi-print* 13 (2003).

92. Y. Yang, C. D. Moen, and J. K. Guest. "Three-Dimensional Force Flow Paths and Reinforcement Design in Concrete via Stress-Dependent Truss-Continuum Topology Optimization". In: *Journal of Engineering Mechanics* 141.1 (2015), p. 04014106. https://doi.org/10.1061/(asce)em.1943-7889.0000819.

93. B.-Y. Youn-Cale and R. Breitenbücher. "Consolidation of single-component grouting mortars in the course of dewatering – Redistribution of particles". en. In: *International Journal of Civil Engineering* 22 (2018).

94. B.-Y. Youn. "Untersuchungen zum Entwässerungsverhalten und zur Scherfestigkeitsentwicklung von einkomponentigen Ringspaltmörteln im Tunnelbau". PhD thesis. Ruhr-University Bochum, 2016.

95. B.-Y. Youn and R. Breitenbücher. "Dewatering and infiltration behavior of annular gap grouts". In: *Proceedings of the ITA-AITES World Tunnel Congress 2015. SEE Tunnel – Promoting Tunneling in SEE Region, HUBITG, Dubrovnik*. 2015.

96. B.-Y. Youn and R. Breitenbücher. "Influencing parameters of the grout mix on the properties of annular gap grouts in mechanized tunnelling". In: *Tunneling and Underground Space Technology* 43 (2014).

97. B.-Y. Youn and R. Breitenbücher. "Optimization of mortars for annular gap grouting". In: *Proceedings of the International Symposium on Tunnelling and Underground Space Construction for Sustainable Development*. 2013.

98. C. Zang, M. Friswell, and J. Mottershead. "A review of robust optimal design and its application in dynamics". In: *Computers & Structures* 83.4 (2005), pp. 315–326.

99. Y. Zhan and G. Meschke. "Analytical Model for the Pullout Behavior of Straight and Hooked-End Steel Fibers". In: *Journal of Engineering Mechanics (ASCE)* 140(12) (2014), 04014091(1–13). https://doi.org/10.1061/(ASCE)EM.1943-7889.0000800.

100. Y. Zhan and G. Meschke. "Multilevel computational model for failure analysis of steel-fiber – reinforced concrete structures". In: *Journal of Engineering Mechanics (ASCE)* 142.11 (2016), 04016090(1–14). https://doi.org/10.1061/(ASCE)EM.1943-7889.0001154.

101. Y. Zhan. "Multilevel Modeling of Fiber-Reinforced Concrete and Application to Numerical Simulations of Tunnel Lining Segments". PhD thesis. Ruhr University Bochum, 2016.

102. C. Zhao et al. "Prediction of tunnel lining forces and deformations using analytical and numerical solutions". In: *Tunnelling and Underground Space Technology* 64 (2017), pp. 164–176. https://doi.org/10.1016/j.tust.2017.01.015.

103. M. Ziegler et al. "Investigations in the new TBM-excavated Belchen highway tunnel – Status update (Part 4)". In: *ENSI Erfahrungs- und Forschungsberichte 2019* (2020), pp. 331–336.

Digital Design in Mechanized Tunneling

6

Abdullah Alsahly , Hoang-Giang Bui , Lukas Heußner ,
Annika Jodehl , Rodolfo Javier Williams Moises, Markus Obel,
Marcel Stepien, Andre Vonthron, Yaman Zendaki, Steffen Freitag ,
Markus König , Elham Mahmoudi , Peter Mark ,
Günther Meschke , and Markus Thewes

A. Alsahly (✉) · R. J. Williams Moises · Y. Zendaki · G. Meschke
Structural Mechanics, Ruhr-Universität Bochum, Bochum, Germany
e-mail: abdullah.alsahly@rub.de

R. J. Williams Moises
e-mail: rodolfo.williamsmoises@rub.de

Y. Zendaki
e-mail: yaman.zendaki@rub.de

G. Meschke
e-mail: guenther.meschke@rub.de

H.-G. Bui
Mechanics of Materials, Ruhr-Universität Bochum, Bochum, Germany
e-mail: giang.bui@rub.de

L. Heußner · P. Mark
Concrete Structures, Ruhr-Universität Bochum, Bochum, Germany
e-mail: lukas.heussner@rub.de

P. Mark
e-mail: peter.mark@rub.de

A. Jodehl · M. Thewes
Tunneling and Construction Management, Ruhr-Universität Bochum, Bochum, Germany
e-mail: annika.jodehl@rub.de

M. Thewes
e-mail: markus.thewes@rub.de

M. Obel
Mark Ingenieure GmbH, Bochum, Germany
e-mail: m.obel@mark-ingenieure.de

Abstract

Digital design methods are constantly improving the planning procedure in tunnel construction. This development includes the implementation of rule-based systems, concepts for cross-document and -model data integration, and new evaluation concepts that exploit the possibilities of digital design. For planning in tunnel construction and alignment selection, integrated planning environments are created, which help in decision-making through interactive use. By integrating room-ware products, such as touch tables and virtual reality devices, collaborative approaches are also considered, in which decision-makers can be directly involved in the planning process. In current tunneling practice and during planning stage, Finite Element (FE) simulations form an integral element in the planning and the design phase of mechanized tunneling projects. The generation of adequate computational models is often time consuming and requires data from many different sources. Incorporating Building Information Modeling (BIM) concepts offers opportunities to simplify this process by using geometrical BIM sub-models as a basis for structural analyses. In the following chapter, some modern possibilities of digital planning and evaluation of alignments in tunnel construction are explained in more detail. Furthermore, the conception and implementation of an interactive BIM and GIS integrated planning system, "BIM-to-FEM" technology which automatically extracts relevant information needed for FE simulations from BIM sub-models, the establishment of surrogate models for real-time predictions, as well as the evaluation and comparison of planning variants are presented.

M. Stepien · M. König · E. Mahmoudi
Computing in Engineering, Ruhr-Universität Bochum, Bochum, Germany
e-mail: marcel.stepien@rub.de

M. König
e-mail: koenig@inf.bi.rub.de

E. Mahmoudi
e-mail: elham.mahmoudi@rub.de

A. Vonthron
Computing in Engineering, VSK Software GmbH, Bochum, Germany
e-mail: andre.vonthron@vsk-software.com

S. Freitag
Institute for Structural Analysis, Karlsruhe Institute of Technology, Karlsruhe, Germany
e-mail: steffen.freitag@kit.edu

6.1 Introduction

With the move toward digitalization in the construction industry, the rapidly developing field of information technology (IT) plays a dominant role in modern construction processes, in particular large projects like tunnel constructions. As a consequence, more and more digital project data is produced by several authorized project partners and is stored in diverse formats using different IT applications during different stages of the project. Additionally, the availability of computer-aided design (CAD) and sophisticated data management tools have also had noticeable impact on the way construction industries (including tunneling industries) record, store, retrieve, access, process, visualize, maintain, display, and manage important project data. However, in most cases the employed IT tools are standalone applications with limited inter-compatibility with other platforms because proprietary format for storing and accessing information are often different. A coherent data exchange between all applications and information sources within a project is for this reason not directly feasible in digital form without human intervention. As a result of this lack of compatibility, a high amount of errors occur during the exchange of information between applications and information is lost. Moreover, different information packages, from different project partners, which often describe the same object/element in the project, make it difficult to maintain the necessary level of integrity and consistency of project information.

In this regard, Building Information Modeling (BIM) has emerged to address these problems generated by decentralized data management. BIM presents an innovative and collaborative solution that allows for an organized and efficient workflow during the entire life cycle of the project: planning, design, construction, operation, maintenance and possible later demolition phases [25]. Although BIM methods were first developed to be applied to improve the organization of above-ground building projects, they have been, and are currently being extended to tunneling projects [11, 32, 43, 74], among other engineering infrastructure projects [39, 69, 85]. The capability of BIM to connect information databases to a graphical representation based on a parametric 3D models allows better visualization, coordination, and management of construction projects and accordingly, leads to a reduction of construction costs and errors [46].

The development of a real-time interactive digital platform for planning and design of tunneling projects, particularly in urban areas, provides a valuable tool to support the design process and enrich the decision-making. Such platform would allow for visual exploration of the whole project including parametric generation of feasible alignments considering all project design criteria [42, 79]. For this purpose, a digital interactive platform has been developed for collaborative planning process in tunneling projects, in which the numerical simulation, the simulation results, i.e., settlements, construction time, and the damage assessment of existing infrastructure, is integrated and visualized in real-time.

The proposed digital platform considerably reduces the user effort connected with the generation of simulation models. This platform supports data acquisition and model generation as well as the visualization of the important results of a numerical simulation in

a 3D graphical model so as to be in line with Building Information Modeling (BIM) concepts. To this end, a fully automatic model generation assistant has been developed and integrated into the so-called TIM, "Tunneling Information Model" in order to enhance the usability and compatibility of a structural tunnel simulation with BIM methods. The automatic model generator is able to correctly model the geometry of the tunnel project, generate all relevant model components, extract geotechnical survey data stored in CAD format, discretize the FE mesh, and control the flow of the simulation.

6.2 Information Modeling

In the BIM-based approach, information is used as a basis for decision-making and project steering. Some information can only be processed through the exploration of constraints and dependencies. Through so-called interaction chains, relevant information can be dissected and structured. An interaction chain can be defined as a sequence of processes that build on each other and whose results can lead directly to the evaluation of relevant project constraints (see Fig. 6.1). The execution of interaction chains needs to be provided with relevant information. This includes existing product data as well as temporary simulation
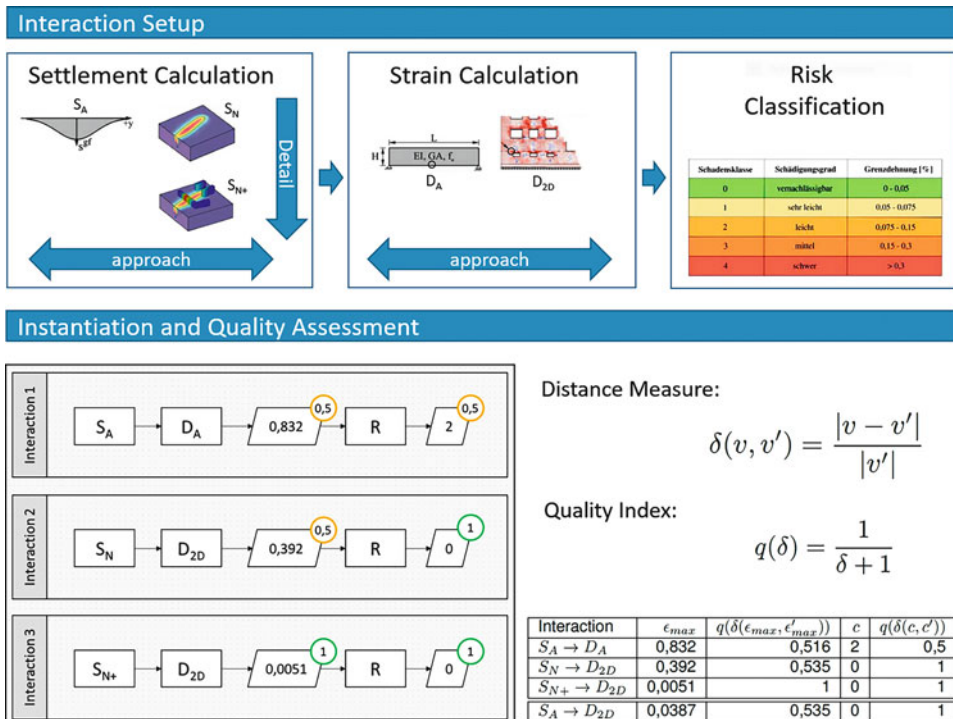
Fig. 6.1 Example of an interaction chain that considers settlement data and strains for risk classification
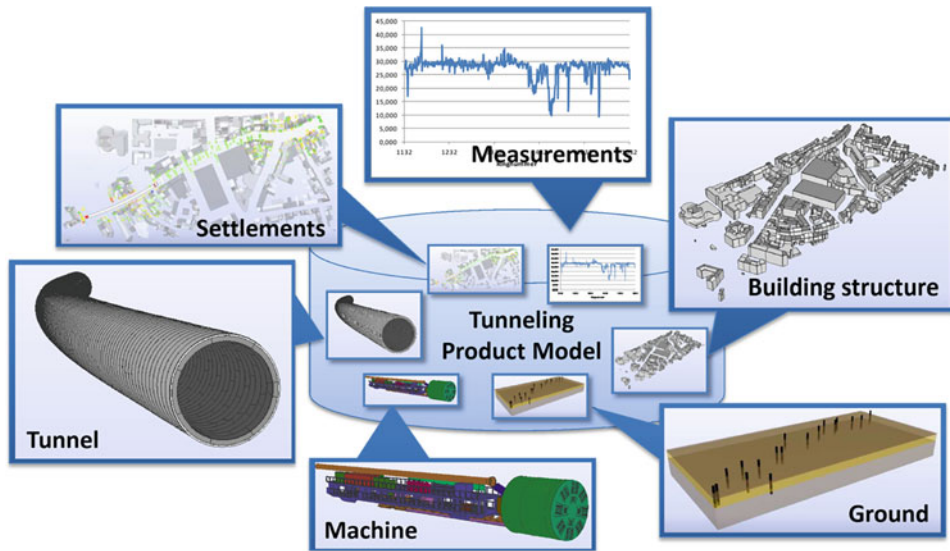
Fig. 6.2 Tunnel information model consisting of the essential four submodels and time-dependent settlement and machine data [74]

results. For the management of these information, a 4D-information model has been developed. In a tunneling project, information is usually time-dependent and is distributed on different systems and various data formats.

In accordance with the BIM concept for tunneling construction domains, the Tunnel Information Model (TIM) [42] establishes a holistic container for tunneling projects that also enables the integration of interaction chains for project evaluation. In the TIM data is integrated and linked by collecting, classifying, structuring and processing necessary information from the planning and construction phase. The structuring of multiple interacting documents has been realized by adopting the multi-model container concept [73]. Compared to existing approaches in the building sector lots of dynamic and time-dependent data must be stored. These include predictive models in the planning phase as well as real settlement data and machine data in the construction phase. A continuously adaption to the ground conditions based on up-to-date measurements and simulation data represents a major challenge. The basis of the TIM is build upon four essential product models, including a hybrid ground model, a boring machine model, a tunnel model and built environment model (Fig. 6.2). A detailed differentiation is provided in the following subsections.

6.2.1 Standards for Digital Design Tunneling

The digital design in construction requires standards for the exchange of information to be applied. In the context of the BIM method, a distinction between semantic information

and geometric representation is made. While the geometry describes the visual representation of an element, the semantic provides descriptive information, such as model structure and object properties. The Industry Foundation Classes (IFC) standard [38] has been established as an open exchange format for BIM models. Traditionally, the IFC schema only supports building construction. However, in recent years, the context of IFC has increasingly being improved to support infrastructure domains in future. An proposal including bridges, rails, roads and port & waterways denoted as IFC4.3 is currently being reviewed by the International Standardization Organisation (ISO) to be the next major officially accepted version of the IFC. An extension for tunnels is also currently being developed by a project group of buildingSmart International [15]. The current version is proposed as IFC4.4, to which the SFB has substantially contributed to the requirements and data models for mechanized tunnels.

6.2.2 Hybrid Ground Model

The ground behavior is a fundamental basis for the overall construction process. A hybrid ground model has been developed in [33] to allow both a global and detailed consideration of the ground conditions. Based on borehole measurements, the profile of the ground can be depicted and transferred to a layer-based ground model. The geometry of these layers, in this case, is based on boundary representations (B-Rep). To support the analysis and assignment in a larger resolution, the layers are decomposed into voxel data (see Fig. 6.3). The detail of the voxel representation is decided upon the specific application. Algorithms, such as octree decomposition, are able to perform efficient decomposition and thus represent the ground model as discretized voxel models [47]. Regions of voxels are then combined based on their properties to represent layers of soil. High detail is required, e.g. when processing data close to the boring machine.

Both formats (B-Rep and voxels) are stored side-by-side, for which methods have been developed to support the integration, consistency and versioning [34]. The versioning also allows to update the ground conditions in the hybrid model and to use it for subsequent analyses. In the overall process, the hybrid ground data model makes it possible to incorporate different version (time-dependent), different resolutions (space) and different geometry representations (format). Throughout all versions, data can be requested and updated in both boundary representations and voxel representations.

Based on the hybrid ground model, analyses and simulation models can efficiently request and process information. For example, a sophisticated octree-based soil model was used to calculate uncertainties based on the knowledge gained from the boreholes locations [47]. This investigation utilized kriging algorithms to map calculated uncertainty directly onto each voxel in the ground model. Several approaches for semivariogram models were tested to illustrate and make optimizations for strategic selection of preferences in projects (Fig. 6.4).
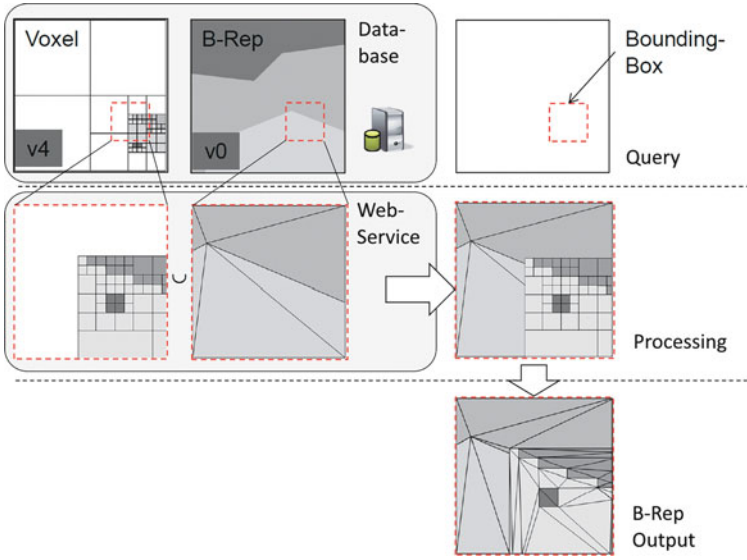
Fig. 6.3 Concept for querying soil properties for a surface model (B-Rep) based on the hybrid ground data model

Applied Variogram Model	Uncertainty Measure		Illustration
Gaussian	U	50.684%	
	s²	0.4777	
Exponential	U	39.502%	
	s²	0.6469	
Spherical	U	53.099%	
	s²	1.421	
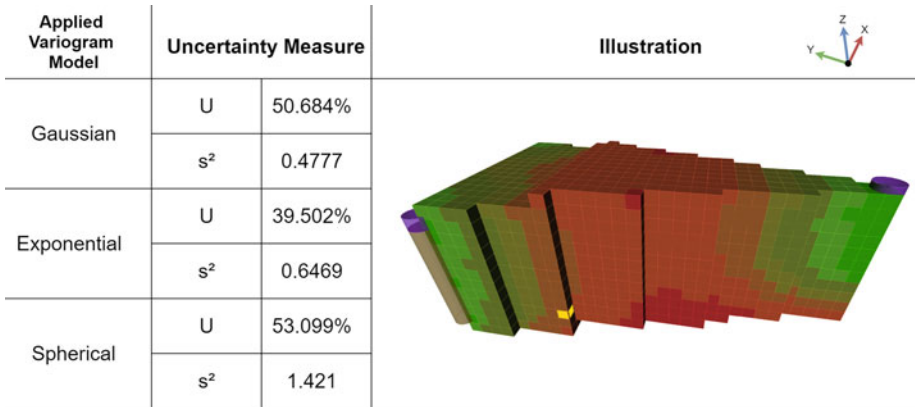
Fig. 6.4 Effect of change in applied semivariogram model for the highlighted voxel [47]

6.2.3 Tunnel Boring Machine Model

The tunnel boring machine has also been modeled and is included in the TIM collection of considered submodels, primarily because of the 4D planning process, that also requires the TBM to be included in planned projects. It is pariculary important to be able to locate the machine, the face of the tunnel and to monitor the progression of the excavation. Here, the focus is on Earth Pressure Balance Shield (EPB) boring machines. To store and exchange
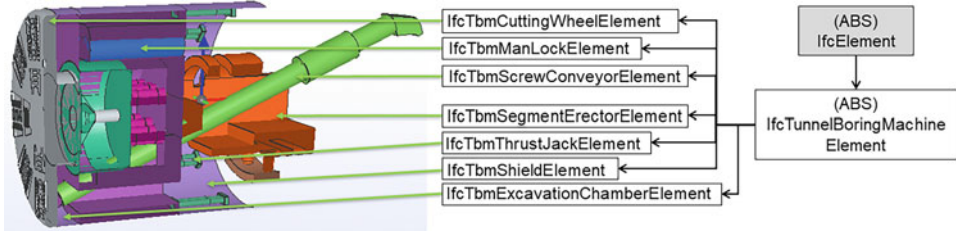
Fig. 6.5 Implemented IFC hierarchy for a TBM in a BIM based process

information regarding the machine, a proposal for the Industry Foundation Classes (IFC) model has been developed (Fig. 6.5). Therefore, a classification for the model elements has been developed by interaction between tunneling and informatics domains within the SFB. These include proper geometric descriptions as well as the assignment of necessary semantic information. In addition, the machine data were linked directly into the model so that they can be updated during tunnel driving and queried, for example, when performing a settlement analysis.

6.2.4 Tunnel Model

The tunnel model itself has also been realized using an IFC-based product model. The geometric representation of such a model can normally not be created by hand, because of the thousands of ring segments. Therefore, parametric modeling methods have been used to automatically create a model based on the cross-section template and the placement of the rings (Fig. 6.6). The placement can be considered as input in both ways, either from the planned positioning as well as from real positions of existing mounted rings. Considering alignment planning variants and settlement calculations, the position can be precisely defined. When calculating the positioning for a planned tunnel, the connectivity of the rings must be considered to calculate the exact position and orientation [57]. Each element is transformed locally to represent the ring rotation and general orientation, using rotation matrices (M_X, M_Y and M_Z) along all axis and defined according to the precise position and direction for the ring on the alignment. Then, the transformed tunnel ring is moved on the position of the alignment (M_T), creating a tunnel model.

Storing the tunnel model as an IFC model data file must also consider resource consumptions. Therefore, an efficient modeling technique has been applied to directly generate a resource preserving model as well as allowing to optimize existing models [88]. When the geometry and properties of each ring or ring segment are clearly represented, the model for individual sections of a tunnel project can easily reach hundreds of megabytes. This affects the external storage in a file format and the performance of visualizations in subsequent analyses. Here, the STEP-format and the flyweight programming-pattern has been utilized to drastically reduce the resources required for modeling and data storage
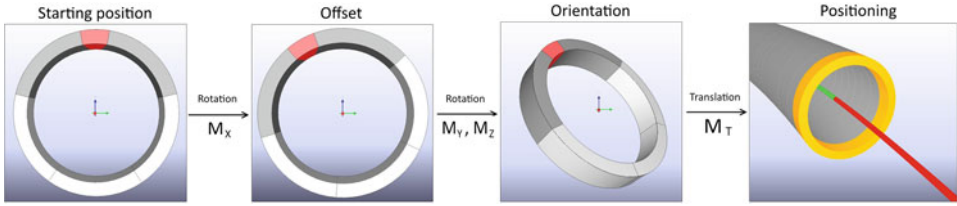
Fig. 6.6 Creating a parametric tunnel model, based on an alignment positioning and orientation
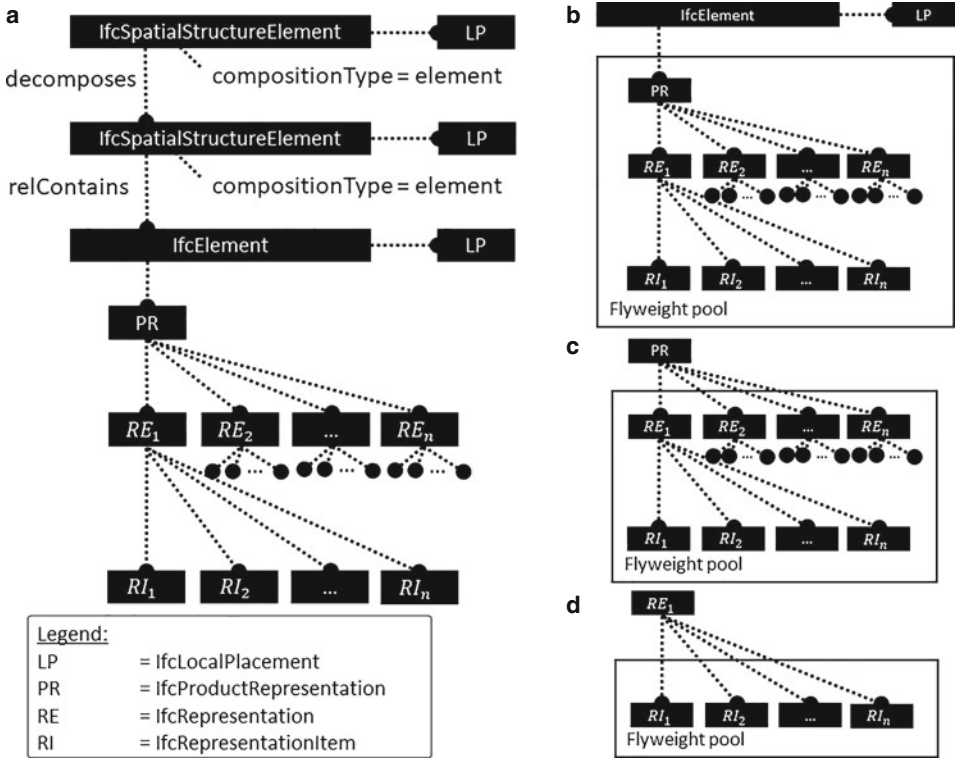
Fig. 6.7 Reuse of recurring elements in the IFC tunnel model (**a**) using either product representation level (**b**), representaion level (**c**) or representation item level (**d**) [88]

(Fig. 6.7). The optimization focuses on single ring segments (A_i) and compares whole tunnel rings. As the types of segments (i.e., an A_1 ring type of k segments) and even complete ring designs (A_1-...-A_k) are highly recurring in a mechanized tunnel model, this can be exploited to share specific information amongst different occurrences. In computer science terms, that is called the flyweight design pattern, which enables the efficient reuse of recurring data. In a tunnel model, this affects both geometry representations as well as common attributes, which do not change among succeeding ring constructions and can be
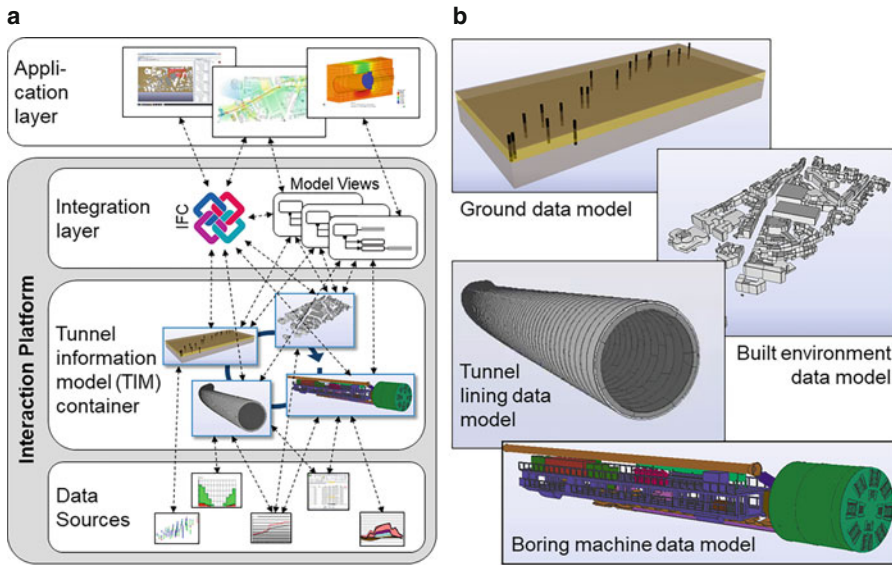
Fig. 6.8 Tunnel information modeling framework based on a unified interaction platform and an application layer (**a**). The tunnel information model contains four main subdomain models (**b**). [42]

stored on a type-based level. Specific information, such as the actual position of rings or the ring number, are then stored on occurrence level.

For existing tunnel models, it is also possible to recalculate an optimized model afterwards. Using a rigid body transformation, these recurring geometries of ring segments can be identified and stored in a resource preserving structure.

6.2.5 Interaction Platform

To access all data of a tunneling project in a uniform and standardized way, an interaction platform has been proposed [42]. The interaction platform that considers the TIM framework (Fig. 6.8) consists of three different layers. The first layer contains the actual data sources, such as machine data or borehole profiles. The second layer represents the TIM, containing models that are linked to one or more data sources. Finally, the integration layer provides a unified interface to support a standardized way to use the data for subsequent tunneling software applications. This is realized by constantly using the IFC data format for the transportation of the product models. By using so-called model views, implemented on top of the IFC format using the Model View Definition (MVD) in MVDxml format. This allows to set specific requirements, which must be included into a model to execute a specific application, as well as it allows to filter only the necessary data.

6.2.6   Visualization of Settlements Based on Analysed Measured Data

An important task for the evaluation of the tunneling process is the analysis of settlements. Based on the reference project "Wehrhahn-Linie" in Düsseldorf, Germany, a case study has been conducted to visualize the amount of settlement during the tunneling process. The settlements must be considered both in the context of the existing built environment and the dynamic position of the current data of the TBM. This allows to identify potentially endangered buildings along the alignment of the tunnel. Also, conclusions about the operational behavior during excavation can be drawn from the settlements, i.e. the values of the excavation advance or grouting pressure can be checked in case of unexpectedly high settlements. For the analysis of settlements, a dedicated model view has been defined (see Fig. 6.9). Only necessary contents are provided, for example, how to provide the built environment, which only is delivered in geometric representation while providing a ground representation is completely discarded in this case. However, the model view ensures, that the required tunnel and the boring machine as well as the settlement values itself are available, before the application can be executed.

Based on the model view, the data was used into a settlement application to analyze and visualize settlements over a period of time corresponding to the excavation process. The visualization is performed step-wise based on a time-step (hours, days and weeks) or ring-wise manner. Based on the current excavation, the installed rings are turned on visible and the position of the machine in front of the tunnel is updated, accordingly. Additionally, the performance data of the boring machine is plotted aside and can be reviewed to the corresponding time step.
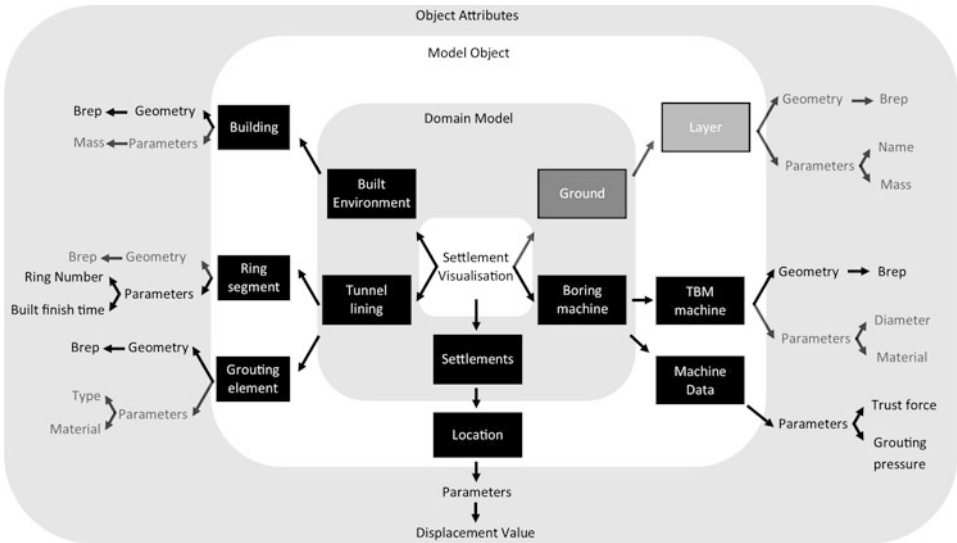
Fig. 6.9 Model View Definition for the settlement analysis

a b
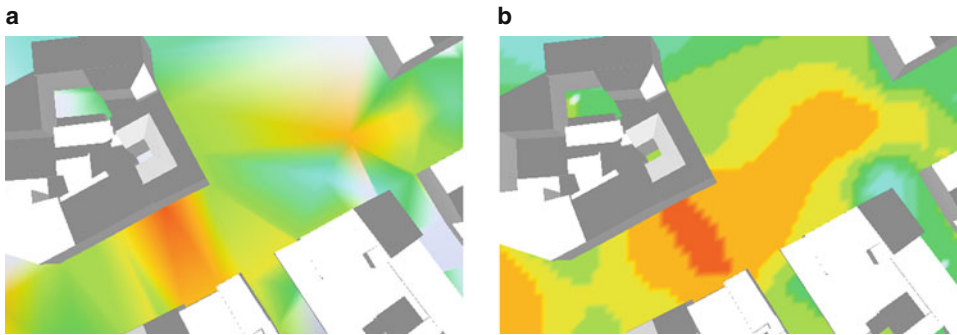
Fig. 6.10 Delauney triangulation (**a**) vs. Kringing method (**b**)

The settlement data, which is input in form of 2d-positions and vertical displacement values, is transferred into surface-based representations and colored according to the displacement value. This allows to easily identify spots of endangering settlement values. A surface-based representation, which can be calculated in real-time, is based on Delauney triangulation (Fig. 6.10a). The accuracy of this method is sufficient, when the measurement points are regularly distributed. However, when settlement values occur scattered or spatial varying, this method is not sufficient. In this case, the application
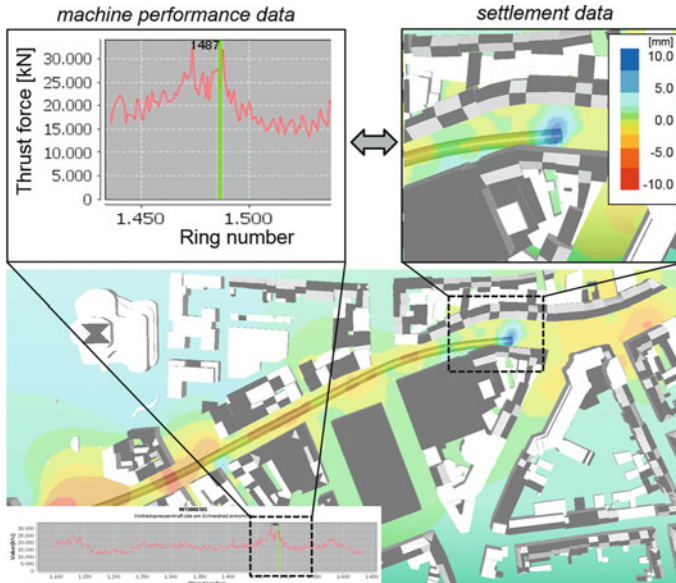
Fig. 6.11 Time-dependent visualization of settlements in context of the existing built environment and the current tunneling advancement

of geo-statistical methods help to create a surface representation. In particular, the Simple Kriging method has been applied, which outputs a statistical interpreted value on a regular grid (Fig. 6.10b). This leads to a smoother indication of the settlement values, where relevant spots can easily be identified. Using this method, points must be pre-calculated for a specific moment in time before executing a time-dependent settlement analysis. Therefore, both resource consumption and performance must be considered, as well as data size, which depends on the step size (e.g., number of days or number of rings), the resolution of the generated grid, and the geostatistical interpolation algorithm itself.

An example of a specific real-project situation of a time-dependent visualization of settlements is presented in Fig. 6.11. Here, a conspicuous heaving above the TBM could be resolved to a peak in the thrust force value, which originated from the boring machine passing through a bearing slurry wall.

6.3 Digital Design of Tunnel Tracks

The investigation of the tunnel track design is one of the most important studies in tunnel construction. Variations of alignments are compared in order to plan cost-efficiently and to reduce the risks for the project. Usually, variations of alignments are valid, as the criteria allow for alternative approaches that must be evaluated by experts. The *Weighted Decision Matrix* (WDM) method is used for the evaluation of such variants, by establishing, weighting and comparing project-specific criteria. A manageable number of alignments are examined, until the best alignment is selected for a project. The variants also consider variables in the tunnel design, such as variations in the tunnel diameter, number of tunnel tubes (dual-tube vs. single-tube design) or a strategic selection of methods in tunnel excavation. However, the most important factors are impacts on the environment, such as critical settlements in protected areas or collision with underground structures.

Traditionally, an alignment is composed of a route and a gradient. The route describes the alignment in a 2D plane, while the gradient adds the elevation depending on the current curve section. Both tracks are defined in segments and modeled by special curves section by section. This is necessary, for example, to take into account geometric criteria of elevation and speed. A significant aspect of this approach is the use of transition segments for alignment definition. These are special curve sections, often modeled as clothoid curves, which enable a smooth transition of the curve curvature between segments. The combination of these two design perspectives creates a 3D alignment that can subsequently be used for placement of elements in a BIM-based process.

A number of tools is required for the investigation of alignment variants. The integrated platform for interactive alignment exploration (Fig. 6.12) has been conceptually developed within the course of the research of the SFB 837. Here, the main focus is on the interactive exploration of alignment variants, new methods for the variant evaluation and the integration of domain-specific information.
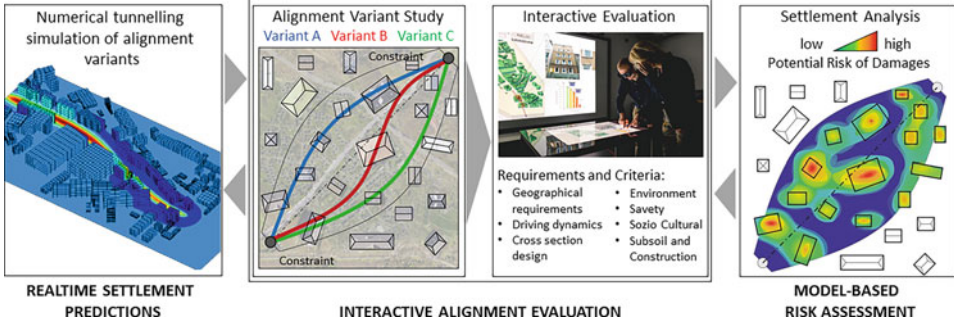
Fig. 6.12 Integration of interactive planning and evaluation between prediction and risk assessment for the digital alignment planning procedure

6.3.1 Integrated Platform

The Tunnel Information Modeling Framework (TIM) [42] has been adapted into an integrated platform and developed further in [79]. The platform (Fig. 6.13) advances the TIM framework by including alignment planning methods, integrating BIM and GIS data, as well as improving the decision-making by establishing an interactive planning environment for the exploration. The framework has been conceived to utilize roomware products, mainly touch-table devices, to enable a collaborative, interactive and ongoing exploration of planning variants. Therefore, a primary feature of the integrated platform is a (multi-)touch-based interaction with the planning environment that enables updates of planning variants in a collaborative environment in real-time. The creation process of the
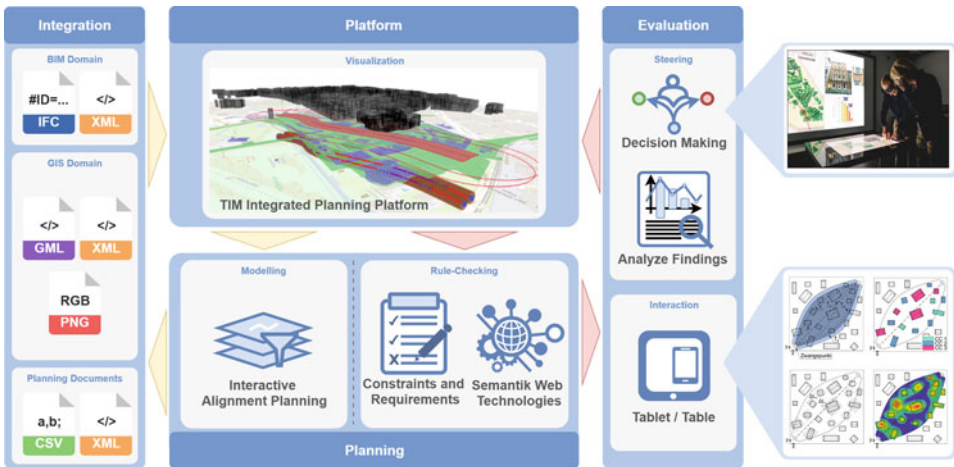
Fig. 6.13 Overview of the Integrated Platform Environment and Processes for Alignment Planning in Tunneling
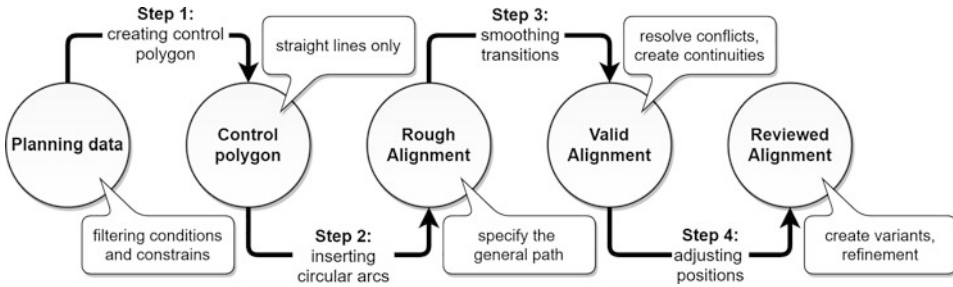
Fig. 6.14 Procedure of planning the route on an alignment [79]

segmented alignment has been generalized using spline curves, especially *Non-Uniform Rational B-Splines* (NURBS), in order to create a more flexible representation for alignment definition.

6.3.2   Interactive Exploration of the Alignment

Alignment planning requires the segmentation and procedural creation of curve sections to create alignments that comply with necessary properties, such as a slowly increasing and decreasing angle of the gradient or a smooth transition of curvature during turns.

Thereby, each segmented curve-type is defined individually, which are primarily a set of lines, circular-arcs, clothoids or parabolas. Handling these curve-types separately, however, complicates the planning process in an interactive environment.

Figure 6.14 displays the step by step approach for alignment modeling. The process starts with a set of planning data, which provides basic constraints to model the alignment on top. The alignment is then refined in each step, by adding more and new types of segments into the alignment definition. In the end, the alignment has to be reviewed against project requirements and constraints, creating a variant for alignment evaluation.

6.3.3   Spline-Based Alignments Planning Approach

Because of their flexibility and consistency, spline curves are often used as a basis for the representation of different types of curves. Whereas lines and circular-arc elements can be displayed quite effortlessly, the implementation of clothoids using splines is much more complex. The main reason for this is that it is difficult to represent the continuously growing curvature of a clothoid curve by splines. This issue has been studied in several articles where different approaches to represent clothoids using splines have been elaborated, e.g., by approximating in a certain interval [90] or parametrically identifying controlled and restrictive computations [89]. This approaches hat been considered for an interactive design of tunnel tracks.

In [79] a set of spline-curves, specifically Non-Uniform Rational B-Splines (NURBS), were investigated to model different types of curves for alignment definition. More specifically, the parameters of these splines had been restricted in specific ways, to emulate the behavior and properties of different curve-types. For example, setting the weights depending on the angle and length of the control polygon can represent circular-arc segments given by start- and end-point. The tangential continuity between segments can then be modeled by splitting the NURBS into subsets of spline-curves or by synchronizing the tangential direction at start- and end-points. While NURBS enable highly adjustable modeling approaches, certain curve-types are modeled as near enough approximations, such as clothoids.

6.3.4 Alignments for Parametric Tunnel-Design

In the context of BIM-based projects, alignments are used for positioning of elements relative to the path and tilt of the alignment axis. For example, in road and rail projects they are used to semi-automatically generate streets- and rails-systems, including technical equipment and information about ablation of ground on the construction site. Considering projects of the tunneling domain, however, alignments are used to generate tunnel models, using a cross-section and design parameters as reference for the modeling process. This process has been evaluated in [78], by using an alignment and cross-section information to generate tunnel models in mechanized tunneling, specifically in segmental ring design (Fig. 6.15). The process of aligning elements to an alignment relies on a sequence of transformations to be applied systematically (see Fig. 6.6).
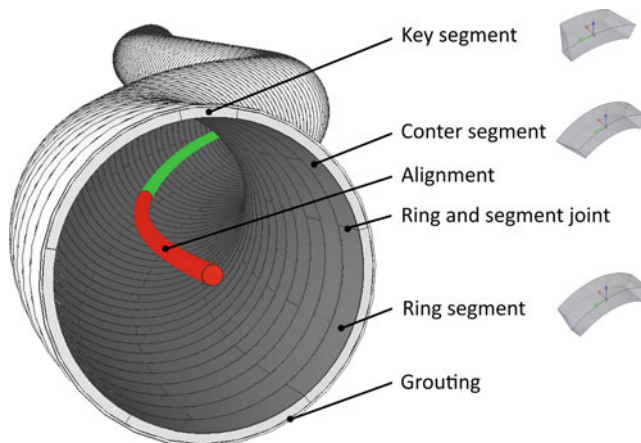
Fig. 6.15 Generated tunnel model in segmented ring design using an alignment and cross-section information as a basis, applying the method in [78]

These models were exported as Industry Foundation Classes (IFC) models and could be used for information delivery in infrastructure and visualization in the tunnel excavation. Here, prototypical instances of the IFC tunnel extension [15] were used to create semantically correct tunnel models and alignments for data exchange, instead of placeholder elements as is common practice in the industry.

6.3.5 Collaborative Exploration Using Roomware Products

The alignments planning process relies on experts feedback and knowledge. In a collaborative environment, results of the planning design and evaluation can be discussed directly. However, common planning tools and evaluation methods are not designed to provide feedback in real time or to involve a group of stakeholders. Here, the benefits of a collaborative approach can lead to significant improvements in the decision-making process of alignment selection. For example, it can lead to a reduction of the number of planning variants and shorten the development time by directly implementing changes.

To allow a collaborative approach for alignment planning to be applied, the interactive exploration is performed on touch-table devices (see Fig. 6.16, Collaborative Planning Environment). Such a roomware device can be surrounded and interacted with by a group of people. To handle user interactions the planning application running on such a device needs to incorporate (multi-)touch-strategies and streamline the planning process in order to enable semi-automatic reevaluation of the modified alignment. For that purpose a set of multi-touch strategies has been investigated in [79] and implemented into the integrated platform. These touch-strategies were mainly designed to handle simultaneous multi-touch interactions by users (Area-Group) and touch-interactions with elements further away from the users perspective (Lock-On). Therefore, with each interaction the alignment can be modified and planned using only touch, while the updated alignment will be reevaluated in real time and results are visualized for validation (Fig. 6.16, Interactive Planning Tools).
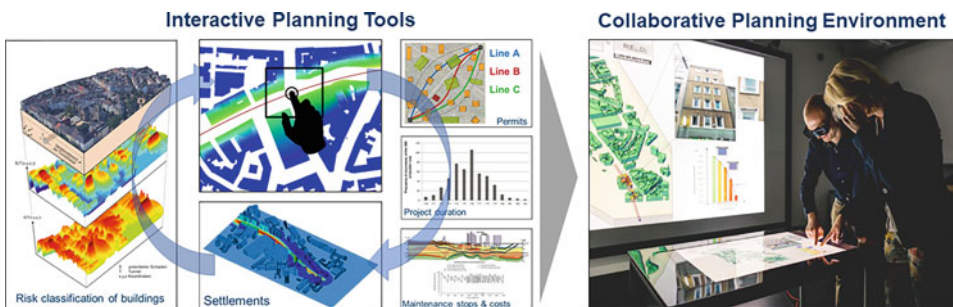
Fig. 6.16 Adopting planning and evaluation tools into a collaborative environment using roomware devices, such as touch-tables and VR-walls, for real time evaluation and live feedback

6.3.6 BIM and GIS Integration

The platform considers the integration of documents and models primarily used in the BIM and GIS domains. These are often considered integrated approaches since their information complements each other in the context of the spatial environment.

The concept of integrating BIM and GIS, however, is often used as an umbrella term that distinguishes between integration approaches in scope and purpose of considered information. For that matter, Beck et al. [6] investigated related research and categorized it based on integration effort and used terminologies. Considering the approaches in [42, 79, 81] the integrated platform falls under the categorization of instance-level information integration of real-world objects that differs in perspective and links based on utilizing queries with spatial reasoning. Also, a multitude of documents and models were investigated for integrated planning. The set of considered documents and models consists of, for example, *map data* (e.g. cadastrals), *built environments* (e.g. city model), *terrain* and *ground models* (Fig. 6.17). However, the integration of both domains has proven to be challenging due to differences in format, detail, and scope of considered data. Documents and models can vary in level of development and contain a variety of geometric representations.

Dealing with geometric differences is a particular challenge since documents and models must be represented superimposed. This requires the handling of transformations of the geo-localization and conversion of the geometry into a uniform representation form in order to be able to perform operations for a comparison. In order to integrate new processes
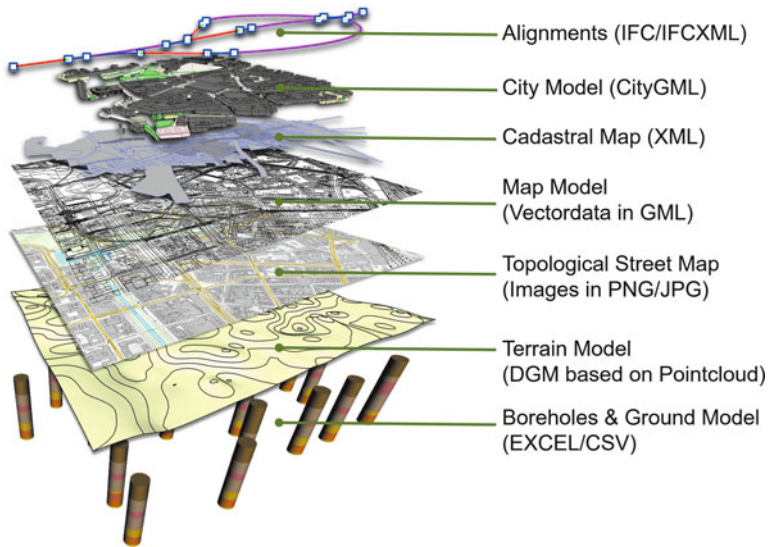
Fig. 6.17 Documents and model considered in a BIM and GIS integrated planning environment of the tunnel domain

and their representation into the planning process, these must first be aligned with those of the integrated environment. For example, in [47] a voxelized approximation of a ground model has been used for the examination of soil and borehole information. This enabled to quantify uncertainties for the ground model and optimize the placement of new boreholes. Integrating such a model based on existing borehole datasets greatly improves decision making, but may require an alternative representation to comply with the superposition of individual documents and models.

6.3.7   Rule-Based Alignment Evaluation and Data Acquisition

When exploring an integrated environment, rule-based exploration can add value to information acquisition process and for checking constraints and requirements. Considering the superimposed nature of documents and models from BIM and GIS domains allows for spatial reasoning approaches to be applied. In [81] the alignment planning context (see Sect. 6.3.8 for details) also has been incorporated into a reasoning approach, creating context rich relations between elements. This relations were then used to query information across documents and models, which enabled a semi-automated evaluation of relevant requirements and constraints.

Further studies examined the use of a decision model for the choice of tunnel systems (single tube vs. double tube) [86] as well as for the selection of a tunnel boring machine [91].

Sets of elements are highlighted by the queries, which can then be examined in more detail for evaluation. For direct visual feedback, such results can be selected and colorized, which allows for visual validation and subsequent investigations. In such an integrated platform, certain requirements and conditions (e.g. range constraint) can be transformed into geometric representation, which further allows for visual feedback in the investigated area.

6.3.8   Constraints and Requirements

For maintaining a context sensitive approach in tunneling and alignment evaluation, a set of relevant requirements and constraints, that must be met for the creation of valid alignments, are incorporated into the reasoning. These constraints and requirements take into account the correlation between the geologic conditions, the built environment, the parameters of the excavation process, and the operating conditions. Specifically, these can be categorized into the types of

- geometrical/geographical requirements,
- driving dynamics,
- cross section design,
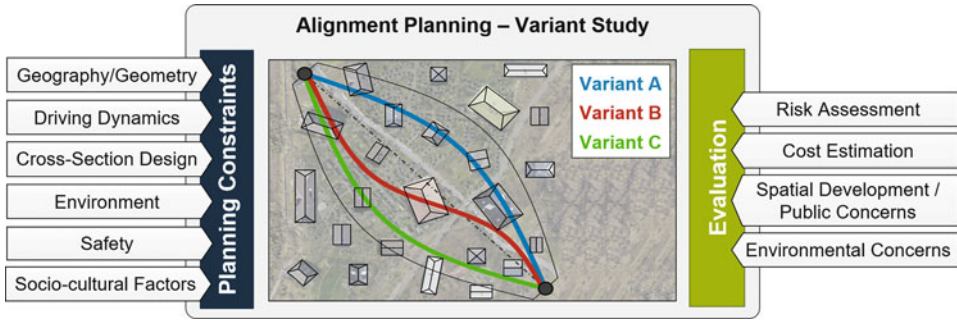
Fig. 6.18 An overview of requirements and constraints affecting the alignment planning process [80]

- built environment,
- safety criteria and
- socio-cultural factors.

Geographical and geometrical requirements include criteria such as stations to be connected or existing infrastructure. Requirements of the type of *driving dynamics* depend mainly on the mode of transport. These include limit values for alignment elements, e.g., maximum radii or the maximum length of straight sections in road tunnels. In addition, the *cross-section*, a double tube or two single tubes, must be determined. Environmental factors include, for example the protection of FFH areas (Flora-Fauna-Habitat). The last two groups consider e.g., the location of emergency exits for *safety criteria* and the protection of cultural heritage for *socio-cultural factors*.

These context-specific requirements are examined and a set of valid variants is formed. These in turn are evaluated using evaluation criteria such as *risk assessments* and *cost estimates* (Fig. 6.18). For the evaluation interaction results from settlement analysis (see Sect. 6.2.6) and risk assessment of building damage (see Sect. 6.5.3) can be incorporated.

Utilizing decision models, which consist of rules performing inferences in an axiomatic system of decisions (IF/THEN), can significantly improve the decision-making process for the tunnel domain. In the field of tunnel construction, the application of decision models has been investigated in [83, 84], by investigating the decision-making process of furnishing tunnels with safety systems. This research demonstrated that decision models can enhance the decision-making process and that the weighting of individual criteria influences the evaluation, which also applies to the alignment analysis and selection.

6.3.9 Utilizing Semantic Web Approaches

Semantic web technologies and approaches can be used to integrate data from the BIM and GIS domains. Using ontology-based data structures, domain-specific information can
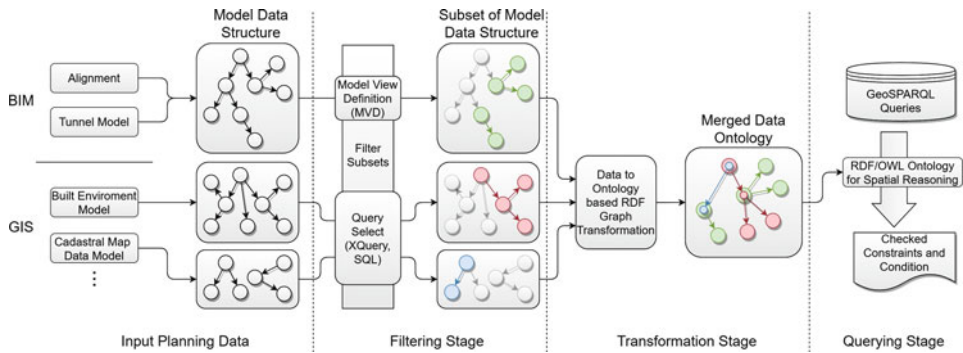
Fig. 6.19 The method of establishing ontology-based data structures to query across multiple documents and models [81]

be reorganized and combined to explore an integrated environment. For that reason, in [81] the ontology for *Spatial Reasoning in Tunneling* (SRT) has been conceived to enable the investigation of geometries for a spatial reasoning approach. With the *SPARQL Protocol and RDF Query Language* resulting data structures can be investigated systematically. However, for exploring a spatial environment, considered geometries must be transformed to describe the same spatial context. This includes handling geo-localization of elements and synchronizing their representation in the level of detail and dimension. This is necessary because considering data from the BIM and GIS domains will result in a blend of 2D and 3D representations, which can also be defined in different *Coordinate Reference Systems* (CRS).

In *Semantic Web*, geometry is usually represented in *Well-Known Text* representations (WKT) [37, 65], which is a compact and streamlined version of most significant geometric representations. By utilizing WKT-CRS [64], an extension of WKT-representations to handle geometries defined in different CRS, the geo-localization of such elements can be handled naturally by *Semantic Web* technologies. The spatial reasoning approach can then be performed by utilized GeoSPARQL [63], an established library and SPARQL extension for investigating spatial relations between geometries. This library uses the *Dimensionally Extended 9-Intersection Model* method (DE-9IM) [26, 44], which uses a set of distinct intersections to distinguish between geometrical conditions, such as *intersect*, *touch*, *within*, *cross*, etc.

This approach of utilizing *Semantic Web* for a linked data and acquisition of relevant information has been validated by numerous publications [8, 35, 87]. Including this approach in the integrated platform enables the semi-automated execution of queries to perform data acquisition and evaluation across documents and models. This concept (Fig. 6.19) has been elaborated and implemented in [81], resulting in the establishment of context-rich relations across documents and models by also including constraints and requirements in the query process.

6.3.10 Application for Decision-Making and Examination

For decision-making in the alignment selection process, commonly different alignment variants are compared with evaluation criteria using e.g., the *Weighted Decision Matrix* Method (WDM). The method takes into account a number of constraints and requirements that are evaluated and compared, leading to the selection of a preferred variant, e.g., based on the examination of cost effectiveness [72] (see Sect. 6.3.8). Such an evaluation method is based on the specifics of the planning environment and the associated data. In order to identify relevant data for examination, the spatial environment must be examined. By using *Semantic Web* technologies, several cases of semi-automated data acquisitions can be performed. In [81], for example, the execution of predefined SPARQL queries enabled the identification of tunneled buildings (Fig. 6.20) or buildings that are under historic preservation and within the vicinity of the alignment (Fig. 6.21). These filtered subsets can be highlighted, providing visual feedback on the results.

Since these queries accommodate for constraints and requirements of the alignment planning process, they can be incorporated into the decision-making process by integrating results as relevant information for the examination of criteria in a WDM approach. For example, for examining geometric geographical requirements, the identification of buildings within the vicinity of the settlement-affected area is important. Deducing the number and status of those buildings provides a significant resource investigating buildings that are subject to potential damages (see Fig. 6.61). In combination with other factors, such as potential expenses for maintenance and compensation, these query results provide valuable inside for decision-making.
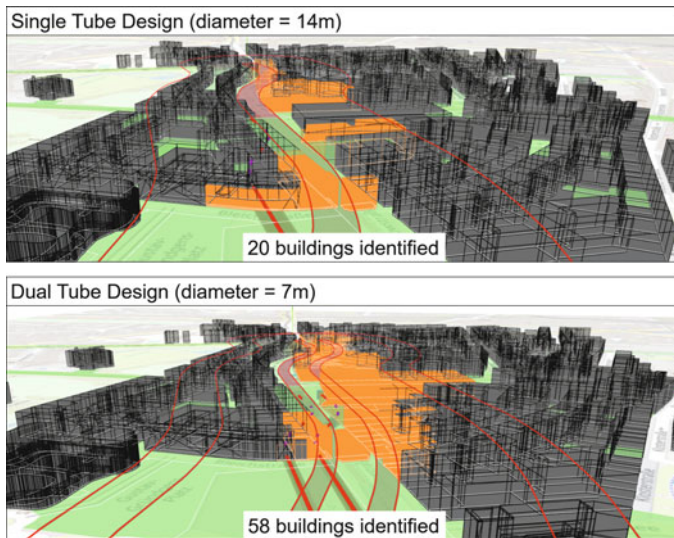
Fig. 6.20 Finding and comparing the number of tunneled buildings in single and dual tube design [81, Case 1]
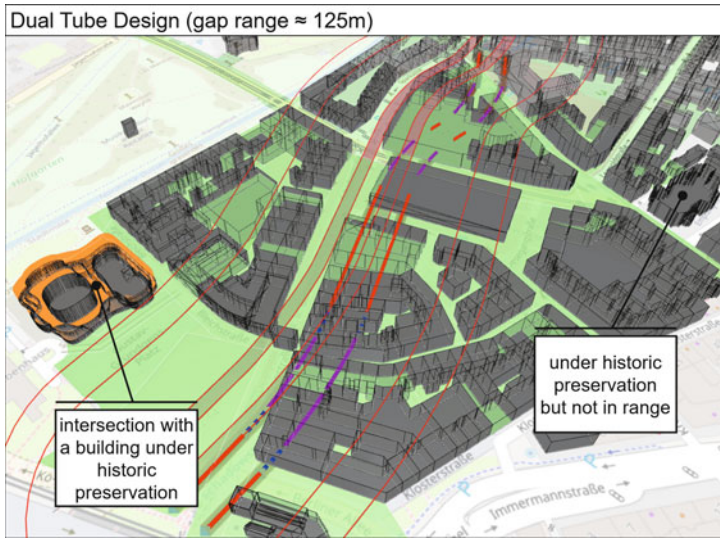
Fig. 6.21 Finding buildings under historic preservation and within the vicinity of the alignment [81, Case 2]

6.4   Process-Oriented Numerical Simulation

This section presents the software that was produced in this project for Advanced Tunneling Engineering (ekate), as well as a Tunnel Analysis Model based on the CUTFEM method. Also, a discussion of an automatic model generation based on BIM with aspects of parallelization are given.

6.4.1   `ekate`: Enhanced KRATOS for Advanced Tunneling Engineering

The simulation model, denoted as ekate (Enhanced KRATOS for Advanced Tunneling Engineering), has been implemented via the object-oriented finite element code KRATOS [22]. The latter is an open-source framework dedicated to perform numerical simulations for multi-physics problems. Its modular structure provides efficient and robust implementations of various algorithms and schemes (e.g. solution methods, time integration schemes, element formulations, constitutive laws, etc). KRATOS is written in C++, in which its kernel provides the basic functionalities and data managements, while, applications characterize the implementation aspects of the numerical model for different physical problems. Herein, the simulation model is developed using KRATOS STRUCTURAL APPLICATION and EKATE AUXILIARY APPLICATION. More detailed discussion about the model can be found in [55], while basic strategies and implementation aspects are presented in [77].
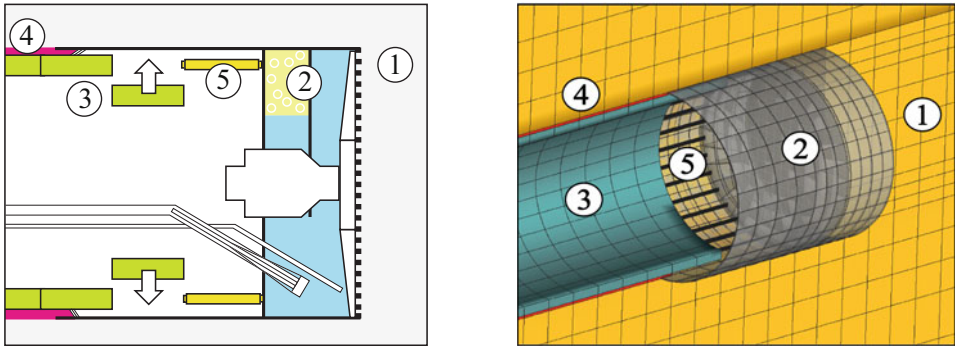
Fig. 6.22 Computational model for mechanized tunneling `ekate`. left: main components involved in the simulation of the mechanized tunneling process and, right: finite element discretization of the model components; (1) Geological and ground Model, (2) Shield Machine, (3) Tunnel Lining, (4) Tail void grouting and (5) Thrust Jacks [50]

The main goal of the model is to provide an efficient yet realistic simulation environment for all interaction processes occurring during machine driven tunnel construction. Therefore, the model includes all relevant components of the mechanized tunneling process as sub-models, representing the partially or fully saturated ground, the tunnel boring machine, the tunnel lining, hydraulic thrust jacks, the tail void grouting and can take into account soil improvement by means artificial ground freezing, which are interacting with each other via various algorithms. The interaction between the shield and the excavated ground is taken into account via frictional contact algorithm. The shield-lining interaction is described with truss elements (hydraulic jacks) connected between the front surface of the last activated lining segment and the shield, by which, the lining acts as a counter-bearing for the hydraulic jacks thrust to push forward the shield machine. Figure 6.22 shows the basic model components on the left and their respective representation in the finite element mesh on the right. In what follows, the basic model components, the steering algorithm for shield advancement and the simulation script for modeling the construction process are discussed in more detail.

6.4.1.1 Modeling of Ground and Ground Support in Shield Tunneling

Ground model The ground model is formulated within the framework of the Theory of Porous Media (TPM) [10] that accounts for the coupling between the deformations of the solid phase and the fluid pressures (i.e. an incompressible water phase and a compressible air phase). In that, deformations and pressures are taken as primary variables. The governing balance equations build a set of partial differential equations as the basis of finite element solution. In the following, the two-phase model for fully saturated soils (Fig. 6.23) is briefly presented.
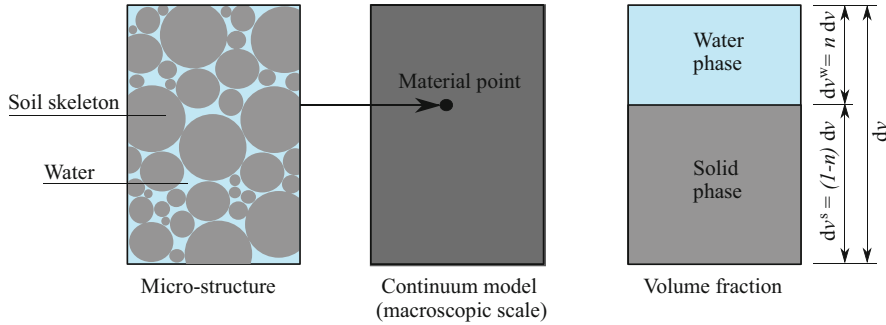
Fig. 6.23 Fully saturated soil modeled according to TPM [50]

The following balance equations prescribe the momentum balance of the mixture, and the mass balance of both solid and fluid phase. Under the assumption of incompressible solid and water phase, the mass balance of each constituent α [$\alpha = s$(olid) or w(ater)] is given by

$$\frac{D_\alpha}{Dt}\rho^\alpha + \rho^\alpha \operatorname{div} \dot{\mathbf{x}}^\alpha = 0, \tag{6.1}$$

where ρ^α is the average density of a constituent α. The porosity n, which defines the volume fraction of water, is used to describe the solid and water phases. Therefore, the average density of the mixture ρ can be determined by the intrinsic density of each constituent ϱ^α as

$$\rho = \sum \rho^\alpha = (1-n)\varrho^s + n\varrho^w. \tag{6.2}$$

In addition, the velocity of the solid skeleton ($\dot{\mathbf{x}}^s = \dot{\mathbf{u}}^s = D_s\mathbf{u}^s/D_t$) and the diffusion velocity ($\boldsymbol{v}^{ws} = \dot{\mathbf{x}}^w - \dot{\mathbf{u}}^s$) are used to describe the motion of the constituents. Thus, Eq. 6.1 yields to

$$\frac{D_s}{Dt}((1-n)\varrho^s) + (1-n)\varrho^s \operatorname{div}\dot{\mathbf{u}}^s = 0 \qquad \text{for solid skeleton} \tag{6.3}$$

and

$$\frac{D_w}{Dt}(n\varrho^w) + n\varrho^w \operatorname{div}(\boldsymbol{v}^{ws} + \dot{\mathbf{u}}^s) = 0 \qquad \text{for pore water.} \tag{6.4}$$

For Eq. 6.3, assuming incompressible solid grains (i.e. $D_s\varrho^s/D_t = 0$), a differential equation for the porosity can be derived as

$$
\begin{aligned}
&-\varrho^s \frac{D_s n}{Dt} + (1-n)\varrho^s \operatorname{div}\dot{\mathbf{u}}^s = 0, \\
&\frac{dn}{dt} = (1-n)\operatorname{div}\dot{\mathbf{u}}^s.
\end{aligned}
\tag{6.5}
$$

For the mass balance of the water phase, the time derivative with respect to the current configuration of the water phase is transformed to the current configuration of the solid phase as

$$\frac{D_w}{D_t}(\rho^w) = \frac{d\rho^w}{dt} + \text{grad}\,\rho^w \cdot \boldsymbol{v}^{ws}. \tag{6.6}$$

The water flow $\tilde{\boldsymbol{v}}^{ws}$ through the pore spaces is described by DARCY's law [23]. Accordingly, the flow is governed by the pressure gradient and the volume of pore spaces and expressed as

$$\tilde{\boldsymbol{v}}^{ws} = -\frac{k^w}{\varrho^w g}(\text{grad}\,P^w - \varrho^w \mathbf{g}), \tag{6.7}$$

where k^w is the hydraulic conductivity that symbolizes the available pore spaces in soil. Using the volume fraction n, the DARCY's velocity is related to the diffusion velocity $\boldsymbol{v}^{ws}$ as $\tilde{\boldsymbol{v}}^{ws} = n\,\boldsymbol{v}^{ws}$. Applying Eq. 6.6 to Eq. 6.4, the mass balance of the incompressible water phase can be written as

$$\frac{d}{dt}(n\varrho^w) + \text{grad}(n\varrho^w) \cdot \boldsymbol{v}^{ws} + n\varrho^w \text{div}(\boldsymbol{v}^{ws} + \dot{\mathbf{u}}^s) = 0,$$

$$\frac{d}{dt}(n) + \text{div}(\tilde{\boldsymbol{v}}^{ws}) + n\,\text{div}(\dot{\mathbf{u}}^s) = 0, \tag{6.8}$$

$$\text{div}(\tilde{\boldsymbol{v}}^{ws}) + \text{div}(\dot{\mathbf{u}}^s) = 0.$$

The second balance relation is introduced by the overall momentum balance of the mixture using the averaged CAUCHY stress $\boldsymbol{\sigma}$ as

$$\text{div}(\boldsymbol{\sigma}) + \rho\mathbf{g} = \mathbf{0}, \tag{6.9}$$

According to [82], the effective stresses define the inner grain interaction (i.e. the stress-strain behavior of the soil skeleton). The effective stresses in a fully saturated soil are determined as

$$\boldsymbol{\sigma}^{s\prime} = \boldsymbol{\sigma} + P^w \mathbf{I}, \tag{6.10}$$

where the effective stresses $\boldsymbol{\sigma}^{s\prime}$ and the water pressure P^w are the stress variables and $\mathbf{I}$ denotes the unity tensor.

The mass balance and the momentum balance equations form the set of partial differential equations to be solved in which the deformations and water pressures are the primary field variables. Further discussion regarding the multi-phase model for partially saturated soils and its numerical implementation has been presented in [55].

The material behavior of the soil skeleton is represented by means of nonlinear elasto-plastic constitutive laws; namely DRUCKER-PRAGER (DP) law or CLAY AND SAND
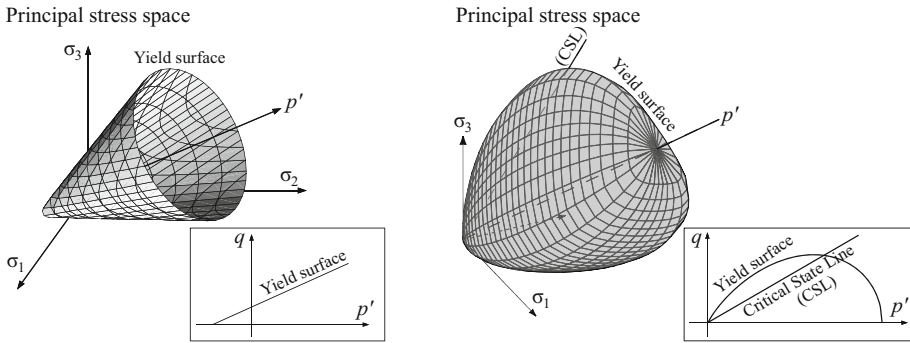
Fig. 6.24 Yield function in principal stress space and in the p'-q plane: DRUCKER-PRAGER-model (left) and CLAY AND SAND-model (right) [50]

MODEL (CASM) [93]. DP-law presents a relatively simple model based on the approximation of the MOHR-COULOMB criteria using a smooth yield function, see Fig. 6.24, left. A generalized behavior for both clay and sand soils can be modelled by CAS-model. Figure 6.24, right, shows the yield surface in the principal stress space. The latter is similar to the CAM-CLAY models, yet, it overcomes the limitation of CAM-CLAY models for the characterization of sands and highly over-consolidated clays.

Grouting mortar The annular gap between the tunnel lining and the excavated ground is filled simultaneously with a pressurized grouting mortar, Fig. 6.25a. The latter is a mixture that consists of a hyper-concentrated two phase material [9]. It should maintain, at the early stage, a certain degree of workability to be distributed uniformly around the lining. On the other hand, hardening should occur to resist the buoyancy of the lining and to prevent the dislocation of the joints. The setting of grouting mortar is characterized by an increase of mechanical stiffness accompanied with a phase change from semi-liquid to solid state, Fig 6.25b.
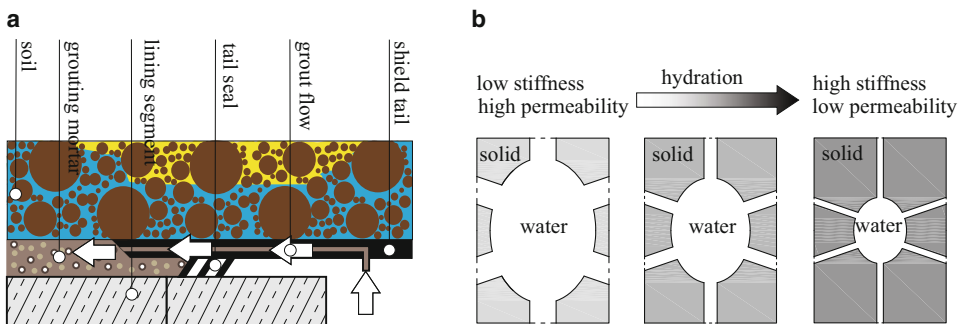
Fig. 6.25 Annular gap grouting. **a** sketch of annular gap grouting through a nozzle in shield skin and **b** the process of grouting mortar hydration with stiffness and permeability evolution [50]
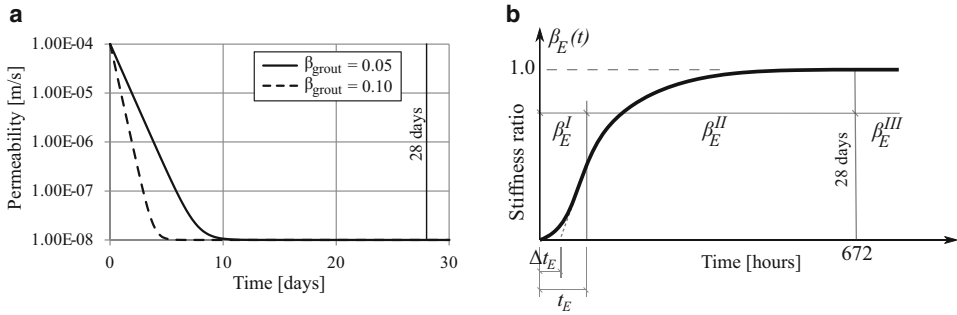
Fig. 6.26 Development of grouting mortar properties with time. **a** permeability evolution for two different analysis parameters and **b** description of the parametric function $\beta_E(t)$ where the grout is fully hardened after 28 days [50]

To model the pressurized grouting mortar, a two-phase (hydro-mechanical) formulation is used, which is similar to the finite element formulation of the ground model. The grouting pressure is applied as pore water pressure to the fresh mortar. Stiffening of the grouting mortar is considered by a time-dependent hyper-elastic material and time-dependent permeability to account for the hydration process. Simultaneous grouting of the annular gap is simulated by the step-wise activation of the corresponding grouting mortar elements with respect to current shield position, while pressurization is realized by a prescribed pressure boundary condition on the face of the elements at the shield tail.

Herein, an exponential relation is used to define the temporal evolution of permeability. This assumption has been already proposed in [41]. The permeability of the grouting element is updated at the beginning of each time step, where the mathematical expression is given by

$$k(t) = (k^{(0)} - k^{(28)})e^{-\beta_{\text{grout}}t} + k^{(28)}, \qquad (6.11)$$

where $k^{(0)}$ and $k^{(28)}$ are the initial permeability and final permeability after 28 days, t expresses the age in hours and β_{grout} is a parameter that controls the change with respect to time. Figure 6.26a shows the time dependent permeability for two different analysis parameters ($\beta_{\text{grout}} = 0.05$ and 0.10). With respect to the stiffness evolution of such cementitious material, the proposed material model follows the basic methodology of hyperelasticity for aging materials, as presented in [52, 53], see Fig. 6.26b.

For the time-dependent increase of elastic modulus, an irrecoverable strain necessarily occurs. Therefore, the strain tensor ε,

$$\boldsymbol{\varepsilon} = \boldsymbol{\varepsilon}^e + \boldsymbol{\varepsilon}^t, \qquad (6.12)$$

is decomposed into a recoverable elastic part $\boldsymbol{\varepsilon}^e$ and a non-recoverable part $\boldsymbol{\varepsilon}^t$ associated with the time-dependent hydration.

According to the theory of hyperelasticity, a time-dependent function of the stored energy defines the stiffening effect and consequently the time-dependent stress tensor as

$$W(\boldsymbol{\varepsilon}, t) = \frac{1}{2}(\boldsymbol{\varepsilon} - \boldsymbol{\varepsilon}^t) : \mathsf{C}^{28} : (\boldsymbol{\varepsilon} - \boldsymbol{\varepsilon}^t), \tag{6.13}$$

$$\boldsymbol{\sigma} = \frac{\delta W}{\delta \boldsymbol{\varepsilon}^e} = \mathsf{C}^{28} : (\boldsymbol{\varepsilon} - \boldsymbol{\varepsilon}^t), \tag{6.14}$$

where C^{28} is the standard elasticity tensor of the hardened material in which the superscript (28) indicates a reference time in days at the end of the aging process. The time-dependent material tensor $\mathsf{C}(t)$ is expressed by the development of the Young's Modulus $E(t)$ as

$$\mathsf{C}(t) = \mathsf{C}^{28} \frac{E(t)}{E^{(28)}}, \tag{6.15}$$

and the experimental observations shows that the stress rate is related to the strain rate by the time-dependent material tensor,

$$\dot{\boldsymbol{\sigma}} = \mathsf{C}(t) : \dot{\boldsymbol{\varepsilon}}. \tag{6.16}$$

The stress increment $\Delta\boldsymbol{\sigma}$ for a certain time interval $[t_n, t_{n+1}]$ is determined from the time integration of Eq. 6.16

$$\Delta\boldsymbol{\sigma} = \int_{t_n}^{t_{n+1}} \mathsf{C}(t) : \dot{\boldsymbol{\varepsilon}}\, dt = \frac{1}{E^{(28)}} \mathsf{C}^{28} : \frac{\Delta\boldsymbol{\varepsilon}}{\Delta t} \int_{t_n}^{t_{n+1}} E(t)\, dt = \frac{\chi}{E^{(28)}\Delta t} \mathsf{C}^{28} : \Delta\boldsymbol{\varepsilon}, \tag{6.17}$$

in which, χ expresses the integration of time-dependent Young's Modulus over the time interval $[t_n, t_{n+1}]$. Comparing Eq. 6.17 with the incremental form of Eq. 6.14, the incremental time-dependent strain yields

$$\Delta\boldsymbol{\varepsilon}^t = \left(1 - \frac{\chi}{E^{(28)}\Delta t}\right)\Delta\boldsymbol{\varepsilon}. \tag{6.18}$$

The elastic algorithmic tangent A^{el},

$$\mathsf{A}^{el} = \frac{\partial\boldsymbol{\sigma}_{n+1}}{\partial\varepsilon_{n+1}} = \frac{\chi}{E^{(28)}\Delta t}\mathsf{C}^{28}, \tag{6.19}$$

can be obtained by the linearization of Eq. 6.14 after inserting Eq. 6.18.

The time-dependent stress-strain behavior of the proposed material is mainly related to the time-variant Young's modulus. The later is expressed as $E(t) = \beta_E(t)E^{(28)}$, see Fig. 6.26b. The coefficient $\beta_E(t)$ is defined, according to [53]

$$\beta_E(t) = \begin{cases} \beta_E^{\mathrm{I}} = c_E t + d_E t^2 & \text{for } t \leq t_E \\ \beta_E^{\mathrm{II}} = \left(a_E + \dfrac{b_E}{t - \Delta t_E}\right)^{-0.5} & \text{for } t_E < t \leq 672h \\ \beta_E^{\mathrm{III}} = 1.0 & \text{for } 672h < t_E \end{cases} \tag{6.20}$$

where a_E, b_E, c_E and d_E are material dependent parameters determined by the ratio $E^{(1)}/E^{(28)}$, the initial time interval t_E and the time step Δt_E, see [53] for more details.

Face support pressures Numerically, two scenarios can be characterized by a *membrane model* and a *penetration model*. They are described in the model by applying adequate boundary conditions, see Fig. 6.27. For the so called *membrane model*, where a perfect filter cake is formed, the fluid flow is set to zero and a prescribed total pressure is applied at the tunnel face as

$$\mathbf{t} = p^{\text{sup}}\,\mathbf{n} \text{ and } q^w = 0. \tag{6.21}$$

For the *penetration model*, i.e. without a filter cake, both fluid pressure and total stresses are prescribed at the tunnel,

$$\mathbf{t} = p^{\text{sup}}\,\mathbf{n} \text{ and } p^w = 0. \tag{6.22}$$

The numerical description of the grouting pressure is achieved in a way similar to the description of face support. At the last face of the newly activated elements, the total stresses and water pressures are prescribed as a linear function using the average grout pressure at the tunnel axis $\bar{p}_{\text{ax}}^{\text{grouting}}$ and its gradient $\operatorname{grad} \bar{p}^{\text{grouting}}$,

$$\bar{p}^{\text{grouting}} = \bar{p}_{\text{ax}}^{\text{grouting}} + z \operatorname{grad} \bar{p}^{\text{grouting}}, \tag{6.23}$$

where z is the distance in the direction of gravity, measured from the tunnel axis. Consequently, the total pressure and the water pressure at the element face can be defined as

$$\begin{aligned} p^w &= \bar{p}^{\text{grouting}}, \\ \mathbf{t}^\star &= -\bar{p}^w \mathbf{n}, \end{aligned} \tag{6.24}$$

where $\mathbf{n}$ is the normal vector to the grouting face. With the previous description, the effective stresses at the last grouting face, where grout injection is executed, are set to zero.
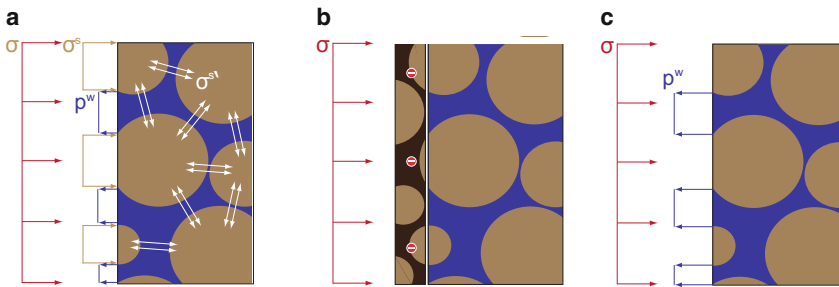
Fig. 6.27 Prescribed boundary conditions of face support pressure. **a** Stresses within the two phase element (total stresses σ, effective stresses $\sigma^{s'}$, partial solid stresses σ^s and water pressure p^w), **b** formation of an impermeable filter cake (Eq. 6.21) and **c** penetration model with no filter cake sealing the tunnel face (Eq. 6.22) [50]

6.4.1.2 Segment-Wise Lining Installation in `ekate`

Shield tunnel linings are constructed by an assembly of segments into a complete ring. The simulation of the segmental lining model including the joints is similar to the continuous model to some extent. The main difference is the assignment of the contact interactions at the joints between the segments. The generation of the segmental lining model starts with the consideration of a single ring as shown in Fig. 6.28. The ring model, generated by GiD, consists of volume elements which represent different segments in which the boundary surfaces of each segment are separately defined. Figure 6.28 shows a ring that consists of 7 segments with equal size including bolts and dowels on joints. Each longitudinal joint contains two bolts at the center line, while each segment has two shear dowels in the ring joint. In total, 14 bolts and 14 dowels are used in each ring. The exact joint geometry is not described in this model since the global structural response is the main interest of this study. As such, the effect of the rubber sealing gasket is not explicitly considered. In addition, only joints with flat contact surfaces will be addressed.

The contact interactions between the segments in one ring and between consecutive rings are shown in Fig. 6.29. The contact algorithm is used to characterize the response of joints; this requires the definition of master and slave surfaces for the possible contact surfaces. Since, the complete lining model consists of a large number of joints, there will consequently exist a large number of master and slave contact surfaces. Therefore, each pair of contacting surfaces is associated with a distinct contact index, as indicated in Fig. 6.29, to speed up the search algorithm.

Beam elements with elastic material properties are used to represent the dowels and bolts in the joints. The geometrical properties of the beam are defined according to the
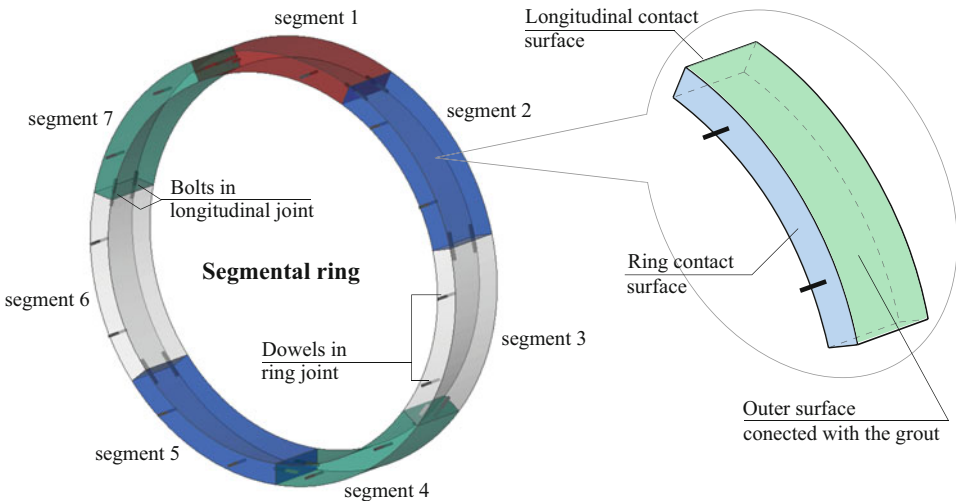
Fig. 6.28 `ekate` representative model for segmental lining geometry including bolts and dowels [50]
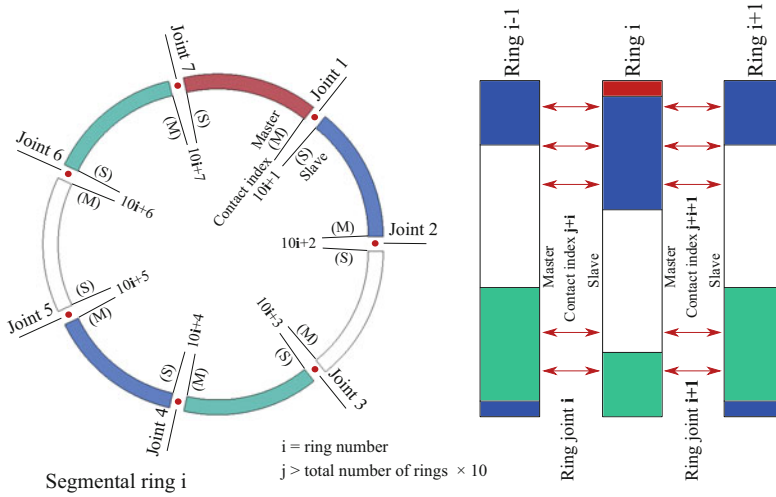
Fig. 6.29 Definition of contact surfaces between the segments as defined in the numerical model [50]

corresponding diameter, length and type, as shown in Fig. 6.30. Pre-stressing in the bolts can be considered by applying a certain pre-stressing force for the corresponding element. In finite element formulation, the internal force vector for the beam element with pre-stressing is defined as

$$\mathbf{R}^{\text{int}} = \mathbf{K} \cdot \mathbf{u} + \mathbf{F}^{\text{Prestress}}. \tag{6.25}$$

The assigned properties to the beam elements describe the desired structural behavior of the elements. For the simulation of shear dowels, only the shear stiffness is required while the axial stiffness can be omitted by setting $A_{\text{axial}} = 0.0$. Bolts are mainly simulated by considering axial stiffness and the pre-stressing force if required, while the flexural stiffness can be either considered or ignored. Generally, the dowels/bolts are assumed to act at the center line of the joints and therefore it is not expected that they contribute significantly to the overall flexural stiffness of the lining ring.
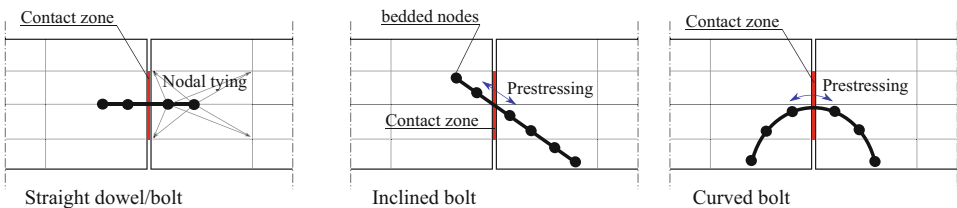
Fig. 6.30 Representation of bolts and dowels in segmental lining joints [50]
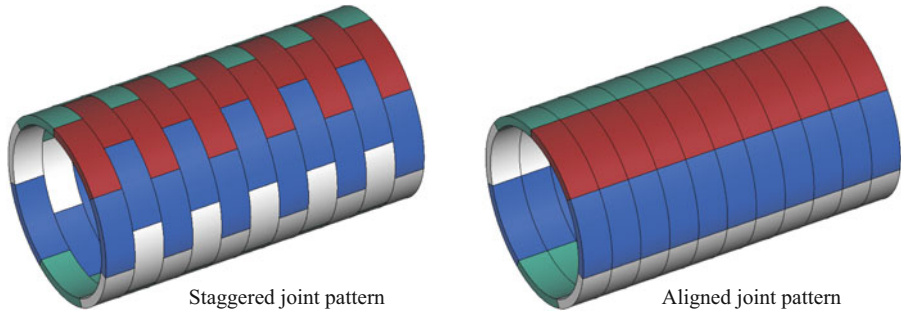
Fig. 6.31 Different joint arrangements in segmental tunnel lining model [50]

The physical interaction between the segments and the dowels/bolts is accounted for by using the node to volume tying, see Fig. 6.30. The nodes at the ends of each bolt are embedded in their corresponding volume elements. In the finite element code `Kratos`, the `EmbeddedPointLagrangeTyingUtility` is used for setting these tying constraints. Within the simulation script, a function, `InitializeEmbedded PointLagrangeTying`, sets the tying condition between the end node of the beam (X^i) and the volume element containing that point. First, the local coordinates $\xi(X^i)$ at the point location inside the volume element are determined. Then, the condition ties the displacements between the point and its projection inside the volume elements using the Lagrange multiplier,

$$(\mathbf{u}^{\text{node}} - \mathbf{u}^{\text{vol}}(\xi(X^i))) \cdot \boldsymbol{\lambda} = \mathbf{0}, \tag{6.26}$$

and the tying condition is added to the system of equations,

$$\begin{bmatrix} \mathbf{K}^{\text{node}} & \mathbf{0} & \mathbf{1} \\ \mathbf{0} & \mathbf{K}^{\text{node}} & -\mathbf{1} \\ \mathbf{1} & -\mathbf{1} & \mathbf{0} \end{bmatrix} \cdot \begin{bmatrix} \mathbf{u}^{\text{node}} \\ \mathbf{u}^{\text{vol}} \\ \boldsymbol{\lambda} \end{bmatrix} = \begin{bmatrix} \mathbf{R}^{\text{node}} \\ \mathbf{R}^{\text{vol}} \\ \mathbf{0} \end{bmatrix}. \tag{6.27}$$

The full description of the numerical model requires the definition of other properties such as material, activation levels, etc., as well. A *python* script is created to automatize the model generation. First, it imports the geometry of the user defined segmental ring. Then, the segmental ring is placed in its location and rotated according to the required staggered joint pattern. The properties and boundary conditions associated with the lining ring are assigned. The desired joint pattern can be generated independently of the finite element discretization of the ground. Figure 6.31 shows a staggered and aligned configurations of lining joints.

It should be noted that the staggered configurations of longitudinal joints are usually preferred in common tunneling practice. In [29], it is explicitly stated that an offset, by half or third of the segment length, should be considered to prevent continuous longitudinal
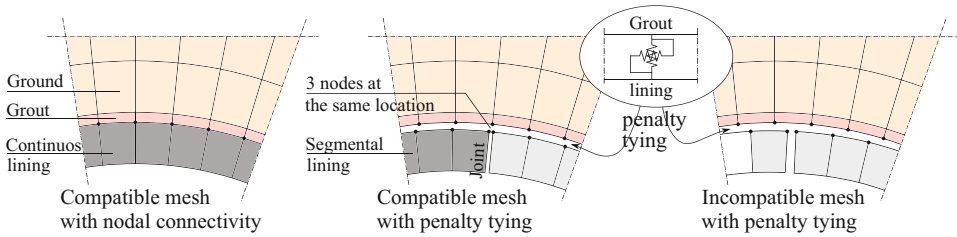
Fig. 6.32 Modeling of lining-soil interactions for the continuous (left) and the segmental lining (right) [50]

joints across multiple rings. This in return strengthens the lining stiffness and the sealing effect. Moreover, it is not suggested to have the hydraulic jacks pads at the location of longitudinal joints. Therefore, the proposed position of joints is adopted in such a manner that they do not match the position of hydraulic jacks.

Lining-soil interaction The relation between the outer boundary of the segment and the surrounding grouting mortar requires a particular consideration in the case of explicit modeling of the segmental lining. As shown in Fig. 6.32, the assumption of mesh compatibility with nodal connectivity between the lining and the grouting is only valid for a continuous lining model. To enable segment-wise ring installation, and the correct kinematics of the joints, the connection between the lining outer surface and the grouting material is modeled by means of a surface-to-surface tying procedure, which does not not require mesh compatibility. The tying constraint preventing the relative displacements is enforced at the GAUSS points using a penalty approach. The energy functional associated with the penalty term is defined as

$$\Pi^{\text{Tying}}(\mathbf{u}) = \frac{1}{2}\,\epsilon\,\|(\mathbf{u}^{\text{lining}} - \mathbf{u}^{\text{grout}})\|^2, \tag{6.28}$$

where ϵ denotes the penalty parameter.

6.4.1.3   TBM Steering and TBM-Soil Interaction

The shield is modeled as an independent, deformable body that interacts with the excavated soil along its outer surface by means of frictional contact conditions. The shield geometry is depicted according to its design, see Fig. 6.33. The respective FE model as shown in Fig. 6.34 accounts for the main structural and load carrying components (i.e. the shield skin, the shield wall and other stiffening parts). Shield weight including the machinery parts are accounted for. The load is distributed on shield front, along approximately two third of the total length, considering the fact that most of the heavy parts are located at the front. The cutting wheel is not modeled explicitly, instead, the equivalent cutting forces in addition to the face pressure are applied on the shield wall. In addition, over-cutting and shield skin tapering are explicitly considered, see Fig. 6.34. This is beneficial
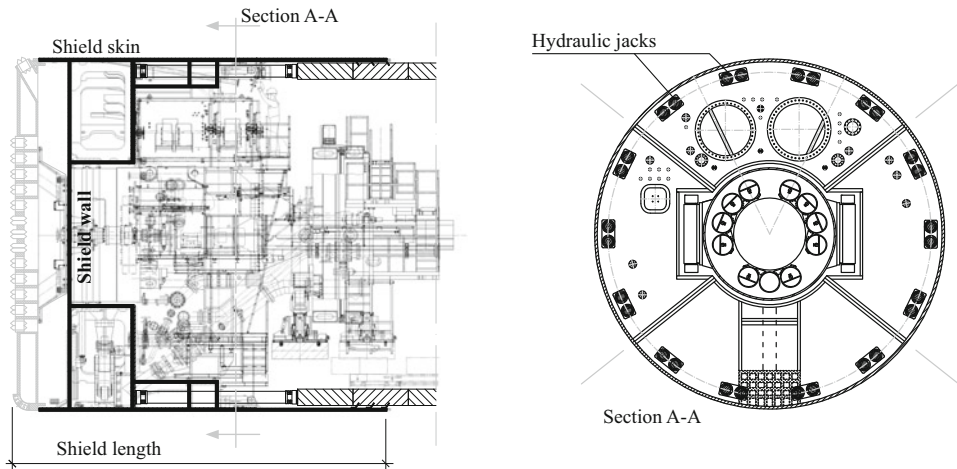
Fig. 6.33 Illustration of the main aspects related to the numerical representation of the shield machine: main structural components represented by the thick black lines (left) and radial distribution of hydraulic jacks (right) [50]
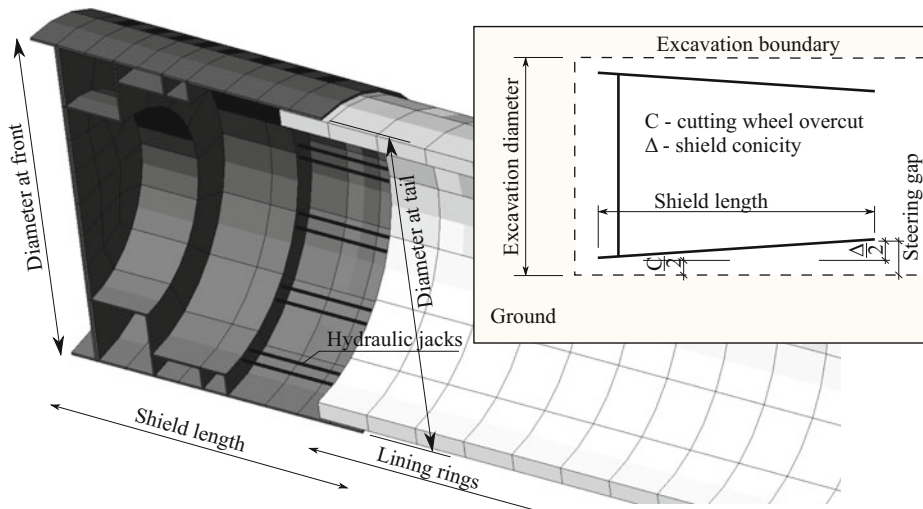
Fig. 6.34 Finite element mesh of the shield machine, the hydraulic jacks and the lining, and the geometrical parameters involved in the definition of the shield model [50]

for a reliable prognoses of the ground settlements, as well, the adequate prediction of the shield soil interaction is feasible, in particular for curved alignments.

The hydraulic jacks are represented by CRISFIELD truss elements [21], that produce the mutual interaction between the shield and the lining and by which shield advancement is achieved. In this context, a steering algorithm is developed to fully automatize the shield

movement [2]. The steering algorithm controls the elongation of each hydraulic jack. Pre-scribed strains and the counter-bearing produced by tunnel lining provides the momentum to move the shield forward. In addition, the steering algorithm includes a correction vector that allows for counter-steering against weight-induced dropping of the shield and keeps the path of the shield on the prescribed tunnel alignment.

The frictional contact characterizes the interaction between the shield skin and the ex-cavated ground. Following the basic concepts in [45, 76], KUHN-TUCKER condition is applied, which defines the separation or direct contact between surfaces. As a result, the simulation model can predict the contact condition between the shield skin and the ground (i.e. whether a gap exists or not). *Slave* and *master* contact faces are assigned to shield skin and excavation boundaries respectively, where the AUGMENTED LAGRANGE method en-forces the contact constraint.

In the simulation model, the governing equations are the weak form of the mass bal-ance equation for the ground water flow and the weak form of the equilibrium equation. Since large movements are required for the positioning of the shield, total LAGRANGIAN FE formulation is used for shield discretization. It should be highlighted that the inertial forces are neglected since the machine advances through the soil with low speed. The final position and orientation of the shield results from the force balance on the shield, where the advancement process is achieved by the elongations of the hydraulic jacks.

6.4.1.4   Computational Modeling for Mechanized Tunneling Process

In tunneling simulations, the size of the domain should be chosen in a way that the model boundaries do not affect the results in the tunneling vicinity. Generally, the primary state of stresses at the boundaries should not change [68]. Figure 6.35 shows the ground do-main with the prescribed boundary conditions for the simulation of a fully saturated soil using two phase formulation. These boundary conditions remain unchanged during the simulation.

To account for the primary stress state in the soil, the respective values can be either explicitly given to the model or implicitly determined. In the simulation model, the sec-ond approach is adopted, in which a two-steps procedure is followed in the beginning of the analysis. In the first step, the ground model is analyzed under its self weight with the aforementioned boundary conditions. At this point, the ground is assumed to behave elas-tically and all the other model components are deactivated. The output stresses of this step correspond to

$$
\begin{aligned}
\sigma'_z &= \sigma_z + u_w; &\text{where} \quad \sigma_z &= -\gamma_{\text{sat}} h \quad \text{and} \quad u_w = \gamma_w h_w, \\
\sigma'_x &= \sigma'_y = K_0 \sigma'_z; &\text{where} \quad K_0 &= \nu/(1-\nu).
\end{aligned}
\tag{6.29}
$$

Using the `InsituStressUtility`, the stresses at the GAUSS points are transmit-ted as pre-stresses. In this utility, a predefined value for K_0 can be imposed. Then, the second step solves the equilibrium equation with gravitational loading and pre-stressing.

Fig. 6.35 FE mesh of the
ground with boundary con-
ditions for the displacement
components u_x, u_y, u_z and
pore pressure P_w [50]
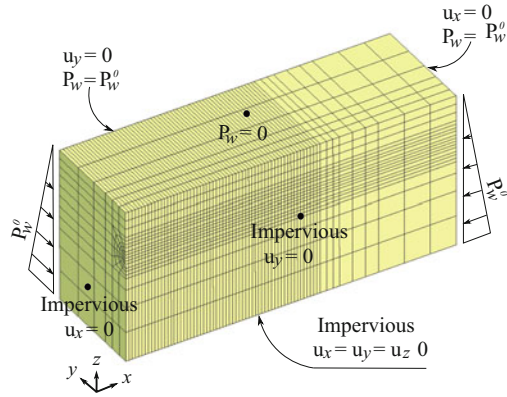
The output ground deformation is checked to ensure that it yields to zero, while the in-situ
state of stress is preserved inside the ground.

The aforementioned scheme serves as a basis to determine the primary stress state,
that is followed by preliminary steps as shown in Fig. 6.36. These steps start with the
initialization of the contact analysis. The shield is activated and positioned at its starting
location and the excavated ground is deactivated (Fig. 6.36a). In addition, the face pressure
and grouting pressures are applied. Then, the hydraulic jacks are initialized and the shield
is allowed to deform. The face pressure and cutting forces are applied on the shield. That
leads to evaluation of shield deformation taking into account the contact forces from the
ground, the applied loads and its self weight (Fig. 6.36b).
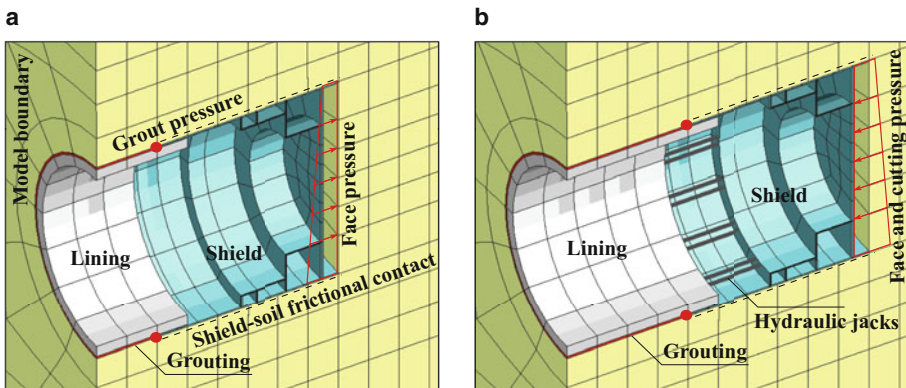
Fig. 6.36 Preliminary steps at the beginning of the simulation of mechanized tunneling. **a** Initial
position of the shield at the model boundary with the initialization of contact analysis, **b** shield with
free deformation supported by the soil pressure and the hydraulic jacks, situation before the start of
step-wise simulation [50]
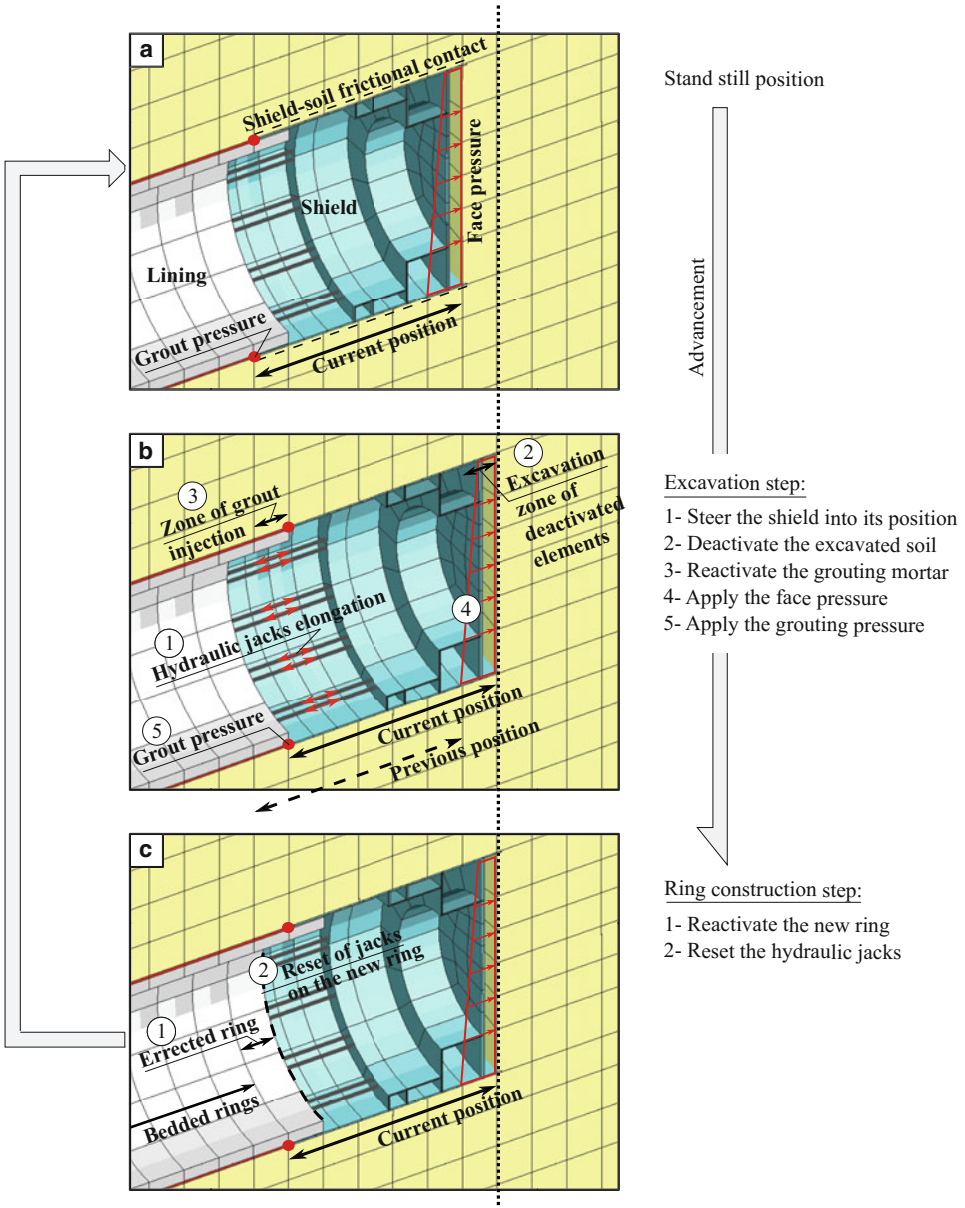
Fig. 6.37 Repetitive scheme for the step-wise simulation of mechanized tunneling process. **a** Stand still position, **b** shield advancement and soil excavation achieved by means of the steering algorithm and the de/re-activation of the respective elements, **c** ring construction and resetting of the hydraulic jacks [50]

Eventually, the step-by-step simulation is carried out as shown in Fig. 6.37. This is achieved by the repetition of two simulation steps: an excavation step and a ring construction step following the predefined time step for each. The excavation step includes the use of the `SteeringUtility` to position the shield. This movement is accompanied with the deactivation of the soil and the activation of the grout. Afterwards, the ring construction step is performed by the activation of the lining ring inside the shield accompanied with the resetting of the hydraulic jacks elements on the face of the newly installed ring. Once the shield reaches the final excavation step, the simulation stops.

6.4.1.5   Computational Modeling of Artificial Ground Freezing in Tunneling

Artificial ground freezing (AGF) is a ground improvement technique which is used to stabilize the soil to provide temporary support and water flow control. In urban environments with settlement-sensitive buildings, AGF is used to provided temporary ground support during tunnel construction. In order to simulate the ground improvement in tunneling by means of AGF, a computational model was developed for the numerical simulation of coupled thermo-hydro-mechanical behavior of soil upon freezing [95]. The freezing soil computational model adopts the theory of poromechanics [20] where the solid particles, liquid water and crystal ice are considered as three separated phases in conjunction with the theory of premelting dynamics.

EULERIAN liquid and ice saturations   At all times the porous volume is assumed to be filled by water, in both liquid form (L) and crystal form (C). Hence, the current LAGRANGIAN porosity ϕ can be written as

$$\phi = \phi_L + \phi_C \,, \tag{6.30}$$

where ϕ_J is the current LAGRANGIAN partial porosity related to phase $J = $ L, C. Once the overall porosity is known, the current partial porosities can be expressed in terms of the degree of saturation as

$$\phi_J = \phi\, \chi_J \,, \quad \text{with} \quad \chi_L + \chi_C = 1 \,, \tag{6.31}$$

where χ_J denotes the EULERIAN saturation and represents the current partial saturation of phase J relative to the current deformed porous volume $\phi \mathrm{D}\Omega_0$, see Fig. 6.38.

Fig. 6.38 Schematic illustration of three-phase freezing soil with averaging principle applied [95]
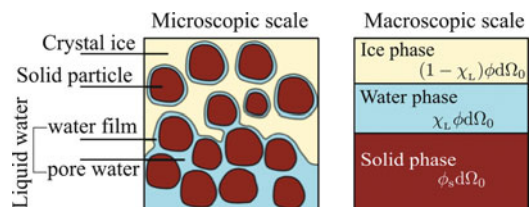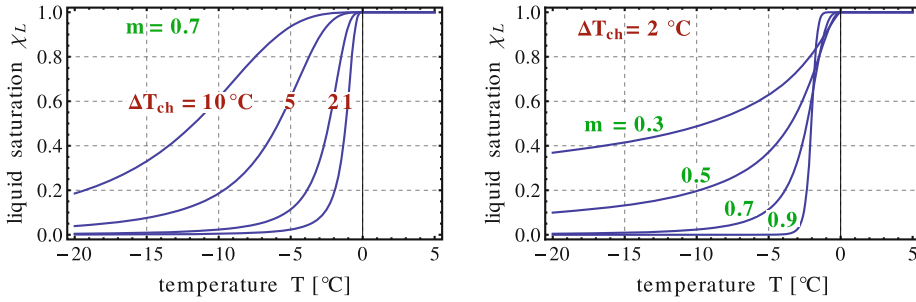
Fig. 6.39 Liquid saturation curve during freezing: Influence of ΔT_{ch} (left) and m (right), [95], [94]

The liquid saturation curve   By analogy with a liquid-gas interface for unsaturated soils and adopting the VAN GENUCHTEN capillary curve, a relationship between the liquid saturation in freezing soils and temperature can be obtained,

$$\chi_{\text{L}} = \left(1 + \left(\frac{T_{\text{f}} - T}{\Delta T_{\text{ch}}} \right)^{\frac{1}{1-m}} \right)^{-m}, \tag{6.32}$$

where $\Delta T_{\text{ch}} = \frac{\mathcal{N}\,\gamma_{\text{CL}}}{S_{\text{f}}\,\gamma_{\text{GL}}}$ is the characteristic cooling temperature related to the most frequently encountered pore radius R_{ch}, $\mathcal{N}$ the capillary modulus, γ_{CL} the liquid-crystal interface energy, γ_{GL} the liquid-air interface energy, S_{f} the freezing entropy per unit of volume and m is an index indicating the pore radius distribution around R_{ch}. The influence of ΔT_{ch} and m on the shape of the liquid saturation curve is illustrated in Fig. 6.39.

The liquid-crystal equilibrium relation   Thermodynamic equilibrium between the liquid pore water (L) and the adjacent crystal ice (C) requires the equality of the chemical potential of both phases,

$$\mathrm{d}\mu_L = \mathrm{d}\mu_C, \text{ with } \mathrm{d}\mu_J = \frac{\mathrm{d}p_J}{\rho_J} - s_J\mathrm{d}T \quad (J = \text{L,C}), \tag{6.33}$$

where μ_J, p_J, ρ_J and s_J are the chemical potential, the pressure, the specific mass density and the entropy per unit mass of phase J, respectively. Integrating the above equation between the reference state $p = 0\,\text{Pa}$, $T = T_{\text{f}} = 273\,\text{K}$ and the current state provides the liquid-crystal equilibrium, we have

$$p_{\text{C}} - p_{\text{L}} = S_{\text{f}}(T_{\text{f}} - T)\,, \text{ with } S_{\text{f}} = \frac{\rho_c L_{\text{f}}}{T_{\text{f}}}. \tag{6.34}$$

Note that Eq. 6.34 can be used to explain the micro-cryo-suction mechanism, which is identified as the driving force of frost heave phenomenon observed for frost-susceptible soils.

The three-phase finite element model for freezing soils   The computational model is a thermo-hydro-mechanical three-phase finite element model which considers the temperature, liquid pressure and solid displacements as the primary variables. The three-phase finite element model captures the most relevant couplings between the phase transition associated with latent heat effect, the liquid transport within the pores, and the accompanying mechanical deformation trough three fundamental physical laws, which are the overall entropy balance, mass balance of liquid water and crystal ice, and overall momentum balance, together with corresponding state relations.

Mass balance of liquid water and crystal ice   Considering the possible phase transition between liquid water and crystal ice, the mass balance equation relative to each phase can be written as

$$\frac{d m_{\mathrm{L}}}{dt} + \nabla \cdot \mathbf{w}_{\mathrm{L}} = -\overset{\circ}{m}_{\mathrm{L} \to \mathrm{C}}, \quad \frac{d m_{\mathrm{C}}}{dt} + \nabla \cdot \mathbf{w}_{\mathrm{C}} = \overset{\circ}{m}_{\mathrm{L} \to \mathrm{C}}, \tag{6.35}$$

where $m_J = \rho_J \phi_J$ represents the current mass content related to phase J per unit of initial volume, with ρ_J being the corresponding specific mass density; $\nabla \cdot (\cdot)$ denotes the divergence operator; $\mathbf{w}_J$ is the EULERIAN relative mass flow vector, and $\overset{\circ}{m}_{\mathrm{L} \to \mathrm{C}}$ is the rate of liquid water mass changing into crystal ice. With the assumption that the flow of ice with respect to the skeleton occurs much slower than the flow of water such that $\mathbf{w}_{\mathrm{C}} = \mathbf{0}$, summation of the mass balance equations yields the combined mass balance for both the liquid water and the crystal ice phase. The mass balance equation for the ice and liquid phases reads

$$\frac{d m_L}{dt} + \frac{d m_C}{dt} + \nabla \cdot \mathbf{w}_L = 0. \tag{6.36}$$

Overall momentum balance   Neglecting dynamic effects, the momentum balance equation for the mixture is given as

$$\nabla \cdot \boldsymbol{\sigma} + \rho \, \mathbf{g} = 0, \tag{6.37}$$

where $\boldsymbol{\sigma}$ denotes the tensor of total stresses, $\rho = (1 - \phi_0) \rho_{\mathrm{S0}} + m_{\mathrm{L}} + m_{\mathrm{C}}$ stands for the overall mass density with ρ_{S0} being the initial mass density of solid particles, and $\mathbf{g}$ is the gravity force per unit volume.

Overall entropy balance   Identifying the spontaneous production of entropy Φ_M, the second law of thermodynamics states the entropy balance for the liquid-ice crystal-solid mixture:

$$T \left(\frac{dS}{dt} + \nabla \cdot (s_L w_L) \right) + \nabla \cdot \mathbf{q} - \Phi_M = 0, \tag{6.38}$$

with $S = S_S + m_L s_L + m_C s_C$ as the overall density of entropy per unit of volume, while S_S is the entropy of the solid matrix and s_J the specific entropy related to phase J, $\mathbf{q}$ is the overall outgoing heat flow vector. Here Φ_M represents only the mechanical dissipation associated with the viscous liquid flow through the porous volume.

Numerical simulation of AGF under seepage flow   The computational modeling of artificial ground freezing (AGF) method represents a challenge due the hydro-thermo-mechanical interactions between the frozen and unfrozen surrounding soil. In tunneling application, the developed computational was used to investigate the influence of horizontal seepage flow on the formation of a frozen arch wall during AGF and an optimization of freeze pipe arrangement was investigated with the goal of speeding up the time to obtain a fully frozen arch, see [51]. Figure 6.40 compares the spatial distribution obtained from three different levels of seepage flow $\mathbf{v}_L = 0$, 0.5 and 1.0 m/d after 3, 6 and 9 days of continuous freezing.

Application of ant colony optimization to find an optimized arrangement of the freeze pipes   The results of Fig. 6.40 lead to the conclusion that a large seepage flow will significantly delay or even avoid the formation of a closed frozen arch around the tunnel profile during freezing process. In such situations, the frost zone around the freeze pipe does not form concentrically around the freeze pipes. It is clear, that an equidistant distribution of the freeze pipes is not the optimal arrangement in case of presence of seepage flow. The success of the freezing process may be endangered in a situation when a steady state is reached without forming a closed frozen arch. For this reason, the groundwater flow must be adequately considered in the design of the freezing operation to achieve a successful freezing process.
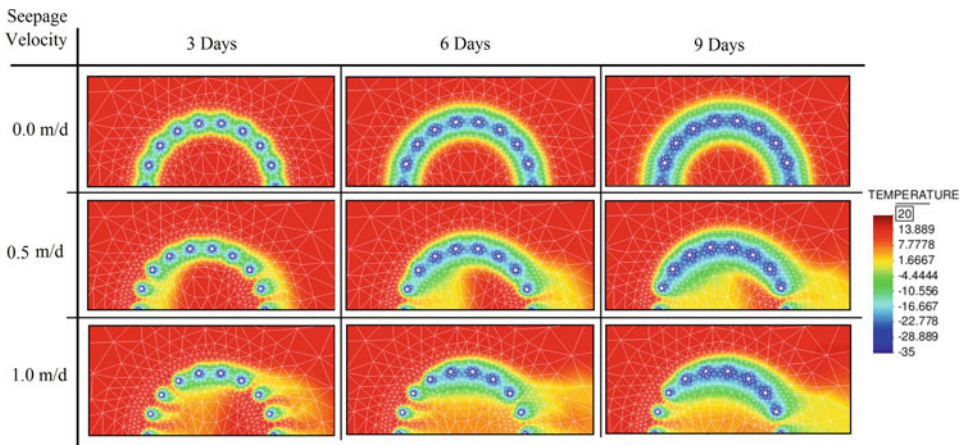
Fig. 6.40   Influence of seepage flow on the formation of a frozen arch, [51], [50]
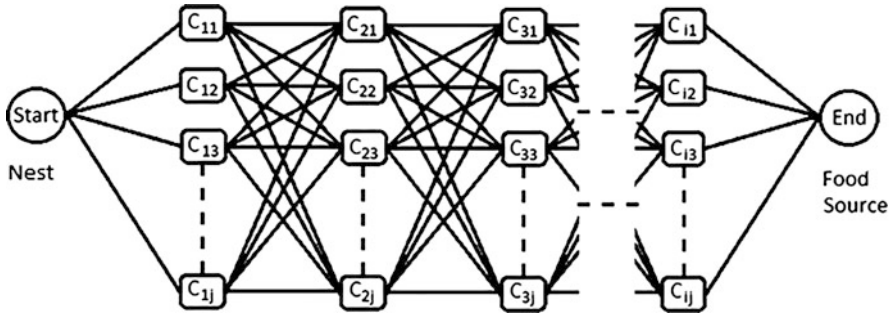
Fig. 6.41 Ant Colony Optimization: Illustration of discrete solution space, of note is that each column resembles one variable including the set of attached discrete values, [51], [50]

In order to enhance the freezing efficiency, the Ant colony optimization (ACO) described herein has been applied to search for the optimal arrangement of freeze pipes depending on the direction and magnitude of the groundwater flow. ACO algorithm is a probabilistic method with the goal to search the optimal path in a graph by mimicking the behavior of ants seeking a path between their colony and a source of food, see [30]. The artificial ant is a simple computational agent of the ACO iterative algorithm. In Fig. 6.41 a walking ant on the graph simulates the solution selection process. At each iteration of the ACO algorithm, each ant moves from a solution state to another solution state creating a partial solution until it constructs the complete solution.

The results after optimization show that an arrangement of the freeze pipes determined by the optimization algorithm considerably reduces the freezing time for the formation of a frozen arch. With increasing seepage velocity, the freezing time increases progressively in case of an even distribution of the freeze pipes. In contrast, only a moderate increase is observed if an optimal placement is chosen. It is notable that the larger the flow velocity of the groundwater, the larger is the improvement obtained from the optimization procedure. The optimum arrangement of freeze pipes is presented in Fig. 6.42 for $v_L = 1.0$ m/d. In Fig. 6.42, note that the pipe locations are shifted against the seepage flow direction and that the spacing between pipes is decreased at the upstream direction. For a seepage velocity of $v_L = 1.0$ m/d, the optimized solution requires a freezing time of 10 days to form a fully frozen arch. In contrast, to the original design with an equidistant placement

Fig. 6.42 Comparison of the optimum arrangement of freeze pipes with an equal distribution of the pipes for $v_L = 1.0$ m/d, [51], [50]
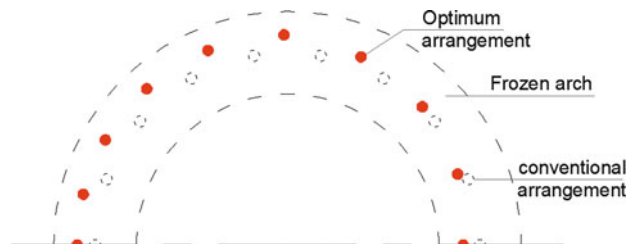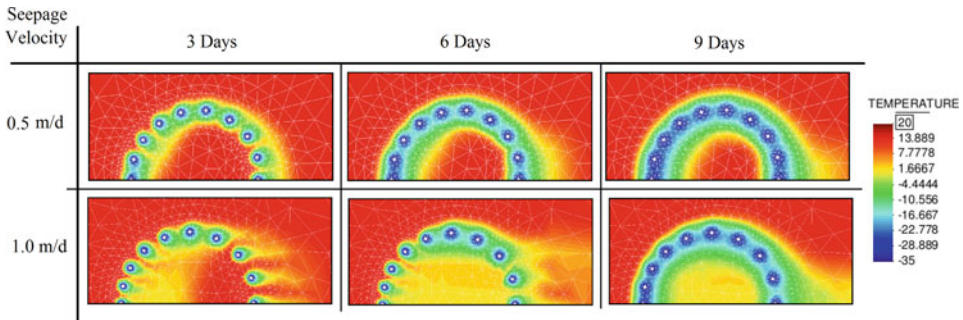
Fig. 6.43 Influence of seepage flow on the formation of a frozen arch for an optimized arrangement of the freeze pipes, [51], [50]

of the freeze pipes, for which more than 50 days of freezing are required. Figure 6.43 shows the formation of the frozen arch by means of the temperature distribution at different days of the freezing process for an optimized placement of the pipes for a seepage velocity of $\mathbf{v}_L = 0.5$ m/d and $\mathbf{v}_L = 1.0$ m/d, respectively. When the optimized arrangement is compared with Fig. 6.40, one observes, that the use of the optimum arrangement results in a more symmetric and homogeneous growth of the frost body as compared to an equidistant arrangement of the pipes.

A development of a failure criteria based on strength upscaling for freezing soils
A novel constitutive model for freezing soils is developed by adopting the CASM [93] for the unfrozen state, and the enhanced BBM [58] together with the homogenized strength criteria obtained for the freezing state [96], [97]. The developed elasto-plastic mechanical constitutive model with failure criterion upscaled through strength homogenization is named as Extended BBM [94]. In contrast to phenomenological elasto-plastic models, the failure criteria is established on the basis of the knowledge of their microstructure, i.e. the volume fractions and strength properties of constituent phases. Therefore, the macroscopic strength properties of drained partially frozen soil obtained through a two-step strength upscaling are incorporated into the extended BBM. Figure 6.44 illustrates the flowchart of the extended BBM with the strength properties from the strength upscaling model and to its integration into the three-phase finite element model for soil freezing.

6.4.2 Model Generation and Simulation Procedure

An automatic modeler which can be integrated within the TIM has been developed to generate realistic three-dimensional tunnel simulation models much simpler than up to now. Details of this approach along with an outlook to possible parallelization are given in the following sections.
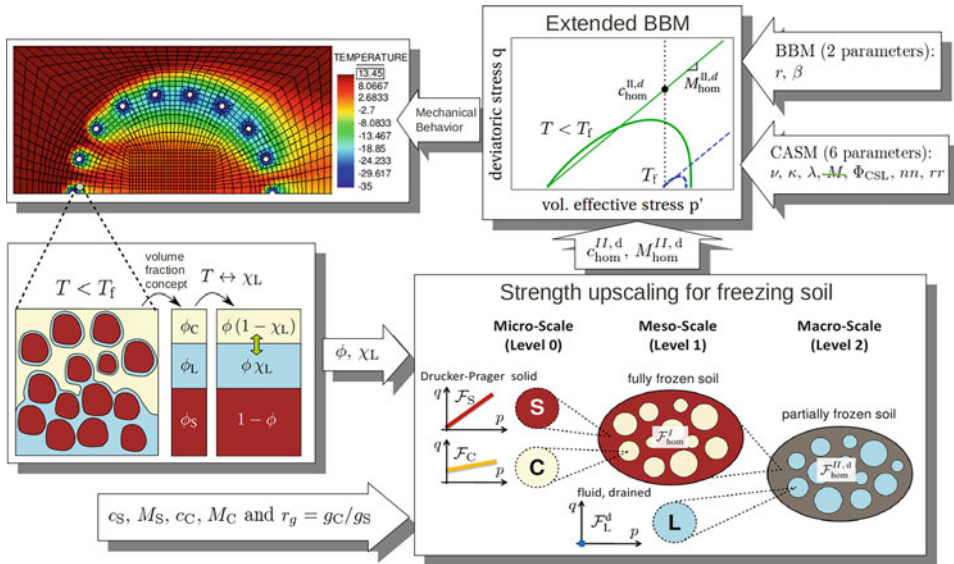
Fig. 6.44 Illustration of AGF simulation under seepage flow considering the developed extended BBM with strength properties from a two set up-scaling strategy, [94]

6.4.2.1   Automatic BIM-Based Model Generation

Generating a realistic three-dimensional tunnel simulation model that is capable of representing all the involved components of a bored tunnel construction process requires considerable effort and experience [7]. In addition to the considerable experience required to generate an accurate numerical model, data from many different sources is required for the construction of such a simulation model. This data is most often not centrally stored and therefore not easily accessible. Additionally, the formats in which project data are stored are typically not compatible with the formats required by an FE program. This is especially true in the case of geometrical data, such as CAD drawings. Although existing design drawings are most often used as the basis for an FE model, a direct import into an FE program is most often not successful as the imported data generates a geometry that does not fulfill the requirements of the FEM model, such as model connectivity. Even if the geometry is successfully imported, other necessary aspects of an FE model, such as boundary conditions and material properties, must be applied manually. These incompatibilities inevitably result in the creation of a new model, which, especially in the case of complex 3D models, is a time consuming process.

To this end, an automatic modeler, which is integrated within the TIM, has been developed as a numerical simulation tool to automate and simplify the modeling process, and to reduce errors due to inexperience. This modeler allows for "BIM-to-FEM" interaction platform, that automatically extracts the relevant information (geology, alignment, lining, material and process parameters), needed for an FE-simulation from TIM sub-models and

subsequently performs an FE-analysis of the tunnel drive. All process data and material parameters are stored and can be exported as text files. Moreover, for all geometrical representation, each individual component is defined as volumetric data with a non-uniform rational basis spline (NURBS) in ACIS® .sat format. The necessary boundary conditions and construction sequences are automatically incorporated based upon the design data. This simplifies the information flow and limits errors that jeopardize the structural analysis.

The modularity of the developed TIM-based modeler has been accomplished by connecting various scripts and software packages, to which a specific task during the model generation is determined. The main involved modules are the GiD pre- and post-processing software, the object-oriented finite element framework KRATOS and library of auxiliary scripts (e.g. Python) used to invoke the TIM, exchange data and generate the complete simulation model. The modular structure of GiD allows automatic model generation using batch files and user-defined routines, written in TCL. These TCL-routines are powerful tools as they can access the data structure of GiD and automatically identify layers and boundaries without any user interactions. On the other hand, the batch files contain every instruction that is necessary to read and create the geometry, assign the boundary conditions and generate the mesh. Furthermore, it has the capability of invoking GiD in silent mode from command line. For this reason, the automatic creation of a number of batch files, based on the input parameters from the TIM is the key feature which simplifies and automates the complete process of model generation. Figure 6.45 outlines the workflow of the proposed automatic modeler. The main tasks that are performed during the automatic model generation are described below:

- **Acquisition of geometry and geology:** The topology of the geological layers, buildings and all relevant components of the tunnel geometry, in addition to the geometrical boundaries (simulation domain) must be defined. This information is imported from the TIM to the modeler as volumetric data with a non-uniform rational basis spline (NURBS) in ACIS® .sat format. ACIS is a geometric modeling kernel used to enable robust and 3D modeling capabilities of Computer-aided design (CAD) software. The tunnel geometry can be either imported using the geometrical data for each individual ring, or as simply a tunnel alignment and a ring thickness and diameter. Initially the modeler stores these geometries separately.
- **Acquisition of input parameters:** Process parameters (e.g. face support pressure and grouting pressure) and material parameters (i.e. for soil, grouting, and lining stiffness) are required to generate the simulation model. This information is available in the TIM and can be provided in .txt format.
- **Generation and execution of the numerical simulation:** A set of batch files will be automatically generated after reading all required data (.txt). These batch files, import all geometrical information from 3D interchange files (ACIS) provided by TIM, generate the geometrical model in GiD, apply boundary conditions and material properties to their corresponding elements and generate the finite element mesh, automatically.
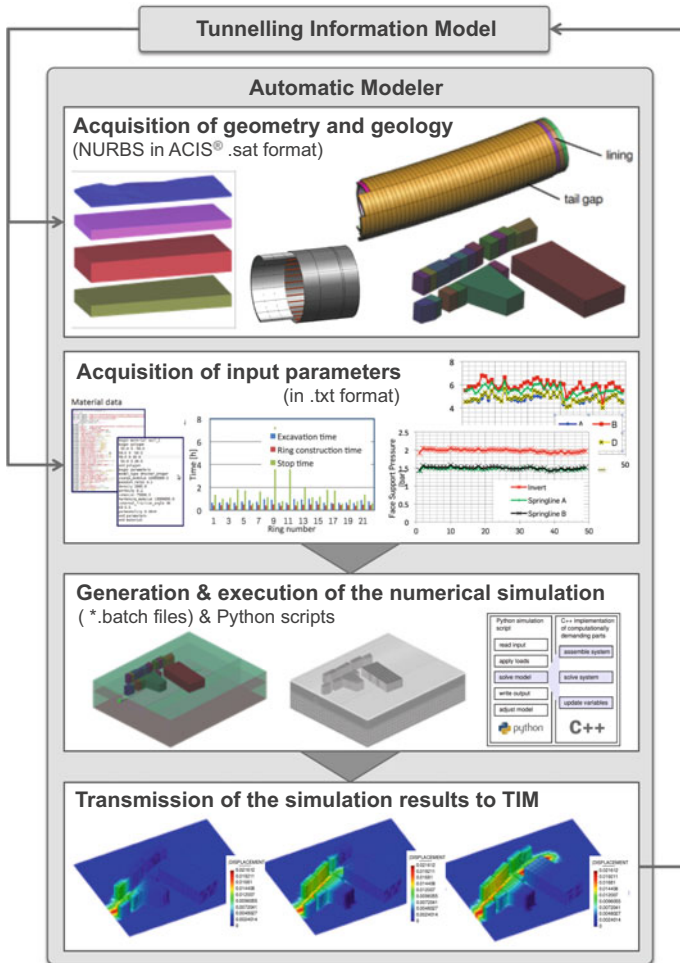
Fig. 6.45 Schematic illustration of the workflow of TIM-based automatic model generation with performed individual task

Finally, a python simulation script is automatically generated, reading all process parameters from the TIM, and executed in order to perform the finite element analysis.

- **Transmission of the simulation results to the Tunnel Information Model:** The modeler is able to automatically incorporate the results of FE simulations into the TIM where the user has continuous access. The simulation data is thus easily visualized and compared to site data, such as building locations, monitoring data, such as settlement measurements, and machine data such as thrust forces.

The object oriented architecture of the computational software ekate and the modularity of the developed automatic modeler, allow for an efficient and robust internet-based interaction with the TIM via web-service.

6.4.2.2 Parallelization Concept

To speed up the computation process, the tunnel advancement analysis can be solved in parallel on a distributed computing platform using the Message-Passing-Interface (MPI). In the first stage, the mesh is decomposed into partitions to support for parallel assembly. As a result, the linear system has to be stored in parallel using a compatible storage scheme [4]. In the second stage, the resulting linear system is solved using a parallel iterative solver. To speed up the convergence of the iteration process, a block preconditioning strategy, taking advantage of the coupled nature of the fully saturated soils problem at hand, is employed.

The domain decomposition algorithm minimizes the interface between the domain to save communication time [40]. An illustration of a typical partitioning for tunnel analysis can be found in Fig. 6.46, left. To accommodate for contact analysis, where the TBM traverses through the computational domain and hence is in contact with the interface, the master contact surfaces are duplicated in all domains as ghost entities. It helps to compute the contact forces properly and avoid sophisticated data exchange, meanwhile the memory overhead is not high. An illustration for this concept is depicted in Fig. 6.46, right.

The parallel iterative solver is GMRES, which is a variant of the Krylov subspace method. In this method, the solution is searched in the subspace $S = \{\mathbf{x}_0, \mathbf{K}\mathbf{x}_0, \ldots, \mathbf{K}^{m-1}\mathbf{x}_0\}$, in which m is the dimension of the Krylov subspace, $\mathbf{K}$ denotes the system stiffness matrix and $\mathbf{x}_0$ is the initial prediction. To speed up the search iteration, a preconditioner is required. For a fully saturated model comprising solid and fluid phases, the stiffness matrix $\mathbf{K}$ can be written in the block form $\mathbf{K} = \begin{bmatrix} \mathbf{A} & \mathbf{B}_1 \\ \mathbf{B}_2 & \mathbf{C} \end{bmatrix}$. This allows to compute an approximation for the inverse of $\mathbf{K}$ based on algebraic decomposition. This approximation can then be used as a preconditioner for the Krylov subspace method. The full algebraic factorization of the block system matrix reads

$$\mathbf{K}^{-1} \approx \mathbf{P}_{sf}^{-1} = \begin{bmatrix} \mathbf{I} & -\mathbf{A}^{-1}\mathbf{B}_1 \\ \mathbf{0} & \mathbf{I} \end{bmatrix} \begin{bmatrix} \mathbf{A}^{-1} & \mathbf{0} \\ \mathbf{0} & \mathbf{S}^{-1} \end{bmatrix} \begin{bmatrix} \mathbf{I} & \mathbf{0} \\ -\mathbf{B}_2\mathbf{A}^{-1} & \mathbf{I} \end{bmatrix}. \tag{6.39}$$
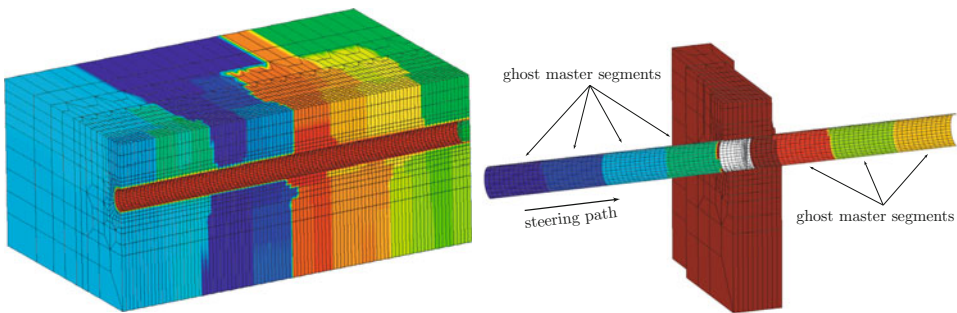
Fig. 6.46 The domain decomposition concept for tunnel analysis: (left) partitioning of the computational model; (right) partition of one domain with contact faces

In Eq. 6.39, **S** is the Schur complement of the system matrix **K**, which can be approximated by $\mathbf{S} = \mathbf{C} - \mathbf{B}_2 \, \text{diag}(\mathbf{A})^{-1} \mathbf{B}_1$. The block preconditioner Eq. 6.39 contains two matrix inversion $\mathbf{A}^{-1}$ and $\mathbf{S}^{-1}$. These inversions can be approximated by using classical preconditioning techniques, such as Incomplete LU factorization (ILU) or the Algebraic Multigrid Method (AMG). The preconditioner Eq. 6.39 can be simplified by dropping the first or last term, leading to the block lower and block upper preconditioner [13], as described in the equations

$$
\mathbf{P}_{\text{sl}}^{-1} = \begin{bmatrix} \mathbf{A}^{-1} & \mathbf{0} \\ \mathbf{O} & \mathbf{S}^{-1} \end{bmatrix} \begin{bmatrix} \mathbf{I} & \mathbf{0} \\ -\mathbf{B}_2\mathbf{A}^{-1} & \mathbf{I} \end{bmatrix} \left(= \begin{bmatrix} \mathbf{A} & \mathbf{0} \\ \mathbf{B}_2 & \mathbf{S} \end{bmatrix}^{-1} \right),
\tag{6.40}
$$

$$
\mathbf{P}_{\text{su}}^{-1} = \begin{bmatrix} \mathbf{I} & -\mathbf{A}^{-1}\mathbf{B}_1 \\ \mathbf{0} & \mathbf{I} \end{bmatrix} \begin{bmatrix} \mathbf{A}^{-1} & \mathbf{0} \\ \mathbf{0} & \mathbf{S}^{-1} \end{bmatrix} \left(= \begin{bmatrix} \mathbf{A} & \mathbf{B}_1 \\ \mathbf{0} & \mathbf{S} \end{bmatrix}^{-1} \right).
\tag{6.41}
$$

Alternatively, to avoid computing the Schur complement, one can employ the algebraic Gauss Seidel decomposition of the block stiffness matrix **K**,

$$
\mathbf{P}_{\text{gs}}^{-1} = \begin{bmatrix} \mathbf{I} & \mathbf{0} \\ \mathbf{0} & \mathbf{C}^{-1} \end{bmatrix} \begin{bmatrix} \mathbf{I} & \mathbf{0} \\ -\mathbf{B}_2 & \mathbf{I} \end{bmatrix} \begin{bmatrix} \mathbf{A}^{-1} & \mathbf{0} \\ \mathbf{0} & \mathbf{I} \end{bmatrix}.
\tag{6.42}
$$

The parallel computation phase in the context of the whole computational workflow for tunnel simulation is depicted in Fig. 6.47.

The domain decomposition strategy is crucial to obtain the perfect parallel scalability of the assembly process. Meanwhile, the performance of the block preconditioner varies and shows a degree of sensitiveness with regards to the permeability of the fluid phase. It is noted that the system stiffness matrix becomes ill-posed when the permeability is low, leading to a poor convergence of the iterative solver. The numerical experiment shows that the computational time is higher with low permeability, nevertheless the speed-up is better, as can be seen in Fig. 6.48.

6.4.3 A Tunnel Analysis Model Based on the CutFEM Method

To accommodate for the flexibility in varying the tunnel alignment in analysis and design, a tunnel analysis model based on the Cut Finite Element Method (CUTFEM) is proposed. In this section, details of the CUTFEM method along with the validation examples are presented. By the end of the section, a numerical example to analyze the induced building damage with regards to different tunnel track variants is performed to verify the effectiveness of the CUTFEM approach.

6.4.3.1 Description of the Computational Model

The CUTFEM tunnel model makes use of the fictitious domain concept [24], where the computational domain covers up the whole underground space, including the excavation
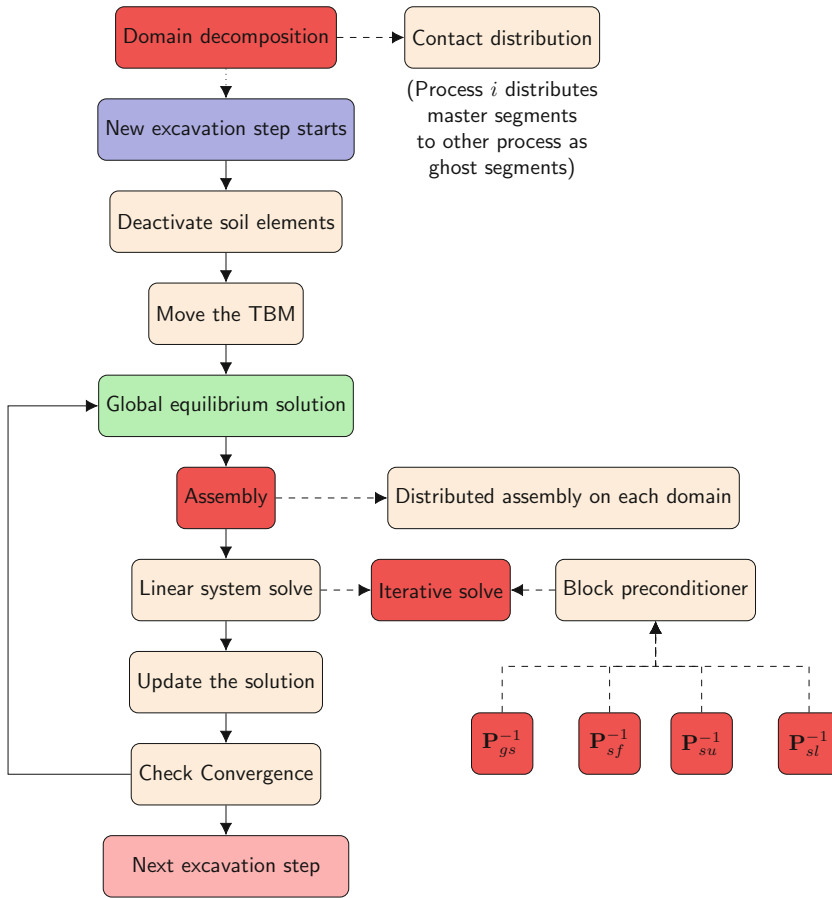
Fig. 6.47 Computational workflow for parallelized tunneling simulations. The parallel computation is highlighted in red, including possible block preconditioning strategies [13]

domain. The material removal during excavation is accounted for in the weak form of the boundary value problem, which is then translated into the system stiffness matrix and residual forces. An illustration of the computational domain can be found in Fig. 6.49.

In making up the computational domain Ω, the fictitious domain Ω_{fict} is perceived as an extension of the physical domain Ω_{phys}. As a result, the computational domain does not contain any geometric constraint and can be meshed arbitrarily. However, it is typical in practice to have structured meshing for simplicity and avoid remeshing. The structured mesh also offers other advantages, such as superior mesh quality and optimal assembly kernel for large simulation.

The indicator function α is defined as $\alpha(\mathbf{x}) = 1, \forall \mathbf{x} \in \Omega_{\text{phys}}$ and $\alpha(\mathbf{x}) = 0, \forall \mathbf{x} \in \Omega_{\text{fict}}$. The indicator function is also used to penalize the stress in the fictitious domain. For a typical two-phase fully saturated soil, under quasistatic conditions and assuming small
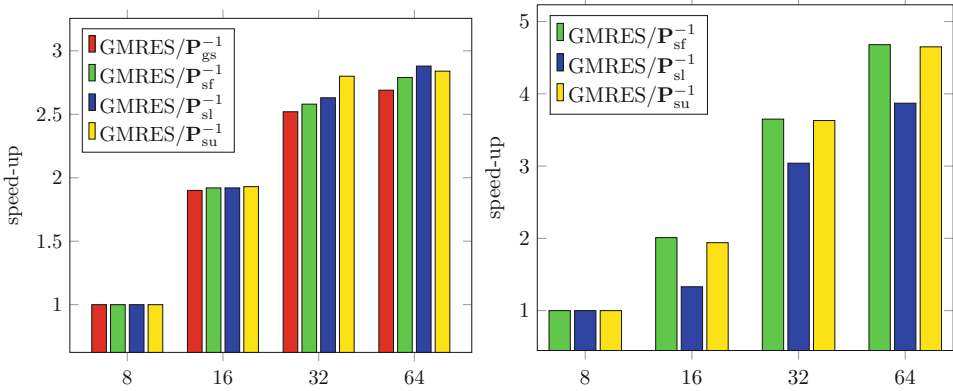
Fig. 6.48 Performance of the block preconditioner with regards to high water permeability (left) and low water permeability (right)
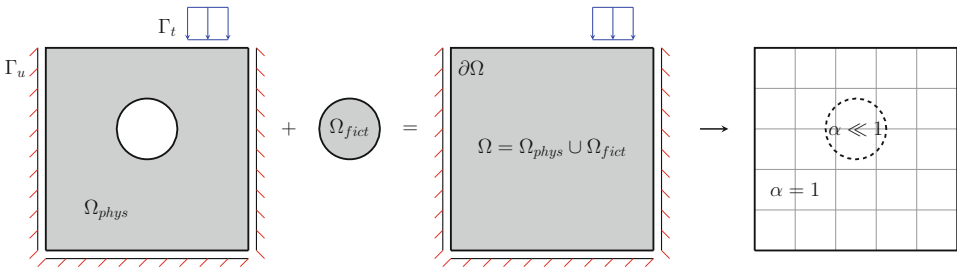
Fig. 6.49 The fictitious domain concept for tunnel analysis: The physical domain Ω_{phys} is extended by the fictitious domain Ω_{fict} to allow structured meshing of the computational domain Ω. The indicator function α implicitly defines Ω_{phys} and Ω_{fict}

strain kinematics, the equilibrium equations read

$$\delta W^s = \int_{\Gamma_N^s} \delta \mathbf{u}^s \cdot \mathbf{t} dA - \int_{\Omega} \alpha^s(\mathbf{x}) \nabla^{sym} \delta \mathbf{u}^s : \boldsymbol{\sigma} \, dV + \int_{\Omega} \alpha^s(\mathbf{x}) \delta \mathbf{u}^s \cdot \rho \mathbf{g} dV = 0, \quad (6.43)$$

$$\delta W^w = \int_{\Gamma_N^w} \delta p^w q^w dA - \int_{\Omega} \alpha^w(\mathbf{x}) \operatorname{grad} \delta p^w \cdot \tilde{\mathbf{v}}^{ws} dV + \int_{\Omega} \alpha^w(\mathbf{x}) \delta p^w \operatorname{div} \dot{\mathbf{u}}^s dV = 0,$$

$$(6.44)$$

in which α^s and α^w are separate indicator functions for solid and fluid phases. In practice, the indicator function takes small values ($10^{-4} \sim 10^{-15}$) at the fictitious domain to avoid ill-conditioning.

The weak forms Eq. 6.43 and Eq. 6.44 are typically integrated using an adaptive quadrature scheme, see e.g. Fig. 6.50, where the integration points are generated by
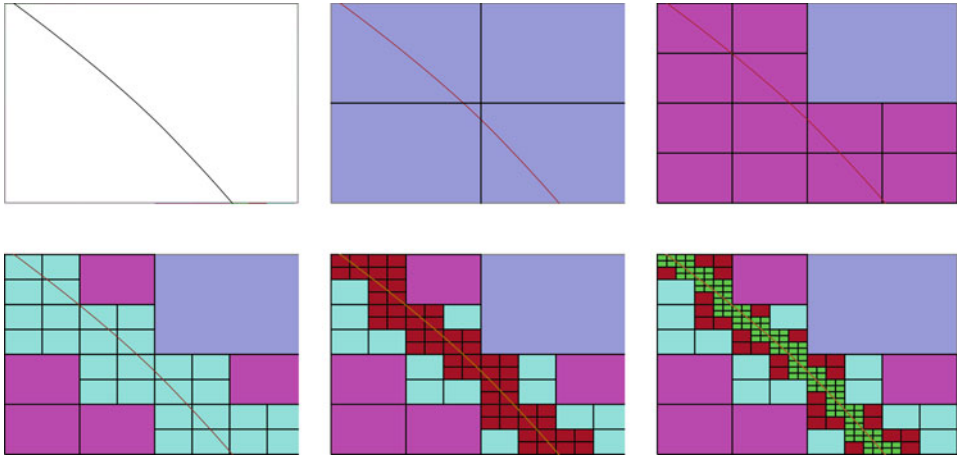
Fig. 6.50 The adaptive quadrature for CUTFEM tunnel analysis

a space-tree subdivision algorithm. The adaptive quadrature scheme is simple to implement and robust with regards to a large number of material models.

To improve the mesh resolution around the excavation domain, and especially to avoid costly global remeshing, the structured mesh can be refined by using a space-tree subdivision approach. This approach involves the hanging node, which can be handled by introducing additional constraints to the resulting linear system, as illustrated in Fig. 6.51.

The fictitious domain approach also allows to mesh the components independently. In the context of tunnel analysis, the tunnel lining and the grouting layer can be meshed in a structured way as a tube mesh, see Fig. 6.52. The tube mesh is then connected to the background mesh using a mesh tying technique, which effectively enhances the weak form by weak tying constraints

$$\delta W^{ut} = \int_{\Gamma_s} \kappa_u (\delta \mathbf{u}_1 - \delta \mathbf{u}_2) \cdot (\mathbf{u}_1 - \mathbf{u}_2) \, dA, \tag{6.45}$$

$$\delta W^{wt} = \int_{\Gamma_s} \kappa_p (\delta p_1 - \delta p_2)(p_1 - p_2) \, dA. \tag{6.46}$$

The simulation of sequential excavation is characterized by continuously adapting the cut elements with the new cut configuration. The cut configuration is changed in each excavation step. There are two possibilities to realize the cut configuration, either using a Boundary Representation (BRep) of an excavation tube or a level set based on the tube BRep. The BRep approach is preferred in practice due to its simplicity, nevertheless the level set approach could provide more options to fine-grain adjust the soil surface. A typical cut changing situation is depicted in Fig. 6.53 and the resulting quadrature in 3D is depicted in Fig. 6.54.
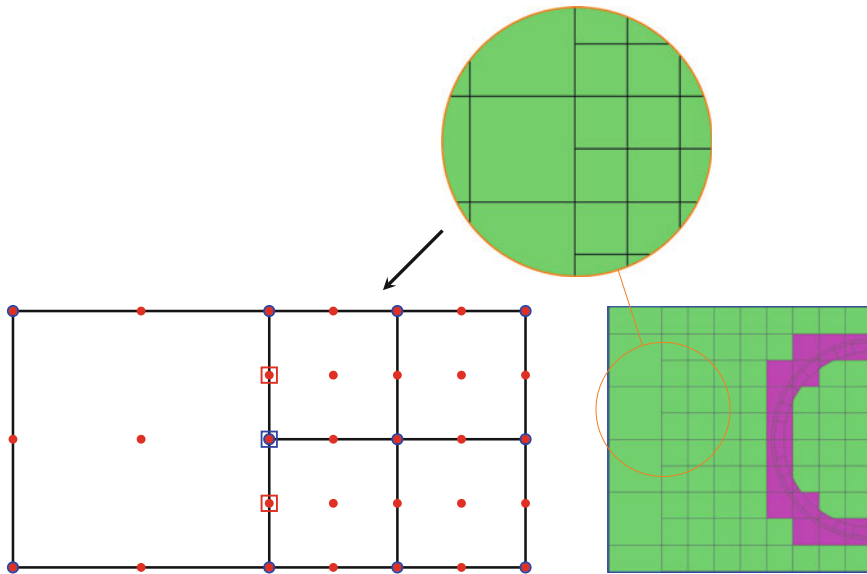
Fig. 6.51 Hanging nodes in adaptive mesh refinement (red dot: displacement node; blue dot: pressure node; red square: hanging displacement node; blue square: hanging pressure node) (left) and the relative location of the refinement domain containing hanging nodes with respect to the tunnel lining (right)
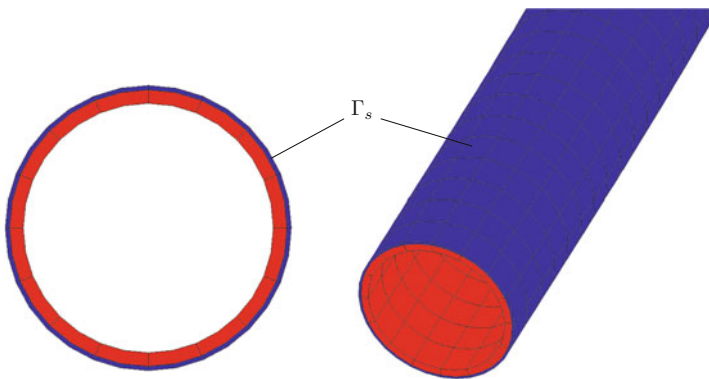
Fig. 6.52 Boundary fitted discretization of the tunnel lining (red) and the grouting layer (blue) (tube mesh). Γ_s denotes the soil surface region, aka integration domain for tying constraints

6.4.3.2   Numerical Examples and Validation

The results of the CUTFEM tunnel model is shown to match excellently with the analysis using FEM [14], as can be seen in Fig. 6.55, where the straight advancement of a TBM with an overburden of $2D$ ($D = 9.5$ m) is simulated. The analysis with CUTFEM, however, takes more computational resources since the refinement is performed excessively
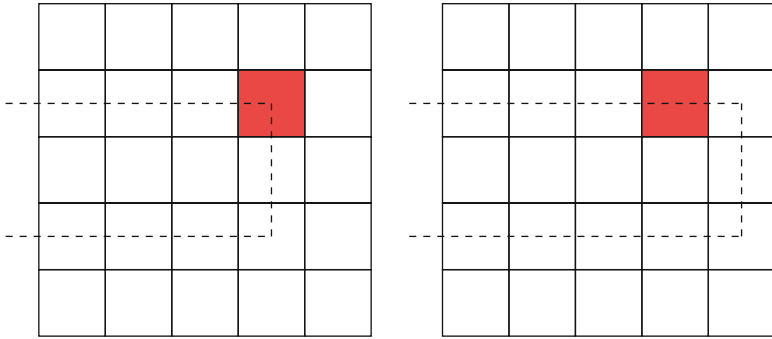
Fig. 6.53 Cut element (red) changes from partially cut to fully cut during tunnel advance
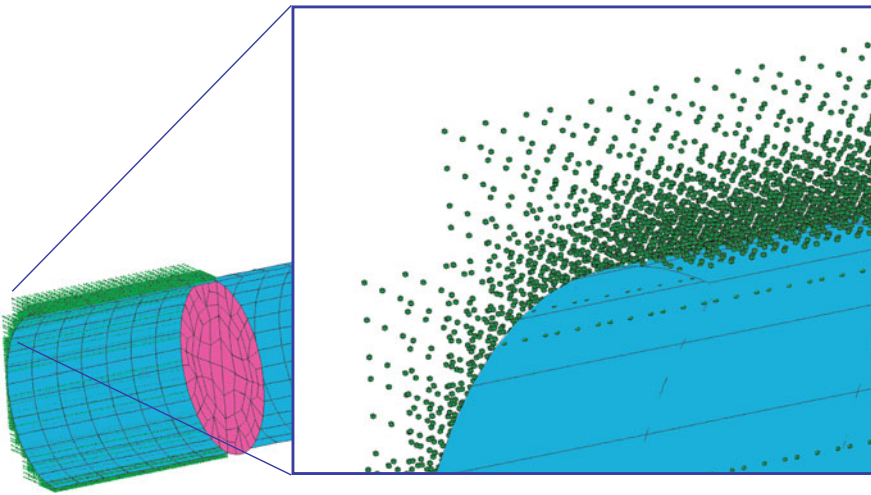
Fig. 6.54 Soil surface (light blue), heading face (purple) and quadrature points in the physical domain (green) evolving during sequential soil excavation

around the tunnel track, leading to more elements. In addition, between excavation steps, CUTFEM simulation requires to transfer the variables to the newly cut cells to maintain the stress accuracy.

Having been fully validated, the CUTFEM model shows a great potential for parametric study and tunnel track design. Figure 6.56 shows an example to evaluate the building damage during excavation for different tunnel track variants. For all analyses, the same background mesh is used for mesh and quadrature refinement. Thanks to the mesh refinement process based on space-tree subdivision, which is highly efficient, the only change in the input given to the analysis is the tunnel track data, characterizing by sampling points along the alignment curve.
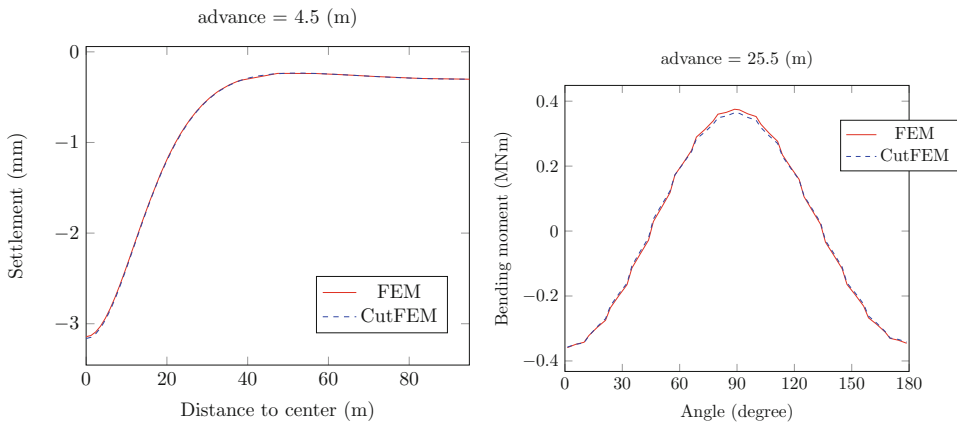
Fig. 6.55 Simulation of mechanized tunnel advance with CUTFEM: (Left) Comparison of the settlement profile at line L at two advancement stages obtained from the finite element and the CUTFEM model; (Right) Bending moment on middle ring of the tunnel
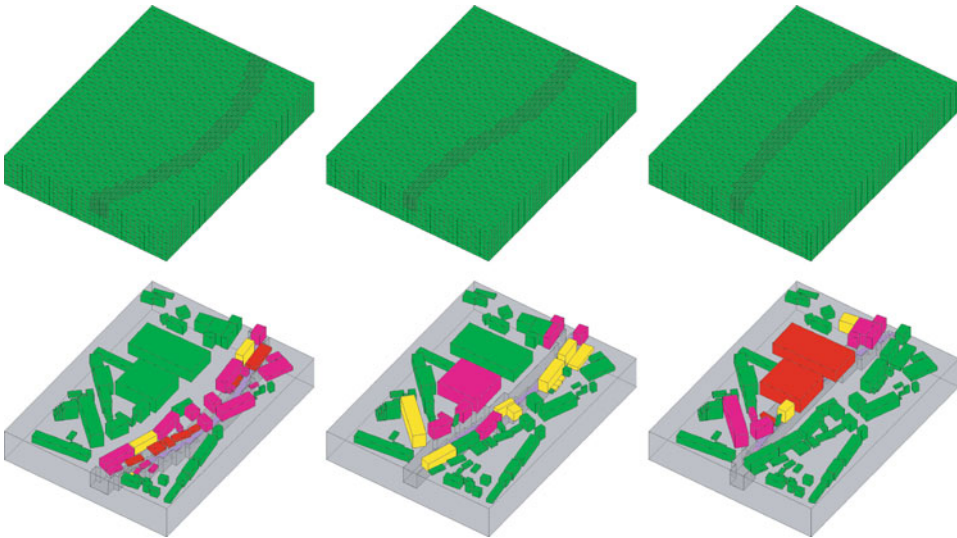
Fig. 6.56 CUTFEM models used to investigate design variants in urban tunneling: Top: Background mesh for three track variants, bottom: Visualization of building damage assessment

6.5 Risk Assessment of Building Damage

Besides the classical damage assessment needed during TBM operations, research was done to determine specific coefficients required for the possible consideration of compensation injections. To aid the assessment, an interactive tool was developed and its usefulness is demonstrated by applying it to a case study involving the Wehrhahn line in Düsseldorf.

Table 6.1 Relationship between category of damage and limiting tensile strains

category of damage	degree of severity	limiting tensile strain (%)
0	negligible	< 0.01
1	very slight	0.01–0.05
2	slight	0.050–0.075
3	moderate	0.075–0.150
4	severe	0.15–0.30
5	very severe	≥ 0.3

6.5.1 Classical Damage Assessment

Damage assessment of buildings is usually based on the category of damage (cod), see e.g. [27, 56, 92]. In this work, the tunneling induced building damage is quantified by comparing the maximum of the calculated structural strains with limiting strains, which – in the case of brittle materials such as concrete or masonry – lead to either no damage, micro-cracking or macro-cracking [48, 59, 62]. Table 6.1 shows a common assignment of limiting tensile strains to corresponding categories of damage. While strains in category 0 cause no damages, categories 1–2 cause usually aesthetic or optical damages, strains in category 3 impair structures' serviceability and strains in category 4–5 even affect the structures' ultimate load bearing capacity [12, 61].

6.5.1.1 Settlement Prediction

The damage-causing event, the settlements can be determined using analytical models like Peck [67] and Attewell [3]. Here the focus was set on the aforementioned settlement prediction using 3D FEM calculations.

6.5.1.2 Damage Evaluation

Based on settlement values for the transversal and longitudinal direction the bending strains ε_b and shear strains ε_d for the hogging (hog) and sagging (sag) areas are obtained by using Eqs. 6.47–6.50, [16]. The individual settlements are referred to as Δ_i, where the index i denotes the settlement area hog or sag. In addition to the settlements, the corresponding lengths L for the hogging L_{hog} and sagging area L_{sag} are taken into account. The height H of the building corresponds to the distance from the foundation to the eaves. The E/G-ratio represents the continuum mechanical relationship for a linear-elastic material. E terms the Young's and G the shear modulus. Influences such as facade openings and degradation effects, which reduce the effective stiffness, can be considered in fictitious E/G values. For ordinary masonry structures with a low tensile strength, E/G equals 0.5 [16] and we have

$$\varepsilon_{b,\text{max,hog}} = \frac{\Delta_{\text{max,hog}}}{L_{\text{hog}}} \cdot \left(\frac{L_{\text{hog}}}{12H} + \frac{H}{2L_{\text{hog}}} \cdot \frac{E}{G} \right)^{-1}, \tag{6.47}$$

$$\varepsilon_{d,\mathrm{max,hog}} = \frac{\Delta_{\mathrm{max,hog}}}{L_{\mathrm{hog}}} \cdot \left(1 + \frac{L_{\mathrm{hog}}^2}{6H^2} \cdot \frac{G}{E}\right)^{-1}, \tag{6.48}$$

$$\varepsilon_{b,\mathrm{max,sag}} = \frac{\Delta_{\mathrm{max,sag}}}{L_{\mathrm{sag}}} \cdot \left(\frac{L_{\mathrm{sag}}}{6H} + \frac{H}{4L_{\mathrm{sag}}} \cdot \frac{E}{G}\right)^{-1}, \tag{6.49}$$

$$\varepsilon_{d,\mathrm{max,sag}} = \frac{\Delta_{\mathrm{max,sag}}}{L_{\mathrm{sag}}} \cdot \left(1 + \frac{2L_{\mathrm{sag}}^2}{3H^2} \cdot \frac{G}{E}\right)^{-1}. \tag{6.50}$$

All four equations must be evaluated if the structure is located in both, in the hogging and sagging area, only the corresponding ones for structures located in either of the two. Furthermore, the strains and the associated damage category have to be determined for each individual structure in transversal and longitudinal direction. To account for a variation from the orthogonal orientation of the buildings, the settlement values Δ_i are determined for the projected facades separately for the longitudinal and transversal direction (see Fig. 6.57). The related length L_i ($i =$ sag, hog) is taken from the building rotated by the angle θ. This means that for wall AD with length L_{sag} the damage caused by the settlement $\Delta_{DA,\mathrm{sag}}$ in transversal and $\Delta_{AD,\mathrm{sag}}$ in longitudinal direction must be determined (Fig. 6.57). The maximum value of the strains is then relevant for the evaluation.

In contrast to the damage assessment in the final state, which assigns single damage to each location of the alignment, the potential damage during the construction process depends on the distance of the building from the tunnel face [28]. The distance that provides the maximum strain and corresponding maximum damage is determined by incrementally changing the location of the building concerning the settlement trough.
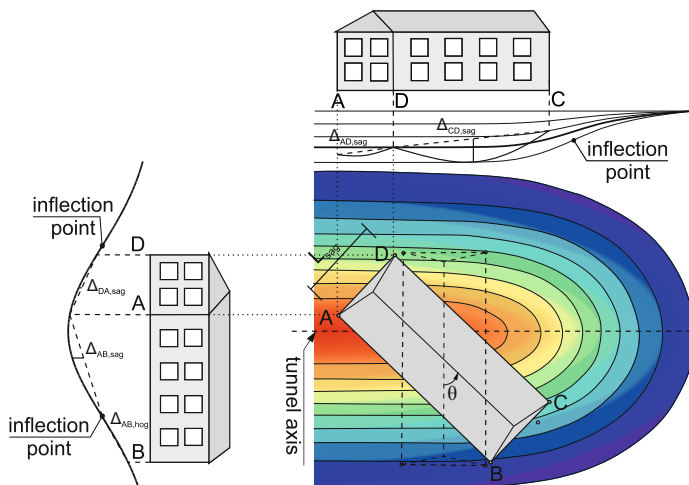
Fig. 6.57 Diagonal excavation; side view in transversal (bottom left) and longitudinal direction (top right); top view (bottom right)

However, it is inefficient to evaluate the damages by using equidistant increments along a whole alignment. On the one hand, this requires a large number of calculations, and, on the other hand, only the maximum damage is usually relevant for each building. An approach based on Artificial Neural Networks (ANN) is derived to determine these maximum damages. The advantage of using an ANN is that any type of building or soil model (analytical or numerical) can be used [18].

ANNs try to approximate data of underlying problems by a combination of simple sub-functions, called neurons. The impact of an input parameter on a certain neuron is determined by optimization that delivers weights as scalar quantities. An arbitrary number of neurons is vertically summarized on a single layer. More layers are optional. The greater the number of neurons or layers, the better the network fits to the data, but the lower the forecast quality of new data is [36]. ANN has often been proved a useful alternative to multiple polynomial regression since it neither is too demanding concerning the quality of input data nor the residuals of approximation. Basically, a variety of ANN's exist which differ regarding the topology of the network and interconnections therein. Most frequently used for approximation, are simple feed-forward networks [1]. To establish an ANN, the total available data is split into three portions: training, validation, and test data.

- Training data serves to determine optimal weights by iteration.
- Validation data provides an indicator for optimal weights. As long as the error of validation data decreases, the weights are improved based on the training data. If the error increases over 6 iterations, training is canceled and the weights associated to the minimal error are used [31].
- Test data finally helps to prove the forecast ability of the ANN [59].

The used ANN consists of one hidden layer with 10 neurons [18, 60] and has seven input variables. These are the building length L, building height H, the rotation angle θ, the distance of the building from the tunnel axis in transversal direction e_y, the dimensionless soil parameter K, the coverage c, and the external tunnel diameter D. The input parameters were chosen for typical urban environments (see Fig. 6.58, above) and generated as uniformly distributed data using the Latin Hypercube Sampling. The eccentricity at which the maximum strain is obtained was used here as the output. Based on the eccentricity value, the strain can then exactly be determined in a subsequent calculation. For computationally expensive models (e.g. FE models), however, it is more appropriate to use the strain itself as the output parameter since this eliminates the need for a subsequent FE calculation.

To generate the ANN's, 120,000 input, 15,000 validation, and 15,000 test data were used. Figure 6.58 shows the comparison between the exact and predicted eccentricity e of the ANN for training (left), validation (middle), and test data (right). In the optimal case, the results of both calculations would lie on a diagonal regression line. Data points above the regression line indicate an overestimation, and those below an underestimation of the eccentricities by the ANN. A scalar quantity for the characterization of the prognosis

input parameter: c = 5 ... 20 [m];   D = 5 ... 20 [m];   K = 0.2 ... 0.4 [-];   L = 5 ... 30 [m];   H = 5 ... 30 [m]
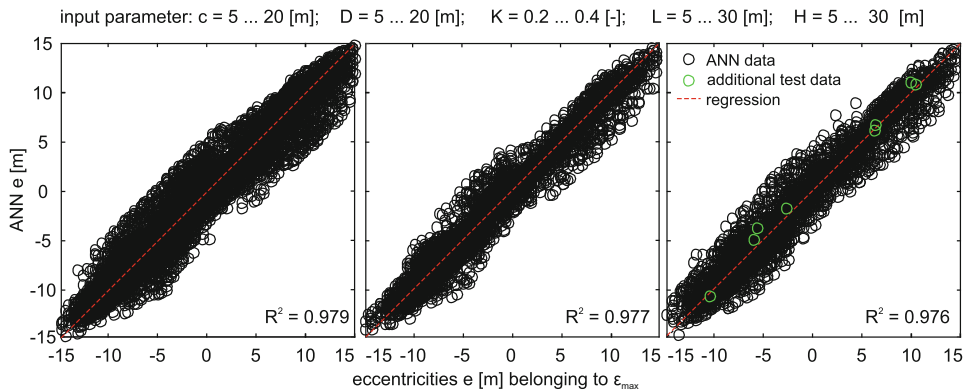
Fig. 6.58 Comparison of the exactly determined eccentricity e and the prediction based on the ANN for training (left), validation (center) and test data (right)

quality is the coefficient of determination R^2. The coefficient is determined concerning the diagonal regression line and is about 0.98, which means that the model has a very high prognosis quality. To evaluate the error and the prognosis time additional eight test data (Fig. 6.58 right, green circles) were used. The prognoses were calculated on average in about 0.1 second and showed a mean deviation of 0.43%. In conclusion, it can be stated that based on the ANN, the location of the maximum strains and the duration of the prognoses are sufficiently accurate for real-time predictions [19, 54].

6.5.2   Advanced Damage Assessment Coefficients

Classical damage assessment is based on mechanical damage only, but does not adequately reflect the background of actual use, the related consequences on maintenance and restrictions of use, and the effects of damage-reducing compensation measures.

Therefore, we propose an approach that combines the mechanical damage, i.e. the categories of damage, with the maintenance costs as well as building-specific properties such as the type of the building and a possible consequence of the damage (Fig. 6.59, left). To compare the maintenance and the prevention of damages, evaluation coefficients for possible consideration of compensation injections are also introduced (Fig. 6.59, right). This concept enables a detailed comparison of maintenance and prevention of damage and can be used to determine the most economical approach during the design of urban tunnel alignments (Fig. 6.59, middle).

6.5.2.1   Effort Coefficients for the Maintenance of Buildings
The transfer of theoretical limiting-tensile-strain-based cods to more practical effort coefficients builds on the damage descriptions of Table 6.1 and statistical maintenance costs for
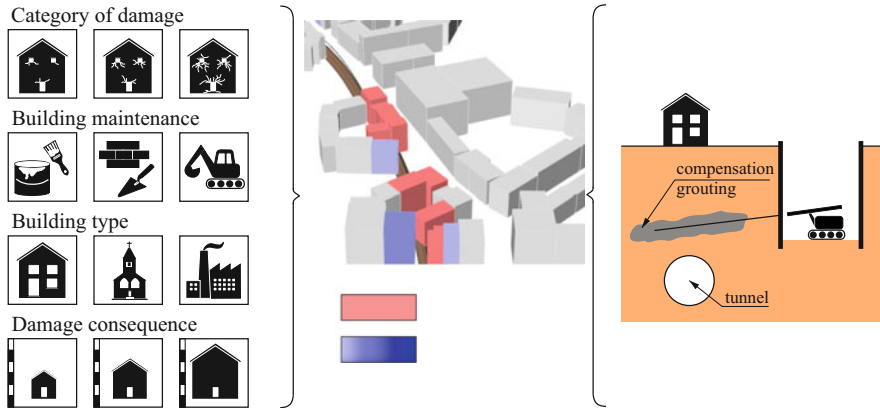
Fig. 6.59 Maintenance coefficients (left), risk assessment (middle), compensation measures (right)

residential buildings according to the German *Baukosteninformationszentrum* [5] (BKI). Naturally, this data basis depends on regional costs and construction methods, as well as highly subjective criteria regarding the demand for maintenance. These criteria should therefore be adapted to regional preferences. The determination of the damage assessment coefficients is a simple additive concept. With increasing cod, i.e., increasing damage, maintenance becomes more elaborate. In the case of cod 1, for example, only painting work is required to restore the building's original condition. For cod 2, the cod 1 painting works are complemented by more extensive maintenance like the backfilling of cracks. This addition of required measures continues up to cod 4. For cod 5 the structure is damaged beyond repair, and a new, equivalent construction is needed. Based on the considered reference project Wehrhahn-Line (WHL), maintenance measures are assumed as follows:

- cod 0: No measures required
- cod 1: Wallpapering, painting and varnishing work
- cod 2: Interior wall maintenance
- cod 3: Plastering, maintenance, and sealing work
- cod 4: Maintenance of supply and disposal pipelines, exterior walls, and exterior wall lining
- cod 5: Build a new building

Due to the minor damage in cod 1, only painting work is assumed here as maintenance measures. With reference to Table 6.1, the main damage to be expected for cod 2 is at the interior walls, and therefore only this area needs to be maintained. As cracks of up to 5 mm are to be expected in exterior walls of cod 3, plastering work as well as necessary auxiliary constructions, like scaffolds, are required to carry out the maintenance of the structure. Since water tightness is no longer guaranteed, appropriate sealing work is required. The measures to remove jammed windows and doors are covered by the mainte-

Table 6.2 Costs and effort coefficients α_i depending on the category of damage

category of damage i	costs (€/m^2)			effort coefficients α_i		
	min.	mean	max.	min.	mean	max.
0	0	0	0	0.00	0.00	0.00
1	6	24	72	0.02	0.07	0.21
2	17	58	133	0.05	0.17	0.39
3	31	104	234	0.09	0.31	0.69
4	69	212	445	0.20	0.62	1.31
5	140	340	610	0.49	1.00	1.79

nance work. In particular, higher levels of damage can lead to the need to replace masonry and the corresponding wall lining. Large settlement differences can also damage supply and disposal lines, which must be replaced. Based on these maintenance measures, the relative evaluation coefficients, also known as effort coefficients, can be derived by means of the statistical BKI costs, which are usually provided per m^2 of a building's gross floor area (GFA). Since the estimated costs also largely depend on the standard of living, i.e., whether, for example, simple wallpaper or a complex filling of a wall is required, they are usually provided in a range of minimum, mean, and maximum values (Table 6.2). In Table 6.2, the mean value of a new building serves as the reference value (1.0) for the normalized effort coefficients α_i. Consequently, maintenance for a building with cod 1 is $1/0.07 = 14$ times more economical on the mean value level than replacing it with a new structure.

6.5.2.2   Building Coefficients Based on Raw Construction Values

Although the effort coefficients provide a generalized maintenance demand with respect to the cods, the specific type of building is still disregarded. To also incorporate this information, additional building coefficients γ are introduced, which take the varying construction expenses of different building types into account. They represent generalized, relative raw construction costs per m^3 of the building volume. For the WHL reference project they are defined according to the values provided by the Ministerial Bulletin of the State of North Rhine-Westphalia, Germany (NRW 2018/27). Table 6.3 presents some relevant av-

Table 6.3 Building coefficients depending on selected raw construction costs

building type	raw construction costs (€/m^3)	building coefficient γ (m^{-3})
residential	129	1.00
office and administration	151	1.17
hospital	169	1.31
school	150	1.16
hotel	149	1.15
church	149	1.15

Table 6.4 Consequence coefficient in relation to the consequence class

consequence class k	characteristic	building example	consequence coefficient ϕ_k
CC 1	minor consequence	residential office and administration	0.5
CC 2	medium consequence	hospital	1.0
CC 3	major consequence	stadium	1.5

erage raw construction costs and their corresponding normalized building coefficients. The value of a residential building serves as the reference. If buildings have higher raw construction costs, the building coefficient increases, whereas it decreases for lower costs.

6.5.2.3 Consequence Coefficients

Although a damage assessment which incorporates building and effort coefficients is already much more accurate, the additional consideration of a building's restricted use after damage is required for a holistic determination of damage consequence costs. Depending on the type of use and duration of the maintenance measures, these impairments can have a considerable influence on the total damage costs. For these consequential costs, however, no publicly accessible, taxable data basis is available. For this reason, here, the influence is estimated by means of deterministic consequence coefficients. They are indicated as a function of the type of building or use, which is classified analogously to the consequence classes (CC) of the VDI Guideline 6200 (2010) (Table 6.4).

CC 2 is used as reference value. Its corresponding consequence index is set to 1.0, i.e. the restricted use costs are equal to the maintenance costs. For CC 1 they only add up to 50 %, for CC 3 to 150 % of the maintenance costs. The final assessment coefficient S of the damage of a building regards maintenance measures as well as the damage consequences and corresponds to the product of the effort coefficient α_i, building coefficient γ, consequence coefficient ϕ_k as well as the total building volume V (Eq. 6.51)

$$S = \underbrace{\alpha_i \cdot \gamma \cdot V}_{\text{maintenance}} + \underbrace{\phi_k \cdot \alpha_i \cdot \gamma \cdot V}_{\text{consequence of damage}} = (1 + \phi_k) \cdot \alpha_i \cdot \gamma \cdot V \quad \text{for} \quad \begin{cases} i = 0, \dots, 5 \\ k = 1, \dots, 3 \end{cases}$$

$$(6.51)$$

6.5.2.4 Reduction of Settlement Induced Damages

The effort of repairing damages according to Eq. 6.51 is opposed by that of avoiding damage by preemptive measures. Depending on the strategy and procedure, different methods for the avoidance can be applied. On the one hand, these are reinforcing measures of the structures, e.g. supporting the facades or reinforcing the foundations, and, on the other hand, a reduction of the expected settlements. These reductions can be achieved, for example, by increasing the tunnel's coverage, actively controlling the excavation (jack forces, annular gap grouting) or using compensation measures.

Here, only compensation measures are regarded, which can be temporary or permanent. Temporary measures include, for example, icing of the soil, whereas permanent measures include, for example, high-pressure mortar injections (HPI). HPIs inject mortar into the ground under high pressure to locally strengthen the ground. The total effort of realizing HPIs, i.e. including mounting and dismounting of the equipment, man power, material, etc., is usually stated per m^3 of mortar injected. It strongly depends on the condition of the soil as well as various environmental conditions. Experience values for standard urban measures lie between 400 and 600 €/m^3. This corresponds to a compensation factor κ of $400/129 = 3.10$ to $600/129 = 4.65$ based on the reference value, the building volume of a residential building. The total cost of an injection K is thus determined by the product of the compensation factor κ, the thickness h of the injection and the base area of a building A,

$$K = \kappa h A .\tag{6.52}$$

6.5.3   An Interactive Tool for Visualizing Building Damage

The visualization as well as the interactive design is implemented via the program Rhinoceros 3D (Rhino 3D) [71]. The required algorithms were created using the associated, visual programming language Grasshopper 3D [70].

To implement the visualization, the building's coordinates must first be available in a suitable file format. The building geometries and the position (distance and rotational angle) in relation to an arbitrary reference coordinate system can then be determined from the provided coordinates (Fig. 6.60, top left).

Figure 6.60 (bottom) shows the developed calculation routine for the visualization of the damages in Grasshopper 3D. First, the building data (blue box) and the tunnel information–outer diameter, depth and alignment (green box)–are imported. In a second step, the distances between the buildings and the tunnel axis are determined, followed by the damage evaluation in the final and construction state (red box). In a final step, the potential damages are transferred to Rhino 3D using the corresponding color code of the categories of damage (turquoise box).

Generally, for any given location of the tunnel, all buildings in the considered urban area have to be analyzed. In case of interactive design as well as in case of a large number of buildings, this leads quickly to a significant computational effort despite using analytical models. For this reason, only those buildings are included in the evaluation which are located at a distance smaller than $r = 2.5K(c + D/2)$ from the tunnel axis. Therein K is the dimensionless soil parameter, c is the coverage, and D is the external tunnel diameter (Fig. 6.60, top right). Investigations in [3] have shown that beyond this distance usually no relevant settlements occur.

During interactive design, the user can adjust the tunnel diameter, the depth and the alignment as desired. The alignment is modeled using non-uniform rational B-splines
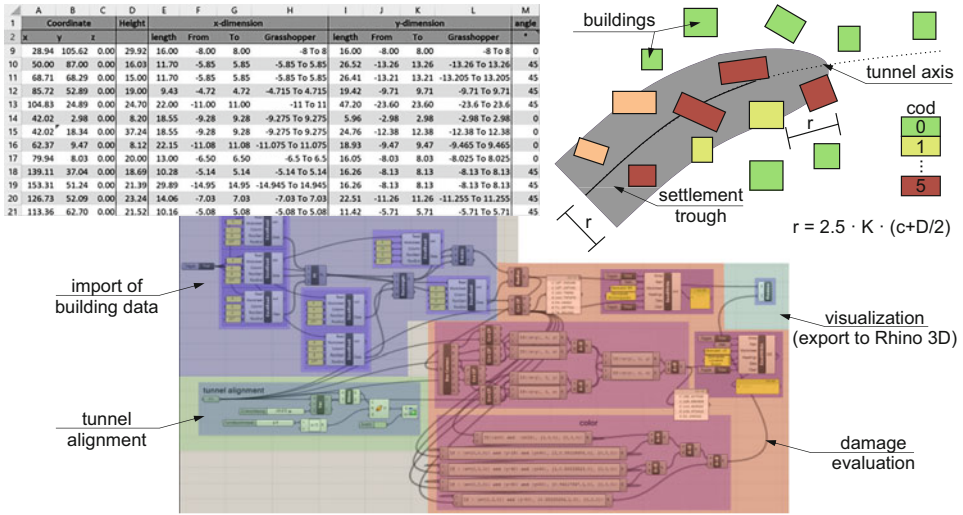
Fig. 6.60 Building coordinates (top left); Computational boundaries (top right); algorithmic implementation in Grasshopper 3D (bottom)

(NURBS). Corresponding constraint points or boundary conditions can be introduced during modeling using NURBS by means of corresponding support points. Furthermore, it is possible to shift an arbitrarily modeled alignment holistically.

6.5.4 Visualized Damage Assessment Illustrated by the Wehrhahn Line

The previously presented methods shall be applied to the reference project Wehrhahn-Linie in Düsseldorf, [49, 75]. The entire WHL has a length of 3.4 km. Here, the east branch of the alignment, which is approximately 800 m long, is used for visualization. Data on 285 buildings are available along this east branch. The tunnel was excavated at a depth of about 12.5 m with an external diameter of 9.2 m in loose to medium dense sands and gravels.

6.5.4.1 Application of Damage Assessment Coefficients

112 structures are located in the vicinity of the WHL tunnel and are evaluated using the aforementioned damage assessment coefficients. Figure 6.61 (top) shows a summary of the maximum cod for all 112 structures. Clearly, a direct underpass of the facade leads to higher damages which decrease with increasing eccentricity. In total, there are 16 out of 112 vulnerable buildings. All of them have a cod > 0.

Following a basic plausibility check of the prognosis, the risk analysis is performed. This analysis serves on the one hand to determine the occurrence or exceedance probability of potential efforts for damage maintenance, and on the other hand to determine the
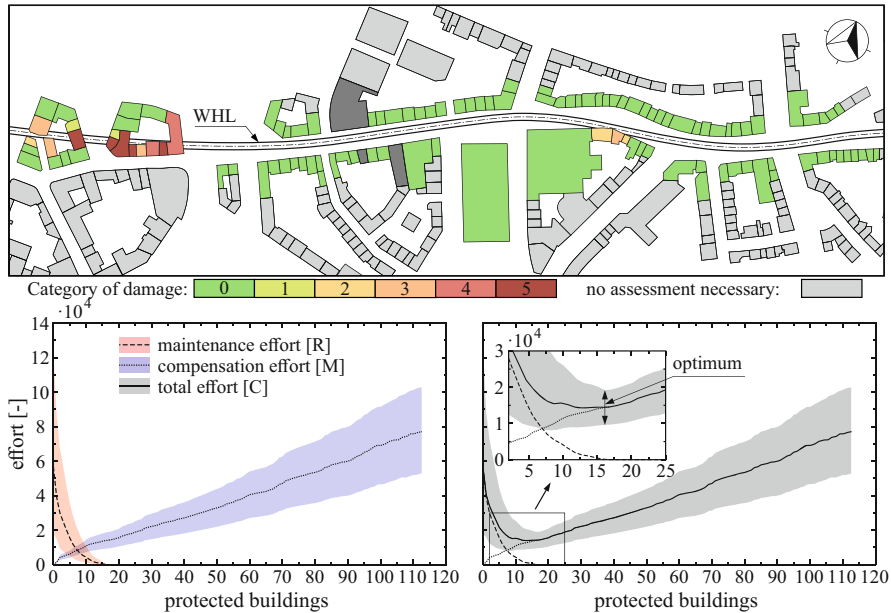
Fig. 6.61 Maximum expected category of damages for buildings along the WHL (top); Uncertain risk simulation: damage risk, compensation measures (bottom left) and total effort (bottom right) [59]

effort and benefit of potential preemptive settlement reducing measures under uncertain boundary conditions, such as compensation injections.

If the risk measures for the minimum, average and maximum maintenance efforts are determined successively for the 112 facades, the uncertain risk of damage can be represented as a function of buildings protected by compensation injections (Fig. 6.61, bottom left).

As expected, this damage risk has the highest maintenance effort at 0 protected structures. It decreases continuously with an increasing number of protected structures until it reaches a minimum effort of $R = 0$ for 16 protected structures. These 16 structures represent the critical buildings of Figure 6.61 (top) with cod > 0. For each building removed from the risk simulation, the uncertain effort of the compensation injections increases. The positive effect of the compensations is recognizable up to 16 protected buildings, whereas for the remaining 96 buildings – which permanently are in cod 0 – the compensations only lead to an increased effort but negligible benefits. The sum of the two curves results in the uncertain total effort (Fig. 6.61, bottom right).

6.5.4.2 Deploying the Interactive Tool

Figure 6.62, (top left) shows the structural damage assessment of the WHL. In the analysis, possible diagonal, corner, and side excavations as well as the construction stages were
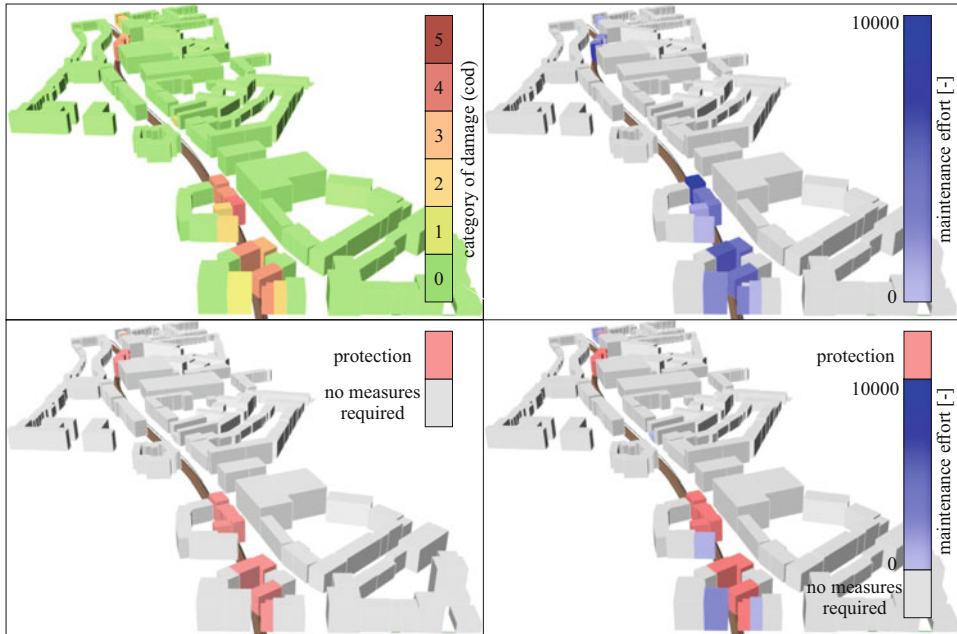
Fig. 6.62 Predicted categories of damage for a possible alignment along the WHL (top left); maintenance as a function of the category of damage (top right); localization of suitable compensation injections (bottom left); visualization of the maintenance and the compensation injections (bottom right)

taken into account. Basically, for all buildings located in the range $r = 2.5K(c + D/2)$ to the tunnel axis, the damage in the final state as well as in the construction state is determined. However, only the maximum damage is shown in the visualization. In addition to the structural damage, the extended damage indices can also be visualized in order to obtain direct visual information on the maintenance effort for a building (Fig. 6.62, top right). Furthermore, a direct visualization of possible compensation measures as well as a comparison between compensation and maintenance measures is possible (Fig. 6.62, bottom).

6.6 Interactive Assessment of Tunnel Alignment

The interactive platform uses information from the planning process to generate new data. Certain boundary conditions can be interpreted as geometry, such as a range constraint or reference points. However, this procedure can become much more significant if, for example, settlement analysis is taken into account.
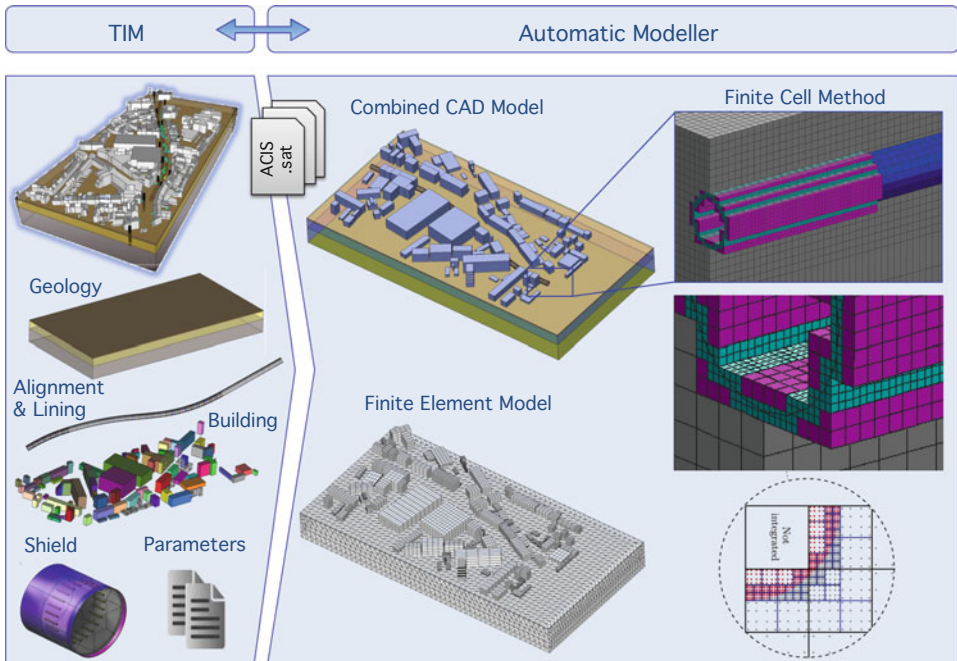
Fig. 6.63 Automated creation and analysis of the FE simulation model ekate 2.0 based on TIM CAD-Models

6.6.1   Simulation Strategy for a Seamless Connection to TIM Models

For the assessment of the impact of various tunnel alignments, e.g., settlements, face stability, damage criteria, a process-oriented finite element (FE) simulation model for mechanized tunneling (ekate) is integrated in the interactive platform for tunnel track design. For this purpose, the FE-simulation model is coupled with the Tunneling Information Model (TIM) (see Fig. 6.63). This coupling allows automatic extraction of all relevant information (geology, alignment, lining, existing infrastructure, material, and process parameters) needed for the numerical model and subsequently performing a FE analysis for the tunnel drive.

6.6.2   Interoperability

In order to keep the TIM independent from the external applications, e.g. the simulation process, the TIM and the automatic modeler (introduced in Sect. 6.4.2) interact using a web-based service (see Fig. 6.64). This allows the TIM to autonomously invoke the sim-
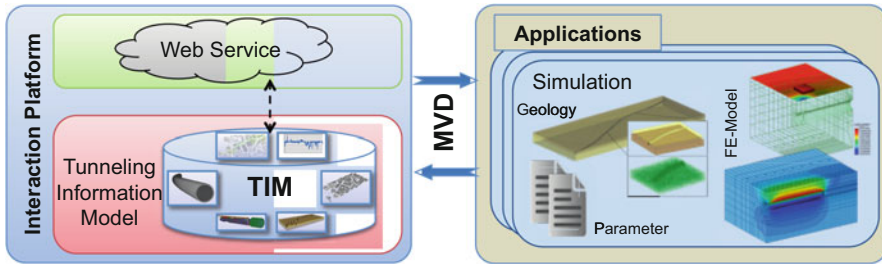
Fig. 6.64 Schematic representation of TIM applications interacting through a web service which enables simulation software to automatically extract the required data and parameters in order to configure and generate the simulation model and perform simulations

ulation for a certain domain and automatically configure, generate and run the required three-dimensional finite element model. The web-based interface provides a simple interaction platform that allows any additional applications to access and exchange data in the TIM through predefined Model View Definitions (MVD's) in a general manner. For the application of numerical simulation, the TIM can be invoked for a set of parameters that are required for the numerical simulation, which is read from the centralized database and automatically provided to the simulation.

6.6.3 Optimizing the Modeler for Various Tunnel Alignments

To further enhance the efficiency of model generation for various tunnel alignments, a new modeling strategy is integrated in the FE-simulation model that is flexible to incorporating various tunnel alignments without requiring generation of a new finite element mesh for each path. This new strategy employs CutFEM, which is based on a structured regular mesh of the entire domain and does not require the spatial discretization to follow the geometry of the (moving) excavation boundaries (see Fig. 6.65). The boundaries of the soil layers, the excavation geometries and the tunnel alignment are directly transferred as NURBS surface geometries in the ekate-software without any need for a new mesh generation. Adaptive Octree algorithms with quadrature refinement is used to realize geometric and material boundaries in the model. This procedure is a pre-requisite to enhance the interoperability with the interactive track design tool. On one the hand, the FE-simulation can be invoked autonomously for various tunnel alignments. On the other hand, the results of the numerical simulation are automatically incorporated in the digital planning tool.

To enable real-time interaction with the platform, a surrogate modeling approach for various tunnel alignments can be trained beforehand based on synthetic data from FE-simulations and then integrated in the interactive platform.
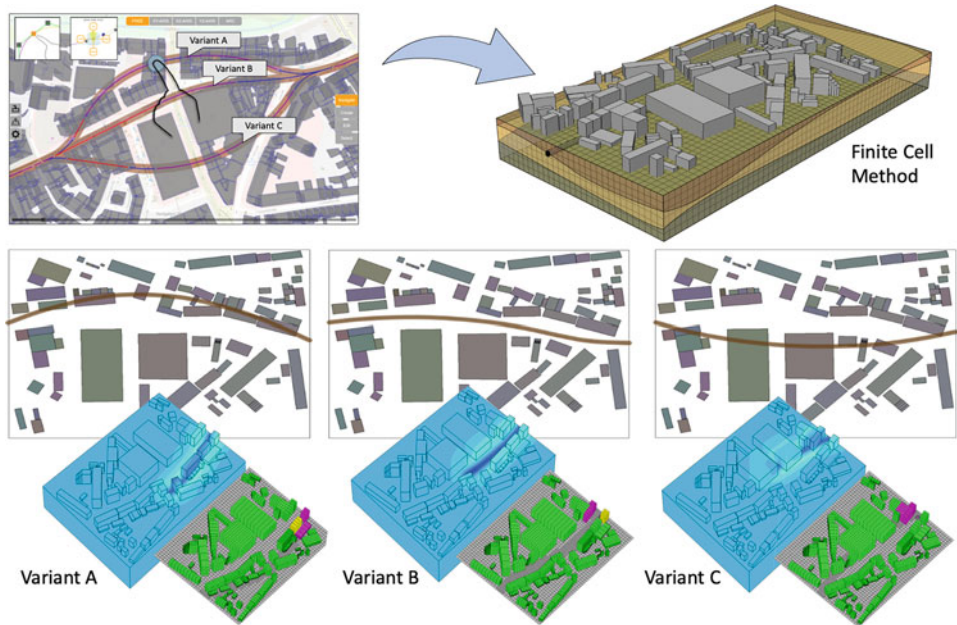
Fig. 6.65 Automatic generation of Finite Cell simulation model for various tunnel alignments based on TIM CAD-Models

6.6.4   A Surrogate Model For Real-Time Tunnel Alignment Assessment

The surrogate model is established and applied during the design stage of a tunnel project with a purpose of interactively investigating different possibilities of tunnel alignment by providing the associated surface settlement field in real-time. In the offline stage, i.e. before the interactive real-time design procedure, the process-oriented CutFEM model described in Sect. 6.4.3 is used to simulate the mechanized tunneling processes with various tunnel alignments. The resulting settlement fields will be used to construct the surrogate model. For each simulation, input parameters are coordinates of a set of points representing the tunnel alignment. In general, tunnel alignments can be in any shape satisfying the predefined design requirements. To have a parametric representation of a tunnel alignment, the alignment is assumed to be represented by a cubic function. As the first step to create an arbitrary alignment, some control points, which divide the tunnel alignment into several parts following the X direction, are generated using the Latin Hypercube sampling. A fitting step is performed to determine parameters of an appropriate cubic function which passes through these control points. Subsequently, coordinates of all input points are determined based on the fitted cubic function. These coordinates are then sent to the CutFEM model to execute the simulations as well as stored as the inputs of the surrogate model. Figure 6.66 presents inputs of the surrogate model for an illustrative example, which are possible tunnel alignments in three-dimensional space.
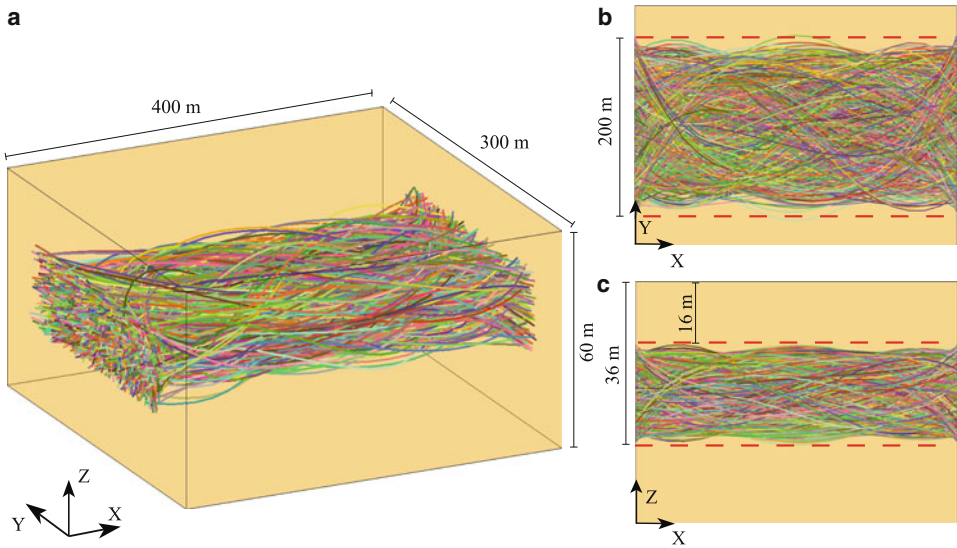
Fig. 6.66 **a** Possible three-dimensional tunnel alignments, **b** design constraints for the width of tunnel alignments, **c** design constraints for the depth of tunnel alignments
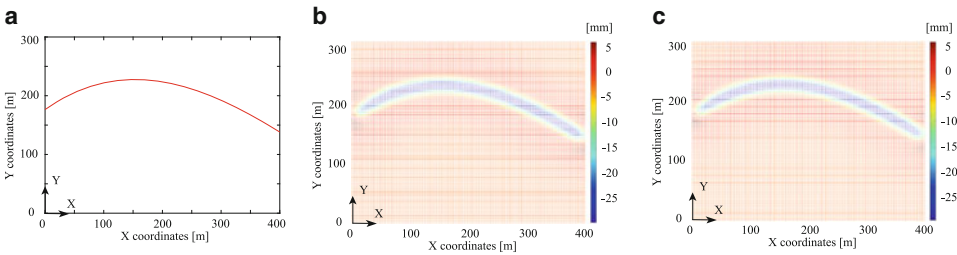
Fig. 6.67 Settlement prediction for a validation tunnel alignment scenario. **a** Tunnel alignment, **b** prediction (POD-RBF), **c** reference (CutFEM simulations)

The objective of the surrogate model is to predict the complete surface settlement field for an arbitrary tunnel alignment with similar accuracy as the original CutFEM model. In the context of real-time applications, with respect to each intuitive alignment change, input points, which are well approximated with the new alignment, will be created using the curve fitting method. With the coordinates of the new input points, a surrogate model based on the combination of Proper Orthogonal Decomposition and Radial Basis Functions (POD-RBF) methods is employed to approximate the spatial field of surface displacements. The predicted results are used to support the design engineer in selecting appropriate alignments for further investigations. More details about the method can be found in [17, 66].

To illustrate the usage of the POD-RBF model, a representative example is performed, in which Fig. 6.67 depicts the very good agreement between the predicted settlement ob-

Table 6.5 Prediction performance of the POD-RBF surrogate model for three-dimensional tunnel alignment design example: L_2 norm error (in %)

No. of samples	10-fold cross validation										Avg.
	1	2	3	4	5	6	7	8	9	10	
500	24.0	23.0	23.8	25.2	23.8	22.0	22.6	23.7	23.8	23.4	**23.5**
2000	2.5	2.5	1.8	2.2	2.2	2.3	3.2	2.0	2.4	2.3	**2.4**

tained from the described POD-RBF surrogate model with 2000 samples and the reference solution from CutFEM model for an illustrative validation alignment.

Table 6.5 summarizes the L_2 norm prediction errors. One can see that, the prediction accuracy of the model is significantly increased when the data set is refined.

The L_2 norm errors from 10 fold-cross validation prove the generalization and reliability of the surrogate model. While maintaining the prediction capability as compared to the CutFEM model, the surrogate model is able to considerably reduce the computation time from 6 to 10 hours to less than 1 second, Therefore, the POD-RBF surrogate model can substitute the CutFEM model for a real-time tunnel track design application.

References

1. H. Adeli. "Neural Networks in Civil Engineering: 1989-2000". In: *Computer-Aided Civil and Infrastructure Engineering* 16.2 (2001), pp. 126–142. ISSN: 1093-9687. https://doi.org/10.1111/0885-9507.00219.
2. A. Alsahly, J. Stascheit, and G. Meschke. "Advanced finite element modeling of excavation and advancement processes in mechanized tunneling". In: *Advances in Engineering Software* 100 (2016), pp. 198–214. https://doi.org/10.1016/j.advengsoft.2016.07.011.
3. P. B. Attewell, J. Yeats, and R. Selby. "Soil movements induced by tunnelling and their effects on pipelines and structures". In: (1986).
4. S. Balay et al. *PETSc Users Manual*. Tech. rep. Argonne National Laboratory, 2016.
5. Baukosteninformationszentrum. *Building costs 2017: Old buildings - Statistical cost parameters for buildings*. 2017.
6. F. Beck, A. Borrmann, and T. H. Kolbe. "The need for a differentiation between heterogeneous information integration approaches in the field of "BIM-GIS Integration": a literature review". In: *ISPRS Annals of the Photogrammetry, Remote Sensing and Spatial Information Sciences* 6 (2020), pp. 21–28. https://doi.org/10.5194/isprs-annals-VI-4-W1-2020-21-2020.
7. G. Beer, ed. *Numerical Simulation in Tunnelling*. Wien – New York: Springer, 2003.
8. J. Beetz and A. Borrmann. "Benefits and limitations of linked data approaches for road modeling and data exchange". In: *Workshop of the European Group for Intelligent Computing in Engineering*. 2018, pp. 245–261. https://doi.org/10.1007/978-3-319-91638-5_13.
9. A. Bezuijen et al. "Field measurements of grout pressure during tunnelling of the Sophia Rail Tunnel". In: *Soils and Foundations* 44.1 (2004), pp. 39–48.
10. R. de Boer. *Theory of Porous Media – highlights in the historical development and current state*. Vol. 2. Berlin, Heidelberg, New York: Springer-Verlag, 2000.

11. A. Borrmann et al. "Multi-scale geometric-semantic modeling of shield tunnels for GIS and BIM applications". In: *Computer-Aided Civil and Infrastructure Engineering* 30.4 (2015), pp. 263–281.

12. M. D. Boscardin and E. J. Cording. "Building Response to Excavation–Induced Settlement". In: *Journal of Geotechnical Engineering* 115.1 (1989), pp. 1–21. ISSN: 0733-9410. https://doi.org/10.1061/(ASCE)0733-9410(1989)115:1(1).

13. H. G. Bui and G. Meschke. "A parallelization strategy for hydro-mechanically coupled mechanized tunneling simulations". In: *Computers and Geotechnics* 120 (2020), p. 103378.

14. H.-G. Bui et al. "A CutFEM based framework for numerical simulations of machine driven tunnels with arbitrary alignments". In: *Computers and Geotechnics* 144 (2022).

15. buildingSMART. *IFC-Tunnel Requirements Analysis Report*. 2020.

16. J. B. Burland and C. P. Wroth. "Settlement of buildings and associated damage". In: *Prentech Press* (1974), pp. 611–654.

17. B. Cao, S. Freitag, and G. Meschke. "A hybrid RNN-GPOD surrogate model for real-time settlement predictions in mechanised tunnelling". In: *Advanced Modeling and Simulation in Engineering Sciences* 3.5 (2016), pp. 1–22.

18. B. T. Cao et al. "Artificial Neural Network Surrogate Modelling for Real-Time Prediction of Soil-Structure Interactions in Mechanised Tunneling". In: *Advances in Engineering Software* 149.11 (2020), pp. 61–67. https://doi.org/10.1016/j.advengsoft.2020.102869.

19. B. T. Cao et al. "Real-time Reliability Analysis of Tunneling-induced Building Damage". In: *Proceedings of the 7th Asian-Pacific Symposium on Structural Reliability and Its Applications*. Tokyo, 2020. https://doi.org/10.15083/00079823.

20. O. Coussy. "Poromechanics of freezing materials". In: *Journal of the Mechanics and Physics of Solids* 53.8 (2005), pp. 1689–1718. ISSN: 00225096. https://doi.org/10.1016/j.jmps.2005.04.001.

21. M. Crisfield. *Nonlinear Finite Element Analysis of Solids and Structures*. 1. Vol. 1. John Wiley & sons, 1991.

22. P. Dadvand, R. Rossi, and E. Oñate. "An Object-oriented Environment for Developing Finite Element Codes for Multi-disciplinary Applications". In: *Archives of Computational Methods in Engineering* 17.3 (2010), pp. 253–297. https://doi.org/10.1007/s11831-010-9045-2.

23. H.-P. G. Darcy. "Les fontaines publiques de la ville Dijon: exposition et application des principes a suivre et des formules a employer dans les questions de distribution déau ; ouvrage terminé par un appendice relatif aux fournitures déau de plusieurs villes au filtrage des eaux à la fabrication des tuyaux de fonte, de plomb, de tole et de bitume." PhD thesis. Paris: Dalmont, 1856.

24. A. Düster et al. "The finite cell method for three-dimensional problems of solid mechanics". In: *Computer Methods in Applied Mechanics and Engineering* 197 (2008), pp. 3768–3782.

25. C. M. Eastman et al. *BIM handbook: A guide to building information modeling for owners, managers, designers, engineers and contractors*. John Wiley & Sons, 2011.

26. M. J. Egenhofer. "A formal definition of binary topological relationships". In: *International conference on foundations of data organization and algorithms*. 1989, pp. 457–472. https://doi.org/10.1007/3-540-51295-0_148.

27. V. Fargnoli, C. G. Gargano, and Boldini, D., Amorosi, A. "3D numerical modelling of soil-structure interaction during EPB tunnelling". In: *Géotechnique* 65.1 (2015), pp. 236–246. https://doi.org/10.1680/geot.14.P.091.

28. V. E. Gall et al. "A Holistic Approach for the Investigation of Lining Response to Mechanized Tunneling induced Construction Loadings". In: *Underground Space* 3.1 (2018), pp. 45–60. https://doi.org/10.1016/j.undsp.2018.01.001.

29. German Tunnelling Committee (DAUB). *Recommendations for the design, production and installation of segmental rings*. Tech. rep. Deutscher Ausschuss für unterirdisches Bauen e. V. (DAUB), 2013.

30. S. Goss et al. "Self-organized Shortcuts in the Argentine Ant". In: *Naturwissenschaften* 76 (1989), pp. 579–581.

31. M. T. Hagan et al. *Neural network design*. 2nd. Wrocław: Amazon Fulfillment Poland Sp. z o.o, 2014. ISBN: 9780971732117.

32. F. Hegemann, K. Lehner, and M. König. "IFC-based Product Modeling for Tunnel Boring Machines." In: *eWork and eBusiness in Architecture, Engineering and Construction*. Ed. by G. Gudnason and R. Scherer. CRC Press, 2012, pp. 289–296.

33. F. Hegemann. "A hybrid ground data management concept for tunneling projects" (2016).

34. F. Hegemann et al. "Hybrid ground data model for interacting simulations in mechanized tunneling". In: *Journal of computing in civil engineering* 27.6 (2013), pp. 708–718.

35. A. H. Hor, A. Jadidi, and G. Sohn. "BIM-GIS integrated geospatial information model using semantic web and RDF graphs". In: *ISPRS Ann. Photogramm. Remote Sens. Spat. Inf. Sci* 3.4 (2016), pp. 73–79. https://doi.org/10.5194/isprs-annals-III-4-73-2016.

36. K. Hornik, M. Stinchcombe, and H. White. "Multilayer feedforward networks are universal approximators". In: *Neural Networks* 5.2 (1989), pp. 359–366. ISSN: 08936080. https://doi.org/10.1016/0893-6080(89)90020-8.

37. International Organization for Standardization. *Geographic information - Simple feature access – Part 1: Common architectur: ISO 19125-1*. 2004.

38. ISO. *ISO 16739-1:2018: Industry Foundation Classes (IFC) for data sharing in the construction and facility management industries — Part 1: Data schema*. International Organization for Standardization, 2018, p. 1474.

39. Y. Ji et al. "Exchange of parametric bridge models using a neutral data format". In: *Journal of Computing in Civil Engineering* 27.6 (2012), pp. 593–606.

40. G. Karypis and V. Kumar. *METIS – A Software Package for Partitioning Unstructured Graphs, Partitioning Meshes and Computing Fill-Reducing Orderings of Sparse Matrices*. Tech. rep. University of Minnesota, 1998.

41. T. Kasper. "Finite Elemente Simulation maschineller Tunnelvortriebe in wassergesättigtem Lockergestein". PhD thesis. Lehrstuhl für Statik und Dynamik, Ruhr-Universität Bochum, 2005.

42. C. Koch, A. Vonthron, and M. König. "A tunnel information modelling framework to support management, simulations and visualisations in mechanised tunnelling projects". In: *Automation in Construction* 83 (2017), pp. 78–90.

43. M. König et al. "Taschenbuch für den Tunnelbau 2017". In: 978-3-433-03168-1. Wilhelm Ernst & Sohn, 2016. Chap. Building Information Modeling (BIM) im maschinellen Tunnelbau, pp. 199–232.

44. Y. Kurata. "The 9+-intersection: A universal framework for modeling topological relations". In: *International Conference on Geographic Information Science*. 2008, pp. 181–198. https://doi.org/10.1007/978-3-540-87473-7_12.

45. T. Laursen. *Computational Contact and Impact Mechanics*. Springer, Berlin-Heidelberg, 2002.

46. G. Lee, R. Sacks, and C. M. Eastman. "Specifying parametric building object behavior (BOB) for a building information modeling system". In: *Automation in construction* 15.6 (2006), pp. 758–776.

47. E. Mahmoudi, M. Stepien, and M. König. "Optimisation of geotechnical surveys using a BIM-based geostatistical analysis". In: *Smart and Sustainable Built Environment* (2021).

48. P. Mark and B. Schnütgen. "Limits of Elastic Material Behaviour of Concrete". In: *Beton- und Stahlbetonbau* 96.5 (2001), pp. 373–378. ISSN: 00059900. https://doi.org/10.1002/best.200100400.

49. P. Mark et al. "Radar interferometry for monitoring of settlements in tunnelling". In: *Bautechnik* 89.11 (2012), pp. 764–776. ISSN: 09328351. https://doi.org/10.1002/bate.201200035.

50. A. Marwan. "Computational Analysis of Segmental Linings in Mechanized Tunneling". PhD thesis. Ruhr University Bochum, 2019.

51. A. Marwan et al. "Optimization of artificial ground freezing in tunneling in the presence of seepage flow". In: *Computers and Geotechnics* 75 (2016), pp. 112–125. ISSN: 18737633. https://doi.org/10.1016/j.compgeo.2016.01.004.

52. G. Meschke. "Consideration of aging of shotcrete in the context of a 3D viscoplastic material model". In: *International Journal for Numerical Methods in Engineering* 39 (1996), pp. 3123–3143.

53. G. Meschke, C. Kropik, and H. Mang. "Numerical analyses of tunnel linings by means of a viscoplastic material model for shotcrete". In: *International Journal for Numerical Methods in Engineering* 39 (1996), pp. 3145–3162.

54. G. Meschke et al. "Real-Time Simulations for Process Steering Support". In: *Tunnel* 1 (2021), pp. 28–33.

55. F. Nagel. "Numerical modelling of partially saturated soil and simulation of shield supported tunnel advance". PhD thesis. Ruhr University Bochum, 2009.

56. M. Neuhausen et al. "Window detection in facade images for risk assessment in tunneling". In: *Visualization in Engineering* 6.1 (2018), pp. 1–16. ISSN: 2213-7459. https://doi.org/10.1186/s40327-018-0062-9.

57. J. Ninić et al. "Integrated parametric multi-level information and numerical modelling of mechanised tunnelling projects". In: *Advanced Engineering Informatics* 43 (2020), p. 101011. ISSN: 1474-0346. https://doi.org/10.1016/j.aei.2019.101011.

58. S. Nishimura et al. "THM-coupled finite element analysis of frozen soil: formulation and application". In: *Géotechnique* 59.3 (2009), pp. 159–171. ISSN: 0016-8505. https://doi.org/10.1680/geot.2009.59.3.159.

59. M. Obel. "Ein konsekutives Konzept zur probabilistischen Risokobewertung setzungsinduzierter Bauwerksschädigungen". Dissertation. Bochum: Ruhr University Bochum, 2019.

60. M. Obel, M. A. Ahrens, and P. Mark. "Metamodel-Based Risk Analysis of Structural Damages due to Tunneling-Induced Settlements". In: *ASCE-ASME Journal of Risk and Uncertainty in Engineering Systems, Part A: Civil Engineering* 88.12 (2020), pp. 61–71. https://doi.org/10.1061/AJRUA6.0001092.

61. M. Obel and P. Mark. "Minimization of Compensation Measures Based on a Probabilistic Risk Simulation Concept". In: *ITA-AITES World Tunnel Congress (WTC2020)* (2020), pp. 103–108.

62. M. Obel et al. "Settlement Risk Assessment by Means of Categorized Surface Infrastructure". In: *Proceedings of the 10th International Conference on Structural Analysis of Historical Constructions*. Leuven, 2016. https://doi.org/10.1201/9781315616995-68.

63. Open Geospatial Consortium. *A Geographic Query Language for RDF Data*. 2012.

64. Open Geospatial Consortium. *Geographic information – Well-known text representation of coordinate reference systems*. 2019.

65. Open Geospatial Consortium. *OpenGIS Implementation Standard for Geographic information – Simple feature access – Part 1: Common architecture [Corrigendum]*. Ed. by J. R. Herring. 2011. https://doi.org/10.25607/OBP-630.

66. Z. Ostrowski, R. Bialecki, and A. Kassab. "'Solving inverse heat conduction problems using trained POD-RBF network inverse method". In: *Inverse Problems in Science and Engineering* 16.1 (2008), pp. 39–54.

67. R. B. Peck. "Deep excavations and tunneling in soft ground". In: *Proceedings of the 7th International Conference on Soil Mechanics and Foundation Engineering*. Vol. 4. 1969, pp. 225–290.

68. D. M. Potts and L. Zdravkovic. *Finite Element Analysis in Geotechnical Engineering*. Thomas Telford, 1999.

69. D. Rebolj et al. "Development and application of a road product model". In: *Automation in construction* 17.6 (2008), pp. 719–728.

70. Robert McNeel & Associates. *Grasshopper 3D*. 2007.

71. Robert McNeel & Associates. *Rhinoceros 3D*. 1980.

72. J. Rudolf, V. Gall, and A. Nitschke. "Selection of alignment and tunneling methods in urban settings". In: *Proceedings of the World Tunnel Congress*. 2008, pp. 22–24.

73. R. J. Scherer and S.-E. Schapke. "A distributed multi-model-based management information system for simulation and decision-making on construction projects". In: *Advanced Engineering Informatics* 25.4 (2011), pp. 582–599.

74. S. Schindler et al. "An interaction platform for mechanized tunnelling. Application on the Wehrhahn-Line in Düsseldorf (Germany) / Eine Interaktionsplattform für maschinelle Tunnelvortriebe. Anwendung am Beispiel der Wehrhahn-Linie in Düsseldorf". In: *Geomechanics and Tunnelling* 7.1 (2014), pp. 72–86.

75. S. Schindler et al. "Radar interferometry based settlement monitoring in tunnelling: Visualization and accuracy analyses". In: *Visualization in Engineering* 4.7 (2016), pp. 1–16. ISSN: 2213-7459. https://doi.org/10.1186/s40327-016-0034-x.

76. J. C. Simo and T. Laursen. "An augmented Lagrangian treatment of contact problems involving friction". In: *Computers & Structures* 42.1 (1992), pp. 97–116.

77. J. Stascheit. "Parallelisation and model generation methods for large-scale simulations of shield tunnelling processes". PhD thesis. Ruhr-Universität Bochum, 2010.

78. M. Stepien, D. Pawlowski, and A. Vonthron. "IFC-basierte Modellierung von Tunnelbauwerksmodellen". In: *Forum Bauinformatik: Tagungsband - Berichte aus der Bauinformatik* (2016), pp. 29–39.

79. M. Stepien, A. Vonthron, and M. König. "Integrated platform for interactive and collaborative exploration of tunnel alignments". In: *International Conference on Computing in Civil and Building Engineering*. Springer. 2020, pp. 320–334.

80. M. Stepien et al. "An Approach for Cross-Data Querying and Spatial Reasoning of Tunnel Alignments". In: *Advanced Engineering Informatics* (2022). submitted.

81. M. Stepien et al. "An approach for cross-data querying and spatial reasoning of tunnel alignments". In: *Advanced Engineering Informatics* 54 (2022), p. 101728.

82. K. Terzaghi. *Theoretical Soil Mechanics*. John Wiley and Sons, 1943.

83. M. Thewes et al. "Decision Model for Furnishing Tunnels with safety technical Systems, Part 1: General Conditions for Transportation Tunnels". In: *Tunnel – International Journal of Subsurface Construction* 32.8 (2013), pp. 38–47.

84. M. Thewes et al. "Decision Model for Furnishing Tunnels with safety technical Systems, Part 2: Comparison of variations and model calculation". In: *Tunnel – International Journal of Subsurface Construction* 33.1 (2014), pp. 17–27.

85. D. Toll et al., eds. *Information Technology in Geo-Engineering. 2nd International Conference on Information Technology in Geo-Engineering*. 2014.

86. H.-P. Vetsch et al. "Gotthard Base Tunnel – Choice of the tunnel system from today's point of view". In: *Geomechanics and Tunnelling* 9.2 (2016), pp. 79–93. https://doi.org/10.1002/geot.201600006.

87. S. Vilgertshofer et al. "Linking BIM and GIS models in infrastructure by example of IFC and CityGML". In: *Computing in Civil Engineering 2017*. 2017, pp. 133–140. https://doi.org/10.1061/9780784480823.017.

88. A. Vonthron, C. Koch, and M. König. "Removing duplicated geometries in IFC models using rigid body transformation estimation and flyweight design pattern". In: *Visualization in Engineering* 6.1 (2018), pp. 1–15.

89. D. J. Walton and D. S. Meek. "A controlled clothoid spline". In: *Computers & Graphics* 29.3 (2005), pp. 353–363.

90. L. Wang et al. "An approximation approach of the clothoid curve defined in the interval $[0, \pi/2]$ and its offset by free-form curves". In: *Computer-Aided Design* 33.14 (2001), pp. 1049–1058.

91. A. Yazdani-Chamzini and S. H. Yakhchali. "Tunnel Boring Machine (TBM) selection using fuzzy multicriteria decision making methods". In: *Tunnelling and Underground Space Technology* 30 (2012), pp. 194–204. https://doi.org/10.1016/j.tust.2012.02.021.

92. W. N. Yiu, H. J. Burd, and C. M. Martin. "Finite-element modelling for the assessment of tunnel-induced damage to a masonry building". In: *Géotechnique* 67.9 (2017), pp. 1–15. https://doi.org/10.1680/jgeot.sip17.P.249.

93. H. Yu. "CASM: A unified state parameter model for clay and sand". In: *International Journal for Numerical and Analytical Methods in Geomechanics* 48 (1998), pp. 773–778.

94. M.-M. Zhou. "Computational simulation of soil freezing: multiphase modeling and strength upscaling". PhD thesis. Ruhr University Bochum, 2015.

95. M.-M. Zhou and G. Meschke. "A three-phase THM coupled FE model for freezing soils". In: *International Journal for Numerical and Analytical Methods in Geomechanics* 37.18 (2013). 10.1002/nag.2184, pp. 3173–3193.

96. M.-M. Zhou and G. Meschke. "Strength homogenization of matrix-inclusion composites using the linear comparison composite approach". In: *International Journal of Solids and Structures* 51 (2014), pp. 259–273.

97. M. M. Zhou and G. Meschke. "A multiscale homogenization model for strength predictions of fully and partially frozen soils". In: *Acta Geotechnica* 13.1 (2018), pp. 175–193. ISSN: 18611133. https://doi.org/10.1007/s11440-017-0538-0.

Real-Time Simulation for Steering the Tunnel Construction Process

Ba Trung Cao , Lukas Heußner , Annika Jodehl , Markus Obel,
Yara Salloum, Steffen Freitag , Markus König , Peter Mark ,
Günther Meschke , and Markus Thewes

B. T. Cao (✉) · G. Meschke
Structural Mechanics, Ruhr-Universität Bochum, Bochum, Germany
e-mail: ba.cao@rub.de

G. Meschke
e-mail: guenther.meschke@rub.de

L. Heußner · P. Mark
Concrete Structures, Ruhr-Universität Bochum, Bochum, Germany
e-mail: lukas.heussner@rub.de

P. Mark
e-mail: peter.mark@rub.de

A. Jodehl · M. Thewes
Tunneling and Construction Management, Ruhr-Universität Bochum, Bochum, Germany
e-mail: annika.jodehl@rub.de

M. Thewes
e-mail: markus.thewes@rub.de

M. Obel
Mark Ingenieure GmbH, Bochum, Germany
e-mail: m.obel@mark-ingenieure.de

Y. Salloum · M. König
Computing in Engineering, Ruhr-Universität Bochum, Bochum, Germany
e-mail: yara.salloum@rub.de

M. König
e-mail: koenig@inf.bi.rub.de

S. Freitag
Institute for Structural Analysis, Karlsruhe Institute of Technology, Karlsruhe, Germany
e-mail: steffen.freitag@kit.edu

Abstract

Currently, in mechanized tunneling, the steering of tunnel boring machines (TBM) in practice is mainly decided based on engineering expert knowledge and recorded monitoring data. In this chapter, a new concept of exploiting the advantages of simulation models to support the steering phase is presented, which allows optimizing the construction process. With the aim to support the steering decision during tunnel construction by means of real-time simulations, predictive simulation models are established in the initial planning phase of a tunnel project. The models are then capable of being continuously updated with monitoring data during the construction. The chapter focuses on explaining models for real-time predictions of logistics processes and tunneling induced settlements as well as the risk of building damage in more details. Additionally, application examples, which are practical-oriented, are also presented to illustrate the applicability of the proposed concept.

7.1 A Concept for Real-Time Simulations During the Tunneling Process

The mechanized tunneling process is characterized by a staged procedure of soil excavation at the tunnel face and lining erection, providing at the same time a continuous support of the soil by means of supporting fluids at the tunnel face and pressurized grouting of the tail gap. The construction logistics, interactions between the TBM, the support measures and the soil, including the groundwater, are the determining factors for the efficiency, the safety of the tunnel advancement and the risk of damage on the built-environment. Currently, decisions affecting the steering of TBMs are based upon engineering expert knowledge and monitoring data. However, using monitoring data implies that information (data) related to already passed situations is used to extrapolate on the future behavior of the soil-tunnel interactions.

In contrast, numerical methods have recently become an important tool to investigate and predict soil-structure interaction effects in the design phase of tunneling projects. The numerical simulations can also be employed to perform the system predictions simultaneously to the construction process in order to support the selection of adequate process parameters. Therefore, as an additional tool to usual process monitoring, process simulations, which must be obtained in real-time, can be used to effectively support controlling and steering of the tunneling construction processes.

The concept of real-time simulations for computational steering requires to set up predictive simulation models in the design stage of a tunneling project, which are continuously updated with monitoring data during the construction process, see Fig. 7.1. This allows to investigate different scenarios of the TBM operational parameters for subsequent excavation steps and can assist the engineers to make informed decisions aiming to optimize the construction process.
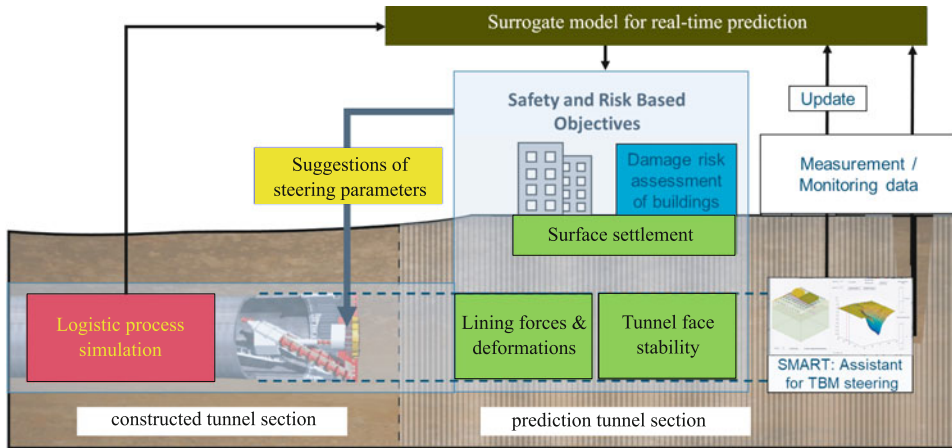
Fig. 7.1 The concept of real-time computational steering in mechanized tunneling with continuous model update

7.2   Process Simulation Models for Logistic Processes

Mechanized tunneling systems are an extraordinary combination of different manufacturing conditions in the construction industry. On the one hand, they consist of the manufacturing processes of a quasi-stationary factory plant, with its performance-determining core processes of tunneling, ring building and the scheduled inspection and maintenance of system-critical components, which are an indispensable part of the production cycle. The overall system performance also depends to a large extent on internal support processes in the supply chain, such as backup logistics, logistics in the tunnel, construction site equipment and the external supply and disposal of the construction site. On the other hand, disruptive influences from the complex interactions between subsoil and tunneling technology (face stability, advance, wear, bonding, groundwater, etc.), which are common in tunneling, as well as further disruptive influences from the machine technology (grout injection, electronics, hydraulics, pipe and cable extensions) and from the supply chain (tunnel trains, mixing plant) must be managed [46]. Figure 7.2 presents the interaction of performance and supply processes in mechanized tunneling.

Typical consequences of the interaction of the many influencing factors are, for example, excavation delays or production downtimes. According to this, the production output of a tunneling machine depends only to a comparatively small extent on the actual advance speed during excavation or on the duration of installation of the segment ring. In previous tunneling projects, unproductive time proportions of 40%-60% of the total working time were found [25]. System decisions have so far mostly been made on the basis of a limited decision horizon. The overall context remains unconsidered due to its complexity.

Nowadays, simulation models are used to support the planning and analysis of production processes. With the help of a simulation model, analyses of complex systems while
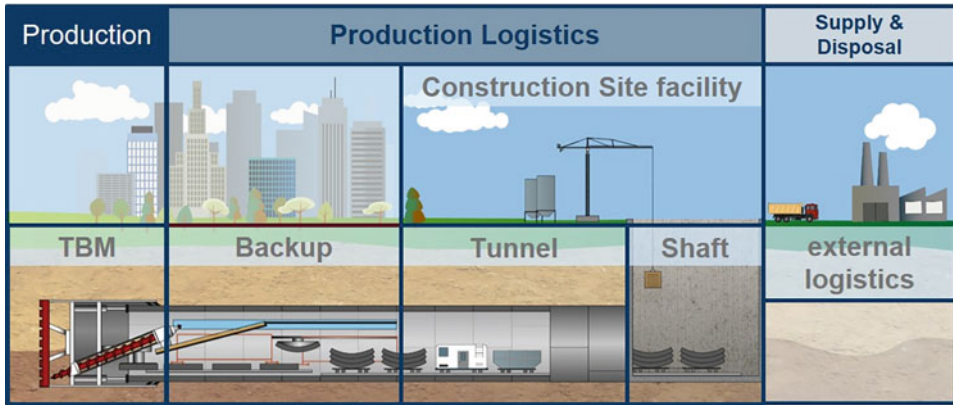
Fig. 7.2 Interaction of performance and supply processes in mechanized tunneling based on [14]

considering uncertainties can be carried out. Process-oriented simulation approaches are particularly suitable for the analysis of mechanized tunneling due to the repetitive construction sequence [39, 66]. Existing simulation approaches for mechanized tunneling, however, have so far mostly been focused on an isolated consideration of the production or logistics processes of a construction site [5, 28, 29]. Detailed models for the analysis of process interactions exist so far only for individual projects [50]. However, such project-specific simulation models can only be transferred to other tunnel construction projects with partly very different logistics systems with great effort [17].

The use of process simulation for an operational analysis and management of the advancement processes including all support processes and the scheduling of maintenance work are investigated and the main results are summarized in the following sections. In Sect. 7.2.1, modular simulation models for mechanized tunneling are described considering interdependencies of production processes, uncertain boundary conditions and disturbances. In the following section, Sect. 7.2.2, the influence of maintenance scheduling on the overall project performance is investigated. New concepts for a robust and optimized planning of maintenance intervals considering the wear of cutting tools are presented. Simulation models support a robust design of logistics processes in the planning stage of a project, but can also support decision making during project execution. The online application of simulation models is therefore presented in Sect. 7.2.3. Concepts for a real time assessment and the computational steering of the logistics and production processes are introduced.

7.2.1 Simulation of Logistics and Production Processes

In mechanized tunneling, there is a high proportion of unproductive time, as various processes are frequently disturbed or the main tunneling processes have to be interrupted for

logistical reasons. Since relationships between the process chains of mechanized tunneling have a major influence on the overall performance and efficiency of the tunnel boring machine (TBM), it is important to identify an overall context and investigate sensitivities of individual processes as well as process interactions. For this purpose, process simulation can be used, which not only provides a static view, but also a representation of the complex dynamic relationships. In this way, stochastic processes can also be analysed and their influence on the important tunneling processes can be investigated.

When modeling the individual core and support processes, a large number of boundary conditions must be taken into account. In addition to resources and material availability, these include current soil characteristics and settlements. This information is partly incomplete and subject to uncertainties. For a realistic analysis of the production processes, these boundary conditions must be classified and modeled. Subsequently, these boundary conditions can be consistently integrated into the simulation models. In addition to the fuzzy boundary conditions, typical production-related disturbances during tunneling must be included in the simulation. Addressing these issues, the simulation of logistics and production processes was investigated in the collaborative research center 837. The main results of this research were published in [46, 64, 70] and are summarized in this section.

7.2.1.1   Classification of Process Interactions

In this research project, the graphical modeling language SysML (System Modeling Language) was used to represent the complex interactions of the numerous processes of a mechanized tunneling system. It represents a subclass of the Unified Modeling Language (UML) according to the Object Management Group [58]. With the help of diagrams, a conceptual model description can be made, with which the production-technical processes and effective relationships can be classified and formalised in the context of mechanized tunneling using shield machines.

The hierarchical structure description is carried out by means of block diagrams (SysML Block Definition Diagram), representations of the intrinsic behavior of all system elements with the help of state diagrams (SysML State Machine Diagram) and a description of the interactions between the system elements with sequence diagrams (SysML Sequence Diagram).

With the help of the state machine diagrams (stm), requirements for the respective element and the consequences of the process execution can be illustrated. In addition, processes and states including their activation conditions can be described in a selected level of detail. As an example, Fig. 7.3 shows the intrinsic behavior of the erector in the state diagram. Processes are shown as rectangles, arrows represent conditions or consequences and the grey elements represent signals. The stm diagram shows the two main states of the erector, *idle* and *ringbuild*. The erector leaves the idle state as soon as the *AdvanceFinished* signal arrives. Then the ring build process starts with its sub-processes *pickUp* and *assemble*. *PickUp* depends in turn on the availability of segments. Thus, the process sequence of the erector including all conditions and requirements is shown within the diagram.
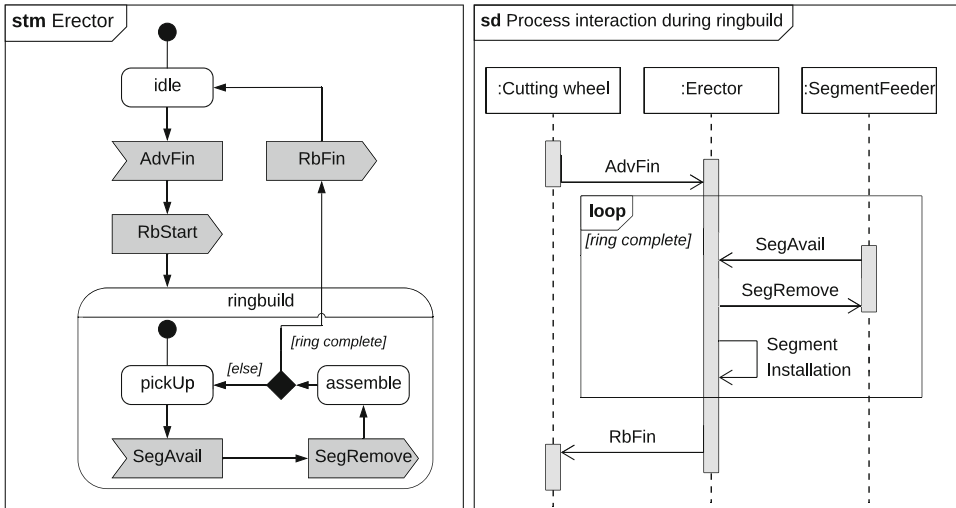
Fig. 7.3 State machine diagram of the erector to illustrate the modeling of processes (left), Sequence diagram to illustrate the modeling of process interdependencies during ring build (right) [64]

In addition to the description of the intrinsic behavior of an element, the formal description of the interactions between the individual system elements is also very important. An interaction describes, which changes of state of a system element leads to which reactions and thus changes of state of another system element. The interactions are structured hierarchically, represent the information to be exchanged and depend on the detail of the system elements used. As an example, Fig. 7.3 shows a sequence diagram to describe the process interaction required for the process ring build described above. It can be seen, that the *AdvanceFinished* signal is sent here from the cutting wheel. The signal whether a segment is available is in turn sent from the segment feeder.

Through formal modeling based on SysML, all essential elements, processes and interactions in mechanized tunneling can be described and discussed with the responsible technical planners. This increases the understanding of the system and simplifies the implementation in the form of discrete-event simulation models [46]. The formal description of all defined system elements can be found in [25, 63, 64, 70].

7.2.1.2   Representation of Uncertain and Incomplete Boundary Conditions

For simulation studies, the quality of the input data is crucial for the quality of simulation results. Therefore, the processing of input data is an essential step in the development of simulation models. In tunneling, many input data are subject to uncertainties (e.g. geological data) and process durations are subject to natural fluctuations. The advance speed of the TBM and the excavation performance of the cutting wheel, for example, are significantly influenced by the ground conditions encountered, which in turn have a high degree of prediction inaccuracy. The installation of the segments by the erector is controlled manually,

so that scattered sub-process durations also occur here. These uncertainties and fluctuations have to be displayed in the input data of the simulation model in order to provide a realistic representation of the real tunneling system [46].

A frequently used method for representing uncertainties and varying input data, which was also selected here, is the use of probability functions [1]. However, generating reasonable probability distributions that are as close to reality as possible is not trivial. Distribution fitting methods can be used for this purpose. In this process, probability distributions are closely fitted to the histogram of a given data set by suitably varying the distribution parameters. In a second step, goodness-of-fit tests should be performed to assess the quality of the fitted distributions to represent the data set [64].

Once a suitable probability distribution is identified, it can be implemented in the simulation model to generate discrete values at random within a Monte Carlo simulation. To generate robust predictions, running a large number of randomised simulations based on well-chosen distribution functions is advisable.

7.2.1.3 Simulation of Disturbances

In order to simulate production disturbances, their causes must be known. The diverse problems and disturbances of mechanized tunneling were divided into the following three classes in this research project: Production disturbances, logistical problems and propagation effects [46]. One speaks of production disturbances when a disturbance occurs directly at one of the main elements, such as the cutting wheel, the erector or the slurry circuit. As a result, the production process must be interrupted directly [46].

Logistical problems, such as disturbances in the delivery of material, lack of capacity or maintenance work, on the other hand, do not usually affect production directly. This is because support processes have a certain buffer time. In this way, troubleshooting can be made possible without, in the best case, interrupting production at all. For example, a malfunction in the delivery of segments has no effect on ring construction if a ring has already been delivered to the TBM. If, on the other hand, the disruption continues until another full driving cycle has been completed, so that no more segments are available for further installation, the production process must be interrupted. The same applies, for example, to malfunctions in the slurry circuit when the excavated material is pumped with liquid [46].

In the class of propagation effects, processes are considered that can react sensitively to disturbances of other processes. For example, a production disturbance that reaches a certain temporal threshold can cause the freshly delivered annular gap mortar to harden. Even if the triggering production disturbance is no longer present, tunneling cannot then continue without a new supply of annular gap mortar [46].

For the simulation of disturbances, time-related assumptions must be made. On the one hand, the time interval until a failure occurs must be determined (TBF: Time Between Failure) and, on the other hand, the time interval how long it takes to repair the failure (TTR: Time To Recover) has to be defined. The characteristic values should be specified for the process simulation with probability distributions. Shift reports, for example,
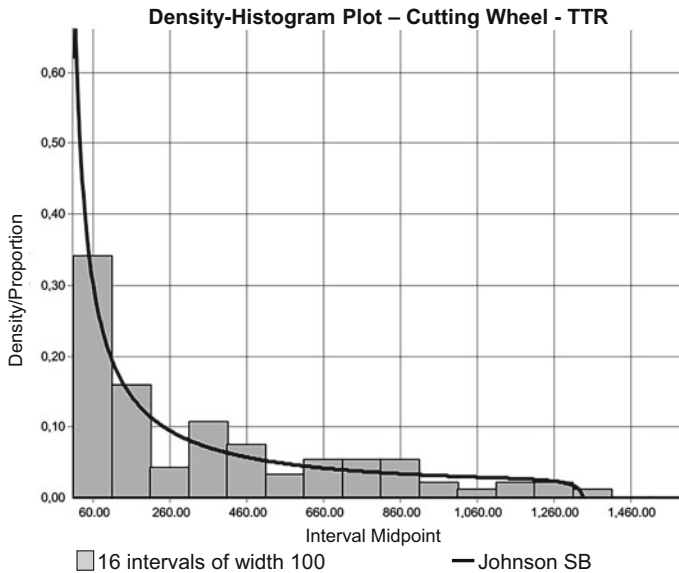
Fig. 7.4 Density-histogram plot for TTR of the cutting wheel with real project data (histogram) and fitted distribution (Johnson SB) [63]

can serve as a data basis. Especially for technical components, these parameters are also supplied by system manufacturers [46].

In this research project, various tunnel excavations were analysed with regard to their disturbances. Typical disturbances were classified and processed for reuse. The classified disturbances were analysed according to both frequency and intensity. Fig. 7.4 shows an example of a distribution function for an evaluation of the MTBF for the cutting wheel, evaluated on the basis of a reference project. Further evaluations of TBF and TTR can be found in [63, 64]. In addition to the time dependency, wear-related disturbances were also identified, the cause of which is triggered by a certain number of process repetitions or a distance driven. Significant correlations were identified between the frequency and intensity of the disruption and factors such as geology, maintenance strategy and quality of the material or lubricants used [46].

Individual disturbances can be combined into disturbance scenarios and scaled if necessary. This allows a set-up configuration to be analysed quickly under different boundary conditions. The analysis of disturbances and other varying variables requires stochastic simulation experiments (Monte Carlo simulation). This means that discrete values are generated for each simulation run based on the distribution functions. Thus, a large number of simulation runs must be carried out to ensure a meaningful and significant estimation of the distribution and statistical measures (e.g. mean values, variances or quantile values) of the resulting variables, such as utilisation, project duration and possible costs [46].

7.2.1.4 Simulation Models for Mechanized Tunneling

For the analysis of the logistics and production processes, process simulation models were developed, taking into account the previously described tunnel construction-specific boundary conditions. Simulations are used when investigations on the real system are not possible or are associated with too much effort and there are no analytical procedures that adequately represent the problem. In particular, the dynamic behavior and uncertain, statistical influences that make a classical investigation difficult can be included in the investigation of logistics and production processes via process simulation.

Implementation The presented simulation approach is implemented in the simulation framework ANYLOGIC [78]. This software allows a multi-method simulation (agent-based modeling, system dynamic modeling, discrete-event modeling). All simulation models created are hierarchically structured and configured according to a modular concept.

ANYLOGIC includes a native Java programming environment with which the complex interactions of the tunnel construction processes can be implemented in detail. The exchange of signals was carried out via an Observer-Observable design pattern (see [36]). Thus, signals are distributed to the corresponding elements via a central event manager instead of a direct exchange between the single elements.

Following the example in Sect. 7.2.1.1, for example, the signal *AdvanceFinished* is sent by the cutting wheel after completion of the advance and received by the event manager (see Fig. 7.5). In parallel, the *SegmentAvailable* signal is sent by the segment feeder to indicate that a segment is ready for installation. The event manager forwards these signals to the erector, which starts ring building. The end of ring building is again transmitted to the cutting wheel via the Event Manager and the signal *RingbuildFinished*. The use of the EventManager thus enables a flexible communication structure that allows the exchange

Fig. 7.5 Conceptual drawing of the event manager to realize a flexible process interaction [64]
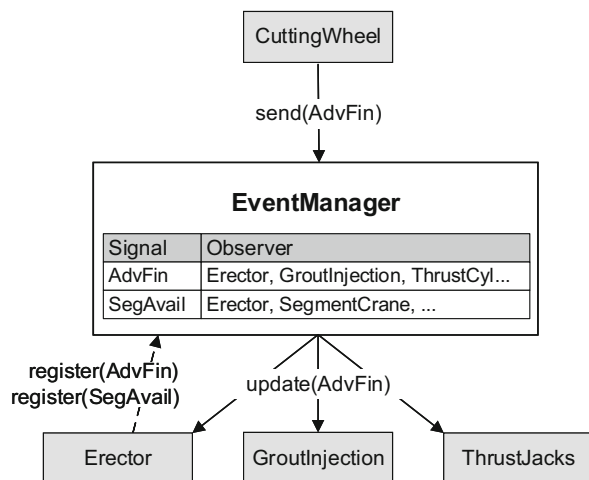
of modular model elements without the need for re-implementation of the entire signal exchange [64].

The individual state diagrams of the model components are visualized directly in the simulation model. This allows the behavior of the overall system to be viewed and checked at any time during the simulation [46].

The disturbance of the individual elements can be passed on to the respective affected elements due to the implemented process dependencies [64]. Analogous to the duration of the production processes for tunneling and ring building, the duration until the next occurrence of a disturbance, as well as the duration for repair (cf. 7.2.1.3), are mapped via distribution functions. In addition, the well-known package Stochastic Simulation in Java (SSJ), which was developed by the University of Montreal, can be integrated via the Java environment. This allows random values to be generated from more specialised probability functions in addition to the basic distribution functions available in ANYLOGIC [64].

Model design   The developed model displays the main elements of a mechanized tunneling project. The structure can vary depending on the main objective of the simulation study and the selected level of detail as well as depending on the project specific characteristics. The model consists for example of the main elements of a project *TBM*, *backup system*, *underground logistics system* and *surface facilities*. Each main element can consist of further sub-elements. For example, a TBM can be designed from individual elements such as a cutting wheel, erector, thrust cylinders and grout injection pump. As an example, a model construction of a project with a slurry shield machine is shown in Fig. 7.6.

In addition to these elements, components for defining geotechnical aspects and visualizing the results were also realised. The material flow between the elements can be defined interactively through special connections. The different components are implemented very
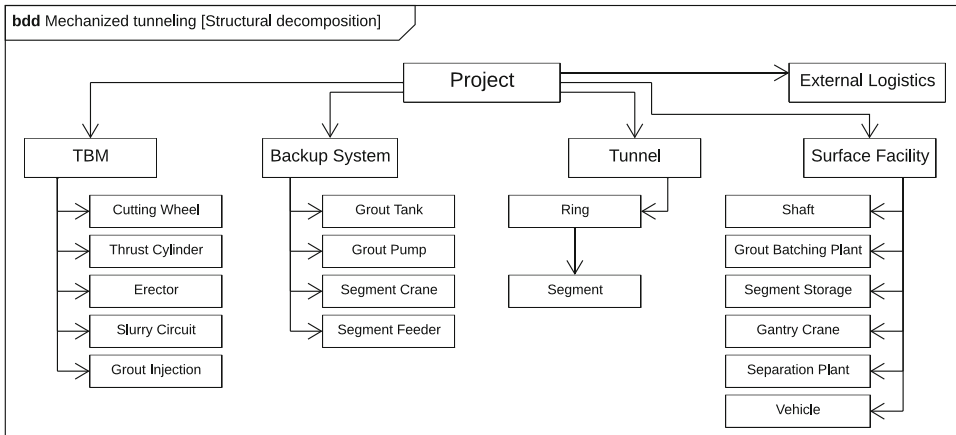
Fig. 7.6 Block definition diagram of a mechanized tunneling project [64]

Table 7.1 Possible Simulation investigations

Topics	Publication (example)
Influences on production, e.g.:	
Logistics	[46]
Disturbances in the main processes	[64]
Disturbances in the logistics processes	[64]
Uncertain parameters	[46]
Variation in above-ground logistics	[70]
Site layout	[69]
Maintenance strategies	[18]
Optimization of logistics components, e.g.:	
Tunnel transport system	[46]
Storage capacities at the construction site and on the trailer	[24]
Transport possibilities on the trailer	[24]
Robust maintenance scheduling	
Tool wear	[16]
Development of an empirical wear prediction model	[19]
Cost forecast related to maintenance and comparison of two project configurations	[14]
Real-time use of process simulation models	[43]

flexibly and can be used for different machine configurations and supply chains. Similar to the SysML formalisation in Fig. 7.6, a second level of hierarchy can be modeled to allow alternative configurations by swapping elements. The behavior of the mechanized tunneling components is implemented directly in ANYLOGIC through state diagrams following the formal descriptor of the interactions in Sect. 7.2.1.1.

Based on the results developed, a brief summary of possible investigations is given in Table 7.1. For each investigation, the objectives are briefly summarised and a corresponding paper is referenced in case of further interest.

7.2.2 Optimization of Maintenance Strategies

The overall efficiency of a project is highly influenced not only by the performance of the support processes, but also by the maintenance of cutting tools. Cutting tools, which are in direct contact with the ground during tunneling, are subject to a constant wear process. When tunneling in unstable ground conditions, however, the maintenance of the cutting tools is very costly and can cause long downtimes due to the tunnel face support. In order to reach the tools, the support medium in the excavation chamber must be replaced by compressed air. The modification of the face support carries the risk of settlements at the surface as well as blow-outs, which can lead to fractures and thus endanger the

surface development as well as the workers in the excavation chamber. The number of entrances into the excavation chamber should therefore be kept as low as possible. However, a condition-based maintenance of the cutting tools is not possible due to the inaccessibility of the tools during the excavation. Also, there are only a few wear prediction models to determine the wear of the tools on the basis of the soil parameters and driving parameters. In addition, uncertainties and fuzziness, especially in the soil parameters, make it difficult to plan maintenance stops accurately. Furthermore, it is not possible to enter the excavation chamber at every point of the tunnel alignment, e.g. due to existing buildings above [19].

7.2.2.1 Formalisation of Tool Wear and Maintenance Strategies

Tool wear In mechanized tunneling, the ground is excavated with a tool-equipped cutting wheel. The cutting tools, whose type varies depending on the ground conditions (e.g. discs, scrapers and bucket), are hence exposed to a constant wear process. The wear pattern depends mainly on soil properties, such as excavatability, consistency, transport behavior and ambient pressure [45], but also on the design of the cutting wheel, e.g. the type of cutting tools and their arrangement on the cutting wheel [47]. A more detailed description and investigation of tool wear can be found in Sect. 3.3.

In materials engineering, several types of material wear are defined. In mechanized tunneling in soft ground, mainly abrasion, adhesion, tribochemical reactions and surface disruption occur. The decisive factor in soft ground is abrasive wear and thus the abrasiveness of the soil [26].

As there is no sufficient possibility to monitor the tool condition during the tunneling process, wear prediction models have to be used to determine necessary inspection intervals and maintenance processes. Currently, prediction models of wear behavior are mostly based on input data obtained in laboratory index tests under idealised boundary conditions [45]. Plinninger and Restner [61] give an overview of the index tests developed over the years to investigate the abrasiveness of soils (e.g. LCPC test). However, these index tests do not consider TBM steering parameters (e.g. penetration or rotational speed of the cutting wheel) and their results can therefore only be transferred to the real system to a limited extent [26, 49].

In order to consider these boundary conditions, Köppl [47] developed an empirical model based on 18 evaluated hydroshield projects. His model takes into account the abrasiveness of the soil using a Soil Abrasivity Index (SAI) and additionally considers the type and arrangement of the tools on the cutting wheel as well as the penetration. The SAI takes into account the equivalent quartz content eQu, the stresses using the shear strength of the soil τ_c and the grain size distribution of the ground using the grain size D_{60} [47],

$$\text{SAI} = \left(\frac{\text{eQu}}{100}\right)^2 D_{60} \, \tau_c \, . \tag{7.1}$$

With the help of the SAI a maximum cutting path for each cutting tool can be calculated depending on the different tool types [47],

$$s_{c,e(z)} = \begin{cases} 312.0 + \exp(-0.0048(SAI_z - 1398.2)), & \text{discs} \\ 280.9 + \exp(-0.0050(SAI_z - 1300.7)), & \text{scrapers/buckets.} \end{cases} \tag{7.2}$$

This enables the estimation of the lifespan for each cutting tool and thus also the maximum advance distance until the next maintenance stop.

During the advance process, each cutting tool follows a helix-shaped path, representing the maximum cutting path $s_{c,e(z),i}$. When considering the cutting wheel geometry and tool position, the maximum cutting path can be translated into the maximum longitudinal length of an excavated tunnel section $L_{c(m)z,i}$ in order to determine the next maintenance position. The wear level of a tool $e_{cd,e(m)z}$,

$$e_{cd,e(m)z} = \frac{s_{d,e(z)}}{s_{c,e(z)}\gamma_{cl}} = \frac{e_{c,e(z)}}{\gamma_{cl}} , \tag{7.3}$$

is estimated by comparing the current driven cutting path of a tool $s_{d,e(z)}$ to the maximum cutting path $s_{c,e(z)}$. The safety factor γ_{cl} reduces the maximum cutting path to ensure a workability of the cutting tools under worse boundary condition ($0 < \gamma_{cl} \leq 1.0$). This wear level, calculated in Eq. 7.3, is used to determine the tools that have to be replaced during a maintenance stop [19].

If the wear limit of a tool is exceeded and the hard-metal parts at the top of the tool are worn out, the wear resistance of the tool decreases significantly. If the tool wears out to a certain extent, even the tool holder can be damaged, which can in turn lead to a significant damage of the cutting wheel and a long standstill (see Fig. 7.7).
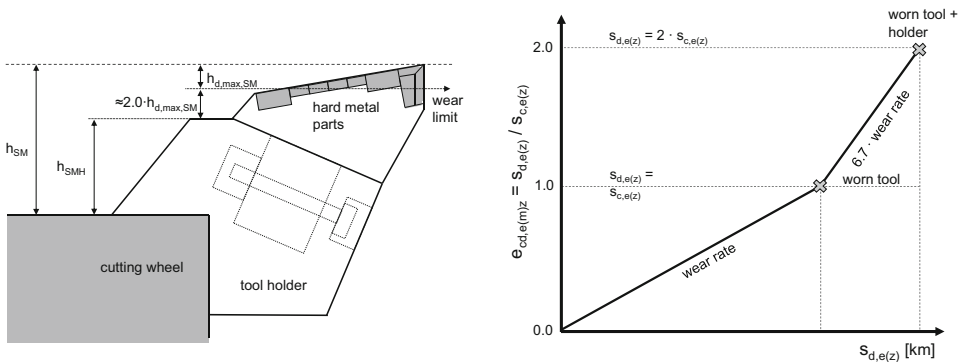
Fig. 7.7 Schematic wear behavior of a cutting tool (left); Wear limit of a scraper defined by the depth of the hard metal parts, wear limit of the tool holder to be damaged given by the geometrical boundaries (here: $2.0h_{d;max;SM}$) (right) based on [19]

Maintenance strategies   The maintenance of cutting tools in tunneling in soft ground is very complex and subject to many uncertainties. Due to the face support, the tools are not freely accessible and prevent condition-based maintenance. Therefore, maintenance is usually carried out periodically, with additional preventive stops before passing a critical tunnel section (e.g. high water pressure or sensitive surface structures). The interval of maintenance is mainly determined by the predicted wear limit of the tools and the expected geotechnical conditions. Depending on the maximum travel distance ($L_{c(m)z,i}$) of the quickest worn out tool, the maintenance stops are planned and the tools that have reached their wear limit (see Fig. 7.8, right, $i = 1, 18$) or will reach this limit in the near future are replaced [19].

The maintenance interval must neither be too long, as otherwise there is a risk that tools will exceed their wear limit and thus increase the risk of massive damage to the cutting wheel, nor must the interval be too short, as maintenance stops are very time-consuming and cost-intensive. Therefore, their number must be limited to a reasonable minimum.

Before maintenance of the cutting tools, the required tools as well as necessary materials must be transported to the TBM. In the case of planned maintenance, the materials can be transported into the tunnel without additional effort already during a regular drive of the tunnel vehicle. In the case of unplanned maintenance in the event of corrective maintenance, additional time for waiting for material has to be added to the maintenance duration, as materials and tools are only transported to the machine after the shutdown has occurred.

The maintenance process itself is then divided into three main processes, the mobilisation process, inspection and replacement of tools, and demobilisation.

The mobilisation process (t_{mob}) describes all preparatory work up to assessing the condition of the tools and replacing them if necessary. To enter the excavation chamber, the support medium in the excavation chamber must first be lowered and replaced by compressed air (t_{low}). However, this process is not always recommendable at all points along the alignment and carries the risk of an unstable face due to insufficient support pressure or even of blow-outs [TTB]. Furthermore, the limited working time under pressure as well
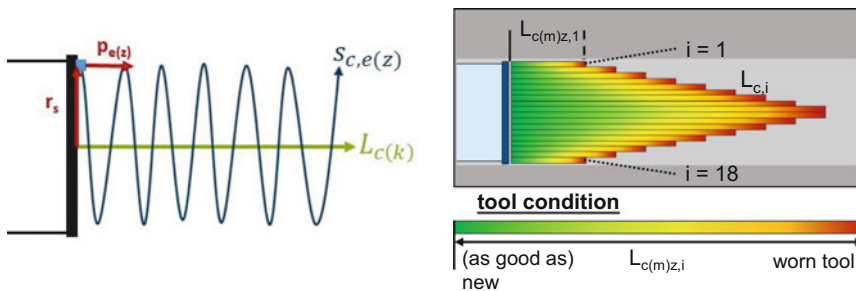
Fig. 7.8 Schematic of the dependencies of maintenance interval $L_{c(m)z,i}$ and lifespan of cutting tools $s_{c,e(z)}$ based on [14, 19]

as compression and decompression times of the workers ($t_{compress}$) have to be considered. The compression durations depend on the level of the prevailing pressure and the duration of stay [41]. After the workers have been successfully compressed, the working platforms are installed ($t_{installation}$). Subsequently, the cutting wheel and tools can be accessed and cleaned ($t_{cleaning}$). Accordingly, the duration of the mobilisation process (t_{mob}) can be calculated as [19]

$$t_{mob} = t_{low} + t_{compress} + t_{installation} + t_{cleaning} \ . \tag{7.4}$$

The replacement work ($t_{replace}$) consists of three processes, a visual tool inspection ($t_{inspect}$) of all tools, retightening of loose bolts (t_{bolt}) and replacement of all worn tools (t_e) (Eq. 7.5). The duration of the tool change depends on the different tool types and the current condition of the tools. If there is severe damage, e.g. worn tool holders or a damaged cutter wheel structure, the maintenance process becomes more time consuming as it requires welding. We have

$$t_{replace} = \sum_{i=1}^{n} t_{inspect,i} + \sum_{i=1}^{n_{bolt}} t_{bolt,i} + \sum_{i=1}^{n_{e,d}} t_{e,d,i} + \sum_{i=1}^{n_{e,s}} t_{e,s,i} + \sum_{i=1}^{n_{e,b}} t_{e,b,i} \ , \tag{7.5}$$

where $t_{replace}$ is the duration of replacement work (min), $t_{inspect}$ is the duration of tool inspection work (min/tool), n is the number of cutting tools (pcs), t_{bolts} is the duration for re-tightening one bolt (min/bolt), n_{bolt} is the number of re-tighted bolts (pcs), $t_{e,d,i}$ is the duration for exchanging one tool (min/tool) and $n_{e,d/s/b}$ is the number of exchanged tools (pcs). Here, d, s and b represent discs, scapers and buckets, respectively.

After the inspection is completed, the demobilisation process (t_{demob}) starts. This comprises the processes of demounting the working platforms ($t_{unmount}$), decompressing the workers ($t_{decompress}$) and refilling the excavation chamber with the support medium (t_{refill}). The total duration for the demobilisation process sums up according to [19]

$$t_{demob} = t_{unmount} + t_{decompress} + t_{refill}. \tag{7.6}$$

These processes are carried out separately one after the other to ensure the safety of the workers. The total duration of a maintenance stop can then be estimated according to [19] as

$$t_{maint} = t_{mob} + t_{replace} + t_{demob}. \tag{7.7}$$

In addition to the replacement of worn tools, tools can also be preventively replaced by new ones during maintenance, that are likely to exceed the wear limit by far until the next maintenance stop to reduces the risk of severe damage to the cutting wheel. This limit for the preventive replacement of tools is a key factor for the performance and efficiency of a project [19].
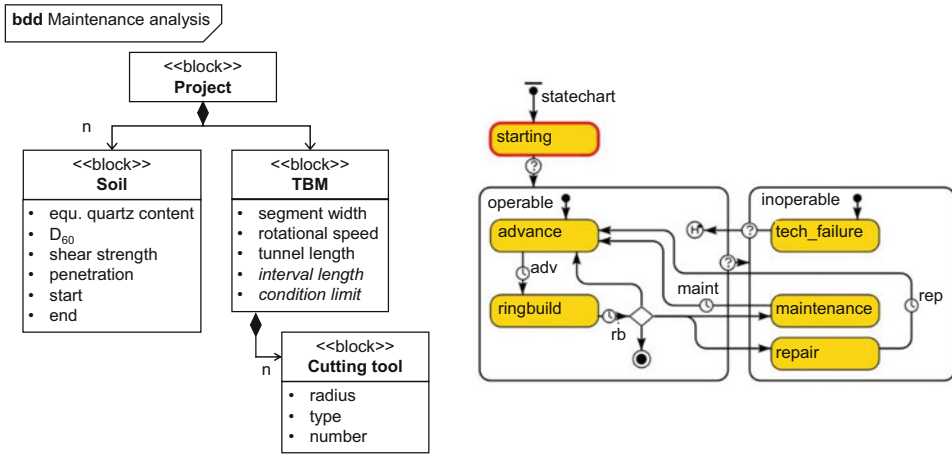
Fig. 7.9 Formal Model description (left) based on [19], state chart of the TBM including the states maintenance and repair (right) [14]

7.2.2.2 Modeling of Wear and Maintenance

For modeling wear and maintenance processes, a new agent is introduced into the simulation approach described in Sect. 7.2.1. The agent *CuttingTool* represents each cutting tool, its condition and remaining lifespan individually. Since the number of rotations is set by the shield driver and can thus be simplistically assumed to be constant, the penetration of the tool depends mainly on the fluctuating advance speed. As a result, the penetration and thus the wear also fluctuates within a homogeneous soil section. For the soil, a new agent is introduced, which contains all important parameters describing the abrasiveness of the soil (see Fig. 7.9, left).

Besides, the agent *cuttingWheel* and *Erector* were simplified and combined in the agent *TBM* to focus on the analysis of wear and maintenance. The states maintenance and repair were added, as well as a list of all cutting tools. If the TBM reaches the maintenance position planned, the agent *TBM* changes its state to maintenance. After each advance, the wear status of each individual tool is determined using the wear model according to Köppl [47] as described above. If a tool reaches its wear limit before scheduled maintenance takes place, the cutting wheel is stopped and changes to the *technicalFailure* state. In this case, a technical failure interrupts the current process. In both cases, the duration for the maintenance of the cutting tools is determined on the basis of the prevailing boundary conditions. After the determined duration has elapsed, the cutting wheel changes back to the operable state.

7.2.2.3 Analysis of Robustness Measures

To evaluate the influence of the uncertainties affecting the wear behavior of cutting tools on the maintenance scheduling and to find a robust and efficient maintenance strategy, a robustness analysis has to be performed.

Robustness is defined as the sensitivity of results to influencing parameters. In mechanized tunneling, influencing parameters are divided into controllable parameters, noisy parameters and uncertain parameters. With regard to maintenance and wear, controllable parameters are the maintenance interval and the safety factor for the wear limit. Uncertain, noisy parameters are soil properties and the penetration of the TBM [19].

The robustness of maintenance strategies can be characterised by three specific values. These are the total duration of maintenance, the number of replaced tools and worn tool holders, and the location of maintenance stops along the tunnel route in relation to the given boundary conditions. A robust maintenance strategy aims to optimize these three values and reduce the risk of unplanned maintenance stops. This is because unplanned maintenance stops not only cause higher costs, but also increase the risk of work accidents and damage to sensitive surface structures [19].

For the assessment of robustness, a comparative value must be used. In the presented research, cost functions for maintenance work are used for a comparable definition describing the robustness and efficiency of a maintenance strategy while considering uncertainties. For this, cost factors are needed, which are divided into the following time dependent and material dependent costs [19]:

- Time-dependent costs:
  - general expenses of the jobsite [Euro/h],
  - planned/unplanned maintenance. stops [Euro/h].
- Material costs:
  - cutting discs [Euro/disc],
  - scraper [Euro/scraper],
  - bucket [Euro/bucket].
- Fix costs:
  - compressing/decompressing operation costs [Euro/ operation],
  - planned/unplanned maintenance. stops [Euro/stop].

In order to find an optimal maintenance strategy, the characterising parameters maintenance interval L_i and safety factor γ_{cl} are varied using the crossed-array method of Taguchi [77]. Thus, all possible parameter variations are considered and evaluated using the cost objective function. Unplanned downtimes should always be avoided as mentioned before, therefore strategies that lead to unplanned maintenance stops are considered unfeasible.

7.2.2.4   Optimization of Logistics and Maintenance Processes

The optimization of maintenance intervals and maintenance strategies always aims at maximising the availability of the system. However, contradictory effects play a decisive role here. For example, regular entries into the excavation chamber allow a better estimation of the wear condition and thus prevent unscheduled stops. Too frequent inspection intervals in turn lead to a reduction in availability. For mechanized tunneling, minimising project
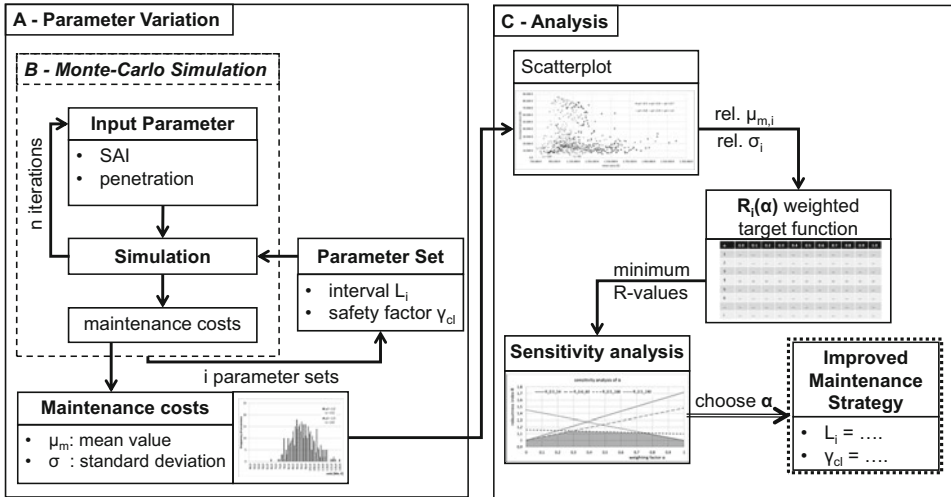
Fig. 7.10 Procedure model for the evaluation of maintenance strategies with regard to their robustness by using process simulation [19]

duration by maximising availability and avoiding unscheduled stops while reducing the number of cutting tools to be changed is of particular importance.

Within the optimization framework, the developed process model was extended so that the influence of different maintenance strategies as well as different wear conditions of cutting tools can be determined (see Fig. 7.10). The variation of the wear condition of a cutting tool that is still classified as acceptable during an inspection process describes the use of a proactive maintenance strategy. The coupling of Monte Carlo simulations and parameter variations thus results in a multi-criteria optimization, which determines a Pareto optimum as a result. The simulation parameters length of the maintenance interval, averaged condition of all cutting tools as well as the limit state of serviceability of a single cutting tool can be used to compare the effects of different maintenance strategies on the project time and the number of cutting tools to be changed. A more detailed description of the optimization framework can be found in [15, 19].

Case study   To illustrate the developed simulation approach, a short case study is presented, which compares a corrective to a preventive maintenance strategy. The case study is based on a metro line project constructed in sand and clay soil conditions. The tunnel alignment is 1800 m long in total and made of four distinct geological sections consisting of either sand or clay with varying support pressure. The TBM is equipped with compressed air work facilities. A man lock and a material lock are used to transfer workers and tools into the excavation chamber. The cutterhead is equipped with disc cutters, scrapers and buckets to excavate the soil. The rotational speed of the cutting wheel is set to 2 rotations per minute, while the advance speeds varies according to Weibull distributions
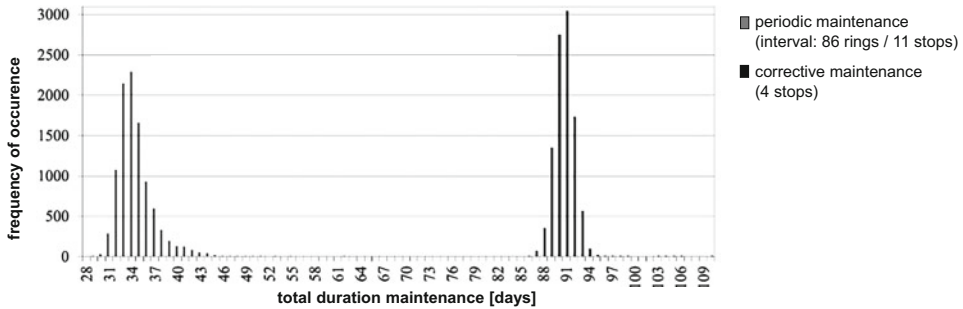
Fig. 7.11 Total downtime in days for 10,000 simulation runs

gained from the evaluation of processing data of finished tunneling projects with an average advance speed of 15.5 mm/min for the one geological section and 25.5 mm/min for the other one. The time for the ring build is set to 40 minutes, since the ring build process has no influence on the wear or maintenance processes, thus does not influence the results of the model [18].

Different maintenance strategies are analyzed by varying the maintenance interval. The first strategy that has been analyzed uses only corrective maintenance. The second strategy considers a maintenance interval of 86 rings, after a first rough estimation. In both cases, the wear limit for the tool exchange is set to 10%, so that the tools, which are nearly worn completely, are exchanged preventively. For each strategy a Monte Carlo analysis has been performed, conducting 10,000 simulation runs. This way, the uncertainty of the input parameters are taken into account. Consequently, the simulation result is not one certain value but can be evaluated using a histogram [18].

First, the total downtime caused by the maintenance processes has been evaluated. The graphical comparison of the results for each strategy (see Fig. 7.11) shows that the total downtime of the corrective maintenance is much higher than for the periodic maintenance, even though the total number of maintenance stops is higher using periodic maintenance. In both cases, there is a small possibility of significantly higher downtimes up to approx. 148 days for corrective maintenance [18].

The number of replaced tools increases with the rising number of maintenance stops. While during the corrective maintenance 406 tools are replaced on average, during the periodic maintenance 551 tools are replaced on average. The utilization of the tools is higher using corrective maintenance, but there are severe damages of the cutterhead and tool holders, which cause an increase of the needed repairing effort [18].

Regarding the position, at which an entering of the excavation chamber is conducted, periodic maintenance has the advantage that the positions are predefined and known beforehand, while in corrective maintenance, they vary according to the position the damage is detected. By varying further parameters, like the wear limit for the tool exchange or the amount of wear at which the damage is detected, it became visible that these parameters

also influence the results of an optimal maintenance interval at which the total downtime
is at its minimum [18].

7.2.3   Real-Time Use of Process Simulation Models

The use of real-time data for online simulation is getting increasingly important for an im-
proved prediction of a projects outcome and also for a support of the steering of processes.

In tunneling, many parameters deviate from their predicted values. The main reasons
are that the assumptions made in the planning phase are subject to uncertainties and fuzzi-
ness. Further, unforeseen events can occur during execution that were or could not be
considered during the planning phase. Therefore, logistics and production processes must
be adapted and controlled continuously. The developed simulation models for the analysis
and optimization of production and logistics processes can also be used for a real-time
analysis and a simulation-based steering of these processes. For this purpose, a control
concept in the form of a control loop has been specified, which includes the recording of
the current status of the production and logistics processes, the evaluation of the current
data and the planning of suitable counter measures (see Fig. 7.12).

First, an adequate recording of real-time data, which reflects the status of the construc-
tion site, is important. In mechanized tunneling, a lot of data is already recorded during
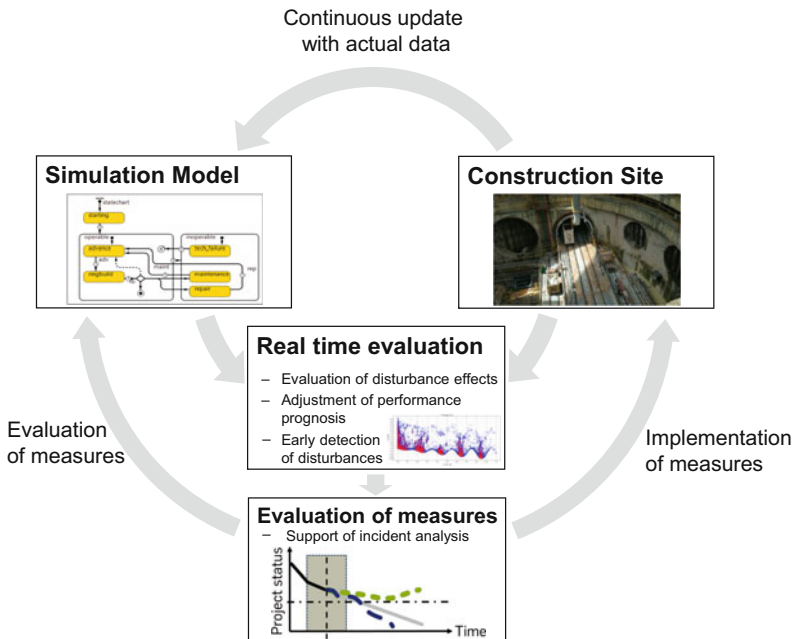
Fig. 7.12 Control loop for the holistic process simulation approach for tunneling projects

excavation. In order to evaluate the current construction progress and to enable an adjustment of the production processes, deviations between the planned and the recorded data are determined. This enables an adaption of the logistics processes and an adjustment of the prognosis. If significant deviations are detected, suitable measures can be taken to accelerate the production progress or prevent possible incidents. The effect of deviations in the project flow can be evaluated and counter measures can be proven with the help of simulation models.

Further, by identifying threshold values, an early detection of disturbances is possible. Simulation models can help to evaluate a real time prediction of disturbance effects and an evaluation of the adaption of control variables.

This section summarizes the main results of the investigated real-time use of simulation models, which were also published in [43, 67].

7.2.3.1 Concept for a Real-Time Use of Simulation Models

Compared with the traditional offline simulation that uses stationary input parameters, the capability of real-time simulation to dynamically incorporate new project data and adapt to changes in the operating environment offers the promise of improving the accuracy of project forecasting [75].

To employ the simulation model to perform the system predictions simultaneously to the construction process, it is essential to provide the ability to do a continuous comparison between the initial and the current values of the input data. If the deviation is significant, an update of the input data could improve the prognosis for the next phase of the project.

During the online-update, real-data and model-generated data is compared during the progress of the constructions. According to this comparison, an update of the simulation inputs is suggested to improve the model and its prediction and to improve the system accordingly when possible.

7.2.3.2 Integration of Real-Time Data

The most essential step to manage the online-update of the simulation system is the effective management of the simulation inputs, which means to be able to update the inputs of the model at any time and to set the suitable data gathering method to collect real-time inputs. In agent-based models, each agent operates in a discrete manner, using the parameters and variables implemented in the agent. The initial values of these variables are set at the beginning of the simulation, and the simulation starts to operate from this state. What is important to consider, is that interaction between the agents is not disturbed by the change of the initial state. However, it is based on the change of state of each variable during the execution of the simulation model.

The main challenge in the update process is to maintain the validity of the model after the update. Although the agents are isolated during execution, to implement the update, extra variables or time-related functions need to be added, which may require a validation step after. Additionally, updating the non-deterministic parameters, which generally are

Step 1	Step 2	Step 3	Step 4
Choose Inputs to Update	Integrate Real-Time Data	Adjust Simulation Model	Validation Test
→ Real System Inputs	→ Non-deterministic Inputs	→ Dynamic Database	→ Fixed Input Values
→ Simulation Internal Inputs	→ Deterministic Inputs	→ Read/write functions	→ Fixed probability Functions
		→ New Communication Messages	
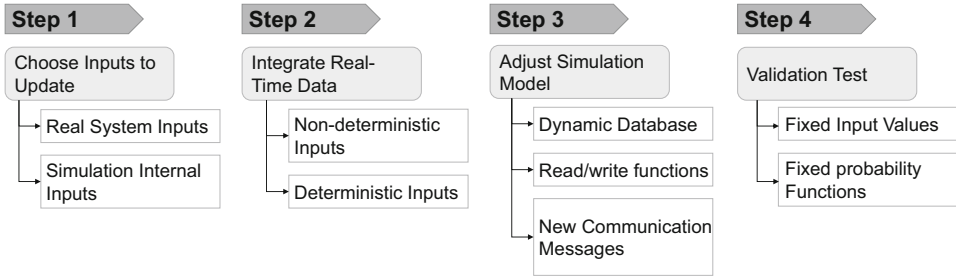
Fig. 7.13 Proposed methodology to update an agent-based simulation model modified based on [67]

represented using probability distribution functions, may affect the model. Updating such data need an external data analysis, before being implemented in the agent-based models.

For offline runs, waiting for the model to complete the run is not as critical or demanding. On the other hand, when the model is providing real-time predictive analytics, model run turn-around time, including multiple scenarios and Monte Carlo runs, become critical. Whether the implementation is for schedule adherence, predictive bottleneck detection, or other efficiency and improvement alerts, two key factors influence the overall solution, the simulation speed, and model validity and accuracy [2].

To optimize speed, many approaches are used to distribute and parallelize the model to speed the model execution without affecting the validity of the system. Model accuracy, on the other hand, can be even more difficult to maintain, especially when real-time data is used. The simulation model should be designed or adjusted in a way that allows growing with the system and expanding to allow a correct relationship with live data. The user should be able to apply real-time constraint changes, and in some case expand the model in order to maintain the correct relationship with live data.

The main concept of the online update of the simulation model can be summarized in four basic steps [67]. The diagram illustrated in Fig. 7.13 displays these four steps in order to achieve a real-time update.

Step 1 First, one should choose the main input parameters to be updated, which affect the objectives of the simulation the most. In the simulation model, hundreds of input parameters are used to simulate the real-time system. These parameters can be divided into two types:

- Real system inputs: This means the input parameters of the main processes in the simulated system, such as velocities, types of soil, the cutting speed, the flowrates of the pumps, etc.
- Internal input parameters which are set by the designer to regulate the flow of the process in the simulation model.

Updating all data can be time-consuming and might not be necessary, if they don't affect, or have a negligible effect on the update of the desired outcomes. It is advisable to do a sensitivity analysis in order to decide the most essential input parameters that can significantly affect the results [67].

Another important process for the update is the collection of the real time data. In mechanized tunneling, hundreds of sensors are used to monitor the production progress, usually with the help of process controlling tools. This data can be requested with the help of API-requests and used for the simulation update [43].

Step 2 For the second step, it is important to choose the integration method to implement the new input parameters, using data collected from the real-time configuration, in the simulation model.

In general, we deal with two types of data in real-time systems, accordingly in simulation models. The data can be deterministic such as amounts of supplied materials or the fluid amount in the tanks, or it can be non-deterministic such as the duration of segment installation, the advance speed through the different types of soils, and the probability of failures occurrence during production.

Different adaption methods are required to integrate these data into the simulation model. For deterministic input parameters, simple methods are used such as fitting the units, finding mean values, find maximum or minimum values of datasets, or excluding irregularities, etc.

To update non-deterministic data, a different approach is used. Figure 7.14 explains the suggested concept to update dynamically the PDF used to evaluate the probability of certain parameters offline. In this figure, the blue curve displays the PDF assumed in planning, which was generated with a probabilistic approach. During the execution of the project a new set of data, the real-time data, is available (green curve). At a point in time, this data is gathered and analyzed to evaluate the validity of the proposed PDF.

Using both sets of data, we can predict an updated posterior PDF (grey curve) that is more realistic and gives a better prediction of the project performance in the next phase of execution. This can be done using simple data fitting methods or more sophisticated methods [43, 67]. In literature, several approaches have been investigated (i.e. [75, 79]), mainly using a Bayesian approach.
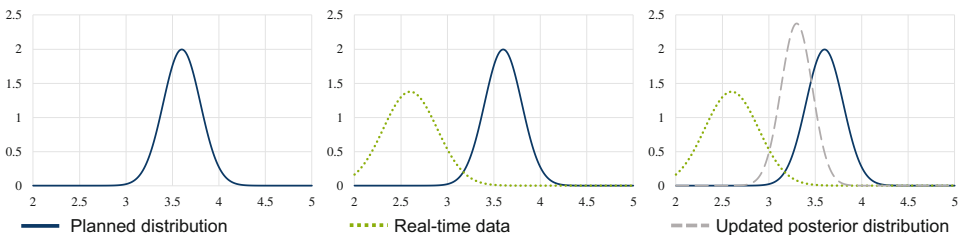
Fig. 7.14 Updating probability distribution functions [67]

Step 3   If the model is designed for offline simulation during the planning phase, some modification might be necessary for the next step to adapt the real-time data for the online-update modeling.

In order to update the input parameters, they are connected to a dynamic database. In an agent-based simulation model, each agent has a set of input parameters. The initial values of these inputs are connected to database tables in order to read and write values during the simulation. Extra read/write functions are added to the model's agents to write/read inputs at different points during the execution of the simulation. The same concept is used to register the simulation outcomes before and after the update.

Step 4   The last step includes the validation of the concept taking into consideration the non-deterministic nature of the simulation variables.

Validation is required to prove that the model is a sufficient representation of the real system, a verification of the results is done after running the simulation by comparing the results with real-time results from similar projects [62]. To ensure the validity of a model after the update, many different techniques are used such as predictive validation, historical data validation, comparison to other models, and fixed value test.

For the application of the online-update concept, validation tests were carried out to verify the results. The scheme in Fig. 7.15 gives a rough overview of the suggested validation concept. The illustrated concept suggests running the simulation in a first run to get an initial prediction of the project duration using a fixed seed (reproducible simulation runs). At a specific point, the output parameters of the simulation will be stored in a database output file and reinserted in a second, updated simulation using the updating concept. The results of these two simulation runs are then compared in expectation of a 100 per cent correlation. Using this principle, further validation tests have been conducted to also proof the update considering randomness.

The conducted validation tests have shown, that the proposed update methodology produces valid results. Details about the validation results can be found in [67].
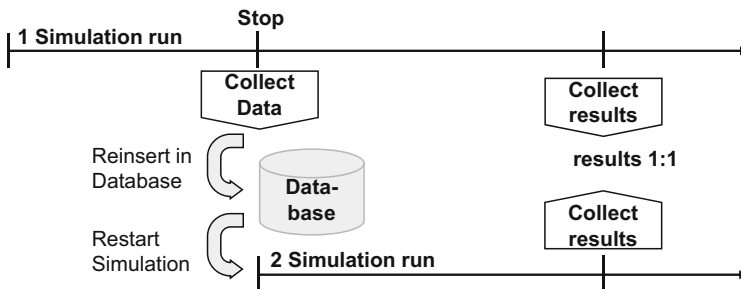
Fig. 7.15   Validation concept for integrating real time data into simulation models based on [67]

The proposed methodology can therefore be used to turn offline simulation models into a useful tool to support the decision making process during the execution of the project. First applications on a real reference project have shown, that integrating real time data and updating simulation models improves the prognosis of a project duration noticeably [43].

7.2.3.3 Simulation-Based Support of an Incident Analysis

Based on the incident analyses and maintenance investigations carried out, robust incident management can be supported on the basis of current actual information, which recognizes problems at an early stage on the basis of the recorded actual data- and simulation-based updated forecasts.

On the one hand, specific countermeasures and suitable measures in the event of a downtime can be evaluated with the help of updated simulation models. With the help of the classification of different measures and the definition of key values, different scenarios can be simulated and evaluated on the basis of the simulation results before being implemented on site. This supports a steering of the processes and enables the best possible control under the given boundary conditions.

On the other hand, during the progress of the construction work, different tools are used to monitor the workflow and record the parameters of each process. These parameters include the most obvious values as the advance speed and the segment installation in addition to hundreds of parameters to monitor pressures and flowrate of the fluids and materials.

A thorough analysis of these data can conclude to correlations between these values and a correlation between the changes in these values and the changes in the workflow. Such analyses can explain the unexpected delay in processes and tasks due to the unexpected disturbances in another section of a project. Good examples would be the relation between the blockage in the mortar lines and the irregular flows and pressure peaks during annular gap grouting. In projects with high tool wear, also a worn cutting wheel can be announced by increased specific energy during dismantling.

7.3 Real-Time Prediction of Tunneling-Induced Settlements

Tunneling-induced settlements can be computed by the process-oriented finite element simulation model presented in Sect. 7.2.1.4. To handle the real-time prediction of tunneling-induced settlements for large, numerically expensive models, surrogate models are needed to obtain numerical values quickly enough to make extensive predictions possible. In particular, so-called hybrid surrogate models have proven to be valuable tools in developing such real-time predictors. Also, aspects of prediction with uncertain data, interval data or fuzzy data have been investigated and assessed. Details are given in the following sections.
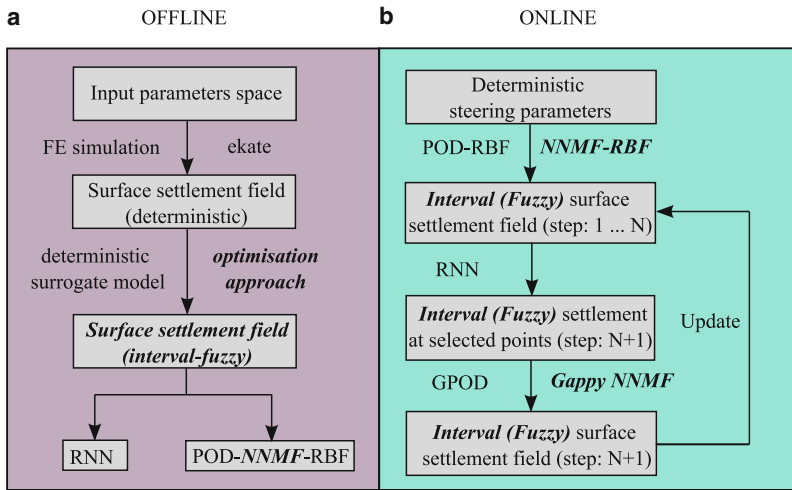
7.3.1   Hybrid Surrogate Modeling Concept

Mechanized tunneling simulations using the process-oriented FE model are time-consuming and therefore best employed in the design stage of a tunneling project. For the purpose of supporting the steering phase in tunnel construction in real-time, surrogate models are required. Various surrogate modeling approaches have been developed for a large number of engineering applications. In mechanized tunneling, different surrogate modeling approaches can be employed for different specific tasks. In [55], an Artificial Neural Network (ANN) with a feed-forward structure has been adopted as a surrogate model with low dimensional outputs for deterministic real time analyses in mechanized tunneling.

With the purpose of delivering real-time predictions of expected surface settlements at multiple surface locations, the benefits of another type of ANN, called Recurrent Neural Networks (RNN), and the Proper Orthogonal Decomposition (POD) approach are combined within a hybrid RNN-POD surrogate model concept. The hybrid surrogate model, which has a low dimensional input and a high dimensional output, can be used for deterministic input-output mapping [12], interval input-output mapping [35] and fuzzy input-output mapping [11]. The concept of hybrid surrogate modeling approach is explained below.

For predefined sections of a tunneling project, the simulation model needs to map the relationship between process parameters, geotechnical parameters and the corresponding time variant surface settlements. The process parameters are taken to be deterministic values, whereas geotechnical parameters may be presented as an interval or fuzzy numbers rather than a specific value. The general concept of hybrid surrogate models is depicted in Fig. 7.16, with the bold italic texts indicating that additional steps are required to handle uncertain input-output data relationships, depending on the type of intervals or fuzzy numbers.

First, in an offline stage, a representative numerical simulation model for a tunnel drive through a specific tunnel section from time step 1 to N is set up, see Fig. 7.16a. By varying the deterministic values of input parameters (both geotechnical and process parameters), deterministic output data (surface settlements) are collected. This deterministic input-output data set is utilized to establish a deterministic surrogate model. This surrogate model can be used directly to predict the complete surface settlement field in step $N + 1$ when there is no uncertainty from geotechnical parameters. When dealing with uncertainty of interval data or fuzzy data type, an additional step to compute the system outputs for uncertain geotechnical parameters is required.

Interval (fuzzy) analyses based on the just-built deterministic surrogate model together with an optimization approach, see [34], are performed for predefined intervals (fuzzy numbers) of soil parameters, which are generally retrieved from geotechnical reports. The result obtained from these analyses is used to create the hybrid surrogate model, which is capable of predicting interval (fuzzy) input-output relationships in the online stage for step $N + 1$.

Fig. 7.16 Scheme of the hybrid surrogate modeling approach

Figure 7.16b shows how to apply the proposed surrogate model in the online stage, i.e. during the tunnel construction. The prediction results depend on deterministic chosen values of the steering parameters in time step $N + 1$ and the recorded history from time step 1 to N. The procedure is performed through three consequent steps. In the first step, an RNN approach is employed to predict the settlement behavior at selected monitoring points for time step $N + 1$. Afterwards, the complete time-variant surface settlement field from step 1 to N is approximated by the POD-RBF approach, which is a combination of the POD method and Radial Basis Functions (RBF). Finally, a reconstruction missing data technique (i.e. Gappy POD) is performed to predict the complete settlement field in time step $N+1$. For the prediction of interval or fuzzy settlement fields in case of uncertain input parameters, Non-Negative Matrix Factorization (NNMF) [59] is employed together with the POD method. More specifically, in case of deterministic data, a trained RNN and a POD-RBF network are required for step 1 and step 2, respectively; GPOD technique is applied in step 3. However in case of interval data, with the adoption of the concept of midpoint-radius representation of interval data, two surrogate models are constructed to handle midpoints and radiuses of interval input and output data separately in each step, step 1 and step 2. In step 3, GPOD and NNMF techniques are employed for the reconstruction of midpoints and radiuses. Similarly, with the concept of Δ representation for fuzzy numbers, several surrogate models based on both POD and NNMF methods are constructed for the prediction of fuzzy input-output data relationships. In the following sections, the methods used in the hybrid surrogate modeling approach are explained in more details.

7.3.1.1 Recurrent Neural Networks

For the prediction of time-variant surface settlement at selected monitoring points, a type of ANN called Recurrent Neural Network (RNN) is utilized. The method is capable of

extrapolating the time-variant processes by means of combining information from the hidden layer of previous time steps and the inputs of the current step to update the values of the hidden layers of the current time step via context neurons. To illustrate the concept of the RNN approach, a simple RNN network structure with 3 layers: an input layer with 2 neurons P_1 and P_2 (representing two common adjustable steering parameters: the tail void grouting pressure and the face support pressure), a hidden layer with H hidden neurons and an output layer S_T with T output neurons (T is the number of selected points), is considered. Input signals of the RNN at each time step n (the steering parameters $^{[n]}P_k$, $k = 1, 2$) are processed layer by layer to get the network outputs (the settlements $^{[n]}S_t$, $t = 1, \ldots, T$). The signal value v of the hidden neuron h, where $h = 1, \ldots, H$, at time step n and the outputs S_t of the network are computed by

$$^{[n]}v_h = \varphi^1 \left(\sum_{k=1}^{2} {}^{[n]}P_k \cdot \omega_{hk} + \sum_{d=1}^{D} {}^{[n-d]}v_h \cdot {}^d c_h + b_h \right), \tag{7.8}$$

$$^{[n]}S_t = \varphi^2 \left(\sum_{h=1}^{H} {}^{[n]}v_h \cdot \omega_{th} + b_t \right). \tag{7.9}$$

Here, ω_{hk} is the weight from input neuron k to hidden neuron h, ω_{th} is the weight from the hidden neuron h to the output neuron t, $^{[n-d]}v_h$ is the output signal of hidden neuron h at time step $[n - d]$, where $d = 1, \ldots, D$ are the time delays, $^d c_h$ is the context neuron weight of the delayed time step d and b_h, b_t are additional bias values of hidden neuron h and output neuron t.

Within the network training, unknown network parameters, i.e. the synaptic weights ω, the context weights c for each delayed time step and the bias values b, are adjusted by iteratively evaluating the error in each training step (epoch). The training process ends, when the stopping criteria is met (e.g. training and validation error smaller than a predefined tolerance, reaching the maximum number of epochs). In this work, the Levenberg-Marquardt back-propagation algorithm, which is one of the most widely used methods for non-linear optimization, is adopted for the training of the RNNs.

7.3.1.2 Proper Orthogonal Decomposition and Radial Basis Functions

Basically, a high-dimensional matrix $\mathbf{S}$ can be approximated as a linear combination of the truncated basis vectors $\hat{\boldsymbol{\Phi}}$ as

$$\mathbf{S} \approx \hat{\boldsymbol{\Phi}} \cdot \hat{\mathbf{A}}. \tag{7.10}$$

The truncated basis vectors are obtained from solving an eigenvalue problem of the covariance matrix

$$\mathbf{C} = \mathbf{S}^{\top} \cdot \mathbf{S}. \tag{7.11}$$

At this step, the truncated amplitude matrix $\hat{\mathbf{A}}$ contains constant values associated with the given matrix $\mathbf{S}$. Hence, they are only an approximation for snapshots that were generated in the original high-dimensional snapshots matrix $\mathbf{S}$.

To obtain a rather continuous approximation, each amplitude vector $\hat{\mathbf{A}}_i$ is expressed as a nonlinear function of input parameters on which the system depends. The amplitudes $\mathbf{A}$ can be related to the function by an unknown matrix of constant coefficients $\mathbf{B}$ as

$$\hat{\mathbf{A}}_i = \mathbf{B} \cdot \mathbf{F}_i. \tag{7.12}$$

with $\mathbf{F}_i$ being a set of predefined interpolation functions $f_j(z)$ of input parameters z. In this work, an inverse multiquadric radial function, a type of RBF (see [40] for a description), is selected as the interpolation function. The output system response corresponding to an arbitrary set of input parameters is thus approximated by

$$\mathbf{S}^a \approx \hat{\boldsymbol{\Phi}} \cdot \mathbf{B} \cdot \mathbf{F}^a. \tag{7.13}$$

7.3.1.3 Gappy Proper Orthogonal Decomposition and Non-Negative Matrix Factorization

To predict the complete settlement field, two dimensionality reduction techniques, named Gappy Proper Orthogonal Decomposition (GPOD) and Non-Negative Matrix Factorization (NNMF) are adopted in the context of missing data reconstruction problems. The GPOD method, which is a combination of the basic POD method with a linear regression [30], is applied in case of an unconstrained output prediction, i.e. in case of a deterministic input-output relationship. Whereas, in case of uncertainties quantified as intervals or fuzzy data, the NNMF method [59] is utilized to guarantee the non-negativity constraints of the reconstructed results.

A complete snapshot $\mathbf{S}_j$, which belongs to a set of snapshots, can be approximated as a linear combination of the first K POD basis vectors $\boldsymbol{\Phi}$ and an amplitude vector $\mathbf{A}_j$. The amplitude vector is calculated by minimising the error norm

$$\min \|\mathbf{S}_j - \hat{\boldsymbol{\Phi}} \cdot \hat{\mathbf{A}}_j\|_{L_2}^2. \tag{7.14}$$

In case of an incomplete data snapshot $\mathbf{S}^*$, the same least square approach can be effectively used to restore missing data by

$$\min \|\mathbf{S}^* - \hat{\boldsymbol{\Phi}} \cdot \hat{\mathbf{A}}^*\|_{L_2}^2. \tag{7.15}$$

However, due to missing elements, the L_2 norm cannot be evaluated correctly. The GPOD procedure thus works following the concept of a gappy norm based on available data. The missing data problem is solved by computing the intermediate repaired vector $\widetilde{\mathbf{S}}^*$ in terms of truncated POD basis vectors $\hat{\boldsymbol{\Phi}}$ and associated amplitude vector $\hat{\mathbf{A}}^*$ as

$$\widetilde{\mathbf{S}}^* \approx \hat{\boldsymbol{\Phi}} \cdot \hat{\mathbf{A}}^*. \tag{7.16}$$

The coefficient vector $\hat{\mathbf{A}}^*$ can be computed by minimizing the error between the intermediate vector $\widetilde{\mathbf{S}}^*$ and the available vector $\mathbf{S}^*$ using the solution of a *least squares* problem given by a linear system of equations

$$\mathbf{M} \cdot \hat{\mathbf{A}}^* = \mathbf{R}, \tag{7.17}$$

$$\mathbf{M} = (\hat{\boldsymbol{\Phi}}^{\top}, \hat{\boldsymbol{\Phi}}), \tag{7.18}$$

$$\mathbf{R} = (\hat{\boldsymbol{\Phi}}^{\top}, \mathbf{S}^*). \tag{7.19}$$

Given a non-negative matrix $\mathbf{S}^+$, the NNMF algorithm is searching for two non-negative matrices $\mathbf{W}$ and $\mathbf{H}^+$ that satisfies the following optimization problem

$$\min \quad \frac{1}{2}\|\mathbf{S}^+ - \mathbf{W} \cdot \mathbf{H}^+\|_{L_2}^2, \text{ subject to } \mathbf{W}, \mathbf{H}^+ \geq 0. \tag{7.20}$$

The alternating non-negative least squares algorithm proposed in [44], which ensures the convergence of the minimization problem, is implemented to find $\mathbf{W}$ and $\mathbf{H}^+$. The reconstruction procedure for a non-negative vector $\mathbf{S}^+$ now can follow the steps of the GPOD method. Similar to the POD approach, the objective function containing the distances between the available incomplete data vector and the predicted vector is minimized. The amplitude vector $\mathbf{H}^+$ is obtained considering the non-negativity constraint by solving the *non-negative least squares* problem

$$\mathbf{M}^+ \cdot \mathbf{H}^+ = \mathbf{R}^+, \tag{7.21}$$

$$\mathbf{M}^+ = (\mathbf{W}^{\top}, \mathbf{W}), \tag{7.22}$$

$$\mathbf{R}^+ = (\mathbf{W}^{\top}, \mathbf{S}^+), \tag{7.23}$$

where the non-negative *basis matrix* $\mathbf{W}$ is extracted from the available non-negative data matrix $\mathbf{S}^+$. Finally, by replacing the missing elements in $\mathbf{S}^*$ and $\mathbf{S}^+$ by those in the corresponding reconstructed vectors, the complete unconstrained and non-negative constrained vectors of the system response are reconstructed.

7.3.2 Surrogate models for Real-Time Prediction with Deterministic Data

In this section, the performance of the proposed hybrid surrogate model for deterministic data is demonstrated by means of an application concerned with the numerical simulation of the advancement process of a TBM driven tunnel. The main goal is to demonstrate the capability of the surrogate model to provide reliable predictions of the expected settlements induced by mechanized tunneling. To this end, the model predictions will be evaluated by comparing the predictions with reference results obtained from the original process-oriented finite element model ekate. Considering S_i as the settlement at point i of
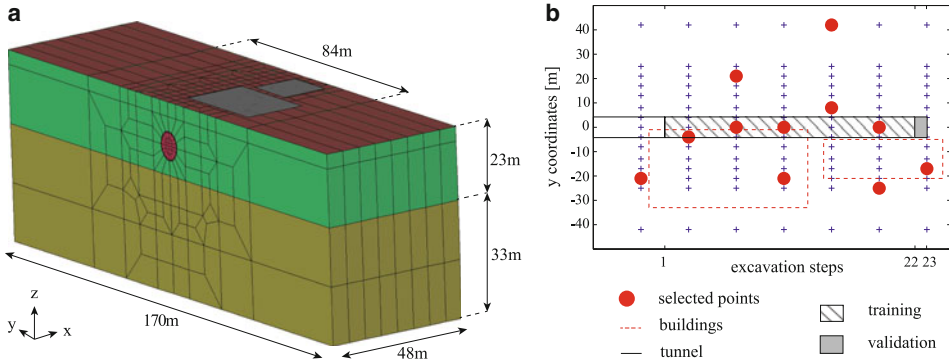
Fig. 7.17 Simulation model of a tunnel section with deterministic input parameters. **a** Model geometry, **b** investigated surface area for settlement prediction

the settlement field and M as the number of outputs of the surrogate model, the error E between the prediction and the FE result is calculated using the L_2 norm error equation,

$$E = \sqrt{\frac{\sum_{i=1}^{M}\left(\mathbf{S}_i^{\text{FE}} - \mathbf{S}_i^{\text{pred}}\right)^2}{\sum_{i=1}^{M}\left(\mathbf{S}_i^{\text{FE}}\right)^2}} \times 100\% . \tag{7.24}$$

A numerical model representing a tunnel section of 48 meters length, constructed with an overburden of 8.5 meters by a TBM, is depicted in Fig. 7.17a. The model is discretized with 11,072 quadrilateral two-field finite elements with quadratic approximations for the displacements and linear approximations of the water pressure. The tunnel lining has a thickness of 0.3 meters and each lining ring has a length of 1.5 meters. The simulation is represented for a tunnel with a diameter of 8.5 meters excavated completely within the first soil layer of a ground model comprising of two layers of soft cohesive soils. The tunnel alignment is assumed to follow an existing street on the surface ground of an urban area, where there are two essential buildings on one side of the street. To consider the existing buildings, rectangular plate-like substitute models are adopted with an equivalent thickness of 5 meters and a stiffness of 50 GPa at the top surface, see Fig. 7.17. A step-by-step procedure of the mechanized tunneling process is considered in the simulation, which consists of different phases: soil excavation at the tunnel face, application of the face support pressure, advancement of the TBM, installation of a tunnel ring and application of the tail void grouting pressure.

The groundwater table is assumed to be at the ground surface. A Drucker-Prager plasticity model is selected for the modeling of the constitutive behavior of the soil, while the material behavior of the tunnel lining and the TBM shield is assumed to be linear elastic. During the tunnel advance, the support pressure, which plays an important role to avoid tunnel face collapse, is kept constant with a value of 180 kPa at the tunnel axis. In contrast, the tail void grouting pressure filling into the annular gap GP, which is necessary

to prevent large deformations of the surrounding soil and large settlements at the ground surface, is simulated as a time variant process parameter. In this example, this operational controllable parameter GP is regarded as one of the input parameters of the surrogate model. Another input parameter is the elastic modulus E_1, which defines the stiffness of the first soil layer. The outputs of the hybrid RNN-GPOD model are the vertical displacements following the Z-direction of surface points. Instead of taking settlements of all surface points as model outputs, settlements of only 105 points within an effective area as depicted in Fig. 7.17b are considered for the generation of the surrogate model due to the fact that surface settlements beyond a distance of 42 meters in Y-direction from both sides of the tunnel axis are almost zero.

To demonstrate the steering supported concept, the proposed hybrid surrogate model is adopted to predict the complete surface displacement field in the subsequent excavation steps with the assumption that the history of TBM advance operation and settlement evolution are available. The prediction is made based on the known history of the excavation process together with future possible applied values of the steering parameters. In this example, the prediction is performed for the step 23 assuming that the TBM currently advances to the 22$^{\text{nd}}$ step of the excavation process. Outputs of the employed RNN are the settlements of 11 selected monitoring points. The position of the 11 points are selected based on the usual position of settlement measurement sensors on the surface in a real tunnel project. For the number of monitoring points, the prediction quality of the GPOD would be theoretically better with a larger number of available data points, however the training and prediction of the RNN might be more complicated. Therefore, the number of monitoring points in the hybrid modeling approach is determined considering both conditions such that the RNN is capable to provide good predictions and to have an appropriate accuracy of the GPOD.

Within the range of the two investigated parameters E_1 and $^{[n]}GP$, ten particular values for E_1 and six scenarios of time varying $^{[n]}GP$ are defined, that constitutes an input space of 60 sampling points. Each sampling point is a combination of one value of E_1 and an applied scenario of grouting pressure $^{[n]}GP$. In total, 60 simulations are carried out using the FE model described in Sect. 6.4.3 to create the surrogate model. The specific variation range of the two input parameters are 20 to 110 MPa for E_1 and 130 to 230 kPa for $^{[n]}GP$, respectively. To validate the prediction capability of the surrogate model, the FE simulation data set is divided into training and validation data sets. The data from 54 randomly selected simulations is used for the training and the data from the rest 6 simulations is employed for the testing of the proposed surrogate model. Figure 7.18 presents a comparison between the prediction results from components of the hybrid surrogate model and the reference FE solutions for a representative validation case with the value of E_1 is 90 MPa. The settlement prediction accuracy of 105 points from all previous excavation steps (steps 1 to 22), i.e. with a total number of 2310 elements, using the POD-RBF model, is shown in Fig. 7.18a. The prediction quality of 11 selected points by RNN and 105 surface points at excavation step 23 by the hybrid RNN-GPOD technique are presented in Figs. 7.18b and (c), respectively. It can be concluded that the settlement prediction obtained from
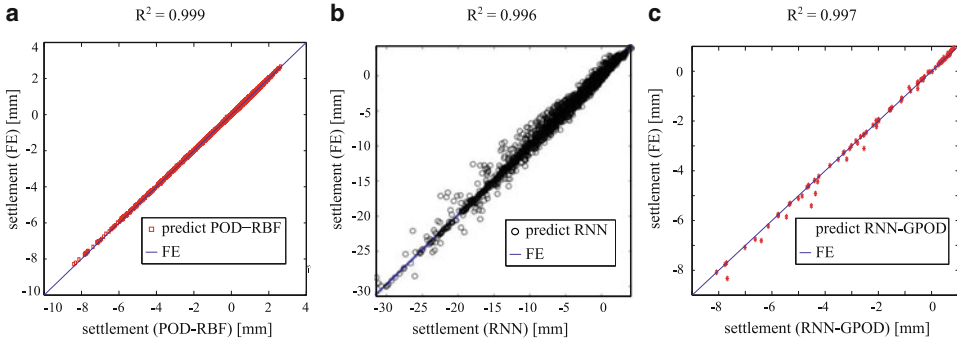
Fig. 7.18 Regression plot between predicted settlements from surrogate models and reference settlements from FE simulations. **a** POD-RBF model, **b** RNN model, **c** RNN-GPOD model

the hybrid surrogate model agrees very well with the reference solutions from FE simulations, which can be indicated by the values of R^2 coefficients. The closer R^2 is to 1, the better the prediction is. The L_2 norm error is only 5%, whereas the computation time is significantly reduced from 6 hours with a FE simulation to less than 1 seconds with the surrogate model. This enables the real-time application of the presented approach for the selection of appropriate steering parameters during tunnel construction to control the surface settlement within a tolerable range.

7.3.3 Surrogate Models for Real-Time Prediction with Uncertain Data

The concept of performing reliability analysis during tunnel construction stage, i.e. to support decision making in steering phase, of mechanized tunneling processes is presented in a synthetic example.

7.3.3.1 Real-Time Prediction with Interval Data

Reliability analyses can be carried out taking into account polymorphic uncertain data using different approaches: stochastic, interval and combined interval-stochastic approaches using the hybrid surrogate model with deterministic input-output data relationship presented in Sect. 7.3.2 [34]. In this section, similar analyses are re-performed with the proposed surrogate modeling strategy for interval data. More details about the proposed strategy can be found in [35], while a detailed description of the representative numerical model can be found in Sect. 7.3.2. The prediction of interval surface settlement fields resulting from interval geotechnical data in a mechanized tunneling process is illustrated by extending the analysis on the synthetic example in Sect. 7.3.2. The direct interval results obtained from the proposed strategy are compared with the reference solution based upon the deterministic surrogate model and an optimization approach within an interval analysis in terms of prediction accuracy and computation time. Similar to the example in
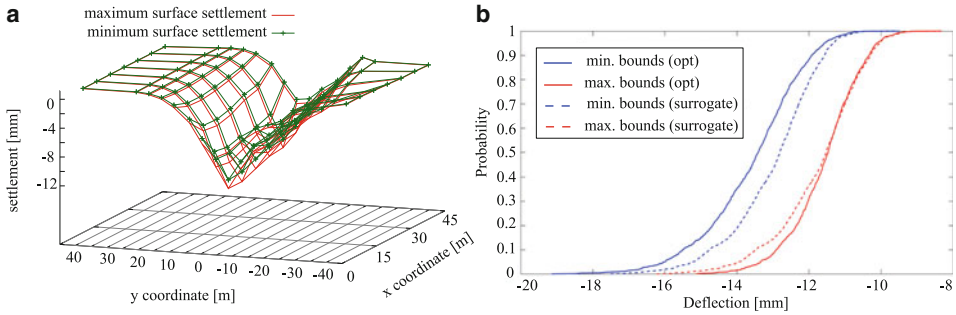
Fig. 7.19 Interval settlement predictions. **a** Interval settlement field with $\bar{E}_1 = [45; 52]$ MPa, **b** P-boxes of the settlement at a monitoring point with E_1 as an interval stochastic number $\mu_1 = [40; 50]$ MPa and $\sigma = 5$ MPa

Sect. 7.3.2, data obtained from FE simulations is utilized for the generation of a deterministic surrogate model. The interval settlement results computed from the deterministic surrogate model and an optimization approach are then employed to train the proposed hybrid RNN-GPOD surrogate model for interval data. As a result, by adjusting the controllable steering parameters, corresponding interval bounds of the surface settlements field for further time steps of the mechanized tunneling process are quickly predicted.

Instead of a deterministic value as shown in the example in Sect. 7.3.2, the modulus of elasticity of the first soil layer E_1 is assumed to be quantified by an interval $\bar{E}_1 = [45; 52]$ MPa in this example. To construct a data set of interval settlements, which can be used for the generation of a surrogate model for an interval input-output data relationship, 100 interval analyses using the deterministic surrogate model together with Particle Swarm Optimization (PSO) approach are executed. Using the midpoint-radius representation for interval data, the interval data set is divided into two sub data sets for midpoints and radiuses. Subsequently, the midpoint and the radius of the settlements at the selected monitoring points are predicted by two individual deterministic RNNs. Regression values between the target values and the predicted values from the trained RNNs for midpoint and radius are $^{\mathrm{mid}}R = 0.9999$ and $^{\mathrm{rad}}R = 0.99761$, which shows a very good prediction capability of the two trained RNNs. For the reconstruction of the complete interval settlement field in the next time step, i.e. step 23, the GPOD method is employed to predict the midpoints of the interval settlements, whereas the NNMF is utilized for the prediction of the radiuses of the interval settlements to satisfy the non-negative constraint.

The computed interval settlement field is represented by its lower and upper bounds as shown in Fig. 7.19a. The proposed prediction strategy shows a good accuracy with respect to the reference solution in both the upper and lower bounds. The L_2 norm errors are 6.2% and 8.9% for the lower and upper bounds, respectively. The interval settlement field is predicted from the proposed approach in only one step with the computation time less than a second, whereas it requires around 1.5 hours to obtain the settlement bounds for all surface points of the field in case of using the optimization approach. The consider-

able reduction in computation time is thus the most important and attractive benefit of the proposed approach. In addition, with the largest absolute prediction error among all monitoring points is just 1.9 mm, the proposed surrogate model shows a promising capability for practical applications.

Another comparison is carried out for a reliability analysis based on the p-box approach. In this approach, the elastic modulus E_1 is treated as a normal distributed interval stochastic number with interval mean value $\mu_1 = [40; 50]$ MPa and deterministic standard deviation $\sigma = 5$ MPa. A reliability analysis is performed using an interval Monte Carlo simulation with 1,000 interval samples. For a comparison purpose, the input samples are used for both approaches: directly within the surrogate model for interval data (midpoint-radius representation) and within the traditional approach combining the PSO optimization approach and the deterministic surrogate model to predict the bounding distributions of the settlements.

The bounds of the cumulative distribution functions (p-box) of the settlement at one representative monitoring point obtained by both approaches are shown in Fig. 7.19b. As compared to the classical optimization approach, the p-box of the settlements obtained by the new surrogate model shows an appropriate performance with relative L_2 norm errors of 5% and 3% for the lower and upper bounds of the cumulative distribution functions, respectively. It should be noted that a computation time of 12 hours is required to obtain the p-box with the optimization approach, while the necessary computation time is only 10 minutes employing the proposed interval surrogate model. The significant time reduction can lead to much more efficiency in case of performing reliability analyses for high dimensional outputs, where optimization runs would be required for obtaining the interval bounds of each output.

7.3.3.2   Real-Time Prediction with Fuzzy Data

In case of uncertainties quantified as fuzzy data, the hybrid surrogate model can also be used to predict time variant fuzzy settlement fields of a mechanized tunneling process. A simulation model for a tunnel section of 144m length constructed by a TBM is shown in Fig. 7.20a. In this example, the TBM is assumed to advance underpassing an existing railway system. Two rail tracks, which are embedded on a compacted ballast layer, are situated on the top ground surface. When the machine advances under the railway system, it is essential to minimize or to reduce the effects of the tunneling process on the existing surface infrastructure. Therefore, the simulation-based real-time surface settlement prediction and reliability analyses performed in this section can support the TBM driver to select appropriate steering parameters for the advancement of the TBM.

The elastic modulus of the top soil layer (the low terrace gravel) E_1 is considered as an uncertain parameter defined by a fuzzy number with 2 α-cuts, i.e. $\tilde{E}_1 = \langle 52, 60, 70, 75 \rangle$ MPa as shown in Fig. 7.20b. A set of 154 selected nodes from the FE mesh constitutes the investigated surface area. The respective settlement of these nodes are considered as outputs of the surrogate model. Inputs of the surrogate model are the two operational steering parameters, the grouting pressure GP and the face support pressure
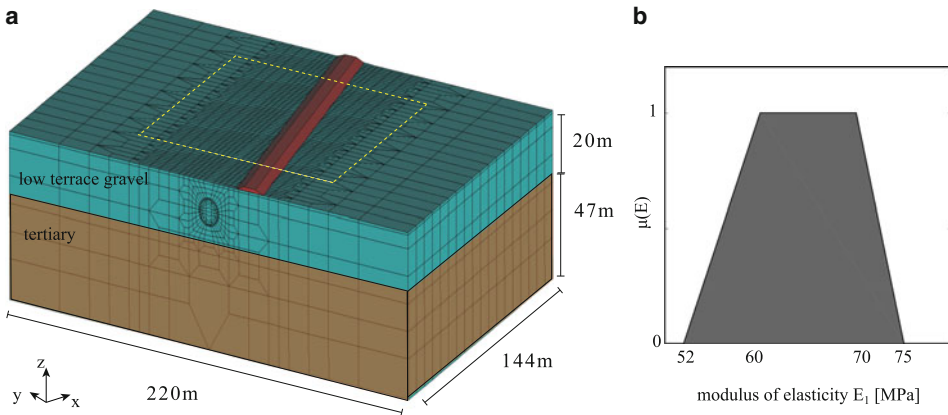
Fig. 7.20 Simulation model of a tunnel section with soil parameters as fuzzy data. **a** Model geometry, **b** modulus of elasticity E_1 as a fuzzy number with 2 α-cuts $\tilde{E}_1 = \langle 52, 60, 70, 75 \rangle$ MPa

SP. With the assumption that the TBM is currently preparing to underpass the railway, which corresponds to the 36th step of the excavation process, different steering scenarios can be investigated to support for the advancement. The surrogate model is thus employed to quickly predict the propagated fuzzy settlements of 154 surface nodes at time step 37 with changes of support and grouting pressures considering the uncertainty of the modulus of elasticity of the top soil layer E_1 under the type of fuzzy data. More details about the surrogate model generation, data split and model validation results can be found in [11].

Four surfaces representing for the predicted fuzzy settlements of the complete surface field at time step 37 are depicted in Fig. 7.21a. Considering settlement predictions from all validation cases, it can be seen that the surrogate model provides the prediction results with a good agreement with reference solutions from pre-performed fuzzy analyses. Specifically, the L_2 average relative errors are around 6% for the inner α-cut 2 and 7.5% for the outer α-cut 1. Similar to the conclusions from the example with interval data, the biggest advantage of the proposed approach is the considerable reduction in the computation time. For a fuzzy input number with two α-cuts, the resulting fuzzy settlement field is predicted in only 2 seconds instead of around 8 hours as compared to the fuzzy analysis with α-cut optimization approach, e.g. a fuzzy analysis for this example requires 8 hours for 154 outputs.

Using the proposed fuzzy surrogate model, reliability analyses are now performed considering polymorphic uncertain data with the p-box approach. In this approach, the grouting pressure $^{[n]}GP$ and the support pressures $^{[n]}SP$ are treated as stochastic processes assuming to follow a Gaussian distribution, while the modulus of elasticity E_1 is regarded as a fuzzy number with two α-cuts ($\tilde{E}_1 = \langle 52, 60, 70, 75 \rangle$ MPa)s. The distribution for both pressures is assumed to have the same standard deviations at the value of
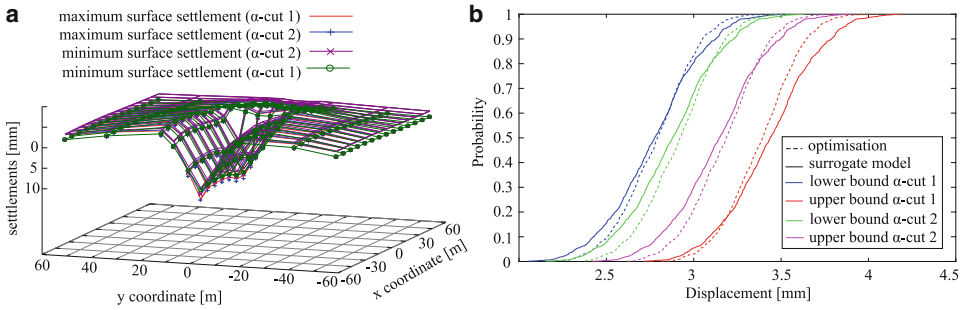
Fig. 7.21 Fuzzy settlement predictions. **a** Fuzzy settlement field with $\tilde{E}_1 = \langle 52, 60, 70, 75 \rangle$ MPa, **b** P-boxes of the settlement at a monitoring point with E_1 as a fuzzy number and $^{[n]}GP$, $^{[n]}SP$ stochastic processes following a Gaussian distribution with mean values of $^{[n]}GP = 170$ kN and $^{[n]}SP = 150$ kN

$\sigma = 30$ kN, whereas mean values of $^{[n]}GP$ and $^{[n]}SP$ are 170 kN and 150 kN, respectively. The reliability analysis is carried out using a Monte Carlo simulation with 1000 samples.

For an illustration, the potential behavior of a surface point lying ahead of the TBM, which belongs to the intersection line between tunnel alignment and the railway, is investigated based on the reliability results. Minimum and maximum cumulative distribution functions of the settlement of the investigated point at time step 37 are depicted as four curves in Fig. 7.21b. The curves corresponds to two nested intervals of $\tilde{E}$ obtained from classical optimization approach and the proposed surrogate model. As compared to the probability boxes obtained from optimization approach, the boxes produced by the surrogate model are in very good agreement with an average relative error of all curves around 2.5%. However, without the help of parallelization techniques, the computation time for an analysis considering a fuzzy input number with two α-cuts drops dramatically to just 20 minutes instead of around 1 day in case of using the optimization approach. For reliability analyses with high dimensional outputs, where a fuzzy analysis is required to produce the fuzzy bounds for each output, the proposed surrogate model approach leads to much more impressive efficiency. The method thus enables the possibility to quickly investigate the consequences of certain process parameters on the expected settlements in the subsequent excavation stages, which opens up an opportunity for real-time predictions to support the machine driver in steering the TBM.

7.4   Real-Time Prediction of Building Damage

To be able to provide adequate real-time predictions of building damage, a variety of models to assess building damage have been investigated. In particular, models based on the finite element method, which are replaced by artificial neural networks (ANN) for real-time applications have proven to be very useful.

The tunneling induced building damage risk can be quantified by comparing the maximum of the calculated structural strains with limiting strains, leading to different kinds of damages (micro-cracking or macro-cracking).

7.4.1 Models for Building Damage Assessment

The theory of sensitivity analysis is a key concept in damage prediction, and along with ANNs and specifically feed-forward neural networks form the basis of the research in this project as described in the following sections.

7.4.1.1 Finite Element Model of the Considered Building

To determine the structural damage of the building, the maximum strains are used regardless of their location within the building. Basically, the building is idealized by means of shell elements for the masonry and slab elements for the reinforced concrete (Fig. 7.22, left).

The behavior of concrete under compression as well as in tension is modeled via the Eurocode II [22] and the Model Code [32] (Fig. 7.22, top right). In compression f_c defines the maximum strength at the corresponding strain ε_c and $\varepsilon_{c,\lim}$ defines the maximum strain. The biaxial material behavior of masonry and concrete is modeled using the failure curves of Kupfer et al. [48, 81]. Under tension, the behavior of the reinforced concrete is
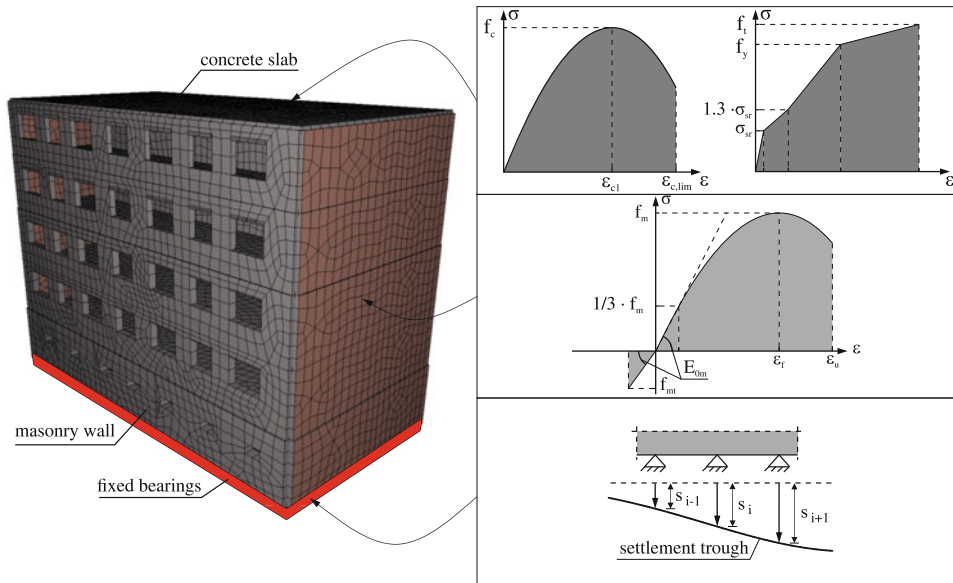
Fig. 7.22 Building model (left); material model in compression and tension for concrete (top right) and masonry (center right); consideration of settlements (bottom right) [13]

assumed to be uncracked up to the stress σ_{sr}. This is followed by cracking, in which the concrete contributes up to a stress of approximately $1.3\sigma_{sr}$. Beyond this point, only the reinforcement bears loads up to the stress f_y. If f_y is exceeded, yielding occurs until the ultimate stress f_t is reached.

An isotropic damage model is used to account for the nonlinear material behavior of masonry. This model is parabolic in compression and linear under tension (Fig. 7.22, center right). The maximum compression strength f_m and the corresponding strain ε_f as well as the failure strain ε_u change for various masonry types. An overview of different masonry types can be found in [42]. The tensile behavior of masonry is assumed to be linear-elastic up to the tensile strength f_{mt} and can be described by Hooke's law. The gradient for the tensile strength can be estimated using the elastic modulus under compression E_{0m} [4]. Due to the brittle character of masonry, usually no tensile softening is applied [37]. Numerous recalculations have shown that the model is capable of predicting the load-bearing behavior in good agreement with experiments [71].

The support type at the footing depends on the settlements determined beforehand. In case the settlements were estimated using simple analytical models, i.e. when no soil-structure interaction (SSI) is considered for the settlement prediction, the bearing should be idealized using nonlinear springs [3, 52]. These springs consider the calculated settlement as an initial gap and provide a realistic representation of the soil [71]. To estimate the spring stiffness of the soil, for example, Pasternak's model [60] can be used.

In the case the settlements were estimated via numerical models–taking an existing SSI into account–the supports should be idealized with fixed bearings (Figure 7.22, bottom right). In this case, the settlements s_i act as constrained variables on the building by displacing the supports. Also, the use of springs would result in a further load distribution in the building, thus causing lower strains.

Altogether, the model defines 21 independent parameters in Table 7.2; 12 capture the geometry, 8 the material properties and one the loading. Due to variable window sizes in the facade the variation of widths and heights are documented in rows 5 and 6 instead of the true dimensions. Moreover the table introduces abbreviations and summarizes sources and belonging distribution functions for all parameters. Characteristic intervals or distribution properties are documented, too. Additionally, the material model accounts for the Young's moduli of concrete and brickwork. Both are modeled fully correlated to the material's compressive strength and thus excluded from the list.

7.4.1.2 Fundamentals of Sensitivity Analysis

By means of sensitivity analysis (SA) the impact of input parameters' variance on the total variance of the result can be highlighted. It often serves to eliminate irrelevant scattering input from complex models beforehand and improves the efficiency of computation. This global approach accounts for variation in all input parameters at once and thus capture potential parameter interaction, too. Another advantage is model independence. Elementary effects might be applied to arbitrary models. By contrast, alternative approaches as regression analysis or sigma normalized derivatives work with linear models only [68]. While

Table 7.2 Stochastic characteristics of input parameters

	parameter		distribution function	source
facade				
geom.	height of the facade (m)	H	$\mathcal{U}(14.48, 14.52)$	[23]
	width of the facade (m)	B	$\mathcal{U}(20.076, 20.124)$	
	height of the foundation (m)	H_{FU}	$\mathcal{U}(0.69, 0.71)$	
	width of the foundation (m)	B_{FU}	$\mathcal{U}(0.49, 0.51)$	
	variation of windows' height (m)	H_F	$\mathcal{U}(-0.012, 0.012)$	
	variation of windows' widths (m)	B_F	$\mathcal{U}(-0.012, 0.012)$	
	concrete cover (m)	c_{nom}	$\mathcal{N}(0.05, 0.01^2)$	[42]
	bending reinforcement (cm^2/m)	A_{sl}	$\mathcal{U}(0, 55.4)$	chosen
	shear reinforcement (cm^2/m)	A_{ql}	$\mathcal{U}(0, 10)$	chosen
mat.	compressive strength of masonry (N/mm^2)	f_m	$\mathcal{LN}(8.1, 1.62^2)$	[42]
	tensile strength of masonry (N/mm^2)	f_{mt}	$\mathcal{LN}(0.51, 0.178^2)$	
	compressive strength of concrete (N/mm^2)	f_c	$\mathcal{LN}(20, 5^2)$	[65, 72]
	yield limit of steel (N/mm^2)	f_y	$\mathcal{N}(400, 24^2)$	[72, 74]
	Young's modulus of steel (N/mm^2)	E_s	$\mathcal{N}(210000, 6300^2)$	[72, 76]
	load (kN/m)	g	$\mathcal{U}(18, 26.4)$	chosen
soil/tunnel				
geom.	coverage (m)	c	$\mathcal{U}(10.9, 11.1)$	[8]
	outer diameter of the tunnel (m)	D	$\mathcal{U}(9.49, 9.51)$	[20]
	eccentricity (m)	e	$\mathcal{U}(-0.1, 0.1)$	[8]
mat.	rigid modulus of the soil (MN/m^2)	E_B	$\mathcal{LN}(85, 37.5^2)$	[27]
	Poisson's ratio (–)	ν	$\mathcal{U}(0.25, 0.35)$	[71]
	dimensionless soil parameter (–)	K	$\mathcal{U}(0.25, 0.5)$	[33]

elementary effects require less simulation to estimate sensitivities of computationally intensive models, but deliver qualitative results only. Sobol' indices evaluate the relative impact of the input's variance on the output's one quantitatively [10, 73]. A comparison between the elementary effects and the sobol indices was performed in [57].

7.4.1.3 Basics of the Elementary Effects Method

The method of elementary effects [53] is based on successive variation of the input and quantifies the impact on the result. Basically a model Y with k independent input parameters $X_i, i = 1, \ldots, k$ is considered. The input is normalized and spans a k-dimensional unit hypercube Ω which is discretized into a p-level grid. Discretization determines the step size $\Delta = p/(2p - 2)$ in which each parameter is varied in random order [68]. Variation of each parameter delivers a trajectory that might be imagined as a virtual diagonal between start and endpoint. For in total r trajectories the elementary effect EE_i is

$$EE_i = \frac{Y(X_1, \ldots, X_i + \Delta, \ldots, X_k) - Y(X_1, \ldots, X_i, \ldots, X_k)}{\Delta}. \tag{7.25}$$

Next, the sensitivity measures are obtained from Eq. 7.26 to Eq. 7.28. The mean μ and the absolute mean μ^* reflect a parameter's mean impact, while the absolute one excludes potential misinterpretation due to signs [9]. The variance σ^2 covers nonlinear effects and interaction to other parameters, so we have

$$\mu_i = \frac{1}{r} \sum_{j=1}^{r} EE_i^j, \tag{7.26}$$

$$\sigma_i^2 = \frac{1}{r-1} \sum_{j=1}^{r} \left(EE_i^j - \mu_i \right)^2, \tag{7.27}$$

$$\mu_i^* = \frac{1}{r} \sum_{j=1}^{r} |EE_i^j|. \tag{7.28}$$

Eq. 7.29 describes the procedure to generate randomly distributed parameters in associated limits. Therein, $\mathbf{J}_{k+1,k}$ and $\mathbf{J}_{k+1,1}$ denote a matrix and a vector of ones, respectively. The input to generate trajectories is summarized in the vector $\mathbf{x}^*$. Its entries are picked from the interval $[0, 1/(p-1), 2/(p-1), \ldots, 1 - \Delta]$ by chance. $\mathbf{B}$ symbolizes a lower triangular matrix of ones. The diagonal matrix $\mathbf{D}^*$ is the identity matrix having random signs $(+, -)$ with equal probability of occurrence. The matrix $\mathbf{P}^*$ permutes the order in which the parameters are augmented by Δ. Thus, the sample matrix $\mathbf{B}^*$ can be calculated as

$$\mathbf{B}^* = \left(\mathbf{J}_{k+1,1} \cdot \mathbf{x}^* + (\Delta/2) \left[(2\mathbf{B}_{k+1,k} - \mathbf{J}_{k+1,k})\mathbf{D}_{k,k}^* + \mathbf{J}_{k+1,k} \right] \right) \mathbf{P}_{k,k}^*. \tag{7.29}$$

Eq. 7.29 can be extended to grouped input, too. Frequently, several input parameters are grouped when suspected irrelevant. The initial procedure to get the elementary effect according to Eq. 7.25 by subtracting a functional value at X from the functional value at $X + \Delta$ cannot be applied to grouped parameters, since they would be altered in different directions. Thus, [9] recommends to use the absolute mean μ_i^* instead. Doing so, it immediately becomes impossible to identify nonlinear relationships or interactions among input parameters. However, investigations in [68] prove the differences between μ_i^* and σ_i negligible and nevertheless document sufficiently precise statements. Just the sample matrix $\mathbf{B}^*$ must be adjusted to a grouped one (index gr) according to Eq. 7.30 to get the elementary effects. Therein $\mathbf{G}$ is a group matrix with k rows and g columns. Similarly g counts the number of groups. If an input parameter X_i belongs to a group j the element $G_{i,j}$ of the group matrix is 1 and 0 otherwise. If $g = k$ each parameter has its own group and thus sampling delivers the same results as the original approach according to Eq. 7.29. We have

$$\mathbf{B}_{\mathbf{gr}}^* = \mathbf{J}_{g+1,1} \cdot \mathbf{x}^* + (\Delta/2) \left[\left(2\mathbf{B}_{g+1,g} \left(\mathbf{G}_{k,g} \mathbf{P}_{g,g}^* \right)^T - \mathbf{J}_{g+1,k} \right) \mathbf{D}_{k,k}^* + \mathbf{J}_{g+1,k} \right]. \tag{7.30}$$

In case of unlimited distribution functions, as it is with the Gaussian distribution, the tails must be truncated. The $\pm\infty$ unit space is mapped onto the new limits by means of Eq. 7.31. Here, $\mathbf{B}^*$ might be put in according to Eq. 7.29 or Eq. 7.30, respectively. The upper quantiles Q_u and the lower quantiles Q_l can be arbitrarily chosen. Most frequently the 0.5% and 99.5% quantiles are picked. Subsequent evaluation of the cumulative density function $F^{-1}(x)$ delivers appropriate values for $\mathbf{B}^*_{\text{new}}$,

$$\mathbf{B}^*_{\text{new}} = F^{-1} \cdot \mathbf{B}^* \cdot [Q_u - Q_l] + Q_l. \tag{7.31}$$

7.4.1.4 Surrogate Models

To gain reliable variance-based sensitivities a great number ($n > 10^4$) of finite element simulations is necessary [68]. In risk analysis, the number of simulations required equals the inverse probability of occurrence of the limit state of interest [6]. Evaluation of such a number of simulation is time demanding. Thus, surrogate models to approximate the interesting model response (e.g. maximum strains induced by settlements) are beneficial. Here, artificial neural networks (ANN) were used. The basis for the ANN is the input data. These are generated by means of the Latin-Hypercube Sampling.

7.4.1.5 Brief Overview on Feed-Forward Neural Networks

In the existing problem of structural damage only the final condition with maximum cracks is simulated and time-dependent crack growth as a result of different settlement states is not investigated. Therefore, feed-forward neural networks (FFNN) provide sufficiently accurate approximations.

Figure 7.23 shows the structure of the used three-layer FFNN with $k = 4$ input parameter x_k, $k = 1\ldots4$. The hidden layer has 20 neurons and the output layer 1 neuron. Each neuron has also a bias neuron b to achieve better approximations [38]. The output is the maximum strain ε_{max} that occurs in the building. In principle, a FFNN can be used to map several response parameter such as displacements or strains according to the applied loads. The procedure to create the network is basically the same, only the number of neurons in the output layer increase.

Fig. 7.23 Structure of the employed FFNN for the damage prediction [13]
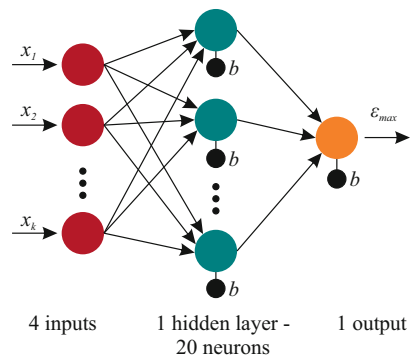
The input for the h-th neuron v_h in the hidden layer is determined by the addition of the bias neuron b_h and the sum of the product of the k-th input value x_k with the corresponding weights w_{hk} (Eq. 7.32). Therefore,

$$v_h = \varphi^1 \left(\sum_{k=1}^{4} x_k \cdot w_{hk} + b_h \right), \quad \text{with} \quad \begin{array}{l} k = 1, 2, \ldots, 4 \\ h = 1, 2, \ldots, 20. \end{array} \tag{7.32}$$

In Eq. 7.32, the tangent hyperbolic activation function φ^1 is used. Compared to the recurrent neural network (RNN) signal processing (see Eq. 7.8), the FFNN has no time delayed context signals. The FFNN output $\varepsilon_{\max}$,

$$\varepsilon_{\max} = \varphi^2 \left(\sum_{h=1}^{10} v_h \cdot w_{\varepsilon h} + b_\varepsilon \right), \tag{7.33}$$

is computed by using the linear activation function.

The unknown variables, the weights w_{hk}, $w_{\varepsilon h}$ and the bias neurons b_h, b_o are determined on the basis of the available data during the training using optimization algorithms by minimizing the quadratic error to the exact solution. Basically, a large number of algorithms can be used to determine the weights. A detailed overview is given in [21]. Analogously to the RNN, the Levenberg-Marquardt algorithm is used here.

7.4.2   Application

Damage assessment of buildings is usually based on the category of damage, see e.g. [31, 54, 80]. In this section, the tunneling induced building damage risk is quantified by comparing the maximum of the calculated structural strains with limiting strains, which– in the case of brittle materials such as concrete or masonry–lead to either no damage, micro-cracking or macro-cracking [51].

Table 7.3 shows a common assignment of limiting tensile strains to corresponding categories of damage. While strains in category 0 lead to no damage, strains in categories 1–2 usually only cause aesthetic or optical damage, strains in category 3 impair structures' serviceability, whereas strains in categories 4–5 even affect the structures' ultimate load-bearing capacity [7].

**Table 7.3** Limiting tensile strains of masonry and related categories of damage

category of damage	degree of severity	limiting tensile strain (%)
0	negligible	< 0.01
1	very slight	0.01–0.05
2	slight	0.05–0.075
3	moderate	0.075–0.15
4	severe	0.15–0.30
5	very severe	≥ 0.3

7.4.2.1 Sensitivity Analysis

In a first step, irrelevant parameters with no impact on the variation of the result are iden-
tified by the method of elementary effects. For this, the elementary effects of grouped
parameters are contrasted to those of the $k = 21$ single parameters. Grouped are the
two reinforcement parameters A_s and the remaining 10 geometry parameters G listed
in Table 7.2. Grouping leads to a reduced number of input parameters $g = 11$. Computa-
tion utilizes $r = 4$ trajectories. Thus, in the grouped case only $r(g + 1) = 48$ instead of
$r(k + 1) = 88$ finite element simulations are necessary. If a parameter is relevant or not
is decided based upon comparison to a threshold value of 5%. The threshold follows from
Eq. 7.34 regarding the absolute mean of the elementary effects μ^*. In case of not uni-
formly distributed parameters the limits are chosen equal to 0.0135% quantiles to grant
meaningful sensitivities not prone to false prognosis due to too small limits,

$$E_i = \frac{\mu_i^*}{\sum_{i=1}^{n} \mu_i^*} \quad \text{for} \quad i = 1, \dots, n. \tag{7.34}$$

Grouped and ungrouped results are qualitatively equivalent (Fig. 7.24). For instance,
the impact of the geometry input turns out negligible for both. Thus, in the following
only 6 relevant material parameters remain to set-up a surrogate model. Three of them
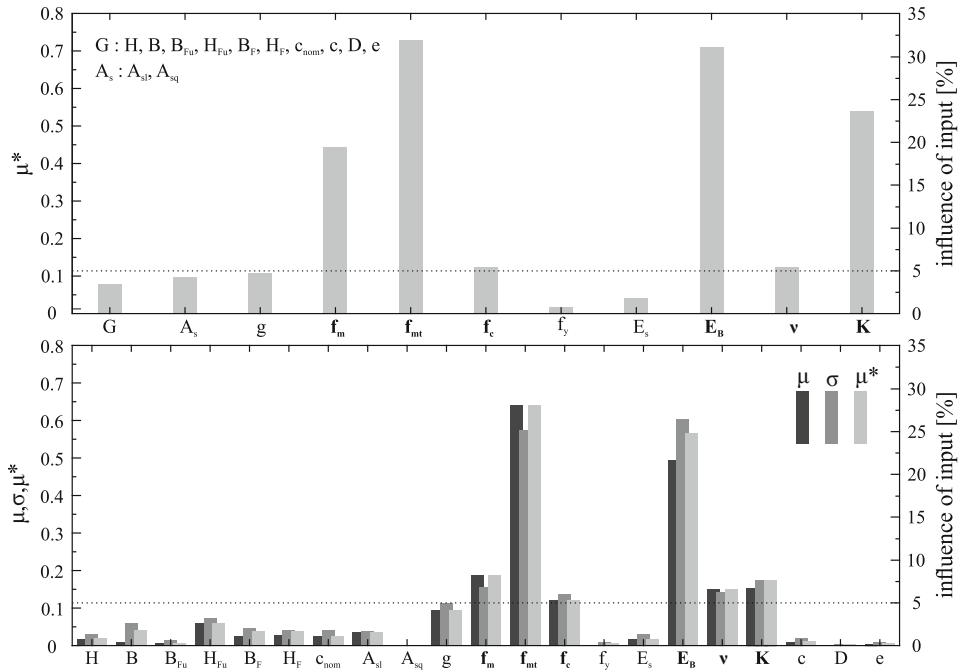

Fig. 7.24 Elementary effects of the nonlinear FE-simulation for 11 (upper) and 21 input parameters
(lower) [56]

determine the material properties of the facade (compressive strength of concrete (f_c) and brickwork (f_m) as well as tensile strength of concrete (f_{mt})), while the rest reflects the settlements s of the soil.

7.4.2.2   Feed-Forward Neural Network

The total data basis for the feed-forward neural networks (FFNNs) are 500 FE calculations. The data is divided into two sets of 250 values each and are obtained using Latin Hypercube Sampling. The same values of the material parameters are used for both sets. The settlement values are derived from the interval analysis, taking into account interval-related soil parameters (Sect. 7.3.3.1). One set is determined via the lower and the other set via the upper limit values of the settlements. Consequently, the difference between these two sets are the settlement values. The 10 settlement values from the soil model are not used for the generation of inputs of the FFNN. Only the difference between the settlement at the building's edge and in the center is used. As a result, the size of inputs of the FFNN (**SB**) is reduced to 4 inputs instead of 10. The reason for this is that the parameter domain can be reduced and less data is needed to generate a suitable FFNN. Based on the 250 data points of the log-normal distributions, about 96 % of all possible values of the material parameters are considered in the FFNN.

To approximate the maximum strains in the building, a neural network architecture with one hidden layer and 20 neurons was used. Tests with this architecture showed the smallest deviation between the training and test data and achieved a coefficient of determination of $R^2 \approx 0.90$ (Fig. 7.25). The data was randomly split into three sub-sets for training, validation and testing with the ratios of 70 %, 15 % and 15 %, respectively.
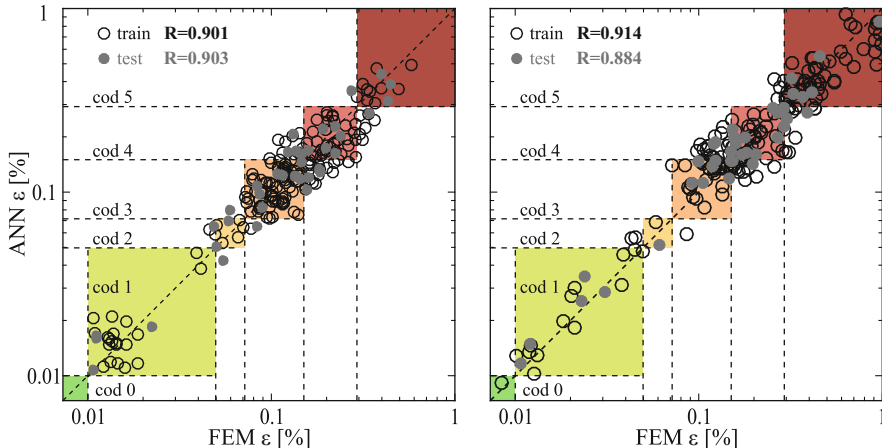
Fig. 7.25 Regression plots of the FFNN; training and testing results for the upper bound settlement values (left) and training and testing results for the lower bound settlements values (right) [13]

Contrary to expectations, more results are located in the higher categories of damage when using the lower bound of the settlements than compared to the upper bound of the settlements (cf. Fig. 7.25). This can be explained by the fact that the absolute settlement value is not significant, but rather the settlement difference between the building's edge and the center.

7.5 Real-Time TBM Steering Support Minimising Building Damage Risks

During the tunneling process, the surface settlement can lead to damage in adjacent buildings through subsidence and tilts of these structures and therefore should be controlled during the tunneling process. In this context, it is essential to predict the surface deformations and then to evaluate the associated risk of damage to existing buildings in the construction phase. To answer the question, if the damage of buildings can be assessed in real-time during the tunnel construction process and if TBM process parameters can be changed to reduce the damage risk, the hybrid RNN-GPOD surrogate model is coupled with a feed-forward neural network (FFNN), which is capable to quickly deliver the strain state in adjacent buildings. More details about the employed FFNN is given in Sect. 7.4.2.2. The model-based TBM steering supported strategy is depicted in Fig. 7.26.

7.5.1 TBM Steering Support with Deterministic Data

The TBM steering support scheme using the expected level of damage of buildings located in the vicinity of the tunnel axis as a target for the adjustment of the operational parameters of the machine is illustrated by means of a synthetic example, characterised by a tunnel section constructed by a TBM in an urban area. The tunnel is assumed to directly
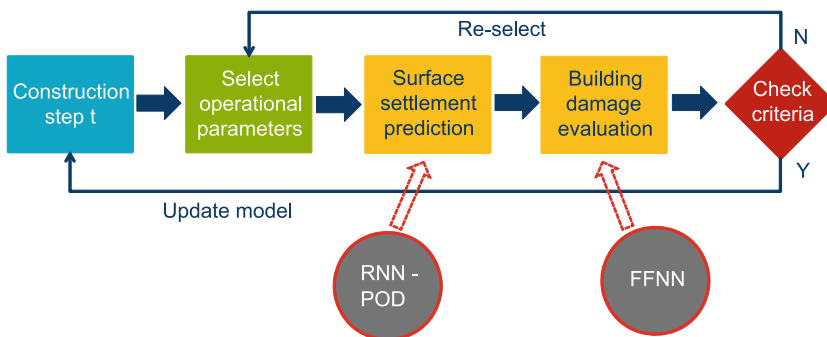
Fig. 7.26 Concept of TBM steering support using the predicted level of building damage as objective for adjusting the operational parameters
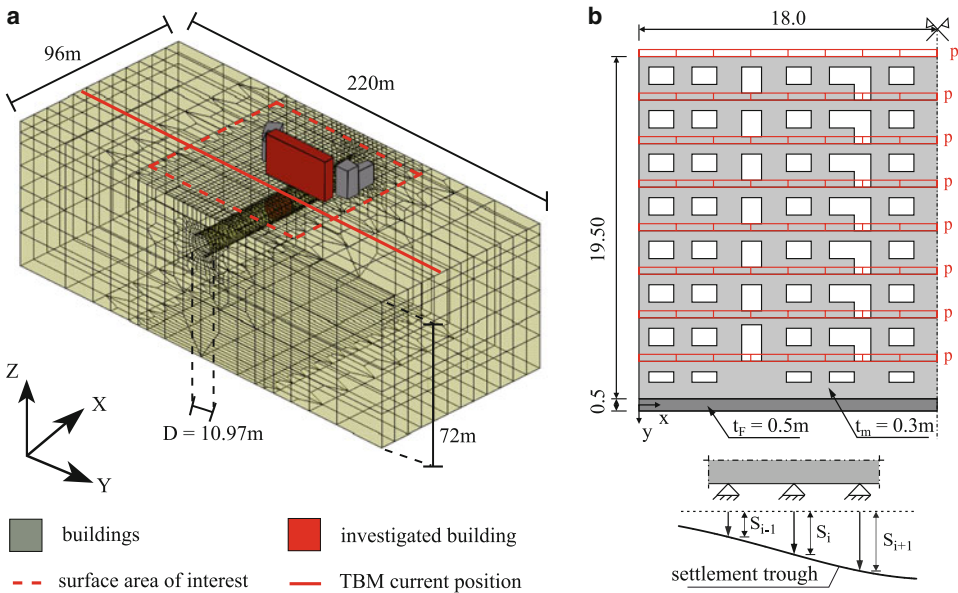
Fig. 7.27 FE simulation model of a tunnel section underpassing a building. **a** Tunnel model geometry, **b** Facade model of the investigated building

underpass a multi-storey building (highlighted in red in Fig. 7.27a). For the analysis of the expected damage caused by tunneling induced settlements, a structural model of a facade is established, see Fig. 7.27b. For the classification of the building in terms of category of damage (cod), the maximum expected strain at the facade is used as the damage indicator. With the fact that damages can emerge in the building due to the tunneling induced settlements during construction, a surface settlement prediction and an assessment of the damage category for the building are performed in real-time to support the TBM driver selecting appropriate steering parameters to minimise or to reduce the influence of the tunneling process to the building. The two-dimensional damage analysis is performed based on the facade model together with the boundary conditions obtained from settlement prediction at the building baseline.

It is assumed that, the TBM has proceeded to the 25th step of the tunneling process and is directly below the investigated building as shown in Fig. 7.28a. A constant level of 120 kPa at the tunnel axis is adopted for the face support pressure from time step 1 to time step 25. Three possible pressure scenarios are investigated to drive the TBM underneath the building. In the first scenario (scenario (1)), the face support pressure is kept unchanged in the next 12 meters, i.e., 6 excavation steps, as illustrated by the black line in Fig. 7.28b. The corresponding settlement trough along the baseline of the building, denoted as black line in Fig. 7.28c, and the corresponding building damage category are quickly predicted and classified by the RNN-GPOD surrogate model and the FFNN
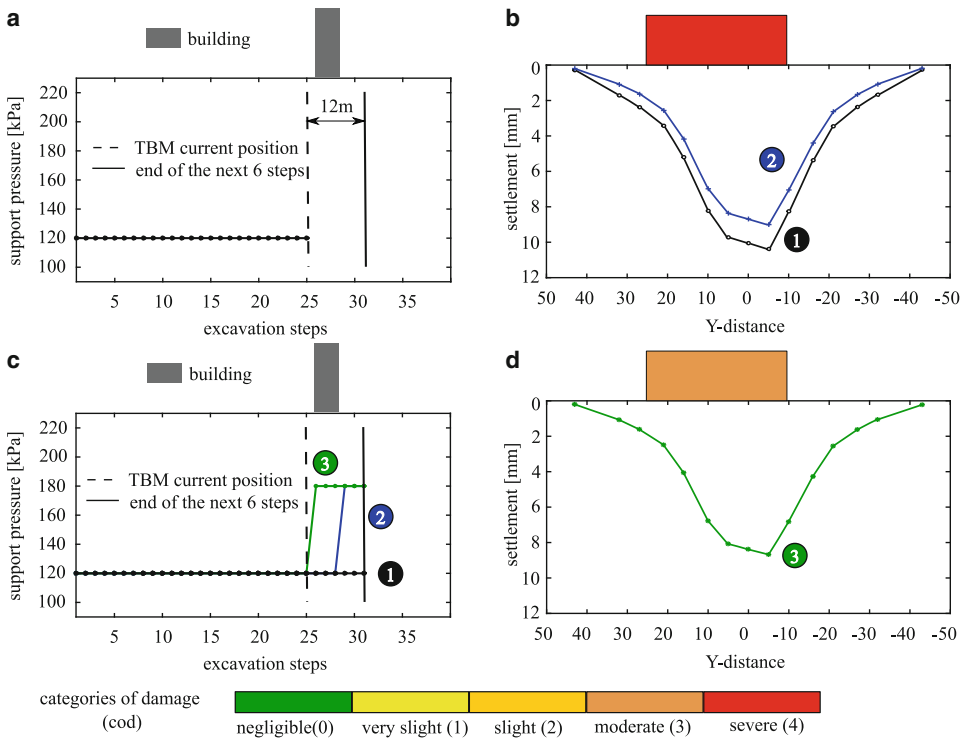
Fig. 7.28 TBM steering support example with deterministic data. **a** Face support pressure history, **b** three investigated pressure scenarios, **c** resulting settlement trough and building damage category for the scenarios (1) and (2), **d** resulting settlement trough and building damage category for scenario (3)

surrogate model, respectively. Five building damage categories representing the damage degrees from negligible damage, very small damage, slight damage, moderate damage and severe damage are depicted in different colors as shown in Fig. 7.28. The criteria for damage groups classification is given in details in Table 7.3. For scenario (1) with an unchanged face support pressure, the building is predicted to have severe damage and thus classified into the fifth category. With this provided information before underpassing the building, the TBM driver has enough time to adjust the face pressure in order to avoid the critical situation. Alternative scenarios for applying the face pressure when advancing underneath the building can be investigated in real-time, using the proposed approach.

Blue and green colors as illustrated in Fig. 7.28 represent two alternative pressure scenarios (2) and (3). In case of increasing the face pressure immediately at the next excavation step (time step 26) to the value of 180 kPa (scenario (3) – green line), the ground settlements along the facade are predicted to be reduced significantly. The category of damage of the building can thus be reduced from "severe damage" to "moderate damage," see Fig. 7.28d. According to scenario (2), where the face support pressure is not immedi-

Table 7.4 Different scenarios of increasing the face pressure and resulting category of damage of the investigated building

applied value [kPa]	applied in step			
	20	23	26	29
120 (no pressure increase)	4	4	4	4
150 (increase to medium pressure)	3	3	4	4
180 (increase to high pressure)	3	3	3	4

ately increased, but only increased when the TBM is already below the building at time step 29, the surface settlement and the resulting maximum strain in the building are reduced, but the building is still estimated to suffer "severe damage" as shown in Fig. 7.28c. Table 7.4 summarizes several possible scenarios, including different steps to increase the pressure and the applied values of the face pressure. It can be seen, that it is necessary to increase the face pressure latest at step 26 to 180 kPa or already at step 23 to 150 kPa in order to reach damage category 3. In addition, although the face support pressure might be increased earlier, e.g. already in step 20, the damage category still remains. This example exemplifies the potential of the proposed concept to consider the building damage risk categorisation as a steering target in order to select appropriate TBM operational parameters in real-time during the construction process in mechanized tunneling.
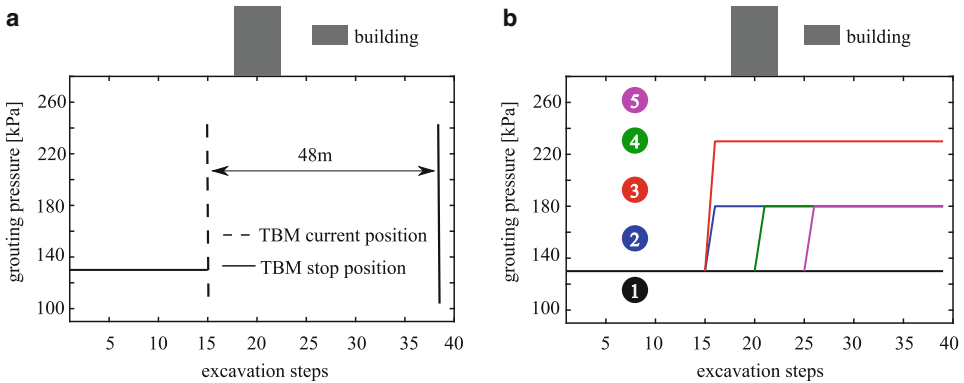
7.5.2 TBM Steering Support with Polymorphic Uncertainty

Polymorphic uncertainties from soil parameters and building characteristics under different types of uncertain data are also taken into account within the prediction. In this context, soil parameters are generally quantified by intervals, building parameters can be represented as random variables. The interval settlement field propagated from interval soil parameters can be predicted using the hybrid surrogate model with interval data. Stochastic analyses for building damage assessment are then carried out considering the interval settlements as boundary conditions. The proposed prediction scheme is applied on a synthetics example, which adopts the risk assessment of building damages as a criterion to drive the TBM.

A tunnel section, which is assumed to be constructed by a TBM in an urban area, is investigated. Figure 7.29a depicts the symmetrical view of the simulated tunnel section. Among a number of existing buildings on the ground surface, the tunnel is excavated directly below a multi-storey building, which is considered as a critical infrastructure. The selected building is modeled with details as illustrated in Fig. 7.29b. In this example, the uncertainty of the elasticity modulus of the second soil layer (the sandy clay), which the tunnel is excavated through, is given as an interval $E_2 = [30; 55]$ MPa. The prediction accuracy of all surrogate models involved in the prediction of interval settlements are in general very high with values of the coefficient of determination R^2 larger than 0.9. For more detailed explanations and descriptions of the surrogate model generation, validation and comparison, readers are referred to [13].
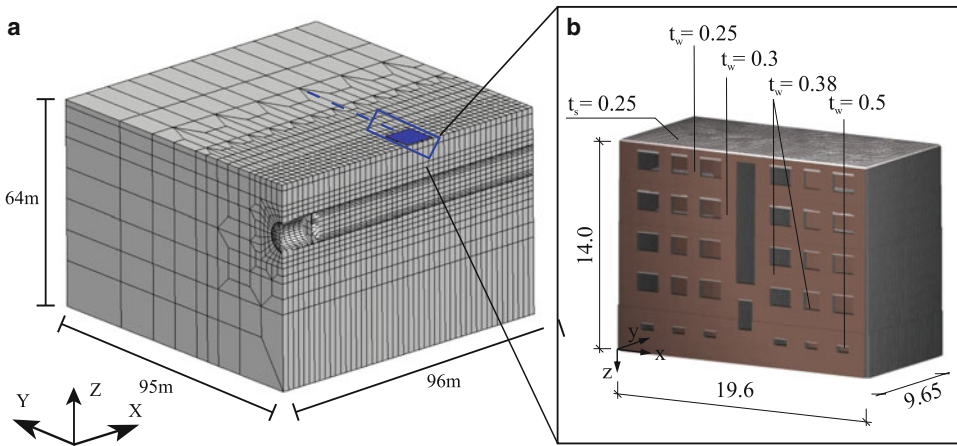
Fig. 7.29 Simulation model of a tunnel section with polymorphic uncertain soil parameters and building properties. **a** Model geometry, **b** detailed 3D model of the investigated building

Fig. 7.30 TBM steering support example with polymorphic uncertainty. **a** grouting pressure history, **b** five investigated pressure scenarios

With the aim to support the selection of appropriate steering parameters during the TBM advance in real-time, a practical oriented investigation is carried out using the established surrogate models to demonstrate the applicability of the proposed scheme. The current TBM position is assumed to be directly in front of the investigated building, corresponding to time step 15. The history of the applied grouting pressure at the tunnel axis is recorded from time step 1 to time step 15 with a value of 130 kPa, as shown in Fig. 7.30a. For the investigation of different advancement scenarios underneath the multi-storey building, five possible applied pressure scenarios from time step 16 are of particular interest, see Fig. 7.30b. The first scenario, i.e., scenario (1), considers the situation with no modifications in the selection of grouting pressure in the next 24 excavation steps (i.e., 48 m). The grouting pressure values are planned to be increased to 180 and 230 kPa start-
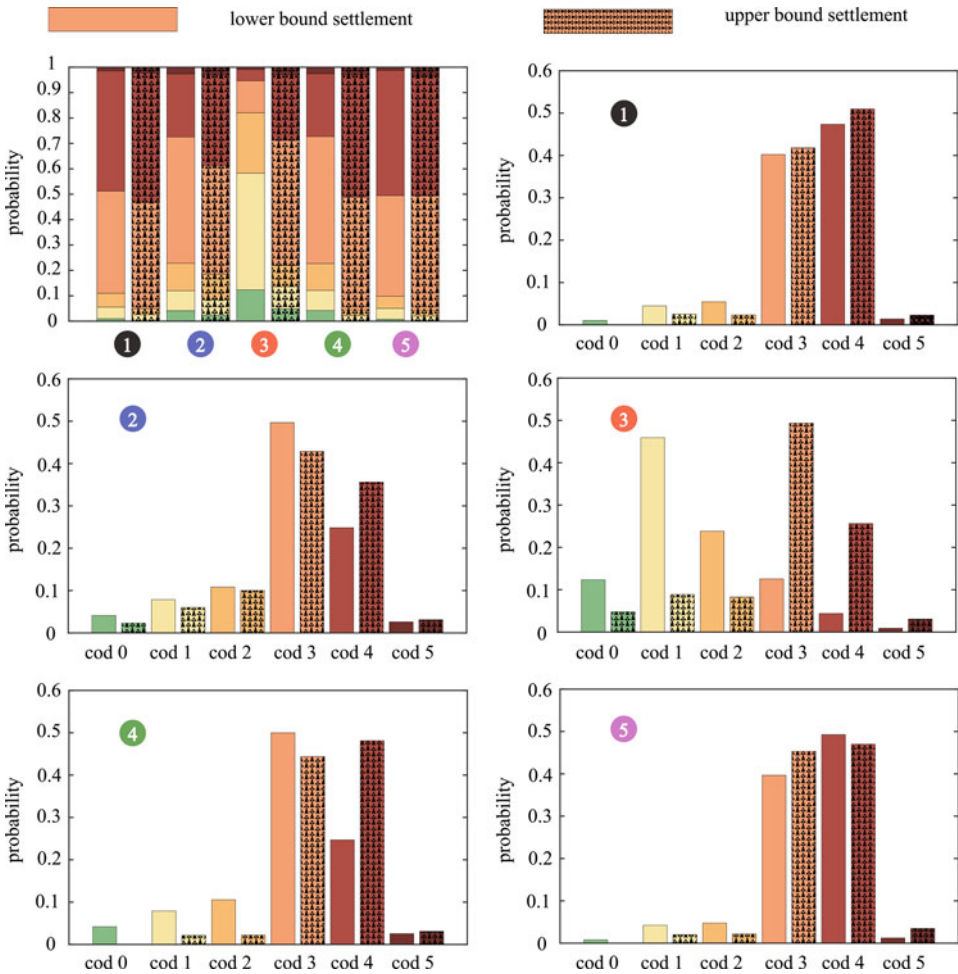
Fig. 7.31 Individual and accumulated building damage probabilities of the five investigated steering scenarios

ing from step 16, respectively, in scenarios (2) and (3). Scenarios (4) and (5) account for the increase in pressure values up to 180 kPa from step 21 or later from step 26. In each steering scenario, two bounds, i.e. the lower bound and the upper bound of the settlement trough involving the building, is given from the settlement surrogate model. As a result, the maximum strain in the building is computed for each bound considering building parameters as random variables. More specifically, following Table. 7.3, the probabilities of the maximum strain can be transformed into probabilities of categories of damages (cod) from 0 to 5 as visualized in Fig. 7.31. The interval bounds of the imprecise classification probabilities (relative frequencies and accumulated probabilities) can also be seen in Fig. 7.31. Considering the five steering scenarios, the evaluation of changing the grouting

pressure when excavating the tunnel in the vicinity of the building can follow two possible strategies. Either different magnitudes of the applied pressure (scenarios (1), (2) and (3)) or different steps starting applying the pressure with the same magnitude (scenarios (1), (2), (4) and (5)) are compared.

Regarding the first evaluation, in case of remaining the pressure according to scenario (1), the building would mainly belong to cod 3 and cod 4 with the respective frequencies of 0.4027 and 0.4736 due to induced damage resulting from the lower settlement bound. With the upper settlement bound, the corresponding relative frequencies in this scenario are 0.4181 and 0.5098, respectively. If the grouting pressure is increased to 180 kPa as planned in scenario (2), the relative frequencies (0.4027 and 0.4181 for lower and upper settlement bounds) can slightly be reversed to 0.4969 and 0.4287 for cod 3, however the categories with the highest relative frequencies are still the same (cod 3 and cod 4). In this scenario, i.e. scenario (2), a certain reduction in the relative frequencies can be observed for cod 4, which changes from 0.4736 to 0.2486 for the lower settlement bound and from 0.5098 to 0.3562 for the upper settlement bound. A very slight damage (cod 1) to the building can be achieved with the lower bound of the settlement trough, when the pressure is further increased to a value of 230 kPa in scenario (3). The relative frequency of cod 1 in this scenario is 0.4593, which is also the highest frequency, while the other frequencies, i.e., for cod 0, cod 2, cod 3, cod 4 and cod 5, are 0.1234, 0.2383, 0.1257, 0.0441, and 0.0092, respectively. Although the lower settlement bound in scenario (3) leads to a re-distribution of relative frequencies of cod as compared to those in scenario (2), the relative frequencies of the damage categories resulting from the upper settlement bound, are just slightly changed as compared to the corresponding distribution in scenario (2).

In the second evaluation, effects of the time steps, where the pressure is applied, are investigated. In case of comparing scenario (1) and scenario (5), in which the pressure remains constant and the pressure adjustment is performed too late respectively, it can be seen that the probabilities are almost the same. If increasing the pressure from time step 16 , i.e. before entering the building area, following scenario (2) and from time step 21, i.e. later when the TBM being under the building, as in scenario (4), differences between the resulting relative frequencies with respect to the lower settlement bound are negligible. However, the difference in the time step of applying pressure leads to a redistribution in the relative frequencies associated to the upper bound of settlement. More specifically, if scenario (4) is applied, the probability for the damages on the investigated building related to the cod 2 with slight damages is 0.0221 instead of 0.1004 in case of applying scenario (2). Similarly, an earlier steering parameter adjustments (scenario 2) can reduce the relative frequency of the severe damage category (cod 4) to 0.3562 from a higher number of 0.4813, when steering parameters are adjusted late as planned in steering scenario (4).

The accumulated imprecise probabilities of building damage categories resulting from the polymorphic uncertain information of the inputs are presented in the stacked plot in Fig. 7.31. For instance, considering driving the TBM with a target of limiting the building damages in cod 3 (moderate damages), the probabilities of satisfying this condition are in a narrow interval [0.467; 0.512] in case of applying steering scenario (1). Higher mag-

nitudes and wider interval probabilities [0.613; 0.725] and [0.488,0.727] can be obtained when the pressure is adjusted earlier and with higher values, e.g. in steering scenarios (2) and (4), respectively. Adopting a high pressure as drafted in scenario (3) would even lead to an assured interval of probabilities of [0.713; 0.947] for the moderate damage group (cod 3). With the presented building damage analyses, it can be concluded that the magnitude of the applied grouting pressure (the first evaluation) and the time step of adjusting the grouting pressure (the second evaluation) are essential for the control of damage risk of existing buildings in mechanized tunneling.

7.6 Application Development for TBM Steering Support

With the aim to support the steering of TBMs during mechanized tunneling, a real-time simulation application is developed based on the algorithms presented in Sects. 7.3 and 7.4. The application SMART (**S**imulation-and-**M**onitoring-based **A**ssistant for **R**eal-time steering in mechanized **T**unneling) is capable of providing a very quick prediction of the system response with user defined inputs. The goal of SMART is to predict the system response, i.e. the surface settlements and the risks of damages on existing buildings (and/or tunnel lining forces etc.), resulting from the TBM-soil interaction in real-time as the response to changes of operational parameters, such as the face pressure or the grouting pressure.

The main flowchart of the application is based on the online algorithm described in Sect. 7.3. Depending on the type of input data, the system responses are predicted under different type: deterministic, interval or fuzzy data. Additionally, reliability analyses can be performed in real-time to support the selection of TBM operational parameters. Thus, the application SMART provides an assistant tool for decision-making in regards to adjusting the support and grouting pressures during the tunnel construction.

Figure 7.32 presents a screenshot of the application SMART with the latest features related to building damage assessment in real-time. All historic data of the tunnel drive are stored. Given the current position of the TBM, by moving the sliders on the right hand side to change the values of operational parameters for the forthcoming advancement step, the software computes and visualizes the corresponding surface settlement field, considering the soil structure interactions, and the expected category of building damage evaluation within just one second.

The application is implemented in MATLAB and is executed on a standard computer. The MATLAB Compiler is used to create a standalone version of SMART which targets to run SMART application on machines without installing the complete MATLAB software. The standalone version together with a free MATLAB Component Runtime library are easily distributed to the end users for demonstration purposes. Before running SMART, the user needs to install the provided Runtime library which is compatible with the operation system of the target machine. SMART application has been successfully installed and tested on Windows, Linux and Mac OS. Since the installation and execution of SMART
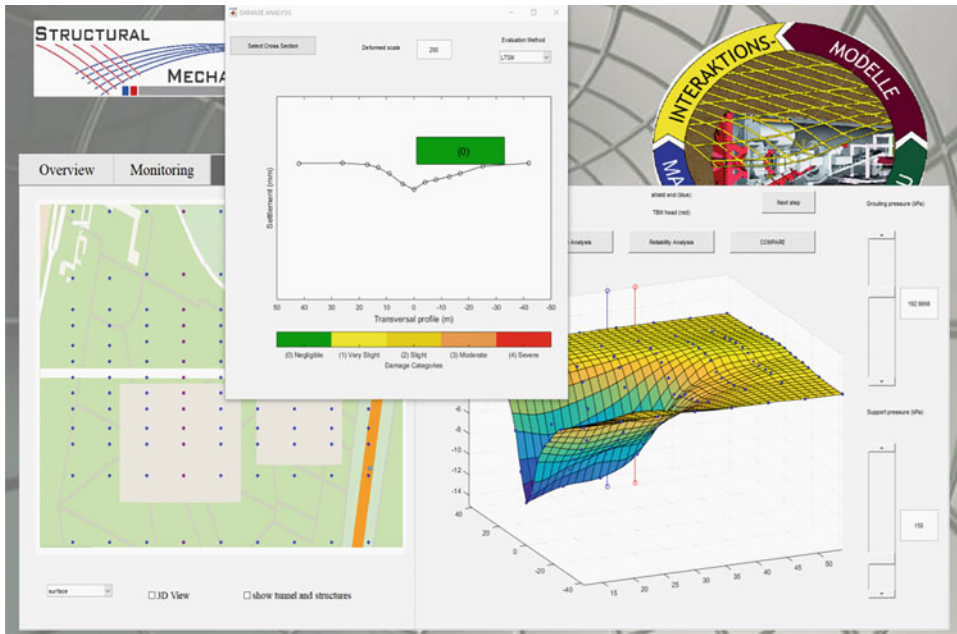
Fig. 7.32 Screenshot of the software application SMART for real-time building damage assessment during tunnel construction

does not require any expensive hardware, the application can run in almost every standard laptop or even tablet.

References

1. S. AbouRizk and D. W. Halpin. "Statistical Properties of Construction Duration Data". In: *Journal of Construction Engineering and Management* 118.3 (1992), pp. 525–544. ISSN: 0733-9364.
2. H. Adra. "Realtime predictive and prescriptive analytics with real-time data and simulation". In: *Proceedings of the 2016 Winter Simulation Conference, USA* (2016).
3. A. Alsahly et al. "Soil-Building Interaction and Risk Assessment of Existing Structures During Mechanized Tunneling". In: *Challenges and Innovations in Geomechanics*. Ed. by M. Barla, A. Di Donna, and D. Sterpi. Cham: Springer International Publishing, 2021, pp. 139–147. ISBN: 978-3-030-64518-2. https://doi.org/10.1007/978-3-030-64518-2_17.
4. H.-P. Backes. "Zugfestigkeit von Mauerwerk und Verformungsverhalten unter Zugbeanspruchung". In: *Mauerwerk Kalender*. 1985, pp. 719–725.
5. M. Al-Bataineh, S. AbouRizk, and H. Parkis. "Using Simulation to Plan Tunnel Construction". In: *Journal of Construction Engineering and Management* 139.5 (2013), pp. 564–571. ISSN: 0733-9364. https://doi.org/10.1061/(ASCE)CO.1943-7862.0000626.
6. T. Bedford and R. Cooke. *Probabilistic risk analysis: Foundations and methods*. 3. printing. Cambridge: Cambridge Univ. Press, 2004. ISBN: 9780521773201.

7. M. D. Boscardin and E. J. Cording. "Building Response to Excavation–Induced Settlement". In: *Journal of Geotechnical Engineering* 115.1 (1989), pp. 1–21. ISSN: 0733-9410. https://doi.org/10.1061/(ASCE)0733-9410(1989)115:1(1).

8. Bundesanstalt für Straßenwesen ZTV-ING. *Zusätzliche Technische Vertragsbedingungen und Richtlinien für Ingenieurbauten, Teil 5 'Tunnelbau'*. 2014.

9. F. Campolongo, J. Cariboni, and A. Saltelli. "An effective screening design for sensitivity analysis of large models". In: *Environmental modelling & software* 22.10 (2007), pp. 1509–1518. ISSN: 1364-8152. https://doi.org/10.1016/j.envsoft.2006.10.004.

10. F. Campolongo, A. Saltelli, and J. Cariboni. "From screening to quantitative sensitivity analysis. A unified approach". In: *Computer Physics Communications* 182.4 (2011), pp. 978–988. ISSN: 0010-4655. https://doi.org/10.1016/j.cpc.2010.12.039.

11. B. Cao, S. Freitag, and G. Meschke. "A fuzzy surrogate modelling approach for real-time settlement predictions in mechanised tunnelling". In: *International Journal of Reliability and Safety* 12.1/2 (2018), pp. 187–217. https://doi.org/10.1504/IJRS.2018.10013808.

12. B. Cao, S. Freitag, and G. Meschke. "A hybrid RNN-GPOD surrogate model for real-time settlement predictions in mechanised tunnelling". In: *Advanced Modeling and Simulation in Engineering Sciences* 3.5 (2016), pp. 1–22. https://doi.org/10.1186/s40323-016-0057-9.

13. B. Cao et al. "Real-time risk assessment of tunneling-induced building damage considering polymorphic uncertainty". In: *ASCE-ASME Journal of Risk and Uncertainty in Engineering Systems, Part A: Civil Engineering* 8.1 (2022), p. 04021069. https://doi.org/10.1061/AJRUA6.0001192.

14. A. Conrads. "Maintenance of cutting tools in mechanised tunnelling - Development of a process simulation model for the scheduling and evaluation of maintenance strategies". Dissertation. Bochum: Ruhr-Universität Bochum, 2019. https://doi.org/10.13154/294-7141.

15. A. Conrads et al. "Maintenance costs for cutting tools in soft ground gained by process simulation". In: *Proceedings of the WTC2019 ITA-AITES World Tunnel Congress, Naples, Italy, 3-9 May, 2019* (2019).

16. A. Conrads et al. "Prozesssimulation für die Leistungsermittlung und -planung beim maschinellen Tunnelbau". In: *Taschenbuch für den Tunnelbau*. Ed. by DGGT Deutsche Gesellschaft für Geotechnik e.V. Berlin: Ernst & Sohn, 2017, pp. 166–198.

17. A. Conrads et al. "Prozesssimulation zur Analyse von Wartungsstrategien im maschinellen Tunnelbau". In: *Simulation in Production and Logistics 2015*. 2015.

18. A. Conrads et al. "Assessing maintenance strategies for cutting tool replacements in mechanized tunneling using process simulation". In: *Journal of Simulation* 11.1 (2017), pp. 51–61. https://doi.org/10.1057/s41273-016-0046-5.

19. A. Conrads et al. "Robustness evaluation of cutting tool maintenance planning for soft ground tunneling projects". In: *Underground Space* 3.1 (2018), pp. 72–85. ISSN: 24679674. https://doi.org/10.1016/j.undsp.2018.01.005.

20. DAUB. *Empfehlung für den Entwurf, die Herstellung und den Einbau von Tübbingringen*. 2013. https://doi.org/10.1002/9783433603574.

21. H. Demuth, M. Beale, and M. Hagan. *Neural Network Toolbox 6: User's Guide*. 2008.

22. Deutsches Institut für Normung. *Eurocode 2: Design of concrete structures – Part 1-1: General rules and rules for buildings*. Jan. 2011.

23. Deutsches Institut für Normung. *Toleranzen im Hochbau - Bauwerke*. Apr. 2013.

24. R. Duhme et al. "TBM Performance Prediction by Process Simulation". In: *EURO:TUN 2013*. 2013.

25. R. Duhme. "Deterministic and simulation based planning approaches for advance and logistic processes in mechanized tunneling". Dissertation. Bochum: Ruhr-Universität Bochum, 2018.

26. J. Düllmann et al. "Practical TBM excavation data processing". In: *Tunnels and Tunnelling* (2014).

27. EAU. *Empfehlungen des Arbeitsausschusses Ufereinfassungen: Häfen und Wasserstraßen; 48 Tabellen*. 8. Aufl. Berlin: Ernst, 1990. ISBN: 978-3433012109.

28. Y. Ebrahimy et al. "Simphony Supply Chain Simulator: A simulation toolkit to model the supply chain of construction projects". In: *SIMULATION* 87.8 (2011), pp. 657–667. ISSN: 0037-5497. https://doi.org/10.1177/0037549710380992.

29. Y. Ebrahimy et al. "Simulation modeling and sensitivity analysis of a tunneling construction project's supply chain". In: *Engineering, Construction and Architectural Management* 18.5 (2011), pp. 462–480. ISSN: 0969-9988. https://doi.org/10.1108/09699981011074600.

30. R. Everson and L. Sirovich. "Karhunen-Loeve Procedure for Gappy Data". In: *Journal of the Optical Society of America A* 12.8 (1995), pp. 1657–1664.

31. V. Fargnoli, C. G. Gargano, and Boldini, D., Amorosi, A. "3D numerical modelling of soil-structure interaction during EPB tunnelling". In: *Géotechnique* 65.1 (2015), pp. 236–246. https://doi.org/10.1680/geot.14.P.091.

32. Fédération internationale du béton. *Model Code for Concrete Structures 2010: First complete draft*. Vol. 65. Bulletin / International Federation for Structural Concrete. Lausanne: International Federation for Structural Concrete, 2010. ISBN: 978-2-88394-095-6. https://doi.org/10.35789/fib.BULL.0055.

33. J. Fillibeck. "Oberflächensetzung bei Tunnelvortrieben im Lockergestein: Prognose, Messung und Beeinflussung". Habilitation. Munich: Technical University of Munich, 2012.

34. S. Freitag et al. "Hybrid surrogate modelling for mechanised tunnelling simulations with uncertain data". In: *International Journal of Reliability and Safety* 9.2/3 (2015), pp. 154–173. https://doi.org/10.1504/IJRS.2015.072717.

35. S. Freitag et al. "Recurrent neural networks and proper orthogonal decomposition with interval data for real-time predictions of mechanised tunnelling processes". In: *Computers and Structures* 207 (2018), pp. 258–273. https://doi.org/10.1016/j.compstruc.2017.03.020.

36. E. Gamma et al. *Design patterns: Elements of reusable object-oriented software*. Addison-Wesley professional computing series. Reading, Mass.: Addison-Wesley, 1995. ISBN: 0-201-63361-2.

37. C. Glock. "Traglast unbewehrter Beton- und Mauerwerkswände: Nicht-lineares Berechnungsmodell und konsistentes Bemessungskonzept für schlanke Wände unter Druckbeanspruchung". Dissertation. Darmstadt: Technical University of Darmstadt, 2004.

38. M. T. Hagan et al. *Neural network design*. 2nd. Wrocław: Amazon Fulfillment Poland Sp. z o.o, 2014. ISBN: 9780971732117.

39. D. Hajjar and S. M. AbouRizk. "Development of an Object Oriented Framework for the Simulation of Earth Moving Operations". In: *IEEE Trans. Knowledge and Data Engineering* (Jan. 1997), pp. 326–330. https://doi.org/10.1109/IIS.1997.645279.

40. R. Hardy. "Theory and Applications of the Multiquadric-biharmonic Method: 20 Years of Discovery 1968-1988". In: *Computers and Mathematics with Applications* 19.8/9 (1990), pp. 163–208. https://doi.org/10.1016/0898-1221(90)90272-L.

41. J. Holzhäuser, C. Mayer, and S. Hunt. *Erfahrungen bei Tunnelvortrieben im Lockergestein und im Fels bei sehr hohem Grundwasserdruck*. Darmstadt, Mar. 2007.

42. JCSS. *Probabilistic Model Code*. 2001.

43. A. Jodehl et al. "Simulationsgestützter Ansatz zur Verbesserung der Leistungsprognose maschineller Tunnelvortriebe mithilfe baubegleitender Prozessdaten". In: *Simulation in Produktion und Logistik 2021*. Ed. by J. Franke and P. Schuderer. Göttingen: Cuvillier Verlag, 2021. ISBN: 9783736974791.

44. H. Kim and H. Park. "Nonnegative Matrix Factorization Based on Alternating Nonnegativity Constrained Least Squares and Active Set Method". In: *SIAM Journal on Matrix Analysis and Applications* 30.2 (2008), pp. 713–730. https://doi.org/10.1137/07069239X.

45. M. Köhler, U. Maidl, and L. Martak. "Abrasiveness and tool wear in shield tunnelling in soil". In: *Geomechanics and Tunnelling* 4 (2011), pp. 36–54. https://doi.org/10.1002/geot.201100002.

46. M. König et al. "Prozesssimulation von maschinellen Tunnelvortrieben Verfügbarkeitsanalysen der Leistungsprozesse unter Berücksichtigung von Stillständen". In: *Bauingenieur* 89.11 (2014), pp. 467–477.

47. F. Köppl, K. Thuro, and M. Thewes. "Suggestion of an empirical prognosis model for cutting tool wear of Hydroshield TBM". In: *Tunnelling and Underground Space Technology* 49.287-294 (2015). ISSN: 08867798. https://doi.org/10.1016/j.tust.2015.04.017.

48. H. B. Kupfer, Gerstle K.H., and H. Rüsch. "Behaviour of concrete under biaxial stresses". In: *Journal of the engineering mechanics division* 99.4 (1973), pp. 853–866. https://doi.org/10.1061/JMCEA3.0001789.

49. J. Küpferle et al. "The RUB Tunneling Device – A newly developed test method to analyze and determine the wear of excavation tools in soils". In: *Tunnelling and Underground Space Technology* 59 (2016), pp. 1–6. ISSN: 08867798. https://doi.org/10.1016/j.tust.2016.06.006.

50. L. Li et al. "Virtual Prototype of the Tunnel Boring Machine and Movement Simulation in DIVISION MOCKUP2000i2". In: *Proceedings of the 6th CIRP-Sponsored International Conference on Digital Enterprise Technology*. Ed. by G. Q. Huang, K. L. Mak, and P. G. Maropoulos. Vol. 66. Advances in Intelligent and Soft Computing. Berlin, Heidelberg: Springer-Verlag Berlin Heidelberg, 2010, pp. 525–532. ISBN: 978-3-642-10429-9. DOI: 10.1007/978-3-642-10430-5{_}40.

51. P. Mark and B. Schnütgen. "Limits of Elastic Material Behaviour of Concrete". In: *Beton- und Stahlbetonbau* 96.5 (2001), pp. 373–378. ISSN: 00059900. https://doi.org/10.1002/best.200100400.

52. A. Marwan et al. "Soil-Building Interaction in Mechanized Tunneling: A Comparison of Modeling and Approaches". In: *Engineering and Innovation Meet Archaeology, Architecture and Art*. Neapel, 2019, pp. 2653–2662. https://doi.org/10.1201/9781003031635-11.

53. M. D. Morris. "Factorial Sampling Plans for Preliminary Computational Experiments". In: *Technometrics* 33 (1991), pp. 161–174. https://doi.org/10.1080/00401706.1991.10484804.

54. M. Neuhausen et al. "Window detection in facade images for risk assessment in tunneling". In: *Visualization in Engineering* 6.1 (2018), pp. 1–16. ISSN: 2213-7459. https://doi.org/10.1186/s40327-018-0062-9.

55. J. Ninic and G. Meschke. "Model update and real-time steering of tunnel boring machines using simulation-based meta models". In: *Tunnelling and Underground Space Technology* 45 (2015), pp. 138–152. https://doi.org/10.1016/j.tust.2014.09.013.

56. M. Obel, M. A. Ahrens, and P. Mark. "Metamodel-Based Risk Analysis of Structural Damages due to Tunneling-Induced Settlements". In: *ASCE-ASME Journal of Risk and Uncertainty in Engineering Systems, Part A: Civil Engineering* 88.12 (2020), pp. 61–71. https://doi.org/10.1061/AJRUA6.0001092.

57. M. Obel and P. Mark. "Minimization of Compensation Measures Based on a Probabilistic Risk Simulation Concept". In: *ITA-AITES World Tunnel Congress (WTC2020)* (2020), pp. 103–108.

58. *Object Management Group (2012). OMG Systems Modeling Language (OMG SysML™) – Version 1.3. Object Management Group*. 2012.

59. P. Paatero and U. Tapper. "Positive matrix factorization: A non-negative factor model with optimal utilization of error estimates of data values". In: *Environmetrics* 5.2 (1994), pp. 111–126. https://doi.org/10.1002/env.3170050203.

60. P. L. Pasternak. "Grundlagen einer neuen Methode der Berechnung von Fundamentplatten mittels zwei Bettungskoeffizienten". In: *Gosudarstvennoe Izdatelstvo Literaturi po Stroitelstvu I Arkhitekture*. 1954, pp. 7–20.

61. R. J. Plinninger and U. Restner. "Abrasiveness Testing, Quo Vadis? – A Commented Overview of Abrasiveness Testing Methods". In: *Geomechanik und Tunnelbau* 1.1 (2008), pp. 61–70. ISSN: 18657362. https://doi.org/10.1002/geot.200800007.

62. M. Rabe, S. Spieckermann, and S. Wenzel. *Verifikation und Validierung für die Simulation in Produktion und Logistik: Vorgehensmodelle und Techniken*. Springer-Verlag Berlin Heidelberg, 2008. ISBN: 978-3-540-35281-5.

63. T. Rahm. "Simulation-based evaluation of disturbances of production and logistic processes in mechanized tunneling operations". Dissertation. Bochum: Ruhr-Universität Bochum, 2017.

64. T. Rahm et al. "Evaluation of Disturbances in Mechanized Tunneling Using Process Simulation". In: *Computer-Aided Civil and Infrastructure Engineering* 31.3 (2015), pp. 176–192. ISSN: 10939687. https://doi.org/10.1111/mice.12143.

65. H. Rüsch, R. Sell, and R. Rackwitz. *Statistische Analyse der Betonfestigkeit*. Vol. Heft 206. Deutscher Ausschuss für Stahlbeton. 1969.

66. J. Y. Ruwanpura and S. T. Ariaratnam. "Simulation modeling techniques for underground infrastructure construction processes". In: *Tunnelling and Underground Space Technology* 22.5-6 (2007), pp. 553–567. ISSN: 08867798. https://doi.org/10.1016/j.tust.2007.05.001.

67. Y. Salloum et al. "From Forecasting to real-time process controlling with continuous simulation model updates". In: *Proceedings of the 37th International CIB W78 Conference* (2020). https://doi.org/10.46421/2706-6568.37.2020.paper032.

68. A. Saltelli et al. *Global Sensitivity Analysis: The Primer*. Wiley, 2008. ISBN: 978-0-470-05997-5. https://doi.org/10.1002/9780470725184.

69. M. Scheffer et al. "Jobsite logistic simulation in mechanized tunneling". In: *Winter Simulation Conference (WSC), 2014*. Ed. by A. Tolk. Piscataway, NJ: IEEE, 2014, pp. 1843–1854. ISBN: 978-1-4799-7486-3. https://doi.org/10.1109/WSC.2014.7020032.

70. M. Scheffer et al. "Simulation-Based Analysis of Integrated Production and Jobsite Logistics in Mechanized Tunneling". In: *Journal of Computing in Civil Engineering* 30.5 (2016), p. C4016002. ISSN: 0887-3801. https://doi.org/10.1061/(ASCE)CP.1943-5487.0000584.

71. S. Schindler. "Monitoringbasierte strukturmechanische Schadensanalyse von Bauwerken beim Tunnelbau". Dissertation. Bochum: Ruhr University Bochum, 2014.

72. J. Schnell et al. *Sachstandsbericht Bauen im Bestand – Teil I: Mechanische Kennwerte historischer Betone, Betonstähle und Spannstähle für die Nachrechnung von bestehenden Bauwerken: Deutscher Ausschuss für Stahlbeton Heft 619*. Vol. Heft 616. Deutscher Ausschuss für Stahlbeton. 2016. ISBN: 978-3-410-65280-9.

73. V. Schwieger. "Nicht-lineare Sensitivitätsanalyse gezeigt an Beispielen zu bewegten Objekten: Zugl.: Stuttgart, Univ., Habil.-Schr., 2004". Dissertation. Munich: Technical University of Munich, 2005.

74. M. Six. *Sicherheitskonzept für nichtlineare Traglastverfahren im Betonbau: Deutscher Ausschuss für Stahlbeton Heft 534*. Vol. Heft 534. Deutscher Ausschuss für Stahlbeton. 2003. ISBN: 3-410-65734-7. https://doi.org/10.2366/61633374.

75. L. Song and N. N. Eldin. "Adaptive real-time tracking and simulation of heavy construction operations for look-ahead scheduling". In: *Automation in Construction* 27 (2012), pp. 32–39. ISSN: 09265805. https://doi.org/10.1016/j.autcon.2012.05.007.

76. A. Strauss, K. Bergmeister, and S. März. "Reliability assessment of ecocentric loaded columns". In: *Beton- und Stahlbetonbau* 102.4 (2007), pp. 223–230. ISSN: 00059900. https://doi.org/10.1002/best.200700537.

77. G. Taguchi, D. Clausing, and L. Watanabe Tung. "System of experimental design: Engineering methods to optimize quality and minimize cost". In: *Quality Resources* (1991).

78. *The AnyLogic Company (2022). AnyLogic 8.7.10 University*. 2022.

79. L. Wu and S. M. AbouRizk. "Numerical-based approach for updating simulation input in real-time". In: *Journal of Computing in Civil Engineering* 35.2 (2021). ISSN: 0887-3801. https://doi.org/10.1061/(ASCE)CP.1943-5487.0000948.

80. W. N. Yiu, H. J. Burd, and C. M. Martin. "Finite-element modelling for the assessment of tunnel-induced damage to a masonry building". In: *Géotechnique* 67.9 (2017), pp. 1–15. https://doi.org/10.1680/jgeot.sip17.P.249.

81. O. C. Zienkiewicz, R. L. Taylor, and J. Z. Zhu. *The finite element method: its basis and fundamentals*. Elsevier, 2005. https://doi.org/10.1016/C2009-0-24909-9.